Provenance of Southern Cape Rivers: Links to Hydroclimate and Early Humans

Thesis submitted for the degree of Doctor of Philosophy

November 2023

Ellie Pryor

School of Earth and Environmental Sciences

Cardiff University

The present day view from Blombos Cave, South Africa. 70,000 years ago this view would have been remarkably unfamiliar, the shoreline would have been further out exposing a vast green plain, where early humans lived and foraged.

Summary

Blombos Cave coastal archaeological site in the southern Cape of South Africa exhibits artifacts from the Late Middle Stone Age (LMSA); 100–50 ka BP - a time interval when human cognition and technological advances underwent rapid development. Two such time intervals which represent important phases in the cognitive and cultural development of Anatomically Modern Humans (AMHs) are the Still Bay (72-71 ka) (SB) and Howiesons Poort (64–59 ka) (HP) industries. Research suggests environmental and climatic conditions in the region facilitated the cultural evolution of AMHs. This hypothesis is particularly relevant for coastal sites located at the dynamic land-ocean interface, which are influenced by the Greater Agulhas Current system in the Southwest Indian Ocean. However, our understanding of climatic conditions in the region is limited by the fact only a few continuous high-resolution archives exist. Terrestrial sediments from river channels of drainage basins between Durban and Cape Town using geochemical ($^{87}Sr/^{86}Sr$ and εNd), clay mineralogy and lithogenic grain size data define two key sediment source regions: the Karoo and Cape Supergroup from South Africa. These new radiogenic isotope endmembers within the <2 µm grain size fraction were generated by unmixing of river sediment radiogenic isotope signatures. The εNd represents source rock age whereas variability in the $^{87}Sr/^{86}Sr$ is due to the degree of chemical weathering. These endmembers are used as a provenance tracer for reconstructions related to palaeoclimate variability utilising marine sediment cores offshore of the Southeast African coastline from modern and Last Glacial Maximum (LGM) dated samples. Major rivers drain into this region, these are the local South African sediments, as well as the Limpopo and Zambezi rivers. Through targeting the <2 µm, 2-10 µm and 10-63 µm size fractions of lithogenic sediments, this study reveals that during the LGM, there was an increase in Zambezi river input in the <2 µm fraction, transported downstream in the Agulhas Current mixed with local South African river sediment and a deep water signal in the 10-63 µm fraction, coming from the South Atlantic Ocean. The temporal variability is further explored in sediment core, MD20-3591 (36°43.707 S; 22°9.151 E, water depth 2464 m) as this site records marine hydrographic (Agulhas Current) and terrestrial hydrological variability. This study finds that during MIS 5, low latitude summer insolation changes, paced by orbital precession, explain the long-term climate variability in εNd whereas abrupt climate oscillations in the northern high latitudes are the main driver for the observed millennial-scale wet phases, inferred from $^{87}Sr/^{86}Sr$ isotope ratios. During MIS 4, the effect of sea level on the local sediment signal is apparent, with a coarser sediment input during this glacial interval. This study further explores the variability of regional hydroclimate in

relation to the early human archaeological record during the MSA interval.

Acknowledgements

What a journey this PhD has been! “If we knew what it was we were doing, it would not be called research, would it?” – Albert Einstein.

Firstly, I offer so much thanks to my primary supervisor Ian Hall for being so supportive and always making time to have regular meetings despite juggling a very busy schedule and the global pandemic as Head of School. You have given me lots of opportunities to improve my writing, my thoughts and the science in this thesis - thank you for all the encouragement helping me strive to be a better scientist! There have definitely been laughs along the way, one ‘key’ memory involves a hire car and a set of keys locked in said car’s boot at the hire car pick-up, after a 3-week cruise and a 1-week river sampling campaign in South Africa! I would also like to thank Margit Simon for guiding me and being an incredible role model in science. Thank you for letting me crash your date night with HC after the first Bergen trip Airbnb disaster, for the dinner parties and for the mushroom hunting trips. More thanks goes to Jeroen van der Lubbe for being another brilliant supervisor. You have taught me so much and for that I am so very grateful. Thank you for showing me the grain size ways in Amsterdam, answering all my questions, for taking me to Brodies for the first time when you were in Cardiff, helping on the South African rivers fieldwork and for cooking me an authentic Dutch meal in Amsterdam. I thank Morten Andersen for helping me with all the hours of lab work in CELTIC, for teaching me Sr and Nd chemistry, measuring lots of my samples and for being so friendly. I enjoyed our train meetings when we were both travelling home after a day in Cardiff!

More thanks go to everyone involved in my lab work in some way, shape or form. I would not have managed to obtain the data used in this thesis if it were not for you. Firstly, thank you Lindsey for being sooooo helpful in the lab, caring and a friendly face - especially during the pandemic when nobody was around! Sandra, you really are an isotopes superstar- thank you for measuring all my stable isotope samples. Edward, thank you for being a super lab manager, it has not been an easy ride for you, and I really appreciate how you always made time for me and all my samples… I also extend my thanks to the rest of the CELTIC lab team, notably, Marc, Sophie, Caps, Katie F and Katie Fr, Carmen, Laura and Hong. What an experience… I wouldn’t have wanted to have ridden this rollercoaster with a better bunch. Another lab where I spent lots of time was the palaeo lab (0.71), thank you to Aidan and Debs for making the long days sieving even more fun! Many thanks to Tony for your guidance with XRD work.

My PhD was funded by the NERC GW4+ DTP. I am grateful for the support and

the opportunities to travel to South Africa, Bergen and Amsterdam, to meet other PhD students and to expand my skillset through different courses. Many thanks to Sara Berrow and Emmi Palk for being so supportive. I thank Claire Waelbroeck, Natalia Vazquez-Riveiros and the rest of the ACCLIMATE 2 team for an amazing time in the Southern Ocean. Thank you for making my 22nd birthday so memorable, it is crazy to think we retrieved the marine sediment core I have used in this thesis on my birthday. What a super day!

Special thanks goes to my friends within the PhD world. I must thank the following people in particular for being such important parts of my PhD journey; Erin, Ana, Sara, Sophie, James K, Joel, Sarah Du Plessis, Charles, Danielle, Anya, Inge, Ben, Erin W and Nea. Many thanks to Erin, Ana and Nea for reading bits of this thesis, I really appreciate your encouragement. When I was in Bergen for all three visits, Karl thank you for being such a friendly face, organising trips and inviting me to social activities with other PhD candidates. A lot of fun as well as work was achieved when I was in Bergen, and I look back on all the trips to Bergen with such fond memories.

To the non-Earth and PhD friends, firstly thank you to the Granny Lyns, we shared an incredible year in Flat 10 Glan y Lyn, drinking tea, growing vegetables, baking bread, learning to knit and watching MAFS. Thank you for providing suitable distractions from PhD work, Sarah, Erin and Katherine. We really had the best time! Southampton housemates and Oceanography girls, thank you for the support from oceanography undergrad to the end of my PhD, I'm so proud of everything we have achieved and where everyone is now! It's amazing how we have all remained in touch with the ocean after all these years. To Anna my best friend and biggest cheerleader. To Katherine, for the trips and adventures through the years.

Many thanks to my dogs Whiskey and Pippa for all the cuddles along the way, for the fun walks and incessant ball throwing... Thanks to the untouchable things, the Netflix fire for making late working evenings a little more possible, the non-fiction books I have read during my PhD which take me away from the present, specifically books by Taylor Jenkins Reid (thank you Katie for the recommendation!). Greg James on BBC Radio 1, I believe I have listened to the breakfast show for 90% of my mornings since starting my PhD, it has given feasible distractions whilst working and made me laugh so much. Music is a big part of my life so through this thesis I reference certain songs which became prominent listening material whilst writing chapters, Ben Howard - I thank you for your intricate lyrics which take me to a peaceful utopia.

To the nature, green spaces, mountains, fresh air, and my new found appreciation for trail running and experiencing the outdoors in a different way. Life is now much better with a good pair of trail shoes and uneven terrain.

To my parents, for their support through life, school, cheering at me from the poolside edge (for many years…) and for all the amazing holidays we've been on together. To Dad, for igniting my love of geography by showing me the raised beaches, stacks, stumps and the 'all famous' recumbent fold at Godrevy, St Ives Bay (yes it must be mentioned!!). Thank you. To Mum, for being so strong, so loving, always being at the end of the phone for a chat and for supplying me with tea, cakeage and rescue remedy in times of need.

Kieran, this is as much your achievement as it is mine. You have been by my side for it all. Thank you for being so supportive and caring, and for making me laugh every day - "there's this peace that comes with knowing you have a person in the world who would do anything for you, that you would do anything for" - Taylor Jenkins Reid.

Contents

Summary iii

Acknowledgement v

List of Figures xiv

List of Tables xviii

1 Introduction 1

1.1 Early Humans . . . 2
1.1.1 The Coastal Zone of South Africa . . . 3
1.1.2 Blombos Cave and SapienCE context . . . 5
1.2 An overview of Climate Variability during the Late Pleistocene . . . 8
1.2.1 Millennial Scale Variability and Rapid Climate Changes . . . 11
1.3 Setting of South Africa . . . 14
1.3.1 Regional Atmospheric and Oceanic Circulation . . . 14
1.3.2 Climate Change in southern South Africa during the LMSA interval 17
1.4 Ocean Circulation . . . 19
1.4.1 Thermohaline Circulation . . . 19
1.4.1.1 North Atlantic Deep Water (NADW) . . . 19
1.4.1.2 Antarctic Bottom Water (AABW) . . . 20
1.4.2 Southern Ocean Circulation . . . 21
1.4.3 Agulhas Current: Past and Present . . . 23
1.4.3.1 Present Agulhas Current System . . . 23
1.4.3.1.1 Northern Agulhas Current . . . 25
1.4.3.1.2 Southern Agulhas Current . . . 26
1.4.4 Palaeoceanographic Reconstructions of the Agulhas Current System 27
1.5 Terrigenous Sediments . . . 29
1.5.1 Modern Sources of Sediment from South Africa . . . 30
1.5.1.1 South Africa Coastal Drainage Basins . . . 30
1.5.1.2 Zambezi and Limpopo Drainage Basins (upstream sediment sources) . . . 31
1.6 Major Themes and Thesis Structure . . . 34

1.7 Questions in this thesis . . . 36

2 Materials and Methods **37**

2.1 Site Settings . . . 38
2.1.1 Modern Oceanography at Site MD20-3591 . . . 40
2.1.2 Sedimentology . . . 40
2.2 Palaeoceanographic Proxies and Techniques . . . 42
2.2.1 Geochemical Proxies . . . 42
2.2.1.1 Environmental Signals in Terrigenous Sediment . . . 43
2.2.1.1.1 Radiogenic Isotopes Systematics . . . 43
2.2.1.1.1.1 Neodymium Isotopes For Provenance . . . 44
2.2.1.1.1.2 Strontium Isotope Compositions . . . 44
2.2.1.1.2 Clay Mineralogy . . . 44
2.2.1.1.3 Bulk Sediment Geochemistry . . . 46
2.2.1.2 Environment Signals in Biogenic Sediment . . . 46
2.2.1.2.1 Foraminifera: Time Machines . . . 46
2.2.1.2.2 Formaminiferal Stable Isotopes . . . 47
2.2.1.2.2.1 Oxygen Isotopes Ratios in Foraminifera . . . 47
2.2.1.2.2.2 Carbon Isotope Ratios in Foraminifera . . . 48
2.2.1.3 Grain Size Analysis . . . 49
2.2.1.3.1 Endmember Modelling . . . 50
2.2.1.3.2 Sortable Silt Mean Grain Size . . . 51
2.3 Analytical Methods . . . 51
2.3.1 Sediment Processing . . . 51
2.3.2 Grain Size Separation - A Case Study . . . 53
2.3.2.1 Experimental Set-Up . . . 53
2.3.2.1.1 Grain Density Parameter (ρ) . . . 54
2.3.2.1.2 The Angular Velocity Parameter (N) . . . 54
2.3.2.1.3 Sediment Material - Initial Sample Size . . . 55
2.3.2.2 Method . . . 55
2.3.2.2.1 Verification of the Centrifugation Set-Up . . . 55
2.3.2.2.2 Pre-treatment of Lithogenic Fraction . . . 55
2.3.2.2.3 Separation of Additional Grain Size Classes . . . 55
2.3.2.2.4 Grain Size Analysis . . . 55
2.3.2.3 Results . . . 56
2.3.2.3.1 Grain Size Isolation . . . 56
2.3.2.4 Discussion . . . 57
2.3.2.5 Recommended Method . . . 58
2.3.2.5.1 Updated Method . . . 58

2.3.3 Radiogenic Isotope Analysis . . . 60
2.3.4 Radiogenic Isotope Endmember Mixing . . . 61
2.3.5 Sediment Source Contribution Modelling . . . 62
2.3.6 Clay Mineralogy . . . 63
2.3.7 Grain Size Analysis . . . 63
2.3.7.1 Endmember Modelling Using Analysize . . . 63
2.3.7.2 Sortable Silt . . . 63
2.3.8 Stable Isotope Analysis of Foraminifera . . . 64
2.3.8.1 Procedure for Isotope Analysis . . . 64
2.3.9 Estimation for Carbonate Content . . . 64
2.3.10 Elemental Records (XRF Core Scanning) . . . 65
2.3.10.1 Calibration of XRF . . . 66
2.4 Statistical Analysis . . . 67
2.4.1 Principal Component Analysis . . . 67
2.4.2 Time Series Analysis . . . 67
2.5 Age - Depth Models . . . 68
2.5.1 Radiocarbon Dating . . . 68
2.5.2 Radiocarbon (^{14}C) - LR04 Age Model . . . 69
2.5.3 Speleothem Age Model: Adjustment to LR04 Age Model . . . 72

3 Rivers of South Africa: Investigating the Provenance of River Sediments Draining into the Southwest Indian Ocean 75
3.1 Introduction . . . 76
3.1.1 Geochemistry and Provenance Tools . . . 78
3.1.2 Research Objectives . . . 79
3.2 Climate and Fluvial Systems in Southern South Africa . . . 79
3.2.1 Modern Climate of South Africa . . . 79
3.2.2 Fluvial Systems of Africa . . . 79
3.2.3 Regional Geology . . . 82
3.3 Sampling and Analytical Methods . . . 84
3.3.1 Sample Selection . . . 84
3.3.2 Geochemistry - Pre-treatment . . . 85
3.3.3 Grain Size Analyses . . . 86
3.4 Results . . . 86
3.4.1 Mineralogy and Geochemistry . . . 86
3.4.1.1 <2 µm fraction . . . 86
3.4.1.2 2 - 32 µm (fine silt) fraction . . . 87
3.4.2 Grain Size . . . 88
3.4.3 Clay Mineralogy . . . 90

3.4.4 Radiogenic Endmember Mixing Calculations . . . 91
3.5 Discussion: Geochemical Fingerprints . . . 93
3.5.1 Signals from Radiogenic Isotopes . . . 93
3.5.1.1 Source Regions . . . 94
3.5.2 The Sr Grain Size Effect . . . 96
3.5.2.1 Chemical Weathering . . . 98
3.5.2.2 Clay Composition . . . 98
3.5.2.3 Soil Type . . . 100
3.5.2.3.1 The Effect of Erosion . . . 100
3.5.3 Anthropogenic Influences . . . 102
3.5.3.1 Dams . . . 102
3.5.3.2 Climate Change . . . 102
3.6 Implications for Palaeoclimate Reconstructions . . . 103
3.7 Concluding Remarks . . . 104

4 The Last Termination: Sediment Source Changes; a Last Glacial Maximum - Modern Day Study 106
4.1 Chapter Outline . . . 107
4.2 Introduction . . . 107
4.2.1 Last Glacial Maximum Climate . . . 107
4.2.1.1 LGM Climate of the Present-Day Winter Rainfall Zone . 109
4.2.1.2 LGM Climate of the Present-Day Summer Rainfall Zone . 110
4.2.1.3 LGM Climate of the Present-Day Year-round Rainfall Zone 111
4.2.1.4 Modern Sources of Sediment from South Africa . . . 112
4.2.2 Grain Size Selection . . . 113
4.3 Methods . . . 116
4.3.1 Site Selection . . . 116
4.3.1.1 Identification Techniques of Last Glacial Maximum Samples 117
4.3.2 Stable Isotopes . . . 117
4.3.3 Sediment Processing and Techniques Applied (Summary) . . . 118
4.4 Results . . . 118
4.4.1 Clay Minerals . . . 118
4.4.2 Radiogenic Isotope Systematics (Sediment Provenance) . . . 119
4.4.2.1 Clay Fraction . . . 119
4.4.2.2 Cohesive Silt Fraction . . . 119
4.4.2.3 Non-Cohesive Silt Fraction . . . 120
4.4.2.4 Latitudinal Extent of Radiogenic Isotopes during Modern and LGM . . . 121
4.4.3 Terrigenous Grain Size Measurements . . . 122

4.4.3.1 Sortable Silt . . . 124
4.4.3.2 Stable Isotope δ^{13}C Measurements . . . 125
4.5 Discussion . . . 126
4.5.1 Hydrography Reconstructions . . . 126
4.5.1.1 Regional Comparison . . . 127
4.5.2 Sediment Provenance . . . 130
4.5.2.1 Detrital Sediment Supply to Northern Sector . . . 134
4.5.2.2 Detrital Sediment Supply to Central Zone . . . 136
4.5.2.3 Detrital Sediment Supply to Southern Sector . . . 136
4.5.3 Sediment Sources and Mixing: Links to Modern and LGM Climate in Southern Africa . . . 137
4.5.3.1 Modern Day . . . 137
4.5.3.2 Impact of Sea Level Shifts during LGM on Local South African Sediment Supply . . . 140
4.5.3.3 South African Regional Hydrology . . . 142
4.5.3.4 Upstream sediment sources (Limpopo and Zambezi) . . . 143
4.5.3.5 Increased Contribution of South Atlantic Sediments during the LGM to the Southern Sector . . . 149
4.6 Concluding Remarks . . . 152

5 Terrestrial Climate Variability from South Africa's southern Cape: Setting the Environmental Scene for Early Modern Humans 155
5.1 Chapter Outline . . . 156
5.2 Introduction . . . 156
5.2.1 Forcings on the Climate Variability in South Africa Today . . . 156
5.2.2 Orbital Forcings Driving Climate Variability in South Africa . . . 157
5.2.2.1 Millennial Forcing driving Climate Variability in South Africa . . . 161
5.2.2.2 Climate during the Late Middle Stone Age (100-50 ka) . . . 161
5.3 Materials and Methods . . . 163
5.3.1 Sampling Strategy and Processing . . . 163
5.4 Results and Discussion . . . 164
5.4.1 ^{14}C – LR04 Age Model . . . 164
5.4.1.1 Time Series Analysis of LR04 timescale . . . 165
5.4.2 Hulu-Sanbao Speleothem Age Model (Speleothem Chronology) . . . 167
5.4.2.1 Time Series Analysis of Speleothem Chronology . . . 168
5.4.3 X-Ray Fluorescence Scanning and Principal Component Analysis . 171
5.4.3.1 XRF Scanning Results of MD20-3591 . . . 171

5.4.3.2 Principal Component Analysis . . . 172
5.4.4 Sea Level Control on Grain Size at Site MD20-3591 . . . 177
5.4.5 Sediment Provenance (Radiogenic Isotopes) in Site MD20-3591 . . . 179
5.4.5.1 Disentangling the εNd and $^{87}Sr/^{86}Sr$ variability . . . 180
5.4.6 South Africa Hydroclimate Patterns at Different Timescales . . . 184
5.4.6.1 Long Term Climate Variability . . . 184
5.4.6.1.1 MIS 4 in South Africa . . . 187
5.4.6.2 Millennial-Scale Variability . . . 196
5.4.7 The Early Human Link . . . 202
5.5 Concluding Remarks . . . 203

6 Synthesis and Future Perspectives **205**
6.1 Summary of Chapters . . . 206
6.1.1 Chapter 3 . . . 206
6.1.2 Chapter 4 . . . 206
6.1.3 Chapter 5 . . . 207
6.2 Wider Perspective . . . 208
6.3 Future Work . . . 209
6.3.1 River Sediments . . . 209
6.3.2 More Sediment Collection . . . 210
6.3.3 Archaeological Evidence . . . 211

Bibliography **212**

Appendix **267**

List of Figures

1.1 Map of southern Africa 4
1.2 Location of two key Middle Stone Age archaeological sites, Blombos Cave and Klipdrift Complex. 6
1.3 Blombos Cave Middle Stone Age (MSA) Sequence. 7
1.4 Benthic foraminiferal calcite δ^{18}O stack. 10
1.5 Late Pleistocene Climate Variability. 11
1.6 Oxygen Isotope and methane data from Greenland and Antarctic ice cores. 12
1.7 Greenland (GISP2) and Antarctic δ^{18}O of ice. 14
1.8 Map of southern Africa showing seasonality of rainfall and climatic gradients. 16
1.9 Pretoria Saltpan Rainfall record (mm/year) (Partridge *et al.,* 1997) 18
1.10 Schematic representation of the global thermohaline circulation. 19
1.11 Schematic of meridional overturning for the Atlantic Ocean 21
1.12 Overturning circulation from a Southern Ocean perspective 22
1.13 Ocean circulation patterns offshore of southern Africa. 24
1.14 Agulhas Current structure. 25
1.15 Geology of southern Africa. 32

2.1 Modern Hydrography of Agulhas Current region with core sites discussed in this thesis. 38
2.2 Offshore South Africa sedimentary environments. 42
2.3 Kaolinite/Chlorite ratio in clay fraction <2 µm for global ocean. 45
2.4 Grain size distribution of separated lithogenic clay fraction (<2 µm). . . . 57
2.5 Grain size distributions from lithogenic sediment grain size separation. . . 58
2.6 Method for separating the <2 µm, 2-10 µm and 10-63 µm fractions. 60
2.7 Downcore variability in $CaCO_3$% and Total Organic Carbon for MD20-3591. 65
2.8 Downcore raw XRF scanning results. 66
2.9 ^{14}C - LR04 Age Model for 100 to 0 ka. 70
2.10 ^{14}C -LR04 Chronology of core MD20-3591 –MIS are highlighted on top (a). 71
2.11 The Bayesian LR04 Age Model obtained from undatable for MD20-3591. . 72
2.12 Speleothem Chronology. 74

3.1 Overview map of all published Sr and/or Nd datasets in the South Africa region. 77
3.2 Annual mean rainfall map of South Africa. 81

3.3 Images of rivers from eastern Cape of South Africa. 82
3.4 South African geology within each drainage basin. 83
3.5 Elevation map of South Africa with major drainage areas. 84
3.6 Radiogenic isotope compositions and clay mineralogies of selected river catchments analysed. 88
3.7 Comparison of $^{87}Sr/^{86}Sr$ isotope composition showing the values obtained from the <2 µm size fraction (circles) and 2-32 µm size fraction (squares). 89
3.8 Grain Size distributions of riverine sediments. 90
3.9 Radiogenic isotope endmember mixing calculation results for both size fractions measured. 93
3.10 Sr-Nd isotope ratios mixing plot based on linear regression between South African river sediments (red) and published terrestrial and marine samples from the region. 95
3.11 Correlation between age of bedrock and Nd from each river catchment. . . 96
3.12 Soil types of South African river catchments. 101
3.13 Erosivity calculations output using empirical-based modelling approach. . . 102

4.1 Map of southern Africa showing seasonality of rainfall and climatic gradients 109
4.2 Modern day core top Sr isotope values from published literature. 114
4.3 (a) Map showing the location of sediment cores. 116
4.4 $^{87}Sr/^{86}Sr$ isotope composition and εNd for each operationally defined grain size class (<2 µm, 2-10 µm and 10-63 µm). 121
4.5 Latitudinal Distribution of radiogenic isotopes on the <2 µm fraction. . . . 122
4.6 Grain size distributions for marine sediments from CD154 core sites. 123
4.7 Mean grain size (µm) of Modern and LGM dated sediments (top) and mean $\overline{SS}$ (µm) of Modern and LGM dated sediments (bottom) 124
4.8 a) Calibration of $\overline{SS}$ (µm) using 'main line' equation from McCave *et al.* (2017), b) Depth profile of calibrated flowspeed (U) (cm/s^{-1}) 125
4.9 Depth profile of $\delta^{13}C$. 126
4.10 Depth profiles of a) modern $\delta^{13}C$, modern day values for NADW and CDW indicated. 127
4.11 Vertical $\delta^{13}C$ for modern (black) and LGM (red) from South Atlantic and Southwest Indian Ocean. 129
4.12 Chemical vs Physical ventilation plots. 130
4.13 Comparison between radiogenic isotopes $^{87}Sr/^{86}Sr$ and εNd. 132
4.14 Correlation matrix showing Pearson Correlation Coefficient (r) between designated records of all CD154 core sites included in this study. 133
4.15 Comparison between $^{87}Sr/^{86}Sr$ values measured on the <63 µm (triangles; from Franzese *et al.,* 2006) and <2 µm fraction (circles; from this study). . 134

4.16 Modern and LGM terrigenous $^{87}Sr/^{86}Sr_{clay}$ variability. 135
4.17 Modern and LGM $\varepsilon Nd_c lay$ variability. 136
4.18 Radar plot of defined radiogenic isotope endmember source contributions during the modern (purple) and LGM (blue). 137
4.19 Conceptual Diagram of Modern Conditions. 139
4.20 Sea level low stand Palaeo Agulhas Plain exposure simulation for LGM shoreline. 141
4.21 Conceptual Image of the sea level effect and more local South African sediment supply during the LGM. 143
4.22 Conceptual Image to show increased Zambezi sediment supply during the LGM. 146
4.23 Conceptual Image presenting Stronger Agulhas Current and enhanced South Atlantic input during the LGM. 148
4.24 Map of core sites shown Table 4.7. 151
4.25 Updated Sr isotope values from published literature and this study 153

5.1 Schematic of primary atmospheric (white arrows) and oceanic circulation systems (red arrows for warm currents, blue arrows for cold currents, with Agulhas Current and Benguela Current labelled). 159
5.2 Time series analysis of XRF PC1 record on LR04 timescale (Bayesian). . . 166
5.3 Comparison of XRF PC1 on both age model chronologies. 169
5.4 Bayesian Speleothem Chronology Age-Depth. 170
5.5 Time series analysis of XRF PC1 record on Speleothem chronology. 171
5.6 Comparison of XRF data to calibration samples using individual element concentrations. 172
5.7 Downcore calibrated XRF scanning results. 173
5.8 Principal Component Analysis results. 175
5.9 Downcore comparison of records. 176
5.10 Pearson's correlation. 177
5.11 Grain size distribution for site MD20-3591 sediments. 178
5.12 Comparison of core site MD20-3591 grain size EM1 (%) (blue) and down-sampled sea level from Grant *et al.* (2014). 179
5.13 Regression plot of sea level from Grant *et al.* (2014) and mean grain size (µm). 180
5.14 Downcore radiogenic isotope reconstructions from core site MD20-3591. . . 182
5.15 Sr-Nd ratios mixing plot based on linear regression between South African river sediments (Chapter 3) and sediment sources offshore of the Limpopo. 184

5.16 Comparison of 30°S summer (DJF) insolation (grey) and (a) LR04 (Lisiecki and Raymo, 2005), (b) MD20-3591 XRF PC1 (purple), (c) MD20-3591 εNd (red), (d) XRF scanning ln(Fe/K) (CD154-10-06P) (Simon *et al.,* 2015a) (green), (e) XRF scanning ln(Fe/K) (CD154-17-17K) (Ziegler *et al.,* 2013). MD20-3591 data are presented on the Speleothem Age Model. 186
5.17 Climate modelling results from Götkürk *et al.* (2023) showing a mean precipitation change (%) (over 30 years) and surface winds (shown by arrows) from 82 to 70 ka for the southern Cape region. 188
5.18 Sea level low stand Palaeo-Agulhas Plain exposure simulation at varying sea level regression. 189
5.19 Coupling of sea level (Grant *et al.,* 2014) and grain size EM1 (%). 190
5.20 Lead lag correlation (root mean square) between sea level from Grant *et al.* (2014) and grain size EM1 performed on Acycle (Li *et al.,* 2019). 191
5.21 Sediment source apportionment for key sediment sources. 192
5.22 Climate Variability during the LMSA. 194
5.23 Conceptual Model of precipitation shifts during minimum 30°S summer insolation (e.g. $\sim$ 82 ka) (top) and maximum 30°S summer insolation (e.g. $\sim$ 72 ka) (bottom). 195
5.24 Climate variability during LMSA. 197
5.25 Spectral Frequencies from the $^{87}Sr/^{86}Sr$ record during MIS 5 and MIS 4. . 199
5.26 Millennial Scale Variability during the LMSA period. 200

List of Tables

1.1 Water Mass properties depicted in Figure 1.14 25

2.1 List of marine sediment core sites used in this study, arranged in order of water depth. 39
2.2 Radiocarbon ACPs for marine sediment core MD20-3591 69
2.3 Tuning points of LR04 Age Model 71
2.4 Speleothem Chronology 73

3.1 Bedrock geology database and weighted average bedrock age 85
3.2 Results table of radiogenic isotope data from South African river sediment. εNd is measured on the clay fraction only 87
3.3 Grain size percentages ordered by class; Sand > 63µm, Silt 2-63µm and clay <2µm. LPS03 to LPS24a are from eastern Cape, LPS28 to LPS45 are from southern Cape. 91
3.4 Clay mineral abundances for river sediment samples. LPS03 to LPS24a are from eastern Cape, LPS28 to LPS45 are from southern Cape 92
3.5 Endmember Values for South African river mud from two regions (Karoo is eastern Cape and Cape is southern Cape) by using radiogenic isotope mixing model (section 2.3.4). 96

4.1 Table of radiogenic isotopes endmembers used in this study from South African coastal rivers and Limpopo and Zambezi rivers. 113
4.2 Collated studies of radiogenic isotopes and/or grain size studies on various size fractions. 115
4.3 Stratigraphic tools used for identifying LGM depth horizon for each CD154 core used in this study. 117
4.4 Clay mineral abundances for CD154 sediment cores during modern and LGM. 119
4.5 Radiogenic isotope data results 120
4.6 Classical grain size percentages for sand, silt and clay for each sediment core (Modern and LGM dated). 124
4.7 List of radiogenic isotope values from published studies with size fraction identified from Southeast Atlantic Ocean and Southwest Indian Ocean for Modern and LGM dates. 150

4.8 Radiogenic isotope compositions for CD154 core sites (this study) measured on 10-63 µm fraction. 152

Abbrieviations

AABW = Antarctic Bottom Water;

AAIW = Antarctic Intermediate Water;

ACC = Antarctic Circumpolar Current;

AL = Agulhas Leakage;

AMH = Anatomically Modern Human (*Homo sapiens*)

AMOC = Atlantic Meridional Overturning Circulation;

ARC = Agulhas Return Current;

CAB = Congo Air Boundary;

CDW = Circumpolar Deep Water;

DBD = Dry Bulk Density;

DIC = Dissolved Inorganic Carbon;

DP = Drake Passage;

IDP = Indian Deep Water;

IRD = Ice-Rafted Debris;

ITCZ = Intertropical Convergence Zone;

IODP = International Ocean Discovery Program;

IOW = Indian Ocean Waters;

ka = Thousand years before present, (kilo annum);

kyr = Thousand years (duration);

LCDW = Lower Circumpolar Deep Water;

LR04 = Lisiecki and Raymo - 2004 benthic oxygen isotope stack;

LSR = Linear Sedimentation Rate;

MAR = Mass Accumulation Rate;

MIS = Marine Isotope Stage;

NADW = North Atlantic Deep Water;

PDW = Pacific Deep Water;

PF = Polar Front;

SAC = South Atlantic Current;

SAF = Subantarctic Front;

SAZ = Subantarctic Zone;

SCW = South Component Water;

SST = Sea surface temperature

STF = Subtropical Front;

STFZ = Subtropical Frontal Zone;

SHW = Southern Hemisphere Westerlies;

UCDW = Upper Circumpolar Deep Water;

VPDB = Vienna Pee Dee Belemnite;

WBC = Western Boundary Current

Chapter 1 | Introduction

The sea the great unifier is man's only hope – Jacques Yves Cousteau

1.1 Early Humans

The earliest traces of humans are observed in the African fossil and archaeological record. *Homo sapiens* evolved from our predecessor species, who evolved from *Homo heidelbergensis* through both gradual and punctuated processes (Stringer, 2016). The evolution of *Homo* since 800 thousand years ago[1] (ka) has been attributed to random genetic mutations which favoured greater cognitive capacity (Klein, 2009). Fossils recovered from Ethiopia indicate that archaic humans were replaced by more gracile, larger brained anatomically modern humans (AMHs) (*Homo sapiens*) by 200 to 155 ka (White *et al.,* 2003; McDougall *et al.,* 2005). The shift towards a bigger brain marks a key movement in the most significant trait associated with the human lineage - *Homo sapiens* means 'wise man' and a key defining feature of AMH is the shape and size of their skull. The AMH brain is bigger, relative to total body size, than its ancestors, and the skull shape is different from ancestral species, with a bulbous appearance and prominent forehead. The appearance of AMHs and the development of modern behaviours suggests increased functional organisation and capacity of the brain (Klein, 2009).

The Middle Stone Age (MSA) ($\sim$ 300 to 30 ka) period of South Africa is a key midpoint within which AMHs developed, diverged and migrated (Behar *et al.,* 2008; Pickrell *et al.,* 2012; Dusseldorp *et al.,* 2013). The archaeological evidence from the African MSA defines our understanding of AMH behavioural evolution as a phase characterised by features such as a focus on prepared core lithic technology, hafting, and long-distance exchange (Mcbrearty and Brooks, 2000; Scerri, 2017; Brooks *et al.,* 2018).

Cultural identity has been suggested to be a defining feature of early AHMs with the dominant narrative of the MSA of South Africa emerging from numerous publications (e.g. Mellars, 2006; McCall, 2007; Villa *et al.,* 2009; Mourre *et al.,* 2010; Villa *et al.,* 2010; Compton, 2011; McCall and Thomas, 2012; Ziegler *et al.,* 2013; Simon *et al.,* 2015a; Wilkins, 2020; Wilkins *et al.,* 2021) is 'Middle Palaeolithic-like' variability that occurred until $\sim$ 77 ka from the earliest MSA. The first time that 'Upper Palaeolithic-like' variability developed was during Marine Isotope Stage (MIS) 4, with increasing innovation and complexity associated with Still Bay (72 - 71 ka) (SB) and Howiesons Poort (64 – 59 ka) (HP) complexes (Jacobs *et al.,* 2008; Reynard and Henshilwood, 2017). During these techno-complexes, the manufacture of products such as bifacial points in blades, which required techniques like pressure flaking and heat treatment of stone, provide evidence of technical sophistication (Henshilwood, 2012). This indicates the cognitive complexity required by AMHs and the high levels of innovation (Wadley *et al.,* 2009) could have been symbolically mediated behaviour (Henshilwood and Marean, 2003).

[1] one thousand years ago = 1 ka

1.1.1 The Coastal Zone of South Africa

The coastal zone of South Africa has transformed our knowledge about the emergence of the complex technological behaviours which characterise the AMH species. The coastal zones are considered a key site for early AMH populations occupation (Fisher *et al.,* 2010). South Africa's archaeological record is world renowned for a diversity of evidence relating to early AMH lifeways (Wadley, 2015). This archaeological record is biased towards the continental margins which is partly due to the favourable conditions in coastal zones for preservation of caves and rock shelters (Wilkins *et al.,* 2021). Through the setting of many archaeological sites being located on the coast, and abundant remains of shellfish being discovered at these sites, a dominant story persists between AMH origins and the coastal region, in which we are intrinsically tied to the coast and marine resources (Wilkins *et al.,* 2021).

The southern Cape coastal platform (known as the Palaeo-Agulhas Plain (PAP)), which extends from Gqeberha (previously Port Elizabeth) in the east to Cape Hangklip in the west and is 800 km along the Cape South Coast (Cawthra *et al.,* 2020b) (Figure 1.1)), is postulated as a glacial-phase refugium whereas the interior of southern Africa is considered climatically and ecologically complex (Carr *et al.,* 2023). The expansion and contraction of habitats in response to glacial and interglacial climate cycles during the last $\sim$ 800 ka (Adams *et al.,* 1997; Carr *et al.,* 2010) may have driven the appearance of increasingly modern behaviour (Compton, 2011). Large amplitude, $\sim$ 120 m, glacial to interglacial sea level fluctuations (Grant *et al.,* 2014) would have directly impacted the exposure of continental shelves off the continent of Africa. The PAP, separated from Africa by rugged sandstone mountains of the Cape Fold Belt, would have greatly expanded during glacial sea level low stands (Dingle and Rogers, 1972; van Andel, 1989; Compton, 2011; Cawthra *et al.,* 2019; Cawthra *et al.,* 2020a) and reconnected during interglacial periods.

Early human populations likely focused on the coastal zone because of the abundance and predictable coastal resources (Jerardino and Marean, 2010; Jerardino, 2016) and changing shorelines and vegetative habitats would have affected AMHs in numerous ways. AMHs were reliant on the low sea level stands for shellfish foraging and exploitation (Marean *et al.,* 2007; Compton, 2011) and there is evidence of this on the PAP (Jerardino and Marean, 2010). Sea level shifts seem to have influenced the southern Cape productivity since during glacial periods, the continental shelf was exposed and likely grazed on by ungulates, hippos and eland (Klein, 1983; Copeland *et al.,* 2016; Hodgkins *et al.,* 2020). The shelf further acted as a refuge for these populations, and as a result, many archaeological sites are situated along this coastal zone (Henshilwood *et al.,* 2002; Jerardino and Marean, 2010; Compton, 2011, 2016; Sealy *et al.,* 2016).

There is evidence of a palaeo river system between Plattenberg Bay and Cape Agulhas (Figure 1.1) (Cawthra *et al.,* 2020b). These rivers extended onto the continental shelf

during sea level low stands crosscutting the PAP and would have provided a freshwater reserve, meaning AMHs would have had a more proximal access to freshwater on the PAP.

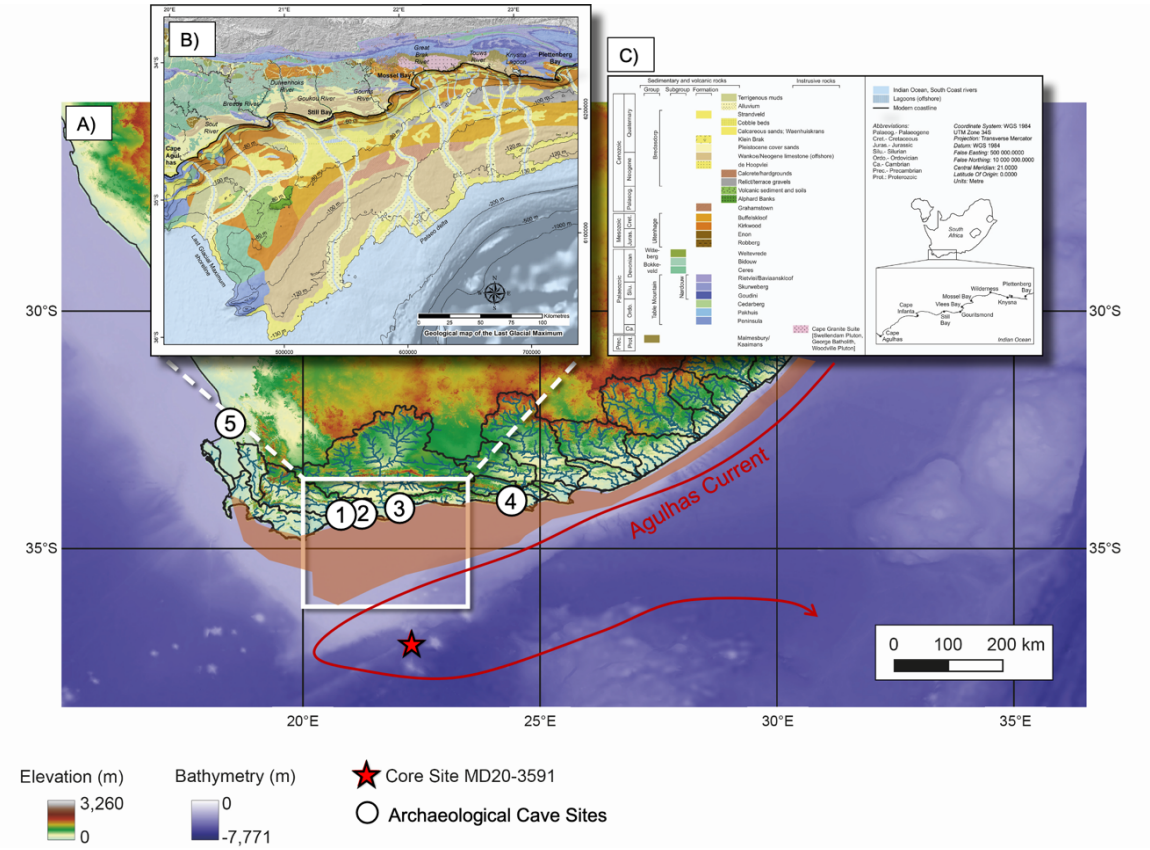

Figure 1.1: Map of southern Africa elevation from Hydro1K and bathymetry from BODC. (A) Location of Marine Core Site MD20-3591 (red star) and sites discussed in this chapter 1) Klipdrift Complex, 2) Blombos Cave, 3) Pinnacle Point, 4) Klasies River, 5) Diepkloof Rock Shelter. The Palaeo Agulhas Plain (PAP) extent in orange, and inset (B) of geology of PAP from Cawthra *et al.* (2019) with inset (C) as key. Agulhas Current trajectory (red arrow).

There is extended evidence that the PAP was highly fertile with many different types of vegetation communities (Cowling *et al.,* 2019). Vegetation diversity is highly dependent on soil type. Reworking of sediment through repeated exposure during glacials, and flooding during interglacials, is conducive to fertile, clay-rich landscapes on the PAP (Cawthra *et al.,* 2020b), supporting the conclusion that a more fertile landscape occurred on the PAP than the contemporary coastal land formation (van Breemen and Buurman, 2002). These fertile clays benefitted the growth of grasslands, which attracted herbivores and provided food resources for hunter-gatherers (Cowling *et al.,* 2019). This attraction to a varied ecosystem habitat on the PAP would have required AMHs to change their hunting style and necessitated more sophisticated toolkits (Marean, 2015; Copeland *et al.,* 2016; Haaland *et al.,* 2020).

The earliest evidence for cultural innovation such as the manufacturing of stone tools,

ornamentation, engravement and implements from organic materials occurs continuously throughout the MSA, both spatially and temporally, with some manufacture and use of specific types of symbolic resources dated to approximately 100 ka. The evidence includes tool kits such as pigment processing and incised ochre at Blombos Cave[2] (Henshilwood *et al.,* 2001; Henshilwood *et al.,* 2009; Henshilwood *et al.,* 2011) (Figure 1.2). Humans were collecting other non-utilitarian objects (non-food marine shells), most likely for symbolic practices around the same time, at sites further along the coastline from Blombos Cave such as Pinnacle Point 13B and Klasies River Main Site (Figure 1.1). Additionally, at Diepkloof Rockshelter, discarded ostrich eggshells have been discovered, with the earliest undecorated ostrich eggshells dated to 105 ka (Wilkins *et al.,* 2021). The evidence for innovation at these sites appears to concentrate in two successive waves, known as cultural industries (e.g. SB and HP), and are units of time from which numerous cave sites depict archaeological artefacts showing behavioural development from AMHs. These industries are recorded in layers at Blombos Cave site (Henshilwood *et al.,* 2001; Henshilwood *et al.,* 2009; Henshilwood and Dubreuil, 2011). The appearance of items such as stone tools, including a spear point and a point tip ranging from 84 to 72 ka (Henshilwood and Sealy, 1997; Henshilwood *et al.,* 2001; Henshilwood *et al.,* 2002; Jacobs *et al.,* 2006; d'Errico and Henshilwood, 2007), processing and engraving ochre artefacts (Henshilwood *et al.,* 2009; Henshilwood *et al.,* 2011), shell beads (Henshilwood *et al.,* 2004) and ostrich eggshells (Texier *et al.,* 2010) concentrate around these two cultural industries. Our ancestors gradually developed new symbolic forms, technological production strategies and subsistence behaviours, yet the mechanistic driver of these industries is not fully understood.

1.1.2 Blombos Cave and SapienCE context

SapienCE (Centre for Early Sapiens Behaviour) scientists have had continuous access to Blombos Cave to research AMH occupation at the site. Blombos Cave is known as the cradle of human culture and AMHs occupied the cave between 100 to 70 ka. At present, Blombos Cave (Henshilwood *et al.,* 2001) is positioned between the Goukou and Duiwenhoks river mouths (Figure 1.2) with a surrounding habitat dominated by fynbos vegetation (evergreen shrubland) (Nel and Henshilwood, 2016; Haaland *et al.,* 2020). The climate sensitivity of coastal southern Africa to changes in glacial sea level variations at $\sim$ 70 ka and associated land extent has been investigated with a high-resolution regional climate model (Göktürk *et al.,* 2023a) downscaled from global model simulations incorporating appropriate external forcing factors. When sea level is lower, the PAP is exposed and the coastline extends away from Blombos Cave, the climate at previously coastal localities shows strong continental characteristics. Notably, diurnal temperature ranges change by up to ± 6°C with, for example, temperature extremes of

[2]Key MSA cave site referred to throughout this thesis.

the modelled marine climate much more probable at Blombos Cave as the coastline shifts (Göktürk *et al.,* 2023b). Additionally, the coastline shifts have been shown to shape the local climate around Blombos by causing local modifications in near-surface atmospheric circulation, reducing the modelled amount of precipitation within the coastal region by 40% (Göktürk *et al.,* 2023b).

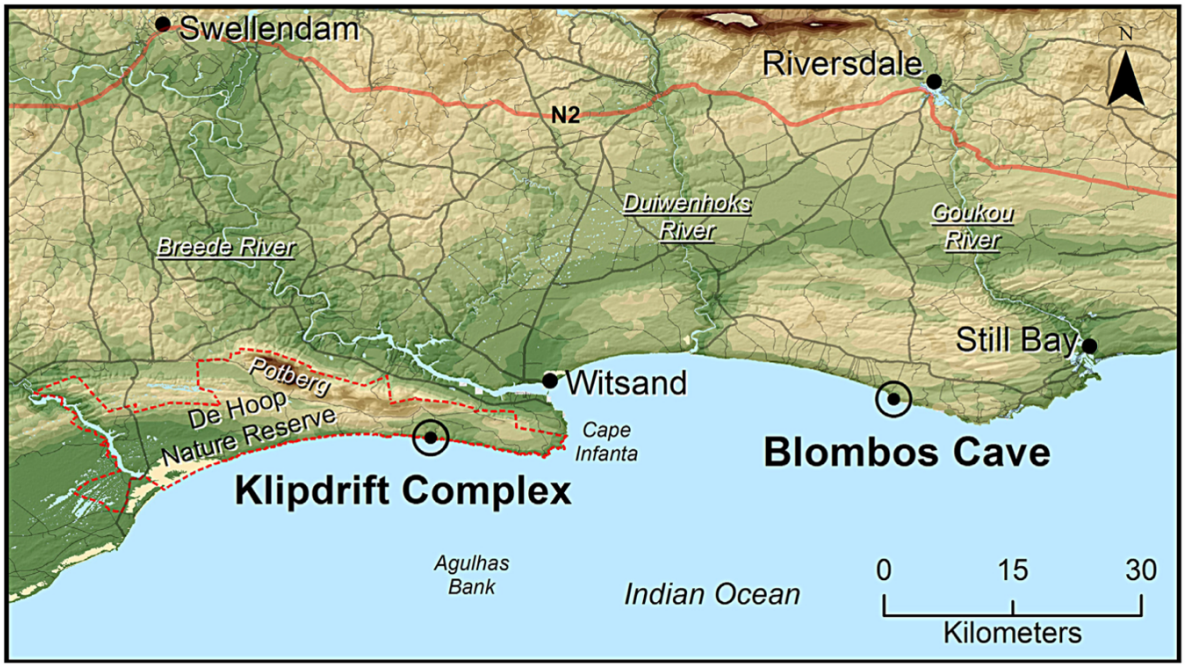

Figure 1.2: Location of two key Middle Stone Age archaeological sites, Blombos Cave and Klipdrift Complex. Image taken from Henshilwood *et al.* (2014). Paleoclimatic changes in South Africa are of intense interdisciplinary interest in the context of human evolution, especially around the southern Cape region, which hosts prominent archaeological sites, including Blombos Cave, Klipdrift Shelter and Klasies River

Blombos Cave has well-stratified sediment and well-preserved fauna. The Blombos Cave MSA sequence occurs below a sand dune sequence, which is known as the Blombos Cave Hiatus (Reynard and Henshilwood, 2017). This gap in the cave site records of the entire western Cape occurs up to $\sim$ 66 ka (Henshilwood, pers.comms). The MSA sequences consist, from top to bottom, of four MSA occupational phases. These are an M1 phase, an upper and lower M2 phase and an M3 phase (Figure 1.3) (Henshilwood *et al.,* 2001; Haaland *et al.,* 2020). The SB period encompasses M1 and upper M2. The upper M2 complex contains shellfish, engraved ochres, perforated shell beads and bone tools, which reveal the complex innovation techniques of our ancestors (Marean *et al.,* 2007).

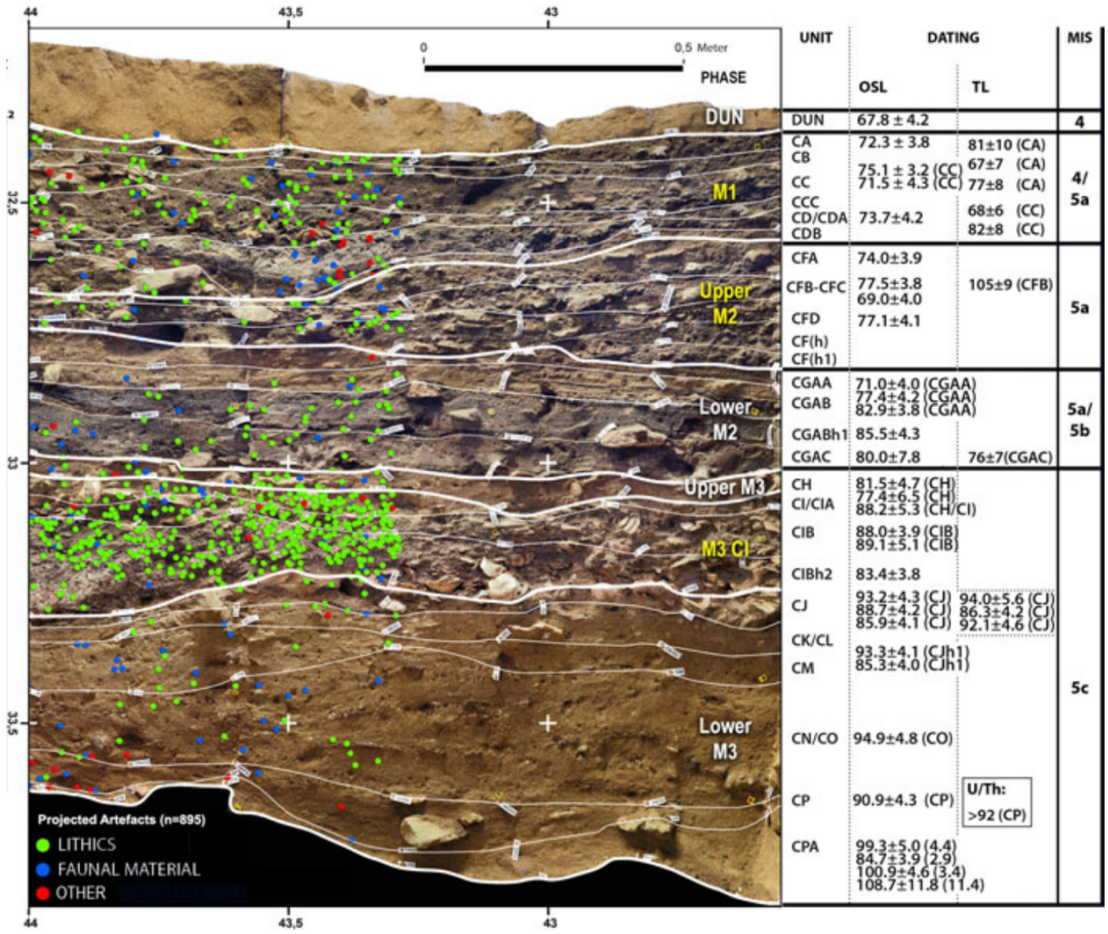

Figure 1.3: Blombos Cave Middle Stone Age (MSA) Sequence. Southern section showing stratigraphic units and main occupation phases. Image from Haaland *et al.* (2020). Projection of plotted MSA artefacts, green (lithics), blue (faunal material), and red (other material, i.e., ochre, eggshell, personal ornaments) dots on half of the section wall.

The Late Middle Stone Age (LMSA), referred to throughout this thesis as the 100-50 ka interval is concentrated on in Chapter 5 as this was a period with significant discoveries in Blombos Cave. The glacial periods MIS 4 and 2 are also a key focus in this thesis because they were times when a large area of the coastal plain south of Africa was exposed. Previous studies suggest the LMSA cognitive evolution of early AMHs was facilitated by environmental and climatic conditions in the region; particularly at the dynamic land-ocean coastal interface influenced by the Greater Agulhas Current system in the Southwest Indian Ocean (Figure 1.1). Understanding the processes that led to the cognitive transformation in AMHs requires palaeoclimate based evidence in the southern Cape area during this LMSA time interval.

The major events of occupation in HP and SB industries observed in Blombos Cave occurred when the North Atlantic climate was colder (Ziegler *et al.,* 2013; Simon *et al.,* 2015a), coinciding with a weaker Asian monsoon and an increase in humid conditions and river discharge in South Africa (Ziegler *et al.,* 2013; Simon *et al.,* 2015a). To link climate

variability to the archaeological records it is necessary to have continuous high-resolution climate archives integrating the ocean and terrestrial signal. The palaeohydrology of the South African continent is documented by a variety of terrestrial and offshore marine records. Records are better resolved in the eastern regions of South Africa, than the southern Cape region. The main issues encountered in the past when attempting to define past climates of South Africa are; a) the lack of records available, largely due to the absence of rift lakes and the dry seasonal climates and b) the difficulties establishing reliable age chronologies using radiocarbon which is limited in its functional range (50 ka). From South Africa, only several continuous and high-resolution archives exist. Of these records, most are restricted to the east (Holmgren *et al.,* 2003; Kristen *et al.,* 2010; Truc *et al.,* 2013), the south coast (Chase *et al.,* 2013; Wündsch *et al.,* 2016; Chase *et al.,* 2021) and the coastal areas in the west (Scott and Woodborne, 2007; Chase *et al.,* 2019; Dupont *et al.,* 2021; Chase *et al.,* 2023). Marine archives offshore of the South African continent often contain terrestrial material delivered by aeolian or riverine transport, so are suitable for investigating terrestrial palaeoclimate conditions. This has been previously shown using the terrestrial versus marine elemental ratio recorded in marine sediments, which can be used as an indication of relative changes in the amount of fine (Fe-rich) terrigenous components supplied to the core site from regional river discharge (e.g. Ziegler *et al.,* 2013).

1.2 An overview of Climate Variability during the Late Pleistocene

Palaeoclimate reconstructions show that major oceanic and climatic changes have occurred during the Pleistocene Epoch (between 2.58 million to 11,700 years ago). These include variations in the Northern Hemisphere ice volume, otherwise known as glacial to interglacial changes, which have been uncovered by geologists and palaeoclimatologists since the 19th Century (Agassiz *et al.,* 1840; Adhémar, 1842).

Cyclic variations in insolation, caused by the precession and obliquity of Earth's spin axis and variations in the eccentricity of Earth's orbit, have been acknowledged as key drivers of Quaternary climate variability. These, principally known external forcings, form the basis for the astronomical theory of palaeoclimates, first identified by Milutin Milankovitch (Milanković, 1941).

Eccentricity is the term used to describe the variation in the shape of the Earth's orbit and deviations between high and low eccentricity is about 6% resulting in small effects on insolation which is integrated over all latitudes (Berger, 1984). Eccentricity is the longest of the orbital cycles of Milankovitch Theory, originally calculated to be 100 thousand years (kyr), although Hays *et al.* (1976) were the first to suggest the possibility of a 400-kyr cycle, with a 100-kyr non-linear climate response. Eccentricity also modulates

the amplitude of the precessional cycle which is the 23-kyr cycle (see below). Obliquity controls the tilt of the earth's axis; it has a $\sim$ 40 kyr pacing (Denton and Hughes, 1983) and affects the strength of the seasons (Ruddiman, 2007). This is because the angle of tilt influences the amount of incoming solar radiation- during periods of high tilt, seasonality is greater. Precession is the change in the rotation of the Earth's axis, referring specifically to the precession of the equinoxes, the position of the solstices and equinoxes in relation to the aphelion (point in the Earth's orbit furthest from the sun) and perihelion (point in the Earth's orbit closest to the sun) (Hays *et al.,* 1976). Precession has two periodicities, the 19 kyr and 23 kyr cycles. These periodicities determine the seasonal distribution of solar insolation which means that the cycle causes an antiphase response between the Northern and Southern Hemispheres, with phases of high boreal insolation also being phases of low austral insolation. Milankovitch proposed that ice accumulation in the Northern Hemisphere coincides with periods of decreased summer insolation. Further derived from Milankovitch's theory is a simplified model of these forcing interactions. July insolation at 65°N is taken as the most useful single quantity for examining the role of orbital variations in glacial cycles as 65°N is the latitude where ice sheets accumulate first and melt last, making it the most sensitive latitude for low insolation values. Changes in high latitude Northern Hemisphere insolation, driven by Milankovitch cycles, act as a global pacemaker, regulating the more complex non-linear internal variations within the climate system.

It was not until the 20th Century that palaeoclimatologists began to test the Milankovitch theories and understand external and internal climate forcings. The development of geochemical tools to extract climate and environmental information from the sediments, such as using the ratio of $^{18}O/^{16}O$ in calcite microfossils (Emiliani, 1955; Shackleton, 1977), became more popularised. Early studies of the ratio of $^{18}O/^{16}O$ or $\delta^{18}O$ recorded by the calcium carbonate microfossils in deep sea sediment provide a first order approximation of continental ice volume (Shackleton, 1967), and other accountable factors, reflecting the climate oscillation in past time. The presence of orbital periodicities in marine sediment cores was confirmed by statistical analysis by Hays *et al.* (1976), highlighting changes in precession and obliquity of the Earth's axis as well as eccentricity of Earth's orbit around the sun. Statistical analysis of long continuous marine oxygen isotope records such as LR04 (Lisiecki and Raymo, 2005) (Figure 1.4) has pioneered studies on the nature of past climate variability by providing the clearest overview of climate change over the Cenozoic era (e.g. Zachos *et al.,* 2001; Lisiecki and Raymo, 2005).

Orbital forcing alone is unable to explain the large amplitude of glacial-interglacial cycles or the abruptness of transitions from one state to another. A mechanism of positive feedback within the climate system must therefore be operating to amplify the orbital signal. These internal variations include changes in ocean circulation and productivity,

the growth and decay of ice sheets and CO_2 feedback loops. These climate non-linearities are often associated with feedback mechanisms which dampen or amplify climate change relative to the forcing.

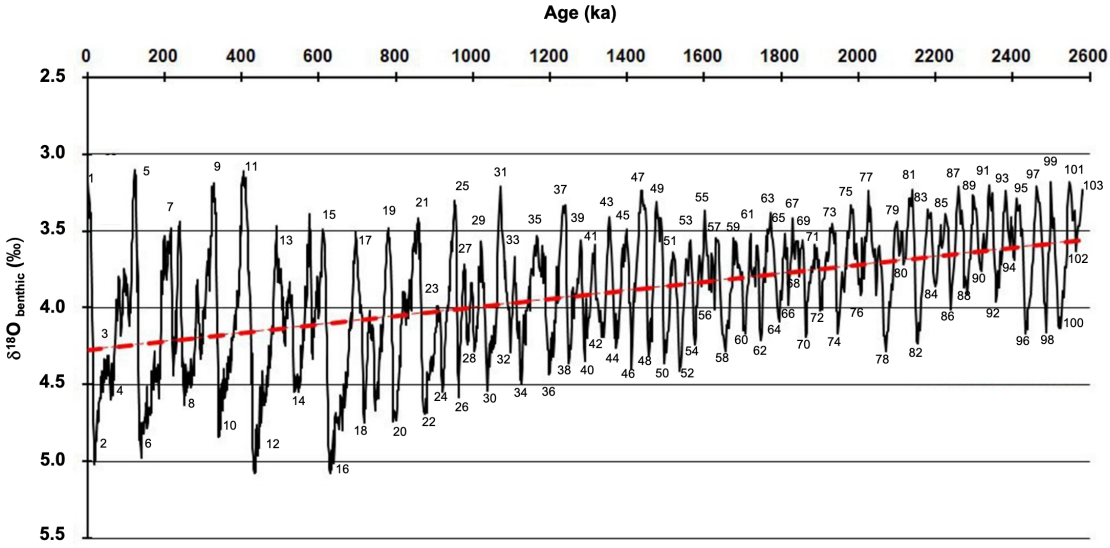

Figure 1.4: Benthic foraminiferal calcite $\delta^{18}O$ stack comprised of averaging 57 individual records showing the glacial-interglacial variability in ice volume and deep water temperature over the last 2.6 Ma known as the Pleistocene (Lisiecki & Raymo, 2005). These glacial – interglacial cycles occurred amid a long-term trend of increasingly heavy $\delta^{18}O$ (red line). This reflects the development of continental ice sheets; even numbers represent glacial stages and odd numbers are interglacial periods. Figure modified from Wieczorek *et al.* (2021).

Milankovitch cycles are the trigger of glacial-interglacial variability, however the classic 'saw-tooth' structure of glacial cycles (Broecker and van Donk, 1970) requires a non-linear response of the ocean-atmosphere system to solar forcing. Across glacial to interglacial cycles ice core records show that air temperature and CO_2 closely followed each other over the last 800 kyr (Figure 1.5) (Petit *et al.,* 1999; EPICA Community Members, 2004). These oscillations are recorded in ice core archives (Johnsen *et al.,* 1972; Dansgaard *et al.,* 1984) and sediment cores, from oceans in proximity to ice sheets and in far-field locations. The cyclic variations were first seen in the Antarctic ice cores (Figure 1.5), but more recently have been identified in high resolution records from Greenland ice cores (Dansgaard *et al.,* 1993; Johnsen *et al.,* 1997). Intense periods of millennial-scale variability within both cold glacial and warm interglacial periods are observed in Greenland ice cores and have since been shown in extended Antarctic ice core records over $\sim$ 430 ka (Figure 1.5) (Petit *et al.,* 1999; EPICA Community Members, 2004).

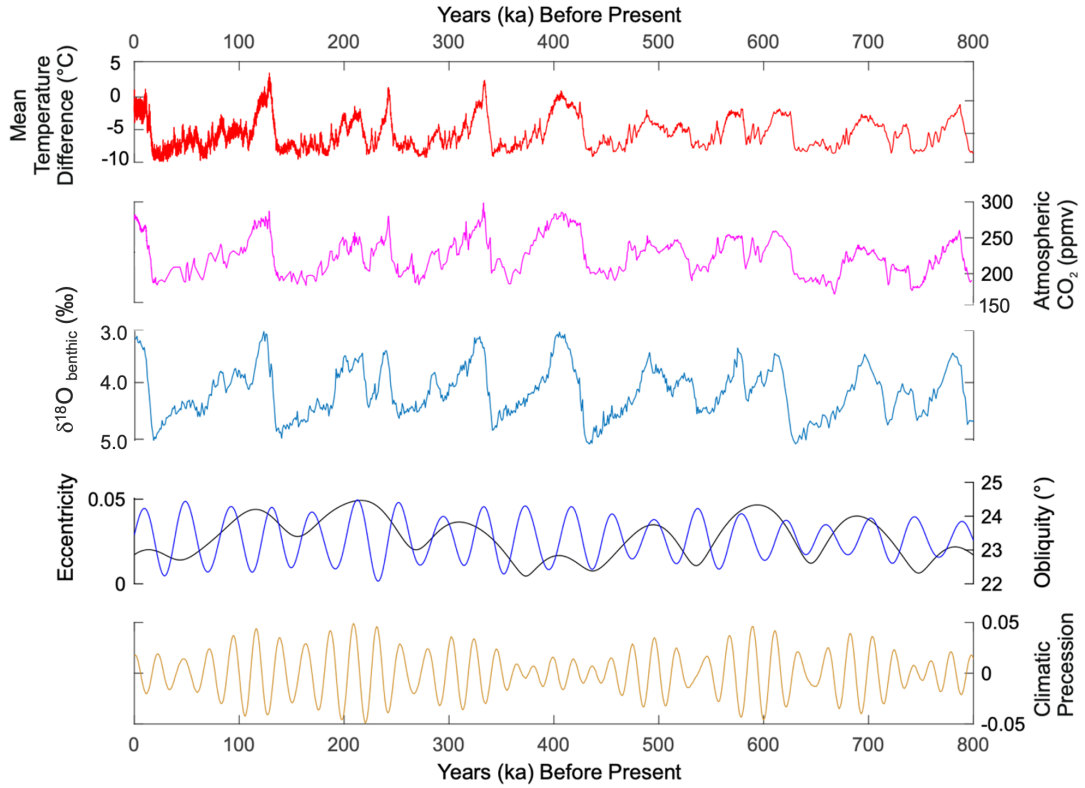

Figure 1.5: Late Pleistocene Climate Variability. Mean temperature variation reconstructed from Antarctic Ice Cores (Jouzel *et al.,* 2007), Atmospheric CO_2 from Luthi *et al.* (2008), Global benthic stack representing global ice volume changes (Lisiecki & Raymo, 2005), and Orbital Parameters (Berger & Loutre, 1999).

1.2.1 Millennial Scale Variability and Rapid Climate Changes

Throughout the last glacial period, several abrupt climate oscillations transitioning between cold (stadial) and warm (interstadial) periods occurred, known as Daansgard-Oeschger (D-O) oscillations (Dansgaard *et al.,* 1993; NGRIP, 2004) (Figure 1.6). The general structure of a D-O event is a slow shift towards colder, stadial conditions followed by relatively abrupt shifts back to warmer conditions. These D-O oscillations can alter global mean temperatures by 5-6°C over periods as little as 10 years or less (Alley *et al.,* 2003). There are 25 of these distinct D-O oscillations during the last glacial period, shifting between cold stadials and warm interstadials with a cyclicity of 1470 years ± 532 (Bond *et al.,* 1997; Bond *et al.,* 1999). Some D-O events are associated with Heinrich Events (HE) (Heinrich, 1988), occurring in the cold stadials proceeding the rapid D-O warming. HEs are associated with increased meltwater and ice rafted debris (IRD) influx into the North Atlantic originating from the Iceland and East Greenland ice sheets (Bond and Lotti, 1995).

Main contenders of the mechanistic driver of glacial D-O type variability include internal mechanisms within the ocean-atmosphere system (Broecker and Denton, 1990; Ganopolski

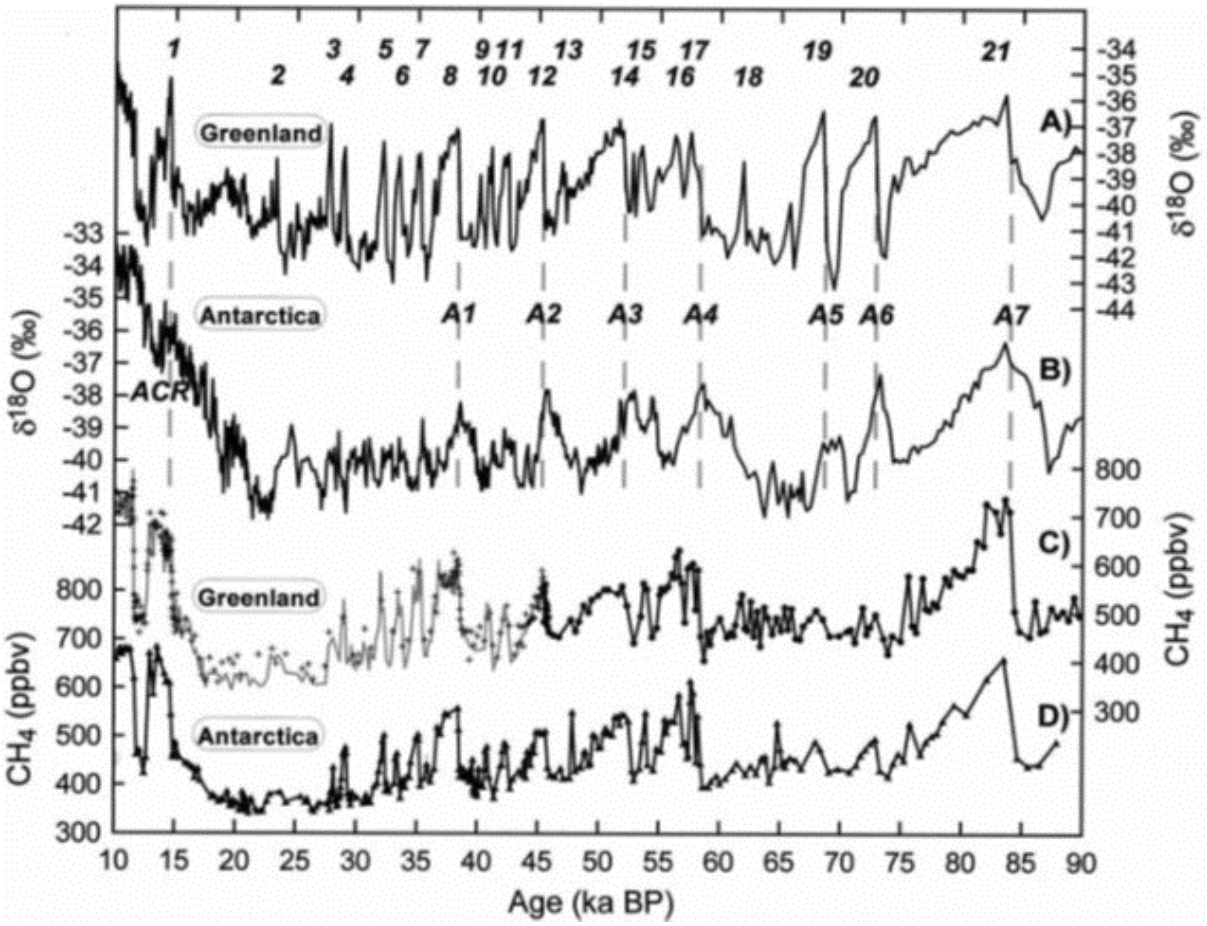

Figure 1.6: Oxygen Isotope and methane data from Greenland and Antarctic ice cores on the GISP2 timescale (from Brunier and Brook, 2001). (A) Greenland temperature proxy, δ^{18}O. Numbers denote D-O events. (B) Antarctica temperature proxy, δ^{18}O. Antarctic Warming Events (A1 to A7 labelled). (C) CH_4 concentrations from Greenland and (D) Antarctic CH_4 concentrations.

and Rahmstorf, 2001; Clark *et al.,* 2002) and periodic calving of the Greenland ice sheet (Van Kreveld *et al.,* 2000). Marine records from the North Atlantic reveal negative δ^{18}O excursions (Bond *et al.,* 1992; Maslin, 1995; Cortijo *et al.,* 1997) every 7-10 kyr (Bond and Lotti, 1995), and prominent IRD layers representing a higher frequency of iceberg discharge. These HEs correspond to stadial intervals within the Greenland air temperature record (Bond *et al.,* 1993) (Figure 1.7).

Synchronising the ice core records from Greenland and Antarctica has shown that these oscillations did not occur across the Hemispheres synchronously. The temperature shifts in Greenland were out of phase with the gradual changes observed in Antarctic ice cores, and the Antarctic records precede Greenland D-O events by $\sim$ 1.5 to 3 kyr (Figure 1.7) (Blunier and Brook, 2001). This contrasting temperature relationship between the two hemispheres is linked to the thermal bipolar seesaw (Broecker, 1998). Therefore, rapid climate variability is likely driven by changes in Atlantic Meridional Overturning Circulation (AMOC) strength (Rahmstorf, 2002) suggesting the ocean played an essential role

in millennial-scale climate fluctuations. Reductions in AMOC have been shown to cause cooling in the Northern Hemisphere and warming in the Southern Hemisphere (Figure 1.7) due to the bipolar seesaw mechanism (Barker *et al.,* 2009). Deglacial climate variability has been suggested to be controlled by ocean circulation via deep water formation reduction (Thornalley *et al.,* 2011; Ritz *et al.,* 2013) through freshwater inputs changing the density structure in deep water formation zones in the Northern Hemisphere (Thornalley *et al.,* 2010). Climate oscillations coeval to Heinrich Events have been discovered in marine and terrestrial records globally, from South Africa (Ziegler *et al.,* 2013; Simon *et al.,* 2015a), South America (Lowell *et al.,* 1995), the Asian Monsoon record from Chinese speleothems (Cheng *et al.,* 2009; Cheng *et al.,* 2016), and from the South China Sea (Wang *et al.,* 1999), suggesting the influence of these meltwater pulses into the North Atlantic is translated globally via teleconnections through the ocean and/or atmosphere.

During the MIS 5-4 transition ($\sim$ 74 to 70 ka), orbital parameters and global sea level were markedly different from each other. MIS 5 ($\sim$ 130 to 71 ka; (Shackleton, 1969)) has been divided into five substages, alternating between higher (MIS 5e, MIS 5c, and MIS 5a) and lower sea level stands (MIS 5d and MIS 5b) (Sánchez-Goñi, 2007). At the MIS 5–4 boundary, there was a rapid global cooling at $\sim$ 70 ka (Lisiecki and Raymo, 2005). During this period, nearly half of the interglacial–glacial drawdown of atmospheric CO_2 occurred over roughly 4 kyr (Ahn and Brook, 2008). This transition also brought extensive global cooling, growth of polar ice sheets, and changes in deep ocean circulation (Cutler *et al.,* 2003; Bereiter *et al.,* 2012; Adkins, 2013). During MIS 5 and MIS 4 intervals, the following D-O events occurred, these were D-O event 21 ($\sim$ 82 ka), D-O event 20 ($\sim$ 75 ka), D-O event 19 ($\sim$ 72.1 ka), D-O event 18 ($\sim$ 65 ka), D-O event 17 ($\sim$ 62 ka) and D-O event 16 ($\sim$ 58 ka) (Dansgaard *et al.,* 1984) (specifically South Africa climates (section 1.3.2)) and Heinrich Stadial 6 (HS 6) at 60 ka.

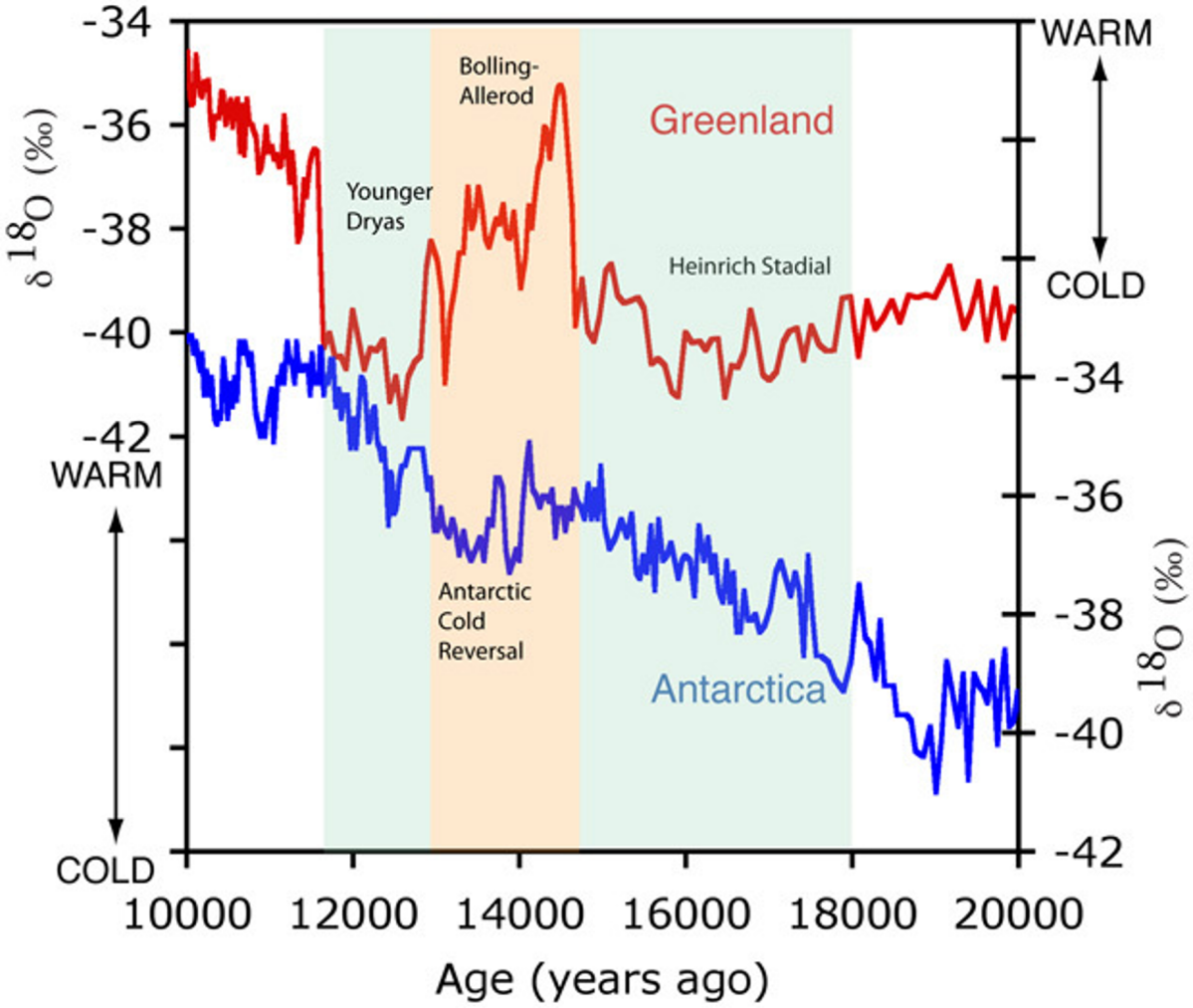

Figure 1.7: Greenland (GISP2) and Antarctic δ^{18}O of ice on a common time scale using methane (Blunier and Brook, 2001). When Greenland experienced cold temperatures between 19 to 15 ka, and during the Younger Dryas, Antarctica was warming. When Greenland was warm during the Bølling-Allerød, Antarctic experienced a cold reversal. Figure taken from Oppo and Curry (2012).

1.3 Setting of South Africa

1.3.1 Regional Atmospheric and Oceanic Circulation

The modern climate of South Africa is highly variable and results from oceanic and atmospheric circulation patterns. The pattern of precipitation in South Africa is governed by tropical convection and the seasonal migration of circulation patterns including the Intertropical Convergence Zone (ITCZ), Congo Air Boundary (CAB), Southern Hemisphere Westerlies (SHW) and the Southeast trade winds (Reason and Rouault, 2002; Castañeda *et al.,* 2007; Gasse *et al.,* 2008; Chevalier and Chase, 2015) (Figure 1.8). During austral summer the ITCZ migrates southward to (5-6°N) with the CAB, and during austral winter the ITCZ is positioned at about 15-18°N (Schneider *et al.,* 2014; Dunning *et al.,*

2016; Dunning *et al.,* 2018; Yang *et al.,* 2023). The CAB marks the zone of moist air convergence from the Atlantic and Indian Oceans and as such, the southwestern region of South Africa is separated from the influence of the South Indian Anticyclone as a moisture source (Vigaud *et al.,* 2009; Tierney *et al.,* 2011; Costa *et al.,* 2014). The SHW transport moisture during austral winter from the South Atlantic Ocean to the southwestern region of South Africa (Weldeab *et al.,* 2013; Chevalier and Chase, 2015). Therefore, both the South Atlantic high-pressure system and easterly flow from the Indian Ocean of the Agulhas Current invoke three rainfall zones; summer, winter and year-round (Dupont *et al.,* 2021). Modern rainfall in the Summer Rainfall Zone (SRZ; Figure 1.8) is modulated by sea surface temperatures (SSTs) of the Indian Ocean (Reason and Mulenga, 1999; Reason, 2001), while winter rainfall in the southwestern Cape mainly comes with cold fronts, especially if the westerlies have a northern position (Compton, 2011; Nash, 2017; Dupont *et al.,* 2021). The WRZ receives moisture from the latitudinal migration of the westerlies (Figure 1.8), which are influenced by Antarctic sea ice (Tyson, 1986; Nicholson, 2000; Tyson and Preston-Whyte, 2000; Chase and Meadows, 2007). The region located between these two zones; the Year-round Rainfall Zone (YRZ; Figure 1.8), receives rainfall in all seasons influenced by both the Southwest Indian Ocean and the South Atlantic Ocean.

The major ocean circulation patterns around South Africa include the cold Benguela Current and the warm Agulhas Current (Figure 1.8) (section 1.4.3). The Benguela Current flows northward along the west coast of South Africa and the Agulhas Current flows southward, down the east coast of South Africa. Upwelling occurs due to Ekman transport caused by the Southeast trade winds along the west coast inducing upwelling of cold nutrient rich waters, initiating highly productive and biological diverse ecosystems and nesting sites in this region. Contrastingly, the warm waters of the Agulhas invoke a regional ocean-land heat flux and precipitation in southern Africa (Walker, 1990). Precipitation is enhanced when onshore winds and SSTs induced convection of warmer and moist air are both stronger (Walker, 1990; Mason, 1995). This is the predominant driver of rainfall in the eastern and southern Cape regions, whereby the easterlies supply most of the precipitation in austral summer months.

Ocean circulation variability (Agulhas Current SSTs) has been proposed as a mechanism of transmitting the Northern Hemisphere signal to southern regions (Walker, 1990; Mason, 1995; Goddard and Graham, 1999; Camberlin *et al.,* 2001; Dupont *et al.,* 2011; Tierney *et al.,* 2013; Simon *et al.,* 2015b; Castañeda *et al.,* 2016). Over shorter timescales, the Southwest Indian Ocean temperatures influence regional rainfall variability (Tierney *et al.,* 2008; Stager *et al.,* 2011) and drive changes in the moisture balance (Walker, 1990; Mason, 1995; Goddard and Graham, 1999; Camberlin *et al.,* 2001; Dupont *et al.,* 2011; Stager *et al.,* 2011; Tierney *et al.,* 2013; Simon *et al.,* 2015b; Castañeda *et*

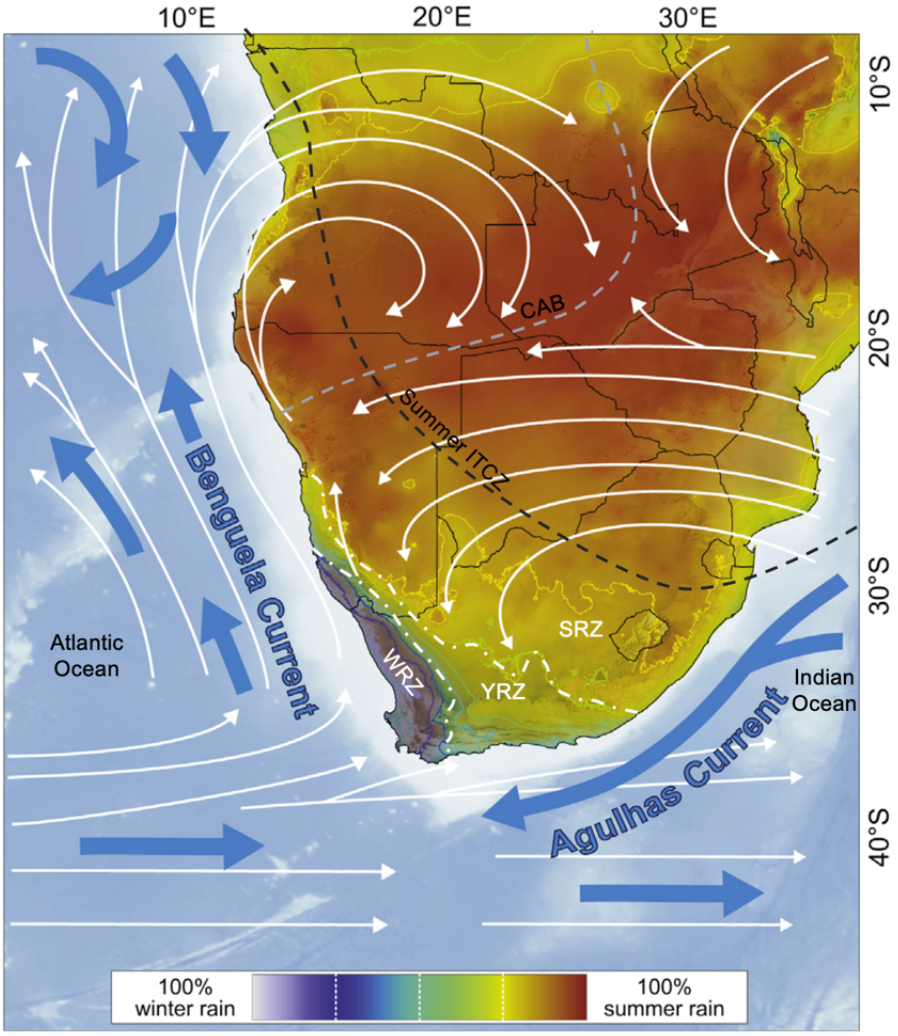

Figure 1.8: Map of southern Africa showing seasonality of rainfall and climatic gradients dictated by the zones of summer/tropical (red) and winter/temperate (blue) rainfall dominance. Major atmospheric (white arrows) and oceanic (blue arrows) circulation systems (Image modified from Chase *et al.* (2021)). WRZ = Winter Rainfall Zone, YRZ = Year round Rainfall Zone, SRZ = Summer Rainfall Zone. Summer ITCZ location and Congo Air Boundary depicted.

al., 2016; Strobel *et al.,* 2019). A warmer SST is associated with enhanced easterlies and moisture convergence over tropical and subtropical regions has been found (Walker, 1990). Principal Component Analysis of SSTs in the southern African region revealed prominent loadings at interannual and decadal scales and a spatial pattern covering the Southwest Indian Ocean (as well as the Mozambique Channel and waters south and southwest of Madagascar) (Mason, 1995). Additional findings from Reason *et al.* (1999, 2000) reveal a significant link between warmer SSTs in Southwest Indian Ocean and increased summer rainfall over South Africa, with warming also occurring in central and eastern tropical Pacific, suggesting the correlation between warmer SSTs in Southwest Indian Ocean and increased summer rainfall may be linked to El Niño Southern Oscillation (ENSO).

Over longer timescales there does not seem to be a precessional rhythm in the SSTs of the Southwest Indian Ocean, as such the influence of SST on the precipitation in the region does not have an effect on the precessional pacing (Caley *et al.,* 2011; Caley *et al.,* 2018) instead it could be considered that the difference in ocean and land temperatures has an effect on precipitation. Additionally, along the western coast of South Africa, records of dinoflagellate cysts from marine sediment core GeoB3603-2 show a strong precessional variability, indicating that stratified waters prevailed when precession was weak (Esper *et al.,* 2004) and the dominance of low latitude forcing during periods of high orbital eccentricity is noted in East Africa (Scholz *et al.,* 2007).

1.3.2 Climate Change in southern South Africa during the LMSA interval

Many climate forcing mechanisms have been proposed to explain the observed climate variability in southern South Africa during the LMSA, such as a breakdown of precession with declining eccentricity at $\sim$ 70 ka (Chase, 2021; Chase *et al.,* 2023) and global cooling at the MIS 5a–4 transition and extensive Antarctic icesheet growth influencing SHW latitudinal position (van Zinderen Bakker, 1967; van Zinderen Bakker, 1976; Cockcroft *et al.,* 1987; Shi *et al.,* 2000; Stuut, 2004; Chase and Meadows, 2007; Neumann and Scott, 2018a). On orbital timescales, Southeast African climate has been associated with local insolation changes, driven by orbital precession (Partridge *et al.,* 1997; Simon *et al.,* 2015a) with higher rainfall in Southeast Africa at summer insolation 30°S maxima (Figure 1.9). Studies have also linked wet conditions in Southeast Africa to strong summer insolation which results in stronger atmospheric convection, increased moisture transport by tropical easterlies and higher precipitation in the region (Schefuß *et al.,* 2011; Chevalier and Chase, 2015). The deterministic mechanism for this is suggested to be the southward displacement of the ITCZ. The effects of a southerly displacement of the ITCZ causing more rainfall, would have been confined to a spatial extent of subtropical southern African between 15 and 21°S (Thomas *et al.,* 2009; Schefuß *et al.,* 2011; Truc *et al.,* 2013; Chevalier and Chase, 2015; Chevalier *et al.,* 2017). On the other hand, precipitation in southern South Africa, specifically in the WRZ, has been shown to be associated with interactions between temperate and tropical systems, which have been linked to the latitudinal movement of the SHW in response to more Antarctic sea ice (Tyson, 1986; Nicholson, 2000; Tyson and Preston-Whyte, 2000; Chase and Meadows, 2007).

Studies of precipitation show rainfall regimes during the LMSA were distinctively different depending on the glacial boundary conditions. For example, during MIS 4, the climate was considerably colder and sea level was lower due to enhanced Northern Hemisphere ice volume. At 70 ka, during 30°S summer insolation maxima, the PAP was exposed and climate at the southern Cape coast was more arid (Göktürk *et al.,* 2023b). At 82 ka when sea level was higher, the shoreline was close to Blombos Cave and the climate was coastal

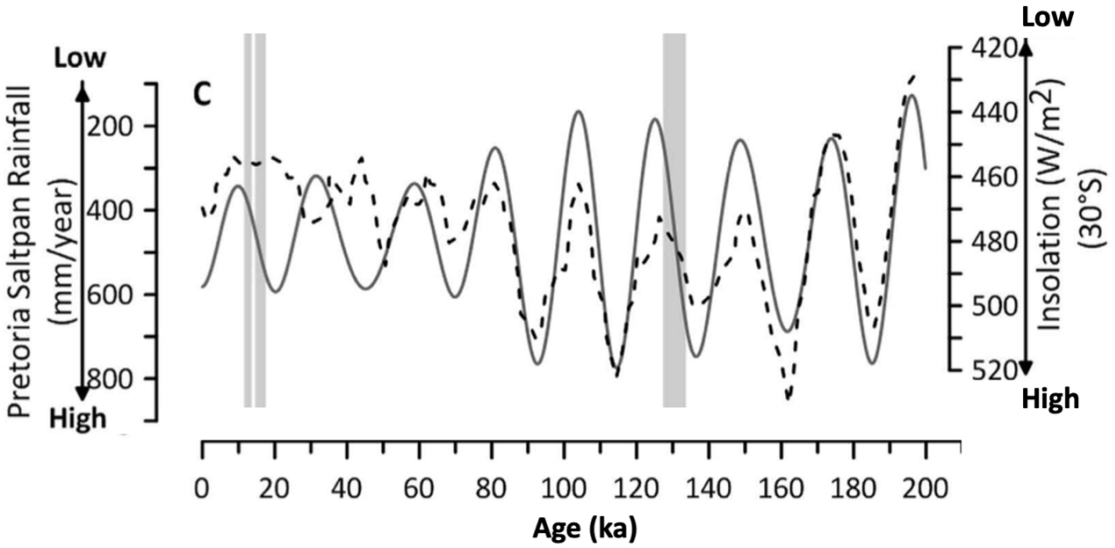

Figure 1.9: Pretoria Saltpan Rainfall record (mm/year) (Partridge *et al.,* 1997) with December insolation at 30 °S. Image modified from Simon *et al.* (2015a).

with more humid conditions in the surrounding landscape and smaller inter-seasonal and diurnal ranges of temperatures (Göktürk *et al.,* 2023b). Climate modelling results reveal that at 70 ka, compared to 82 ka, a more continental climate persisted on the coastline, due to a southward coastline shift and an increased land surface expansion, whereas inland experienced more humid conditions (Göktürk *et al.,* 2023a).

On shorter timescales, Northern Hemisphere cold events correspond to wetter conditions in eastern South Africa (Ziegler *et al.,* 2013). These humid conditions are likely caused by a southward shift in the tropical rain belt and associated rain-bearing systems which has been suggested to enhance the monsoonal precipitation in the Southern Hemisphere (Schefuß *et al.,* 2011; Ziegler *et al.,* 2013; Simon *et al.,* 2015a). The South African hydroclimate is sensitive to regional oceanic-continent interactions and atmospheric forcings (Reason *et al.,* 2000). As such, these humid periods which occurred during cold North Hemisphere events and a weak Asian Monsoon (Ziegler *et al.,* 2013), provide evidence for a teleconnection between the Northern and Southern Hemispheres, linked to the bipolar seesaw. This bipolar seesaw behaviour has been linked to changes in the strength of the AMOC and its effect on the distribution of heat between the hemispheres (Broecker, 1998). It is therefore necessary to explore in greater detail the present understanding of ocean circulation as this will enhance understanding of major ocean currents distributing heat and moisture to South Africa, influencing the continental hydroclimate.

1.4 Ocean Circulation

1.4.1 Thermohaline Circulation

Thermohaline Circulation (THC) is a conceptual view of global circulation (Figure 1.10), it is driven by fluxes of heat and freshwater across the surface waters (Rahmstorf, 2006). The North Atlantic is one of the regions where the thermohaline system is set up, composed of the northward flowing warm saline water in the upper layers of the Atlantic where the heat is released to the atmosphere with substantial impacts on climate over large regions, and a southward flow of colder saline water at depth.

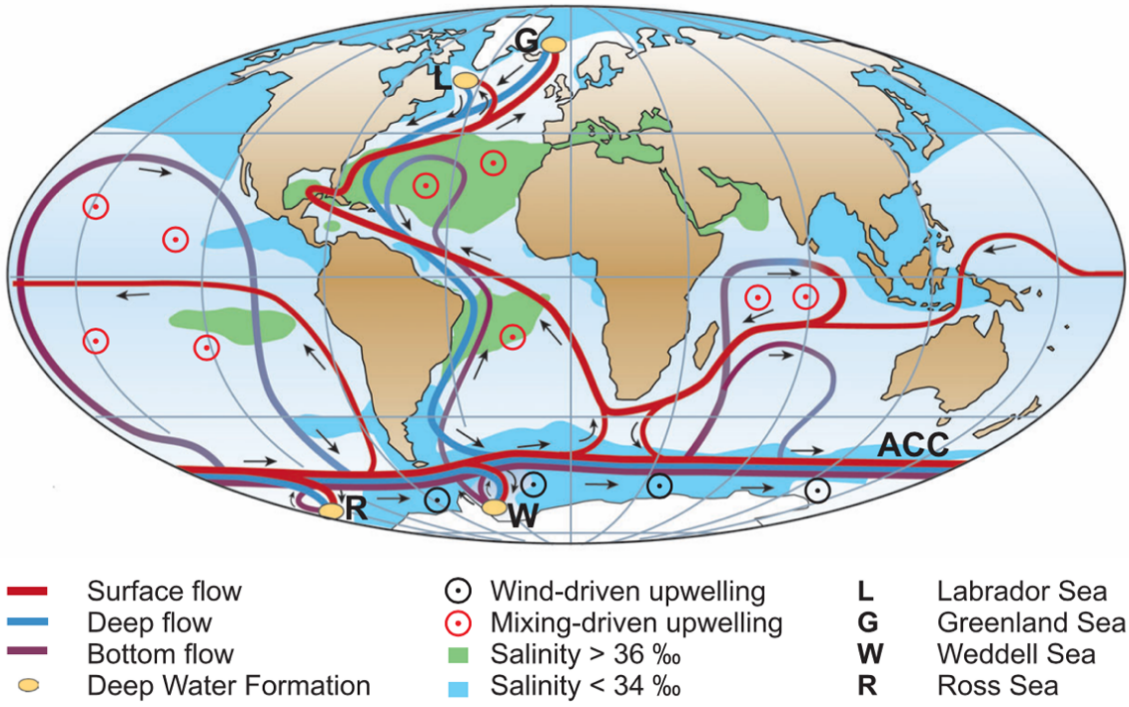

Figure 1.10: Schematic representation of the global thermohaline circulation. Surface currents are shown in red, deep waters in light blue and bottom waters in dark blue. The main deep water formation sites are shown in orange, image taken from Rahmstorf *et al.* (2006).

1.4.1.1 North Atlantic Deep Water (NADW)

North Atlantic Deep Water (NADW) formation sites are situated in the Nordic and Labrador Sea and Antarctic Bottom Water (AABW) forms in the Ross and Weddell Sea (Figure 1.10; 1.11) (Jacobs *et al.,* 1970; Foster and Carmack, 1976). The warm, shallow water in the Atlantic sector transported poleward from the tropics warms the air over the northern region of the North Atlantic and Arctic, where the near-surface waters cool becoming dense and sinking to form NADW (Toggweiler *et al.,* 2006; Talley, 2013). The densification of near-surface waters in the high latitude North Atlantic occurs through

cooling. This is because high latitude North Atlantic waters are generally less saline than low latitudes. After production in the North Atlantic, the NADW is transported southward in the deep-water cell through the Atlantic basin, then it intercepts the Antarctic Circumpolar Current (ACC) and travels eastward around southern Africa entering the southern Indian Ocean (Toggweiler *et al.,* 2006; Talley, 2013). Only a small amount of NADW moves into the Indian Ocean north of the ACC. It eventually upwells becoming Indian Deep Water (IDW) (Talley, 2013). Equatorial warming and wind driven upwelling of deep waters (Toggweiler *et al.,* 2006; Talley, 2013) in the Indian and Pacific Ocean forms surface currents which act to redistribute the warmer and fresher water masses back into the Atlantic, through the Indian Ocean (Talley, 2013). This outflow of deep-water from the Atlantic Basin is balanced by the return of surface and thermocline water across the Indian-Atlantic Ocean Gateway (IAOG) and through the Drake Passage. This is the warm water route constituting the Agulhas Leakage (section 1.4.3.1.2). Thermocline and intermediate waters travel through the Drake Passage and return to the Atlantic Ocean, this is known as the cold water route. The warm water route is believed to dominate the return supply to AMOC over the cold water route which is via the Drake Passage (Beal *et al.,* 2011a).

1.4.1.2 Antarctic Bottom Water (AABW)

The second known overturning cell is associated with Antarctic Bottom Water (AABW). AABW production in the Ross Sea, Weddell Sea and Adelie Land sectors of the Southern Ocean (Foster and Carmack, 1976; Jacobs et al., 1970) is fed predominantly by deep upwelling south of the ACC. AABW production is partly fed by northern sourced deep-water upwelling south of the ACC, as discussed above. There is a connection between the shallower circulation cell and this bottom cell. The Circumpolar Deep Waters (CDW) represent a mixing between the northern sourced NADW and the southern sourced AABW (Figure 1.11). In the Southern Ocean, the NADW experiences a negative surface buoyancy forcing and downwells forming AABW (Kuhlbrodt *et al.,* 2007). Here the AABW can follow one of two routes: if it is dense enough, the AABW sinks and propagates north. It can either flow out into the Atlantic Basin, or into the Indian and Pacific basins. At lower latitudes the AABW upwells in the Atlantic, Indian or Pacific basins, as local deep waters, to combine with NADW, IDW or Pacific Deep Water (PDW) respectively (Figure 1.12) (Talley, 2013; Ferrari *et al.,* 2014). These deep-water masses then flow back towards regions of AABW formation as Lower Circumpolar Deep Water (LCDW) (Toggweiler *et al.,* 2006). These water masses diffusively upwell, experiencing a positive surface buoyancy forcing and they return to the Southern Ocean. The less dense water masses, known as the Upper Circumpolar Deep Water (UCDW) upwell in the Southern Ocean, within the Sub-Antarctic Zone (SAZ) and eventually flow northward to complete the loop (Toggweiler *et al.,* 2006) (Figure 1.12).

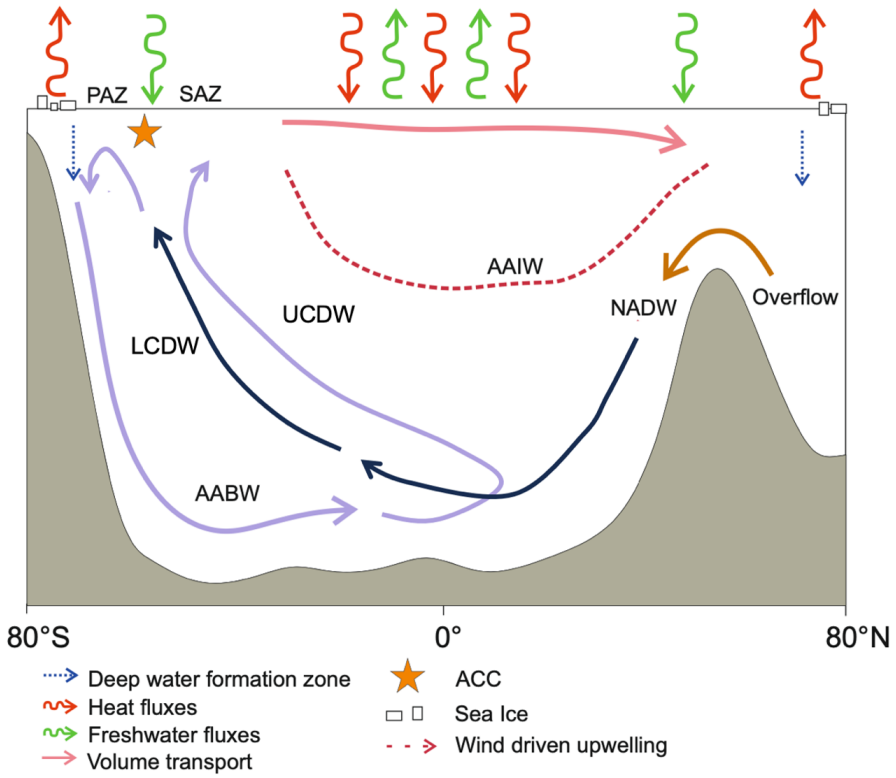

Figure 1.11: Schematic of meridional overturning for the Atlantic Ocean following Talley (2013). The navy-blue arrow represents the North Atlantic Deep Water (NADW) cell feeding into the Lower Circumpolar Deep Water (LCDW). The purple arrows represent the Antarctic Bottom Water (AABW) cell, feeding into the Upper Circumpolar Deep Water (UCDW). Upwelling occurs in the Southern Ocean in response to the Ekman Divergence across the Antarctic Circumpolar Current (ACC). The blue dashed arrows represent deep water formation in the northern North Atlantic and Southern Ocean. The dashed lines represent water- mass boundaries. PAZ = Polar Antarctic Zone.

1.4.2 Southern Ocean Circulation

The Southern Ocean is an intersection in the global ocean's water masses, connecting the Atlantic, Pacific, and Indian Oceans as well as connecting the deep ocean to the surface (Orsi *et al.,* 1995; Russell *et al.,* 2006). The SHW are the strongest oceanic winds in the world (Russell *et al.,* 2006), which drive the deep and vigorous ACC eastward around the Antarctic continent. Through Ekman Transport, these winds push the surface waters away from the Antarctic continent. This creates divergence-driven upwelling south of the current, bringing intermediate – depth water (2000–3000 m) water into contact with the atmosphere. The flow of the ACC is estimated to transport 130 Sverdrup (Sv, 1 Sv = 10^6 m^3 s^{-1}) of water (Orsi *et al.,* 1995). A series of ocean fronts which are large circumpolar bands of horizontal density gradients are associated with the ACC (Orsi *et al.,* 1995). These fronts are the Polar Front (PF) and Subantarctic Front (SAF). The PF (or Antarctic Convergence) separates Antarctic surface water from Subantarctic

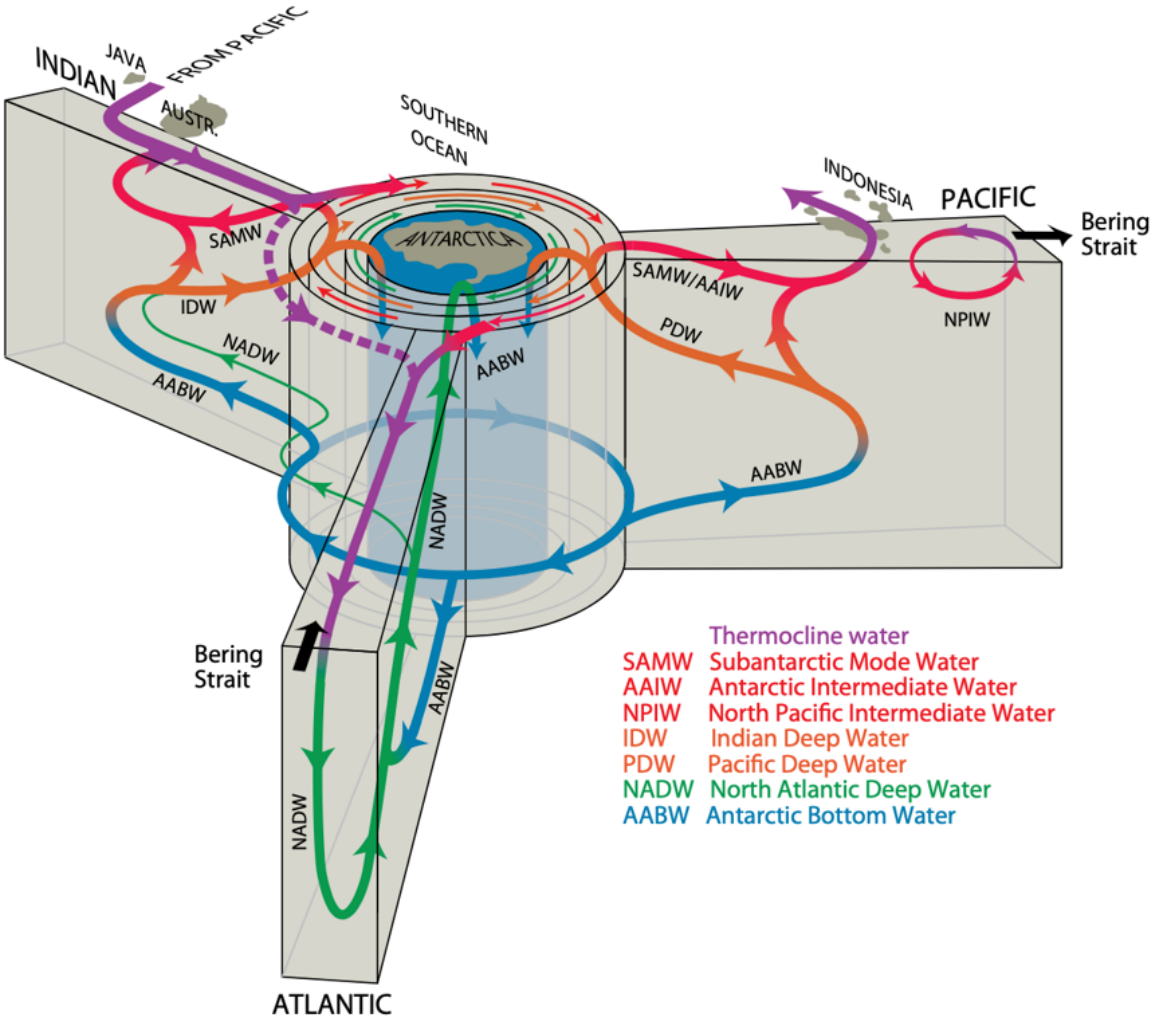

Figure 1.12: Overturning circulation from a Southern Ocean perspective, schematic from Talley *et al.* (2013). NADW transport to the south with conversion into AABW close to Antarctica (blue cylinder). Low oxygen Pacific and Indian Deep Water (PDW & IDW) further north in Antarctic Circumpolar Current (ACC) are the most direct source of the surface water that flows northward out of the Southern Ocean.

surface waters. Studies have suggested that during glacial periods, enhanced production of deep waters occurred in the zone south of the PF (Rosenthal *et al.,* 1997; Mackensen *et al.,* 2001; Bickert and Mackensen, 2003). The SAF marks the boundary between Subantarctic surface waters and Transitional surface waters associated with the rapid northward sinking related to AAIW (Orsi *et al.,* 1995). The Subtropical Front (STF) marking the northern most extent of subantarctic waters, is at times considered to be a strong current (Stramma and Peterson, 1989), rather than a surface water mass boundary yet another frequent definition of the STF is the southern boundary of the subtropical gyres (Bard and Rickaby, 2009; Beal *et al.,* 2011).

1.4.3 Agulhas Current: Past and Present

1.4.3.1 Present Agulhas Current System

The Agulhas Current System is located around southern Africa (Figure 1.13). It comprises the Southwest region of the Indian ocean, bordering the Southeast coast of Africa and separating South Africa from the ACC. The current transports waters from both the South Indian subtropical gyre, comprised of Red Sea and Arabian Sea waters, and the Indonesian Throughflow (Meyers, 1996; Tillinger and Gordon, 2009; Hall *et al.,* 2016; Wang, 2019). The waters of the Mozambique Channel, known as the Mozambique Current, and the East Madagascar Current join to form the Agulhas Current at $\sim$ 25°S (Lutjeharms, 2006; Lutjeharms, 2007). The Agulhas Current is considered the largest Western Boundary Current (WBC) in the global ocean (Lutjeharms, 2007) and transports approximately 75 Sv (Beal and Bryden, 1999; Bryden *et al.,* 2005; Lutjeharms, 2006) of surface and intermediate waters with tropical Indian Ocean origins southward towards the tip of Africa. The waters characteristic of the Agulhas have high SSTs of 22-26°C, observations suggesting 26°C in summer and 22°C in winter (Lutjeharms, 2006), and high surface salinities (approximately 35.4) (Gordon *et al.,* 1987). Upon reaching the southern limit of the South African coastline, the current retroreflects and flows eastward into the Indian Ocean as the Agulhas Return Current (Feron *et al.,* 1992). The remainder of the Agulhas Current waters 'leaks' into the South Atlantic, mostly as large warm core eddies known as Agulhas rings. The Agulhas Leakage forms part of the THC, transporting warm salty waters towards the subpolar North Atlantic as the upper limb of the overall overturning circulation. It therefore impacts global climate in a number of different ways, most notably through altering the thermohaline conditions and deep water formation in the Atlantic Ocean (Knorr and Lohmann, 2003; Biastoch *et al.,* 2008a; Marino and Zahn, 2015).

Previous studies have outlined detailed research in the spatial characteristics of the Agulhas Current (e.g. Beal and Bryden, 1999), although before The International Indian Ocean Expedition (1962-1965) and the Two World Ocean Circulation Experiment (1995) (Ffield *et al.,* 1997) there was a lack of sufficient evidence for the volume transport and geostrophic current flow of the Agulhas Current. The inaccurate measurements of the past, hampered by a lack of direct observations and means to implement this led to more contemporary scientific studies being completed, including studies (e.g. Beal and Bryden, 1999) on Agulhas System dynamics and the Indian Ocean. Previous estimates for the transport of the Agulhas Current have varied from 9 to 90 Sv (Beal and Bryden, 1997). Observations of the Agulhas Current flux using Acoustic Doppler Current Profiler (ADCP) and current moorings at the southern tip of Africa show that here, the mass transport increases to 137 Sv (Jacobs and Georgi, 1977), however Gordon *et al.* (1987) estimated this baroclinic Agulhas Current transport here to be approximately 95 Sv, indicating a spatial variability of the Agulhas Current. To discover this variability, Bryden

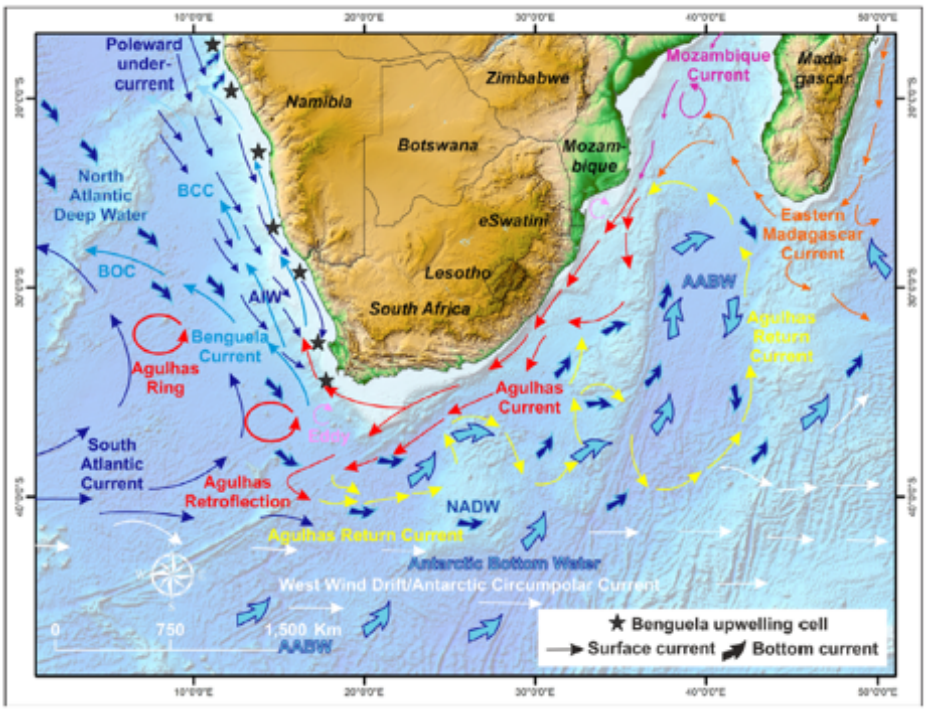

Figure 1.13: Ocean circulation patterns offshore of southern Africa from Cawthra *et al.* (2022). Abbreviations: NADW= North Atlantic Deep Water, AABW=Antarctic Bottom Water, AAIW = Antarctic Intermediate Water, BCC = Benguela Coastal Current, BOC = Benguela Ocean Current.

et al. (2005) used a moored array of current meters South of Durban, South Africa, in collaboration with the World Ocean Circulation Experiment (WOCE) to measure the transport and variability of WBCs at approximately 30 S in each ocean. The authors discovered a variation in Agulhas Current flow of between 9 Sv to 121 Sv. Further study reveals the level of no motion across the Agulhas Current which displays a V shaped pattern and detected an undercurrent flowing equatorward at ∼1000m depth (Beal and Bryden, 1999). The current itself can be considered to consist of a northern and southern section with different characteristics.

The Agulhas surface layer transports Indian Tropical Surface Water (Figure 1.14; Table 1.1) with potential temperatures greater than 20°C and salinity values between 34.7 and 35.3. This water mass, along with the South Indian Ocean Subtropical Surface Water contribute to the flow through the Mozambique Channel (Figure 1.14; Table 1.1). The Agulhas Current flows at depths of up to 1000 m and below this depth the Agulhas Undercurrent carries AAIW and NADW north-eastward below the south-westward flowing Agulhas Current (Biastoch *et al.,* 2009). Direct measurements from four different latitudes in the Agulhas Current shows the presence of the undercurrent from Gqeberha (previously Port Elizabeth) (36°S) to Port Shepstone (32°S) (Cásal *et al.,* 2009). Transport of NADW (below 2000 m) within the undercurrent is 2.3 ±3.0 Sv (Biastoch *et al.,* 2009).

Table 1.1: Water Mass properties depicted in Figure 1.14

Water Mass	Abbreviation	Temperature	Salinity
Tropical surface water	TSW	>20°C	<35.3
Subtropical surface water	STSW	>17°C	>35.6
South Indian central water	SICW	8-15°C	34.6-35.5
Antarctic Intermediate Water	AAIW	9-12°C	<34.7
North Atlantic Deep Water	NADW	3-4°C	34.8

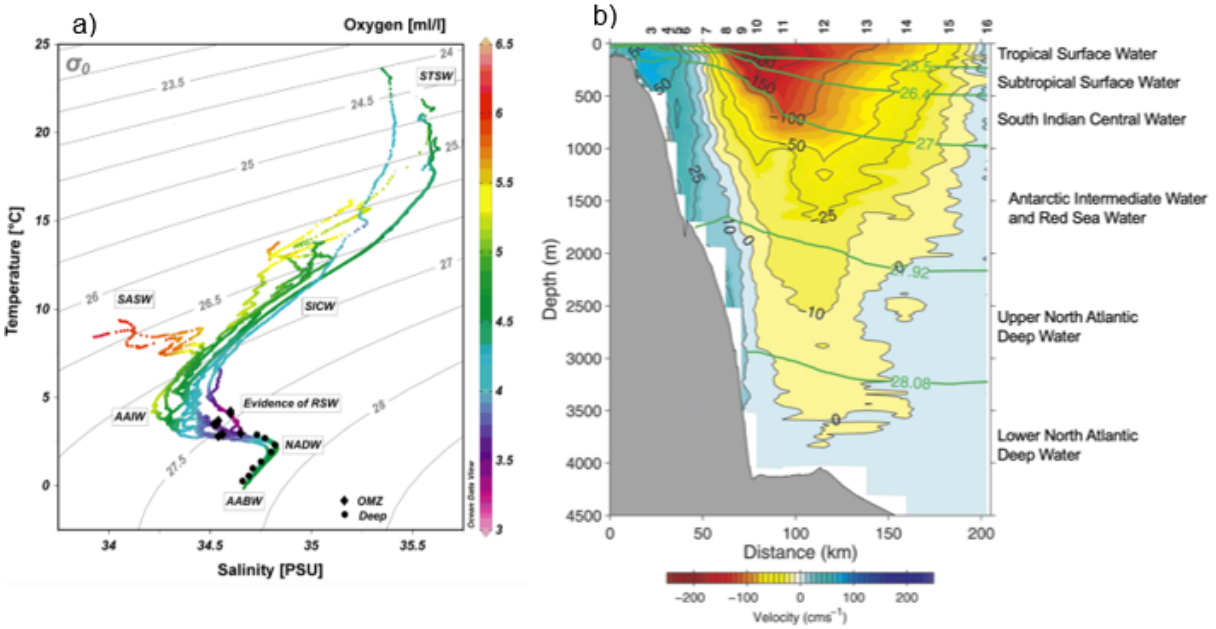

Figure 1.14: Agulhas Current structure. (a) Temperature-Salinity diagram depicting the water masses in the Agulhas Current included in Table 1.1. Oceanographic profile shows Oxygen Minimum Zones (OMZ) and deep samples based on in situ measurements of temperature (°C), salinity (psu) and oxygen (m/l). Image modified from Phoma *et al.* (2018) generated using Ocean Data View (Schlitzer, R., Ocean Data View, http://odv.awi.de, 2017). (b) Direct velocities (along-stream) across the Gqeberha (previously Port Elizabeth) section (nominally 36°S) from Beal *et al.* (2006). Red and yellow colours depict the south- westward flow of the Agulhas Current. Overlaid contours in green show neutral density layers of water masses labelled (please refer to Beal *et al.* (2006) for more information on these water masses. Boldface numbers along the top axis are station numbers.

1.4.3.1.1 Northern Agulhas Current

After the Mozambique and East Madagascar Currents join, the Agulhas Current flows southward down to the latitude of Gqeberha (33.91° S) (de Ruijter *et al.,* 1999) following the bathymetry. The current is relatively stable along the shelf break, unlike any other WBC (de Ruijter *et al.,* 1999), however when the bank widens the current loses stability and shear eddies form (Lutjeharms, 2006). The bathymetry influences the mesoscale eddy variability, these meanders and eddies are regularly able to reach the sea floor. On the Southeast African margin there is frequent sediment instability and slumping (Flemming, 1980), the movement of sediment on the narrow shelf is parallel to the current except

when the shelf widens (Lutjeharms, 2007) indicating the effect of shear eddies.

The most striking variability within the Agulhas Current are Natal Pulses. These are occasional, large, offshore meanders with associated cold core cyclonic ocean circulation within the nearshore region, propagating downstream, along the South African coast (Lutjeharms *et al.,*2001). They originate off the tip of Madagascar as eddies shed here (de Ruijter *et al.,* 1999). These Mozambique eddies moving poleward have been shown to be absorbed by the Agulhas Current (Schouten *et al.,* 2002a; de Ruijter *et al.,* 2005), triggering Agulhas ring shedding in one of two ways. Firstly, they are likely to trigger a Natal pulse (cyclonic) which subsequently brings about Agulhas ring shedding at the Agulhas Retroreflection (Schouten *et al.,* 2002a; Lutjeharms, 2007). Secondly, the migration of the eddies may lead to an occlusion of the retroreflection loop, and bring about an early retroflection (Schouten *et al.,* 2002b). These Agulhas Rings are mesoscale eddies. Natal pulses occur about 6 times per year and propagate downstream at approximately 10 km/day (Lutjeharms *et al.,* 2003). When these pulses arrive in the Agulhas Retroreflection region, they appear to trigger the formation of warm Agulhas Rings which move into the South Atlantic region (van Leeuwen *et al.,* 2000; Bryden *et al.,* 2005).

1.4.3.1.2 Southern Agulhas Current

Downstream of Gqeberha the continental bank widens, and meanders begin to form (Lutjeharms, 1989), the bottom water topography and coastline guide the current. This is where retroreflection primarily occurs, providing evidence of shedding Agulhas Rings and large vortices (Lutjeharms, 2007). The energetic rings are able to occlude themselves and form an independently circulating ring (Gordon *et al.,* 1987; Lutjeharms, 1989), carrying a substantial amount (2-15 Sv) of Indian Ocean water into the South Atlantic (Gordon, 1985). After a ring is spawned, the retroreflection retrogrades eastwards. These rings are much more consistent with WBC characteristics, they reach the southern tip of Africa, and the current can exit in one of two ways, through the Return Current which reconnects waters to the Subtropical Indian Ocean gyre (STIOG), or through a westward passage by Agulhas Leakage (Van Sebille *et al.,* 2009). The retroreflection periodically sheds anticyclonic eddies at its western extension, these rings enclose relatively warm and saline Indian Ocean water and travel westward into the South Atlantic which has temperatures and salinities lower than that of the Indian Ocean. This warm water link is likely to have a strong influence on global climate (Gordon, 1985). Shortly after flowing into the South Atlantic, the current retroreflects in an almost 180° anticyclonic turn and carries the bulk of its waters eastwards as the Return Current, back into the Indian Ocean (Feron *et al.,* 1992). The Return Current carries most of the Agulhas current back into the Indian Ocean, approximately 70-75% feeding the Subtropical Indian Ocean Gyre (STIOG) (Gordon *et al.,* 1987). The Agulhas Undercurrent flows equatorward, directly below the southwest flowing Agulhas Current. The Agulhas Undercurrent carries 40% of the Indian

Ocean overturning at 32°S (Bryden and Beal, 2001). There is evidence of an undercurrent found in the Mozambique Channel and this may be a continuation of Agulhas Undercurrent (de Ruijter *et al.,* 2002). The composition of the Agulhas Undercurrent is both NADW and AAIW (Beal and Bryden 1997). Peak undercurrent transport coincides with passing a Natal Pulse, whereas peak Agulhas Current is associated with the concurrence of Mozambique eddies (Biastoch *et al.,* 2009).

The Agulhas Leakage is the mechanism of warm water return flow to the THC. The principal carriers of the Agulhas Leakage waters are the Agulhas rings, formed through the Agulhas Retroreflection (Beal *et al.,* 2011) which acts as a control on the eastward and westward transport (Van Sebille *et al.,* 2009). It has been speculated that the Agulhas Leakage is a necessary requirement for the NADW formation, although estimations of magnitude of Agulhas Leakage and its importance for northward heat transport in the Atlantic are often contradictory (de Ruijter *et al.,* 1999; Beal *et al.,* 2011). Heat and salt loading the rings help stabilise AMOC (Biastoch *et al.,* 2008b; Beal *et al.,* 2011), this heat dispersal is highly dependent on the strong interactions between the air-sea exchanges of the atmosphere and Agulhas Current (Lutjeharms, 2007). Essentially, an increase in the exchange of positive density anomalies from the Indian Ocean leads to a more saline Atlantic and a stronger and more stable AMOC (Beal *et al.,* 2011).

1.4.4 Palaeoceanographic Reconstructions of the Agulhas Current System

In addition to direct observations of present-day Agulhas Current, palaeoceanographic studies have been carried out on materials from deep sea sediments. The factors controlling the timing and magnitude of Agulhas Leakage remain poorly understood. The two most important factors seem to link to the position of Agulhas Retroflection and Agulhas Current strength. The retroflection location may also be dependent on the volume transport and variability of the upstream Agulhas Current, in addition to the latitude of the STF.

Some studies suggest there is a negative correlation between Agulhas Current strength and Agulhas Leakage (Van Sebille *et al.,* 2009), a stronger Agulhas Current results in a reduced leakage and a more upstream (eastward) Agulhas Retroreflection, whilst other research implies a weaker Agulhas Current allows an increased leakage and a more westward Agulhas Retroreflection (Caley *et al.,* 2011). Models of the Agulhas Current predict further eastward Retroflection for larger transports and further westward penetration of the current for smaller volume transports (Lutjeharms and van Ballegooyen, 1984; Cásal *et al.,* 2009). This relationship has been confirmed by observation, but only for the case of increased transport (de Ruijter *et al.,* 2005; Cásal *et al.,* 2009). Observed increases in volume transport were caused by eddies, which increase the turbulent energy of the

Agulhas Current as well as its transport. There are uncertainties regarding whether an increased volume transport and variability are always correlated in the Agulhas Current system, or which factor is more important for the Agulhas Retroflection and Leakage.

In addition, there is inconsistent data revealing glacial-interglacial variations with Agulhas Current strength as well as the magnitude of Agulhas Leakage. Some studies show that the Agulhas Current may have been less intense during glacial times (Bé and Duplessy, 1976; Hutson, 1980; Franzese *et al.,* 2006) however, more recent studies reveal an increased transport during glacials through utilising the sortable silt flow speed proxy (van der Lubbe *et al.,* 2021). Some studies show that Agulhas Leakage was reduced during glacial periods and at its maximum at glacial terminations (Flores *et al.,* 1999; Cortese and Abelmann, 2002; Peeters *et al.,* 2004; Civel-Mazens *et al.,* 2021). Faunal assemblage studies have revealed that Agulhas Leakage reduced during glacial intervals (Peeters *et al.,* 2004; Caley *et al.,* 2014). These records revealing the surface conditions suggest that during glacial periods, a reduced Agulhas Leakage coincided with an equatorward shift in the STF (Peeters *et al.,* 2004; Bard and Rickaby, 2009; Caley *et al.,* 2012; Marino and Zahn, 2015), forcing an early retroflection (Cásal *et al.,* 2009; Van Sebille *et al.,* 2009). Some data suggests the STF may have been as far north as 31°S during glacial stages (Bé and Duplessy 1976; De Boer *et al.,* 2013; Graham and De Boer, 2013; Kohfeld *et al.,* 2013). Subsequent work shows that during the LGM, a reduced Agulhas Leakage must be explained by a weaker Agulhas Current (Franzese *et al.,* 2006; Franzese *et al.,* 2009). However, the Agulhas Current itself is a poor indicator of the strength of leakage, despite changes in temperature and salinity in Agulhas Leakage being resultant of variability in the composition of the Agulhas Current (Simon *et al.,* 2015b).

As noted above, variability in Agulhas Leakage may be related to the movement of the STF. Extensive studies researching the changes in Agulhas Current and STF off the coast of South Africa and Madagascar find changes in the position of the STF during glacial and interglacial periods (Peeters *et al.,* 2004; Bard and Rickaby, 2009; Caley *et al.,* 2012; Marino and Zahn, 2015). The planktonic foraminifera assemblage record from the Cape Basin (Peeters *et al.,* 2004) reveals a northward migration of the STF position across the last five glacial periods coinciding with a reduced Agulhas Leakage. This northward migration of the STF during glacial periods alters the distribution of high productivity sub-polar water masses (Bard and Rickaby, 2009). Variable SSTs and regional productivity are observed alongside changing westerly wind patterns and a reduced strength of circumpolar currents (Lamy *et al.,* 2015). There is still much discussion on which mechanisms drive the migration of the STF. Cartagena-Sierra *et al.* (2021) suggest the STF related reductions in Agulhas Leakage are not extensive and only occur during extreme northward migrations while Peeters *et al.* (2004) propose solar forcing related changes in the regional wind field would directly control these STF migrations, with other studies

(e.g. Bard and Rickaby, 2009) corroborating a close relationship between STF position and westerly wind patterns. However, it is unlikely that the westerly wind position and strength would alone be strong enough to force this migration, as the zero-wind stress curl and position of the STF are decoupled as the STF may migrate independently of the position of the zero westerly wind stress curl (De Boer *et al.,* 2013; Graham and De Boer, 2013). Instead, a dynamic STF is proposed to mark the eastward extension of the western boundary current of each basin and marks the southern limit of the subtropical gyre circulations. In the Indian Basin, the dynamic STF is the Agulhas Return Current (Graham and De Boer, 2013). Adding to the general understanding of the transport of the Agulhas Current System is important for improving our grasp on global climate as it plays a role in the inter-ocean link in the global THC and determining global climate mechanisms.

1.5 Terrigenous Sediments

Terrigenous sediment can be used for tracing sediment transport pathways associated with oceanic circulation patterns (e.g. Diekmann *et al.,* 2000; Diekmann, 2007; Franzese *et al.,* 2009; Noble *et al.,* 2012; Hahn *et al.,* 2017). The products of weathering from the continent are delivered to the oceans by rivers and winds, and further distributed by ocean currents. These sediments are generally deposited on continental shelves. Bottom currents redistribute sediments from the continental shelves that are originally carried to the deep ocean by turbidity currents and gravity flows. Changes in ocean current flow speed alters the transport capacity of sediment. An accelerating flow speed may cause winnowing whereas a decreasing flow speed leads to deposition (McCave *et al.,* 2017). A small amount of terrestrial material makes it to the surface of open ocean via winds, where it aggregates together through flocculation and sinks to the sea floor.

Significant amounts of terrigenous particles rain out of the Agulhas Current. These particles would be further redistributed by deep and bottom currents which they fall into (Cronin *et al.,* 2013). Sediments deposited south of Africa encompassed in this study have likely been exposed to continental weathering, fluvial and/or aeolian transport into the ocean. Linking these deposited sediments in the deep sea to their continental source region (provenance) provides a means of reconstructing past sediment input and transport mechanisms (e.g. Prospero *et al.,* 2002) to the site of deposition, as well as mechanisms occurring on land, such as hydroclimate changes. Several studies have used terrigenous sediment distribution to interpret both glacial - interglacial and modern surface and deep ocean circulation (Diekmann *et al.,* 1996; Diekmann *et al.,* 1999; Rutberg *et al.,* 2005; Franzese *et al.,* 2006; Latimer *et al.,* 2006; Franzese *et al.,* 2009; Noble *et al.,* 2012; Beny *et al.,* 2020). The Agulhas Current is capable of transporting sediment a significant distance downstream. The surface velocities of the Agulhas Current exceed approximately 2 m/s and at a 1000 m water depth flow speeds have been recorded at 10 cm/s within the

Agulhas Current (Lutjeharms, 2006; Beal *et al.,* 2011a). The speed of the ocean current relative to the settling velocity of the particles is proportional to grain size, determines the extent of long-distance transport of particles by an ocean current. Strong bottom currents which are capable of transporting sediments have flow speeds of $\sim$ 10 to 15 cm/s (McCave and Hall, 2006). Provenance tools like strontium and neodymium isotope systems (section 2.2.1.1.1) can disentangle climate-induced changes in aeolian and fluvial sediment input to the marine environment, as the communication of terrigenous sediment from on-land source via the continental shelf to the deep ocean is unique for each margin environment (Grousset *et al.,* 1988; Biscaye *et al.,* 1997; Grousset *et al.,* 1998; Diekmann *et al.,* 2003; Grousset and Biscaye, 2005).

1.5.1 Modern Sources of Sediment from South Africa

Rivers of southern South Africa have a sediment yield of $\sim 10\text{x}10^6\text{m}^3$/year supplied to the Southwest Indian Ocean (Flemming, 1981; Rooseboom *et al.,* 1992). These rivers have an average catchment size of 5,400 km^2. Sediments are an inherent mixture of particles from various sources. The Agulhas Passage located South of Africa receives sediments from local South African rivers. Sediments are additionally transported in the Agulhas Current from upstream, northern rivers such as the Limpopo and Zambezi rivers (Figure 1.15). The Zambezi and Limpopo have bigger contributions of total riverine sediment flux than the local South African rivers (see below for more information). Prevailing winds are the southeast trade winds and consequently very little aeolian sediment enters the Cape Basin from southern Africa. The Walvis Ridge acts as a barrier to the North, and little sediment enters with NADW. This means distant source regions such as South America and Antarctica, in addition to the Limpopo and Zambezi rivers can be relatively important contributors to the Agulhas Passage sediments.

1.5.1.1 South Africa Coastal Drainage Basins

There are a small number of South African rivers which drain the coastal region of the eastern Cape and southern Cape (Figure 1.15). The eastern Cape river catchments are composed of Palaeozoic Karoo sedimentary rocks (Scheffler *et al.,* 2004; Catuneanu *et al.,* 2005; Riley *et al.,* 2005; Moore *et al.,* 2009; Neumann *et al.,* 2011) and some catchments surrounding Durban drain Mesozoic Karoo basalts and Proterozoic metamorphic rocks which outcrop at various locations such as the Drakensberg Mountains. Ecca sandstones of the Karoo Supergroup have εNd bulk rock values of -7.8 +/-0.2 (Andersson *et al.,* 2003; Neumann *et al.,* 2011). The basalts which intrude the Drakensberg Mountains have a εNd value of -7.5 (Riley *et al.,* 2005). The southern Cape catchments drain the older Proterozoic Cape Granite suite, which is part of the Cape Supergroup.

1.5.1.2 Zambezi and Limpopo Drainage Basins (upstream sediment sources)

Sediments carried by the Agulhas Current have sources in the catchments of the Limpopo and Zambezi River systems, which drain to the east towards the Indian Ocean. The Zambezi River mouth is upstream of the Agulhas Current, near 19°S (Figure 1.15), and the mouth of the Limpopo River is near the latitude where the major source currents converge to form the Agulhas Current at ∼25°S.

The Zambezi Catchment is the fourth largest river catchment in Africa, with a catchment area of 1,390,000 km^2(Frenken *et al.,* 1997). It is the largest eastward draining river in Africa with an annual discharge of nearly $18x10^{12}m^3$/year (Frenken *et al.,* 1997). The geology of Zambezi catchments is characterised by Archean cratons (>2500 Ma) separated by geologically younger belts, which are eroded by the drainage of the Zambezi River (Figure 1.15) (Hargrove *et al.,* 2003).

To the South of the Zambezi, the Limpopo river is the second largest eastward draining river in Africa (Figure 1.15), with a river catchment size of 408,000 km^2, and is associated with sediment input with a signature of older, more radiogenic (higher) $^{87}Sr/^{86}Sr$ ratios and lower εNd values. The Limpopo deposits sediment (discharge of $4.8x10^{12}m^3$/year (Frenken *et al.,* 1997)) into the Delagoa Bright which is a distinct indentation in the continental margin (Lamont *et al.,* 2010). It drains the oldest geological basements on the African continent, the Kaapvaal and Zimbabwe cratons (Jelsma and Dirks, 2002; Eglington and Armstrong, 2004). The oldest parts of these cratons comprise of small low grade Palaeo-Archean volcano-sedimentary greenstone belts (>2700 Ma), which are dominated by gneiss and granite (SADC, 2010). These older cratons are surrounded by a series of younger orogenic belts comprising of metamorphic rocks and granites (SADC, 2010). The oldest of these younger orogeneses is the Limpopo Belt, which developed from a collision of the Kaapvaal and Zimbabwe cratons during the late Archean (Kreissig *et al.,* 2000) - it is made from reworked older cratonic rocks through high grade metamorphism (SADC, 2010).

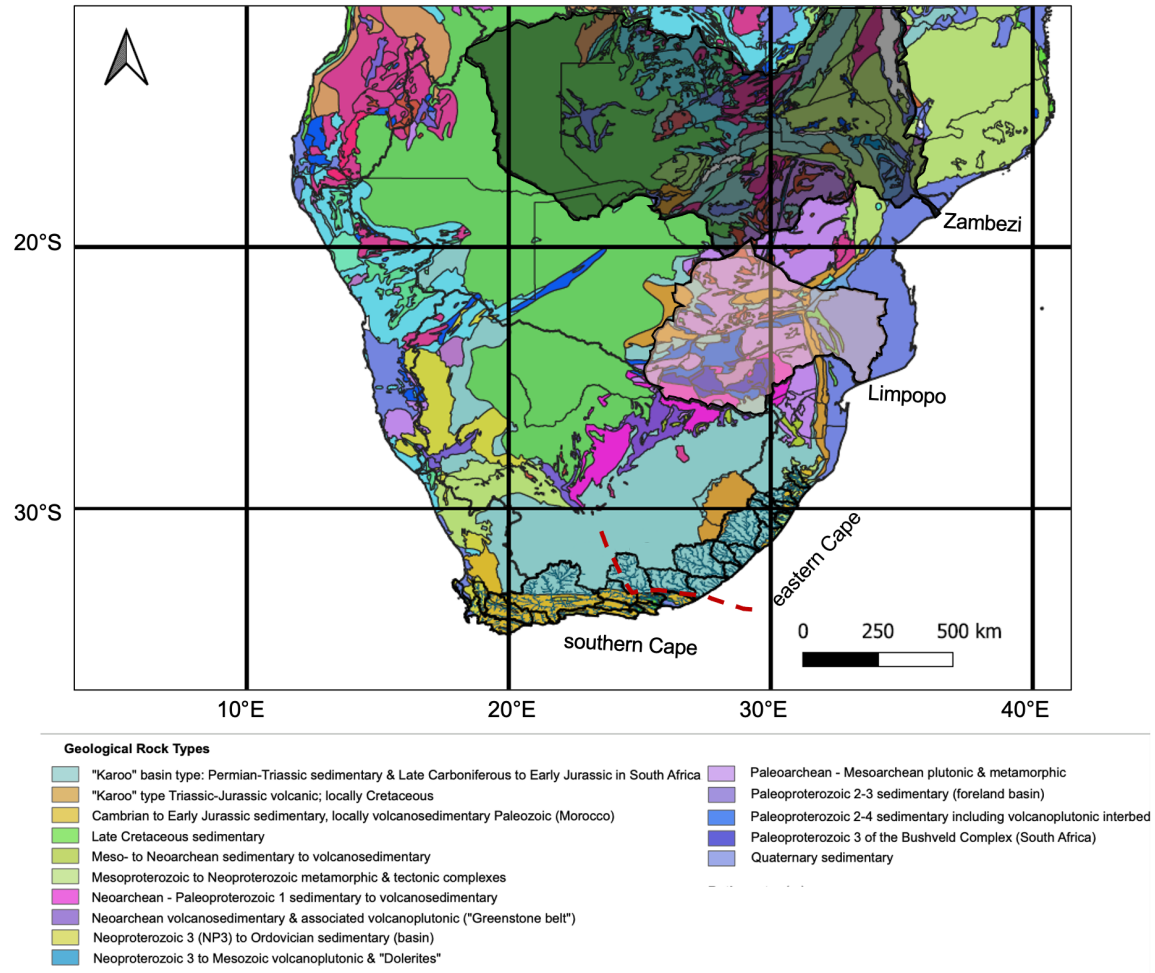

Figure 1.15: Geology of southern Africa from Thieblemont *et al.* (2017) with major river catchments overlain (South African coastal rivers, Limpopo and Zambezi rivers). Red dashed line represents the cut off between eastern Cape and southern Cape referred to throughout this thesis.

The previous published results documented below give catchment fingerprints of the Zambezi and Limpopo catchments. The surface sediments of the Mozambique Shelf clays have εNd values indicating a strong influence of Zambezi between -17.7 to -16.2. This value is indicative of a pure Zambezi signal because the Mozambique Shelf receives sediments directly from the Zambezi River (van der Lubbe *et al.*, 2014, 2016). Clays extracted from the adjacent continental slope display more radiogenic (higher) εNd values of -15.8 to -14.7. Modern detrital clays in the central Mozambique Channel at 17°S and 2700 m water depth and from the continental slope at 15°S and 2800 m water depth yield respective εNd values of -14.4 and -11.2. Site IODP U1476 (15.49°S, water depth 2166 m; (Hall *et al.*, 2016)) yields radiogenic εNd values of $\sim$ -13.0 from surface samples (i.e. the first 60 cm of sediment). Offshore Zambezi sediments which are applied in Chapter 4 for provenance reconstructions are mixed to some extent with clays characterised by more radiogenic εNd signatures from the North (cf; van der Lubbe *et al.*, 2016). The $^{87}Sr/^{86}Sr$ isotope composition from inland Zambezi are $^{87}Sr/^{86}Sr = 0.721$ and $\varepsilon Nd = -13.024$ from Garzanti

et al. (2014), and offshore Site IODP U1476 values are $^{87}Sr/^{86}Sr$ = 0.731 (<2 µm) and εNd = -13.758. There is limited data from the region on $^{87}Sr/^{86}Sr$ isotopes. We note that $^{87}Sr/^{86}Sr$ isotopes are affected by a grain size offset and that the study conducted by Garzanti *et al.* (2014) used a coarser size fraction (<32 µm) than targetted in this thesis (<2 µm). Therefore, grain size offsets might explain these Sr isotope differences.

South of the Zambezi sourced regions, sediment from the Limpopo catchment yield unradiogenic εNd values of –26 and –31, draining the Kaapvaal and Zimbabwe Cratons (Garzanti *et al.,* 2014). Site IODP U1478 (25°49.26'S, water depth 488 m; (Hall *et al.,* 2016)) sediment displays more radiogenic εNd values than the Limpopo catchment with values between –19.8 to -17.5 (Simon *et al.,* 2020a). Muds from the Limpopo tributaries draining the Kaapvaal and Zimbabwe Cratons have distinctly high $^{87}Sr/^{86}Sr$ signatures (between 0.73 and 0.78) (Simon *et al.,* 2020a). However, Limpopo mud has a lower $^{87}Sr/^{86}Sr$ value (<2 µm) and less negative εNd, with a younger Paleoproterozoic age, suggesting a more significant contribution from Karoo basalts (Simon *et al.,* 2020a). River sediment radiogenic isotope endmembers used in this study are from upstream Limpopo and Zambezi rivers based on published data from Simon *et al.* (2020a); van der Lubbe *et al.* (2014) and Garzanti *et al.* (2014), as well as local South African river endmembers generated from data in Chapter 3.

Sediments delivered to the Agulhas Passage and Natal Valley by the South Atlantic Current (SAC) and ACC have their sources in South America, as well as the Antarctic Peninsula and the Falkland and Shetland Islands. South American sediment sources are generally younger than South African sources, due to the presence of the Andean volcanic arc. Model results reveal there was significant Patagonian dust in the Southern Ocean during the LGM (Li *et al.,* 2008) and radiogenic isotope studies also reveal that Patagonian dust is the most significant glacial source region to Antarctica (Grousset *et al.,* 1992; Basile *et al.,* 1997; Delmonte *et al.,* 2008). This is likely controlled by glacial - interglacial fluctuations in Patagonian glaciers (Diekmann *et al.,* 2000; Marinoni *et al.,* 2008; Sugden *et al.,* 2009). During the LGM, a lower sea level distributed vast amounts of sediment via outwash plains and fluvial systems from the Andes, providing a major source of dust. Studies show that during the LGM, these Patagonian sourced sediments were capable of longer distance transport because the SAC and the ACC increased in strength during the LGM (Hemming *et al.,* 2007; Noble *et al.,* 2012).

Bulk $^{87}Sr/^{86}Sr$ data from the Antarctic peninsula range from 0.7030 to 0.7043 and εNd from +3.6 to +7.3 (Lawver *et al.,* 1995). Holocene bulk sediments from two deep-sea cores in the Scotia Sea have $^{87}Sr/^{86}Sr$ = 0.7090 and 0.7123 and εNd = -4.4 and -5.7 (Walter *et al.,* 2000), reflecting mixing of the South American and Antarctic sources. Walter *et al.* (2000) do acknowledge the Sr grain size offset and find lower $^{87}Sr/^{86}Sr$ ratios in the clay fraction compared to the silt fraction. South Atlantic studies show a $^{87}Sr/^{86}Sr$ range of

0.708 to 0.714 and εNd = -4 to -8 on the <63 µm fraction (Franzese *et al.,* 2006).

The AABW may carry sediments with a younger provenance from the Antarctic Peninsula and the islands in the Weddell Sea, as well as sediments with a much older provenance from East Antarctica. Mesozoic Karoo-related basalts from Dronning Maud Land, Antarctica, have $^{87}Sr/^{86}Sr$ ratios ranging from 0.7045 to 0.7083 and εNd from -17.4 to +2.5 (Luttinen *et al.,* 1998). Rocks from East Antarctica have εNd values ranging from -7 to -46 and $^{87}Sr/^{86}Sr$ values from 0.71 to 0.78 (Basile *et al.,* 1997). These East Antarctic sources do not seem to affect the composition of sediments offshore of South Africa but may influence South Atlantic sediments south of ∼50°S, especially during the LGM (Hemming *et al.,* 2007)

In general, it appears that the bottom waters transport particles of a similar composition to those transported by the ACC (young continental material, with relatively low Sr and high Nd). One exception may be the NADW passing through the Agulhas Passage, it is possible that these waters pick up sediment during their passage. This material would have a composition representing a mixture of all the various sources described in this section.

1.6 Major Themes and Thesis Structure

Blombos Cave coastal archaeological site in the southern Cape of South Africa, exhibits artefacts from the LMSA interval, 100-50 ka; a time interval when human cognition and technological advances underwent rapid development. Research suggests this cognitive evolution of early modern humans was facilitated by environmental and climatic conditions in the region. A huge effort is being made by SapienCE to understand the drivers of these technological advances, by using archaeological evidence from MSA cave sites located in the southern Cape.

This thesis aims to advance the understanding of the terrestrial hydroclimate of South Africa and oceanic variability in the Agulhas Current region during the key LMSA time interval. The terrigenous sediment fraction of river material from South African coastal river catchments has a distinct sediment signature which drains into the Southwest Indian Ocean. The fine sediment (clay fraction; <2 µm) is transported within the Agulhas Current. Marine sediment from core sites located within the main flow of the Agulhas Current serve to reconstruct the provenance changes of sediment, through a source to sink approach to reconstruct the hydroclimatic record during the LMSA interval.

One such marine sediment core, MD20-3591 (36° 43.707 S; 22° 9.151 E, water depth 2464 m) (Figure 1.1), located offshore of Blombos Cave, extends back to 450 ka. It has the potential to record both terrestrial and oceanic variability. The provenance of deposited terrestrial sediments at site MD20-3591 could play an important role in reconstructing sediment delivery by different South African rivers related to terrestrial hydrology and

transport pathways from continental sources further afield such as upstream from the Limpopo and Zambezi rivers (transported downstream in the Agulhas Current). This is of key importance for understanding transport history and characterising sediment source regions in the marine and terrestrial environment.

The Agulhas Current traverses the core site location, before retroflecting back into the Southwest Indian Ocean. This ocean current may have behaved differently in the past, having significant implications on coastal human settlements in the region. Further to this, sea level is an important driver in this region, oscillating between high stands during interglacials and low stands during glacial periods. During the last glacial low stand, the wide continental shelf South of Africa was sub-aerially exposed, and rivers flowed across this plain within a subdued incised valley delivering their sediments to the ocean.

The first part of this thesis aims to identify the origin of sediments deposited within the Agulhas Current region, and specifically in proximity to marine core site MD20-3591. This is achieved by using river sediments from coastal river catchments between Durban and Cape Town in South Africa. The provenance source is identified through mixing bedrock geology signatures with radiogenic isotope compositions to find two key endmembers, from the Karoo and Cape Supergroup. Additionally, grain size analysis and clay mineralogy help to understand what is driving the sediment composition of the South African river catchments to fingerprint each drainage basin for provenance work.

The second part of this thesis considers whether it is possible to distinguish local South African provenance signals from distal (far-field) signatures by isolating different sediment size fractions. This is achieved by using geochemical proxies measured in Modern and Last Glacial Maximum dated time-splices from a suite of sediment cores along the south and southeast African coastline. Different size fractions are more prone to certain transport signals or processes, therefore differentiating transport signals based on size fractions (<2 µm, 2-10 µm and 10-63 µm) allows the interpretation of possible sorting mechanisms.

A central theme to this research is the connection between continental and oceanic processes operating on the southern and southeastern coastline of South Africa determining the sediment supply and distribution during the last glacial cycle. This study uses geochemical proxies to identify the terrestrial sediment source of clay sized detrital sediment, transport pathways and hydroclimate changes on the southern Cape region of South Africa, and the timing of these changes, which likely linked with the early human archaeological record. The third part of this thesis analyses all multiproxy records of bulk geochemistry (XRF), grain size data and radiogenic isotopes ($^{87}Sr/^{86}Sr$, εNd) from marine sediment core MD20-3591 during the LMSA interval to infer the driving mechanism of hydroclimate variability this time period of archaeological significance.

1.7 Questions in this thesis

The main aims of this research are:

- To identify modern day river sediment as radiogenic isotope endmembers for provenance reconstructions.
- To provide new insights in sediment dynamics through linking terrestrial sediments, primarily eroded from South African river catchments with offshore terrigenous sediment deposition during the last glacial cycle.
- To identify Modern and Last Glacial Maximum changes in sediment sources offshore of South Africa.
- To develop a robust age model for marine sediment core MD20-3591 using radiocarbon dating and graphical tuning to LR04 to help address whether the terrestrial fraction of marine sediments reveal variability in southern Cape river catchments hydroclimate during the past 450 ka by comparing to other marine core records.
    - To additionally fine tune to the Hulu-Sanbao record to infer millennial scale variability
- To link hydroclimate changes to the archaeological record during the MSA in harmony with the SapienCE key findings.

The scientific results and findings are structured into three main chapters (Chapters 3, 4 and 5) addressing the main objectives detailed above. Chapter 6 synthesises key results from Chapters 3,4 & 5 and links to the archaeological record and concludes the main scientific results and future ideas. Chapter 2 summarises techniques and methods used in this study.

Chapter 2 | Materials and Methods

What tempest blow me into that deep ocean of ages past, I do not know – Ole Worm

So far from home, where the ocean stood, down dust and pine cone tracks - Old Pine - Ben Howard

2.1 Site Settings

The main palaeoclimate archive discussed and used in this thesis is marine sediment core MD20-3591 (36°43.707 S; 22°9.151 E, water depth 2464m; Figure 2.1), a CALYPSO giant piston core recovered onboard the R.V Marion Dufresne during the cruise MD225 ACCLIMATE-2 (09/02/2020 – 01/0/3/2020 Durban – Durban). This research cruise was dedicated to collecting high resolution marine sediment cores from different latitudes and water depths in the Southeast Atlantic Ocean (Vazquez-Riveiros and Waelbroeck, 2020).

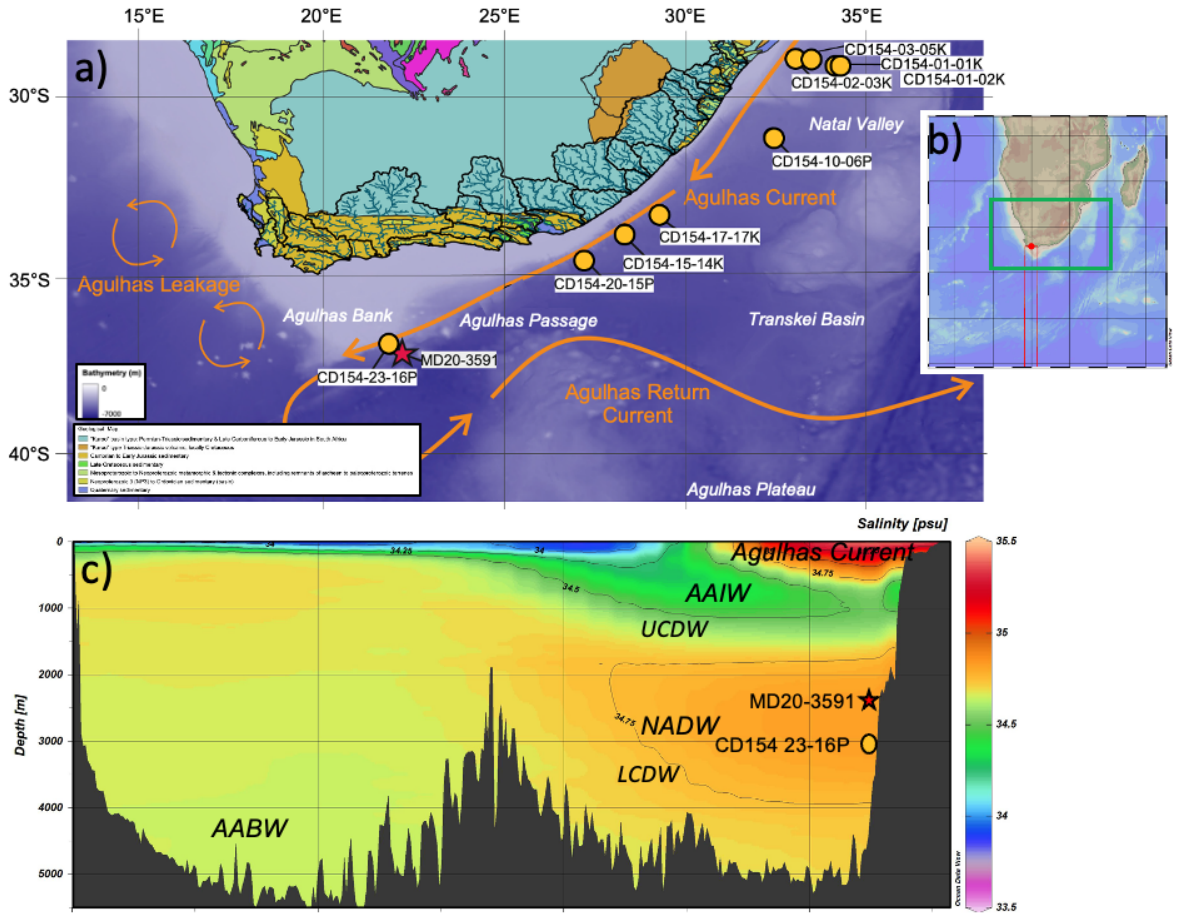

Figure 2.1: Modern Hydrography of Agulhas Current region with core sites discussed in this thesis. (a) Map of South Africa included in green box in inset (b). Geological base rock with key on left (Thieblemont, 2017). Bathymetry from BODC, drainage basins and rivers from Hydro1K. (b) Map of the Agulhas region with sections (red for salinity profile (from World Ocean Atlas) and green box for map of South Africa); (c) Present day latitudinal transect of salinity from the coast of South Africa to 70°S.

Additional marine core sites used and discussed in Chapter 4 of this study are CD154-02-03K, CD154-03-05K, CD154-01-01K, CD154-01-02K, CD154-10-06P, CD154-15-14K, CD154-17-17K, CD154-20-15P and CD154-23-16P (Figure 2.1; Table 2.1). The NERC funded project 'Agulhas Leakage and Abrupt Climate Change: the past 50,000 years' onboard the RV Charles Darwin cruise CD154 aimed to retrieve sediment samples in

the Agulhas Current region. River sediments from South African drainage basins were collected systematically between Durban and Cape Town (29°48.583 S - 34°18.8 S) during March 2020, the collection of these materials is discussed in Chapter 3.

Table 2.1: List of marine sediment core sites used in this study, arranged in order of water depth.

Site	Latitude (°S)	Longitude (°E)	Water Depth (m)
CD154-02-03K	29.070	32.770	1626
CD154-03-05K	29.120	32.890	1747
CD154-01-01K	29.300	33.150	1997
CD154-01-02K	29.280	33.160	2019
MD20-3591	36.910	22.150	2464
CD154-10-06P	31.180	32.160	3076
CD154-23-16P	36.820	22.000	3189
CD154-15-14K	33.730	28.200	3236
CD154-17-17K	33.270	29.120	3333
CD154-20-15P	34.460	27.150	3583

The aim of this chapter is to describe sedimentary settings of the marine sediment cores collected and used in this study. Furthermore, it will describe the palaeoceanographic and geochemical proxies applied in this study and their analytical details used for specific research questions.

2.1.1 Modern Oceanography at Site MD20-3591

The intersection between the Atlantic and Indian Ocean is one of many oceanic gateways connecting surface and deep-water masses around the globe, redistributing heat, salt, and nutrients between oceans. South of the Agulhas Bank is an intersection for oceanic currents (Figure 2.1) as such major surface currents interact in this zone. These are Antarctic Circumpolar Current (ACC), South Atlantic Current (SAC) and the Agulhas Current. The Agulhas Current is the main oceanographic feature of the surface waters in this region (Figure 2.1c). It flows south along the coastline of South Africa, following the narrow continental shelf and steep continental slope (Speich *et al.,* 2006). It marks the western boundary current of the Southwest Indian Subtropical Gyre (SWIOG) with a total volume flux of 70 Sverdrup (Sv, 1 Sv = 10^6 m^3 s^{-1}). Site MD20-3591 is located off the continental shelf of South Africa (Figure 2.1a (red star)) within the Agulhas Passage. The Agulhas Passage is situated between the Agulhas Bank and Agulhas Plateau, connecting the Transkei Basin and Natal Valley (Figure 2.1). The MD20-3591 core site is presently located directly under the southernmost reach of the Agulhas Current, close to the region where the current detaches from the continental shelf and undergoes a retroreflection forming the Agulhas Return Current. At a water depth of 2464m, Site MD20-3591 lies within the present day Agulhas Undercurrent and is bathed in North Atlantic Deep Water (NADW) and Upper Circumpolar Deep Water (UCDW) (Vazquez-Riveiros and Waelbroeck, 2020) (Figure 2.1c). It is approximately 1000 m below Antarctic Intermediate Water (AAIW) and $\sim$ 1000 m above Lower Circumpolar Deep Water (LCDW) (Figure 2.1c).

2.1.2 Sedimentology

The Agulhas Passage, situated south of the Natal Valley receives sediment from upstream carried in the Agulhas Current, from the South Atlantic via NADW and from South Africa through river discharge. The narrow continental shelf has deliveries of large volumes of clastic sediment delivered by rivers from the South African continent (Figure 2.2) (Cawthra *et al.,* 2014; Hahn *et al.,* 2018).

The inner and outer continental shelf is powerfully swept southwest by the surface Agulhas Current (Goodlad, 1986), influencing the bedload transport along the continental shelf and delivering sediment to the heads of well-developed submarine canyon systems (Flemming, 1981; Green, 2009). This reveals the importance of the Agulhas Current concerning sediment transport and redistribution (Flemming, 1981). The velocity of the Agulhas Current fluctuates which means it is relatively unsteady like other geostrophic flows, transporting approximately 75 Sv (Beal and Bryden, 1999; Bryden *et al.,* 2005; Lutjeharms, 2006). This is probably caused by combined effects of local wind stress, meandering, and lateral migration of the mean flow path (Flemming, 1981). These changes

in velocity likely drive the mechanism for large-scale sand dunes, ripples and sand-streams seen in this region (Flemming, 1980).

The sediment is further distributed across the steep continental slope by wave regime and wind-driven circulation (Flemming, 1981). The area is classified as a high-energy environment, dominated by south-westerly swells, with average wind speeds exceeding 15 knots. Topographically induced eddies have been observed in this region, due to the vorticity structure of the Agulhas Current (Flemming, 1981), alongside a direct correlation between wind stress and velocity (Pearce *et al.,* 1978).

Sea level is another likely driver of sediment distribution across the Agulhas Bank, referred to as the Palaeo-Agulhas Plain (PAP) throughout this thesis. Large amplitude ($\sim$ 120 m) (Grant *et al.,* 2014) glacial to interglacial sea level fluctuations would have directly impacted the exposure of the PAP with more exposure during glacial low stands. When the PAP was sub-aerially exposed, rivers flowed across this plain within subdued incised valleys delivering terrigenous sediments to the ocean. These rivers changed their courses during glacial sea level low stands, cutting through the PAP and creating different routes to the Southwest Indian Ocean (Cawthra *et al.,* 2020). It is likely bedload sediment dispersal is more dominant during the glacial low stands as very little fine to medium-grained Holocene sediment is being further distributed via submarine canyons (Green, 2009). These canyons aid the transfer of hemipelagic sediment to the margin and offshore currents redistribute these continental sediments.

There is evidence of deep-sea circulation zones of erosion, reflected by the flow of Antarctic Bottom Water (AABW) and NADW (Rogers, 1987; Niemi *et al.,* 2000; Reznikov *et al.,* 2005). One such zone is at the foot of the continental rise, fed by slumps, debris flows and canyon-fed turbidity currents, perpendicular to the margin (Figure 2.2). These topographic configurations restrict the northward flow of AABW. Contouritic drifts have been known to form from AABW at water depths greater than 4500 m in the Transkei Basin (Reznikov *et al.,* 2005). The presence of contourites has been shown along the southeast African margin (Flemming, 1981; Ramsay, 1994; Faugères *et al.,* 1999; Preu *et al.,* 2011) but at present distinguishing between contourites and other deep-sea deposits such as fine sand turbidites of mixed composition solely based on lithological facies in cores is not widely recognised (Rebesco *et al.,* 2014). Seismic data provides evidence of strong current systems present which have formed the Agulhas Drift, orientated east-west deposited as AABW exits the Agulhas Passage into the Transkei Basin. Here AABW dissociates from NADW which continues to flow eastward into the Natal Valley. The Mozambique Ridge drives the NADW east and then south, back to the mouth of the Natal Valley. Here it flows into the Indian Ocean (Niemi *et al.,* 2000).

Deep-sea sediments can be divided into terrigenous, non-biogenic material originating mostly from adjacent continents, and biogenic components of deep-sea sediments origi-

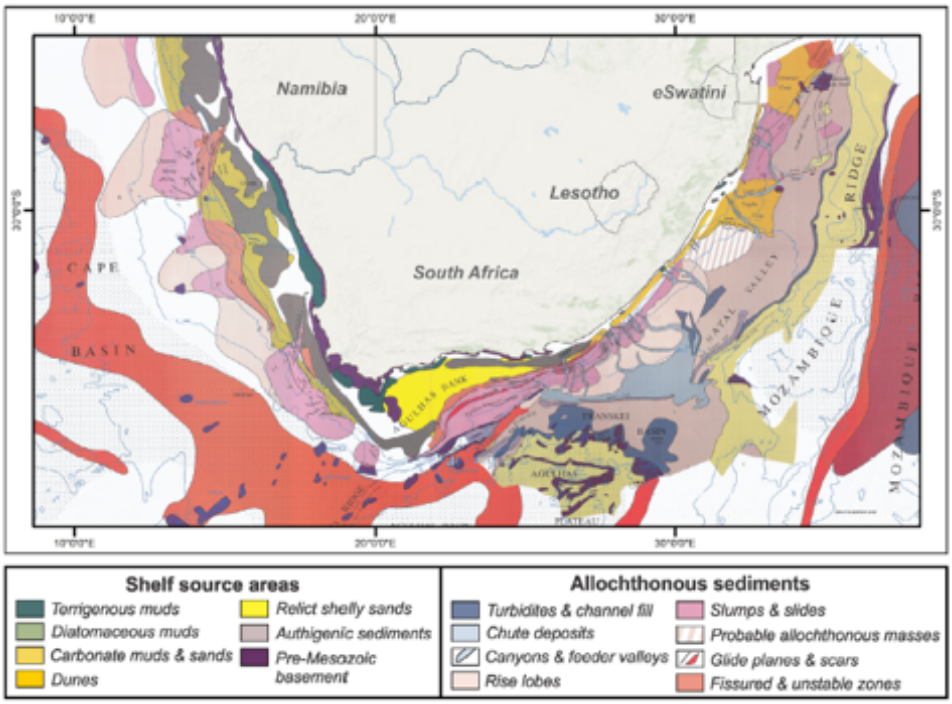

Figure 2.2: Offshore South Africa sedimentary environments, from Cawthra *et al.* (2021). Site MD20-3591 is indicated by the black star and is sourced in a region with prevalent slumps and slides.

nating mostly in the local water column. The latter, derived from skeletal assemblages of marine organisms, contains carbonate ($CaCO_3$) ooze or silicious ooze. Its preservation is controlled by the $CaCO_3$ saturation state of overlying seawater. Pressure increases with depth, which leads to increased $CaCO_3$ dissolution. This causes a limit below which dissolution exceeds preservation (known as the Carbonate Compensation Depth (CCD)). Studies have shown that the carbonate dissolution was minimal during the Late Pleistocene (Diz *et al.,* 2007; Molyneux *et al.,* 2007). As site MD20-3591 is located at a water depth of 2400m which is shallower than the CCD at 4000m, this prevents significant dissolution and means well-preserved carbonate rich organisms such as foraminifera will be present. Preservation does however depend on the prevalence of super-saturated NADW and more corrosive southern-sourced deep waters (González-Dávila *et al.,* 2011).

2.2 Palaeoceanographic Proxies and Techniques

2.2.1 Geochemical Proxies

In this study, geochemical proxies are used as a reference indicator for reconstructing environmental change such as determining the physical, biological and chemical properties of the ocean and atmosphere of the past. These archives rely on applying the techniques specific to the compound in use such as sediments, ice and tree rings. The most widely used proxies in palaeoceanography utilise the biogenic component of marine sediments.

These originate mostly in the local water column and are mainly carbonate rich. Deep sea sediment can also be classified as the terrigenous component, which is non-biogenic, and originates mostly from far-field continents. This section briefly introduces the proxies used in this study to reconstruct various palaeoclimatic parameters.

2.2.1.1 Environmental Signals in Terrigenous Sediment

2.2.1.1.1 Radiogenic Isotopes Systematics

Neodymium (Nd) is a Rare Earth Element (REE). REEs have low boiling points so are known as refractory elements (Taylor, 1980). ^{143}Nd is the radiogenic daughter of ^{147}Sm, therefore Sm/Nd and ^{143}Nd/^{144}Nd differences are considered important in radiogenic isotopes studies and can indicate provenance changes. This is because it is assumed that the relative abundances of REEs in Earth are the same as in the chondritic meteorites. There is a general assumption that the solar system was isotopically homogenous when the Earth formed, hence the initial ^{143}Nd/^{144}Nd ratio should be identical to the initial ^{143}Nd/^{144}Nd ratio of other bodies formed 4.55 billion years ago (Jacobsen and Wasserburg, 1980). As the bulk Earth ^{143}Nd/^{144}Nd ratio at any given time is known, it is useful to consider the relative deviation of ^{143}Nd/^{144}Nd from the bulk Earth value (Depaolo and Wasserburg, 1976; Jacobsen and Wasserburg, 1980; Dickin, 1995). These deviations are small so are written in parts in 10,000 as an epsilon notation (ε). The εNd value is defined as follows:

$$\varepsilon Nd = \left(\frac{(^{143}Nd/^{144}Nd)_{sample} - (^{143}Nd/^{144}Nd)_{CHUR}}{(^{143}Nd/^{144}Nd)_{CHUR}}\right) \times 1000 \tag{2.1}$$

where CHUR stands for 'chondritic uniform reservoir' as (^{143}Nd/^{144}Nd) $_{CHUR}$ is the value of the ratio in chondrites (Jacobsen and Wasserburg, 1980). The value of (^{143}Nd/^{144}Nd) $_{CHUR}$ is 0.512638 for the present (Depaolo and Wasserburg, 1976; Jacobsen and Wasserburg, 1980).

Radiogenic isotopes such as neodymium (εNd) and strontium (^{87}Sr/^{86}Sr) are widely used to trace sediment provenance because the neodymium and strontium isotopes of continental detritus depend on their Sm/Nd and Rb/Sr ratios and rock ages (Grousset and Biscaye, 2005). The isotopic composition of bulk sediments can provide information regarding the provenance of the sediment over time (Grousset *et al.,* 1988; Goldstein and Hemming, 2003; Riley *et al.,* 2005; Jonell *et al.,* 2018; Carter *et al.,* 2020). The primary control on neodymium and strontium isotopes is bed rock geology, different source regions have a varied geology, therefore the input from different regions is reflected in the radiogenic isotope composition of the bulk sediment (McLennan *et al.,* 1989; Clift *et al.,* 2002; Bayon *et al.,* 2015; Hahn *et al.,* 2016; Maccali *et al.,* 2018; Bayon *et al.,* 2020; Carter *et al.,* 2020; Blanchet *et al.,* 2021).

This primary Sr signature is determined by (^{87}Sr/^{86}Sr) and the parent-daughter ratio (Rb/Sr). As Rb is more incompatible than the daughter Sr, a higher Rb/Sr is found

in igenous rocks which make up the continental crust and a lower Rb/Sr signature is found in mafic igneous rocks from the oceanic crust. Rivers draining older crust should have a relatively radiogenic Sr and unradiogenic Nd than rivers draining younger crusts (Goldstein and Jacobsen, 1987). $^{87}Sr/^{86}Sr$ isotopes and εNd therefore have an inverse relationship, tying these two systems together and making it possible to estimate an average isotopic composition of Sr based on Nd isotopic data (Goldstein and Jacobsen, 1987).

2.2.1.1.1.1 Neodymium Isotopes For Provenance

Many εNd studies have utilised the detrital fraction to constrain sediment sources. Detrital clays in marine sediments retain their Nd isotopic signatures from continental weathering through transport processes to diagenesis (Goldstein *et al.,* 1984; Depaolo, 1988).

εNd can be used as a tracer of geological provenance of the terrigenous fraction of marine sediments as it does not fractionate significantly during processes, such as chemical weathering so is largely unaffected by grain size (Goldstein *et al.,* 1984; Blum and Erel, 2003; Fagel *et al.,* 2004; Fagel, 2007; Meyer *et al.,* 2011; Garzanti *et al.,* 2014; van der Lubbe *et al.,* 2014; Hahn *et al.,* 2016; van der Lubbe *et al.,* 2016; Hahn *et al.,* 2018). However, studies dealing with chemical weathering and Nd isotopes are sparse.

2.2.1.1.1.2 Strontium Isotope Compositions

In contrast to Nd isotopes, strontium isotopes are affected by secondary impacts such as weathering and grain size, therefore a change in $^{87}Sr/^{86}Sr$ does not necessarily reflect a change in provenance (Banner 2004; Feng *et al.,* 2009; Meyer *et al.,* 2011; Jonell *et al.,* 2018). $^{87}Sr/^{86}Sr$ isotope ratios increase with decreasing grain size (Dasch, 1969; Biscaye and Dasch, 1971; Grousset *et al.,* 1992; Blum and Erel, 2003; Feng *et al.,* 2009; Meyer *et al.,* 2011). The first study of radiogenic isotope behaviour during weathering was initiated with a comparison of fresh and altered igneous rocks, which found that a high $^{87}Sr/^{86}Sr$ ratio of sediments indicate a higher rainfall intensity and chemical weathering rate (Dasch, 1969), this is because Sr isotopes are easily removed from the source region (Blum and Erel, 1997, 2003). As Sr isotopes fractionate during weathering and transport processes; therefore, they are a powerful tool to represent changes in on-land hydrology and chemical weathering (Goldstein and Jacobsen, 1988; Blum and Erel, 2003; Meyer *et al.,* 2011; Noble *et al.,* 2012; Bayon *et al.,* 2015; Hahn *et al.,* 2016; Roddaz *et al.,* 2020).

2.2.1.1.2 Clay Mineralogy

Clay minerals are good indicators of environmental changes as the oceans are fed sediments from riverine and aeolian inputs and have been used as a tracer of provenance in studies of the world's ocean (Figure 2.3) (Biscaye, 1965; Diekmann *et al.,* 1996; Diekmann *et al.,* 2000; Marinoni *et al.,* 2008). Clay particles are produced through geochemical pathways, most significantly from weathering. Clay minerals consist of tetrahedral and octahedral sheets (given as ratio 1:1 (kaolinite) or 2:1 (montmorillonite and illite) or 2:1:1 (chlorite))

comprising the interlayered cations (Chamley, 1989). Clay minerals are either formed by in situ precipitation from a solution in continental or marine sedimentary basins (authigenic clays) or by continental weathering processes (detrital clays) (Fagel, 2007). Authigenic clays provide insight into the geochemical environment, whereas detrital clays record weathering conditions in the adjacent landmass (Velde, 1995). Detrital clays are broken down from rocks by physical or chemical weathering and transported by major rivers, via surface runoff, and atmospheric circulation to their sedimentary deposits (Fagel, 2007).

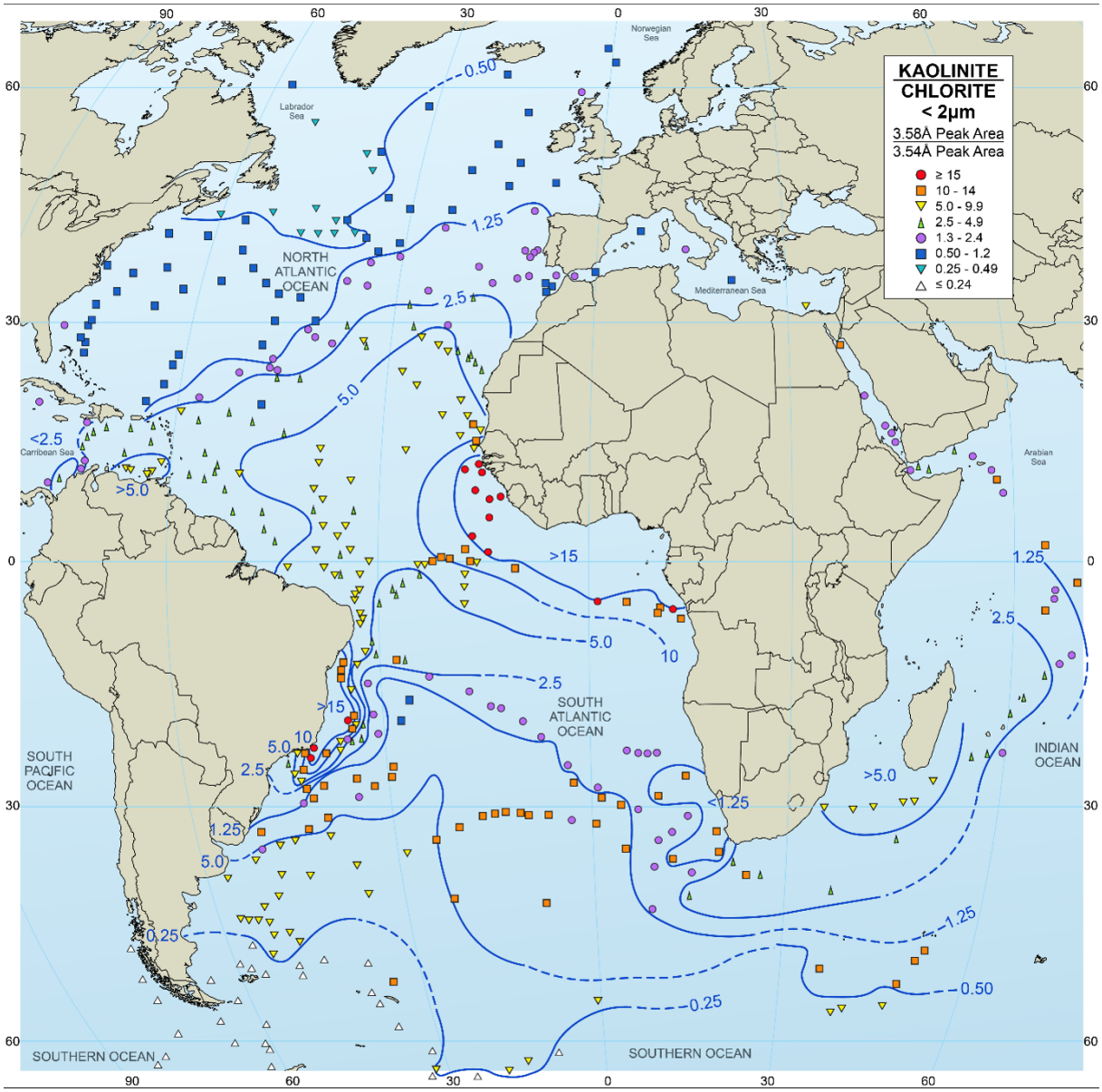

Figure 2.3: Kaolinite/Chlorite ratio in clay fraction <2 µm for global ocean, image updated from Biscaye, 1969.

Provenance studies often utilise clay mineralogy as the clay-based sediments reflect their origin (Figure 2.3). Clay mineralogy has been used to trace ocean transport (Biscaye, 1965; Petschick *et al.,* 1996) as in given water mass, fine-grained clay minerals can be advected over considerable distances to finally settle far away from their original source.

Previous studies over large oceanic areas (Figure 2.3) (Biscaye, 1965) show that major clay mineral abundance patterns are influenced by the interaction of continental sources and ocean distribution mechanisms (Moriarty 1977). In Atlantic Ocean sediments, there is a striking geographical distribution patterns for the main clay minerals (Figure 2.3) (Biscaye, 1965); and these patterns are controlled by climatic and weathering zonation on adjacent land masses, which suggests that most clay minerals are terrigenous (Biscaye, 1965; Chamley, 1989). In addition, the abundance of clay minerals does not solely reflect changes in weathering conditions of the continental source area, this is because diagenesis can entirely remove the palaeoenvironmental record of deposited clay minerals (e.g. Zabel *et al.,* 1999; Worden and Morad, 2000; Fagel, 2007). The provenance signal can be removed by erosion and transport processes, certain other processes like sediment recycling, transport processes or sorting by the energy of transport medium may make the relationship of the geology in the source area and endmembers observed in the deposited sediments difficult to deconvolve (Singer, 1984; Haughton *et al.,* 1991). Therefore, coupling radiogenic isotope analyses with clay mineralogy is a more powerful method of identifying sediment provenance.

2.2.1.1.3 Bulk Sediment Geochemistry

Insights into past climate can come from measuring the chemistry of the sediments. X-Ray Fluorescence (XRF) scanning is a relatively quick way of measuring the elemental concentrations of bulk sediments. XRF scanning is a non-destructive technique which allows continuous records of elemental intensities. However, it is important to convert elemental intensities measured by XRF core scanners to quantitative element concentrations. There are numerous approaches for quantitative applications, such as mass-balance and flux fusion calculations, therefore XRF core scanning is usually presented in the form of count rates (a unit time per unit area), or as ratios of counts (Dunlea *et al.,* 2020).

Ratios between elements can provide additional information on the palaeoenvironment, such as variation Fe/Ti, K/Ti and K/Fe, used to characterise terrigenous sources (Kujau *et al.,* 2010). Additionally, Stuut *et al.* (2007) found geochemical XRF data documented latitudinal shifts in precipitation gradients based on terrigenous input through aeolian and fluvial sources. K/Ti ratios have been used to emphasise differences in terrigenous material relating to illite and mica presence (Diekmann *et al.,* 2008), and finally, Fe can be used as a terrigenous indicator and Ca to record marine productivity and biogenic Ca input (Møller *et al.,* 2006).

2.2.1.2 Environment Signals in Biogenic Sediment

2.2.1.2.1 Foraminifera: Time Machines

Foraminifera are unicellular, eukaryotic organisms abundantly distributed in the global oceans. They secrete a shell, known as a test, made of calcium carbonate ($CaCO_3$). The information extracted from these tests, using geochemical proxies, can help determine the

environmental conditions the foraminifera experienced at the time it secreted the test. When microorganisms in the ocean take ions (Ca^{2+} and CO_3^{2-}) from the surrounding water to grow their calcite shells, the composition of the surrounding water is reflected in the isotopic composition of the calcite matrix. There is an isotopic equilibrium between H_2O and CO_3^{2-} where the isotopic ratios of oxygen isotopes are proportional between the two molecules, which means that the isotopic composition of the foraminifera shell is directly linked to the isotopic composition of the surrounding seawater (Cooke and Rohling, 1999). Species of foraminifera live in different depths of the water column. Benthic foraminifera are deep sea dwelling organisms, living at the seafloor whereas planktic foraminifera are free-floating and drift through the surface layers of the water column via ocean currents.

Foraminifera can be referred to as time machines due to their good preservation, abundance, and widespread distribution in marine sediments. Stable isotope measurements on foraminifera (Emiliani, 1955; Shackleton & Opdyke 1973; Shackleton, 1977) have helped improve marine stratigraphy through graphical correlations of oxygen isotope records to reference curves (Prell *et al.,* 1986). This advance in palaeoclimate studies is perhaps the most renowned way method of age model generation, through tuning sediment core records to an astronomical timescale such as the orbitally tuned benthic oxygen isotope stack of LR04 (Lisiecki and Raymo, 2005).

In addition to utilising the stable isotope composition of foraminifera tests, the chemistry of a foraminifera test can provide a suite of additional geochemical proxies, such as palaeothermometers (such as Mg/Ca (Rosenthal *et al.,* 1997), nutrient proxies (e.g., Cd/Ca, (Boyle, 1988)) and carbonate chemistry proxies (such as boron isotopes (Yu and Elderfield, 2007)).

2.2.1.2.2 Formaminiferal Stable Isotopes

2.2.1.2.2.1 Oxygen Isotopes Ratios in Foraminifera

The two main forms of oxygen isotopes are ^{16}O and ^{18}O when concerning the oxygen isotope analysis in marine sediments. The ratios of these two isotopes are measured as deviations, not as absolute terms, relative to a laboratory standard (Equation 2.2). The oxygen isotope ratio of foraminiferal calcite tests ($\delta^{18}O_{foram}$) is well established as a proxy for palaeoceanographic work.

$$\delta^{18}O = \left(\frac{(^{18}O/^{16}O)_{sample} - (^{18}O/^{16}O)_{standard}}{(^{18}O/^{16}O)_{standard}}\right) \times 1000 \tag{2.2}$$

For planktic foraminifera analysis we used *Globerigerinoides ruber* and for benthic foraminifera we picked *Cibicicoides wuellerstorfi* (Schwager, 1886) which is an epifaunal foraminifera. *G. ruber* is a warm water species and is highly abundant in tropical-subtropical waters, where SST is between 14 and 30°S (Funnell and Riedel, 1971). *G. ruber* is dependent on the symbiotic relationship with dinoflagellate algae for nutrients in low nutrient olig-

otrophic surface waters.

The temperature dependency of $\delta^{18}O$ fractionation between water and $CaCO_3$ has been applied to reconstruct past variations in sea surface temperatures for long standing times (Emiliani, 1955). Later work on oxygen isotope variations observed in marine sediments revealed that the past variations of whole-ocean seawater $\delta^{18}O$ ($\delta^{18}O_{sw}$) are largely driven by the growth and decay of large ice sheets during glacial-interglacial cycles (Shackleton, 1967). Though this complicates the use of $\delta^{18}O_{foram}$ as a proxy for ocean temperatures, its use in palaeoceanography is invaluable. This means the isolation of the temperature dependent component of $\delta^{18}O_{foram}$ and extraction of the $\delta^{18}O_{sw}$ component is possible, when this $\delta^{18}O_{sw}$ is corrected for the effects of changing ice volume with sea level records (Waelbroeck *et al.,* 2002), it becomes possible to constrain the local $\delta^{18}O_{sw}$ signal of $\delta^{18}O_{foram}$ providing a qualitative indication of salinity changes (Rohling, 2007).

Estimation of an absolute value of $\delta^{18}O_{sw}$ is difficult in deep time due to a number of variables such as the absence of direct measures, errors associated with the proxies which the $\delta^{18}O_{sw}$ is derived from, and the variability of $\delta^{18}O_{sw}$ with respect to global ice volume and evaporation-precipitation. Vital effects are additional biases which are needed to be understood when studying foraminiferal test stable isotopes. These are biological processes which can cause the tests to be calcified out of equilibrium with seawater dissolved inorganic carbon (DIC) (Ravelo and Hillaire-Marcel, 2007). For example, calcification at lower temperature decreases the metabolic uptake of ^{12}C, increasing the stable carbon isotopic composition of foraminiferal calcite ($\delta^{13}C$) (Bemis *et al.,* 2000) and higher carbonate ion concentrations have been shown to decrease $\delta^{13}C$ (Spero *et al.,* 1997). Physiological processes such as respiration can also cause this disequilibrium (Spero *et al.,* 1991).

2.2.1.2.2.2 Carbon Isotope Ratios in Foraminifera

Carbon isotopes are non-conservative, reflecting the partitioning between organic and inorganic carbon phases. The $\delta^{13}C$ reflects the carbon isotopic composition of the DIC of the ambient seawater in which they calcified ($\delta^{13}C_{DIC}$). Carbon has two naturally occurring isotopes which are fractionated during a range of natural processes with their ratio being calculated as a deviation from a laboratory standard (Equation 2.3).

$$\delta^{13}C = \left(\frac{(^{13}C/^{12}C)_{sample} - (^{13}C/^{12}C)_{standard}}{(^{13}C/^{12}C)_{standard}}\right) \times 1000 \tag{2.3}$$

Biological production at the ocean surface leaves the $\delta^{13}C$ of inorganic carbon at higher values and remineralisation in the subsurface drive the $\delta^{13}C$ of inorganic carbon to lower values. *C.wuellerstorfi* is an epifaunal benthic foraminifera (Schwager, 1886), hence they are capable of recording ambient near surface bottom water chemical and isotope composition (Duplessy *et al.,* 1984). This benthic species is widely used as a palaeoceanographic tool as it believed to precipitate calcite with $\delta^{13}C$ in or close to the ambient bottom water

$\delta^{13}C_{DIC}$ (Mackensen *et al.,* 2001).

The δ^{13}C of benthic foraminiferal calcite is a tool used to trace deep water masses. Differences in source water and deep-water formation mechanisms for northern (i.e. NADW), southern sourced water masses (AAIW and AABW) has lead to different δ^{13}C values upon formation, recorded in the foraminifera. This can be attributed to the caveats associated with benthic foraminiferal calcite, such as biological productivity changes (Mackensen Effect), air-sea gas exchanges and changes in in the distribution of carbon between various reservoirs, and changes in water mass geometry and water mass mixing. The biological control on δ^{13}C involves photosynthesis in surface waters which primarily uses ^{12}C and nutrients, as they are more bioavailable, enriching the waters in ^{13}C and depleting them in nutrients. The formation of organic matter, enriched in ^{12}C and nutrients, in the surface, sinks through the water column and eventually settles on the ocean floor, which through time is oxidised releasing ^{12}C and nutrients. This means young, nutrient depleted water masses such as NADW, (or the region where NADW forms), have high δ^{13}C signatures (heavy), and older nutrient rich waters that have been isolated for a long time from the atmosphere have increasingly negative values of δ^{13}C with increasing age. The δ^{13}C at a given location within the ocean may change through time as a function of variations in the regional water-mass geometry (and ocean circulation), and changes in mixing ratios between water masses with different characteristic carbon isotopic compositions (Curry and Oppo, 2005). The mean δ^{13}C of the whole ocean is determined by the partitioning of carbon between the ocean, atmosphere, and terrestrial reservoirs. The changes in the size of the terrestrial biosphere on glacial- interglacial timescales impacts the mean δ^{13}C of the whole ocean, the preferential uptake of ^{12}C during photosynthesis by terrestrial plants results in the sequestration of carbon with a low δ^{13}C ratio during photosynthesis (-10 to -30% depending on the photosynthetic pathway (Bender, 1971)).

2.2.1.3 Grain Size Analysis

The size of a particle of marine sediment is directly dependent on the type of environmental setting and the mechanisms of transport, production and depositional conditions (e.g. McCave and Hall, 2006). The purpose of grain size analysis is to 1) obtain a deeper understanding of palaeo-environmental features (e.g. Weltje and Prins, 2003; Holz *et al.,* 2004; van der Lubbe *et al.,* 2014; van der Does *et al.,* 2021), 2) to reconstruct past sedimentary transport histories (Stuut *et al.,* 2002; McCave *et al.,* 2014; Lamy *et al.,* 2015), or 3) analyse in detail instantaneous depositional events such as debris flows (e.g. Harvey *et al.,* 2022). Different size fractions are more prone to transport via certain processes therefore by isolating specific grain size classes, it is possible to separate the transport mechanisms such as ocean currents and river or aeolian transport (Meyer *et al.,* 2011). For example, the 10-63 µm size fraction is notably known to reflect bottom flow speeds (McCave and Hall, 2006) through reflecting a current sorting signal, or the

aeolian dust signal within the 10-40 µm fraction (Meyer *et al.,* 2011) found also through endmember decomposition (Stuut *et al.,* 2002).

2.2.1.3.1 Endmember Modelling

In terms of grain sizes of sediments supplied from the continent and deposited offshore, the terrigenous grain size distributions represent a mixture of fluvial discharged mud, wind-blown dust particles and ice rafted debris, and therefore show either a bimodal or polymodal grain size distribution pattern (Weltje and Prins, 2003). The mix of sediment populations derived from different sources and transported to the site of deposition by different mechanisms represents a problem with palaeoclimatic reconstructions from the terrigenous fraction of marine sediments (Weltje and Prins, 2003). Therefore, an approach is needed to distinguish the groups of sediment, i.e., allochthonous[1] and autochthonous[2].

Endmember modelling is based on a mathematical-statistical algorithm which attempts to explain the observed variations in sediments as a result of mixing (Weltje, 1997). It unravels measured polymodal grain size distributions into sub-populations (Weltje, 1997). The mixing model is subject to strict non-negativity and constant sum of constraints on endmember compositions and mixing coefficients to ensure the model parameters can be interpreted. An endmember modelling algorithm was applied to determine the proportion of distinct sediment components contributing to the measured particle size signal (Weltje, 1997; Stuut *et al.,* 2002). The algorithm output is a series of models, each model explains a different amount of variance. The higher the number of endmembers, the more the variance explains the data.

There are several assumptions implemented to derive a mixing model from a series of compositions. One such assumption is the endmembers must be independent and cannot be expressed as a mixture of the other endmembers as this is required to estimate their number independent of their compositions. Several studies do verify endmembers for distinct sediment types i.e. for ice rafted debris (Prins *et al.,* 2001; Prins *et al.,* 2002), fluvial mud (Prins *et al.,* 2000), and aeolian dust (Stuut *et al.,* 2002). In this thesis, the endmembers have been successfully calculated from measured detrital grain size distributions for marine sediment offshore South Africa, and terrestrial river samples from South Africa, to provide a representative interpretation of observed terrigenous grain size distributions with regard to dominant transport mechanisms offshore of South Africa.

Mechanisms of sediment production, transport and deposition favour certain characteristics such as sediment grain size (McCave, 2008). Endmember modelling is a metric for describing particle size distribution of different sub-populations. Here, we decompose the grain size distributions of the total grain-size dataset into discrete endmembers, which allows us to identify the major grain size components in the overall size distribution, which

[1] displaced from the original site of origin

[2] in situ

are typically different transport processes. This can be further related to the grain-size effects on the isotopic measurements to verify whether it is possible to target certain fractions (i.e. <2 µm). Through identifying endmembers, we can assign each endmember with a particular mode in the size distribution to a certain sediment transport process.

2.2.1.3.2 Sortable Silt Mean Grain Size

The sortable silt mean grain size ($\overline{SS}$) palaeo-current proxy is a measure of the mean grain size of the 10-63 µm size fraction of the terrigenous sediment component (McCave *et al.,* 1995). This $\overline{SS}$ proxy can be used to infer relative changes in the near-bottom speeds of the currents which deposit the material because of its non-cohesive nature and the dependence of its size sorting on hydrodynamic processes. The <10 µm fine end of the $\overline{SS}$ size fraction is not included because the presence of clays results in aggregation and flocculation. The deposition of the fine end of this size fraction is unrelated to the hydrodynamic processes which determine the size sorting of the 10-63 µm. The 10-63 µm fraction generally displays size sorting in response to hydrodynamic processes and is hence a sensitive tool for inference of palaeo-current intensity. This is because the resuspension and deposition actions of sediment by particle size selection depends on the particle settling velocities and fluid shear stress acting on them. At a given shear stress, some grains are deposited whilst other grains with a lower settling velocity remain in suspension (McCave *et al.,* 1995). Therefore, by determining the mean grains size of the non-cohesive 10-63 µm fraction, it is possible to reconstruct the strength of near-bottom flow. Larger particle mean grain size (i.e. higher $\overline{SS}$) results from stronger near-bottom flow speeds and smaller particle mean grain size (lower $\overline{SS}$) from slower near-bottom currents (McCave and Hall, 2006)

2.3 Analytical Methods

2.3.1 Sediment Processing

Marine sediment core MD20-3591 was sliced in half – the archive and working half are stored in Norwegian Research Centre (NORCE), University of Bergen (UiB). All samples were taken from the working side and have various spacing depending on the time interval.

For this work, samples were taken from marine sediment core MD20-3591 for;

i.) radiogenic isotope analyses on samples every 4 cm (∼ 0.63 ka resolution) for the LMSA (384-660 cm) and every 16 cm (∼ 2 ka resolution) for the remaining glacial cycle

ii.) grain size analyses every 4 cm for the last glacial cycle (0-896 cm)

iii.) for planktic stable isotope analyses every 8 cm (∼ 1 ka resolution) for the first 896 cm and every 24 cm (∼ 3 ka) for the remaining core

iv.) benthic stable isotope analyses on samples every 2 cm (0.3 ka resolution) for depths 412-564 cm (80-60 ka), every 4 cm for 384-660 cm (same samples as radiogenic isotopes and grain size) and every 24 cm for rest of core (same samples as planktic stable isotopes).

20 marine sediment samples were also taken for bulk elemental analysis for major element analysis in order to calibrate the XRF scanning data, these selected sampling depths were based on Ti/Ca ratios. See section 2.5.3 on Speleothem age model for more information on how ages (ka) based on sediment depth (cm) were generated.

In preparation for radiogenic isotope (Sr and Nd) work, marine and riverine sediment were washed and wet sieved at 63 µm to separate the coarse (>63 µm) and fine (<63 µm) sediment fraction. 1-2 g of the <63 µm dry fraction was placed in 40 ml of 2M acetic acid on a shaker table for >8 hours. The samples were topped up with de-ionised (DI) water and left to settle overnight. The diluted acid was removed by siphon and 20ml of 6% Hydrogen Peroxide was added to the samples and put on the shaker table for 6-8 hours. The samples were topped up with DI water and left to settle overnight. The diluted acid was removed by siphon and samples were placed in 40 ml of buffered acetic acid on a shaker table for >8 hours. The samples were topped up with DI water and left to settle overnight. The diluted acid was removed by siphon and the samples were transferred to 50 ml centrifuge tubes. Subsequently, 20 ml of Hydroxylamine Hydrochloride (HH) solution was added to the samples and samples were put on the shaker table for a minimum of 8 hours. The samples were then centrifuged for 30 minutes (2400 rotations per minute) and the clear HH solution was decanted. If the HH solution was colourless, only one leach was necessary. If the HH solution was (red/orange) tinted, the HH leaching was repeated until the supernatant appeared colourless. Samples were subsequently cleaned with DI water. This is the sequential leaching procedure used for removal of organic component, carbonates, and Fe-Mn oxyhydroxides based numerous methods (Bayon *et al.,* 2002; Gutjahr *et al.,* 2007; Blaser *et al.,* 2016; Simon *et al.,* 2020a; Simon *et al.,* 2020b). The separation of particles smaller than 2 µm was carried out using 5 ml 0.5% sodium metaphosphate using a centrifuge (section 2.3.2) and after fully suspending the sample by vortexing. To separate the 2-32 µm fraction, the residual samples (>2 µm) were wet sieved using a <32 µm sieve and dried at 40°C overnight.

Fe-Mn coatings provide a sink for REEs, therefore must be removed via a leaching procedure (Blaser *et al.,* 2016). Additionally, carbonates act as a buffer preventing acid-induced mobilisation of the Fe-oxides, this is why a two-step decarbonation is performed, to ensure all carbonates are removed. The terrigenous fraction inherently carries non-authigenic Nd isotope signatures and pre-formed Fe-Mn (not derived from contemporary, ambient sea water) which can be a source of contamination.

2.3.2 Grain Size Separation - A Case Study

Given radiogenic isotope datasets reflect analyses on a variety of size fractions, a grain size separation method is presented which will lead to more comparable datasets with consistent size fraction separation. A wide range of techniques have been used to separate different grain size fractions from a bulk sediment sample. These include: 1) wet and dry sieving (e.g. Buller and Mcmanus, 1972; Gee and Bauder, 1986), 2) micro-filtration (e.g. Minoletti *et al.,* 2009), 3) settling and decanting (e.g. Simon *et al.,* 2020b) and 4) centrifugation (e.g. Stumpt, 2011; Bayon *et al.,* 2015). These methods typically require significant amounts of bulk sediment (often up to ∼3g) (Bayon *et al.,* 2015) or require considerable amounts of time during sediment processing (Bayon *et al.,* 2015; Simon *et al.,* 2020b). For radiogenic isotopes sample preparation and analysis (typically requiring a minimum of 20mg of sediment in a specific size fraction), the common method for isolating size fractions prior to analysis is either settling and decanting (Simon *et al.,* 2020b) or centrifugation (Stumpt, 2011; Bayon *et al.,* 2015); however, there is no standard protocol identified with a low time cost and small sample size of the initial sediment.

Here the experimental design and tests are introduced. These were employed to present the recommended method for isolating precise grain size classes from the <63 µm fraction. This study focuses on the use of centrifugation as this approach provides the shortest processing times and is therefore most likely to provide a suitable approach for high throughput sample processing necessary to support proxy reconstructions that require many samples (typically high-resolution or long timescale studies).

2.3.2.1 Experimental Set-Up

According to Stokes' Law, the settling velocity of a particle is proportional to the density difference between the particle type and the liquid phase, inversely proportional to the viscosity of the liquid, and proportional to the square of the particle diameter. Equally, within a centrifuge, Stokes' Law, can be used to calculate the time of rotation required to separate specific size fractions according to Equation 2.4 (Hathaway 1955), which describes the relationship between time (T) and different components of the centrifuge and material being processed.

$$T = \left(\frac{\eta log_{10}(\frac{R_2}{R_1})}{3.81 r^2 N^2 (\rho - \rho_0)}\right) + \left(\frac{2(t_a + t_d)}{3}\right) \tag{2.4}$$

Where:
T = total time (sec)
η = viscosity (poises)
R_2 = final distance from rotation axis (cm)
R_1 = initial distance from rotation axis (cm)

N = angular velocity (rev/sec)
r = particle radius (cm)
ρ = density of particle (g/cm^3)
ρ_0 density of displaced media (g/cm^3)*
t_a = time of acceleration (sec)
t_d = time of deceleration (sec)

* The grain density of quartz (2.65 g/cm^3) is used for this method.

To determine the specific settings for the experiment, the effect of the different key variables in Equation 2.4 were considered. These are, a) grain density parameter, ρ, b) angular velocity, N. The effect of changing the initial sample size was also explored to determine if this affected final clay fraction (wt %).

All experiments were carried out using a Thermo Scientific™ Sorvall™ ST 16 Centrifuge Series. The following initial settings were selected: R_1 = 6cm, R_2 = 17cm, acceleration = 5.26 seconds and deceleration = 15.2 seconds, according to Equation 2.4. These parameters were designed to reduce sediment processing time.

2.3.2.1.1 Grain Density Parameter (ρ) The lithogenic composition of most marine sediment is dominated by light minerals, mainly quartz (Grain density = 2.65 g/cm^3) and feldspar (2.57 to 2.77 g/cm^3). The dominance of these light minerals results in average grain densities for marine sediments of about 2.65 g/cm^3 for most grains > 63 mm (i.e., sand). This grain density assures the removal of the majority the quartz grains if a 2 µm separation is carried out, although some particles of less dense minerals could remain in suspension (Hathaway 1955). As some studies utilising this updated centrifuge method will be using carbonate-rich sediments (e.g. coccolith studies), we considered the higher grain density for calcite particles (2.71 g/cm^3) we calculate the difference in centrifuge time, relative to a quartz grain density, to be ∼0.3 seconds in our experiments. Given this increase in centrifuge time is negligible compared to the time of centrifuge deceleration time (∼15.2 seconds) we applied a grain size density of 2.65 g/cm^3 for calculating the centrifuge times for all experiments.

2.3.2.1.2 The Angular Velocity Parameter (N) The effect of changing parameter N, the angular velocity, was tested for various spins when separating the finest fraction (2 µm) from the lithogenic sediment samples. Adjusting the angular velocity modified the total spin time (T), resulting in either a time too low for the centrifuge setting (<1 minute), or increasing the processing time. The revolutions per minute (rpm) tested were 500, 1000 and 2000, and all tests resulted in a successful size fraction isolation for the lithogenic sediment samples. However, 500 rpm took longer for the sediment to settle and 2000 rpm resulted in a very settled sediment which for future steps took longer to unsettle when

using the vortex. Therefore the angular velocity was set to 1000 rpm for the first three steps of separation to maximise the low processing time.

2.3.2.1.3 Sediment Material - Initial Sample Size The second test determined the initial sample size (weight) of the <63 µm dry sediment fraction (not leached) necessary to result in a final weight of 20-50 mg for the <2 µm fraction of lithogenic sediment (after leaching) - a requirement for radiogenic isotope analysis (van der Lubbe *et al.,* 2016). Through testing different starting weights of dry <63 µm sediment (not leached), the study found that a starting weight of 1.5-2 g of dry <63 µm sediment (not leached) results in a sufficient amount of <2 µm fraction of lithogenic sediment after centrifugation for subsequent analysis such as radiogenic isotope analysis.

2.3.2.2 Method

2.3.2.2.1 Verification of the Centrifugation Set-Up The values obtained in the Experimental Design using Equation 2.4 helped determine specific settings for the new proposed method. Samples from two common marine sediment types dominated by (i) lithogenic (ii) biogenic carbonate (specifically coccoliths) were used to test the updated protocol. Both sediment types demonstrate the utility of the protocol by isolating three grain size classes, the <2 µm, 2-10 µm and 10-63 µm fractions from the total <63 µm material, with minor uncertainty using Equation 2.4. These specific size fractions were selected because they are commonly used in palaeoceanographic studies (Meyer *et al.,* 2011) (Table 4.2); however, the specific grain size fractions can easily be varied using Equation 2.4.

2.3.2.2.2 Pre-treatment of Lithogenic Fraction Marine sediment from marine core site MD20-3591 was initially wet sieved at <63 µm to separate the coarse and fine sediment fraction (n = 12). Prior to grain size separation, approximately 1-2 g of the <63 µm freeze dried sediment fraction was pre-treated following the method described above (Bayon *et al.,* 2002; Stuut *et al.,* 2002; Gutjahr *et al.,* 2007; Simon *et al.,* 2020a; Simon *et al.,* 2020b). The separation of particles smaller than 2 µm was carried out using 5ml 0.5% sodium metaphosphate and 15ml of DI water, then centrifuging following Stokes' Law (see full method below).

2.3.2.2.3 Separation of Additional Grain Size Classes For both lithogenic and biogenic sediment types, we tested the accuracy of the updated centrifuge method calculations for larger size fractions (2-10 µm and 10-63 µm). To isolate the 2-10 µm and 10-63 µm fraction we utilised Equation 2.4 and values obtained in the Experimental Design testing to determine the centrifugation steps, assuming a typical grain density of quartz (2.65 g/cm^3).

2.3.2.2.4 Grain Size Analysis

Verifying the accuracy/precision of the size class separation in two sample types

The grain size distributions of the lithogenic sediment were measured to confirm the

size isolation was successful. For the 2-10 µm and 10-63 µm size fractions, the Beckman Multisizer IV Coulter Counter was used and for the <2 µm size fractions the HELOS laser particle analyser was used at the Vrije Universiteit (VU) Amsterdam in the Sediment Lab because clays are platy and difficult to distinguish with the Beckman Multisizer IV Coulter Counter.

In addition to classical grain size analysis of lithogenic sediment (using Coulter Counter and/or laser particle analyser), microscope image analysis on the separated size classes was used to investigate the separation of grain size classes for both the lithogenic and biogenic fractions. Smear slides of the separated grain size fractions (<2 µm, 2-10 µm and 10-63 µm) were prepared for microscopy. A total of 20 images for each size fraction were taken using the Leica DMLB transmitted light microscope fitted with Leica Application Suite imaging software and applied count analysis on MATLAB 2022b using the image processing toolbox, by tracing the boundaries of grains within a microscope image (of a set size). The same image size and resolution was used across the images as the minimum grain size depends on the pixel size. The background noise was removed from the image and a binary image was created as by having the original image and the binary image, it was possible to count the objects and perform image analysis, through subtracting the difference in the image contrast.

2.3.2.3 Results

Firstly, the size separation needed to be verified.

2.3.2.3.1 Grain Size Isolation The <2 µm fraction was successfully isolated, with 99% of the sediment isolated recording as clay (<2 µm) using the HELOS laser particle analyser (Figure 2.4). Particles on images were also manually counted by measuring the length, width, and equivalent diameter to determine the percentage of grains within each size fraction class.

Over 90% of the grains between 2-10 µm were isolated and over 70% of the grains 10-63µm were successfully isolated using Multisizer IV Coulter Counter (Figure 2.5).

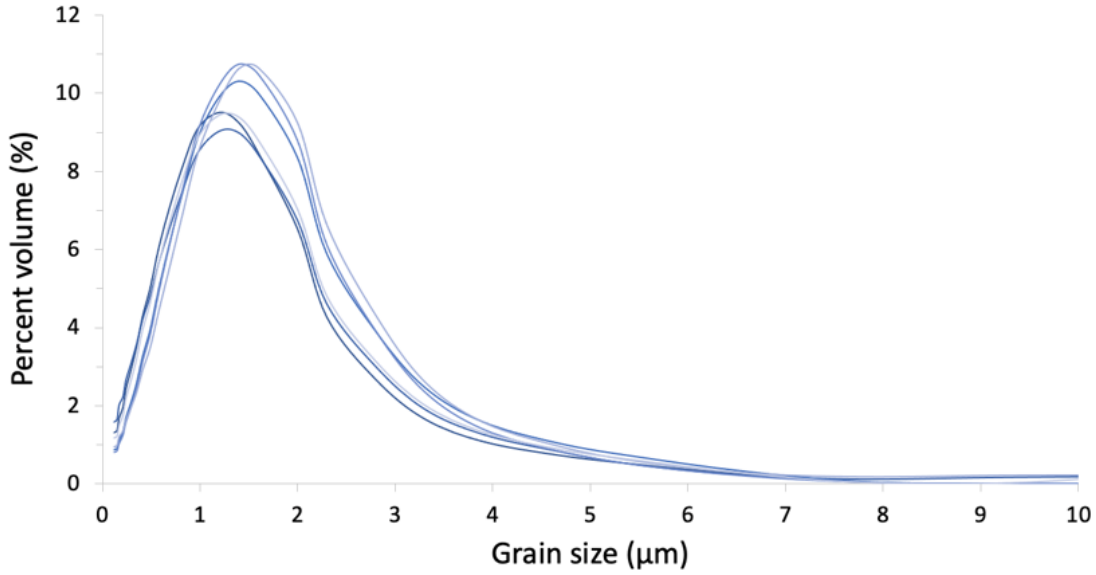

Figure 2.4: Grain size distribution of separated lithogenic clay fraction (<2 µm).

2.3.2.4 Discussion

This updated protocol provides a straightforward and step by step protocol for lithogenic sediment grain size isolation. Previous techniques used for size separation include sieving, settling and micro-filtration, however this separation method relies on standard equipment such as a centrifuge because this approach provides the shortest processing times compared to previous techniques which can take 48 hours to 3 weeks. Importantly, this method takes less than 1 hour to separate the varying size fractions and requires 1-2 g of starting bulk sediment. This amount of starting sediment is much less than previous methods which use a significant amount of bulk sediment (up to $\sim$ 3 g).

This size separation protocol can be routinely used as a method prior to radiogenic isotope analysis (for lithogenic sediment) or coccolith geochemical and isotopic analysis (for biogenic carbonate rich sediment) as it offers the possibility of retrieving sufficient sample material for subsequent analysis at low human resource.

For the finest sediment class, grain size analysis reveals that 99% of the sediment isolated in the lithogenic sediment was from the <2 µm size class. This clay fraction is an effective fraction to use for radiogenic isotopes (specifically $^{87}Sr/^{86}Sr$) because of the strong grain size effect witnessed on $^{87}Sr/^{86}Sr$ isotopes (Dasch, 1969; Grousset *et al.,* 1992; Blum and Erel, 2003; Feng *et al.,* 2009; Meyer *et al.,* 2011). Given radiogenic isotope datasets reflect analyses on a variety of size fractions, this size separation method will lead to more comparable datasets with consistent size fraction separation to improve studies on palaeoclimate reconstructions and environmental variability.

There is no standard protocol identified with a low small sample size of the initial sediment.

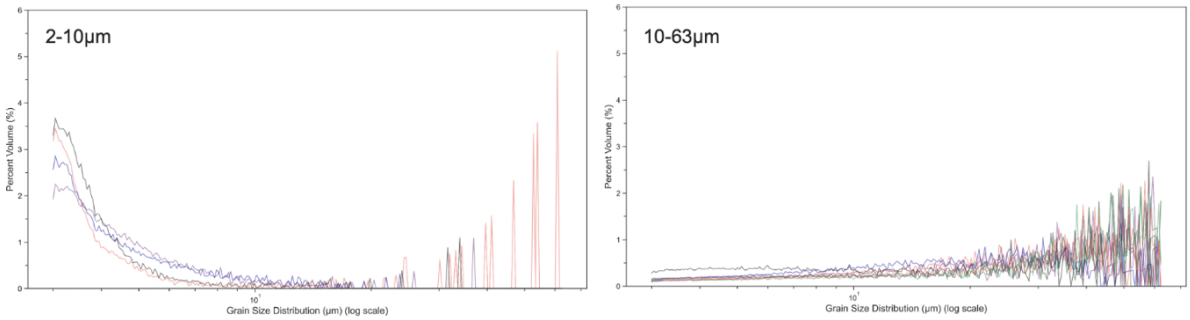

Figure 2.5: Grain size distributions from lithogenic sediment grain size separation; 2-10 µm (left), 10-63 µm (right). Colours indicate different sediment samples from same core site.

For both sediment types tested, this protocol provides enough sediment (20-50 mg) for further analyses in less than 1 hour by following the new method. Overall, the usability of this method means it can be applied to many types of sediment and will increase the sample throughput as well as reducing time costs and financial lab costs.

2.3.2.5 Recommended Method

The updated method for the separation of the <2 µm fraction focuses on Step 6 (see below). NB: tube refers to 50 ml centrifuge tube.

Pre-treatment of marine sediment for lithogenic fraction:

1. Take 1-2 g of dry sediment <63 µm fraction (sieved),
2. Removal of carbonates,
3. Removal of organics,
4. Removal of eventual remaining carbonates,
5. Leach of Fe-Mn coatings of the lithogenic fraction,
6. Centrifugation to isolate <2 µm fraction using 50 ml centrifuge tubes (see below for in detail steps),
7. Drying of samples,
8. Total sample digestion for radiogenic isotope analysis.

2.3.2.5.1 Updated Method Updated Method for isolation of <2 µm fraction*:

1. Add 5 ml sodium metaphosphate solution (0.2%), 15 ml DI water to tube 1.
2. Vortex at 3000 rpm until fully suspended then centrifuge 1000 rpm, 2 minutes for fractions ∼2 µm.
3. Decant solution of tube 1 into tube 2 and place tube 2 aside.
4. Pour 5 ml Calgon solution (0.2%), 15 ml DI water into tube 1 again.

5. Vortex tube 1 until fully suspended then centrifuge 1000 rpm, 2 minutes. This two-step centrifugation begins the separation and ensures the fine silts are isolated from the coarser silts.
6. Pour solution of tube 1 into tube 2. Tube 2 contains 40 ml now.
7. Vortex tube 2 until fully suspended then centrifuge 1000 rpm, 4 minutes. This removes the >2 µm fraction (settled) and the suspended solution contains the <2 µm clay fraction.
8. Pour supernatant into tube 3, this contains the <2 µm clay fraction.
9. Vortex tube 3 until fully suspended then centrifuge for 10 minutes at 2500 rpm.
10. Rinse samples using DI water (40 ml) three times.
11. After cleaning, place samples in tubes in an oven at 40°C. Or can pipette sample onto a glass slide under the fume hood and allow to air dry for XRD work.

*To isolate the 2-10 µm and 10-63 µm fraction we utilised Equation 2.4, assuming a typical grain density of quartz (2.65g/cm^3), to determine the following centrifugation steps:

i. 1000 rpm tube 1 for 2 minutes isolating the 10-63 µm fraction,
ii. centrifuge tube 1 at 1000 rpm for 2 minutes,
iii. pour tube 1 solution into tube 2 centrifuge at 1000 rpm for 4 minutes. Pour into tube 3. The resulting supernatant in tube 3 contains the <2 µm (in suspension) and 2-10 µm (settled) (Figure 2.6). The <2 µm fraction can be poured (ensuring none of the settled material escapes) into an additional tube for subsequent analyses.

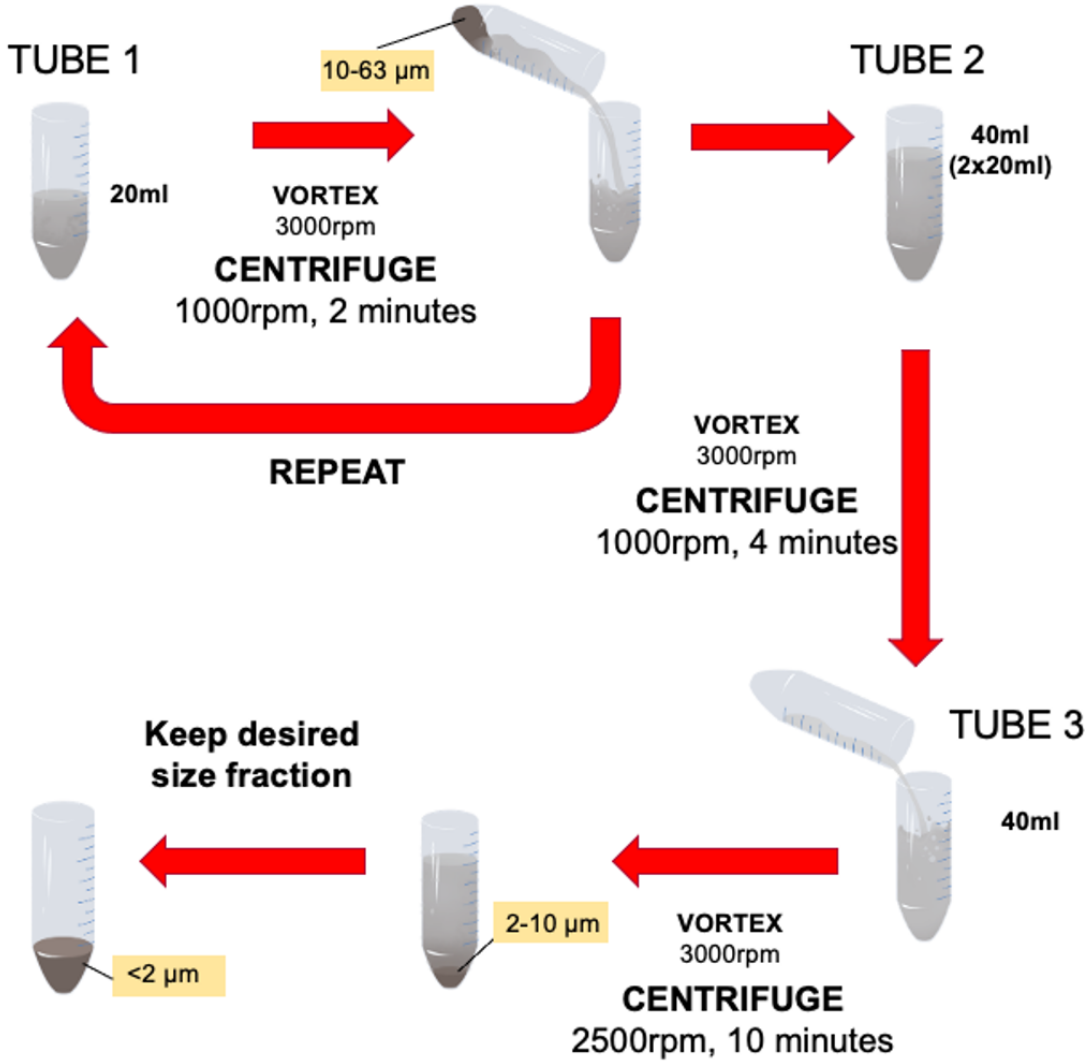

Figure 2.6: Method for separating the <2 µm, 2-10 µm and 10-63 µm fractions through calculations using Equation 2.4.

2.3.3 Radiogenic Isotope Analysis

Preparation and analysis for the radiogenic isotopes were performed at the School of Earth and Environmental Sciences, Cardiff University in The Cardiff Environmental Laboratory for Trace Element and Isotope Chemistry (CELTIC). Approximately 20-50 mg of homogenised and powdered sample material from the separate size fractions (<2 µm, 2-32 µm, 2-10 µm and 10-63 µm) were completely dissolved in a mixture of concentrated HF-HNO_3 on a hotplate at 120°C for >24 hours, following evaporation to incipient dryness the samples were taken up in 6M HCl and dried down. The sample was retaken up in 6M HCl and dried down before being finally dissolved in 8M HNO_3. The rock standards JB2 Basalt (National Institute of Advanced Industrial Science and Technology) and USGS Marine Sediment Standard MAG-1, were processed as standards. For each sample batch (n = 9), one of these standards was dissolved alongside 22 samples and a full procedural

blank. This means one batch equates to 24 beakers.

Strontium extraction from the sediment used Sr SpecTM resin, following a similar protocol from published methods (e.g. Charlier *et al.,* 2006; Font *et al.,* 2007; Scorrer *et al.,* 2021). Samples were loaded into the resin columns in 1ml 8M HNO_3. Matrix elements (including Nd) were collected in separate sample beakers through several washes of 8M HNO_3 before the Sr was eluted and collected in 0.05M HNO_3. Samples were dried overnight on a hotplate and the column separation process was repeated for a second pass to ensure the effective collection of Sr and removal of the matrix elements. The Sr cuts were dried and redissolved in 0.3M HNO_3. The $^{87}Sr/^{86}Sr$ ratios were measured using a Nu Plasma II multi-collector inductively coupled plasma mass spectrometer (MC-ICP-MS) in CELTIC. All data were first corrected for on-peak blank intensities then mass bias corrected using the exponential law and normalisation ratio of 8.375209 for $^{88}Sr/^{86}Sr$, Scorrer *et al.* (2021) for further details of the measurements. Analysis of NIST SRM 987 during the analytical session gave a $^{87}Sr/^{86}Sr$ value of 0.71023735 $\pm$0.00000540867 (n = 15) and all data are corrected to NIST SRM 987 of 0.710248 (Avanzinelli *et al.,* 2005). Typically, the total procedural blanks are less than 20 pg of Sr, a negligible result relative to the Sr in the samples (>20 ng). The repeated runs of the JB2 Basalt yields a mean of 0.703685 $\pm$0.00010 over five batches, compared to published JB2 values from GeoREM database with a mean of 0.703682313 (n = 32).

The Nd separation followed a 2-stage column separation using cation column exchange with AG-50W-X8 resin collecting the rare Earth elements and then Nd separation via Ln-spec resin, using methods described in (Mccoy-west *et al.,* 2017). The chemistry procedure lead to Nd cuts, purified for Sm whole and some Ce are present. The latter have no impact on the $^{143}Nd/^{144}Nd$ ratios. The $^{143}Nd/^{144}Nd$ ratio of the samples was measured on the Nu Plasma II MC-ICP-MS. The $^{143}Nd/^{144}Nd$ was corrected for mass bias using the measured $^{146}Nd/^{144}Nd$ ratio to the a ratio of 0.7219. The $^{143}Nd/^{144}Nd$ measured for the Jndi-1 standard were normalised to 0.512100 and off-sets applied to unknown data. Data where converted to εNd notation (Jacobsen and Wasserburg, 1980) using the standard formula from Equation 2.1. Typically, the total procedural blanks are less than 100 pg of Nd while the obtained εNd values of +8.8$\pm$0.2 for JB2 are consistent with literature data.

2.3.4 Radiogenic Isotope Endmember Mixing

Mixing equations performed by Dr Alex Lipp

The percentages of main geological units in each river catchment were calculated from data outputted from QGIS (Chapter 3) and used in the mixing calculations. The Nd and Sr isotopic endmembers for the Karoo and Cape Supergroup basement rocks were generated by inverting a simple linear mixing model to explain the isotopic composition of the river sediments. For this mixing model, each sample is assumed to be only a mixture

of the Karoo Supergroup rocks and Cape Supergroup rocks given their dominant areal extent in the study region. Additionally, the exposed areas of each of these lithologies within the upstream catchment are believed to be equal to the mixing proportions. The final model assumption is that across the studied region, the lithological supergroups have the same composition. Making these assumptions the following expressions can be written for the isotopic composition of a sample i:

$$\varepsilon Nd_i = A_{karoo,i}\varepsilon Nd_{karoo} + A_{cape,i}\varepsilon Nd_{cape} \tag{2.5}$$

$$Sr_i^{87/86} = A_{karoo,i}Sr_{karoo}^{87/86} + A_{cape,i}Sr_{cape}^{87/86} \tag{2.6}$$

where A is the exposed area of the given lithology upstream, and $\varepsilon\mathrm{Nd}_{karoo}$, $\varepsilon\mathrm{Nd}_{cape}$, $Sr_{karoo}^{87/86}$, and $Sr_{cape}^{87/86}$ are the endmember compositions we seek. Because there are multiple observations, n, we can represent the resulting *2n* expressions in matrix form:

$$Ax = b \tag{2.7}$$

where A is a n x 2 matrix giving the areas of each lithology, x is a 2×2 matrix containing the endmember isotopic compositions of the two lithologies, and b is our n x 2 observations matrix of isotopic compositions. This equation can be inverted to find x given A and b. To perform this inversion a linear least-squares approach was used to minimise the misfit between predictions and observations implemented using the NumPy Python package (Harris *et al.,* 2020). Prior to solving the equation, the observations were normalised to vary between 0 and 1 so as to weight each isotope system equally. The calculated endmembers are therefore 'consensus' endmembers which best fit all our observations downstream, given variable areal exposure upstream.

2.3.5 Sediment Source Contribution Modelling

Radiogenic isotopes endmembers defined using the method above were put into the Bayesian mixing model endmember mixing model tool on Excel™ (EMMTE) (Cao *et al.,* 2023), configured for detailed quantification of source contributions to individual samples. This endmember mixing model uses Monte Carlo simulation and constrains the relative deviation between the observed and the predicted radiogenic isotopes values. It provides comprehensive mass balance constraints and includes compositional range of endmembers. The uncertainty of the model output is predominantly driven by the isotopic variability of the endmembers included in the model.

2.3.6 Clay Mineralogy

Quantitative XRD measurements were completed on the sample clay fraction (<2 µm) using Philips PW1710 Automated Powder Diffractometer. Samples were prepared on glass slides (randomly orientated) and continuously scanned in 2ø-ø scanning mode from 2-32 degrees 2ø using the Philips PW1710 diffractometer with a CuKa radiation (35kV voltage and 40mA current). Quantitative mineral phase analysis was determined using the PW1877 APD version 3.6 software programme via the graphical user interface PW1876 PC-Identify version 1.0b for identification. This is for the estimation of peak areas of the reflection for main clay mineral groups of smectite (17 Å), illite (10 Å), and kaolinite/chlorite (7 Å). Relative clay mineral abundances are given in percentages. For consistency, all the clay mineralogical data referred to in this study was calculated based on the Biscaye method (Biscaye, 1965).

2.3.7 Grain Size Analysis

Grain size analysis was performed at the Vrije Universiteit (VU) Amsterdam in the Sediment Lab using a Sympatec HELOS KR laser diffraction particle sizer. This allows grain size to be measured on the range 0.12-2000 µm. Samples are oxidised using 30% Hydrogen Peroxide (H_2O_2) and boiling until an aggressive reaction occurs, then cooling down. Carbonates were removed using 10% HCl and the boiling until a vigorous reaction occurs. This was different to the sequential leaching procedure (section 2.3.1) As the grain size analysis was measured on the sediment after the geochemical pre-treatment (section 2.3.1), the grain size distribution is representative of the geochemistry and grain size isolation. Samples were poured into the particle sizer and measured. Data was subsequently cleaned with 57 bins.

2.3.7.1 Endmember Modelling Using Analysize

A data set of N specimens with P grain size bins resulting in mixtures from J endmembers can be unmixed in a matrix notation as: X = AS

Where X is a NxP matrix of observed data (one specimen per row), A is the NxJ abundance matrix of the constituent endmembers whose forms are given by the JxP matrix S (one endmember per row).

This forms the basis of the Analysize package within MATLAB 2022b (Paterson and Heslop, 2015), which was applied to the grain size measurements from the HELOS laser particle analyser.

2.3.7.2 Sortable Silt

For the $\overline{SS}$ mean grain size measurements, the Beckman Multisizer IV Coulter Counter was used. Prior to analysis, carbonates and opal were removed from the <63 µm. The $\overline{SS}$ mean grain size (µm) measurements were converted to flow speed (cm/s). This allows a

quantitative comparison between the modern and LGM and locations of marine sediment core sites discussed in this study. For the conversion from $\overline{SS}$ to flow speed, there are numerous calibration techniques, however the widely applied 'main-line' equation from McCave *et al.* (2017) is used, rather than more region specific calibration lines like from the Drake Passage (Wu *et al.,* 2019) or the Scotia Sea (McCave *et al.,* 2017)

2.3.8 Stable Isotope Analysis of Foraminifera

2.3.8.1 Procedure for Isotope Analysis

Bulk sediment was wet sieved at 63 µm and the dry >63 µm sediment was used for stable isotope analysis. Three specimens of *C.wuellerstorfi* were picked from the 250-315 µm size fraction with a fine dampened paintbrush using Milli-Q (MQ) water (18.2 Mø) under a binocular light microscope. Where possible individuals with poorly preserved shells were rejected although the bottom of the core had more poorly preserved shells. Individuals with broken shells were rejected, and a mixture of specimen sizes were selected (within the 250-315 µm size class) as there is no evidence for a size-dependency in the *Cibicicoides* stable isotope composition (Corliss *et al.,* 2002). For δ^{18}O measurements, when abundances of *C.wuellerstorfi* were low, Uvigerina species were picked instead.

Stable oxygen isotopes were measured in carbonate samples of the calcite tests of planktonic (surface-dwelling) foraminifera G.ruber. Stable isotope analysis was performed on whole test samples. Analysis for planktic δ^{18}O and δ^{13}C were performed at the Norwegian National Infrastructure FARLAB (Facility for advanced isotopic research and monitoring of weather, climate, and biogeochemical cycling) at the University of Bergen, Norway. The instrument used was an Finnigan MAT 253 mass spectrometer with an on-line coupled Kiel Carbon device. Benthic stable isotopes measurements were performed at Cardiff University on a Thermo Finnigan MAT 253 mass spectrometer linked online to a Carbo Kiel- II carbonate preparation device. All isotope data is referenced to the Vienna PeeDee Belemnite (VPDB) scale through repeated analysis of the NBS Standard. This means the results are defined in the conventional δ-notation in ‰ relative to VPDB for δ^{18}O calcite. The internal standard deviation for measurements over 3 batches (n = 596) at Cardiff for δ^{18}O is ±0.031 and for δ^{13}C is ±0.022. From this, the standard error of the mean for each sample can be estimated by dividing by the square-root of the number of shells measured (n). This gives error values of ±0.150 ‰ for δ^{18}O and ±0.183 ‰ for δ^{13}C. For Bergen, the error of the measurements is ±0.040 ‰ for δ^{18}O and ±0.020 ‰ for δ^{13}C (n = 260).

2.3.9 Estimation for Carbonate Content

Bulk sediment was dried and crushed, 3 mg of unprocessed bulk sediment was placed in tin capsules and 100 mg of unprocessed bulk sediment was dissolved in 10% HCl, in order to decarbonate the sediment. The supernatant was dried once neutral after three subsequent cleans with DI water, and 10 mg of this decarbonated material was placed

in tin capsules. The samples were measured on the Element Analyser. The difference between the unprocessed and decarbonated sediments was subtracted, resulting in the carbonate content (Figure 2.7).

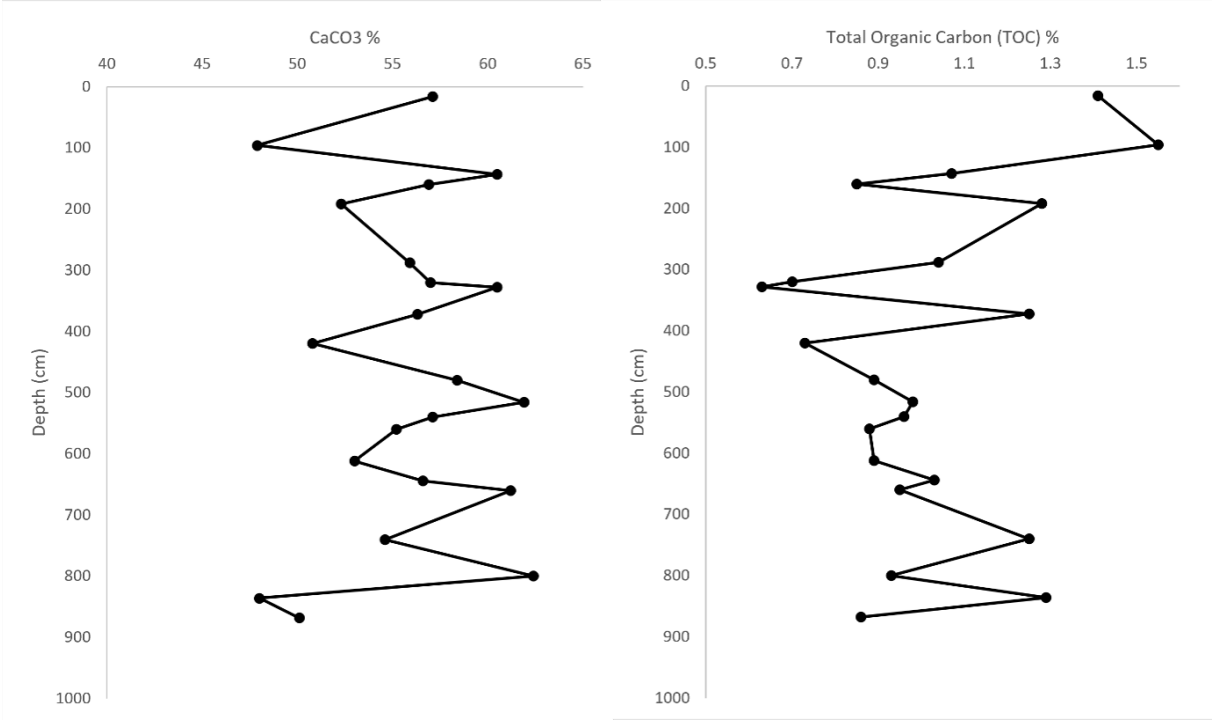

Figure 2.7: Downcore variability in $CaCO_3$% and Total Organic Carbon for MD20-3591.

The $CaCO_3$% is calculated assuming the inorganic carbon comes from $CaCO_3$ by using the following calculation (Equation 2.8), $CaCO_3$ % can be calculated. This corrects for the atomic weight of carbon.

$$CaC0_3\% = (\frac{(InorganicCarbon)}{12}) \times 100 \tag{2.8}$$

The Total Organic Carbon (TOC) is determined by taking approximately 100 mg of unprocessed crushed sediment and treating it with 10% HCl, then re-weighing the decarbonated sample. This ensures the carbonate carbon is eliminated prior to analysis. The analysis consists of heating the carbonate-free sample in an oxygen-rich atmosphere so that the carbon in the sediment is converted to carbon dioxide. The carbon dioxide is then measured using the Element Analyser, and the TOC content is calculated.

2.3.10 Elemental Records (XRF Core Scanning)

Core scanning for MD20-3591 was carried out in University of Bergen GEO department in September 2020 using the ITRAX XRF Scanner from Cox Analytical Systems. Measurements were made every 0.2 cm. Count time per second (cps) was set to 10 seconds and the XRF voltage and amplitude were set to 30 kV and 45 mA respectively.

2.3.10.1 Calibration of XRF

Measuring the real element concentrations in the sediment demonstrates the qualitative XRF scans are good quantitatively and ground-truths the XRF scanning results. Sediment samples from MD20-3591 were taken at points of maxima and minima elemental counts and at midpoints to gain a full spectrum of variability in the count data downcore. These measurements were calibrated with discreet samples as shown previously (e.g. Govin *et al.,* 2012; Simon *et al.,* 2015a; Babin *et al.,* 2020) (Figure 2.8).

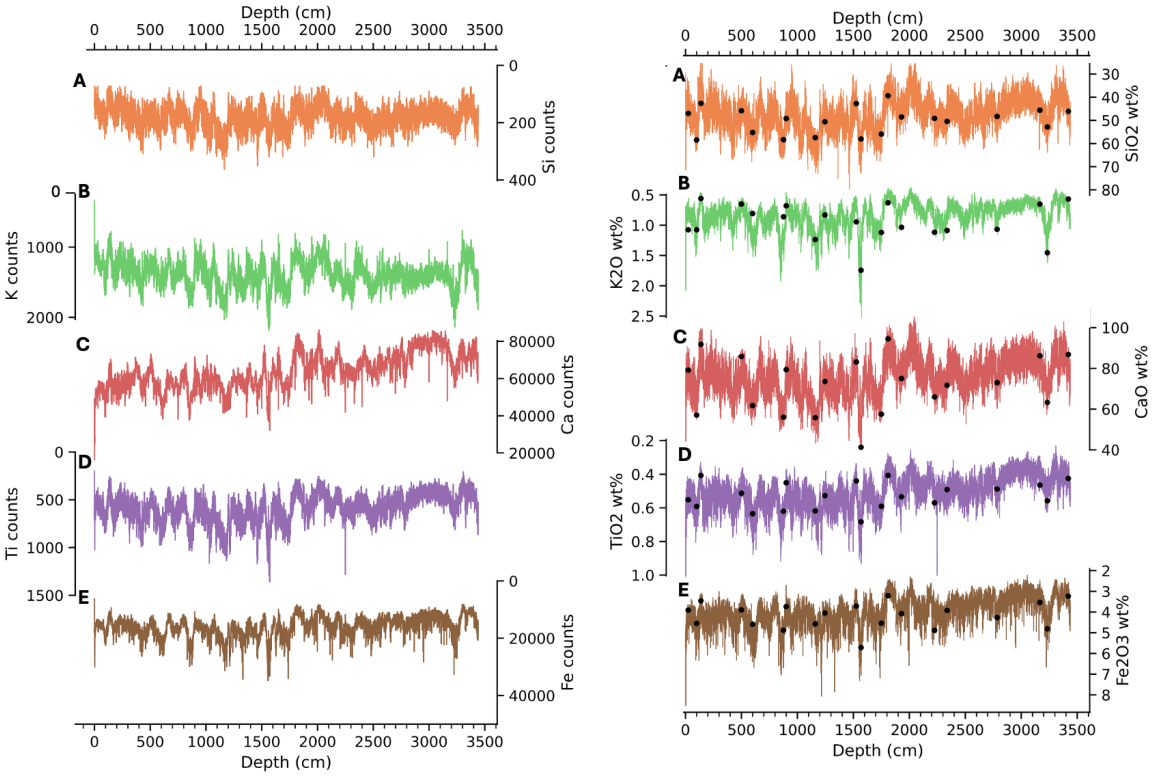

Figure 2.8: Downcore raw XRF scanning results as count data (left) and calibrated XRF elements as concentrations (right) with black dots showing where samples were taken at depth.

Approximately 12 g of freeze-dried and ground bulk sediment was ignited in a furnace at 1000°C and loss on ignition (LOI) values were calculated. This is achieved through knowing the sample weight and weighing the following, (i) the empty crucible, (ii) the crucible and sample before oven, and (iii) the crucible and sample after oven. Bulk sediment major element concentrations were obtained following lithium metaborate flux-fusion method (the samples powders were mixed with $Li_2B_4O_7/LiBO_2$ with a 1:4 dilution and fused to glass beads) (Saini *et al.,* 2000; Babin *et al.,* 2020; Balaram, 2021; Balaram and Subramanyam, 2022). The major elemental concentrations were measured on a PANalytical Axios mAX instrument. The oxide concentrations were derived from the interference corrected major element spectra using a calibration curve based on 28 international standards including USGS BIR-1, W-2 and BCR-2.

Other studies calibrate the scanning XRF to quantitative concentrations using different approaches. The most common method is calibrating the scanning results on an element-by-element basis with the assumption that there is a linear correlation (Wirth *et al.,* 2013; Hunt and Speakman, 2015). The equation of regression from the calibration curve is then used to convert the XRF log ratios to concentrations. However, there is occasionally a need to correct for moisture effects (Tjallingii *et al.,* 2007) and a normalised median weight percentage is also calculated prior to the linear calibration (Lyle *et al.,* 2012; Chen *et al.,* 2016; Li *et al.,* 2022). For MD20-3591, the XRF scanning data was normalised to 100% following Lyle *et al.* (2012) after the removal of section ends and other pre-processing methods (e.g. Babin *et al.,* 2020). I used the uni-variate log-ratio calibration of Weltje and Tjallingii (2008) to turn elemental intensities (cps) to element concentrations with depth, with Ca as the common denominator as this element has the stronger XRF average signal intensity and quantitative concentration (Figure 2.8).

2.4 Statistical Analysis

2.4.1 Principal Component Analysis

Principal Component Analysis (PCA) is a statistical method employed to find elements with common signals and to reduce dimensions. PCA was performed on MATLAB 2022b using the 'pca' function and 'xcorr', which utilise a singular value decomposition function to introduce unit variances. The elements included in the PCA are Al, Ca, Fe, K, Rb, Si, Sr, Ti, and Zr. Results from the PCA and the XRF PC1 record are utilised and discussed in Chapter 5.

2.4.2 Time Series Analysis

Time series analysis helps to identify or isolate periodic components in a signal such as a wavelength of a cycle which might be present in a time series record. Multitaper Spectral (MTM) and Evolutive Harmonic (EHA) analyses were performed in the astrochron R software package (Meyers, 2014; R Core Team, 2019) using the functions 'mtm' and 'eha'. This method analyses the potential presence of dominant frequencies and cycles in the Fourier-space of the depth scale in a proxy record facilitating the assignment of these cycles to orbital frequencies. In addition, to test the amplitude of precessional scale modulations, the function 'testPrecession' (Zeeden *et al.,* 2015) was applied, a function incorporated in the astrochron R software package (Meyers, 2014; R Core Team, 2019). This function utilises the astrochronological testing method and compares observed modulations in the precession-scale amplitude to those expected from the theoretical eccentricity La2004 solution (Laskar *et al.,* 2004). The analysis applies a series of filters to prevent artificial introduction of precession modulations during tuning and data processing and evaluates the significance of the tuned age model using Monte Carlo simulations.

Additional testing of dominant frequencies was carried out on Pyleoclim, a python package (Khider *et al.,* 2022). The XRF PC1 record (see section 5.2.3.1) was analysed using both spectral and wavelet analysis appropriate for unevenly spaced data and results were the same as using astrochron. In this thesis, the Weighted Wavelet Z-Transform ((Foster, 1996; Kirchner and Neal, 2013), WWZ) for both spectral and wavelet analysis are presented. The significance is assessed against AR(1) benchmark. The method for the assessment of significance identifies the asymptotic approximation to the distribution of the AR(1) benchmarks. The default method which makes a direct AR(1) simulation yields a similar result.

2.5 Age - Depth Models

In this study, the term 'age control points' (ACPs) is used for direct age assessments such as radiocarbon dates and for tuned, and hence indirect age assessments obtained via 'wiggle matching' or proxy alignment, the term tie point is used.

2.5.1 Radiocarbon Dating

Radiocarbon dating is an invaluable technique for constructing chronologies in deep sea sediment through dating organic matter which is younger than 50 ka. The radioactive carbon isotope ^{14}C is produced in the atmosphere by the interaction of cosmic rays with nitrogen (^{15}N) in the upper atmosphere, it is mostly in the form of $^{14}CO_2$ molecules which enter the global carbon cycle. Determining the ^{14}C age assumes the concentration of radiocarbon in the atmosphere has remained constant over time, however atmospheric levels of radiocarbon have fluctuated over the past 50 ka, hence it is necessary to measure and compare ^{14}C dates with a modern-day standard. This accounts for magnetic field intensity and solar variability (Stuiver and Braziunas, 1993b), as well as changes in the distribution of ^{14}C between various reservoirs (particularly the ocean) (Siegenthaler and Sarmiento, 1973). Considerations for additional biases such as bioturbation, fragmentation and dissolution must also be accounted for. The age difference between a terrestrial radiocarbon date and a date obtained from the marine environment is 400 radiocarbon years. This age offset is due to the delay in exchange rates between atmospheric carbon and ocean carbonate (Stuiver and Braziunas, 1993a). This marine reservoir effect is further caused by the mixing of surface waters with upwelled deep waters which are older. The reservoir effect is geographically variable, surface waters in the Atlantic Ocean are 400 years older than atmospheric ^{14}C, whereas deep waters in the Pacific are 2000 years older. This is due to the thermohaline circulation owing to the Atlantic being in contact with the atmosphere more recently.

2.5.2 Radiocarbon (^{14}C) - LR04 Age Model

The core chronology produced for the sediment core MD20-3591 was based on radiocarbon (^{14}C) dates in the upper parts of the record (Table 2.2; Figure 2.9). The accelerator mass spectrometer (AMS) ^{14}C dates were measured from samples containing approximately 1000 tests of *G. ruber* (250–315 m). The ^{14}C ages were calibrated using the Marine20 calibration curve (Heaton *et al.,* 2020). The ^{14}C measurements were made at the Eidgenössische Technische Hochschule (ETH) Radiocarbon Laboratory.

This is the basic age model which was extended via benthic δ^{18}O (Figure 2.10). Beyond the limits of the ^{14}C dating ($\sim$ 50 ka), an orbitally tuned age model for MD20-3591 was generated by correlating the *C. wuellerstorfi* and *Uvigerina spp* δ^{18}O record to the LR04 stack (Lisiecki and Raymo, 2005) (Table 2.3). This age model is referred to as the LR04 timescale.

Table 2.2: Radiocarbon ACPs for marine sediment core MD20-3591

Sample ID	Depth 1 (cm)	Depth 2 (cm)	Age (ka)	Age error
ETH118406.1.1	1.0	2.0	2.464	57
ETH118407.1.1	26.0	27.0	6.362	86
ETH124493.1.1	80.5	81.5	11.795	100
ETH111020.1.1	120.0	121.0	16.680	120
ETH111021.1.1	144.0	145.0	18.880	150
ETH124494.1.1	160.5	161.5	19.445	200
ETH111022.1.1	192.0	193.0	28.090	380
ETH111023.1.1	216.0	217.0	30.660	440
ETH111024.1.1	240.0	241.0	33.760	680
ETH111025.1.1	264.0	265.0	37.060	920
ETH111026.1.1	288.0	289.0	37.130	930
ETH124495.1.1	296.5	297.5	32.100	500
ETH111027.1.1	312.0	313.0	47.670	3250

From the selected age points (n=27; consisting of 13 radiocarbon dates and 12 tie points) (Table 2.2; 2.3), the final age-depth model was constructed using the deterministic age modelling routine Undatable (Lougheed and Obrochta, 2019), with 10^5 bootstrap simulations. This derives the 95% (2σ) and 65% uncertainty on the calibrated ages providing an uncertainty envelope for each estimated time point (Figure 2.11).

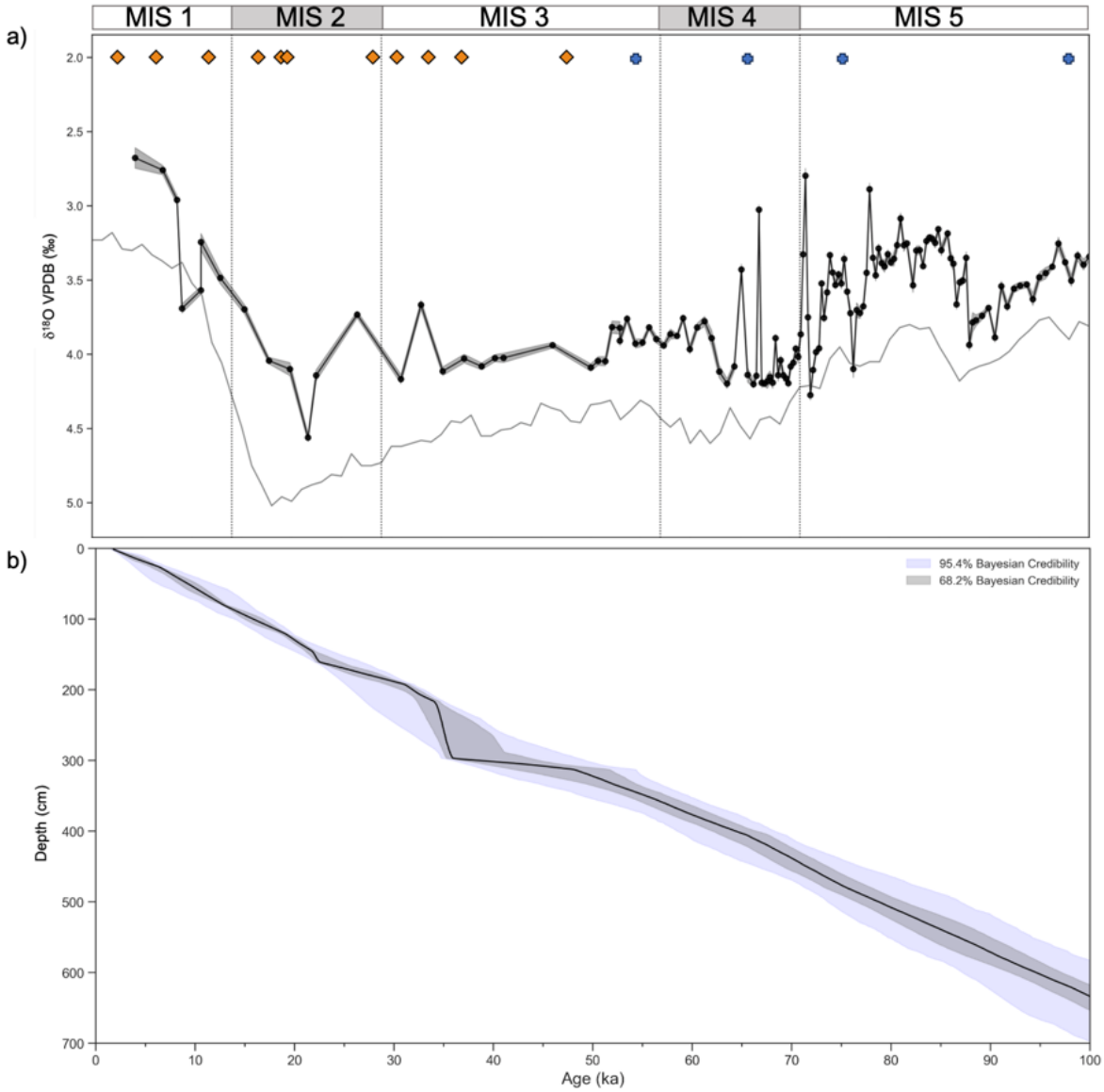

Figure 2.9: ^{14}C - LR04 Age Model for 100 to 0 ka – Marine Isotope Stages (MIS) are highlighted on top. The first 50 ka is based on radiocarbon dates only. (a) Downcore of MD20-3591 δ^{18}O record with LR04, with grey shading indicating the measurement error for each sample. Yellow diamonds indicate radiocarbon dates, blue symbol indicates tie points to LR04. (b) Age- Depth of Bayesian ^{14}C – LR04 Age Model (black line), Bayesian uncertainty thresholds (95.4% light grey; 68.2% dark grey shading).

Table 2.3: Tuning points of LR04 Age Model

Date Type	Depth (cm)	Age (ka)
Tie point	384	58
Tie point	400	64
Tie point	500	78
Tie point	620	98
Tie point	800	126
Tie point	880	130
Tie point	1240	175
Tie point	1340	205
Tie point	1550	245
Tie point	2100	320
Tie point	2257	337
Tie point	2640	370
Tie point	3432	450

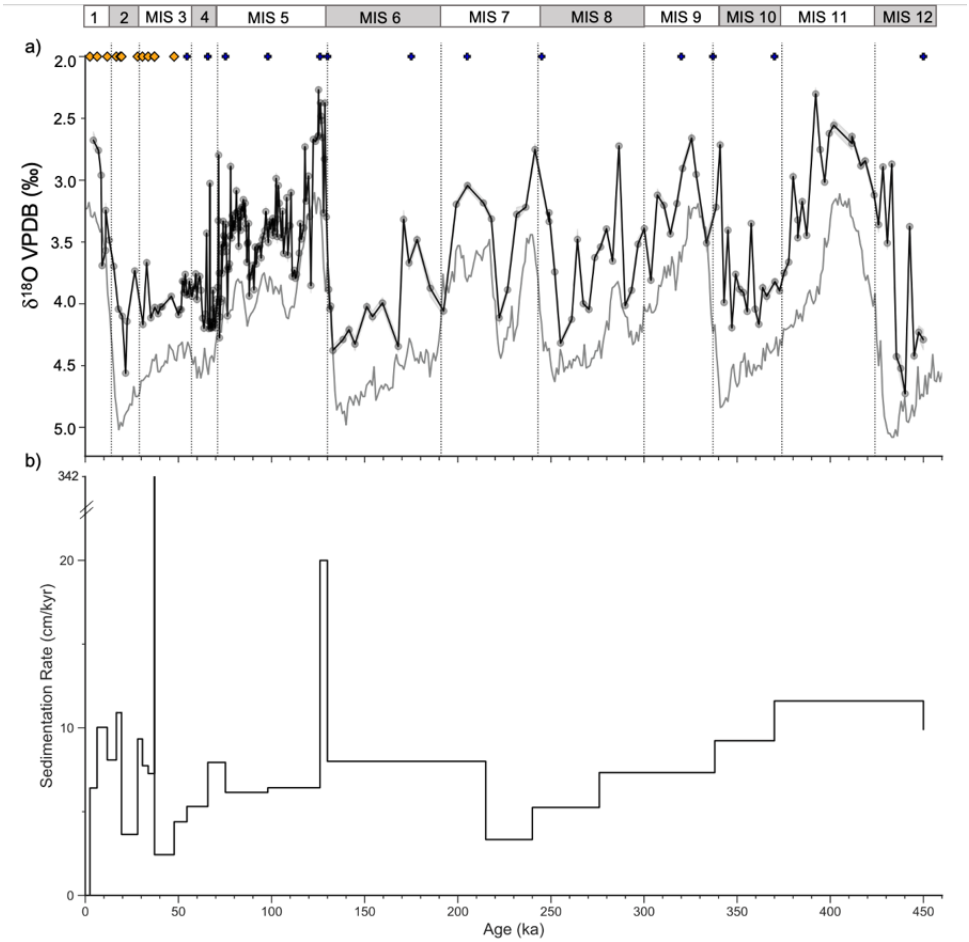

Figure 2.10: ^{14}C -LR04 Chronology of core MD20-3591 –MIS are highlighted on top (a). Benthic δ^{18}O record and global benthic δ^{18}O stack (LRO4, grey) is shown for comparison (Lisiecki and Raymo, 2005). (b) Sedimentation rates for site MD20-3591.

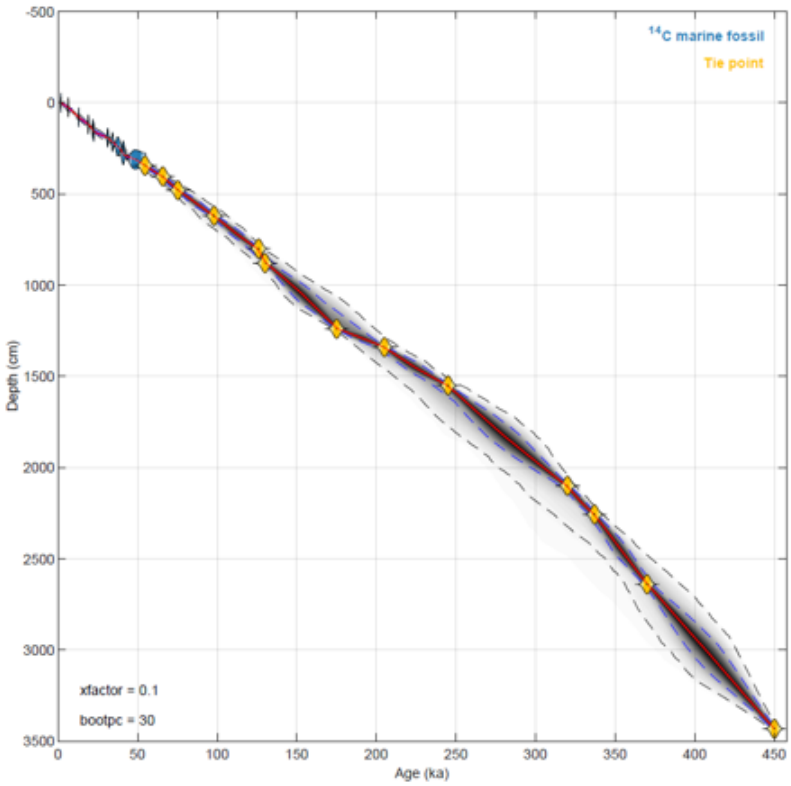

Figure 2.11: The Bayesian LR04 Age Model obtained from undatable for MD20-3591 incorporating local reservoir uncertainty of 400 years. Each date is represented by the credibility threshold of the intersection between the radiocarbon ages at the depth and the Marine20 calibration curve. The grey shadings represent the 65% and 95% probability based on the calibrated dates using the Bayesian toolbox in MATLAB 2022b, undatable.

2.5.3 Speleothem Age Model: Adjustment to LR04 Age Model

Additional chronostratigraphic fine-tuning was employed using the Chinese caves (Hulu and Sanbao) speleothem record (Cheng *et al.,* 2016) and pattern matching it to the full XRF Principal Component 1 (PC1) (section 5.4.3.2) record of MD20-3591 using tie points at the mid-points of transitions. This fine-tuning approach applied 34 tie points to the Chinese caves (Hulu and Sanbao) speleothem record (Cheng *et al.,* 2016) (Table 2.4) in addition to 13 ACPs. The deterministic age-depth modelling approach (Lougheed and Obrochta, 2019) was employed to provide the Bayesian age-depth model with uncertainty estimates. This age model is referred to as the speleothem-chronology, which is used for the time interval of 100-50 ka in Chapter 5 unless otherwise stated (Figure 2.12). Originally ages between each control point were estimated by linear interpolation, this does not give Bayesian uncertainty windows but gives a similar age to the Bayesian speleothem-chronology.

Table 2.4: Speleothem Chronology

Date Type	Depth (cm)	Age (ka)
Tie point	329.500	49.647
Tie point	337.100	51.326
Tie point	345.300	55.000
Tie point	378.600	58.277
Tie point	397.800	59.000
Tie point	404.800	65.000
Tie point	425.000	68.500
Tie point	455.600	72.300
Tie point	480.100	75.261
Tie point	531.400	84.233
Tie point	551.700	87.140
Tie point	581.700	89.871
Tie point	620.000	98.000
Tie point	711.200	108.533
Tie point	774.200	120.992
Tie point	825.500	128.779
Tie point	1082.000	149.425
Tie point	1194.700	165.295
Tie point	1210.000	168.910
Tie point	1274.500	178.865
Tie point	1401.900	198.755
Tie point	1438.500	210.330
Tie point	1455.100	226.136
Tie point	1540.000	242.000
Tie point	1868.200	294.928
Tie point	2220.500	334.299
Tie point	2764.400	394.928
Tie point	3202.200	416.285
Tie point	3324.000	450.299
Tie point	3439.000	463.240

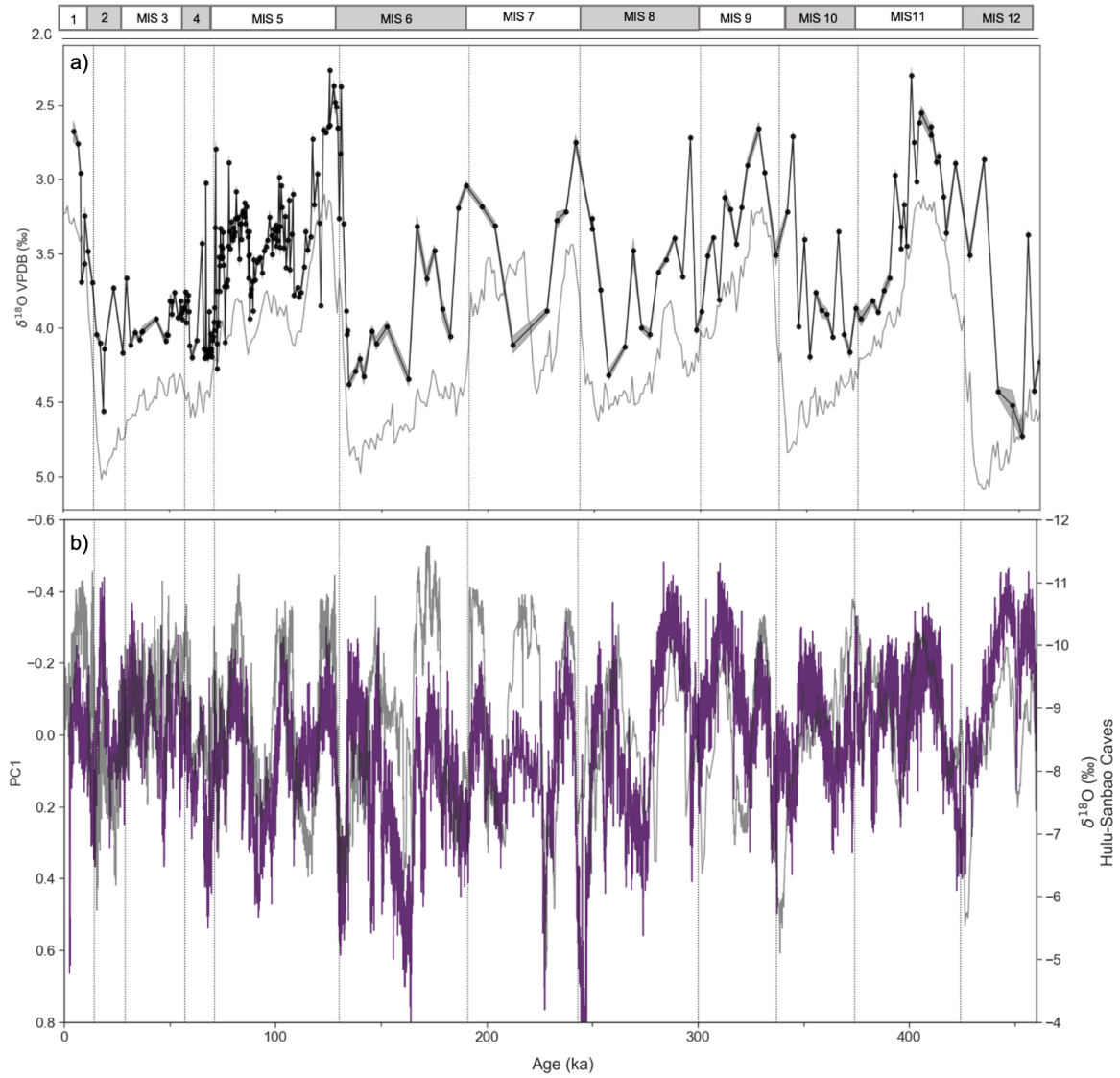

Figure 2.12: Speleothem Chronology. (a) δ^{18}O benthic isotopes on Speleothem Chronology (black) compared to LR04 (grey) (Lisiecki and Raymo, 2005), (b) XRF PC1 scores (purple) with Hulu-Sanbao cave record (grey) (Cheng *et al.*, 2016).

Chapter 3 | Rivers of South Africa: Investigating the Provenance of River Sediments Draining into the Southwest Indian Ocean

But the majestic river floated on, out of the mist and hum of that low land – Matthew Arnold's Sohrab and Rustum

You were talking to the spirit kingdom, Fox, Hare, Kestrel skull the movement large, the weather dull, pick again until the cards can form our meaning - Follies Fixture - Ben Howard

3.1 Introduction

Marine sediment cores provide long-lasting continuous archives of marine climates and provide insight to terrestrial climate changes e.g. through reconstructing run off and subsequently on-land precipitation patterns. These sediments store information on environmental conditions and act as archives of climate changes in the Earth's past. These past climate conditions can be inferred through proxy reconstructions, for example, via specific geochemical signals recorded in the detrital minerals and fossils that can be analysed and correlated with climate or environmental parameters in the modern world (e.g. salinity, temperature, ice cover, oxygen levels, nutrient levels).

Likewise, the provenance of marine sediments (e.g. determination of geographical source areas of lithogenic sediments) can also be used as an indicator of past environmental and climate conditions, through understanding erosion and pedogenic processes in the terrestrial source regions and transport pathways by which the sediment arrived at the core site. The terrigenous signal from marine sediment represents the distal and/or local erosional products from the source region (Meyer *et al.,* 2011; Garzanti *et al.,* 2014; Hahn *et al.,* 2018; Maccali *et al.,* 2018; Dinis *et al.,* 2020; He *et al.,* 2020; Blanchet *et al.,* 2021).

The interpretation of sediment provenance in marine sediments can be complicated as the source signal of sediment transported and supplied from regional river systems to the site of deposition may be overprinted by other material supplied from distal sources via long distance transport (Hahn *et al.,* 2018; Blanchet *et al.,* 2021). Riverine sediments are also prone to hydrodynamic sorting (physical fractionation) processes during transport, affecting the grain size, shape, density, and durability of this lithogenic fraction of terrigenous sediment which can modify the geochemical provenance signals (Petschick *et al.,* 1996; Compton *et al.,* 2009; Govin *et al.,* 2012). Different transport mechanisms (bedload versus suspension) often contribute preferentially to specific grain size fractions, and therefore leave a characteristic grain size signal on the sediment it carries (Stuut *et al.,* 2002; Meyer *et al.,* 2011; McCave *et al.,* 2017; Beny *et al.,* 2020). Hence, in combination with radiogenic isotope provenance reconstructions, it is potentially possible to identify transport pathways from grain size. However, this also means it is crucial that the precise grain size fraction is selected and isolated when utilising the sedimentary geochemical imprint to isolate specific environmental and climate processes.

To decipher terrigenous sediment input to the marine realm, various proxies have been implemented on fluvial and aeolian sediments, with geochemistry and clay mineralogy proving to be the most effective (Goldstein *et al.,* 1984; Grousset *et al.,* 1988, 1998; Garzanti *et al.,* 2014; van der Lubbe *et al.,* 2014; van der Lubbe *et al.,* 2016; Hahn *et al.,* 2018; Dinis *et al.,* 2020; He *et al.,* 2020). Most of the geochemical and isotopic determinations which have been carried out so far on channel riverine sediments are of the

coarse-grained fraction (sands (>63 µm) and gravels (>2 mm)), which are not directly comparable to the fine-grained (<63 µm) deep-sea sediment (Hjulström, 1955). This chapter uses the lithogenic clay fraction (<2 µm) as it has been previously recognised to be good indicator of transport processes of suspended sediments (Chamley, 1989; Walter *et al.,* 2000; Bayon *et al.,* 2015).

Geochemical and isotopic indicators of riverine sediments have been determined for numerous localities across southern Africa (Weldeab *et al.,* 2013; Garzanti *et al.,* 2014; Hahn *et al.,* 2016, 2018; Dinis *et al.,* 2020), however their spatial coverage remains sparse and often intermittent (Figure 3.1). Along the Southeast African coastline, provenance studies are limited to within and offshore of the Limpopo river catchment (e.g. Garzanti *et al.,* 2014; Simon *et al.,* 2020a) and further north offshore of the Zambezi catchment (van der Lubbe *et al.,* 2016). Specifical within South Africa, several studies have identified the terrestrial geochemical signals in marine sediments such as Hahn et al. (2015, 2018) and offshore southwestern rivers such as the Orange river (Compton and Maake, 2007; Weldeab *et al.,* 2013). These studies have successfully linked marine lithogenic sediments with generalised drainage basins rather than individual source rock lithologies. Here, for the first time, a consistent systematically sampled transect from northeast South Africa (Durban) to Southwest (Cape Town) is presented (Figure 3.1; pink triangles), which allows for establishing land-sea linkages and deciphering terrigenous input to the marine realm.

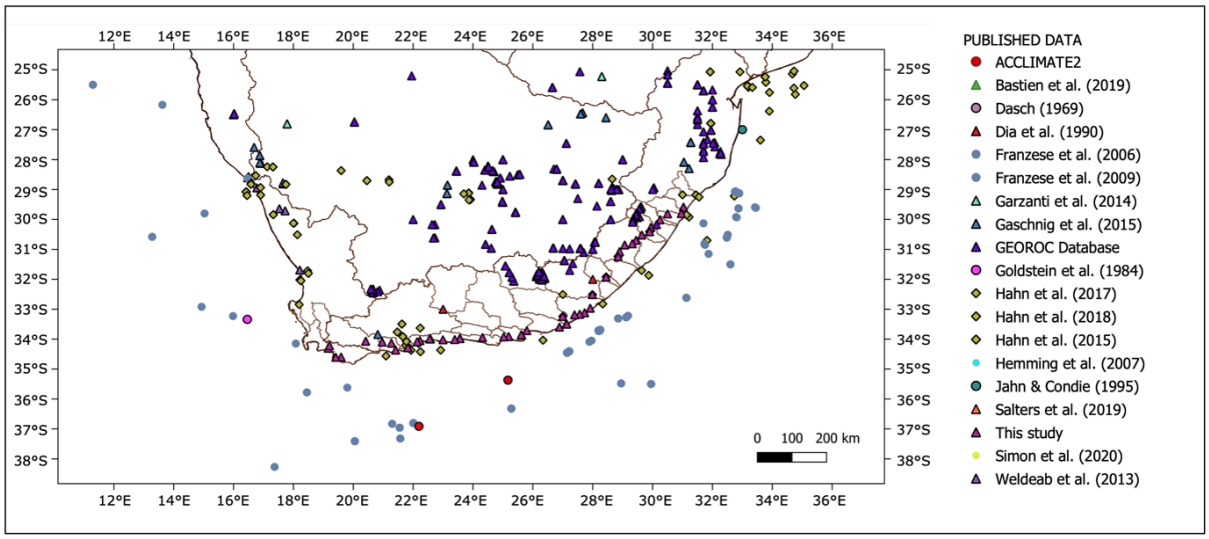

Figure 3.1: Overview map of all published Sr and/or Nd datasets in the South Africa region with outlines of individual river catchments discharging into the ocean. Key for publications. Circles = sediment cores, triangles = on-land samples (either whole rock or river sediments), diamonds = studies by Hahn et al. (2016, 2017, 2018).

3.1.1 Geochemistry and Provenance Tools

Radiogenic isotope compositions (such as $^{87}Sr/^{86}Sr$ and εNd isotopes) are well known tools for provenance reconstructions of the lithogenic fractions in detrital sediment in marine deposits. Sr and Nd isotope variations of continental detritus produced by long-lived radioactive decay mainly depend on their initial Sm/Nd and Rb/Sr ratios, respectively and the rock ages (Goldstein *et al.,* 1984; Grousset and Biscaye, 2005; Hu *et al.,* 2012).

Continental rocks have different Sr and Nd isotope ratios depending on their age, geological history and type. The isotope signatures of river sediments reflect both the initial bedrock and weathering process, which which can be used to determine the provenance of river sediments and weathering type in the drainage basin. Sr and Nd isotope signatures measured on the clay fraction provide robust fingerprints of source regions over long geological timescales and geographic distances as they are transported over long distances and integrate large source areas (Jewell *et al.,* 2020a).

Unlike Nd, the $^{87}Sr/^{86}Sr$ isotopic signature is also defined by the variability in initial Rb content in different mineral types as Sr is more mobile than Rb. Sr is easily removed, leaving Rb behind, which increases the Rb/Sr ratio and the $^{87}Sr/^{86}Sr$ in highly weathered rock (Meyer *et al.,* 2011; Jung *et al.,* 2004). Sr isotopes fractionate during weathering and transport processes by mineral sorting; therefore, they are a powerful tool to represent changes in on-land hydrology and chemical weathering. Since Dasch et al. (1969), it has become clear that $^{87}Sr/^{86}Sr$ ratios increase with both decreasing grain size and increasing weathering intensity, which has later been confirmed repeatedly by other studies (Grousset *et al.,* 1992; Blum and Erel, 2003; Feng *et al.,* 2009; Meyer *et al.,* 2011). In contrast the radiogenic neodymium isotopic signature, expressed as εNd for convenience [$^{143}Nd/^{144}Nd$ normalised to the Chondritic Uniform Reservoir] (Jacobsen and Wasserburg, 1980) bears the same isotopic composition as the current rock source, since Nd isotopes are not altered or fractionated during processes such as chemical weathering. They are therefore considered a more reliable provenance tracer (Goldstein *et al.,* 1984; Blum and Erel, 2003; Fagel *et al.,* 2004; Fagel, 2007; Meyer *et al.,* 2011; Garzanti *et al.,* 2014; van der Lubbe *et al.,* 2014; Hahn *et al.,* 2016, 2018; van der Lubbe *et al.,* 2016).

Initial Sr-Nd isotope provenance studies utilised a mixed range of grain size fractions (Meyer *et al.,* 2011; Hahn *et al.,* 2016), and/or bulk sediments (Riley *et al.,* 2006; Jonell *et al.,* 2018; Carter *et al.,* 2020). However, it has increasingly become apparent that it is necessary to consider size selective mineralogical effects and sediment transport mechanisms in order to accurately quantify the source area variability and reconstruct regional weathering regimes (Garzanti *et al.,* 2014; Dinis *et al.,* 2020; He *et al.,* 2020). Proxy studies have shown that different transport mechanisms (e.g. wind, fluvial) preferentially support different grain size fractions (Stuut *et al.,* 2002; Meyer *et al.,* 2011). The influence of these differential transport pathways needs to be accounted for when employing proxy

reconstructions to interpret environmental variability (Meyer *et al.,* 2011).

3.1.2 Research Objectives

This chapter investigates the factors controlling the Sr and Nd isotopic signatures of terrigenous sediments and clay mineralogy on each major river catchment between Durban and Cape Town to provide information on sediment composition and continental weathering of sediments transported by South African river sediments. These sediments are supplied to the marine system and subsequently deposited at proximal sites from which they are further transported to greater water depths by gravity and near bottom currents. These marine deposits are often used for palaeoclimate reconstructions. It also aims to specifically quantify the magnitude of the grain size effect on radiogenic isotopes by targeting the clay <2 µm fraction and fine silt 2-32 µm fraction of lithogenic sediments to ensure the reported grain size offset of Sr isotopes is accounted for.

Secondly, this chapter determines the implications of our results for palaeoclimate reconstructions through generating radiogenic isotope endmembers and understanding how the signal integrating the bedrock can be used for marine sediment core studies and past climate reconstructions.

3.2 Climate and Fluvial Systems in Southern South Africa

3.2.1 Modern Climate of South Africa

The modern climate of southern South Africa is driven by the interaction of atmospheric and oceanic processes with the surface Agulhas Current along the East and South coasts, and Benguela Current to the West, which results in three distinct rainfall zones in southern Africa (Figure 3.2). Today, precipitation occurs mainly during the austral summer months (November to February) as the easterly trade winds transport tropical moist air from the Southwest Indian Ocean to southern Africa towards Summer Rainfall Zone (SRZ) (Reason and Mulenga, 1999). Rainfall reaches up to 1000 mm in the SRZ and ranges between 5 and 350 mm in the Winter Rainfall Zone (WRZ) (Compton, 2011; Nash, 2017) (Figure 3.2). The WRZ receives moisture from the latitudinal migration of the westerlies, which are influenced by the northward advancing Antarctic sea-ice (Tyson, 1986; Nicholson, 2000; Tyson and Preston-Whyte, 2000; Chase and Meadows, 2007). The region located between these two zones; the Year-round Rainfall Zone (YRZ; Figure 3.2), receives rainfall in all seasons influenced by both the Southwest Indian Ocean and the South Atlantic Ocean.

3.2.2 Fluvial Systems of Africa

Between Durban and Cape Town, there are 10 major rivers draining into the Southwest Indian Ocean. These are: Mgeni, Umzimkulu, Umzimvubu, Great Kei, Great Fish, Sundays, Gamtoos, Kynsa, Gourritz and Breede.

The eastern and southern coastline of South Africa comprises of many smaller coastal river catchments with an average annual sediment yield of $\sim$ 10x10^{6}m^3/year supplied to the Southwest Indian Ocean (Flemming, 1981; Rooseboom *et al.,* 1992). The eastern coastline region has been dramatically affected by past global climate change and associated changes in sea-level rise. More recently under anthropogenic climate change and land-use change, expansive gullies have been formed, which contribute to mass soil degradation and erosion (Figure 3.3) (Hoffman and Todd, 2000; Le Roux, 2007; Birkett *et al.,* 2016; Seutloali *et al.,* 2016). The rivers from the eastern Cape are all typical brown-water rivers, with high sediment loads. The sediments within the catchment areas, are notably rich in iron (Fe) oxides. Consequently, iron rich sediments and geochemical elements such as the Fe/K ratio recorded in marine core sites (such as CD154-17-17K; (Ziegler *et al.,* 2013)) can be used as a first-order indication of relative changes in the amount of fine (Fe-rich) terrigenous components supplied to the core site from regional river discharge.

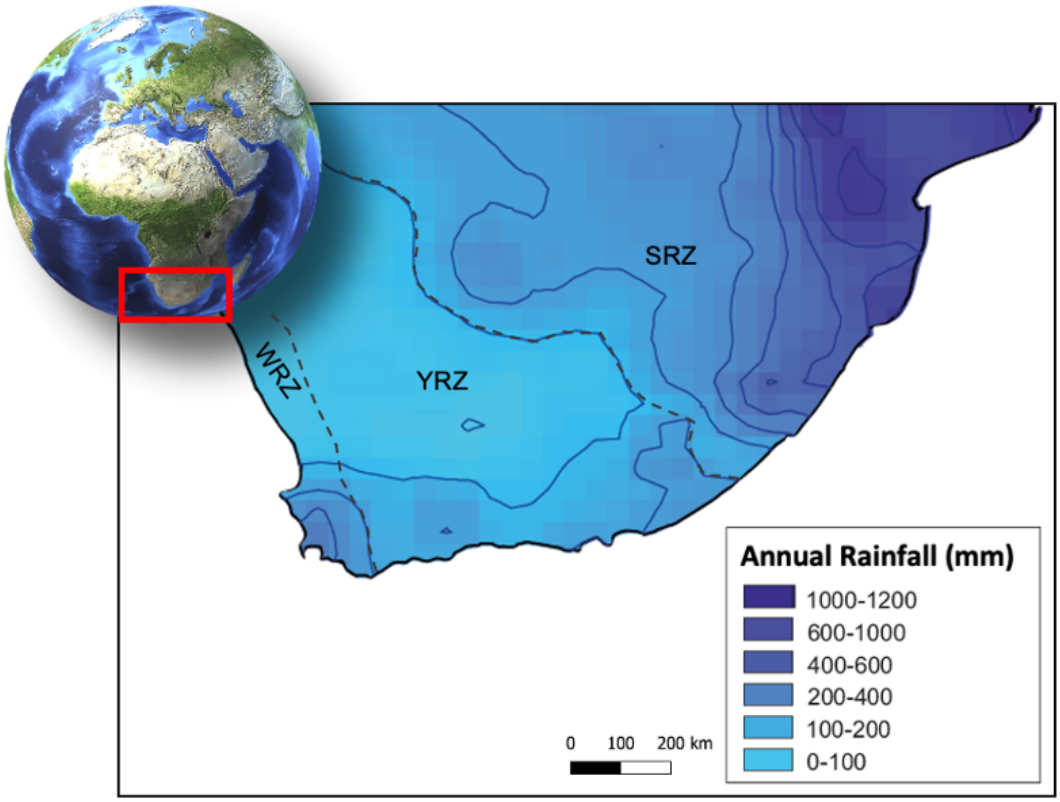

Figure 3.2: Annual mean rainfall map of South Africa, dotted lines display rainfall zones (labelled). WRZ corresponds to Winter Rainfall Zone, YRZ is Year-round Rainfall Zone, and SRZ is Summer Rainfall Zone. Data from Climate Research Unit (CRU), 50km gridded resolution, smoothed to 3x3 squares with contoured intervals.

Along the southern Cape, the major rivers draining from the interior of South Africa and the Cape Fold Mountains are the Gamtoos, Kynsa, Gourritz and Breede. The Gourritz river catchment has a large annual runoff (488 x 10^6 m^3/year (Maitre *et al.,* 2009)) with a catchment size of 45,715 km^2. This river catchment drains within the Klein Karoo vegetative region, within the Swartberg Mountain pass which rises 2000 m above sea level within 100 km of the coast (Hahn *et al.,* 2017). Another major river, the Breede river, has the fourth largest annual runoff in South Africa (Taljaard., 2003). It flows along 322 km in a southeast direction and discharges into the ocean near Cape Infanta on the South coast (Cawthra *et al.,* 2020; Dupont *et al.,* 2021). The transported sediments are partly sequestered in the delta plains and/or submarine deltas, and the remaining sediment is transported to the adjacent upper continental slope from where it is further distributed downslope via submarine canyons and subsequently to the deep sea by ocean currents (Hu *et al.,* 2012). During glacial sea level low stands, when the continental shelf was subaerially exposed, the Breede river mouth was probably situated south of Cape Agulhas, further west than its present-day location (Dupont *et al.,* 2021).

Figure 3.3: Images of rivers from eastern Cape of South Africa, (a) Extant erosional action in Mvalweni River in eastern Cape of South Africa; (b) Mbashe River in the eastern Cape province.

3.2.3 Regional Geology

The regional geology surrounding Durban (in the KwaZulu-Natal) and the eastern Cape is considerably different to the southern Cape (Figure 3.4). The Karoo Supergroup is the prominent source rock in the former region. It overlies the older Cape Supergroup which forms southern Africa's most extensive geological series, central to the Drakensberg Mountain system (Stewart *et al.,* 2020) and extend east-west across central South Africa. The topographic lower parts of the Karoo basin are composed of the Dwyka, Ecca and Beaufort Groups from the lower Carboniferous to Early Jurassic (Catuneanu *et al.,* 2005; Riley *et al.,* 2005; Moore *et al.,* 2009; Neumann *et al.,* 2011), which consists mainly of mudstones and siltstones. These sedimentary rocks are capped by the Drakensberg Group, which is a succession of basalts such as the Karoo flood basalts (Compton, 2004). The KwaZulu-Natal region is additionally cut by numerous dolerite dykes and sills (Riley *et al.,* 2005).

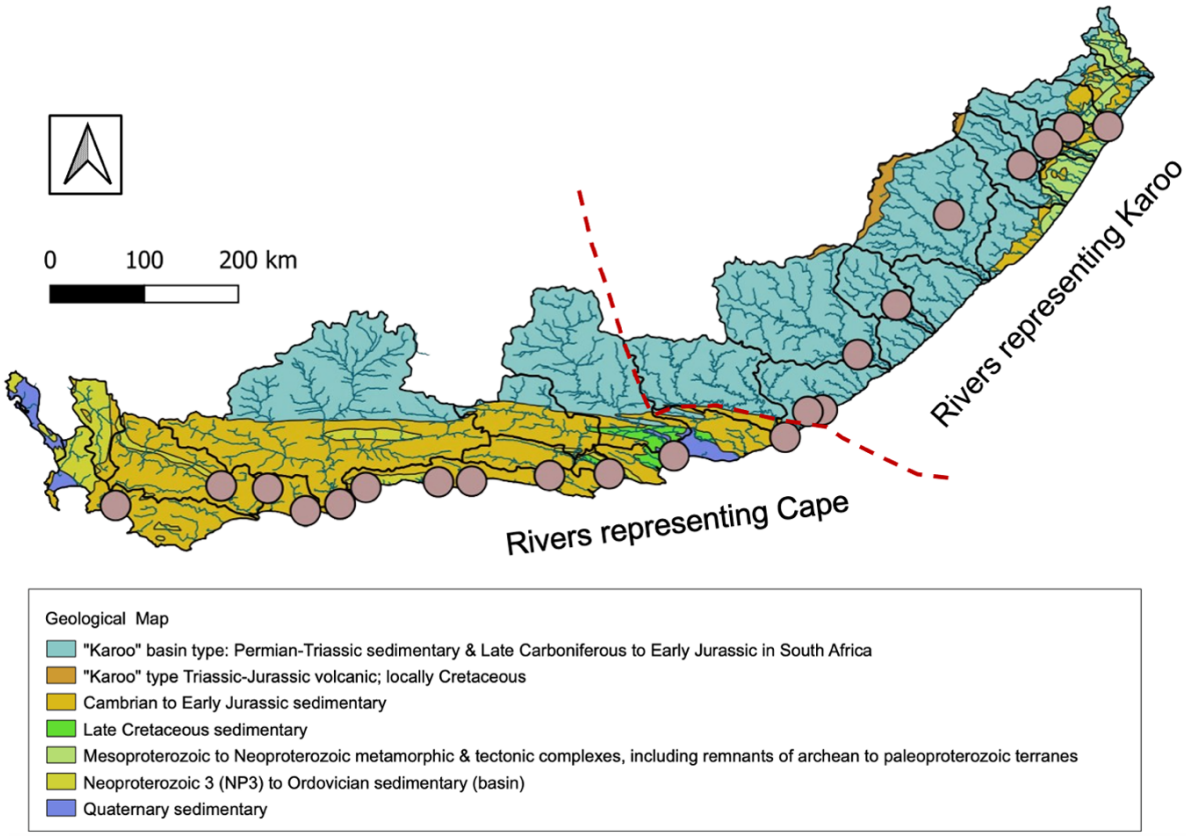

Figure 3.4: South African geology within each drainage basin, with legend indicating ages of bedrock types. Solid grey circles mark sample localities in this present study. Red line shows boundary between rivers draining Karoo Supergroup rocks in the eastern region, and rivers draining the Cape Supergroup, in the southern Cape.

Most of the river courses in the southern Cape do not erode the Karoo Supergroup, due to the Cape Fold Mountain Belt acting as a barrier (Stewart *et al.,* 2020). The Cape Supergroup is an Early Palaeozoic unit (Cambrian-Ordovician) and extends ~1000 km across the southern and western Cape of South Africa. It is subdivided into groups predominantly consisting of young mudstone of the Witteberg and Bokkeveld Groups as well as sandstones and shales of the older Table Mountain Group (Compton, 2004). The oldest sequences are the Cape Granite Suite and Malmesbury Group which are a metamorphosed shale. The Cape Granite Suite is stratigraphically below the Table Mountain Group (Harris et al., 1999). The later rocks sequences are part of the Cape Fold Belt Mountains which traverse the southern Cape from west to east. The Cape Supergroup is mainly composted of micas which weather to illite (Compton and Maake, 2007; Hahn *et al.,* 2016). The weathering products of these distinct bedrock geologies are weathered and transported across the river catchment areas to be finally discharged and deposited into the ocean.

3.3 Sampling and Analytical Methods

3.3.1 Sample Selection

This study was performed on 22 modern river sediment samples collected from riverbanks of active and abandoned river channels covering each major river catchment between Durban and Cape Town (Figure 3.5). The rivers selected are complementary to the study of Hahn *et al.* (2017, 2018) which uses <63 µm and <120 µm size fractions from 10 rivers in South Africa. The overlap between the two studies exists only within the Gourritz river catchment, their study uses 8 samples from the Gourritz as an upstream transect but does not include radiogenic isotopes. Our study fills gaps in the existing datasets (Figure 3.1) cumulating into a complete dataset from river samples on a restricted grain size range from the eastern and southern Cape of South Africa.

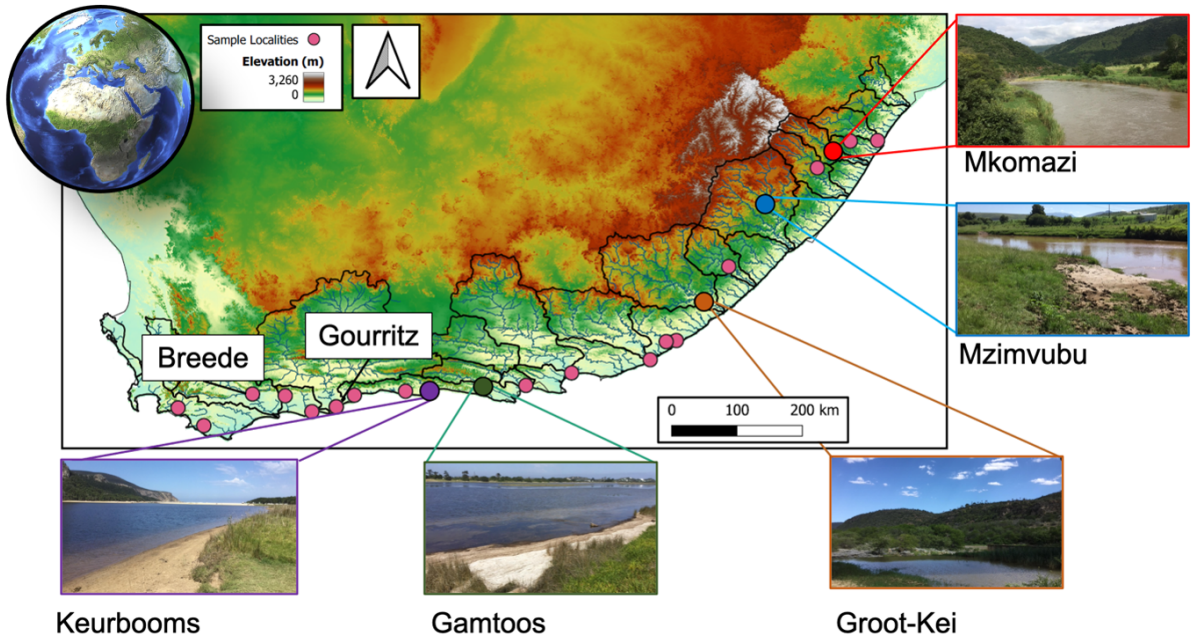

Figure 3.5: Elevation map of Southern Africa with major river drainage areas and sample locations (circles). Colours of sample locations correspond to the those of the outline of photographs (red: Mkomazi, blue: Mzimvubu, orange: Groot-Kei, green: Gamtoos, Purple: Keurbooms). Elevation map is from the Hydro1K dataset.

Twenty river catchments located within South Africa were sampled for this study. The catchments have two main geological bedrock types; the Karoo Supergroup and Cape Supergroup. In order to estimate the percentage bedrock type in each river catchment, the drainage networks of the sampled rivers were defined using Global Runoff Data Centre (GRDC) HydroRIVERS dataset (Lehner and Grill, 2013). The Global 30 Arc-Second Elevation Data Set (GTOPO30) was applied to obtain the drainage basins from the GRDC Major River Basins (MRB) of the World, which incorporates datasets from the HydroSHEDS. A geological map was obtained from the French Bureau de Recherches

Géologiques et Minières (BRGM) geological survey (Thieblemont, 2017) and was overlaid by the catchment boundaries using the union tool in Quantum Geographic Information System (QGIS) to quantify the main geological units within in each drainage basin and river catchment area was calculated based on the surface areas.

A bedrock database was generated from the union tool outputs of QGIS (Table 3.1). This was achieved by calculating the spatial extent of each type of bedrock within the area (km^2) of each river catchment, using the tabulate spatial analyst tool in QGIS. The mean weighted bedrock age (million years) was generated by multiplying the spatial extent of each bedrock type by its known age (from the BRGM shape file (Thieblemont, 2017)). The use of this bedrock database and mean bedrock age gives useful information on the isotopic signature of the material in each river catchment.

Table 3.1: Bedrock geology database and weighted average bedrock age (Ma). Cambrian to Early Jurassic and Neoproterozoic to Ordovician are considered to be Cape Supergroup. Late Carboniferous to Early Jurassic are considered to be Karoo Supergroup based on section 3.2.3

River	Sample	Mesoproterozoic to Neoproterozoic metamorphic	Neoproterozoic to Ordovician sedimentary basin	Cambrian to Early Jurassic sedimentary	Late Carboniferous to Early Jurassic	Triassic-Jurassic volcanic	Late Cretaceous sedimentary	Quaternay sedimentary	Weighted Average Age
Age of Rock		1.6-1.0 Ga	635-443 Ma	485-359 Ma	299-145 Ma	201-145 Ma	105.5-66 Ma	2.6-0 Ma	Million (Ma)
Mgeni	LPS03	15.295	0.000	20.887	63.819	0.000	0.000	0.000	336.113
uMlazi	LPS04a	29.622	0.000	35.467	34.911	0.000	0.000	0.000	561.638
Mkomazi	LPS05a	7.028	0.000	4.597	87.702	0.673	0.000	0.000	179.463
Mzimkulu	LPS06	4.540	0.000	1.495	89.750	4.216	0.000	0.000	141.723
Mzimvubu	LPS11a	0.000	0.000	0.000	91.211	8.789	0.000	0.000	85.438
Mbashe	LPS14	0.000	0.000	0.000	100.00	0.000	0.000	0.000	77.000
Groot-Kei	LPS15	0.000	0.000	0.000	98.930	1.070	0.000	0.000	78.027
Tyolomnqua	LPS18	0.000	0.000	2.298	97.702	0.000	0.000	0.000	84.928
Keiskamma	LPS19	0.000	0.000	2.298	97.702	0.000	0.000	0.000	84.928
Groot-vis	LPS21	0.000	0.000	8.143	91.857	0.000	0.000	0.000	105.093
Sundays	LPS24a	0.000	0.000	8.567	82.136	0.000	7.039	2.258	100.816
Gamtoos	LPS28	0.000	15.400	41.402	0.000	0.000	43.198	0.000	198.032
Krom	LPS29	0.000	14.281	85.649	0.000	0.000	0.069	0.000	375.164
Keurbooms	LPS32	0.000	14.281	85.649	0.000	0.000	0.069	0.000	375.164
Kynsa	LPS33	0.000	14.281	85.649	0.000	0.000	0.069	0.000	375.164
Kleinbrak	LPS37b	0.000	14.281	85.649	0.000	0.000	0.069	0.000	375.164
Gourritz	LPS38a	0.000	2.990	46.542	50.467	0.000	0.000	0.000	238.138
Gourritz	LPS38b	0.000	2.990	46.542	50.467	0.000	0.000	0.000	238.138
Goukou	LPS39	0.000	0.000	100.000	0.000	0.000	0.000	0.000	422.000
Duisenhoks	LPS41	0.000	0.000	100.000	0.000	0.000	0.000	0.000	422.000
Bree	LPS42	0.000	7.397	92.603	0.000	0.000	0.000	0.000	397.885
Bot	LPS43	0.000	24.963	70.015	0.000	0.000	0.000	5.023	319.492
Bot	LPS45	0.000	24.963	70.015	0.000	0.000	0.000	5.023	319.492

3.3.2 Geochemistry - Pre-treatment

Approximately 20-30 g of wet river sediment was collected from the riverbanks and 20 g of wet sediment was processed. The 22 samples were split into two different size fractions, so a total of 44 sediment samples were processed and analysed (see section 2.3.1 and 2.3.2). The radiogenic isotopes geochemistry is outlined in section 2.3.3. To separate the 2-32 µm fraction, the residual samples (>2 µm) were wet sieved using a <32 µm sieve and dried at 40°C overnight. This method order means the geochemistry is representative of the lithogenic terrigenous fraction. To derive radiogenic isotope endmembers for the southern Cape, the percentages of main geological units in each river catchment were calculated

from data outputted from QGIS (Table 3.1) and used in a simple linear mixing model (section 2.3.4).

3.3.3 Grain Size Analyses

To confirm grain size isolation (detailed in Chapter 2) was successful, grain size distributions on selected samples were determined on both the <2 µm and 2-32 µm size class. Grain size analysis of both isolated fractions (<2 µm and 2-32 µm) indicated that there was no overlap between these size fractions. As the grain size analysis was measured on the sediment after the geochemical pre-treatment (section 2.3.1), the grain size distribution is representative of the geochemistry and grain size isolation.

Additional grain size analyses were performed on the bulk sediment fraction (0.2 - 2000 µm) at the Vrije Universiteit (VU) Amsterdam, in the laboratory for sediment analysis using a Sympatec HELOS KR laser diffraction particle sizer. Prior to analysis, organic material, biogenic silica and calcium carbonate were removed from the bulk. To verify all components were removed successfully microscope analyses were carried out on selected sediment samples.

Grain size endmember modelling is a metric for unmixing grain size distributions into possible sub-populations. Here, the grain size distributions of all samples are decomposed into discrete endmembers, which allows the identification of the major terrigenous grain size components in the overall size population. The resulting endmembers can be related to the grain-size distributions which provide an interpretation of transport mechanisms of South African river systems, and the abundance of the targeted grain-size ranges in these samples (section 2.2.1.3.1 and 2.3.7.1).

3.4 Results

3.4.1 Mineralogy and Geochemistry

To differentiate between the $^{87}Sr/^{86}Sr$ isotopes measured on clay fraction (<2 µm) and on the fine silt 2-32 µm fraction, the $^{87}Sr/^{86}Sr$ isotope ratios are referred to as $^{87}Sr/^{86}Sr_{clay}$ and the $^{87}Sr/^{86}Sr_{finesilt}$ values for <2 µm and 2-32 µm fractions respectively

3.4.1.1 <2 µm fraction

Lithogenic riverine sediments display a systematic geographical variation in εNd_{clay} composition related to the regional geology (Figure 3.6). Within the KwaZulu-Natal province, εNd values are the most unradiogenic ranging between -12.50 to -10.00 (LPS03-06; Figure 3.6; Table 3.2). The $^{87}Sr/^{86}Sr_{clay}$ values from the KwaZulu-Natal are remarkably homogenous (with a low $\sigma = 0.003$) and vary from 0.741 to 0.747 ($\pm$0.00001).

Within the southeast rivers (LPS11a – LPS24a; Figure 3.6; Table 3.2), isotopic εNd_{clay} ratios discriminate the younger Karoo sediments displaying $^{87}Sr/^{86}Sr_{clay}$ as low as 0.729 and

εNd values > -9.000 (±0.200). River sediments from within the Karoo Supergroup have a geologically younger $^{87}Sr/^{86}Sr_{clay}$ isotope fingerprints (from 0.729 to 0.747 (±0.00001)).

The southern rivers of the Cape Supergroup have a larger data range of εNd_{clay} and $^{87}Sr/^{86}Sr_{clay}$ compositions (LPS28- LPS45; Figure 3.6; Table 3.2), with higher $^{87}Sr/^{86}Sr_{clay}$ ratios ranging from 0.732 to 0.766 (±0.00001), compared to the rivers of KwaZulu Natal and southeast region. The εNd_{clay} values show a distinct difference between the drainage regions further South and those draining in the eastern coast. In the southern Cape, εNd values range between -10.500 to -9.000 (±0.200) and are somewhat more unradiogenic than the eastern Cape (Figure 3.6).

Table 3.2: Results table of radiogenic isotope data from South African river sediment. εNd is measured on the clay fraction only

WS_ID	Sample	Latitude	Longitude	$^{87}Sr/^{86}Sr_{clay}$	$^{87}Sr/^{86}Sr_{finesilt}$	ϵNd
5242	LPS03	-29.798	30.959	0.748	0.731	-11.277
5256	LPS04a	-29.810	30.500	0.746	0.744	-12.066
5245	LPS05a	-30.008	30.245	0.742	0.748	-8.141
5252	LPS06	-30.258	29.944	0.743	0.723	-8.533
5291	LPS11a	-30.850	29.070	0.738	0.717	-7.827
5289	LPS14	-31.920	28.448	0.730	0.720	-8.399
5288	LPS15	-32.508	27.987	0.738	0.716	-8.609
5311	LPS18	-33.166	27.565	0.732	0.714	-7.843
5311	LPS19	-33.185	27.393	0.735	0.711	-7.611
5309	LPS21	-33.489	27.124	0.742	0.712	-8.241
5302	LPS24a	-33.711	25.798	0.747	0.713	-8.900
5326	LPS28	-33.922	25.027	0.743	0.727	-10.154
5329	LPS29	-33.945	24.318	0.736	0.733	-10.439
5329	LPS32	-34.012	23.391	0.745	0.726	-9.679
5329	LPS33	-34.020	22.996	0.732	0.723	-9.963
5329	LPS37b	-34.087	22.134	0.741	0.732	-9.885
5322	LPS38a	-34.283	21.827	0.756	0.732	-9.359
5322	LPS38b	-34.283	21.827	0.760	0.728	-8.942
5331	LPS39	-34.364	21.416	0.766	0.751	-9.966
5331	LPS41	-34.096	20.966	0.746	0.730	-9.453
5321	LPS42	-34.067	20.414	0.749	0.738	-10.171
5323	LPS45	-34.300	19.158	0.738	0.731	-9.344

3.4.1.2 2 - 32 µm (fine silt) fraction

The $^{87}Sr/^{86}Sr_{finesilt}$ ratios from the KwaZulu-Natal are predominantly lower than the $^{87}Sr/^{86}Sr_{clay}$ values. The $^{87}Sr/^{86}Sr_{finesilt}$ values have a larger range, from 0.711 to 0.752 (±0.00001) in the KwaZulu-Natal region than the $^{87}Sr/^{86}Sr_{clay}$ from the co-registered sample (Figure 3.7). There is one exception identified from the Mkomazi River (LPS 05a) as the $^{87}Sr/^{86}Sr_{finesilt}$ value is more radiogenic (larger) than the clay fraction (Figure 3.7). Sediments from the southeast rivers carry a lower $^{87}Sr/^{86}Sr_{finesilt}$ value by 0.022 (±0.00001) than the $^{87}Sr/^{86}Sr_{clay}$ value. The $^{87}Sr/^{86}Sr_{finesilt}$ versus $^{87}Sr/^{86}Sr_{clay}$ values from within the southern Cape are 0.015 (±0.00001) lower. No εNd measurements were carried out on the 2-32 µm fraction. Overall, the $^{87}Sr/^{86}Sr_{clay}$ values are higher than the $^{87}Sr/^{86}Sr_{finesilt}$ values by 0.01513 but differences range between +0.03 to 0.001 (Table 3.2; Figure 3.7).

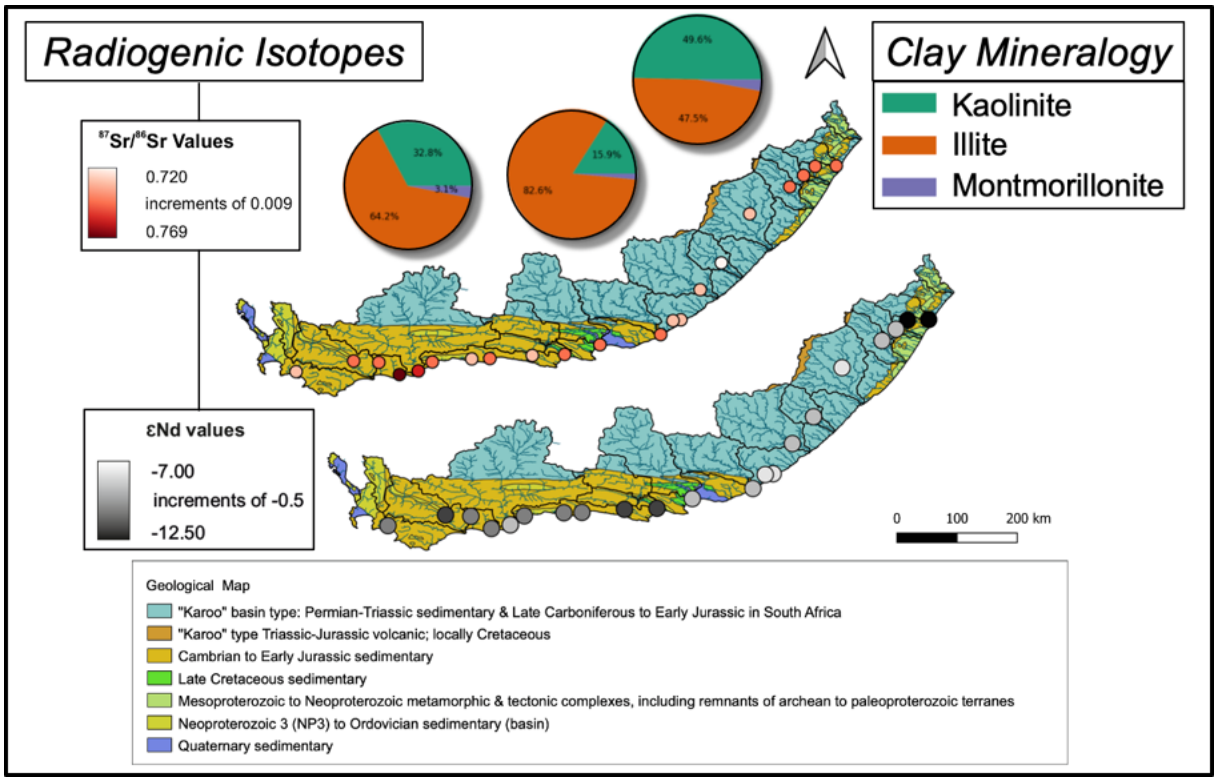

Figure 3.6: Radiogenic isotope compositions and clay mineralogies of selected river catchments analysed. The three pie charts represent the clay mineral composition of three regions, KwaZulu-Natal, eastern Coastline and southern Coastline (top to bottom) (key on right). River catchment geology: circles indicate sample localities and circle colour represents the radiogenic isotope values, indicated by the keys (left).

3.4.2 Grain Size

Riverine sediments have either unimodal and polymodal grain size distributions with a mean grain size of 160 µm. In general, sediments originating from the Karoo Supergroup are finer grained than those from the Cape Supergroup (Figure 3.8a). Karoo sediments have an average grain size of 88 µm as opposed to Cape Supergroup with a mean size of 238 µm (Figure 3.8a). Consequently, samples from rivers dominantly draining the Cape Supergroup (LPS28 to LPS38b) contain high amounts of sand (>80%) and low clay amounts compared to the samples from the Karoo Supergroup (eastern Cape) (Table 3.3; LPS 03 to LPS 21).

The grain size of these riverine sediment samples can be unmixed into three endmembers, which have an overall fit with an r^2 of 0.89 between the measured and modelled grain-size distributions. The finest grain-sized endmember has a distribution centred around 44 µm (Figure 3.8b) and is likely to be the suspension mode of these dominantly seasonal rivers. The coarsest endmember is centred around 350 µm and therefore represents riverine bedload transport of river sediments (Figure 3.8b). South African river sediments are coarser than terrestrial fraction in marine sediments e.g. offshore the Zambezi river (van

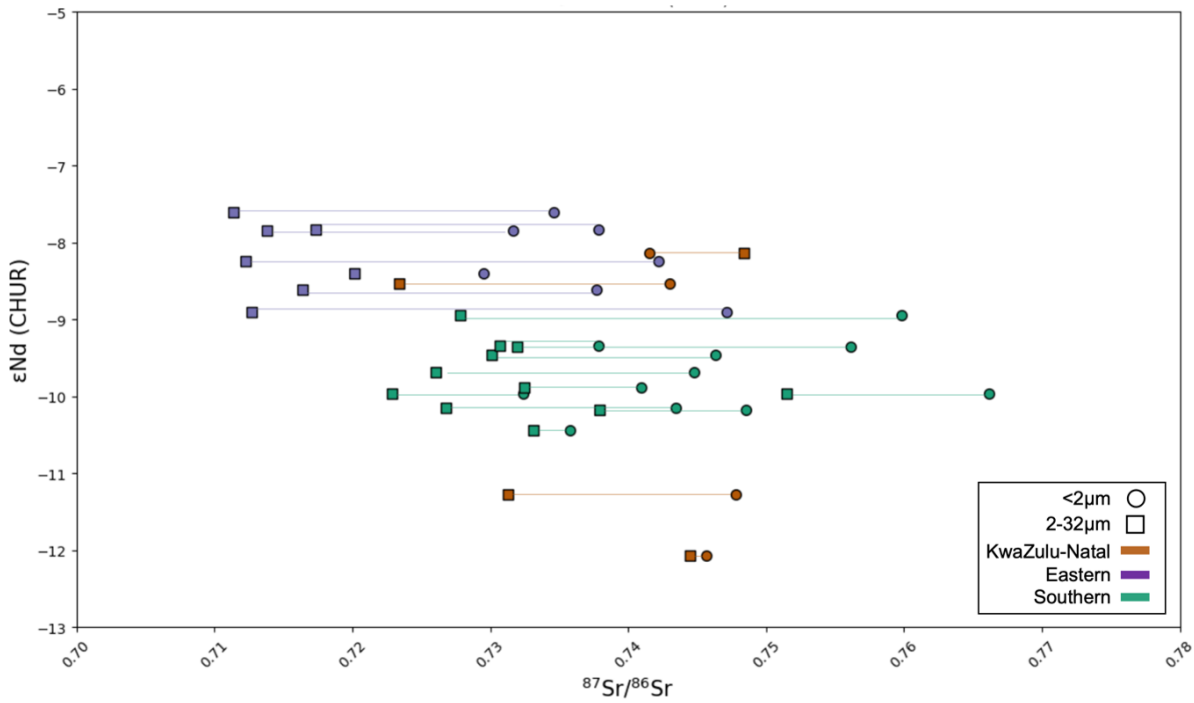

Figure 3.7: Comparison of $^{87}Sr/^{86}Sr$ isotope composition showing the values obtained from the <2 µm size fraction (circles) and 2-32 µm size fraction (squares) follow the same trend but have an average offset of +0.03 to 0.001 in <2 µm data. Note: No Nd analysis was carried out on 2-32 µm so the same Nd value from <2 µm analysis is used.

der Lubbe *et al.*, 2014).

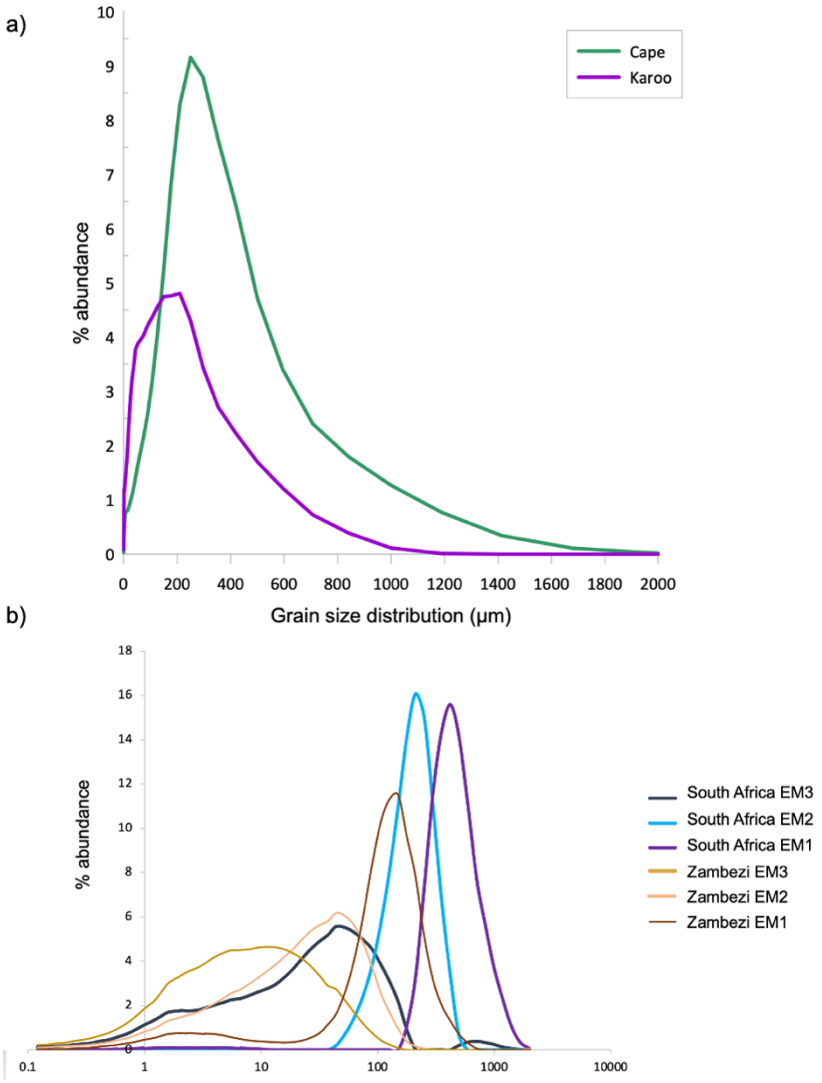

Figure 3.8: Grain Size distributions of riverine sediments; a) Mean grain size distributions for Karoo (southeast rivers) and Cape (southern Cape rivers). b) Endmember % abundance of EM1 (coarsest), EM2 and EM3 (finest) for South African rivers (this study) and Zambezi sediment (van der Lubbe *et al.*, 2014)

3.4.3 Clay Mineralogy

River sediments from the KwaZulu-Natal (LPS03-LPS06; Table 3.4) have high kaolinite abundances (between 44 and 57%) (Figure 3.6). Within the southeast river beds (LPS11a – LPS24a; Table 3.4), sediments have lower kaolinite (< 26%) and contain more illite compositions than the KwaZulu-Natal (Figure 3.6). In general, the southern Cape river sediments (LPS28 – LPS45; Table 3.4) contain more kaolinite than the eastern Cape rivers (Figure 3.6).

Table 3.3: Grain size percentages ordered by class; Sand > 63µm, Silt 2-63µm and clay <2µm. LPS03 to LPS24a are from eastern Cape, LPS28 to LPS45 are from southern Cape.

Sample	Latitude	Longitude	Sand (%)	Silt (%)	Clay (%)
LPS03	-29.798	30.959	69.563	27.220	3.217
LPS04a	-29.810	30.500	84.613	12.185	3.202
LPS05a	-30.008	30.245	14.977	71.622	13.401
LPS06	-30.258	29.944	28.750	60.067	11.183
LPS11a	-30.850	29.070	79.404	18.197	2.399
LPS14	-31.920	28.448	92.301	6.686	1.013
LPS15	-32.508	27.987	10.192	79.099	10.709
LPS18	-33.166	27.565	33.000	54.860	12.140
LPS19	-33.185	27.393	43.064	48.407	8.528
LPS21	-33.489	27.124	29.603	62.878	7.519
LPS24a	-33.711	25.798	89.063	9.158	1.779
LPS28	-33.922	25.027	87.291	10.841	1.868
LPS29	-33.945	24.318	93.881	4.971	1.149
LPS32	-34.012	23.391	96.820	2.482	0.698
LPS33	-34.020	22.996	81.274	16.962	1.763
LPS37b	-34.087	22.134	94.128	5.155	0.718
LPS38a	-34.283	21.827	93.111	5.584	1.305
LPS38b	-34.283	21.827	96.541	2.663	0.796
LPS39	-34.364	21.416	28.507	63.675	7.818
LPS41	-34.096	20.966	63.554	32.930	3.516
LPS42	-34.067	20.414	95.550	3.704	0.746
LPS45	-34.300	19.158	58.386	37.049	4.565

3.4.4 Radiogenic Endmember Mixing Calculations

The Lipp *et al.* (2021) endmember mixing model requires two inputs; 1) bedrock type in the studied river catchments and 2) the radiogenic isotopes signatures from the corresponding river catchments.

In order to understand the bedrock geology, the South Africa study region was mapped on GIS to understand the bedrock geologies mixing with each river sample and therefore determine the source rocks. This was exported from GIS giving the main geological units within in each drainage basin. River catchment area was calculated based on the surface areas from the Hydro1K catchment dataset. This allowed the spatial extent of each bedrock type within the catchment area to be calculated and determine the % bedrock make up of each river catchment. Based on this output the bedrock age was calculated, which allowed the weighted average age of each catchment to be determined (Table 3.1).

The Sr and Nd values of each river sample and the corresponding bedrock type which each sample sits in, was inputted into the Lipp *et al.* (2021) mixing model on Python and generated the results (Figure 3.9). This model does assume that mixing is solely between the rock types entered, but the model generated two endmembers for both the <2 µm

Table 3.4: Clay mineral abundances for river sediment samples. LPS03 to LPS24a are from eastern Cape, LPS28 to LPS45 are from southern Cape

Sample	Latitude	Longitude	Kaolinite (%)	Illite (%)	Montmorillonite (%)
LPS03	-29.798	30.959	44.448	52.965	2.587
LPS04a	-29.810	30.500	51.291	47.068	1.641
LPS05a	-30.008	30.245	45.469	52.813	1.718
LPS06	-30.258	29.944	57.333	37.072	5.595
LPS11a	-30.850	29.070	18.753	81.070	0.177
LPS14	-31.920	28.448	9.869	87.226	2.905
LPS15	-32.508	27.987	26.784	70.315	2.901
LPS18	-33.166	27.565	20.288	78.863	0.849
LPS19	-33.185	27.393	8.217	90.709	1.075
LPS21	-33.489	27.124	17.520	81.321	1.159
LPS24a	-33.711	25.798	9.958	88.663	1.378
LPS28	-33.922	25.027	13.036	85.089	1.875
LPS29	-33.945	24.318	58.823	34.804	6.373
LPS32	-34.012	23.391	35.862	61.283	2.854
LPS33	-34.020	22.996	42.378	54.991	2.631
LPS37b	-34.087	22.134	29.923	65.947	4.130
LPS38a	-34.283	21.827	16.387	82.989	0.624
LPS38b	-34.283	21.827	19.027	80.227	0.746
LPS39	-34.364	21.416	20.649	74.916	4.435
LPS41	-34.096	20.966	25.190	69.431	5.379
LPS42	-34.067	20.414	27.925	68.636	3.439
LPS43	-34.067	20.414	43.729	53.070	3.201
LPS45	-34.300	19.158	60.114	38.535	1.351

fraction and the 2-32 µm fraction for the Karoo and Cape Supergroups. The endmembers do fit with the general bedrock picture (Karoo Supergroup has a younger Nd signal than the older Cape Supergroup).

The model expects the data to sit along the mixing line (Figure 3.9)- for Nd there is a good fit which shows Nd is likely influenced solely by the mixing of source rocks, supported by previous studies regarding the credibility of Nd as a provenance tracer. As Sr is not sitting as close to the mixing line, it is likely another process is driving the Sr signal, likely in addition to Karoo and Cape Supergroup (Figure 3.9). This is the first indication in this Chapter that the Sr signal is not just showing provenance.

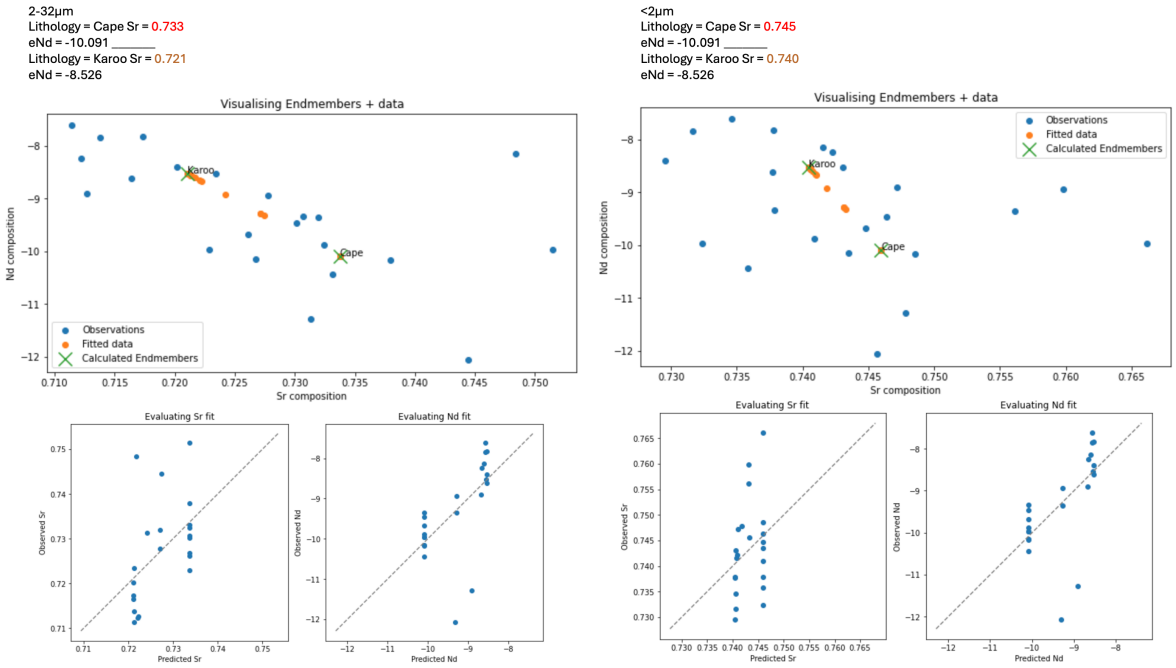

Figure 3.9: Radiogenic isotope endmember mixing calculation results for both size fractions measured. The observed data is the real measured data for εNd and $^{87}Sr/^{86}Sr_{clay}$ isotopes and the predicted data is what the model predicts by assuming mixing between radiogenic isotopes endmembers. The calculated endmembers for the Karoo and Cape are plotted in green.

3.5 Discussion: Geochemical Fingerprints

Here the processes driving the trend in the radiogenic isotopes and clay minerals are explored. The first part of this discussion investigates possible biases of the radiogenic isotopes ($^{87}Sr/^{86}Sr$ and εNd) and then subsequent discussions are applied to the use of the radiogenic isotopes endmember mixing in palaeoclimate studies. The variability in εNd values from South African rivers reflects two major source regions: 1) Karoo sediments, and 2) Cape Supergroup. The sediment from the eastern Cape river bed material originates from the Karoo sediments and the southern Cape rivers are from the rocks comprising the Cape Supergroup.

3.5.1 Signals from Radiogenic Isotopes

The radiogenic isotope composition of weathering products is initially influenced by the isotopic composition of the parent rocks and subsequently by mixing between different sediment sources during transport through the catchment. εNd isotopes are almost unaffected by chemical weathering (Goldstein *et al.,* 1984; Blum and Erel, 2003; Fagel *et al.,* 2004; Fagel, 2007; Meyer *et al.,* 2011; Garzanti *et al.,* 2014; van der Lubbe *et al.,* 2014; Hahn *et al.,* 2016, 2018; van der Lubbe *et al.,* 2016), therefore εNd is utilised as a tracer for geological provenance. The εNd data show a significant difference between the eastern drainage basins (-8.529 εNd $\pm$0.200) and southern river catchments (-10.091 εNd

±0.200) (Figure 3.10; Table 3.2). This observed difference in εNd values can be explained by the distinct geology in the region. The weighted average bedrock age of each river catchment (Table 3.1) is linearly regressed against εNd from the corresponding catchment with older provenance ages of bedrock correlating with more unradiogenic εNd (r^2= -0.82) (Figure 3.11). Thus, εNd clearly discriminates between the sediments of the Karoo and Cape Supergroup (Figure 3.6). Most of the eastern Cape basement is composed of the Karoo Supergroup extending along the eastern coastline of South Africa and with the river catchments cut off inland by the Drakensberg Mountains. Along the southern Cape, the more unradiogenic εNd values reflect the older Cambrian-Ordovician basement rocks of the Cape Supergroup which extend east-west across the southern Cape region (Figure 3.6). This confirms that the εNd primarily reflects the bedrock geology and is a provenance tool, supported by previous studies (Goldstein *et al.,* 1984; Blum and Erel, 2003; Fagel *et al.,* 2004; Fagel, 2007; Meyer *et al.,* 2011; Garzanti *et al.,* 2014; Van der Lubbe *et al.,* 2014; van der Lubbe *et al.,* 2016; Hahn *et al.,* 2018).

3.5.1.1 Source Regions

This study identifies two new South African radiogenic isotope endmembers (Table 3.5) (based on radiogenic isotope endmember mixing (section 2.3.4)), which are visibly different isotopically from the northern Zambezi river and offshore the Limpopo river (Figure 3.10). Nearshore the mouth of the Limpopo river, the <2 µm fraction yields $^{87}Sr/^{86}Sr_{clay}$ values of 0.767 (± 0.000012) and εNd_{clay} values of -19.200 (± 0.07), based on data from Simon *et al.* (2020a) and the radiogenic isotopes mixing calculations. Isotopic compositions of the Zambezi catchment (Garzanti *et al.,* 2014; van der Lubbe *et al.,* 2014) are less radiogenic than offshore Limpopo sediment ($^{87}Sr/^{86}Sr_{clay}$ = 0.723 (± 0.00003) and ε_{clay} = -13.798 (± 0.2)). The generation of these radiogenic isotope values is discussed further in Chapter 4. Both the Limpopo and Zambezi rivers drain geologically older cratonic sediment (Jelsma and Dirks, 2002; Eglington and Armstrong, 2004).

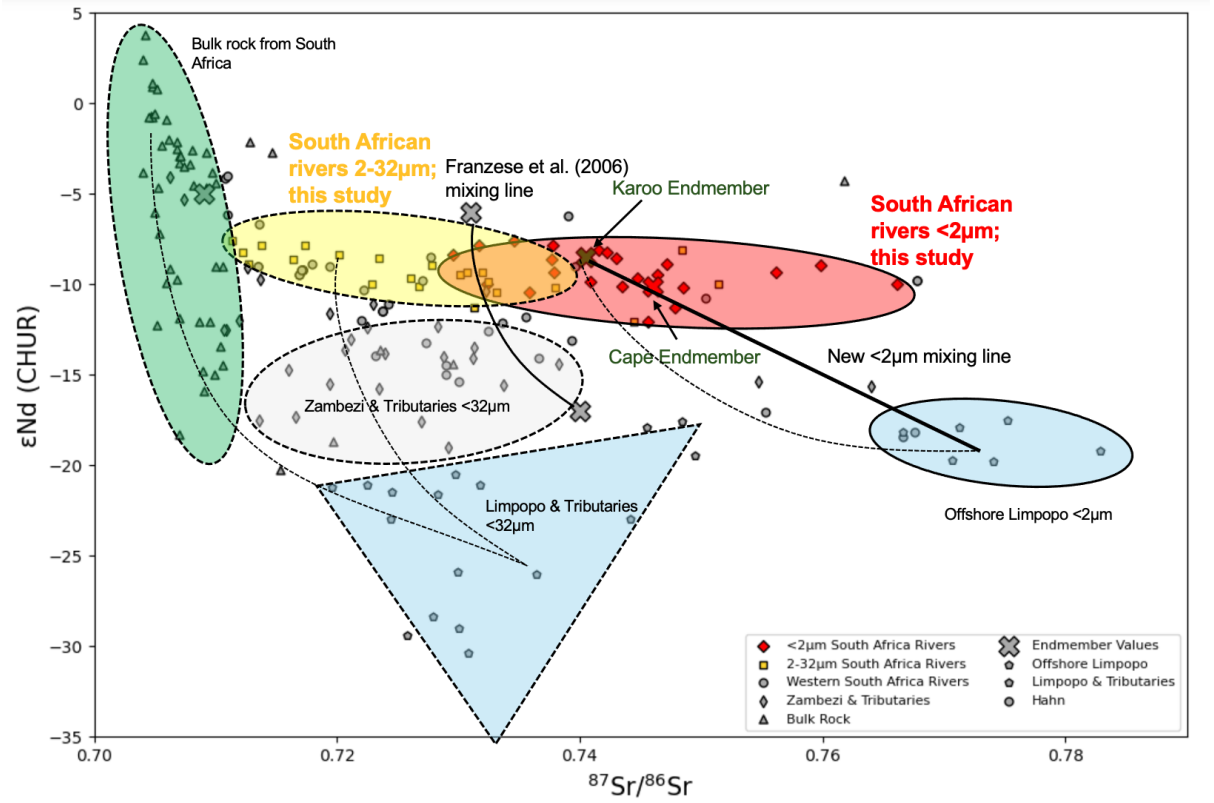

Figure 3.10: Sr-Nd isotope ratios mixing plot based on linear regression between South African river sediments (red) and published terrestrial and marine samples from the region. Samples measured in this study are in colour (red and yellow) and discriminate from Limpopo and Zambezi sourced sediments. Theorised mixing line from samples of the same grain size (<2 µm) from South Africa (our study) and offshore Limpopo (Simon *et al.*, 2020a). Mixing line from Franzese *et al.* (2006) mixing of local marine South African endmember and Agulhas endmember included (labelled as Franzese et al. (2006) mixing line), as well as theoretical mixing lines between 2-32 µm South Africa and <32 µm Limpopo (Garzanti *et al.*, 2014), as well as bulk rock samples from South Africa (Riley *et al.*, 2005; Neumann *et al.*, 2011) and <32 µm Limpopo (Garzanti *et al.*, 2014).

The mixing model, generated using linear regression agrees well with previous radiogenic isotope studies from the region, these are; western rivers from South Africa (Herbert, 2009; Weldeab *et al.*, 2013) and offshore Limpopo (Simon *et al.*, 2020a) (Figure 3.10) - the mixing line from this present study fits between local South Africa rivers (this study) and offshore the Limpopo. A previous mixing line generated by Franzese *et al.* (2006) (based on lithogenic sediment from marine sediments) also supports the values identified in our study. However, the local endmember (identified as South African rivers) (Franzese *et al.*, 2006), bears a somewhat more unradiogenic Sr value to our new endmembers (Table 3.5). This offset is attributed to grain size fractionation (Figure 3.10) as Franzese *et al.* (2006) analysed the radiogenic isotopic compositions on the <63 µm grain size fraction. The grain size fractionation could be due to the influence of marine strontium and authigenic clay formation resulting in a shift to lower $^{87}Sr/^{86}Sr$ values in the <63 µm class or additionally due to the effect of marine barite on the $^{87}Sr/^{86}Sr$ signal (Jewell

et al., 2022). However, the εNd values from Karoo and Cape endmembers are not too different from the local endmember εNd identified in Franzese *et al.* (2006) (εNd = -6) which gives further evidence that the εNd isotope system is less sensitive to grain size or authigenic processes, as found in previous studies (Bayon *et al.,* 2009).

Table 3.5: Endmember Values for South African river mud from two regions (Karoo is eastern Cape and Cape is southern Cape) by using radiogenic isotope mixing model (section 2.3.4).

Location	**$^{87}Sr/^{86}Sr$ value**	**εNd value**
Karoo	0.740	-8.526
Cape	0.745	-10.091

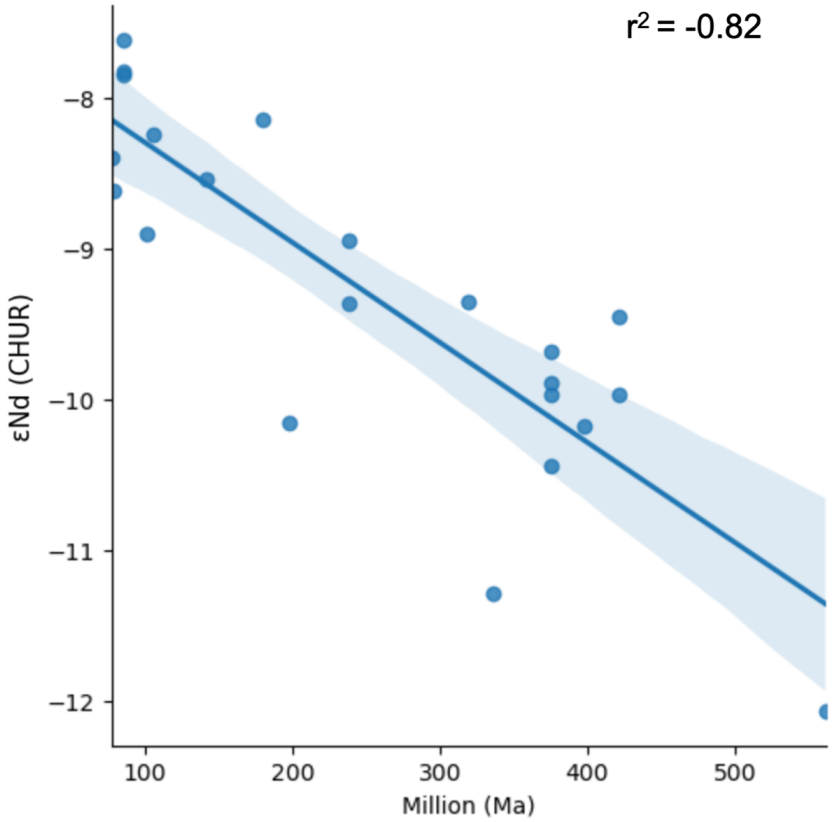

Figure 3.11: Correlation between age of bedrock and Nd from each river catchment, confidence interval is 95% (shaded blue). Blue circles indicate samples.

3.5.2 The Sr Grain Size Effect

The $^{87}Sr/^{86}Sr$ ratios analysed in two different size fractions to identify the magnitude of the grain size effect on the isotopic composition of $^{87}Sr/^{86}Sr$ ratios. The 2-32 µm fraction was chosen to fit with existing studies that analysed the <32 µm fraction (Garzanti *et al.,* 2014). The clay fraction was used because it has the greatest potential to integrate

the different bedrock geologies in the catchment areas as it is the finest fraction so can be mixed and transported long distances compared to coarser material.

All clay samples display a more radiogenic (higher) $^{87}Sr/^{86}Sr_{clay}$ value (circles) than the $^{87}Sr/^{86}Sr_{finesilt}$ fraction (2-32 µm) (squares) on average by + 0.01513, except from sample LPS05a from the Mkomazi River (Figure 3.7). This difference is 0.00001 (e^{-5}) orders of magnitude higher than the $^{87}Sr/^{86}Sr$ isotope variability usually considered significant (Biscaye and Dasch, 1971). This significant grain size induced offset is supported by previous studies (Meyer *et al.,* 2011; Jonell *et al.,* 2018; Carter *et al.,* 2020). One such study (Hahn *et al.,* 2016) identified a +0.02 - offset in $^{87}Sr/^{86}Sr$ isotope data measured in the <2 µm fraction compared to <120 µm fraction. We find a smaller offset between <2 µm and 2-32 µm, compared to the offset between <2 µm and <120 µm from Hahn *et al.* (2016). This could be because Hahn *et al.*. (2016) use the <120 µm fraction which includes the clay fraction, whereas we have removed the clay fraction from 2-32 µm. This means that the 2-32 µm contains less weathered products which have a more radiogenic Sr signature (Blum and Erel, 2003).

The grain size effect observed between the <2 µm and 2-32 µm is likely due to the mineralogy of the samples. The Sr isotopes in the finer fractions are strongly controlled by potassium feldspar and clay minerals (Jonell *et al.,* 2018). Where there is a bigger offset in $^{87}Sr/^{86}Sr$ ratios between size fractions (Figure 3.7), samples contain more illite, indicative of less intense weathering rates. In contrast, when the offset between $^{87}Sr/^{86}Sr$ ratios on size fractions is smaller, samples contain a higher kaolinite composition. This smaller offset is indicative of a higher degree of chemical weathering as feldspar is harder to weather into kaolinite than illite. This geochemical differentiation between clay and coarser material is primarily dependent on mineralogy, as specific mineral phases strongly control Sr isotope compositions and to a less extent Nd (e.g. feldspar weathers to clay, quartzite weathers to sand) and may be enriched or depleted in a certain size fraction during transport (Garzanti *et al.,* 2009; Garçon *et al.,* 2014). In the absence of chemical weathering, bulk sediment would contain minor clay minerals and more feldspar particles and the contrast compositionally between mud and sand would be smaller (c.f. Garzanti *et al.,* 2013). As such, the weathering products in clay would be reduced, which means less Rb rich material (from the feldspars) would be in the clay minerals and a less radiogenic Sr would be recorded.

This chapter shows that the grain size effect must be considered when comparing radiogenic isotopes between samples of varying size fractions. By comparing the $^{87}Sr/^{86}Sr$ isotopes of two separate size fractions, the grain size effect on the $^{87}Sr/^{86}Sr_{clay}$ variability has been ruled out since all radiogenic isotopes are compared in the clay fraction is this thesis (Figure 3.7). Therefore, the $^{87}Sr/^{86}Sr_{clay}$ variability between different <2 µm river samples is driven by another mechanism such as the degree of chemical weathering which

is explored next, using additional lines of evidence such as clay minerals, soil composition and erosivity calculations to understand potential on-land climate processes biasing the Sr and Nd isotope composition.

3.5.2.1 Chemical Weathering

During chemical weathering, the Sr is removed from the source material leaving behind the Rb-rich minerals (e.g. micas), increasing the Rb/Sr ratio and the $^{87}Sr/^{86}Sr$ in the weathered rock (Meyer *et al.,* 2011; Jung *et al.,* 2004; Blum and Erel, 2003). Hence, the observed deviations in $^{87}Sr/^{86}Sr_{clay}$ isotope values likely represent the degree of chemical weathering (Dasch, 1969; Åberg *et al.,* 1989; Blum *et al.,* 1993; Derry and France-Lanord, 1996; Blum and Erel, 1997, 2003; Capo *et al.,* 1998; Jung *et al.,* 2004).

The river sediments from the KwaZulu-Natal bear higher $^{87}Sr/^{86}Sr_{clay}$ values (0.741 to 0.747 ($\pm$0.00001) and are likely subject to more intense chemical weathering than the rivers further South in South Africa. This difference in $^{87}Sr/^{86}Sr_{clay}$ isotope values can be attributed to higher annual rainfall amounts (Åberg *et al.,* 1989) and subsequent weathering intensity in the Drakensberg Mountains and SRZ of South Africa. The southeastern coastline of South Africa experiences more rainfall due to the high sea surface temperatures of the Southwest Indian Ocean, advecting warm moist air on land (Walker, 1990; Mason, 1995; Goddard and Graham, 1999; Camberlin *et al.,* 2001; Dupont *et al.,* 2011; Stager *et al.,* 2011; Tierney *et al.,* 2013; Simon *et al.,* 2015a; Castañeda *et al.,* 2016; Strobel *et al.,* 2019). More rainfall increases physical disaggregation and weathering of sediments in this region, causing a higher $^{87}Sr/^{86}Sr$ isotope signal. The effect of chemical weathering is further explored next by interpreting the clay composition.

3.5.2.2 Clay Composition

Karoo sourced river sediment has been found to be dominant in feldspar (70%) (Compton and Maake, 2007). The data in this chapter shows high kaolinite compositions in the riverine sediments from the KwaZulu-Natal (Table 3.4; LPS03 to 11a) which can be attributed to weathering of the feldspars within granites of the Karoo sediment. This is supported by previous work which finds granites weather to form kaolinite in regions of rainfall rates averaging 800-900 mm per year (van der Merwe and Weber, 1963). A positive relationship has been reported between higher amounts of kaolinite and the total amount of rainfall with the catchments in Southwest Africa (Dinis *et al.,* 2020). The Drakensberg Mountains and KwaZulu-Natal region receive the greatest amount of rainfall in South Africa of approximately 1000 mm per year (Rooseboom and Annandale, 1981; Rooseboom *et al.,* 1992) (Figure 3.2). The rivers from the KwaZulu-Natal have a high sediment yield (601-1000 tonnes/km^2 (Walling, 1984; Compton and Maake, 2007)) compared to the lower yield from the eastern Cape rivers. The high abundance of kaolinite in the KwaZulu-Natal Province can therefore be characteristic of the weathering of granites, coincident with

higher $^{87}Sr/^{86}Sr$ ratios which indicate high weathering rates (Blum and Erel, 2003). High levels of kaolinite has been recorded on the eastern side of Maputo, in sediments from Nelshoogte, suggesting sediments from this region and close to Lesotho are more kaolinite rich (van der Merwe and Weber, 1963) than further south.

Some rivers in the eastern Cape drain from the eastern flank of the Drakensberg (e.g. LPS 06 and 11a), these sediments have a different composition to those draining from the westerly flank of Drakensberg (Compton and Maake, 2007; Compton and Wiltshire, 2009). These westerly flank river sediments are dominant in volcaniclastic mud (Garzanti *et al.,* 2013). The volcaniclastic mud would have a different Nd isotopic signature to Karoo sediments. Significant differences are not observed in Sr and Nd composition of rivers draining from the eastern flank of the Drakensberg Mountains (e.g. LPS 06 and 11a; Table 3.2), compared to those from the eastern Cape which do not have a Drakensberg sediment source (e.g. LPS 14 to 24a; Table 3.2). There is high smectite in riverine mud derived from the weathering of the Karoo basalts originating from the westerly Drakensberg Mountains (Compton and Maake, 2007). These riverine muds are carried by the Orange river westward to the Southeast Atlantic. As our sediments contain small amounts of montmorillonite (<10%) (Table 3.4), this likely indicates that rivers east of the Drakensberg Mountains do not share the same provenance to that of Orange river and/or the volcaniclastic muds from the westerly flank.

Further south of Durban, Karoo sedimentary rock soils (eastern Cape) are more commonly rich in illite (Compton and Maake, 2007). There is a regional change in geology expressed in the clay assemblages, with riverine sediments from the eastern Cape containing more illite than further north. In general, the ratio between kaolinite and illite in the terrestrial signals corroborates well with marine records from the region from previous studies (Petschick *et al.,* 1996; Kuhn and Diekmann, 2002). Comparative studies show that South Africa is within a high illite zone (Petschick *et al.,* 1996; Kuhn and Diekmann, 2002) and marine sediment from the Cape Walvis Ridge, offshore of South Africa also reveal high illite assemblages (Petschick *et al.,* 1996). In this chapter, river sediments with high illite have lower $^{87}Sr/^{86}Sr$ isotope values than sediments from the KwaZulu-Natal. This is apparent in the eastern and southern Cape region, as Karoo sediments and rocks of the Cape Supergroup contain more illite, because sediments in this region contain easily weathered material such as illite (Compton and Maake, 2007; Hahn *et al.,* 2016).

The southern drainage basins mainly contain older rocks reflecting the Cape Supergroup (Table 3.1). The Cape Supergroup is mainly composted of micas which weather to illite (Compton and Maake, 2007; Hahn *et al.,* 2016). The Goukou and Gourritz river drainage basins from the southern Cape have the most radiogenic $^{87}Sr/^{86}Sr_{clay}$ isotope value of 0.766 and 0.759 ($\pm$0.00001) respectively between all samples in this study. The higher $^{87}Sr/^{86}Sr$ ratios are probably associated with a higher proportion of old micas and detrital

illite from basement rocks which contain highly radiogenic $^{87}Sr/^{86}Sr$ isotopes in the clay fraction, eroded along the course of these rivers and brought by tributaries with radiogenic $^{87}Sr/^{86}Sr$ (Hahn *et al.,* 2016).

Conversely, the river catchments located closest to Cape Town have a clay assemblage analogous to the sediment from the KwaZulu-Natal Province, high kaolinite and low illite abundances. This is likely explained by contact between sandstones and Cape granite in the area (Harris *et al.,* 1999). This is supported by other studies (e.g. Van der Merwe & Weber, 1963) which found samples close to Llandudno, Cape Town contain abundant kaolinite, representative of the geology surrounding Cape Town.

3.5.2.3 Soil Type

Soil type, determined from the Soil and Terrain Database for South Africa (Framework Programme of the Global Assessment of Land Degradation (GLADA)), reveals more red brown ferrallisol soils from the KwaZulu-Natal region, with more radiogenic $^{87}Sr/^{86}Sr$ ratios (Figure 3.12). The soil type is indicative of more intense weathering in this region, as opposed to more fluvisols in the southern Cape. This interpretation is supported by other studies that show more rainfall along the southeast coastline and inland of South Africa from various climate proxies such as plant wax δD (Hahn *et al.,* 2018), weathering indices (Garzanti *et al.,* 2014) and modelling, forecasting and historical results (Nicholson, 2000; Compton, 2011). The presence of weathering products in the soils infers high weathering rates (van der Merwe and Weber, 1963; Garzanti *et al.,* 2014), which we couple with more kaolinite (inferred as a conversion of feldspars to kaolinite due to weathering) and more radiogenic $^{87}Sr/^{86}Sr$ ratios.

3.5.2.3.1 The Effect of Erosion

Clay principally derives from mature soil profiles representing the ultimate product of chemical weathering whereas coarser material results from physical erosional processes (i.e. landslides triggered by concentrated rainfall (Attal and Lave (2006)). Therefore, accounting for singular episodic events such as a flash flood when understanding the provenance of sediments is complicated. Changes in on-land rainfall magnitudes cause shifts in river sediment discharges and wetter conditions are believed to be linked to variations in erosive power (Zabel *et al.,* 2001). The capacity of rain to produce erosion (erosivity) and the susceptibility of the soil to erode (erodibility) both have a different effect on the sediment regime. The transfer of soils to the deep sea can be caused by physical erosion or abrasion but depends also on vegetative cover. Therefore, the interpretation that more rainfall leads to more sediment erosion should be considered cautiously when accounting for the erosivity vs erodibility and hydrodynamic controls in the region, especially when viewing offshore variations in $^{87}Sr/^{86}Sr$ values. This is explored through applying the Revised Universal Soil Loss Equation (RUSLE) in combination with GIS (Babin, pers. comms), using NASA Global Precipitation Measurements (GPM_3IMERGHH)

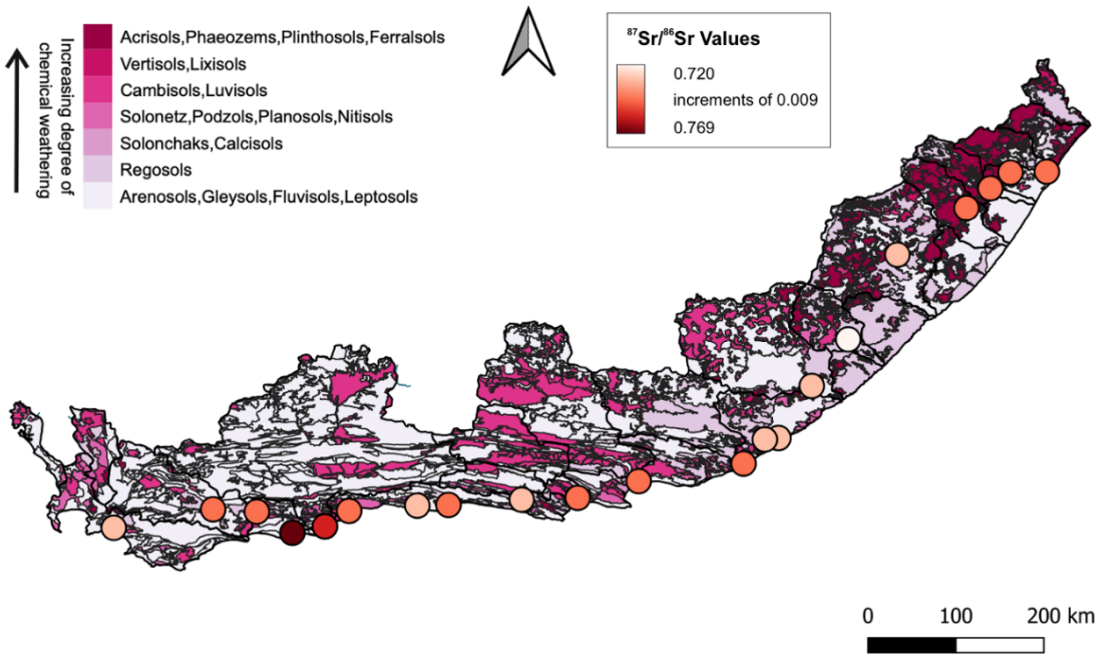

Figure 3.12: Soil types of South African river catchments with $^{87}Sr/^{86}Sr$ isotope values indicated for each river catchment by the circle colour (right key). Soil type indicated by left key.

from 2017 (Huffman *et al.,* 2019). Erosivity calculations were carried out in the study region by using an empirical based modelling approach incorporating the RUSLE model of erosion (e.g. Ganasri and Ramesh, 2016). The results were compared to the Zambezi and Limpopo river catchment (Babin, pers. comms) and the results from this chapter find that the South Africa study region has less erosivity on average than the Zambezi and Limpopo catchments (Figure 3.13). This means the vegetative cover and soil erodibility is lower in South Africa than the Zambezi and Limpopo catchments, suggesting stronger inputs from these two more northern river catchments. This integrative approach allows the modelling of soil erosion in coastal river catchments as a response to changes in land use from anthropogenic sources.

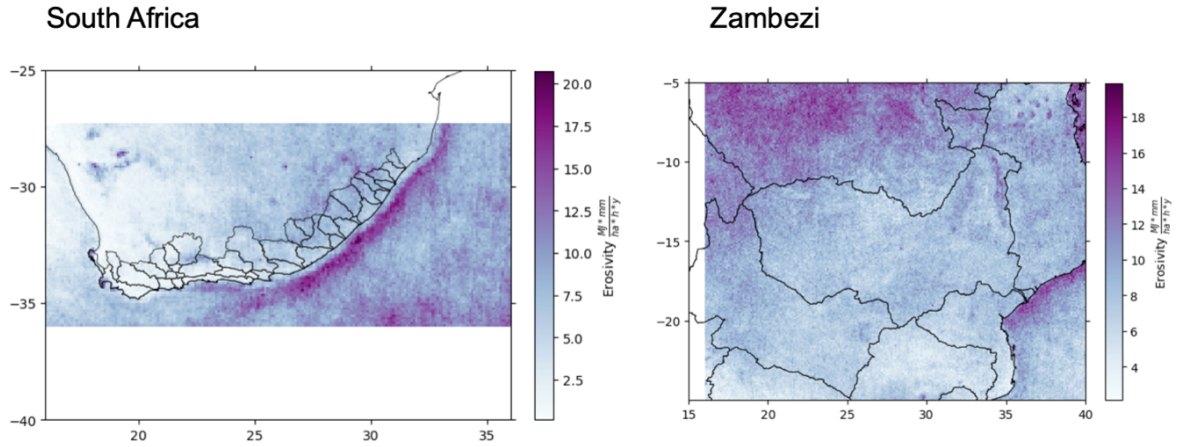

Figure 3.13: Erosivity calculations output using empirical-based modelling approach predicting the long-term average annual rate of soil erosion for South African river catchments and the Zambezi catchment (from Babin, pers.comms).

3.5.3 Anthropogenic Influences

3.5.3.1 Dams

A potential consequence of sampling in this region is the isotopically traced anthropogenic perturbations which may alter the radiogenic signatures, such as dams trapping sediments upstream and reduced riverine flow. This must be considered in riverine sediments when reflecting their source regions. The riverine sediment is well-mixed so integrates the local geology of the drainage area and does not assess seasonality. The material from rivers which are dammed was, where possible collected downstream of the dams, to ensure the same sediment signal is integrated in the marine environment.

3.5.3.2 Climate Change

Flash floods have recently caused more erosional degradation on the KwaZulu-Natal region, creating gullies which cut through the region affecting farmland (Figure 3.3). These flash floods are high energy and offload the coarser sediment material downstream and the finer sediment is transported further. The ability of the soil to erode is increased in more humid areas, and as evidenced in numerous studies on gullies in this region (Hoffman and Todd, 2000; Le Roux, 2007; Birkett *et al.,* 2016; Seutloali *et al.,* 2016). The erosional degradation is increasing with enhanced climate change. This reveals a need for more studies along sediment transport pathways in order to reduce socio-economic impacts to South Africa.

Overall, the above evidence presented suggest the $^{87}Sr/^{86}Sr_{clay}$ ratios variability is likely an effect of the degree of chemical weathering. Despite this, the elemental concentrations of each sample would provide additional evidence to support this hypothesis.

3.6 Implications for Palaeoclimate Reconstructions

As the smallest grain size fraction, clay settles from the water column at a much slower rate, allowing the clay particles to travel much further, at a transfer time an order of magnitude shorter than that of the coarse fraction transported with the bedload (Granet *et al.,* 2010; Carter *et al.,* 2020). The clay fraction differs fundamentally from the sand and silt fractions, not only in grain size but generally in mineralogy as well. It typically contains minerals which are products of chemical weathering such as kaolinite and illite. Other studies have shown that the clay fraction is a more reliable provenance tracer as more likely integrates the bedrock in the drainage area as it is transported over longer distance undergoing extensive mixing (Jonell *et al.,* 2017; Carter *et al.,* 2020). Based on data presented, this study highlights that the $^{87}Sr/^{86}Sr_{clay}$ reflects the weathered material and the εNd represents the same composition as the parent source rock. This is an important finding for palaeoclimate reconstructions as the study shows that the <2 µm fraction is weathered from the source rock but can reflect the source rock radiogenic isotope signature. The <2 µm fraction has a higher potential of long-distance transport so can be used as a provenance tracer for reconstructions related to past climate variability.

This study defines two new South African radiogenic isotope endmembers that allow the provenance of riverine sediments in South Africa to be identified (Table 3.5 and Figure 3.9) and will reconstruct the palaeoclimate and hydrological changes through time. These data suggest the use of the Karoo and Cape $^{87}Sr/^{86}Sr$ and εNd endmembers as a local South African provenance endmember can be adequately differentiated from the river discharge from the two major northern rivers with high sediment fluxes, the Limpopo and Zambezi rivers when utilising downcore sediment signals for palaeoclimate reconstructions (Figure 3.10).

As the radiogenic isotopes bear the same isotopic signature and geological history as the sediment source (Goldstein *et al.,* 1984), it is believed the radiogenic isotopes endmembers are stable on timescales relevant to the studies included in Chapter 4 and 5. As the εNd is the deviation of $^{143}Nd/^{144}Nd$ from the bulk earth value, the measured εNd values in this chapter reflect the initial crustal age of source rocks - the source rocks are geologically older than the timescales in the subsequent studies presented in this thesis, despite small amounts of quaternary cover present in some river catchments (Table 3.1), therefore these endmembers can be used to provide adequate understanding of source rock changes and fluvial discharge variability from South Africa. Furthermore, the river catchments analysed in this study are short and the area is small (<45,715 km^2) compared to the Zambezi or Limpopo rivers and the rivers do not have additional tributaries bringing sediment from other sources. As such, it is unlikely mixing upstream and changes from source to sink will affect the radiogenic isotopes provenance signatures as found in other studies (Clift *et al.,* 2002; Hahn *et al.,* 2018).

These South African rivers drain substantial sediment loads into the Southwest Indian Ocean, which will be picked up by sites further afield, making it possible to trace changes in local South African hydroclimate. At glacial-interglacial timescales, the location of the river mouths has not always been the same as their present-day sites. The emergence of the Palaeo-Agulhas Plain (PAP) at glacial low stands would influence the sediment yield to the ocean and the dominant source areas may have shifted. It is hypothesised that 20,000 years ago (ka) during a glacial period (LGM), the coastal regions of South Africa experienced dry conditions whereas further inland, wetter conditions prevailed (Chase *et al.,* 2017). This would influence the amount of sediment and source region of material deposited in the Southwest Indian Ocean. Therefore, the new radiogenic isotope endmembers of the Karoo and Cape from this study will help to reconstruct transport pathways and distinguish different source regions of southern Africa to help improve that understanding of downcore past climate variability.

3.7 Concluding Remarks

This study identifies the provenance source of coastal South African river sediments through mixing bedrock geology signatures (from QGIS) with radiogenic isotope compositions to find two key radiogenic isotope endmembers that characterise the regional river systems. Rivers of the eastern Cape drain soils of the Karoo Supergroup and Drakensberg granites ($^{87}Sr/^{86}Sr$ of 0.740 and εNd of –8.526 ($\pm$0.200)), whereas rivers of the southern Cape drain the Cape Supergroup province with more radiogenic $^{87}Sr/^{86}Sr$ ratios of 0.745 and unradiogenic εNd values of –10.091 ($\pm$0.200).

This study shows that in the KwaZulu-Natal fluvial sediments, the $^{87}Sr/^{86}Sr_{clay}$ bears a more radiogenic signature, the εNd values are more unradiogenic with a greater kaolinite composition. The soil type is indicative of ferralsols, suggesting high degrees of chemical weathering. This region experiences more rainfall from the warmer sea surface temperatures (SSTs) of the Indian Ocean, bringing moisture in land. The rainfall amount is typically regarded as higher weathering and shows that $^{87}Sr/^{86}Sr$ ratios can be influenced by regional hydrology.

Along the eastern coastline the kaolinite abundance decreases and illite composition increases, coincident with lower $^{87}Sr/^{86}Sr_{clay}$ ratios and higher εNd. This change is reflecting the geology, with younger Karoo sediment dominating the eastern Cape. The older Cape Supergroup in the southern Cape has a more radiogenic $^{87}Sr/^{86}Sr_{clay}$ isotope signature and unradiogenic εNd fingerprint. The εNd is negatively correlated with $^{87}Sr/^{86}Sr$ ratios (Figure 3.10), highlighting the importance of bedrock geology at the source regions driving the radiogenic isotopes and clay minerals. Clay mineralogy, soil composition, erosivity calculations and endmember mixing all reveal a different mechanism is driving the $^{87}Sr/^{86}Sr$ values compared to the εNd, which we attribute to the degree of chemi-

cal weathering. The εNd signature is a provenance tracer reflecting source rock geology, supported by the weighted average bed rock age database generated.

Finally, it is well established that $^{87}Sr/^{86}Sr$ isotope increase with decreasing grain size. This grain size offset observed between the <2 µm and 2-32 µm in this chapter study is similar to a study which compares the <2 µm and <120 µm (Hahn *et al.,* 2016). This highlights that the coarser material likely reflects a mixed signal of all size fractions and the grain size offset is between sands (> 63 µm) and fine silts (2-32 µm). The grain size effect observed between the <2 µm and 2-32 µm is likely due to the mineralogy of the samples. The influence of different grain size fractions on provenance analyses needs to be carefully accounted for, especially when interpreting land-sea linkages or comparing radiogenic isotope datasets (Meyer *et al.,* 2011). Thus, as a prerequisite for such studies, the accurate separation of the grain size classes is essential. The grain size sensitivity of $^{87}Sr/^{86}Sr$ isotope compositions has caused inconsistencies when comparing different core sites used for proxy-based provenance reconstructions. Hence, limitations persist concerning the utility of Sr isotope data from the bulk sediment fraction, or when comparing existing data from different grain size fractions (Meyer *et al.,* 2011; Hahn *et al.,* 2016; Jewell *et al.,* 2020; Simon *et al.,* 2020a; Kunkelova *et al.,* 2022).

Chapter 4 | The Last Termination: Sediment Source Changes; a Last Glacial Maximum - Modern Day Study

Time speeds and bends around planets and suns, is different in mountains than in the valleys, and is part of the same fabris as space, which curves and sweels as does the sea - Delia Owens - Where the Crawdads Sing

Agatha and I go, down to the courtyard slinging, last year's Sundays in the river of time - Days of Lantana - Ben Howard

4.1 Chapter Outline

This chapter uses sediment cores from 29.07°S to 36.91°S offshore eastern South Africa and the southern Cape. The study aims to identify modern and LGM dated sediment provenance using cohesive clay (<2 µm), cohesive silt (2-10 µm) and non- cohesive silt (10-63 µm) fraction radiogenic isotopes, terrigenous grain size analysis, clay mineralogy and δ^{13}C benthic as indicators of potential sediment provenance and transport pathways. In this chapter, temporal variability is addressed in terrigenous sediment supply during the LGM compared to modern day. The transport pathways are inferred based on the spatial patterns of sediment provenance, and grain sizes and bottom water current strengths are utilised to understand the water-mass configurations. Finally, the impact of regional climate variability on sediment input and transport pathways is discussed.

The study aims to:

- decipher the provenance of sediments supplying these marine sediment core sites,
- investigate possible sediment transport mechanisms through targeting the <2 µm, 2-10 µm and 10-63 µm size fractions of terrigenous sediments.

4.2 Introduction

4.2.1 Last Glacial Maximum Climate

The Last Glacial Maximum (LGM) is defined as a period of maximum global ice volume during 25–19 ka before present (Clark *et al.,* 2009). The Earth's climate system operated under profoundly different key boundary conditions during the LGM. Large parts of the high latitude landmasses were covered by ice sheets. Northern Hemisphere ice sheets were larger and ice caps and glaciers extended closer to the equator than under present day conditions (Jansen *et al.,* 2007). Atmospheric CO_2 levels were lower (Wang *et al.,* 2013b) and the Palaeoclimate Modelling Intercomparison Project (PMIP) phases 1, 2 and 3 estimate global average near-surface atmospheric temperatures to be 3-7°C lower than present day (Masson-Delmotte *et al.,* 2006). Sea levels are estimated to have been $\sim$ 120 m lower than present day levels (Peltier, 2004). The ice volume increase through the LGM is the result of reduced amounts of solar radiation reaching the Earth surface of the Northern Hemisphere surface during the boreal summer, as a consequence of the Milankovitch Cycles (Imbrie *et al.,* 1992). Polar amplification occurs when these cooling conditions causing the poles typically cool more than the global average, resulting in an enhanced meridional temperature gradient (Masson-Delmotte *et al.,* 2006). The changes in the hemispheric thermal gradient can influence global atmospheric wind patterns and associated hydroclimate.

A range of climate forcing mechanisms have been proposed to explain the observed climate

and precipitation variability in southern South Africa during the LGM. They broadly include shifts in the Intertropical Convergence Zone (ITCZ), Congo Air Boundary (CAB) and Southern Hemisphere Westerlies (SHW) (Figure 4.1). One site from the Gulf of Aden (Tierney *et al.,* 2013) (11.9 °N; 44.3°E) reveals reduced rainfall, based on δD during the LGM compared to the present-day. This site is north of the ITCZ whereas sites south of the ITCZ such as the South Africa southern precipitation stack based on pollen-based reconstructions (Chevalier and Chase, 2015) record wetter conditions during the LGM. The SHW transport moisture during austral winter from the South Atlantic Ocean to the southwestern region of South Africa. For example, during the LGM it has been suggested that there was an equatorward displacement of the SHW (Kohfeld *et al.,* 2013), under the thermal wind balance (Holton, 1973). Although other factors may have contributed to this displacement during glacial maxima, such as sea ice and the expansion of high-pressure cells (van Zinderen Bakker, 1967; Stuut, 2004). A recent study shows the climate variability of the Winter Rainfall Zone (WRZ) during the last glacial period was controlled by the position of the mid-latitude storm track, linked to an equatorward shift in SHW (Chase *et al.,* 2023). However, alternative evidence suggests no change in the westerlies or a weakening occurred, which can result in the same conditions experienced during the LGM (Kohfeld *et al.,* 2013). General Climate Model (GCM) projections from PMIP3 also display uncertainties regarding the changing strength of the SHW, such that some models display equatorward displacements whilst others project a weakening (Chavaillaz *et al.,* 2013; Rojas, 2013).

Three rainfall zones in South Africa (Figure 4.1) form because of the varying climate mechanisms. These mechanisms include the South Atlantic high-pressure systems influencing the Southwest Africa climate and the easterly winds carrying warm moist air from the Southwest Indian Ocean, driving the Southeast Africa climate. The Winter Rainfall Zone (WRZ; Figure 4.1) receives moisture from the latitudinal migration of the westerlies (Compton, 2011; Nash, 2017; Dupont *et al.,* 2021) which are influenced by Antarctic sea ice and South Atlantic Ocean temperatures. During colder glacial intervals, the SHW are suggested to be located more northward (van Zinderen Bakker, 1967; van Zinderen Bakker, 1976; Cockcroft *et al.,* 1987; Shi *et al.,* 2000; Stuut, 2004; Chase and Meadows, 2007; Neumann and Scott, 2018a) and some studies show the SHW migrated by 5° during glacials (De Boer *et al.,* 2013; Hahn *et al.,* 2020; Miller *et al.,* 2020), although this is still debated (Kohfeld *et al.,* 2013). The Summer Rainfall Zone (SRZ) is modulated by SSTs of the Indian Ocean (Reason and Mulenga, 1999; Reason, 2001). The region located between these two zones; the Year-round Rainfall Zone (YRZ; Figure 4.1), receives rainfall in all seasons influenced by both the Southwest Indian Ocean and the South Atlantic Ocean (Figure 4.1).

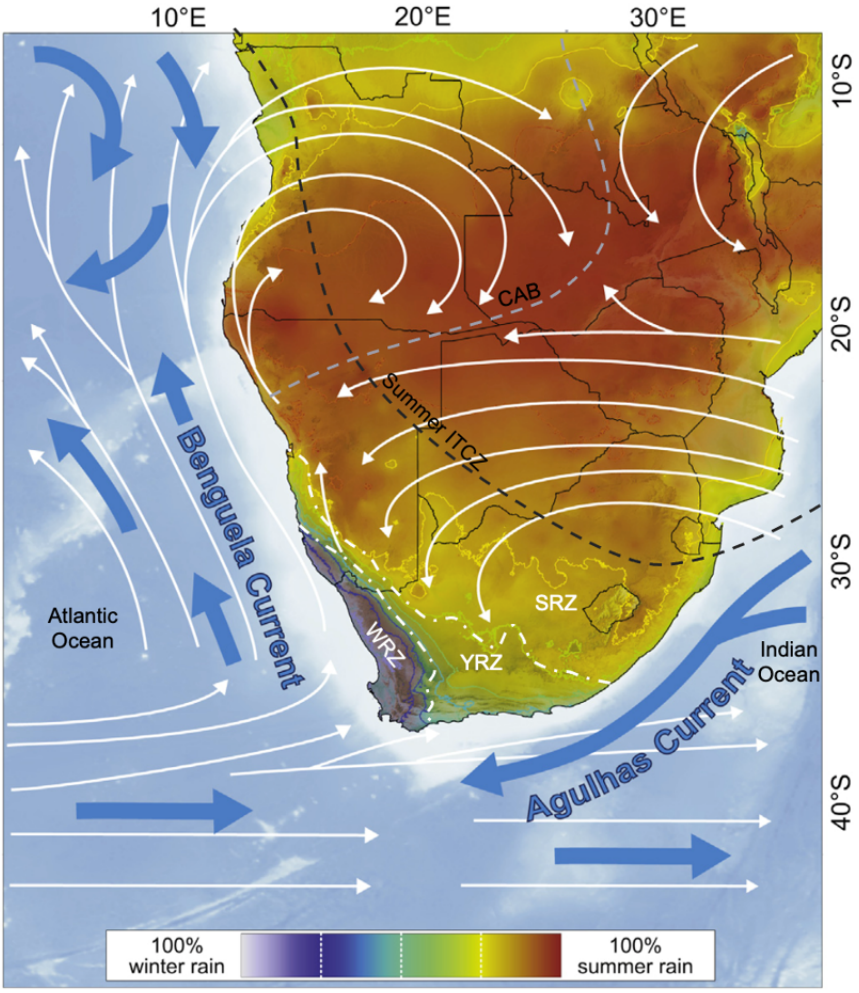

Figure 4.1: Map of southern Africa showing seasonality of rainfall and climatic gradients dictated by the zones of summer/tropical (red) and winter/temperate (blue) rainfall dominance. Major atmospheric (white arrows) and oceanic (blue arrows) circulation systems. South Africa rainfall zones Summer Rainfall Zone (SRZ), Year round Rainfall Zone (YRZ) and Winter Rainfall Zone (WRZ). (Image updated from Chase *et al.* (2017)).

4.2.1.1 LGM Climate of the Present-Day Winter Rainfall Zone

The suggested northward expansion of the WRZ beyond its present-day location, is a key aspect in understanding the LGM climate over southern Africa. It is suggested the expansion is a consequence of the equatorward displacement of the SHW (van Zinderen Bakker, 1967; van Zinderen Bakker, 1976; Cockcroft *et al.,* 1987; Shi *et al.,* 2000; Stuut, 2004; Chase and Meadows, 2007; Neumann and Scott, 2018a). The WRZ is the part of southern Africa that receives more than 66% of its annual rainfall during the austral winter half-year of April to September (Figure 4.1). Studies on the extent of the WRZ have been adjusted for the LGM, with the earliest conceptual model proposing the WRZ reached significantly more northerly latitudes as far north as the Free State province of central South Africa (∼ 29°S; 26°E) as well as central Namibia (∼ 22°S; 17°E) (van

Zinderen Bakker, 1967) (Figure 4.1) and similarly, Cockroft *et al.* (1987) suggested similar expansions of the WRZ, as far north as 25°S and as far east as 30°E. This conceptual model has since been adjusted to propose a mechanism of SHW system intensification (Neumann and Scott, 2018a).

Despite the growth in archives of southern African proxy data covering the LGM (Faith *et al.,* 2019; Chase *et al.,* 2021; Chase *et al.,* 2023), conclusive indications of WRZ expansion during the LGM remain elusive because observed moisture fluctuations cannot easily be translated to seasonality (Scott *et al.,* 2004). There are many inconsistencies regarding the climate patterns of the WRZ. Studies providing evidence that the WRZ expanded during the LGM include charcoal studies from Elands Bay Cave (Cartwright and Parkington, 1997; Cowling *et al.,* 1999), which indicate mesic thicket and Ericaceae pollen (Meadows and Baxter, 1999) and thus higher soil moisture for the LGM compared to the present-day. Geomorphological evidence suggests that the present-day WRZ of South Africa was significantly colder than today during the LGM, to the extent that periglacial features may have been present in the region's mountains with winter temperatures 8-10°C lower than the present-day values (Boelhouwers, 1999; Boelhouwers and Meiklejohn, 2002; Mills *et al.,* 2012). Conversely, dry conditions during the LGM were recorded in archives of pollen in hyrax dung from the Pakhuis Pass, Cederberg (Scott and Woodborne, 2007a; Scott and Woodborne, 2007b) and another record from the same region, at De Rif, does not show major changes in the mountain fynbos vegetation, whereas δ^{13}C and δ^{15}N records from the De Rif from the same region indicate dry conditions during the last period of the LGM (Chase *et al.,* 2011). Finally, downscaling model results for the present-day WRZ, indicate substantial increases (in the order of 2 mm/day) in winter rainfall with particularly large increases over the south-north aligned Cape Fold Mountains to the north of Cape Town and further northwards along the western escarpment (Engelbrecht *et al.,* 2019).

4.2.1.2 LGM Climate of the Present-Day Summer Rainfall Zone

The SRZ of southern Africa was thought to be significantly colder during the LGM, when compared to present-day temperatures. Studies from north-eastern South Africa show temperatures were 5-6°C cooler based on the altitudinal lowering of vegetation belts (Scott, 1982), and 2-6°C cooler based on pollen probability density functions (Truc *et al.,* 2013). Other records also support lower temperatures, such as pollen evidence which suggest the possible occurrence of short-lived glaciers in the Drakensberg mountains (Mills *et al.,* 2012).

In addition, the eastern region of South Africa is believed to be wetter during the LGM with respect to present-day (Butzer *et al.,* 1978). The deterministic mechanism for this is suggested to be the southward displacement of the ITCZ, supported by a proxy record from the Kalahari (Lancaster, 1979). However, other studies argue the eastern Cape was drier during the LGM (Cockcroft *et al.,* 1987), based on proxy data, further examined by

Chase and Meadows (2007). These authors indicate that the effects of a southerly displacement of the ITCZ causing more rainfall, would have been confined to a spatial extent of subtropical southern African between 15 and 21°S (Thomas *et al.,* 2009; Schefuß *et al.,* 2011; Truc *et al.,* 2013; Chevalier and Chase, 2015; Chevalier *et al.,* 2017). The Tswaing Crater record located north of Pretoria also reveal drier indications during the LGM (Partridge *et al.,* 1997), concurrent with less precipitation records in the Wonderkrater region compared to present-day (Truc *et al.,* 2013; Chevalier and Chase, 2015).

4.2.1.3 LGM Climate of the Present-Day Year-round Rainfall Zone

The year-round rainfall zone (YRZ) is the region between the present-day summer and winter rainfall regions (Figure 4.1) (Van Rooy, 1972; Bond *et al.,* 2003; Taljaard. 2003; Engelbrecht *et al.,* 2009; Engelbrecht *et al.,* 2015). Based on microfauna and speleothem proxies a temperature drop of 5-6°C has been inferred for the LGM, compared to the present-day (Heaton *et al.,* 1986; Thackeray, 1990; Talma and Vogel, 1992). There are however contrasting views on the distribution of rainfall during the LGM across the WRZ and southern Cape coast. The perceived expansion of the WRZ during the LGM suggests all-year rainfall occurred during the LGM, as a consequence of the perceived all-year occurrence of frontal rain (van Zinderen Bakker, 1967; van Zinderen Bakker, 1976). Elands Bay Cave, located on the western Cape coast, charcoal analysis indicate that during the LGM the Cape south coast region was drier, whereas the WRZ was wetter (Cartwright and Parkington, 1997; Cowling *et al.,* 1999). More recently modelling results coupled with leaf waxes suggest that during an earlier glacial (MIS 4), the coastal region of the southern Cape was drier whereas inland experienced wetter conditions (Göktürk *et al.,* 2023a). The same assumption that the Cape south coast was drier than the southwestern Cape region during the LGM has been shown (Meadows and Baxter, 1999). The authors deduced from cave sites that the YRZ may have experienced more arid conditions during the LGM, with the southwestern coast of the WRZ simultaneously experiencing increased rainfall. More recently, a coastal versus inland signal has been shown for the Holocene (Chase and Quick, 2018). Records from Boomplaas Cave led to differing climate interpretations during the LGM. Charcoal, pollen and micromammals records reveal it was cold and either dry or moderately wet (Lancaster, 1979; Klein, 1980; Thackeray, 1987; Deacon and Lancaster, 1988), whereas based on isotope studies from bovine teeth enamel and an assessment of ungulate diversity for the LGM, increased winter rainfall conditions and an increase of C3 grasslands (and high moisture levels) have been suggested for the same location (Klein and Cruz-Uribe, 1991; Sealy *et al.,* 2016). Finally, a faunal analysis of Nelson Bay Cave at Plettenberg Bay, suggests an increase of grassy vegetation for the southern coast representing the exposed coastal platform at the sea level low- stand (Klein, 1980; Klein, 1983; Fisher *et al.,* 2010). Clearly diverging interpretations exist for the nature of rainfall in three rainfall zones during the LGM with contradicting lines of evidence in terms of

moisture availability and to what extent weather systems from the SHW to the WRZ on the one hand, and tropical systems (e.g. ITCZ) from the north on the other hand, influenced the region.

In addition to these varying climate mechanisms influencing the rainfall zones during the LGM, sea level changes would have also influenced precipitation variability in South Africa (Göktürk *et al.,* 2023b). Sea level regression, due to increased ice in the Northern Hemisphere, exposed the continental plain south of South Africa, otherwise known as the Palaeo-Agulhas Plain (PAP; (Cawthra *et al.,* 2020a)). As such its extent and accessibility were directly impacted by large-amplitude ($\sim$ 120 m) glacial to interglacial sea-level fluctuations. The PAP has been suggested to influence human migration patterns (Compton, 2011). For example, an expanding glacial PAP may have served as a refuge to large herd animals and humans as interior climates became drier (Morris, 2002; Marean, 2010). There is conflicting evidence showing the contraction of the SRZ and expansion of the WRZ during the LGM. However if these coeval effects did occur, this may have resulted in a seasonal reduction of the arid corridor and allowed large and varied grazer populations such as those documented at Florisbad (Brink, 1987) to move between the coastal plain and the interior during glacial-interglacial climate transitions (Compton, 2011). During the last glacial low stand, rivers flowed over the aerially expanding PAP, delivering sediment to the ocean. This may have served as another reason for refuge to humans and large animals as freshwater reserve was higher and close by.

4.2.1.4 Modern Sources of Sediment from South Africa

Rivers of southern South Africa have an annual sediment yield of $\sim$ 10 x 10^6 m^3/year supplied to the Southwest Indian Ocean (Flemming 1981; Rooseboom *et al.,* 1992). These rivers have an average catchment size of 5,400 km^2. Sediments are an inherent mixture of particles from various sources. The Agulhas Passage located South of Africa receives sediments from local South African rivers. Sediments are additionally transported in the Agulhas Current from upstream, northern rivers such as the Limpopo and Zambezi rivers. These have larger annual sediment fluxes (annual discharge of nearly 18 x10^{12} m^3/year (Frenken *et al.,* 1997); 4.8 x10^{12} m^3/year (Frenken *et al.,* 1997) respectively). Distant source regions such as South America and Antarctica are also important contributors to the Agulhas Passage sediments. These sediments are mainly carried by the Antarctic Circumpolar Current (ACC) (Diekmann *et al.,* 2000; Walter *et al.,* 2000; Diekmann *et al.,* 2003) and also the South Atlantic Current (SAC), which has been shown to increase in flow speed during the LGM (Hemming *et al.,* 2007; Noble *et al.,* 2012). A summary of the sediment sources and their associated radiogenic isotope endmembers is given in Chapter 1.5.

This chapter compliments prior radiogenic isotope provenance studies by presenting radiogenic isotopes from offshore sediment cores retrieved from the continental margin of

South Africa (south of the Limpopo and Zambezi rivers) in context to the study by Franzese *et al.* (2006, 2009) to provide important information on transport regimes and regional hydrology. The marine sediment cores used in this chapter are from 29.07°S to 36.91°S and record climate changes from eastern South Africa to the southern tip of South Africa. The strong surface current in this region, the Agulhas Current, transports sediment from upstream (i.e., Zambezi and Limpopo) making it an ideal location to research the terrigenous sediment supply and understand potential sediment source changes.

Sediment radiogenic isotope endmembers used in this study (Table 4.1) are from upstream Limpopo and Zambezi rivers based on published data from Simon *et al.* (2020); van der Lubbe *et al.* (2014) and Garzanti *et al.* (2014), as well as local South African river endmembers generated from data in Chapter 3. The error for these endmembers are taken as the analytical error from the associated publications.

Table 4.1: Table of radiogenic isotopes endmembers used in this study from South African coastal rivers and Limpopo and Zambezi rivers.

Endmember	**$^{87}Sr/^{86}Sr$ value**	**εNd value**
Karoo	0.740	-8.526
Cape	0.745	-10.091
Zambezi	0.723	-13.798
Limpopo	0.767	-19.200

4.2.2 Grain Size Selection

Accurate and precise grain size separation is an essential requirement during sample preparation for studies focussed on the marine sediment provenance studies prior to analyses, because different transport processes may contribute preferentially to specific grain size fractions (Stuut *et al.,* 2002; Meyer *et al.,* 2011). For example, a key tool used to identify sediment provenance are radiogenic isotopes of the lithogenic clay fraction (Meyer *et al.,* 2011; van der Lubbe *et al.,* 2014; van der Lubbe *et al.,* 2016).

There is an ongoing effort to determine the extent to which $^{87}Sr/^{86}Sr$ isotope ratios are sensitive to grain size variability and chemical weathering (Dasch, 1969; Grousset *et al.,* 1992; Blum and Erel, 2003; Feng *et al.,* 2009; Meyer *et al.,* 2011). It is widely recognised that the $^{87}Sr/^{86}Sr$ composition of marine sediment typically increases with decreasing grain size (Dasch, 1969), since clay minerals are preferentially derived from Rubidium-rich minerals such as biotite and K-feldspars, which are more prone to chemical rather than physical weathering processes (Jung *et al.,* 2004; Garzanti *et al.,* 2014). The grain size sensitivity of $^{87}Sr/^{86}Sr$ isotope compositions has caused inconsistencies when comparing different marine sediment cores used for proxy-based provenance reconstructions. The extent of the inconsistencies is shown in Figure 4.2, which presents all $^{87}Sr/^{86}Sr$ ratios measured on varying size fractions from the South African region (Table A1). Limitations

persist concerning the utility of $^{87}Sr/^{86}Sr$ isotope data from the bulk sediment fraction, or when comparing existing data from different grain size fractions (Meyer *et al.,* 2011; van der Lubbe *et al.,* 2014; Hahn *et al.,* 2016; van der Lubbe *et al.,* 2016; Jewell *et al.,* 2020; Simon *et al.,* 2020a; Kunkelova *et al.,* 2022). For example, (Hahn *et al.,* 2016) identified a +0.02 - offset in $^{87}Sr/^{86}Sr$ isotope data measured in the <2 µm fraction compared to <120 µm fraction, 0.00001 (e^{-5}) orders of magnitude higher than the $^{87}Sr/^{86}Sr$ isotope variability usually considered significant (Biscaye and Dasch, 1971). Unlike $^{87}Sr/^{86}Sr$ isotope ratios, the εNd signatures are less sensitive to chemical weathering and thus grain size variation (Meyer *et al.,* 2011). For palaeoclimate reconstructions, the influence of different grain size fractions on provenance analyses needs to be carefully accounted for, especially when interpreting land-sea linkages (Meyer *et al.,* 2011). Thus as a prerequisite for such studies the accurate separation of the grain size classes is essential (Chapter 2.3.2).

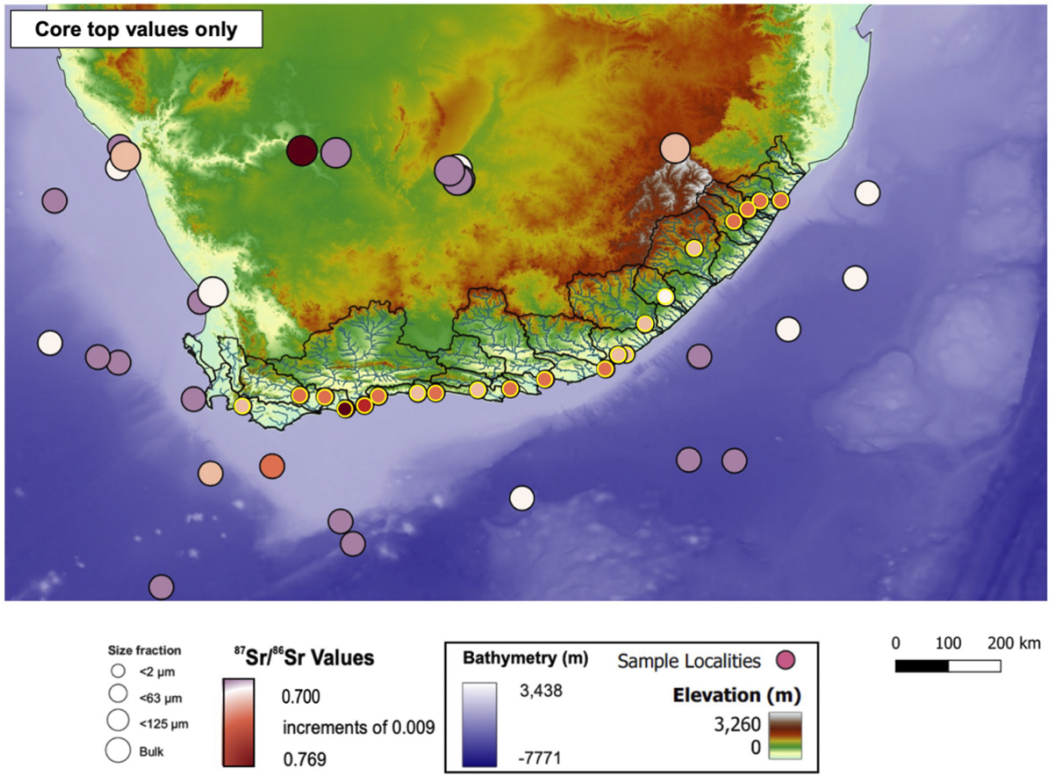

Figure 4.2: Modern day core top Sr isotope values from published literature (Franzese *et al.,* 2006; 2009; Garzanti *et al.,* 2014; Hahn *et al.,* 2015; 2016; 2017) on varying size fractions (in key) for the study region. Data from Chapter 3 are encircled in yellow. All data in this figure from references stated are included in Table A1.

From Chapter 3, a large grain size variability in the river sediment is observed (between <2 µm and 2-32 µm size classes) which has been attributed to chemical weathering in the river catchments. Isolating the clay fraction means the grain size population is the same and the variability can be assumed to be related to provenance or transport. In this study

the clay fraction of terrigenous sediment is used because it has a potential to travel large distances integrating source regions, if not directly flocculated. Clay minerals in the <2 µm fraction of deep-sea sediments are useful indicators of marine sedimentary processes, particularly those involving the transport of land-derived solids to and within the oceans (Griffin *et al.,* 1968). This <2 µm grain size class was also chosen to be more consistent with other studies by Simon *et al.* (2020a) and van der Lubbe *et al.* (2014, 2016) which use the <2 µm fraction for radiogenic isotopes work.

Further to the clay fraction, the 2-63 µm class comprises a large range of sediment grain size populations which covers different sedimentary transport processes. Chapter 4 also targets the 2-10 µm and 10-63 µm size fractions of terrigenous lithogenic sediments. This study is different from other studies designed on different size fractions (Table 4.2) because the two additional size fractions selected were informed based on incorporating the main grain sizes transported by bottom currents and heavy minerals consideration. The 2-10 µm fraction may help to rule out the effect of authigenic clays as some studies suspect the effect of secondary clay minerals formed in the ocean through reverse weathering reactions (Mukai e*et al.,* 2016; Bayon *et al.,* 2021; Kwon *et al.,* 2023). The 10-63 µm fraction was selected as it is non-cohesive and is transported by bottom currents (sortable silts) (McCave and Hall, 2006). As suggested by previous studies it is likely that the influence of hydrodynamic sorting and sediment transport processes will cause less bias on the provenance signal of the clay fraction, given its transport potential and cohesive behaviour once deposited (van der Lubbe *et al.,* 2014; van der Lubbe *et al.,* 2016; Simon *et al.,* 2020a).

Table 4.2: Collated studies of radiogenic isotopes and/or grain size studies on various size fractions.

Author	Grain Size Studied	Named Term	Reason for Study/Conclusion
Beny *et al.,* 2020	<2 µm, 2-10 µm, 10-63 µm	Clay, cohesive silt, sortable silt	Transport
Bayon *et al.,* 2015	<2 µm, 2-63 µm	Clay, silt	Weathering
Garzanti *et al.,* 2013	<32 µm	Cohesive silt	Provenance
Meyer *et al.,* 2010	0-10 µm, 10-40 µm	Fluvial, aeolian	Provenance
Compton and Maake, 2007	<2 µm, 2-38 µm, 38-63 µm	Clay, fine silt, coarse silt	Petrography
Franzese *et al.,*2006	<63 µm	<63 µm terrigenous sediment fraction	Provenance
Grousset *et al.,*1998	<30 µm	Dust	Wind provenance
Rutberg *et al.,* 2005	<63 µm	-	Provenance
Weldeab *et al.,*2013	<120 µm	River sediments	Provenance

4.3 Methods

4.3.1 Site Selection

The marine sediment cores utilised in this study are from three distinct zones within the Agulhas Current with respect to the Southeast coast of South Africa and river catchments analysed in Chapter 3. These are: (i) the northern sector of the Agulhas Current which encompasses 29 to 33°S latitudes and (ii) the central sector which is 33 to 35°S and iii) the southern sector of the Agulhas Current (south of 35°S) (Figure 4.3). The marine sediment cores provide a North-South transect along the Southeast African continental margin from ~29°S to 37°S (Figure 4.3) with water depths ranging between 1626 m and 3583 m. The shallowest sites were sampled near 29°S sitting in Antarctic Intermediate Water (AAIW) with two deeper marine sediment cores sampled near 36°S (Arhan *et al.*, 2003). The deep waters in this region are North Atlantic Deep Water (NADW) and Circumpolar Deep Water (CDW; mixture of NADW and Antarctic Bottom Water (AABW) (Curry and Oppo, 2005)) at approximately 3000 m (Figure 4.3). The NADW is transported within the Agulhas Undercurrent (section 1.4.3.1).

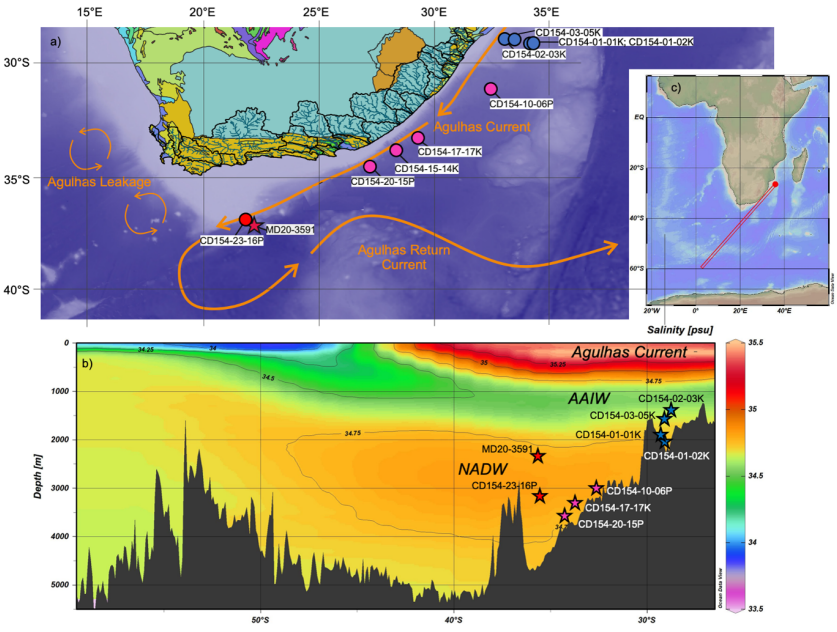

Figure 4.3: (a) Map showing the location of sediment cores (filled circles; blue = northern sector (sites CD154-02-03K, CD154-03-05K, CD154-01-01K, CD154-01-02K), pink = central sector (sites CD154-10-06P, CD154-17-17K, CD154-20-15P), red = southern sector (sites MD20-3591 and CD154-23-16P)) discussed in this chapter. Elevation from Hydro1K (see Figure 4.16 for lithology key) and bathymetry from BODC; (b) Deep water reconstruction of core sites (same colour coding as in (a)) included in this study of transect (c) of study region.

4.3.1.1 Identification Techniques of Last Glacial Maximum Samples

Table 4.3 shows the means of which the depth of the LGM horizon (defined as 19-26 ka) was identified. Preliminary stratigraphic determinations were made onboard the ship (Hall and Zahn, 2004), however in some cases i.e. for sediment cores CD154-10-06P and CD154-17-17K, the most straightforward method involved using more recent existing data, this is $\delta^{18}O_{benthic}$ (Simon *et al.,* 2020c) and $\delta^{18}O_{planktic}$ (Simon *et al.,* 2013) (Table 4.3).

To determine the LGM core depth for sites CD154-20-15P and CD154-23-16P, unpublished planktic $\delta^{18}O$ data and radiocarbon dates for respective marine sediment cores courtesy of Dr Margit Simon were supplied. The LGM depth for CD154-02-3K was determined based on benthic $\delta^{18}O$ data. The LGM depth of MD20-3591 was determined using benthic $\delta^{18}O$ values and the generated age models discussed in Chapter 2. For modern samples, the core top sample was taken, or as close to 0-1 cm was sampled if no other depths were available. This was the case for CD154-23-16P, the closest core top sample was 7-8 cm.

Table 4.3: Stratigraphic tools used for identifying LGM depth horizon for each CD154 core used in this study.

Site	Water Depth (m)	LGM Core Depth (cm)	Reason/Technique
CD154-02-03K	1626	145-146	$\delta^{18}O_{benthic}$ measurements from Franzese *et al.* (2009) and this study
CD154-03-05K	1747	65-66	$\delta^{18}O_{benthic}$ measurements (this study)
CD154-01-01K	1997	42-43	MS, L* and Core description (Hall and Zahn, 2006)
CD154-01-02K	2019	128-129	$\delta^{18}O$, MS and L* (Hall and Zahn, 2006)
CD154-10-06P	3076	73-74	$\delta^{18}O_{benthic}$ from Simon *et al.* (2020c)
CD154-15-14K	3236	50-51	Mag Sus (Hall and Zahn, 2006), $\delta^{18}O_{benthic}$ Franzese *et al.* (2009)
CD154-17-17K	3333	51-52	$\delta^{18}O_{planktic}$ from Simon *et al.* (2013)
CD154-20-15P	3583	304-305	$\delta^{18}O_{planktic}$; unpublished (Simon)
CD154-23-16P	3189	336-337	Radiocarbon dates, L*, Fe/K; unpublished (Simon)
MD20-3591	2464	144-145	$\delta^{18}O_{benthic}$; This study

4.3.2 Stable Isotopes

All stable isotope records were measured on three specimens of benthic foraminifera *Cibicidoides wuellerstorfi* from the 250-315 µm size fraction. All isotope data is referenced to the Vienna PeeDee Belemnite (VPDB) scale and the error value for over 3 batches (n = 596) for $\delta^{18}O$ is ±0.031 and for $\delta^{13}C$ is ±0.022. For more information, please refer to Chapter 2.3.6.1. The LGM $\delta^{18}O$ values from all CD154 marine sediment cores are higher

than the modern signifying glacial conditions. During glacial periods, more ^{16}O is trapped in glacial ice and the oceans become even more enriched in ^{18}O. This shows the LGM depths are trustworthy at indicating glacial conditions.

4.3.3 Sediment Processing and Techniques Applied (Summary)

Grain size analysis was performed on the Sympatec HELOS KR laser diffraction particle sizer at the Vrije Universiteit (VU) Amsterdam in the Sediment Lab. More information can be found in Chapter 2.3.7. The 'sortable silt' flow speed proxy was reconstructed by measuring the mean grain size of the 10-63 µm terrigenous size fraction. These measurements were performed at Cardiff University on the Beckman Multisizer IV Coulter Counter and converted to flow speed (cm/s). This allows a quantitative comparison between the modern and LGM and locations of marine sediment core sites discussed in this study. For the conversion from $\overline{SS}$ to flow speed, there are numerous calibration techniques, however the widely applied 'main-line' equation from McCave *et al.* (2017) is used, rather than more region specific calibration lines like from the Drake Passage (Wu *et al.,* 2019) or the Scotia Sea (McCave *et al.,* 2017). For radiogenic isotopes methods please refer to Chapter 2.3.3. For clay mineralogy methods, refer to section 2.3.6. In order to separate the sediment size fractions (<2 µm, 2-10 µm and 10-63 µm), the centrifuge protocol was followed from section 2.3.2. Note there are no radiogenic isotope reconstructions for marine sediment cores CD154-02-01K, CD154-02-02K and CD154-03-05K, and no clay minerals for these study sites or for MD20-3591.

4.4 Results

4.4.1 Clay Minerals

The clay mineralogy results are shown in Table 4.4. Sediment core CD154-02-03K contains the highest abundance of kaolinite than the other sites included in this study (Table 4.4). The CD154-02-03K LGM sample contains more kaolinite than the corresponding modern sample. The modern CD154-02-03K sample contains more montmorillonite than any other modern or LGM sample. All other sites are richer in illite than kaolinite (Table 4.4).

Table 4.4: Clay mineral abundances for CD154 sediment cores during modern and LGM.

Marine Core	Age (ka)	Water Depth (m)	Latitude	Longitude	Kaolinite (%)	Illite (%)	Montmorillonite (%)
CD154-02-03K	Modern	1626	29.074	32.770	44.541	38.051	17.408
CD154-10-06P	Modern	3076	31.177	32.159	39.329	7.236	3.436
CD154-15-14K	Modern	3236	33.734	28.204	28.878	66.284	4.838
CD154-17-17K	Modern	3333	33.270	29.125	40.238	53.005	6.757
CD154-20-15P	Modern	3583	34.461	27.147	24.199	73.561	2.240
CD154-23-16P	Modern	3189	36.819	22.001	19.902	74.791	5.306
CD154-02-03K	LGM	1626	29.074	32.770	50.686	40.106	9.208
CD154-10-06P	LGM	3076	31.177	32.159	32.524	60.968	6.508
CD154-17-17K	LGM	3333	33.270	29.125	32.440	49.398	18.162
CD154-20-15P	LGM	3583	34.461	27.147	30.111	63.251	6.638
CD154-23-16P	LGM	3189	36.819	22.001	27.318	66.290	6.392

4.4.2 Radiogenic Isotope Systematics (Sediment Provenance)

Firstly, to differentiate between radiogenic isotopes measured on the different grain size classes the $^{87}Sr/^{86}Sr$ and εNd isotope ratios are hereafter defined as $^{87}Sr/^{86}Sr_{clay}$, εNd_{clay}, $^{87}Sr/^{86}Sr_{cohesivesilt}$, $\varepsilon Nd_{cohesivesilt}$ and $^{87}Sr/^{86}Sr_{non-cohesivesilt}$, $\varepsilon Nd_{non-cohesivesilt}$ for the clay fraction (<2 µm), cohesive silt 2-10 µm fraction and non-cohesive silt fraction (10-63 µm) respectively.

The radiogenic isotope data for each grain size fraction for all sediment cores is shown in Table 4.5. In all comparisons between the measured clay fraction and the cohesive or non-cohesive fractions, differences are measured as clay fraction minus other size class.

4.4.2.1 Clay Fraction

The modern $^{87}Sr/^{86}Sr_{clay}$ isotope composition have the most radiogenic isotope values (between 0.745 and 0.760 (±0.00001)) and the least radiogenic εNd_{clay} (between -11.527 and -18.640 (± 0.137)) (Table 4.5). The LGM $^{87}Sr/^{86}Sr_{clay}$ isotope ratios range between 0.738 and 0.760 (±0.000011). These LGM $^{87}Sr/^{86}Sr_{clay}$ values are less radiogenic (lower) than or the same as the respective modern values (Figure 4.4). The LGM εNd_{clay} values range between -11.469 and -17.827 (± 0.156), these values are more radiogenic (higher) than the modern values (Figure 4.4).

4.4.2.2 Cohesive Silt Fraction

The modern $^{87}Sr/^{86}Sr_{cohesivesilt}$ ratios range between 0.739 and 0.754 (± 0.0000109) (Table 4.5) and are less radiogenic than the $^{87}Sr/^{86}Sr_{clay}$ fraction (by ∼ -0.006). Similar to the $^{87}Sr/^{86}Sr_{clay}$, LGM $^{87}Sr/^{86}Sr_{cohesivesilt}$ values range between 0.732 and 0.751 (±0.00000976) are also less radiogenic than their modern equivalent, with the same relative difference between the two size fractions (∼-0.006) (Figure 4.4). The modern $\varepsilon Nd_{cohesivesilt}$ values range from -18.420 to -11.047 (± 0.208) and the LGM depth splices range from -17.707 to -11.167 (± 0.162) (Table 4.5; Figure 4.4). There is a small difference of -0.066 between $\varepsilon Nd_{cohesivesilt}$ values and εNd_{clay} values (Figure 4.4).

4.4.2.3 Non-Cohesive Silt Fraction

The modern $^{87}Sr/^{86}Sr_{non-cohesivesilt}$ ratios range between 0.714 and 0.736 (± 0.00000924) (Table 4.5) and LGM values are between 0.714 and 0.728 (± 0.00000901) (Table 4.5). The least radiogenic $^{87}Sr/^{86}Sr_{non-cohesivesilt}$ values are recorded in the LGM (0.714 (± 0.00000862)), the LGM $^{87}Sr/^{86}Sr_{non-cohesivesilt}$ ratios are on average lower by 0.000994 than the modern values. The modern $^{87}Sr/^{86}Sr_{non-cohesivesilt}$ range are lower than the modern $^{87}Sr/^{86}Sr_{clay}$ values by -0.296. Similarly, LGM $^{87}Sr/^{86}Sr_{non-cohesivesilt}$ are lower than the LGM $^{87}Sr/^{86}Sr_{clay}$ values of -0.277. These differences are well beyond the analytical error (∼0.000005) and indicate a strong grain size fractionation effect with less radiogenic values with increasing grain size. Consistent with previous studies (Meyer *et al.,* 2011; Hahn *et al.,* 2017; Jonell *et al.,* 2018) more radiogenic Sr phases are concentrated in the finer fractions and less radiogenic in the coarser fractions. The Sr isotopes in the finer fractions are strongly controlled by potassium feldspar, micas and clay minerals (Jonell *et al.,* 2018). This was previously found in Chapter 3, with the more radiogenic $^{87}Sr/^{86}Sr_{clay}$ ratios containing more weathered material such as micas.

Table 4.5: Radiogenic isotope data results from each core site in this study (modern and LGM depths) for each operationally defined grain size classes. Clay indicates <2 µm, cohesive silt is 2-10 µm and non-cohesive silt is 10-63 µm size fractions which Sr and Nd were measured on.

Marine Core	Age (ka)	Water Depth (m)	Latitude	Longitude	$^{87}Sr/^{86}Sr_{clay}$	εNd_{clay}	$^{87}Sr/^{86}Sr_{cohesivesilt}$	$\varepsilon Nd_{cohesivesilt}$	$^{87}Sr/^{86}Sr_{non-cohesivesilt}$	$\varepsilon Nd_{non-cohesivesilt}$
CD154-02-3K	Modern	1626	29.074	32.770	0.760	-18.639	0.754	-18.420	0.736	-17.372
CD154-10-6P	Modern	3076	31.177	32.159	0.749	-14.406	0.747	-14.200	0.720	-12.571
CD154-15-14K	Modern	3236	33.734	28.204	0.748	-12.703			0.715	-11.486
CD154-17-17K	Modern	3333	33.270	29.125	0.750	-13.404	0.740	-13.121	0.718	-11.073
CD154-20-15P	Modern	3583	34.461	27.147	0.745	-12.967	0.739	-12.175	0.714	-10.336
CD154-23-16P	Modern	3189	36.819	22.001	0.748	-11.527	0.741	-11.047	0.719	-10.738
MD20-3591	Modern	2464	36.913	22.154	0.750	-12.402	0.747	-14.202	0.719	-11.831
MD20-3591	LGM (∼20ka)	2464	36.913	22.154	0.744	-11.469	0.737	-12.872	0.718	-11.706
CD154-02-3K	LGM (∼20ka)	1626	29.074	32.770	0.760	-17.827	0.751	-17.707	0.728	-18.032
CD154-10-6P	LGM (∼20ka)	3076	31.177	32.159	0.747	-12.685	0.741	-10.000	0.724	-11.200
CD154-15-14K	LGM (∼20ka)	3236	33.734	28.204		-11.519			0.714	-13.435
CD154-17-17K	LGM (∼20ka)	3333	33.270	29.125	0.743	-12.808	0.739	-13.264	0.717	-10.571
CD154-20-15P	LGM (∼20ka)	3583	34.461	27.147	0.743	-11.748	0.737	-11.167	0.716	-10.654
CD154-23-16P	LGM (∼20ka)	3189	36.819	22.001	0.738	-11.694	0.732	-14.538	0.717	-10.759

The modern $\varepsilon Nd_{non-cohesivesilt}$ have the highest values (radiogenic) ranging between -17.372 and -10.336 (± 0.177) and the LGM values are between -18.032 and -10.571 (± 0.161) (Table 4.5). The $\varepsilon Nd_{non-cohesivesilt}$ values are 1.175 (± 0.17120156) lower than εNd_{clay} values which might signify a potential grain size fraction on the εNd.

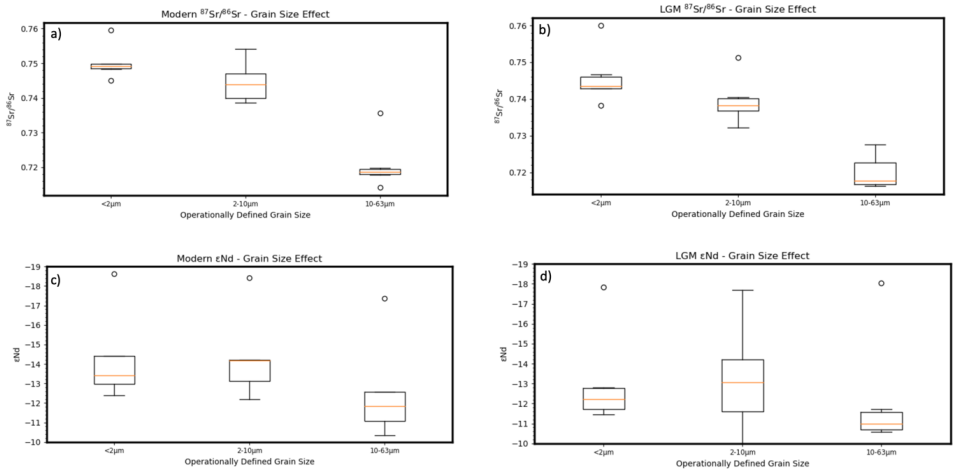

Figure 4.4: $^{87}Sr/^{86}Sr$ isotope composition and εNd for each operationally defined grain size class (<2 µm, 2-10 µm and 10-63 µm). a) Modern $^{87}Sr/^{86}Sr$ isotope, composition, b) LGM $^{87}Sr/^{86}Sr$ isotope composition, c) Modern εNd, d) LGM εNd. Refer to Table 4.5 for number of data points per box plot.

4.4.2.4 Latitudinal Extent of Radiogenic Isotopes during Modern and LGM

There is a latitudinal gradient during the modern and LGM for both $^{87}Sr/^{86}Sr_{clay}$ and εNd_{clay}. The highest $^{87}Sr/^{86}Sr_{clay}$ ratios (0.760 for both modern and LGM ± 0.000009 and 0.000008 respectively) and lowest εNd_{clay} (-18.639 (± 0.134) and -17.827 (± 0.164) for modern and LGM respectively) are observed in the northern sector (core site CD154-02-03K) (Figure 4.5). The central sites have modern $^{87}Sr/^{86}Sr_{clay}$ ratios between 0.745 and 0.750 (± 0.00001) and LGM $^{87}Sr/^{86}Sr_{clay}$ ratios between 0.743 and 0.747 (± 0.00001). The central sites have modern εNd_{clay} values between -14.406 and -12.703 (± 0.137) and LGM εNd_{clay} values between -12.808 and -11.748 (±0.166). The southern sector sites (CD154-23-16P and MD20-3591) have modern $^{87}Sr/^{86}Sr_{clay}$ ratios of 0.748 (± 0.000008) and 0.750 (± 0.000010^{6}8) respectively and LGM $^{87}Sr/^{86}Sr_{clay}$ ratios of 0.738 (0.000007) and 0.744 (± 0.000022) respectively. The southern sites have modern εNd_{clay} values of -11.527 (± 0.151) and -12.402 (± 0.153) and LGM εNd_{clay} values between –11.694 (± 0.117) and -11.469 (± 0.148) respectively.

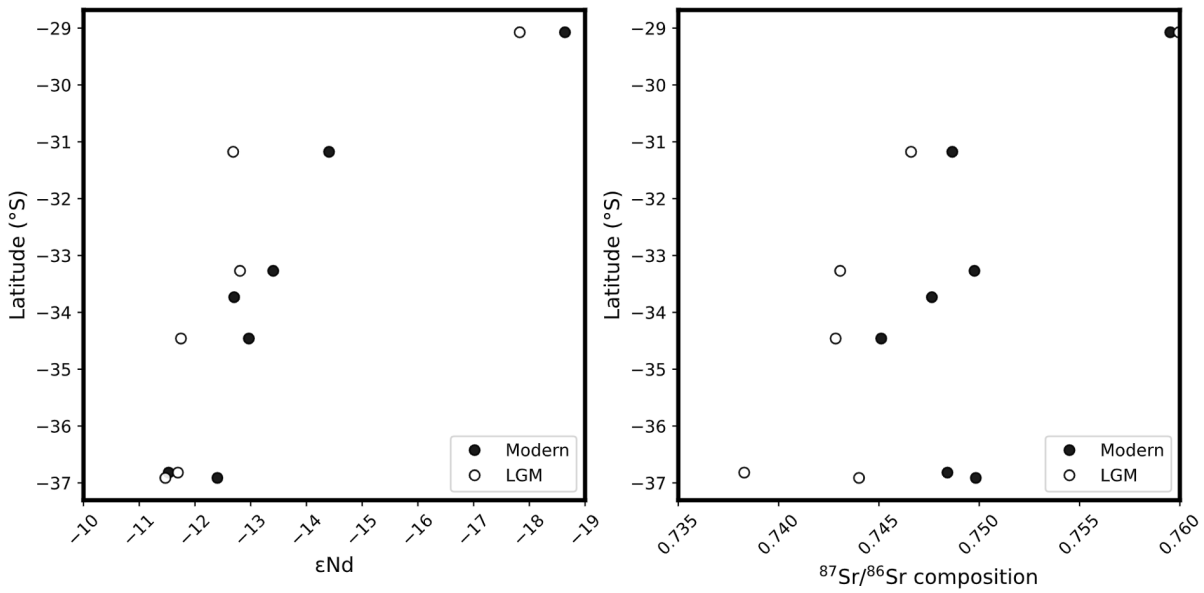

Figure 4.5: Latitudinal Distribution of radiogenic isotopes on the <2 µm fraction, a) εNd_{clay} isotope composition, b) $^{87}Sr/^{86}Sr_{clay}$ ratios. For both panels, filled circles = modern, unfilled circles = LGM dated splices.

4.4.3 Terrigenous Grain Size Measurements

All sediment samples have a bimodal distribution (with peaks in fine silts and fine sand fractions). The samples have a mean grain size within the fine-coarse silt, ranging between 7-33 µm (Figure 4.6). Overall LGM sediments are on average slightly coarser than the modern sediments by ∼2 µm (Figure 4.7). The LGM contain higher sand abundance (%) in comparison to the modern sediment which are more abundant in clay (Table 4.6). CD154-15-14K (0-1 and 145-146cm) contains the highest sand abundance (Table 4.6) (modern 34.00 wt % and LGM 47.30 wt %), suggesting it might be indicating down slope deposition at the site, this LGM sample is therefore not counted in any further work as may not give a true representation of the LGM provenance.

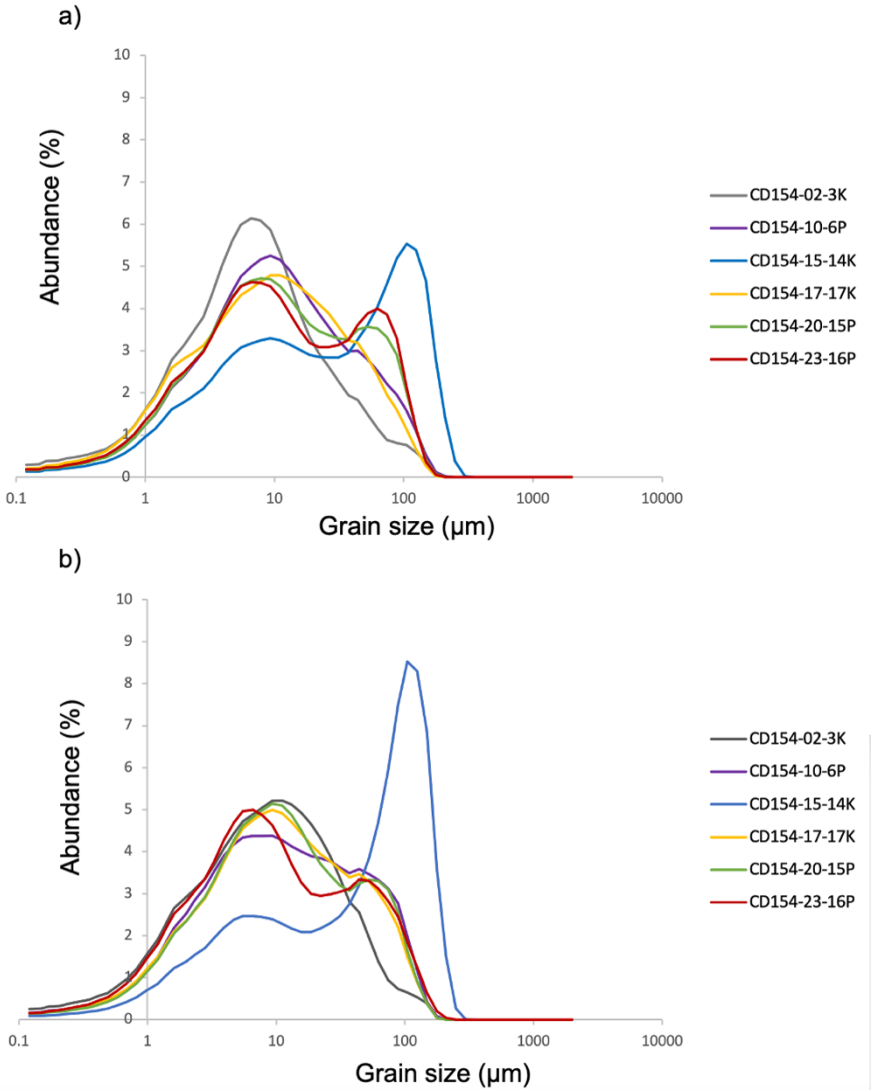

Figure 4.6: Grain size distributions for marine sediments from CD154 core sites (a) Modern and (b) LGM for core sites included in this study (see key for sample ID).

There is more sand (%) in all depths from the LGM compared to the core top samples, except for the southerly marine sediment cores (CD154-20-15P and CD154-23-16P) where the reverse is observed (i.e., less sand (%) LGM) (Table 4.6). However, site CD154-23-16P contains the highest sand content (12.30 wt %) during the LGM compared to all other CD154 sites included in this study.

Table 4.6: Classical grain size percentages for sand, silt and clay for each sediment core (Modern and LGM dated).

Core Site	Age	Depth	Sand (%)	Silt (%)	Clay (%)
CD154-02-03K	Modern	0-1 cm	4.600	79.800	15.500
CD154-10-06P	Modern	3-4 cm	10.100	78.400	11.600
CD154-15-14K	Modern	0-1 cm	34.000	57.300	8.700
CD154-17-17K	Modern	1-2 cm	8.100	77.700	14.300
CD154-20-15P	Modern	1-2 cm	13.500	75.300	11.300
CD154-23-16P	Modern	6-7 cm	14.900	73.000	12.200
CD154-02-03K	LGM	145-146 cm	4.700	80.500	14.700
CD154-10-06P	LGM	69-70 cm	12.900	75.900	11.200
CD154-15-14K	LGM	50-51 cm	47.300	46.400	6.400
CD154-17-17K	LGM	51-52 cm	10.700	78.200	11.100
CD154-20-15P	LGM	304-305 cm	11.900	77.600	10.400
CD154-23-16P	LGM	36-337 cm	12.300	74.500	13.100

4.4.3.1 Sortable Silt

The $\overline{SS}$ mean grain size values range from 22.5 µm to 29.5 µm (Figure 4.7). The mean grain size is slightly larger (by 0.08 µm) during the LGM compared to present-day.

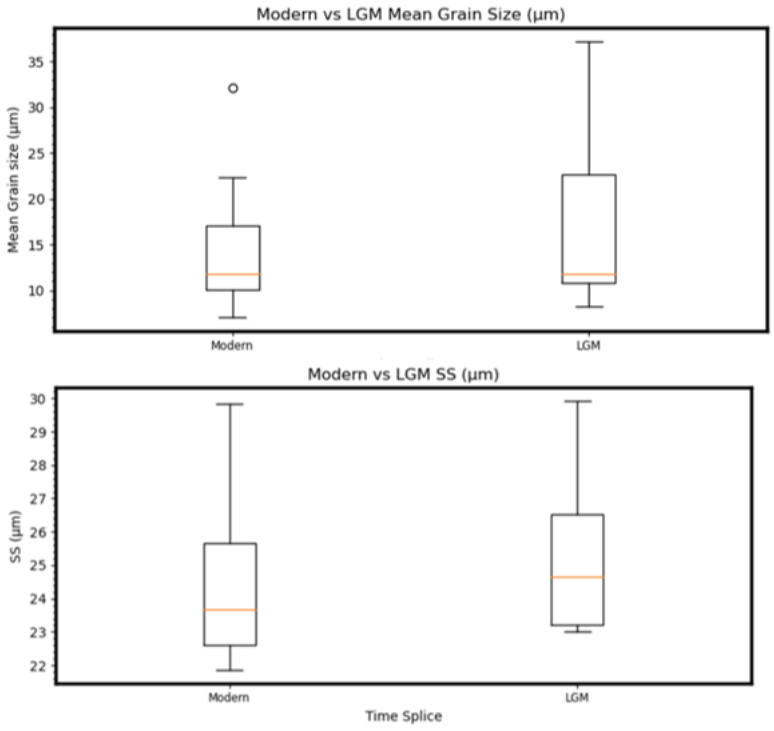

Figure 4.7: Mean grain size (µm) of Modern and LGM dated sediments (top) and mean $\overline{SS}$ (µm) of Modern and LGM dated sediments (bottom)

The "main-line" equation (McCave *et al.*, 2017) is used to convert $\overline{SS}$ (µm) to flow speed (U). It gives a sensitivity of 1.26 ±0.18 cm s^{-1}/µm (±2s.d.) for Coulter Counter data and 1.36 ±0.19 cm s^{-1}/µm for Sedigraph data (McCave *et al.*, 2017). Comparisons of modern $\overline{SS}$ and UModern and LGM $\overline{SS}$ with ULGM are shown in Figure 4.8a. Figure

4.10b reveals the depth profile of flow speed for modern and LGM time splices. There is a peak in flow speed at water depth ∼ 3250 m in the modern within the analytical error mentioned above, and a peak at a shallower water depth (∼ 2500 m) during the LGM within the analytical error.

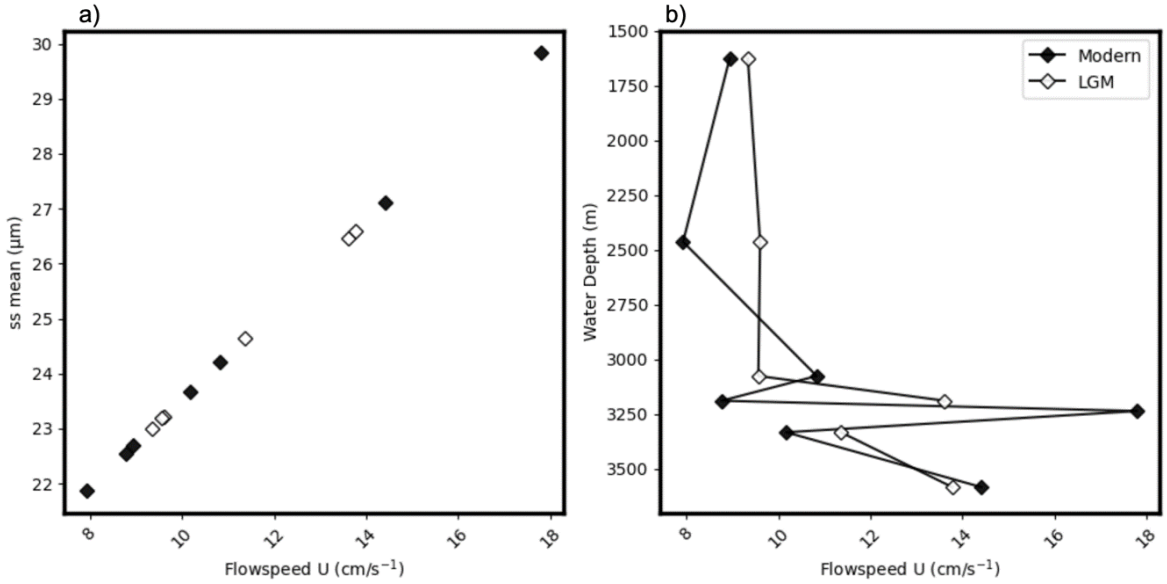

Figure 4.8: a) Calibration of $\overline{SS}$ (µm) using 'main line' equation from McCave *et al.* (2017), b) Depth profile of calibrated flowspeed (U) (cm/s^{-1})

4.4.3.2 Stable Isotope δ^{13}C Measurements

The average benthic δ^{13}C modern values are 0.81‰ and the LGM average δ^{13}C values are 0.32‰. Mean ocean shifts in δ^{13}C have been observed during glacials of ∼0.32‰ (Duplessy *et al.,* 1988) to 0.40‰ (Curry *et al.,* 1988). To account for this shift, a correction of 0.32‰ was applied to the LGM δ^{13}C values (Figure 4.9). This gives an average δ^{13}C value of 0.62‰ during the LGM. There is a maximum benthic δ^{13}C value at ∼ 3000m which indicates the presence of a well-ventilated water mass such as NADW. For the LGM, there is no change in the corrected benthic δ^{13}C values at depths shallower than 2500 m, however deeper than 2500 m there is a lower benthic δ^{13}C value which indicates a dominance of South Component Water (SCW) (Figure 4.9b)

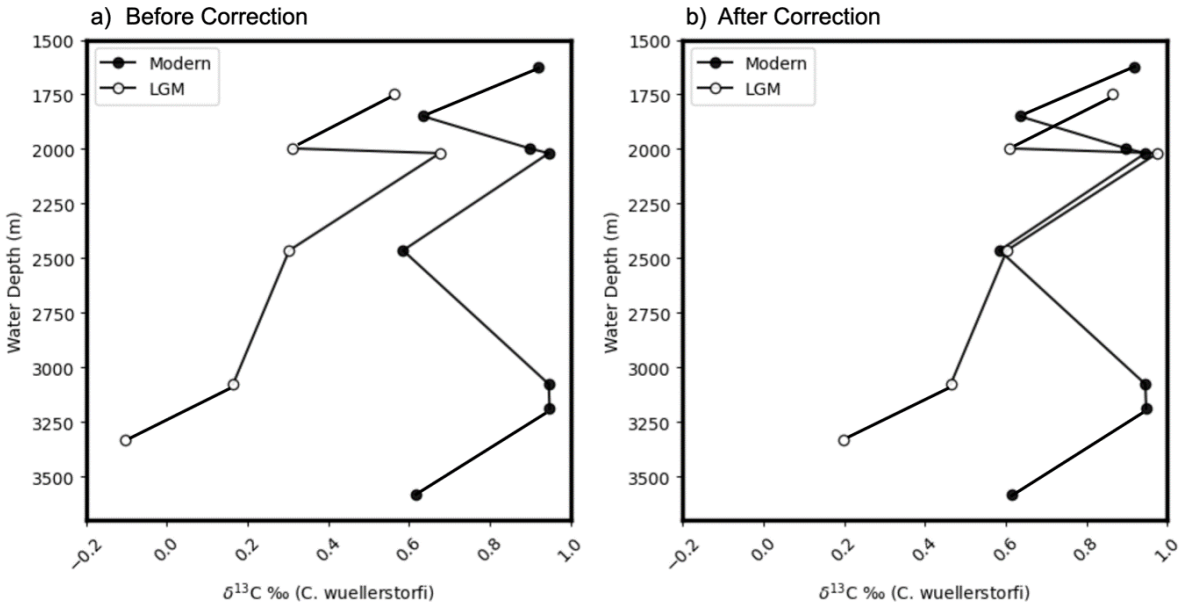

Figure 4.9: Depth profile of δ^{13}C (a) not corrected and (b) corrected by applying the mean ocean correction of 0.32‰ to the LGM samples.

4.5 Discussion

4.5.1 Hydrography Reconstructions

Using the available benthic δ^{13}C data from the region, the first aim relates to characterising the intermediate and deep-water mass geometry in this section. This will help synthesise the regional δ^{13}C data and give an indication of whether bottom waters transporting sediments will influence the radiogenic isotopes provenance signature in the Southwest Indian Ocean.

Major water masses in the region are NADW, AAIW and CDW. NADW originates with δ^{13}C values above 1‰ in the North Atlantic (Kroopnick, 1985) and as it reaches further South, it mixes with the South Ocean source waters resulting in lower δ^{13}C values (0.8‰; (Bickert and Wefer, 1996)). Modern day CDW has a typical δ^{13}C value of 0.5‰ (Kroopnick, 1985), recently confirmed by GEOTRACERS programme section GI04 (a transect from Tokyo, Japan to Cape Town, South Africa (Gamo and Obata, 2010)). Interestingly, the average modern δ^{13}C value of the deeper CD154 marine sediment cores (>3000 m) (Figure 4.10a) is higher than the CDW values for section GI04 by ∼0.3‰. This may be due to the location of the GI04 transect, situated further East compared to the CD154 marine sediment cores in this chapter. This means the transect could be reflecting more CDW dominated waters, which dominate further to the East (Wyrtki, 1971). As modern NADW δ^{13}C values are 0.8‰ in the South Atlantic (Bickert and Wefer, 1996), it is reasonable to suggest there is dominance of NADW at water depths ∼ 3000 m (Figure 4.10a) in this study region during present-day, supported by studies from the modern

Cape Basin which show the core of NADW is located along the South African margin at around 2500 m water depth (Hines *et al.,* 2021).

During the LGM, there is a change to lower δ^{13}C values at water depths greater than 2000m (Figure 4.10b), which are suggesting a dominance of SCW. SCW is a mixture of AABW and AAIW (Reid, 1989; Reid, 2005) so is a nutrient-rich bottom water which has aged and has a lower δ^{13}C value than NADW (Figure 4.10). A similar trend was observed in both benthic δ^{13}C (Hu *et al.,* 2016) and sedimentary ^{231}Pa/^{230}Th records (Lippold *et al.,* 2016), presenting a northward advancement of SCW in the deep Atlantic ($>$ 3000 m) during the LGM. In contrast, no change is observed between the modern and LGM in intermediate waters ($<$ 2000 m), this suggests a continued enhanced mid-depth ventilation during the LGM, supported by other studies (Molyneux, 2007).

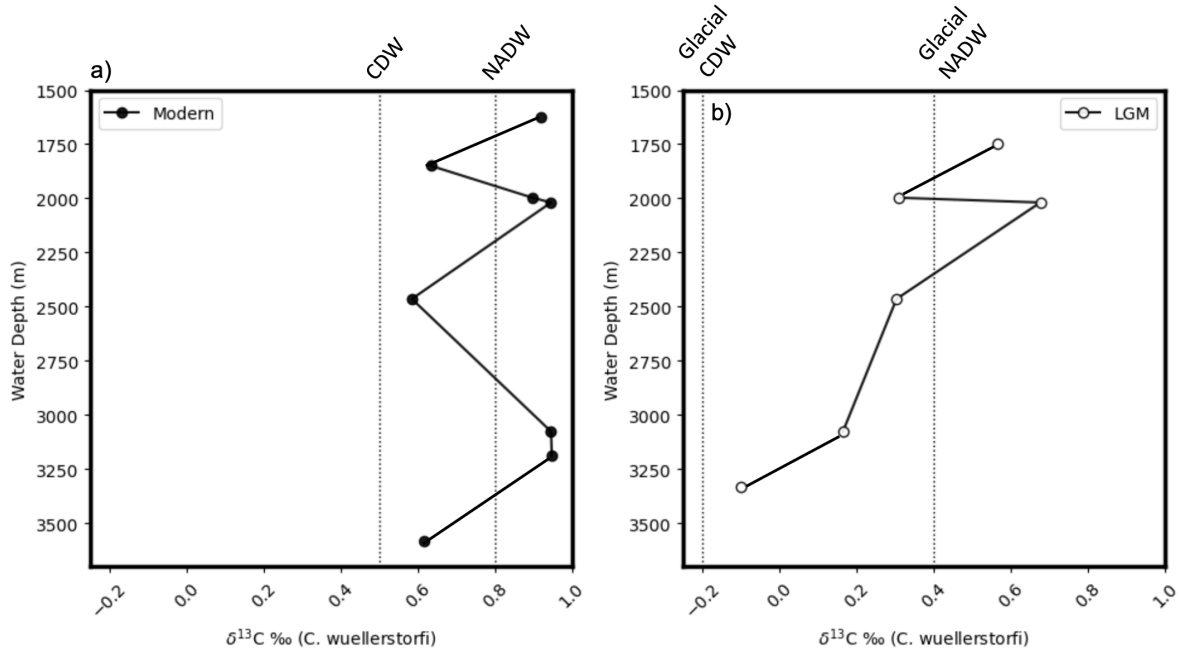

Figure 4.10: Depth profiles of a) modern δ^{13}C, modern day values for NADW and CDW indicated. b) LGM δ^{13}C values with depth with glacial NADW from Lynch-Stieglitz. (2007) and CDW from Oppo and Curry. (2005). Note these δ^{13}C values are not corrected to mean ocean values.

4.5.1.1 Regional Comparison

Comparison of the modern and LGM benthic δ^{13}C values from this study with equivalent records from the South Atlantic and Southwest Indian Ocean is shown in Figure 4.11. No mean ocean δ^{13}C correction has been applied to any values as all δ^{13}C values were equally affected by the mean ocean shift. All data points taken are either modern or LGM dated through radiocarbon dating techniques from the associated publication. Additionally, all benthic isotope values were measured on *Cibicoides spp.*

The modern signal in Figure 4.11 is reflecting a higher modern δ^{13}C signature at depths $\sim$

3000 m indicating NADW. The amplitude of change between modern and LGM in these sites positioned in present-day NADW is small compared to deeper sites, positioned below NADW. Deep abyssal cores in the region have a lower modern δ^{13}C signature compared to the shallower sites (Figure 4.11). Values are on average $\sim$0.8‰ more negative in modern deeper sites compared to shallower sites, which is associated with a greater influence of CDW which has a lighter δ^{13}C signature, indicating its mixing of AABW and NADW (Curry and Oppo, 2005). This pattern is also consistent for the LGM. Studies have shown core sites at water depths > 4000 m (not shown in Figure 4.11) persisted under the influence of AABW during both glacial and interglacial conditions (Charles *et al.,*1996; Ninnemann and Charles, 2002), indicating the difference between modern and LGM δ^{13}C reduces with depth below 4000 m.

Records across the South Atlantic reveal that during glacials lower δ^{13}C values signify older, nutrient-enriched Antarctic water masses, with lower ventilation due to an enhanced seclusion from the atmosphere (Ninnemann and Charles, 2002; Hodell *et al.,* 2003). The lower δ^{13}C values observed during the LGM suggest a reduced influence of NADW and an increase in poorly ventilated SCW in the Southwest Indian Ocean. During glacial conditions, this increase in SCW dominance coincident with a reduction in δ^{13}C values is observed in all marine sediment cores in this chapter (Figure 4.11). Some studies suggest that ocean circulation was different during the LGM, with a shoaling of NADW and a 'two cell' circulation loop (Figure 1.11) (Curry and Oppo, 2005; Ferrari *et al.,* 2014; Sikes *et al.,* 2017). However, in recent times, some authors have re-examined this glacial shoaling (Hines *et al.,* 2021), as most work has been based on carbon isotopes. These studies have instead argued that the glacial ocean has a similar structure to the modern with very little changes in NADW depth (Gebbie, 2014; Howe *et al.,* 2016; Oppo *et al.,* 2018).

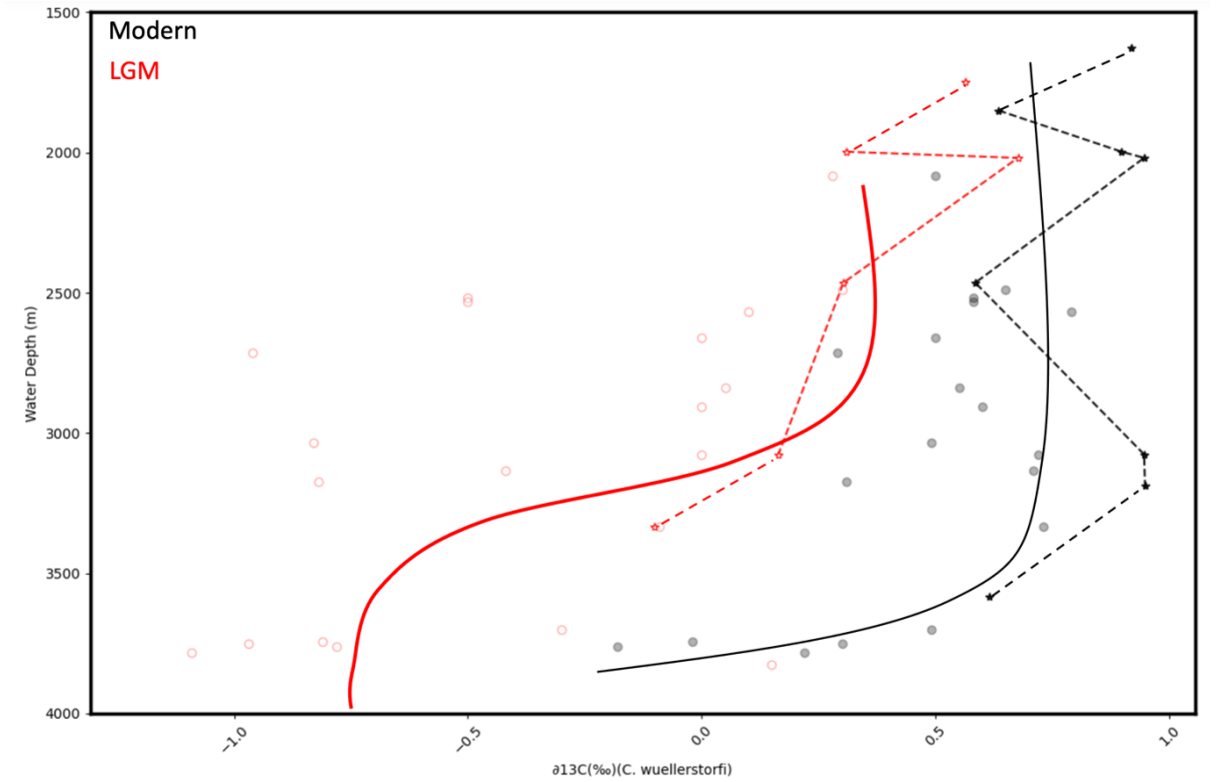

Figure 4.11: Vertical δ^{13}C for modern (black) and LGM (red) from South Atlantic and Southwest Indian Ocean. Sites in this chapter are joined by dashes. Image modified from Hodell *et al.* (2003)

The δ^{13}C values presented alongside the flow speed reconstructions for the study sites show the influence of NADW in the region during present-day at 3000 m (Figure 4.12). The δ^{13}C and flow speed records reveal a stronger influence of SCW during the LGM at depths greater than ∼2500 m (Figure 4.12), this means that more sediment is transported from the southern regions such as South America via the ACC. This evidence of a water mass hydrographic change and physical flow speed shifts between modern and LGM intervals provides an indication of the deep-water transport regimes in the region. This is beneficial for provenance reconstructions during the LGM to enhance understanding of where the sediment in the CD154 cores has come from, based on water mass transport.

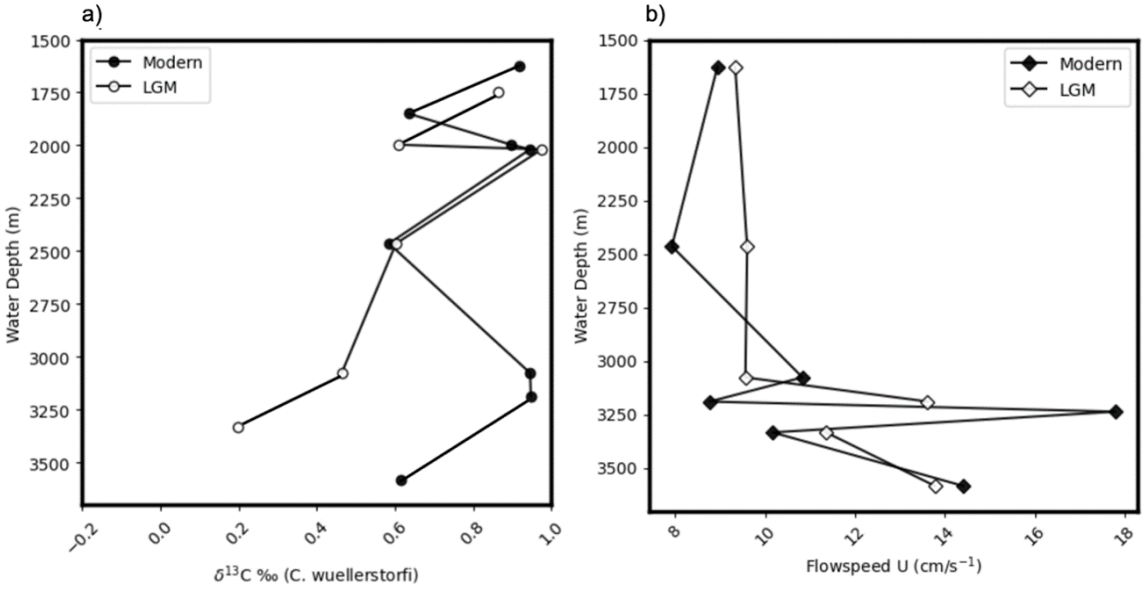

Figure 4.12: Chemical vs Physical ventilation plots. (a) Vertical δ^{13}C reconstructions (corrected) and (b) depth profile of flow speed for modern (filled symbols) and LGM (unfilled symbols).

4.5.2 Sediment Provenance

In this next section, the influence of the surface Agulhas Current carrying sediment from upstream sources, South African regional climate changes and a deep-water mass change are discussed to understand the key processes influencing provenance reconstructions occurring during the modern and LGM. Previously discussed deep water hydrography around South Africa can be put in the context of linking a potential provenance change of sediments during the LGM through sediment transport from the South Atlantic Ocean. The provenance data (radiogenic isotopes) of the marine sediment cores from the defined sectors mentioned above (i) northern sector of the Agulhas Current which encompasses 29 to 33°S latitudes and (ii) the central sector which is 33 to 35°S and iii) the southern sector of the Agulhas Current (south of 35°S) are compared to the radiogenic isotope compositions of likely source regions in Figure 4.13. The simplest scheme for representing the composition of sediment deposited at the core sites utilised in this study is as an admixture of sediment from, 1) proximal sources delivered by rivers discharging along the local South African coastline, 2) distal sources (e.g. Limpopo and Zambezi river systems) carried downstream by the Agulhas Current, or 3) transported at depth via the South Atlantic Ocean.

Based on radiogenic isotope endmember mixing calculations of the <2 µm clay fraction used in Chapter 3, radiogenic isotope endmembers for the Limpopo and Zambezi rivers have been generated in the same way. This is because it is not possible to distinguish between solely Karoo and Cape Supergroup endmembers (from Chapter 3), so we use

additional endmembers from sources further afield to understand the climate picture. Sediment derived from the Limpopo river is characterised by a cratonic signature due to older crust material ($^{87}Sr/^{86}Sr_{clay}$ = 0.767 (± 0.000012) and εNd_{clay} = -19.200 (± 0.07)) (Table 1.1). In comparison, to generate the Zambezi endmember, offshore Zambezi sediments are mixed to some extent with clays characterised by more radiogenic εNd signatures from the North (cf; van der Lubbe *et al.,* 2016) and inland values from Garzanti *et al.* (2014), whereas for $^{87}Sr/^{86}Sr$ isotopes, there is limited data in the Zambezi region. Therefore, inland $^{87}Sr/^{86}Sr$ isotopes from Garzanti *et al.* (2014) are used with offshore surface samples from Site IODP U1476 (15.49°S, water depth 2166m; (Hall *et al.,* 2016)). This yields a radiogenic isotope endmember value of $^{87}Sr/^{86}Sr_{clay}$ = 0.723 (± 0.00003) and εNd_{clay} = -13.798 (± 0.2) for the Zambezi. South Atlantic sediments from the LGM are characterised by lower $^{87}Sr/^{86}Sr_{clay}$ values (Beny *et al.,* 2020) than sediments from the Agulhas Current region ($^{87}Sr/^{86}Sr_{clay}$ = 0.7115 and εNd_{clay} = -5.300). Previous work has identified potential endmember values, but these are based on different size fraction measurements such as <63 µm (Kuhn and Diekmann 2002; Franzese *et al.,* 2006; Noble *et al.,* 2012). Franzese *et al.* (2006) define three endmembers (<63 µm), these are the Agulhas Current endmember which is a combination of Zambezi and Limpopo values ($^{87}Sr/^{86}Sr$ = 0.740; εNd= -17.000), local South Africa ($^{87}Sr/^{86}Sr$ = 0.731, εNd = -6.000) and South Atlantic ($^{87}Sr/^{86}Sr$ = 0.709, εNd= -5.000).

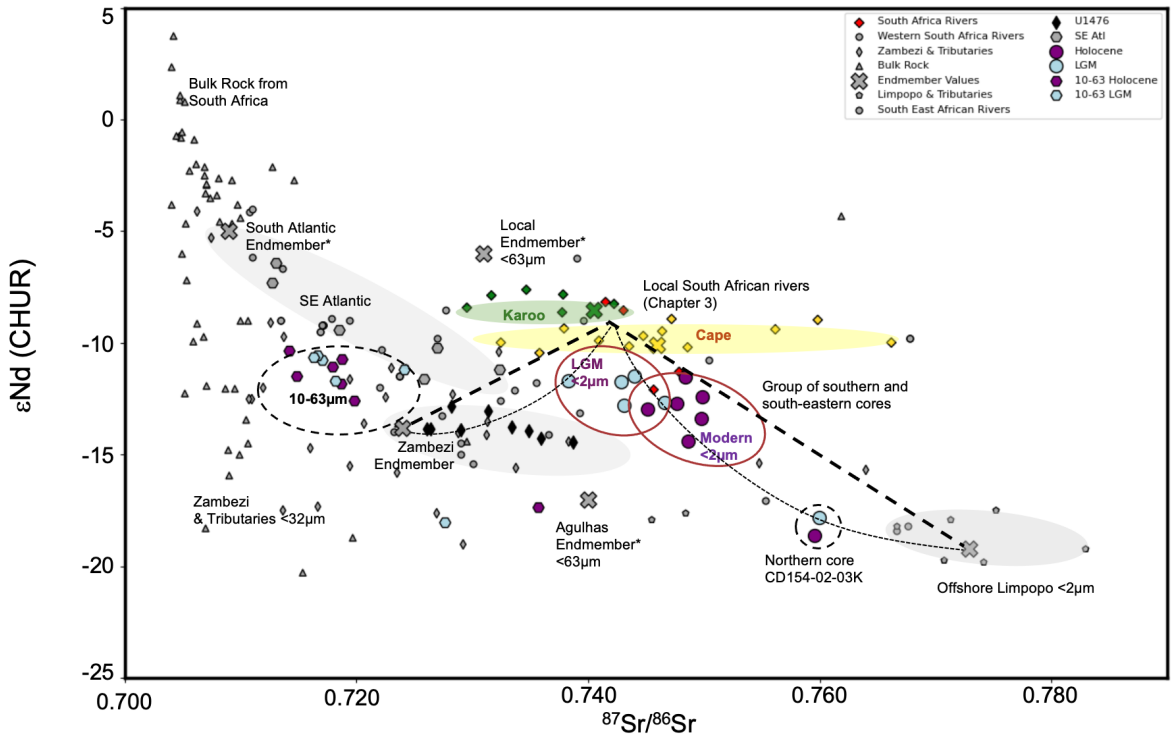

Figure 4.13: Comparison between radiogenic isotopes $^{87}Sr/^{86}Sr$ and εNd. Distinctions between modern (purple) and LGM (blue) source provenance can be seen. During modern the southern sites sit below the mixing line (purple) between offshore Limpopo and local South African river endmembers and during the LGM period, sites are closer to the Zambezi – local mixing line. All published data in grey, these are offshore Limpopo (U1478) (Simon *et al.,* 2020a), Zambezi and Tributaries (Garzanti *et al.,* 2013), Bulk rock values from South Africa (Riley *et al.,* 2005; Neumann *et al.,* 2011), South East Atlantic (Franzese *et al.,* 2006), Western South African rivers (Weldeab *et al.,* 2013), South East African rivers (Hahn *et al.,* 2020), U1476 (van der Lubbe, pers.comms).

From this present study, the εNd_{clay} and $^{87}Sr/^{86}Sr_{clay}$ have a strong anti-correlation (r = -0.80) (Figure 4.14), which suggests the differences are related to sediment provenance changes, rather than transport process (e.g. sedimentary sorting). This is because εNd is strongly controlled by provenance and is not as sensitive to other influences as Sr (e.g. weathering, transport) (Goldstein *et al.,* 1984; Blum and Erel, 2003; Fagel *et al.,* 2004; Fagel, 2007; Meyer *et al.,* 2011; Garzanti *et al.,* 2014; van der Lubbe *et al.,* 2014; Hahn *et al.,* 2016; van der Lubbe *et al.,* 2016; Hahn *et al.,* 2018). This is consistent to results in Chapter 3 with εNd_{clay} and $^{87}Sr/^{86}Sr_{clay}$ values also being anti-correlated. As such, a strong correlation indicates the measured $^{87}Sr/^{86}Sr_{clay}$ values are dominated by provenance, supported by other studies (Franzese *et al.,* 2006; Carter *et al.,* 2020). The average grain size of sediment deposited at these sites is weakly correlated with the $^{87}Sr/^{86}Sr_{clay}$ ($r = -0.15$, $p > 0.05$) and more strongly correlated with $^{87}Sr/^{86}Sr$ non-cohesive silt ($r = -0.6$, $p < 0.05$) (Figure 4.14). As the average grain size increases, the $^{87}Sr/^{86}Sr$ ratios decrease and εNd increases. The stronger correlation of the $^{87}Sr/^{86}Sr$ non-cohesive

silt and average grain size may be due to hydrodynamic sorting.

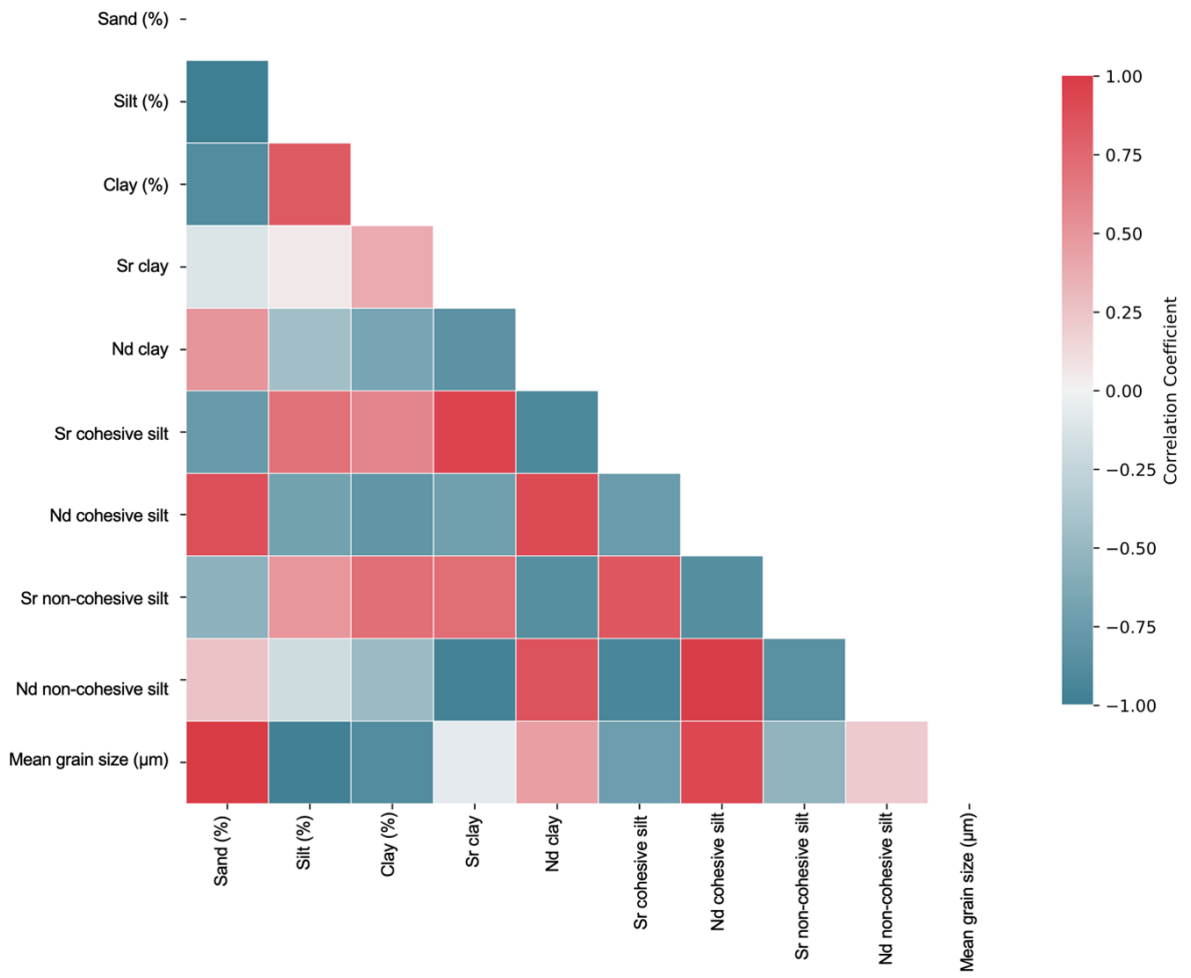

Figure 4.14: Correlation matrix showing Pearson Correlation Coefficient (r) between designated records of all CD154 core sites included in this study. Colours indicate strength and direction of correlation between records (dark red – strong positive, light red – weak positive, white – very weak/ none, light blue – weak negative, dark blue – strong blue).

Franzese *et al.* (2006), based on the <63 µm fraction, found lower $^{87}Sr/^{86}Sr$ values during LGM compared to the modern and interpreted this shift as an indication of changing sediment provenance. Encouragingly, the magnitude of this shift is broadly equivalent to the observed difference in the $^{87}Sr/^{86}Sr_{clay}$ found in this study (Figure 4.15). Taken together this suggests that our $^{87}Sr/^{86}Sr_{clay}$ isotope data is likely faithfully recording provenance variability.

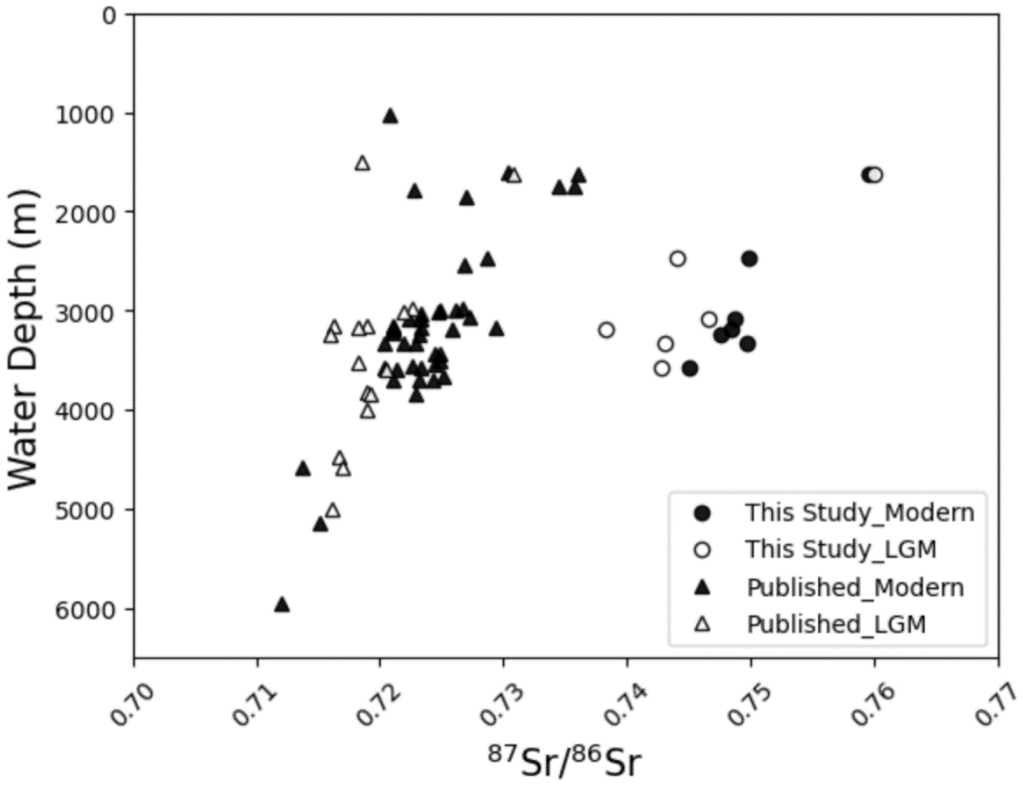

Figure 4.15: Comparison between $^{87}Sr/^{86}Sr$ values measured on the <63 µm (triangles; from Franzese *et al.,* 2006) and <2 µm fraction (circles; from this study). Filled in symbols = modern, unfilled symbols = LGM.

4.5.2.1 Detrital Sediment Supply to Northern Sector

During the modern, there is a radiogenic $^{87}Sr/^{86}Sr_{clay}$ (0.760 ± 0.00000896) composition (Figure 4.16) and unradiogenic εNd_{clay} value (-18.639 ± 0.132) (Figure 4.17) in the most northerly marine sediment core (CD154-02-03K). This means the northern sector reflects an older sediment source supply which could be supplied from the Limpopo river sediments. Figure 4.18 is a radar plot which shows the relative contributions of sediment sources between Limpopo, Zambezi and local South African rivers during present-day and LGM at each CD154 core site discussed in this chapter. Each sediment source is presented on separate axes within the radar and the length on the axis is proportional to the sediment contribution. Based on this sediment source contribution mixing, Limpopo contribution is 85%, Zambezi supply is 10% and local South African rivers supply 5% during the modern to the northern sector (Figure 4.18). Details on this calculation are found in section 2.3.5

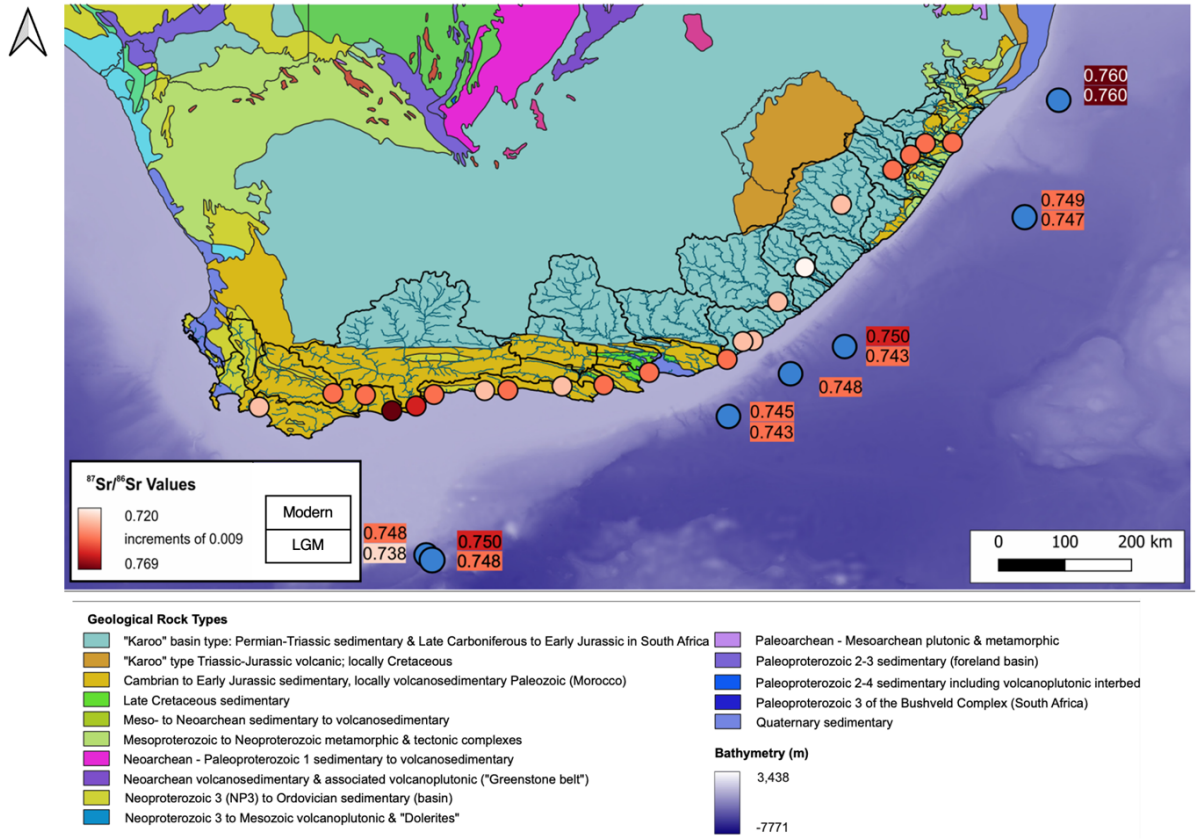

Figure 4.16: Modern and LGM terrigenous $^{87}Sr/^{86}Sr_{clay}$ variability. Symbols marking core locations are not colour coded, however the modern and LGM values for the terrigenous $^{87}Sr/^{86}Sr_{clay}$ are given next to each core, these are colour coded, refer to key. For the cores analysed, the LGM value is lower than or the same as the modern value.

In the northern sector during the LGM the εNd_{clay} signature is higher (εNd_{clay} = -17.827 ± 0.164) than modern, but the $^{87}Sr/^{86}Sr$ signature bears the same radiogenic values as modern (Figure 4.16; 4.17). This finding is similar to Franzese *et al.* (2006) where Holocene and LGM $^{87}Sr/^{86}Sr$ values are similar in northern core site VM19-214 (23.37°S). During the LGM, based on sediment source contribution mixing between Limpopo, Zambezi and local South African rivers, the Limpopo contribution is 75%, Zambezi contribution is 17% and local rivers from South Africa are 7% (Figure 4.18). This shows the contribution of Limpopo reduces and Zambezi increases during the LGM, compared to the modern in the northern sector. Radiogenic isotope mixing plot (Figure 4.13) reveals that CD154-02-03K sits below the mixing line (on the εNd axis) between offshore Limpopo sediment site U1478 (Simon *et al.,* 2020a) and local sediments during both modern and LGM time intervals. This reveals the mixing between an older sediment source indicative of the Limpopo river and a younger sediment source such as South African rivers in the northern sector.

4.5.2.2 Detrital Sediment Supply to Central Zone

Compared to the northern zone, all sites in the central zone (between 33°S to 35°S) present lower modern $^{87}Sr/^{86}Sr_{clay}$ values (Figure 4.16) and higher εNd_{clay} values (Figure 4.17). Based on radiogenic isotope endmember mixing, these data suggest the central sites are influenced by a significantly lower proportion of Limpopo river sediment (Figure 4.18), and reflect high inputs from local South African river sediment (Figure 4.16; 4.17; 4.18).

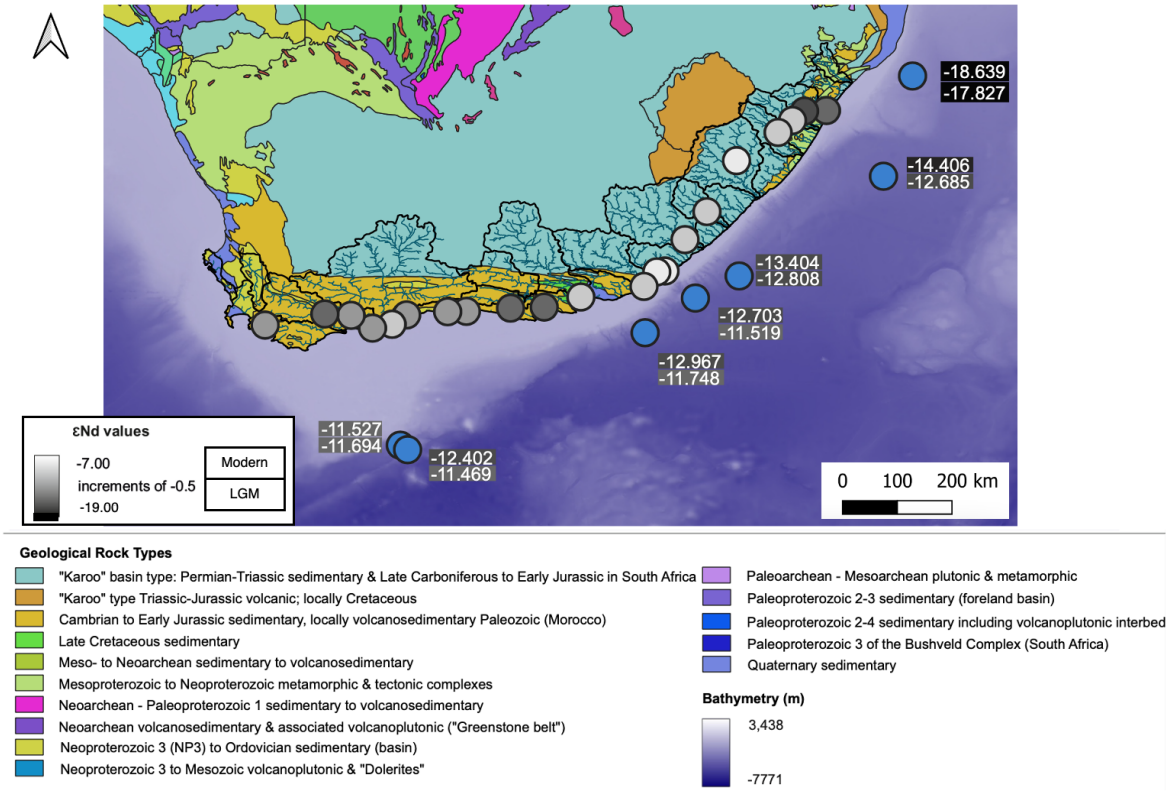

Figure 4.17: Modern and LGM εNd_clay variability. Symbols mark core locations, they are not colour coded, however the modern and LGM values for the εNd_clay are given next to each core. For most of the cores analysed the LGM value is higher than the modern value.

4.5.2.3 Detrital Sediment Supply to Southern Sector

The glacial $^{87}Sr/^{86}Sr_{clay}$ values are lower than the modern $^{87}Sr/^{86}Sr_{clay}$ ratios in the southern zone by 0.010 (Figure 4.16). The LGM εNd_{clay} value is higher (more radiogenic) than the present-day value in MD20-3591 by 0.933 but in CD154-23-16P the εNd value is lower than the associated present-day value by 0.167 (Figure 4.17). This value is beyond the average error for the εNd_{clay} ($\pm$0.147)). In addition to a reduced southward extension of high $^{87}Sr/^{86}Sr$ values during the LGM, as found by Franzese *et al.* (2006), this study observes that low εNd values do not extend south during both modern and LGM.

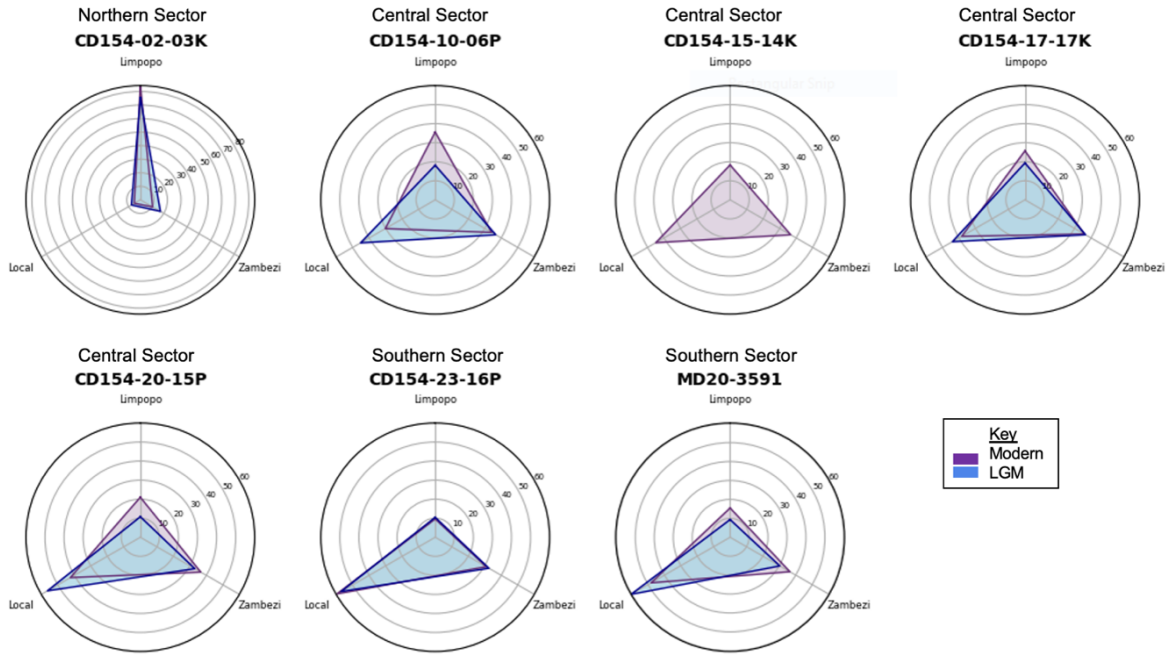

Figure 4.18: Radar plot of defined radiogenic isotope endmember source contributions during the modern (purple) and LGM (blue) for each sediment cores within associated labelled sector (Northern, Central and Southern). The higher the number for each individual plot, the more sediment contributes to the site from the source. Sediment source written around the radar plots, Limpopo (top of each plot), local South Africa (bottom left of each radar plot), Zambezi (bottom right of each radar plot). Note: no LGM data for core site CD154-15-14K. Details on calculation in section 2.3.5

4.5.3 Sediment Sources and Mixing: Links to Modern and LGM Climate in Southern Africa

In this next section, the sediment sources for each region are discussed. These main sources discussed above and in Chapter 1.5 are local South African rivers, the Limpopo and Zambezi rivers characterised as upstream sources and distal sources such as South America and Patagonia, transported via the ACC.

4.5.3.1 Modern Day

The dominant sediment sources during the modern to the CD154 sites are from the proximal South African and distal Limpopo and Zambezi rivers based on radiogenic isotope reconstructions (Figure 4.13; 4.18). Figure 4.18 reveals that the northern sector is influenced mainly by sediments from the Limpopo river during modern (Figure 4.18; purple shading) whereas the central and southern sectors are mainly influenced by local South Africa sediment. This is shown in Figure 4.19 which is a conceptual diagram of modern conditions based on the source contribution model (section 2.3.5). Sediments from the Limpopo and Zambezi are carried downstream by the Agulhas Current to the CD154 core

sites. The present-day regional hydrological reconstructions from South Africa, which reveal three rainfall zones are shown in Figure 4.19. The criteria by which the present day rainfall regions have been defined varies, but a commonly employed method is the percentage of mean annual rainfall during the winter (>66% = WRZ, <33% = SRZ, 33%-66% = YRZ; (Chase and Meadows, 2007) (Figure 4.19)). The following studies discussed below suggest modern day South African rainfall amounts would influence sediment discharge from South African rivers and Limpopo catchment.

In the east, the warm SSTs of the Agulhas Current fosters increased evaporation and the transport of moisture into the interior (Tyson and Preston-Whyte, 2000; Rouault *et al.,* 2002). In the west, tropical moisture advection from the Atlantic Ocean is generally limited to regions north of ∼15°S (Rouault *et al.,* 2003; Crétat *et al.,* 2019). The summer rains in the Limpopo catchment are also influenced by SSTs of the Southwest Indian Ocean and 90% of the rainfall experienced in the Limpopo catchment is during Southern Hemisphere summer (FAO, 2004).

Further south, the cold Benguela Current flows equatorward along the South African coasts, limiting evaporation and supressing convection (Tyson 1986; Nicholson and Entekhabi, 1987). This results in a marked east-west rainfall gradient across the subcontinent at these latitudes, and the dominant moisture-bearing systems are northerly flows over Angola and easterly flows from the Indian Ocean. Southern African climates are also strongly influenced by extra-tropical systems. Poleward of the subcontinent, the SHW dominate mid-latitude atmospheric circulation. Perturbations in the SHW create fronts that produce the majority of rainfall received by the southwestern Cape (Reason and Rouault, 2002). The influences of these various systems have strong seasonal biases, with the tropical systems being most vigorous in the warm summer months, and the extra-tropical frontal systems being most prevalent during the winter, when the Antarctic anticyclone expands and the zone of frontal activity is displaced equatorward (van Zinderen Bakker, 1967; van Zinderen Bakker, 1976; Cockcroft *et al.,* 1987; Shi *et al.,* 2000; Stuut, 2004; Chase and Meadows, 2007; Anderson and Burckle, 2009; Sigman *et al.,* 2010; Neumann and Scott, 2018b).

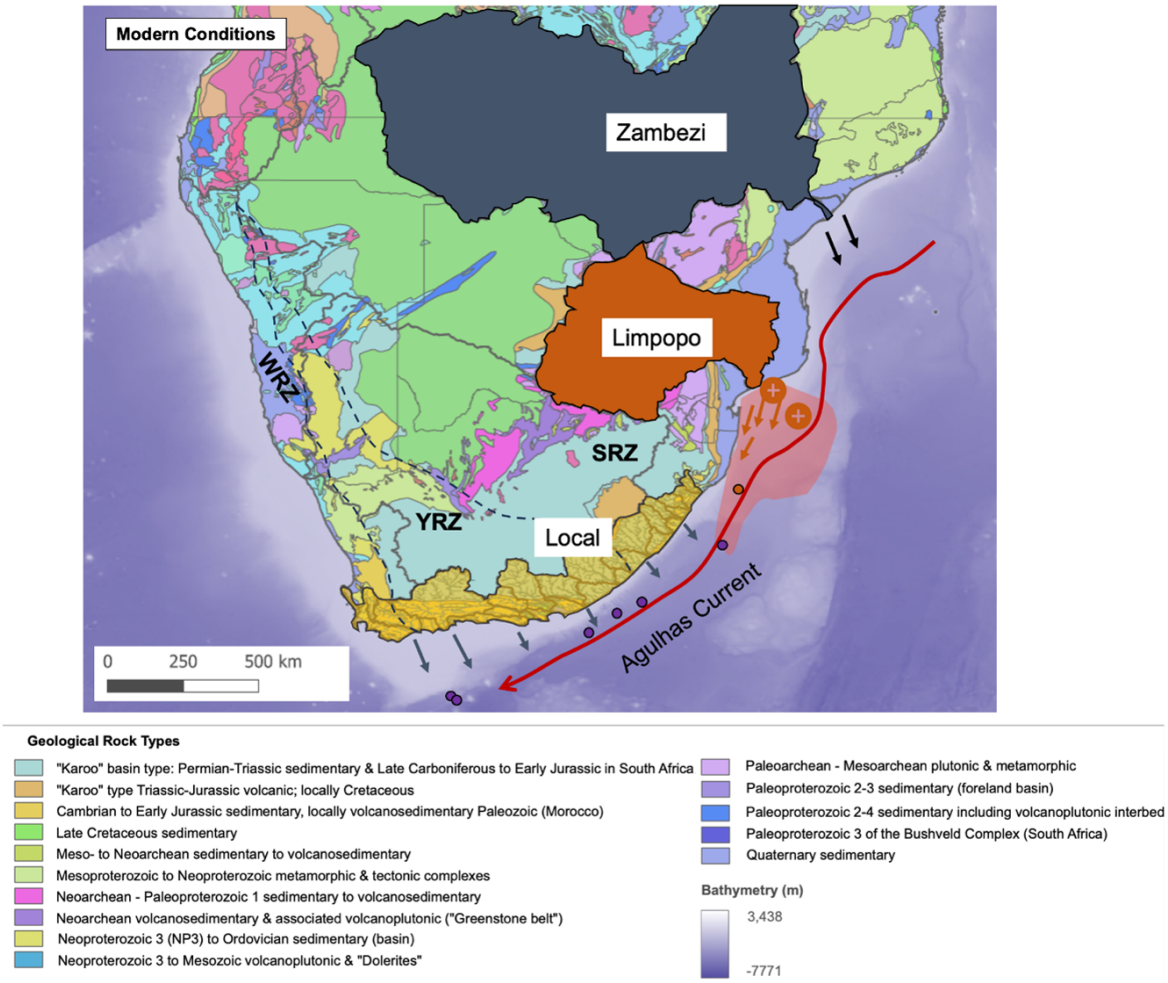

Figure 4.19: Conceptual Diagram of Modern Conditions. Major source regions are Zambezi river catchment (grey), Limpopo river catchment (orange) and local South African river catchments (yellow). Arrow number represents relative contribution to Southwest Indian Ocean, i.e. more arrows, high contribution of sediment from this source to core sites. Agulhas Current (red arrow). Rainfall zones of South Africa, Winter Rainfall Zone (WRZ), Year-round Rainfall Zone (YRZ), Summer Rainfall Zone (SRZ) shown.

In line with these studies, radiogenic isotope results from this chapter show local sediment dominates in the central and southern sector but with some mixing from a more radiogenic source such as the Limpopo and/or Zambezi (Figure 4.18). This is because the $^{87}Sr/^{86}Sr_{clay}$ (average 0.750 ± 0.00001) and εNd_{clay} (-13.721 ± 0.147) values are too high for only local South African river input (Chapter 3) so indicate a mixed source region signature. The northern sector bears radiogenic isotope signatures ($^{87}Sr/^{86}Sr_{clay}$ = 0.760 ± 0.00000896 and εNd_{clay} value = -18.639 ± 0.132) similar to offshore of the Limpopo catchment ($^{87}Sr/^{86}Sr_{clay}$ = 0.767 (± 0.000012) and εNd_{clay} = -19.200 (± 0.07)) (Figure 4.13) and it is likely the sediment is distributed downstream within the Agulhas Current.

Next, the potential hydroclimate mechanisms during the LGM are compared with existing literature to explain the provenance signals observed in the radiogenic isotopes (Sr and Nd) measured on the <2 µm fraction, by utilising other proxies such as clay minerals and terrigenous grain size. The radiogenic isotope signals observed during the LGM in the three different sectors (Figure 4.16; 4.17) are explored further, through focusing on the changes in the individual sediment source regions outlined above. These are the local South African sources, the upstream sources i.e. Limpopo and Zambezi rivers, and distal sources such as South America.

4.5.3.2 Impact of Sea Level Shifts during LGM on Local South African Sediment Supply

Sea level was ∼ 120 m lower during the LGM than it is today (Peltier, 2004). For South Africa, this translates to a large expansion of the PAP (the continental plain south of the continent) and increased exposure with habitable land stretching to 80-100 km further south during the LGM (Figure 4.20) than the present-day location of Cape Agulhas (Fisher *et al.,* 2010; Compton, 2011; Fisher *et al.,* 2020). The PAP is composed of fertile soils derived from siltstone and shale bedrock (Cawthra *et al.,* 2014; Cawthra *et al.,* 2020b) and therefore more sediment was available to be eroded from this shelf and transported via fluvial discharge. The river courses changed considerably during glacial sea level low stands, cutting through the PAP and creating different routes to the Southwest Indian Ocean as mapped in Cawthra *et al.* (2019). There is evidence of bedload transport along the continental shelf, as a function of the topographic forcing and the Agulhas Current flowing over the submarine canyons (Green, 2009). As such this reveals the potential driver of sea level fluctuations in sediment dynamics and distribution and the importance of the Agulhas Current concerning sediment transport. There is a coarser terrigenous grain size during the LGM at sites in the central and southern sectors (Figure 4.8) attributed to a closer proximity of the rivers to the core sites via an exposed PAP.

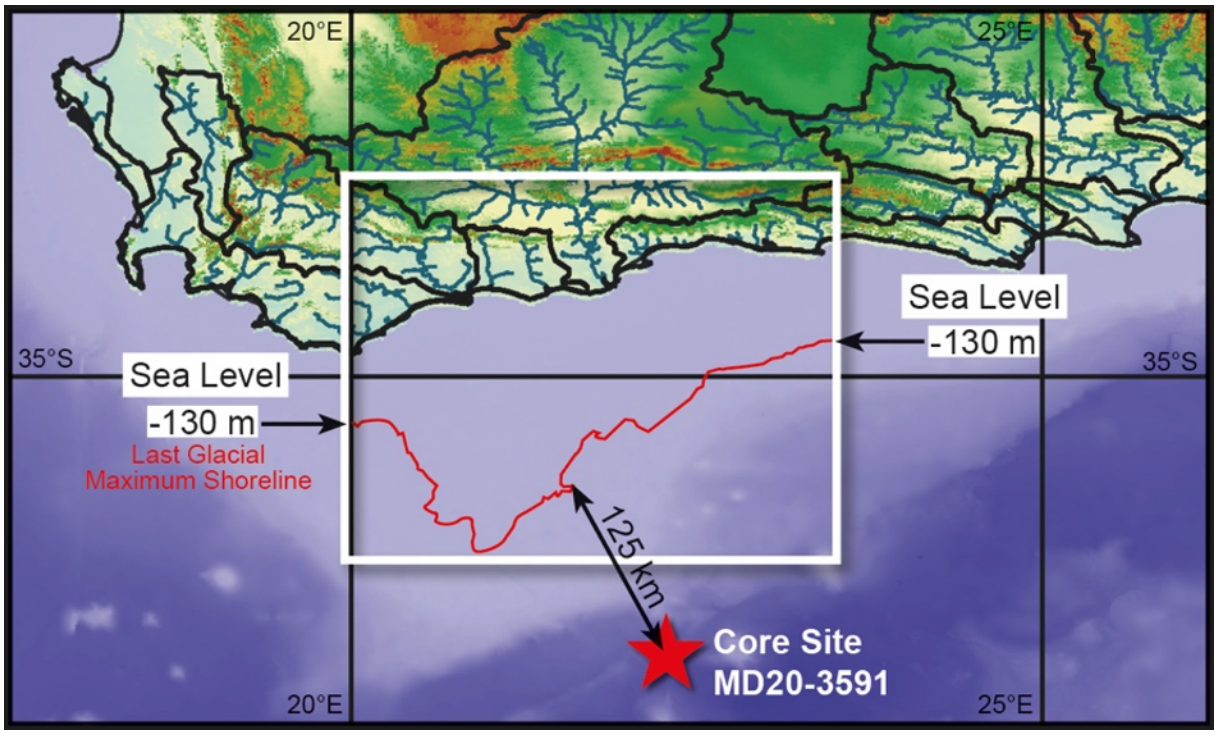

Figure 4.20: Sea level low stand Palaeo Agulhas Plain exposure simulation for LGM shoreline. Arrow represents distance the Gourritz river mouth (largest catchment in southern Cape) to core site MD20-3591 based on mapping by Cawthra et al. (2019). See Chapter 5 for more information on this simulation.

Building on results from Chapter 3, most coastal river sediments from South Africa contain abundant illite. Sites in the central and southern sector contain significantly more illite (%) (by 32%) than kaolinite (Table 4.4) during both modern and the LGM period suggesting a supply of South African river sediment to the core sites. During the LGM, the rivers incised the exposed PAP and the rivers changed their course across the plain, such as the Breede river which drains more kaolinite rich material closer to site CD154-23-16P (Chapter 3), this high kaolinite can be explained by the regional geology around Cape Town (Harris *et al.,* 1999). The amount of kaolinite increases during the LGM compared to modern in the southern sector by 7%, however the amount of illite in the LGM compared to modern only increases by 2% in the central sector. This can be explained by the expansion of the PAP. Along the southern coast of South Africa, the PAP expanded much more than along the south eastern coastline. The PAP is narrower along the south-east coast and the margin is steeper (Green, 2009) so is not so greatly influenced by sea level. Source contribution mixing suggests an increased relative influence of local South African sediment during the LGM in the southern sector and central sector compared to present-day (Figure 4.18). This is supported by a coarser grain size during the LGM in the southern sector by 5 µm and the highest sand content (12.30 wt %) in the LGM compared to other CD154 sites suggesting coarser sediment input, indicative of river sediment (Figure 4.8). Results from Chapter 3 reveal that the rivers draining from the southern

Cape are coarser than the rivers draining in the eastern Cape. Encouragingly, Franzese *et al.* (2006) find there was a greater influence of the local endmember driven by a lower supply of Agulhas endmember sediment during the LGM.

4.5.3.3 South African Regional Hydrology

In addition to the effect of sea level on the southern sector, the regional hydrology of South Africa would have influenced the CD154 sediment provenance signals during the LGM. For the southern Cape region, frontal systems making landfall over western South Africa at more northerly locations can bring rainfall along the Cape Fold mountains and further to the north along the western escarpment. It may be postulated that under a northward displacement of the SHW during the LGM (van Zinderen Bakker, 1967; van Zinderen Bakker, 1976; Cockcroft *et al.,* 1987; Shi *et al.,* 2000; Stuut, 2004; Chase and Meadows, 2007; Anderson and Burckle, 2009; Sigman *et al.,* 2010; Neumann and Scott, 2018b) (Figure 4.21), such a change would be associated with enhanced rainfall along the Cape Fold mountains and the western escarpment. These wetter conditions over the WRZ would explain our pattern in the radiogenic isotopes mixing results.

Model projections from Engelbrecht *et al.* (2019) are indicative of the southern African region being generally wetter during the LGM. Winter frontal rainfall is projected to have had a significant equatorward reach, with the SRZ receiving significantly more rainfall in winter during the LGM than under present-day climate. This is supported by other studies which show an increase in precipitation for the Drakensberg region during the LGM (Botha *et al.,* 1992; Mills *et al.,* 2012). The largest rainfall increases across the southern African region are projected for the WRZ during glacial periods (Engelbrecht *et al.,* 2019). This agrees well with our the lower $^{87}Sr/^{86}Sr$ ratios, higher εNd values, high illite and coarser terrigenous grain size in the core sites located in the central and southern zones during the LGM. It is likely the core sites are picking up signals from the sediment transported in the surface Agulhas Current from upstream sources and mixing with the local sediment supplied from South African rivers.

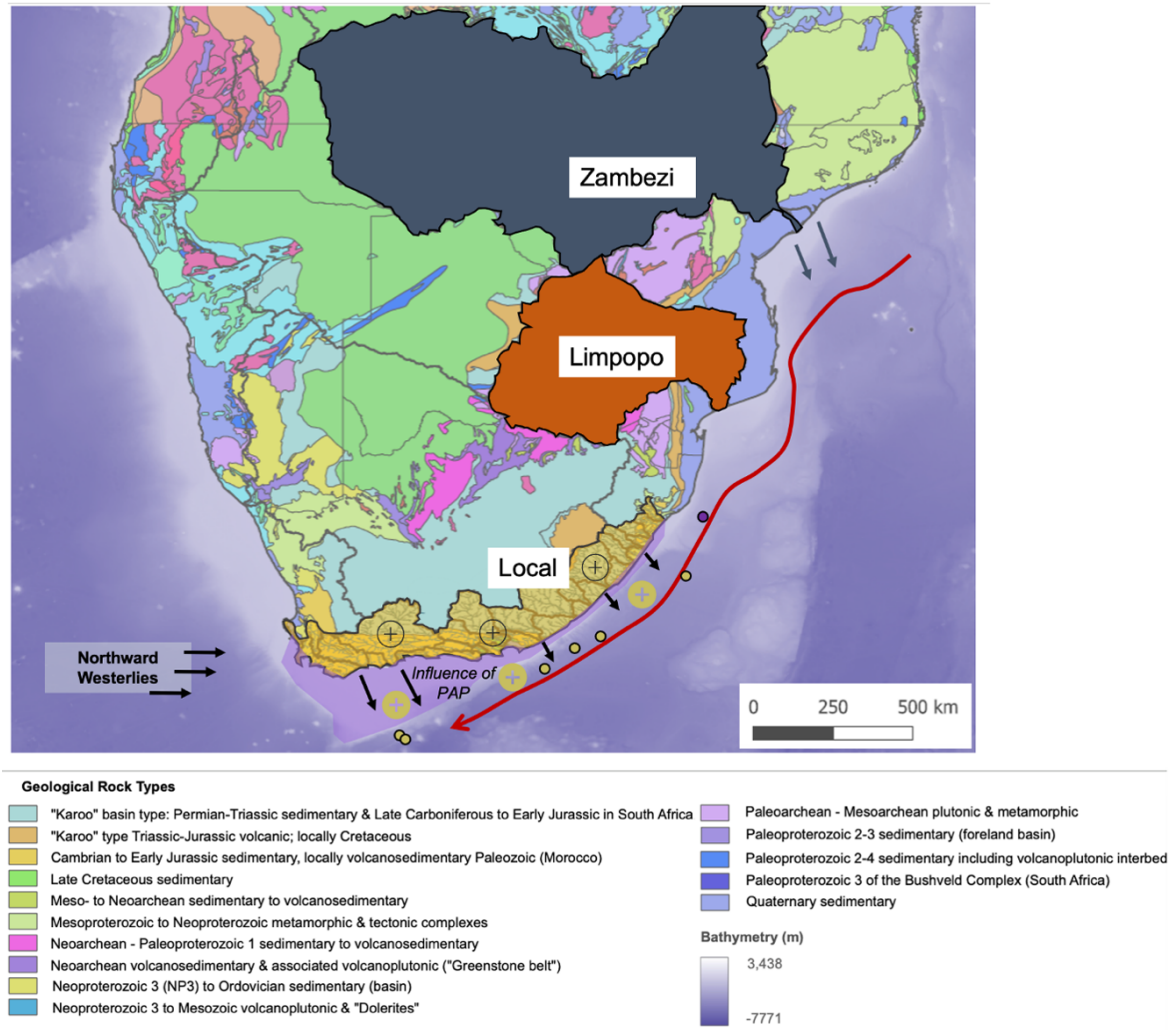

Figure 4.21: Conceptual Image of the sea level effect and more local South African sediment supply during the LGM. Major source regions are Zambezi river catchment (grey), Limpopo river catchment (orange) and local South African river catchments (yellow). Arrow number represents relative contribution to Southwest Indian Ocean, i.e. more arrows, high contribution of sediment from this source to core sites. Agulhas Current (red arrow).

4.5.3.4 Upstream sediment sources (Limpopo and Zambezi)

There is a reduction in Limpopo sourced sediment during the LGM in the northern sector (Figure 4.18). This could be interpreted as a reduction in humidity and precipitation during the LGM in the Limpopo catchment, which is supported by other studies. Close to St Lucia, records from the Mfabeni peatlands on the Indian Ocean coast, have been used to postulate that a sharp decline in % total organic carbon (TOC) and a decrease in $\delta^{13}C_{wax}$ values indicate a change from a denser vegetation to a grass dominated and a drier environment occurred after ~23 ka (Finch and Hill, 2008; Baker *et al.,* 2017; Miller *et al.,* 2019) (Figure 4.22). Other sedimentological evidence from Tswaing Crater indicate drier conditions during the LGM (Partridge *et al.,* 1997) as well as less precipitation recorded from the Wonderkrater region (Truc *et al.,* 2013; Chevalier and Chase, 2015)

whereas Lobatse Cave stalagmite isotope suggest more moisture (Holmgren *et al.,* 1995; Brook *et al.,* 1997) (Figure 4.22). These indications for dry conditions on the eastern coast are somewhat contradicted by an ocean core record off the eastern Cape coast (CD154-10-06P) (Simon *et al.,* 2015b) and Voordrag pollen records (Botha *et al.,* 1992). This suggests there is evidence for drier conditions near and within the Limpopo catchment, which corroborates well with the endmember mixing in Figure 4.18 but reveals more investigation on the nature of rainfall from southeastern Africa is required to disentangle the diverging interpretations regarding rainfall patterns during the LGM. However, low Indian Ocean SSTs have been proposed for arid conditions during the LGM experienced in the Limpopo catchment observed in a marine core (MD96-2048, 26°S) offshore the Limpopo (Dupont *et al.,* 2011).

Based on sediment source endmember mixing (Figure 4.18), the relative influence of the Zambezi endmember increases (by ∼1.5%) during the LGM, affecting the sites located along the Southeast African coastline. This is inferred by a lower or equal $^{87}Sr/^{86}Sr_{clay}$ value during the LGM and a more radiogenic (higher) εNd_{clay} value in the CD154 sites (except CD154-23-16P for εNd_{clay}). Figure 4.13 reveals a shift in the LGM samples (blue) towards the Zambezi - Local mixing line when compared with the modern samples (purple). This Zambezi signal is explored with regards to climate dynamics in the Zambezi catchment during the LGM.

Previous work defines the Agulhas region to have an endmember indicative of the Limpopo and Zambezi rivers (Franzese *et al.,* 2006). Our results advance on these findings from Franzese *et al.* (2006), as this present study defines both the Limpopo and Zambezi as separate endmembers. The previous study (Franzese *et al.,* 2006) find a higher terrigenous flux in the Agulhas source region, but less contribution of upstream Agulhas Current endmember reaching the southerly sites during the LGM. A higher Agulhas flux from Franzese *et al.* (2006) can be accredited to the higher Zambezi and local contributions recorded from sediment source contribution mixing (Figure 4.18). In addition, this chapter presents results which show the proportions of the Zambezi endmember and the local South African endmember increase in the LGM compared to modern, and the contribution of Limpopo endmember reduces. The decreased contribution of Agulhas endmember found in the southern sites by Franzese *et al.*(2006) can be explained in terms of the relationship between the input of Limpopo/Zambezi/Local. Limpopo has a more pronounced radiogenic signature than both the Zambezi and local South African rivers. Therefore, a lower Sr signal is attributed to a proportional increase in Zambezi and local (which have lower $^{87}Sr/^{86}Sr_{clay}$ values) rather than a decrease in overall contribution of Agulhas sourced endmember (and/or decreased Limpopo contribution).

The hydrological records from the Zambezi catchment from core sites GeoB9307-3 (Schefuß *et al.,* 2011) and GIK 16160-3 (Wang *et al.,* 2013a) display wetter climate conditions,

as the African rain belt was displaced South. This suggests more sediment was discharged from the Zambezi and transported southwards in the Agulhas Current. To conceptualise the region where more sediment input in the Zambezi region comes from, a narrow band of increased precipitation during periods of Northern Hemisphere cooling is identified between 15-20°S (Chevalier and Chase, 2015), i.e. the Zambezi catchment (Figure 4.22). Conditions around Lake Tanganyika (north of this band) are more arid during the LGM, similar to conditions in South Africa (south of this band) (Chase, 2021). The main proposed control on the reflected change of source area in this region is suggested to be the shifting rainfall maxima (Just *et al.,* 2014). This shifting rainfall maxima is associated with southward ITCZ displacements associated with colder Northern Hemisphere conditions, leading to higher rainfall in the Zambezi catchment (Schefuß *et al.,* 2011; Wang *et al.,* 2013a) (Figure 4.22).

Modelling simulations reveal an overall coherent signal to the implied increase in Zambezi contribution based on radiogenic isotope provenance, the PMIP3 model ensemble reveals wetter conditions during the LGM over the Zambezi catchment, compared to preindustrial precipitation, linked to shifts in the ITCZ (Chevalier *et al.,* 2017). Additionally, studies suggest the positive rainfall anomalies are linked to changes in the strength of the zonal atmospheric circulation over the Indian Ocean basin, in response to lower LGM sea levels, exposing the Sahel and Sunda shelves in the middle of the Indo-Pacific Warm Pool (DiNezio *et al.,* 2018).

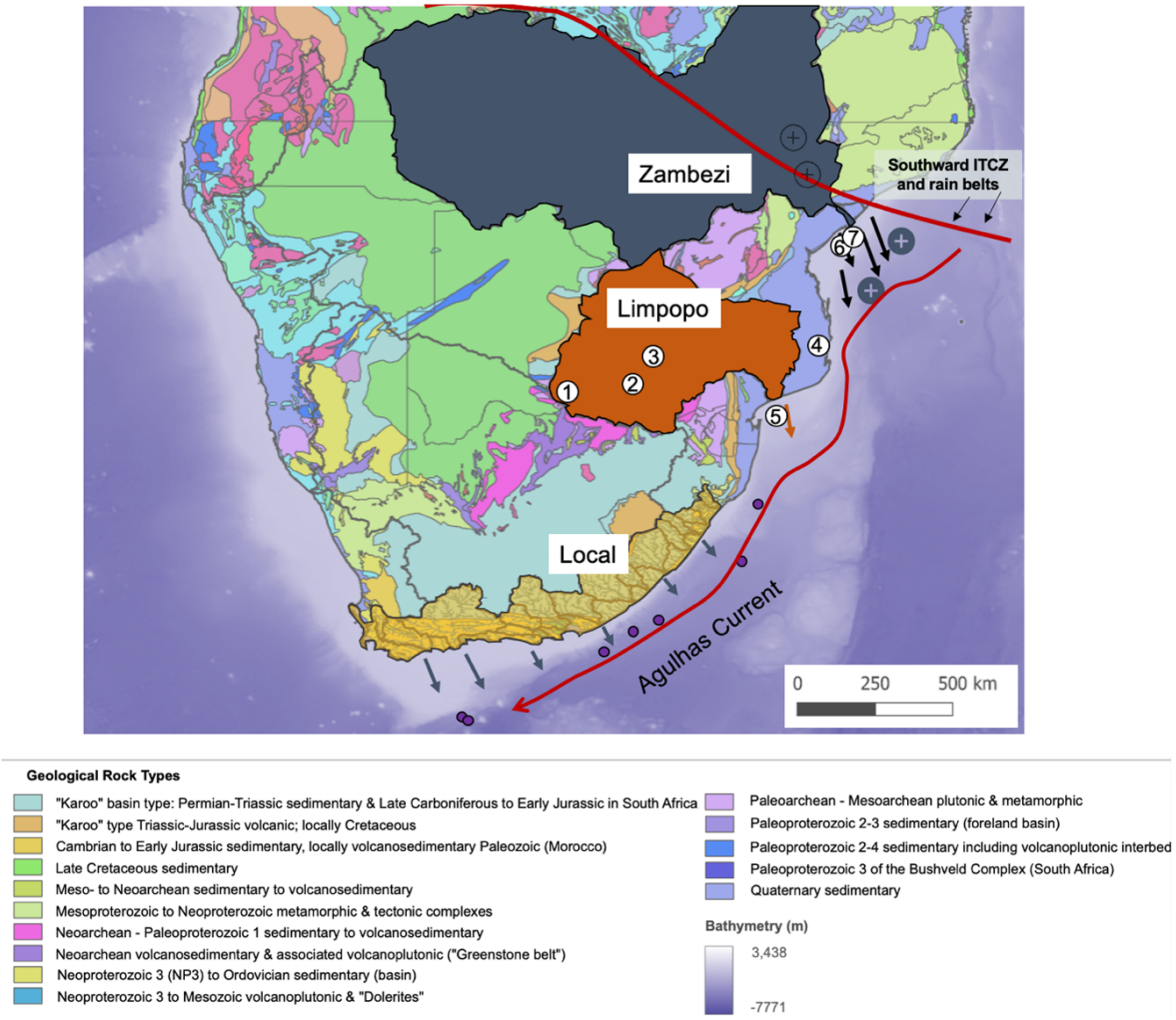

Figure 4.22: Conceptual Image to show increased Zambezi sediment supply during the LGM. Major source regions are Zambezi river catchment (grey), Limpopo river catchment (orange) and local South African river catchments (yellow). Arrow number represents relative contribution to Southwest Indian Ocean, i.e. more arrows, high contribution of sediment from this source to core sites. Agulhas Current (red arrow). Sites discussed are indicated by numbered dots as follows: (1) Lobatse Cave (Holmgren *et al.,* 1995; Brook *et al.,* 1997); (2) Tswaing Crater (Partridge *et al.,* 1997); (3) Wonderkater (Truc *et al.,* 2013; Chevalier and Chase, 2015); (4) Mfabeni Peat (Finch and Hill, 2008; Baker *et al.,* 2017; Miller *et al.,* 2019); (5) MD96-2048 (Dupont *et al.,* 2011); (6) GeoB 9307-3 (Schefub *et al.,* 2011); (7) GIK 16160-3 (Wang *et al.,* 2013a).

The Mozambique Channel also experienced lower sea level during the LGM, resulting in more proximal location of the Zambezi outflow to the study core site (GeoB9307-3) (Schefuß *et al.,* 2011). The Zambezi sediment represents the hinterland geology, with high concentrations of heavy minerals. It consists of igneous (granites, basalts) and metamorphic (gneisses) basement (USGS 2007; van der Lubbe *et al.,* 2014) and the soils are rich in kaolinite (FAO and ISRIC, 2009; Just *et al.,* 2014). The marine sediment cores in the northern and central sectors (specifically sites CD154-02-03K, CD154-10-06P, CD154-17-17K and CD154-20-15P) have kaolinite abundances $> 30\%$ during the LGM which

indicates the transport of more tropical sediment from the north during the LGM (Table 4.4).

Both a lower sea level during the LGM in the Mozambique Channel and a wetter regional climate over the Zambezi catchment favour increased sediment input from the Zambezi. This is in line with the results presented in this chapter. Finally, based on grain size analysis, the Zambezi sediment is typically finer than the Limpopo sediment (van der Lubbe, pers. comms), which highlights how the Zambezi sediment could potentially be distributed further downstream via the Agulhas Current; as finer sediment is carried for longer than coarser bedload sediment (Granet *et al.,* 2010; Carter *et al.,* 2020).

In addition to an increase in the supply of Zambezi sourced sediments during the LGM, the question remains as to whether the Agulhas Current increased in strength enhancing the transport of Zambezi sourced material to the CD154 marine sediment core sites. Few studies have concentrated on the Agulhas Current strength itself. Various models have presented the connection between Agulhas Current strength and Agulhas Leakage, although the relationship between the two is not well understood. Studies on the Agulhas Current strength and Agulhas Leakage propose a decoupling of Agulhas Current variability from Agulhas Leakage (Loveday *et al.,* 2014), whereas van Sebille *et al.* (2009) concluded a weaker Agulhas Current would lead to more Agulhas Leakage.

Palaeoclimate reconstructions using faunal assemblage studies have revealed that Agulhas Leakage reduced during glacial intervals (Peeters *et al.,* 2004; Caley *et al.,* 2014). These records revealing the surface conditions suggest that during glacial periods, a reduced Agulhas Leakage coincided with an equatorward shift in the STF (Peeters *et al.,* 2004; Bard and Rickaby, 2009; Caley *et al.,* 2012; Marino and Zahn, 2015). Additional work shows that during the LGM, a reduced Agulhas Leakage must be explained by a weaker Agulhas Current based on Sr isotope ratios (Franzese *et al.,* 2006; Franzese *et al.,* 2009). However more recent work confirms that the Agulhas Current itself is a poor indicator of the strength of leakage, despite changes in temperature and salinity in Agulhas Leakage being resultant of variability in the composition of the Agulhas Current (Simon *et al.,* 2015b). Studies show an increased transport during glacial periods through the sortable silt flow speed proxy (van der Lubbe *et al.,* 2021) and Franzese *et al.* (2006) find that the sediment load carried by the glacial Agulhas Current was probably at least twice what it is today mainly affecting sites within the northern Agulhas region.

If the Agulhas Current was stronger during the LGM, this can invoke an early retroflection further eastward (Franzese *et al.,* 2006; Cásal *et al.,* 2009) (Figure 4.23) due to changes in the dynamics of Indian Ocean gateway. This could be translated into a different signature between sites within the northern and central zone and the sites in the southern zone. This highlights the potential that the southern sites are cut off from receiving the Zambezi sediment which could be due to an early retroflection from the Agulhas Current

(Figure 4.23). The LGM $^{87}Sr/^{86}Sr_{clay}$ value is significantly lower (= 0.738 ± 0.000007) in site CD154-23-16P and εNd values are higher (= -11.694 ± 0.117; -11.469 ± 0.148) in sites CD154-23-16P and MD20-3591 respectively, compared to the northern and central sectors. Site CD154-23-16P contains abundant kaolinite during the LGM compared to the more northerly sites in this study. These considerable differences from the other marine core sites in this study suggest the sediment is partly being entrained from a different source region for these southerly sites. The next section focuses on the southern sector and investigates the possibility of the South Atlantic region as a substantial source of sediment during the LGM.

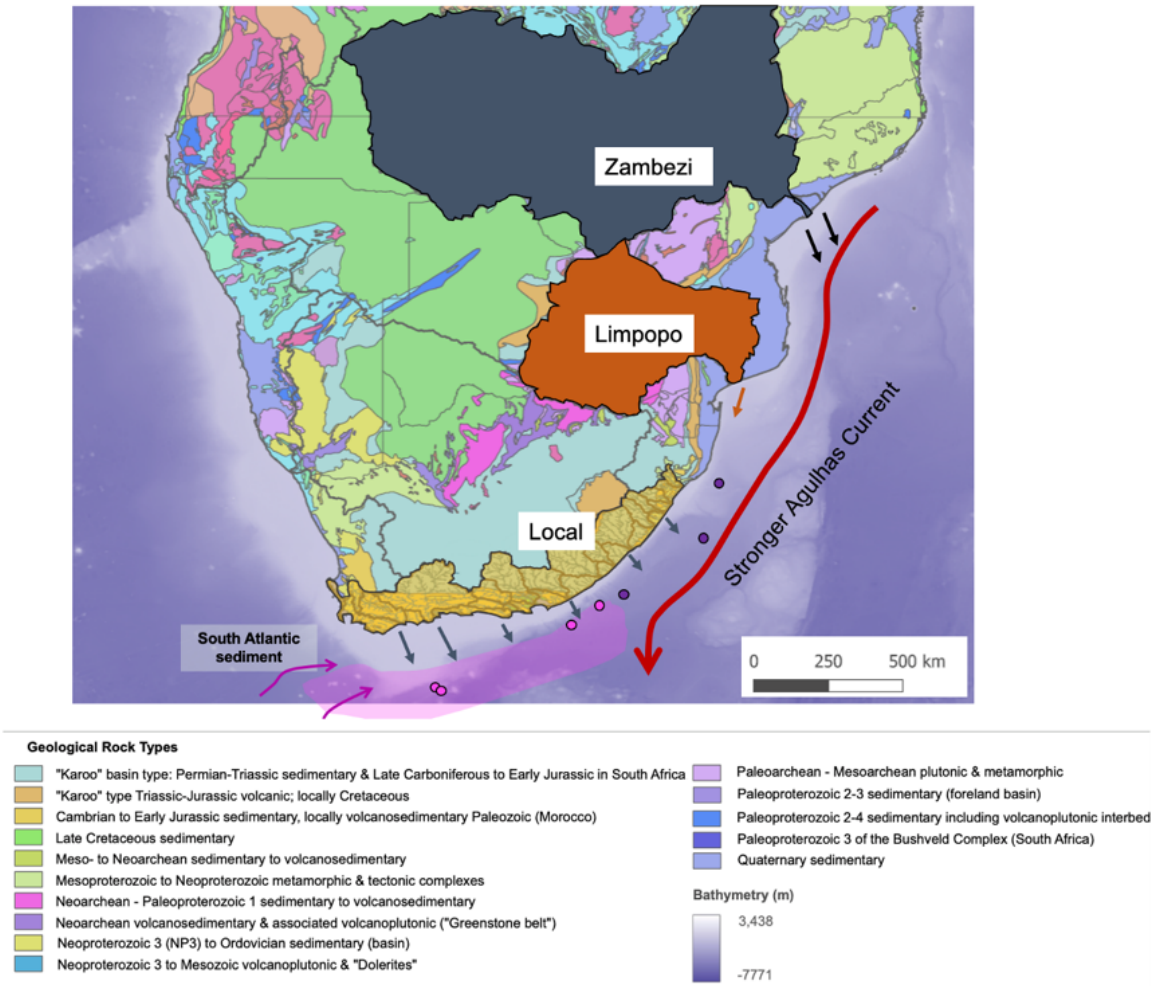

Figure 4.23: Conceptual Image presenting Stronger Agulhas Current and enhanced South Atlantic input during the LGM. Major source regions are South Atlantic (pink), Zambezi river catchment (grey), Limpopo river catchment (orange) and local South African river catchments (yellow). Arrow number represents relative contribution to Southwest Indian Ocean, i.e. more arrows, high contribution of sediment from this source to core sites. Agulhas Current (red arrow), note early retroflection depicted.

4.5.3.5 Increased Contribution of South Atlantic Sediments during the LGM to the Southern Sector

The δ^{13}C reconstructions presented alongside the flow speed reconstructions for the CD154 study sites show the influence of NADW in the region during present-day at 3000 m (Figure 4.12). However, during the LGM, the δ^{13}C values are lower and flow speed records reveal a stronger influence of SCW at $\sim$ 2500 m (Figure 4.12), this means that an older, nutrient rich water mass is transported to the CD154 sites. This water mass is likely transported from southern regions such as the South Atlantic and/or South America via the ACC. The transport of material entrained from South Atlantic to the South Africa region is complicated. The SAC and ACC are postulated to be responsible for the long distance transport of fine grained (<63 µm) material with lower $^{87}Sr/^{86}Sr$ values from South America, across the Atlantic Ocean to, at least, the Cape Basin during the LGM (Franzese *et al.,* 2006; Hemming *et al.,* 2007). However, for material to be transported to the Indian Ocean via the ACC, it must be transported northward by AABW flow (Franzese *et al.,* 2006). The bottom water flow within the Cape Basin redistributes sediment brought in from distal sources such as South Atlantic Ocean and mixes with locally derived sediment (Latimer and Filippelli, 2007). As the SCW is a mix of AABW and AAIW (Reid, 1989; Reid, 2005), this water mass is likely entraining sediment from the South Atlantic which has a radiogenic isotope signature reflecting the South Atlantic (low $^{87}Sr/^{86}Sr$).

Published radiogenic isotope values from the South Atlantic region for modern and LGM (Rutberg *et al.,* 2005; Franzese *et al.,* 2006; Latimer *et al.,* 2006; Noble *et al.,* 2012; Beny *et al.,* 2020) are compiled in Table 4.7 (Figure 4.24). Compared to the CD154 LGM $^{87}Sr/^{86}Sr_{clay}$ ratios (Table 4.5), the published data are lower by $\sim$ 0.038 . This is most probably due to the grain size effect as most published $^{87}Sr/^{86}Sr$ compositions are measured on the <63 µm. Franzese *et al.* (2006) defined the South Atlantic radiogenic isotope endmember (<63 µm) ($^{87}Sr/^{86}Sr$ = 0.709; εNd = -5.000) and found an increased LGM flux of this endmember, transporting sediment with lower $^{87}Sr/^{86}Sr$ ratios and higher εNd from the Southwest Atlantic Ocean to the Cape Basin. The same trend as Franzese *et al.* (2006) is observed in the CD154 southern sector in this chapter, with low $^{87}Sr/^{86}Sr_{clay}$ values during the LGM. This is especially true for site CD154-23-16P which has a LGM $^{87}Sr/^{86}Sr_{clay}$ value of 0.738 ($\pm$ 0.000007) which is lower by 0.013 than sites in the central zone and lower by 0.022 than the northern sector.

Table 4.7: List of radiogenic isotope values from published studies with size fraction identified from Southeast Atlantic Ocean and Southwest Indian Ocean for Modern and LGM dates.

Age (ka)	εNd	$^{87}Sr/^{86}Sr$	Size Fraction	Site	Citation
1.2	-11.000	0.718	<63 µm	ODP1088	Latimer *et al.* (2006)
Holocene	-12.800	0.726	<63 µm	WIND-1B	Noble *et al.* (2012)
Endmember	-5.000	0.709	<63 µm	South Atlantic Ocean	Franzese *et al.* (2006)
6.62	-	0.723	<63 µm	RC11-83	Rutberg *et al.* (2005)
20.28	-	0.718	<63 µm	RC11-83	Rutberg *et al.* (2005)
21.1	-5.300	0.712	<2 µm	MD07-3076Q	Beny *et al.* (2020)
21.1	-3.900	0.708	2-20 µm	MD07-3076Q	Beny *et al.* (2020)
22.72	-2.100	0.708	20-32 µm	MD07-3076Q	Beny *et al.* (2020)
23.1	-9.400	0.716	<63 µm	ODP1088	Latimer *et al.* (2006)

Studies such as Latimer *et al.* (2006) and Beny *et al.* (2020) present εNd records for the modern and LGM periods from sites in the South Atlantic, the LGM values are higher by ∼3.000 to 7.000 εNd values than the southern sector εNd_{clay} from this chapter (Table 4.5). However, the chemical ventilation and physical flow speed reconstructions do reveal a dominance of SCW with lower δ^{13}C gradients at water depths ∼ 2500 m from CD154 sites and increased flow speeds at ∼ 2500 m (Figure 4.12). Further investigation regarding the possibility of deeper water masses to transport sediments to the Agulhas region and associated core sites from the South Atlantic requires the use of the non-cohesive fraction (10-63 µm) radiogenic isotopes from the CD154 sites (Table 4.8). This 10-63 µm size fraction is notably known to reflect bottom flow speeds (McCave and Hall, 2006) and could provide further evidence for the presence of a transport regime such as SCW bringing sediment from the South Atlantic. The LGM $^{87}Sr/^{86}Sr_{non-cohesivesilt}$ ratios range between 0.710 to 0.719 and for $\varepsilon Nd_{non-cohesivesilt}$ (-11.706 to -10.759) for all the CD154 sites in this study (Table 4.8) which are similar values to the South Atlantic from studies (Table 4.7). The LGM $^{87}Sr/^{86}Sr_{non-cohesivesilt}$ and $\varepsilon Nd_{non-cohesivesilt}$ values at sites in the southern sector are particularly similar to the South Atlantic radiogenic isotope values (Rutberg *et al.,* 2005; Franzese *et al.,* 2006; Latimer *et al.,* 2006; Beny *et al.,* 2020): the LGM $^{87}Sr/^{86}Sr$ values from Beny *et al.* (2020) are 0.005 lower than LGM $^{87}Sr/^{86}Sr_{non-cohesivesilt}$ from the southern sector and LGM εNd from Latimer et al. (2006) (Table 4.7) are higher than LGM $\varepsilon Nd_{non-cohesivesilt}$ by 1.359. This closer similarity with LGM $^{87}Sr/^{86}Sr_{non-cohesivesilt}$ from the southern sector highlights that the sediment deposited in the southern sector could be entrained from the South Atlantic in SCW as they are considerably similar to the published data in Table 4.7 from the South Atlantic. This is consistent with δ^{13}C hydrographical and physical flow speed reconstructions which present low LGM δ^{13}C value at 2500m and high flow speeds (Figure 4.12). This could reveal SCW transporting sediment from the South Atlantic to these southern CD154 sites.

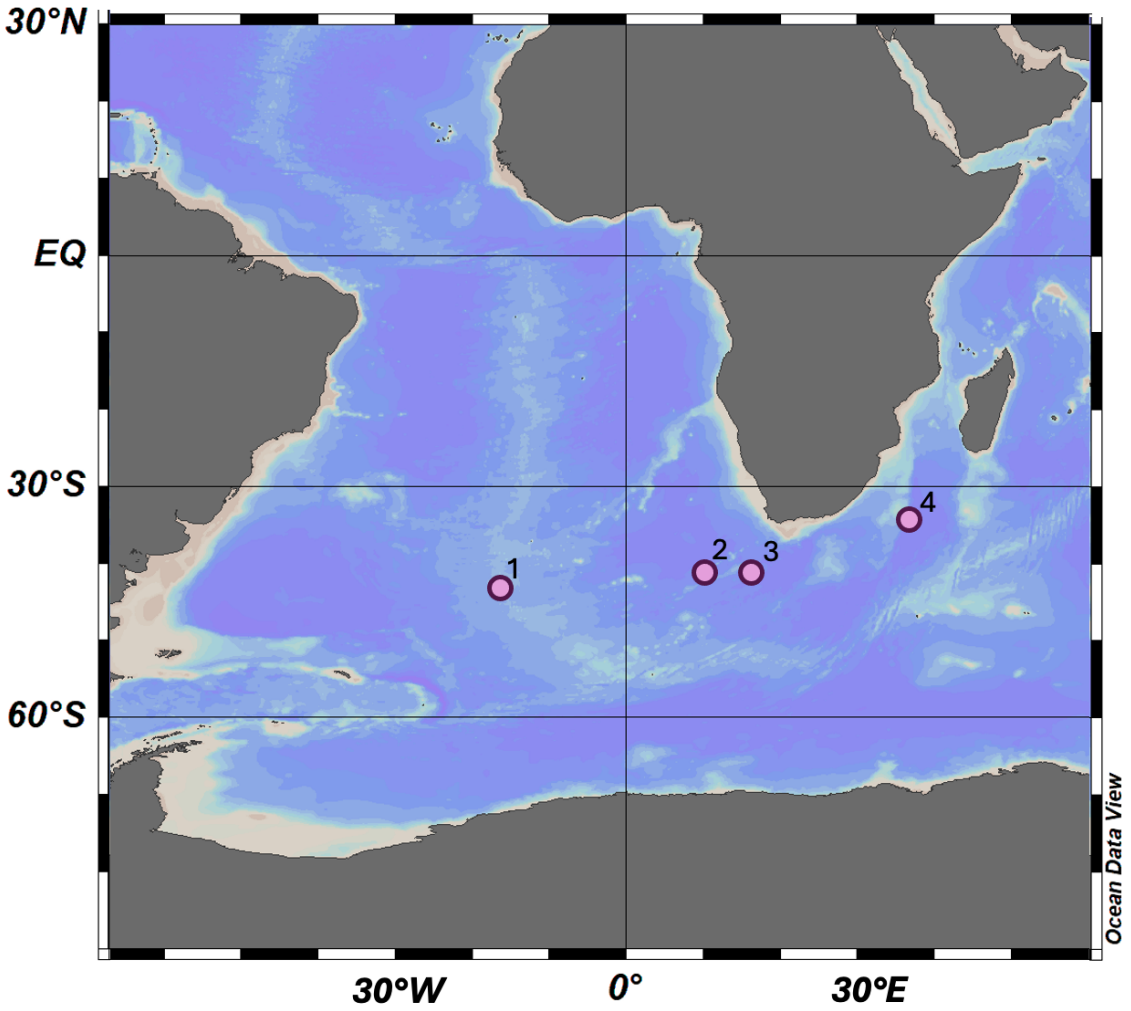

Figure 4.24: Map of core sites shown Table 4.7. 1) MD07-3076Q (Beny *et al.,* 2020), 2) RC11-83 (Rutberg *et al.,* 2005), 3) ODP 1088 (Latimer *et al.,* 2006) 4) WIND-1B (Noble *et al.,* 2012). Figure made on ODV.

Studies show an increase in the sediment transport by the ACC and SAC cause a greater contribution of material supplied from the Southwest Atlantic to the Cape Basin (Franzese *et al.,* 2006; Noble *et al.,* 2012). Provenance data from other sites in the Cape Basin also suggest a stronger input of sediment from distant Antarctic and/or Patagonia carried northwards to the Cape Basin by deep currents during glacial periods (Franzese *et al.,* 2009). The increased contribution of sediments from South America and West Antarctica during glacial times is a significant component of the downcore variability in the $^{87}Sr/^{86}Sr$ record of marine sediment core site RC11-83 (Rutberg *et al.,* 2005). The increased sediment load was probably the result of an increase in glaciogenic sediment input from the Patagonian and Antarctic ice sheets during the LGM. Under glacial conditions the westerlies were likely stronger (van Zinderen Bakker, 1967; van Zinderen Bakker, 1976; Cockcroft *et al.,* 1987; Shi *et al.,* 2000; Stuut, 2004; Chase and Meadows, 2007; Anderson

Table 4.8: Radiogenic isotope compositions for CD154 core sites (this study) measured on 10-63 µm fraction.

Site	Age	$^{87}Sr/^{86}Sr_{non-cohesive}$	$\varepsilon Nd_{non-cohesive}$
CD154-02-3K	Modern	0.736	-17.372
CD154-10-6P	Modern	0.720	-12.571
CD154-15-14K	Modern	0.715	-11.486
CD154-17-17K	Modern	0.718	-11.073
CD154-20-15P	Modern	0.714	-10.336
CD154-23-16P	Modern	0.719	-10.738
CD154-02-3K	LGM ($\sim$ 20ka)	0.728	-18.032
CD154-10-6P	LGM ($\sim$ 20ka)	0.724	-11.200
CD154-15-14K	LGM ($\sim$ 20ka)	0.714	-13.435
CD154-17-17K	LGM ($\sim$ 20ka)	0.717	-10.571
CD154-20-15P	LGM ($\sim$ 20ka)	0.716	-10.654
CD154-23-16P	LGM ($\sim$ 20ka)	0.717	-10.759

and Burckle, 2009; Sigman *et al.,* 2010; Neumann and Scott, 2018b), consistent with studies based on flow speed reconstructions which have shown the ACC is faster during glacial times (Molyneux *et al.,* 2007; Martinez-Mendez *et al.,* 2009; Starr *et al.,* 2021) and stronger, therefore capable of carrying more sediment (Hemming *et al.,* 2007). A strengthened ACC suggests the possibility of a greater influence of SCW (Molyneux *et al.,* 2007) which is consistent with the lower $\delta^{13}C$ gradients at water depths $\sim$ 2500 m from CD154 sites and increased flow speeds at $\sim$ 2500 m (Figure 4.12).

Finally, this also demonstrates that the total <63 µm fraction encompasses a mixed signal that includes the influence of transport regimes such as bottom water flow speeds and hydrography as well as possible authigenic weathering effects in the finer fraction and will therefore not reflect a pure signal such as provenance. This finding is supported by other studies (Weltje and Prins, 2003; Meyer *et al.,* 2011; Jonell *et al.,* 2018) and further shows the benefit of isolating the <2 µm clay fraction which appears to more faithfully reflect provenance changes.

4.6 Concluding Remarks

The impact of the grain size effect on radiogenic isotope fractionation is a well-known, yet often a neglected problem. Most previous Sr-Nd isotope provenance studies focus on the bulk (or whole rock) sediments (Riley *et al.,* 2005; Jonell *et al.,* 2018; Carter *et al.,* 2020) and/or single size fractions (Meyer *et al.,* 2011; Hahn *et al.,* 2016) yet numerous proxy reconstructions suggest that there are variable contributions of sediment to individual sediments from distinctly different grain size fractions. This can be related to different transport regimes such as aeolian dust supply or riverine sediment input. Figure 4.25 shows an updated version of Figure 4.2 and reveals the importance of comparing radiogenic isotopes on the same grain size.

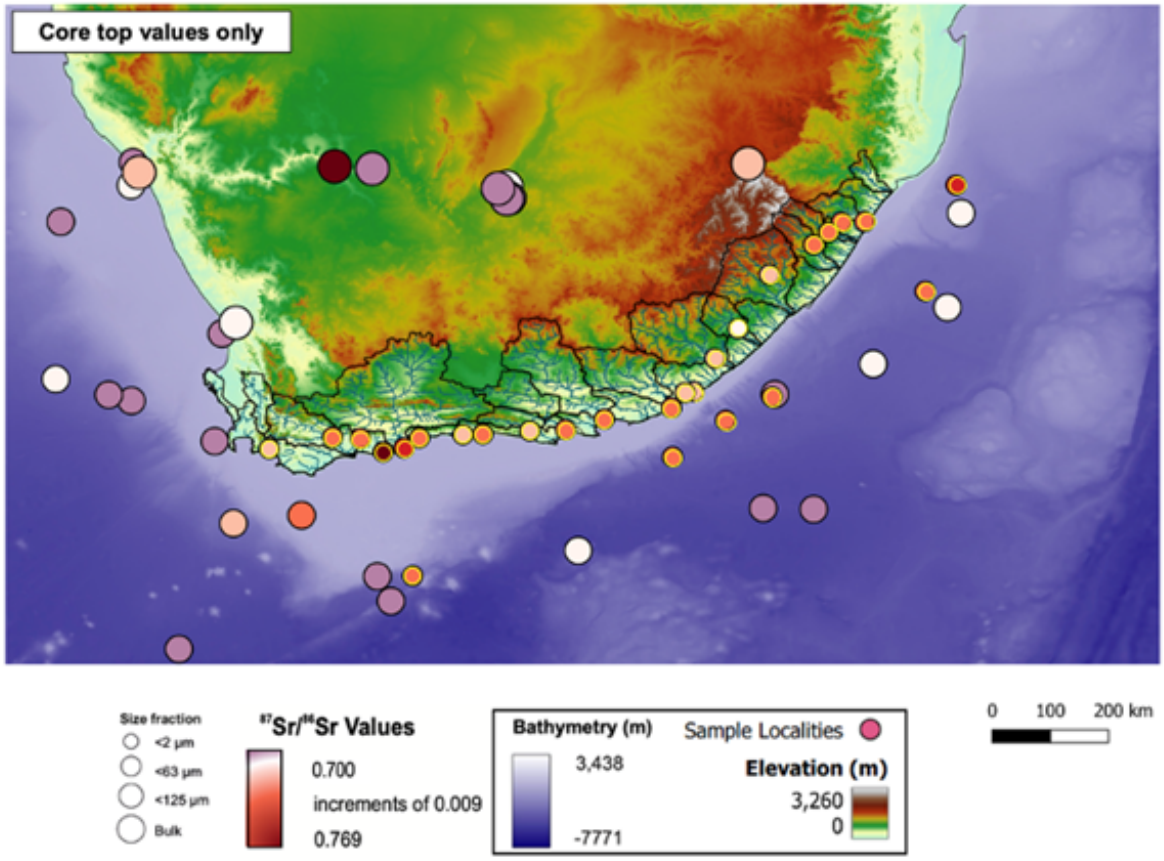

Figure 4.25: Updated Sr isotope values from published literature and this study (Franzese *et al.,* 2006; 2009; Hahn *et al.,* 2015; 2016; 2017; Garzanti *et al.,* 2014); on varying size fractions (in key) for the study region. Data from Chapter 3 and this Chapter are encircled in yellow.

Based on the data available, it is not possible to distinguish between just Karoo and Cape Supergroup endmembers (from Chapter 3), therefore we use additional endmembers from sources further afield to understand the climate picture. A provenance change from modern day Limpopo vs local South African river sediment supply to the CD154 marine sediment cores is inferred to more Zambezi input during the LGM. During the LGM, coherent with hydrological records and modelling simulations, an increase in Zambezi sediment supply was transported southwards to the core sites within the Agulhas Current. This is based on our results revealing lower $^{87}Sr/^{86}Sr_{clay}$ values, more kaolinite contribution in the northern sector and some central sites (CD154-10-06P) and the εNd_{clay} signal, attributed to a proportional increase in Zambezi sediment and a local South African sourced sediment influence. The LGM radiogenic isotope values sit closer to a theoretical mixing line (on both the Sr and Nd axes) between local South African sediment signatures and Zambezi (Figure 4.13). Breaking apart the Agulhas Endmember advances on previous work by Franzese *et al.* (2006), which finds an increased Agulhas Endmember flux but reduced Agulhas Endmember contribution during the LGM. This

reduced contribution is likely due to the balance between the input of Limpopo / Zambezi / local sediments. Limpopo has a more pronounced radiogenic signature than both the Zambezi and local South African rivers. However, more work on analysing the radiogenic isotope composition of sediment samples from within the Zambezi and offshore the Zambezi is needed for the time splices of modern and LGM to increase the number of samples and reproducibility. This was planned but due to a lab closure was not possible. In addition, further investigation is needed to determine whether the Agulhas Current strength changed during the LGM. However, if the Agulhas Current strengthened, this would support the above hypothesis of enhanced Zambezi contribution being transported south.

Despite some studies showing arid conditions during the LGM in southern South Africa (Cartwright and Parkington, 1997; Cowling *et al.,*1999; Meadows and Baxter, 1999; Scott and Woodborne, 2007a; Scott and Woodborne, 2007b; Chase *et al.,* 2011), model projections from Engelbrecht *et al.* (2019) suggest that the southern South African region in the WRZ experienced generally wetter conditions during the LGM. There is additional supported evidence that the WRZ expanded due to a northward shift in westerlies (van Zinderen Bakker, 1967; van Zinderen Bakker, 1976; Cockcroft *et al.,* 1987; Shi *et al.,* 2000; Stuut, 2004; Chase and Meadows, 2007; Neumann and Scott, 2018) and the SRZ received significantly more rainfall in winter during the LGM than under present-day climate (Engelbrecht *et al.,* 2019). This agrees well with radiogenic isotopes, clay minerals and terrigenous grain size results from this chapter which all support local sediment supply during the LGM, likely driven by on-land hydrology increases.

Finally, there is a deep-water transport signal in the 10-63 µm fraction of the Sr and Nd isotopes, likely representing bottom flow from the South Atlantic within SCW, which coincides with lower $\delta^{13}C$ and enhanced flow speeds during the LGM at water depths of 2500m. This highlights the potential that there is a surface signal in the <2 µm fraction coming from the upstream sources, transported in the Agulhas Current and a deep-water signal in the 10-63 µm fraction. However, to affirm these findings, more radiogenic isotope data is needed from the South Atlantic, as to date, no such records exist on the <2 µm.

Chapter 5 | Terrestrial Climate Variability from South Africa's southern Cape: Setting the Environmental Scene for Early Modern Humans

Life evolves to fit the world in which it finds itself, but geography, of ocean currents, the position of the continents, wind patterns and atmospheric chemistry defines the parameters of that world. - Thomas Halliday - Otherlands: A Journey Through Earth's Extinct Worlds

Maybe you were the ocean, when I was just a stone – Blackflies - Ben Howard

5.1 Chapter Outline

This chapter presents palaeoclimate records from marine sediment core MD20-3591 which will be interpreted through utilising the framework of South Africa river sediment provenance and LGM transport patterns outlined in Chapters 3 and 4. Downcore records of stable isotopes measured on benthic foraminifera, terrigenous grain size, radiogenic isotopes and elemental X-Ray Fluorescence (XRF) scanning from sediment core MD20-3591 are presented. All stratigraphic series display coherent orbital modulation and where the sampling resolution is high enough, millennial-scale variability is also evident. Despite presenting the entire MD20-3591 record, the main focus of this chapter is the LMSA time interval in order to characterise the provenance hydroclimate signal during this key human technological development period.

The main aims of this chapter are:

- To develop a robust age model for marine sediment core MD20-3591 using radiocarbon dating and graphical tuning to LR04.
  - To additionally fine tune to the Hulu-Sanbao record to infer millennial scale variability.
- To reconstruct the South African climate variability during the 100-50 ka period using radiogenic isotope provenance.
- To link hydroclimate changes to the archaeological record during the MSA in harmony with the SapienCE key findings.

5.2 Introduction

5.2.1 Forcings on the Climate Variability in South Africa Today

Southern Africa (0-35°S) experiences much greater climate diversity than the same latitudes in the Northern Hemisphere (i.e. 0-35°N) (Peel *et al.,* 2007) due to several factors related to the country's latitudinal position and geomorphology. Southern Africa has a small east to west extent of 3000 km which limits the development of high pressure over the continent and enables incursions of moisture from adjacent tropical Indian and Atlantic Oceans (Chase, 2021). In the west, moisture advection from the South Atlantic Ocean is generally constrained to regions north of ∼15°S (Rouault *et al.,* 2003; Crétat *et al.,* 2019). In the east, the warmth of the Agulhas Current promotes increased evaporation and the transport of moisture into the continent (Tyson and Preston-Whyte, 2000; Rouault *et al.,* 2002; Crétat *et al.,* 2012). Further south, the cold Benguela Current flows equatorward along the South African and Namibian coasts, limiting evaporation and supressing convection (Tyson, 1986; Nicholson and Entekhabi, 1987). This results in a marked east-west rainfall gradient across South Africa and the dominant moisture-bearing system is

an easterly flow from the Indian Ocean (Stuut *et al.,* 2002; Crétat *et al.,* 2012; Tierney *et al.,* 2013; Chase, 2021). South African rainfall is also strongly influenced by extra-tropical systems poleward of South Africa, the southern westerlies dominate mid-latitude atmospheric circulation and the variability in the westerlies creates fronts that produce most of the rainfall received by the southwestern Cape (Reason *et al.,* 2002). The influences of these various systems vary seasonally; the tropical systems are most prevalent in the warm summer months, and the extra-tropical frontal systems are most dominant during the winter, when the Antarctic anticyclone expands, and the zone of frontal activity is displaced equatorward (Figure 5.1). Seasonal distributions in rainfall over South Africa occurs due to these distributions of atmospheric and oceanic circulation systems forming the three rainfall zones in South Africa. These are Summer Rainfall Zone (SRZ), and the Southwestern region referred to as the Winter Rainfall Zone (WRZ) (Figure 5.1) and the Year-round Rainfall Zone (YRZ).

5.2.2 Orbital Forcings Driving Climate Variability in South Africa

Changes in South African climate dynamics in southern most Africa were partly paced by periodic variations in Earth's orbital parameters (Milankovitch, 1930; Chappell, 1973; Hays *et al.,* 1976; Imbrie, 1982; Berger, 1984; Imbrie *et al.,* 1984). These changes include eccentricity, obliquity and precession. Each of these orbital parameters vary the amount of solar insolation the Earth receives and as such their influence on long term South African climate change is still a matter of debate (Partridge *et al.,* 1997; Stuut *et al.,* 2002; Dupont *et al.,* 2011; Collins *et al.,* 2014; Chase *et al.,* 2019).

Generally orbital forcing on South African climate is structured in two classes; high latitude forcing vs direct low latitude mechanisms (van Zinderen Bakker, 1976; Partridge *et al.,* 1997). High latitude ice sheet development as well as the expansion and contraction on global atmospheric and oceanic circulation dynamics are related to high latitude forcings (van Zinderen Bakker, 1967; Stuut *et al.,* 2002; Stuut, 2004; Schefuß *et al.,* 2011; Otto-Bliesner *et al.,* 2014; Chase *et al.,* 2015; Chevalier and Chase, 2015). Whereas low latitude forcing relates to the impact of precession. Precession drives changes in insolation seasonality, with high Southern Hemisphere summer insolation driven by maximum precession, and the associated impact on both regional and local precipitation through dynamical monsoon systems (Kutzbach 1981; Rossignol-Strick, 1983; Partridge *et al.,* 1997; Ruddiman 2006; Kutzbach *et al.,* 2020).

High latitude forcing is considered to be an important factor in driving shorter-term climate change (e.g. Heinrich Events). The high latitudes are sensitive to changes associated with global temperature variability, Northern Hemisphere ice sheet development and Antarctic sea ice extent. As such, global cooling (initiated by reduced declining Northern Hemisphere insolation (Milankovitch, 1930), eccentricity (Broecker and van Donk, 1970; Hays *et al.,* 1976) and ice sheet extent (Ruddiman, 2006)) is thought to have reduced

precipitation in the SRZ. This is because of the lower amount of moisture advection from adjacent oceans resulting in a reduction in evaporative and convective potential (van Zinderen Bakker, 1976; Cockcroft *et al.,* 1987). In the WRZ, during glacial periods, an expansion of Antarctic sea ice and a subsequent equatorward shift of the storm tracks embedded in the Southern Hemisphere Westerlies (SHW), would have resulted in an increased occurrence of precipitation events in the WRZ (van Zinderen Bakker, 1976; Cockcroft *et al.,* 1987; Stuut, 2004).

The variation in the orbital precession parameter results in an anti-phase evolution of the summer insolation between hemispheres (Berger and Loutre, 1991). There are available records obtained from both terrestrial (Partridge *et al.,* 1997; Chase *et al.,* 2019) and marine sediments (Collins *et al.,* 2014; Simon *et al.,* 2015a) suggesting that precession primarily relates to low latitude climate variability in South Africa. This is not surprising considering South Africa has a largely subtropical position, hence there is a strong influence of direct insolation on regional climates. There is evidence in both terrestrial (Partridge *et al.,* 1997; Chase *et al.,* 2019) and marine sediment records (Collins *et al.,* 2014; Simon *et al.,* 2015a) of a strong influence orbital precession variability on regional South African climates. The variability of orbital precession relates to changes in the range of Intertropical Convergence Zone (ITCZ) migrations and associated rain belts. Generally, changes in hydroclimate associated with precessional forcing exist as more (less) summer rainfall under higher (lower) summer insolation. These changes are believed to be anti-phased between the Northern and Southern Hemispheres (Kutzbach, 1981). A northward shift in the mean annual position of the ITCZ by $\sim$ 10 degrees occurs during periods of high summer insolation in the Northern Hemisphere (Nicholson and Flohn, 1981; Clement *et al.,* 2001; Johnson *et al.,* 2002; Chiang *et al.,* 2003; Schefuß *et al.,* 2005; Castañeda *et al.,* 2007; Gasse *et al.,* 2008; Schefuß *et al.,* 2011; Hahn *et al.,* 2017).

Despite the increasing number of southern African paleoclimate studies, large data gaps remain. The interpretation of the antiphase response between the Northern and Southern Hemispheres, with phases of high Northern Hemisphere summer insolation also being phases of low Southern Hemisphere summer insolation has however led to some contradictory interpretations of whether low or high latitude forcing is responsible for a given precession signal (Stuut *et al.,* 2002; Collins *et al.,* 2014). The interpretation is also dependent on the region. In line with this, a sedimentological record from Lake Tswaing in southeastern Africa dating back to 200 thousand years (ka) suggests that precipitation increased during precession related summer insolation maxima in the Southern Hemisphere (Partridge *et al.,* 1997), due to an enhancement of the Southern Hemisphere summer East African monsoon (Tierney *et al.,* 2013). More recent studies have confirmed the importance of the precession component forcing South African climate. Increased pre-

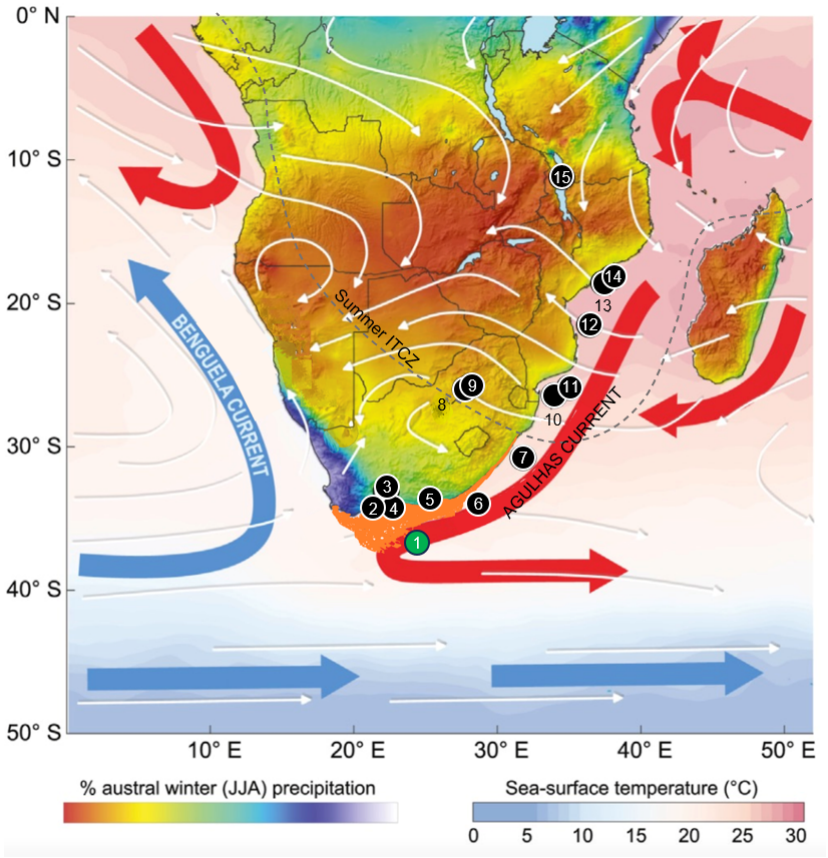

Figure 5.1: Schematic of primary atmospheric (white arrows) and oceanic circulation systems (red arrows for warm currents, blue arrows for cold currents, with Agulhas Current and Benguela Current labelled). Palaeo-Agulhas Plain in orange. Terrestrial colour gradient represents the seasonal distribution of precipitation, blues (reds) indicating a dominance of winter (summer) rainfall linked to temperate (tropical) moisture-bearing systems. Summer ITCZ location (black dashed line). Sites discussed in this chapter are shown by numbered black dots as follows; (1) MD20-3591; (2) Blombos Cave (Henshilwood *et al.,* 2003); (3) more inland Cango Cave (Chase *et al.,* 2021) (4) Pinnacle Point (Braun *et al.,* 2020; (5) Klasies River (Oyster Bay; Carrion *et al.,* 2000); (6) CD154-17-17K (Ziegler *et al.,* 2013); (7) CD154-10-06P (Simon *et al.,* 2015a); (8) Cradle of Humankind; (9) Tswaing Crater (Partridge *et al.,* 1997); (10) MD96-2048 (Braun *et al.,* 2020; Caley *et al.,* 2011, 2018; Dupont *et al.,* 2011); (11) IODP site U1478 (Simon *et al.,* 2020a); (12) GeoB 9311-1 (Dupont and Kuhlmann, 2017); (13) GeoB 9307-3 (Schefuß *et al.,* 2011); (14) GIK 16160-3 (Wang *et al.,* 2013a); (15) Lake Malawi (Johnson *et al.,* 2016). Image updated from Chase *et al.* (2021)

cipitation occurred during precession maxima in the SRZ of South Africa (Daniau *et al.,* 2013; Urrego *et al.,* 2015; Daniau *et al.,* 2023), while marine sediment core records from the Southwest Indian Ocean reveal a precessional driven river discharge in the Limpopo and Tugela rivers (Simon *et al.,* 2015; Caley *et al.,* 2018). Similarly, a leaf-wax hydrogen isotope record from the Zambezi river suggests relatively dry conditions during Southern Hemisphere summer insolation minima (Schefuß *et al.,* 2011). It has also been suggested that southwestern African climate responds in phase with Northern Hemisphere sum-

mer insolation (Chase *et al.,* 2009), as progressive drying is evident during the mid to late Holocene and wetter conditions prevail during mid-Holocene Southern Hemisphere summer insolation minimum. Palaeo-environmental archives from central, eastern and southern Africa have led to suggestions of a climatic hinge zone with a northern mode of orbital scale climate variability and a southern mode (Singarayer and Burrough 2015) responding directly to Southern Hemisphere insolation forcing south of the equator (Barker and Gasse, 2003; Schefuß *et al.,* 2011; Tierney *et al.,* 2011; Costa *et al.,* 2014). This divide appears north or west of Lakes Malawi and Masoko which generally exhibit a southern mode of climate variability (Garcin *et al.,* 2006; Konecky *et al.,* 2011).

In addition to these low latitude forcings, the Subtropical Front (STF) is a southern high latitude forcing which is thought to influence the WRZ of South Africa through influencing Antarctic sea ice extent and SHW (Figure 5.1) (van Zinderen Bakker, 1967; van Zinderen Bakker, 1976; Cockcroft *et al.,* 1987; Shi *et al.,* 2000; Stuut, 2004; Chase and Meadows, 2007; Anderson and Burckle, 2009; Sigman *et al.,* 2010; Neumann and Scott, 2018). The STF is the principal water mass boundary between sub-Antarctic and subtropical surface waters within the Subtropical Frontal Zone (STFZ) and circumnavigates the globe except for the South America region (Orsi *et al.,* 1995). The STF is at the southern boundary of the STFZ and a northern boundary is identified by additional sea surface temperatures and salinity gradients between the STFZ and high salinity sub-tropical gyre waters, often referred to as the North Subtropical Front (NSTF). Enhanced productivity has been observed at the Agulhas Plateau during glacial periods which has been linked to a glacial northward STF migration (Tangunan *et al.,* 2021). The extent that cool, highly productive Southern Ocean surface waters extend northward into ocean basins is highly variable and relates to glacial cycles (Starr *et al.,* 2021). During glacial periods of increased South Atlantic sea ice extent the westerlies, along with the STF, shift northward (van Zinderen Bakker, 1967; van Zinderen Bakker, 1976; Cockcroft *et al.,* 1987; Shi *et al.,* 2000; Stuut, 2004; Chase and Meadows 2007; Anderson and Burckle, 2009; Sigman *et al.,* 2010; Neumann and Scott, 2018). Temperate systems related to the westerly wind belt bring moisture to South Africa, shifting high pressure cells more inland of South Africa and resulting in more humid conditions. As such, the position of the westerlies affects ocean circulation. An equatorward shift in the westerlies would induce a reduced upwelling of the Benguela Current and an inhibited Agulhas Current flow (Partridge *et al.,* 2004; Stager *et al.,* 2011, 2012). However, a southward shift in the westerlies and subsequently a strengthening of the easterlies would lead to an intensification of upwelling and a drying in the South African region (Chase, 2010). As discussed in Chapter 4, the expansion of the WRZ during the LGM is a key feature in understanding South African climate and it is thought this expansion is a consequence of the equatorward displacement of the westerlies (van Zinderen Bakker, 1967; van Zinderen Bakker, 1976; Cockcroft *et al.,* 1987; Shi *et al.,* 2000; Stuut, 2004; Chase and Meadows, 2007; Anderson and Burckle, 2009; Sigman

et al., 2010; Neumann and Scott, 2018). Other studies argue the eastern Cape was drier during the LGM such as the Tswaing Crater record, located north of Pretoria (Partridge *et al.,* 1997). This reveals the diverging interpretations over the drivers of rainfall in the WRZ and SRZ of South Africa, linked to tropical systems from the north or the SHW from the south.

5.2.2.1 Millennial Forcing driving Climate Variability in South Africa

Abrupt changes to more humid conditions in South Africa have been demonstrated to be associated with Greenland stadials and periods of weak East Asian Monsoon. This results in an anti-phasing between rainfall variability in the two Hemispheres on a millennial scale over the last glacial cycle (Schefuß *et al.,* 2011; Ziegler *et al.,* 2013). These millennial scale climate fluctuations are characterised by abrupt (often within decades) and large (up to 10°C in mean annual temperatures) changes in Northern Hemisphere high latitude temperatures as recorded in Greenland ice core records, and antiphased but equally abrupt temperature changes in the South Atlantic Ocean (Barker *et al.,* 2009) with more gradual changes over Antarctica (Blunier and Brook, 2001). This phenomenon known as the Bipolar Seesaw has been linked to changes in the strength of the Atlantic Meridional Overturning Circulation (AMOC) and its effect on the distribution of heat between the Hemispheres (Broecker, 1998). Leaf wax records from marine sediment core site GeoB 9307-3 (Figure 5.1) have found that in response to abrupt Northern Hemisphere cooling, the annual average position of the ITCZ shifts to a more southward position (Schefuß *et al.,* 2011). This ITCZ displacement results in an opposing response between the Northern Hemisphere, where monsoons weaken (Weldeab *et al.,* 2007; Wang *et al.,* 2008), and the Southern Hemisphere, where monsoons strengthen (Wang *et al.,* 2004; Kanner *et al.,* 2012). The presence of a large-scale atmospheric teleconnection linking Northern Hemisphere cold events and precipitation changes in sub-Saharan Africa is also consistent with climate modelling experiments (Chiang *et al.,* 2003; Mulitza *et al.,* 2008). Other studies infer that rainfall variability in the areas south of the ITCZ can be additionally influenced by the sea surface temperature (SST) of the Indian Ocean (Tierney *et al.,* 2008; Stager *et al.,* 2011), with notable effects from the warm waters transported in the Agulhas Current impacting regional atmospheric circulation (Reason, 2001). Numerical modelling results link rainfall in eastern and southern Africa to increased SST in the western and southwestern Indian Ocean, respectively (Reason and Mulenga, 1999).

5.2.2.2 Climate during the Late Middle Stone Age (100-50 ka)

Terrestrial proxy records showing past environmental change, both spatially and temporally in South Africa, are sparse. There are very few long, continuous terrestrial records because the region's semi-arid to arid climates does not favour the development of rift lakes and wetlands. In addition, there are few records which span Marine Isotope Stage (MIS) 5–3, and therefore little is known about the environmental conditions and climate

dynamics during this the Late Middle Stone Age (LMSA), referred to throughout this thesis as the 100-50 ka interval.

This interval is of key importance because of the link between our ancestors evolution and climate changes; it therefore represents a crucial time for human technological and cultural innovation including the Still Bay (SB) (72-71 ka) and Howiesons Poort (HP) (64-59 ka) industries (Jacobs *et al.,* 2008; Reynard and Henshilwood 2017). The rapid development of early human cognition and technological advances is recorded in numerous LMSA cave sites in the Southern Cape region of South Africa (Potts, 1998; Chase, 2010; Fisher *et al.,* 2010; Henshilwood, 2012; Marean *et al.,* 2014; Sealy *et al.,* 2016). One such archaeological cave site is Blombos Cave (Figure 5.1), located in the southern Cape region of South Africa on the coast in the YRZ, between the Goukou river and Duiwenhoks river. Many key LMSA artefacts have been found in Blombos Cave which show the cultural expression of early modern humans through engraved ochre artefacts (Henshilwood *et al.,* 2002, 2009), stone tools including a spear point and a point tip ranging from 84 to 72 ka (Henshilwood and Sealy, 1997; Henshilwood *et al.,* 2001; Jacobs *et al.,* 2006; D'Errico and Henshilwood, 2007) and shell beads (Henshilwood *et al.,* 2004).

As this chapter focuses on understanding changes in on-land hydrology during the LMSA, the climate of the WRZ and SRZ is important to the study. Of particular interest within this context are northerly displaced frontal systems and tropical systems i.e. ITCZ migrations linking the tropics and subtropics (Taljaard, 1996; Engelbrecht *et al.,* 2015). This is because at present, Blombos Cave is located in the YRZ, which is an area influenced by interactions between the tropical, subtropical and temperate weather systems. The Blombos Cave area at present receives annual rainfall of 500-600 mm (Nel and Henshilwood 2016). Studies of precipitation show rainfall regimes during the LMSA were distinctively different depending on the global climate conditions. For example, during MIS 4, the climate was considerably colder and sea level was lower due to enhanced Northern Hemisphere ice volume. The Palaeo-Agulhas Plain (PAP) (Figure 1.2), a large land area adjacent to the present coastline, was exposed at 70 ka due to the falling sea level. When the shoreline was close to Blombos Cave during periods of higher sea level, the climate was coastal with more humid conditions in the surrounding landscape and smaller inter-seasonal and diurnal ranges of temperatures (Göktürk *et al.,* 2023b). At 70 ka, compared to 82 ka, new high-resolution regional climate modelling, downscaled from global model simulations and incorporating concurrent external forcing factors reveal a more continental climate persisted on the coastline due to a southward coastline shift and an increased land surface expansion, whereas inland experienced more humid conditions (Göktürk *et al.,* 2023a).

The two techno-complexes SB and HP are interpreted to be separated by a period of $\sim$ 2.7 to 9.3 kyr (Jacobs and Roberts, 2008), a period which overlaps with the MIS 4 glacial

maximum (70-61 ka). The relation of the SB and HP industries to climate is debated (Jacobs and Roberts, 2008; Bar-Matthews *et al.,* 2010; Chase, 2010); however, both have a direct relation to sea level. The SB is associated with the rapid lowering of sea level whereas the HP coincides with the rise in sea level and closure of the continental shelf south of the African continent associated with the MIS 4 glacial termination (65 to 61 ka). During these two industries, geoarchaeological evidence conveys that human occupation was more frequent but short term, suggesting that sea level fluctuations affected the lives of coastal cave inhabitants and their access to land and sea resources (Haaland *et al.,* 2020; Göktürk *et al.,* 2023a). For example, an expanding glacial PAP may have served as a refuge to large herd animals and humans as interior climates became drier (Morris 2002; Marean 2010). The expansion of winter rainfall inland in relation to a northward SHW shift and a contracted SRZ may have resulted in a seasonal reduction of the arid corridor and allowed large and varied grazer populations, such as those documented at Florisbad (Brink, 1987), to move between the coastal plain and the interior during glacial-interglacial climate transitions.

5.3 Materials and Methods

Full details on the methodology are described in Chapter 2 of this thesis. To avoid repetition, the following is a summary of the materials and methods relevant to data presented in this research chapter.

Marine sediment core MD20-3591 was retrieved during research cruise ACCLIMATE-2 off the continental shelf of South Africa (36° 43.707 S; 22° 9.151 E, water depth 2464 m). The core retrieved 34.32 m of sediment mainly composed of silty clay (Vazquez-Riveiros and Waelbroeck, 2020) with a carbonate content of 48-62% (Figure 2.7). Retrieved from beneath the main flow of the Agulhas Current, this core site reflects the hydrography of the southern Agulhas Current. The core collection aimed to recover sediment from a high sedimentation rate site targeting the LMSA interval (100-50 ka). The core site was a reoccupation of Site CD154-23-16P (RV Charles Darwin 2004; (Hall and Zahn, 2004)), which recovered material with high sedimentation rates ($\sim$ 18 cm/ka) extending back to 58 ka; (58 ka in 11 m), hence the need for a new marine sediment core. Site MD20-3591 is additionally from a shallower water depth than site CD154-23-16P avoiding complications related to carbonate dissolution. Carbonate preservation is influenced by the depth of the Carbonate Compensation Depth (CCD) which is 3500 and 4500 m in the Indian Ocean today (Bickert, 2009). This means at depths shallower than the CCD it is possible to use inorganic proxies such as foraminiferal $\delta^{18}O_{foram}$ calcite as the carbonate is preserved.

5.3.1 Sampling Strategy and Processing

For this work, samples were taken from marine sediment core MD20-3591 (section 2.3.1). Details on the Speleothem age model detailing how ages (ka) based on sediment depth

(cm) were generated (section 2.5.3). Stable oxygen isotopes were measured in carbonate samples from the calcite tests of planktonic (surface-dwelling) foraminifera *Globigerinoides ruber* and deep-dwelling benthic foraminifera species *Cibicoides wuellerstorfi* and *Uvigerina spp* (section 2.3.8). The benthic isotopes were picked from the 250-315 µm size fraction. For the radiogenic isotope analysis, carbonates, organic material and Fe-Mn coatings were removed prior to analysis (section 2.3.1 for a detailed method). The sediment grain size fraction <2 µm was isolated prior to Sr and Nd isotope chemistry. XRF-scanning was performed every 0.2 cm, and 20 discrete samples were taken from the working half of the sediment core to capture the range of variability in the XRF scan data. These samples were digested using lithium metaborate flux-fusion method and elemental concentrations were measured using ICP-MS (Saini *et al.,* 2000; Babin *et al.,* 2020; Balaram, 2021; Balaram and Subramanyam, 2022). All the grain size analyses were performed at the Vrije Universiteit (VU) Amsterdam in the sediment lab using a Sympatec HELOS KR laser diffraction particle sizer for size fractions 0.2 µm to 2000 µm. Previously defined radiogenic isotopes endmember values from Chapter 3 and 4 for the Limpopo, Zambezi and local South African (combination of Karoo and Cape endmembers) rivers were put into the Bayesian mixing model end-member mixing model tool on Excel™ (EMMTE) (Cao *et al.,* 2023), configured for detailed quantification of source contributions to individual samples (see section 2.3.5).

5.4 Results and Discussion

5.4.1 ^{14}C – LR04 Age Model

Firstly, radiocarbon dates (n = 13) were used to construct the first 50 ka of the record (Figure 2.9). This is the basic age model which was extended via benthic δ^{18}O from *C.wuellerstorfi* and *Uvigerina spp* (Figure 2.10). The data spans 34.32 m of sediment core (n = 278 samples) which equates to a 460 ka long record. The $\delta^{18}O_{benthic}$ values range from between 2 and 3 ‰, with no apparent long-term trend towards heavier or lighter values with age (Figure 2.10). The average difference (‰) between LR04 and $\delta^{18}O_{benthic}$ remains equally spaced throughout the full record (Figure 2.10). The *Uvigerina spp* was used in replacement of *C.wuellerstorfi* in the deeper core sections and the $\delta^{18}O_{Uvigerinaspp}$ value was converted to the *C.wuellerstorfi* scale by subtracting 0.64 ‰ from the *Uvigerina* value (Shackleton and Hall, 1997). Without the *Uvigerina spp* isotope values, the record was sparse in intervals, with no or little *C.wuellerstorfi* specimens present.

The full LR04 age model is provided in Tables 2.3 and 2.4. The Undatable age model is very similar to the linear age model, however it provides a Bayesian approach as well as threshold envelopes which are the age uncertainty estimates. On average the 95% uncertainty for the LR04 timescale is 2 kyr, with a range of 0.508 kyr. In the range of the ^{14}C dates (2.464–47.67 ka; Table 2.3), average sedimentation rates are $\sim$ 37 cm/ka.

Beyond that, average sedimentation rates are $\sim$ 7 cm/kyr (Figure 2.10). There are two ACPs closely dated (37.06 ka and 37.13 ka), however the sedimentation rate reaches a maximum here of 342 cm/kyr due to the sample depth from which these radiocarbon ages were dated (240 cm and 264 cm respectively).

5.4.1.1 Time Series Analysis of LR04 timescale

Time series analysis of the LR04 timescale was performed on the MD20-3591 XRF PC1 record (see section 5.4.3.2 for Principal Component Analysis (PCA)) and find the 23 kyr periodicity significant above the 99% uncertainty band which are delineated by the white lines. The 23 kyr periodicity is particularly pronounced between 100-200 ka and 250-300 ka, while there are some shorter periodicities centered around 0-5 ka for the full record (Figure 5.2) - this is inferred from observing the wavelet within the cone of influence (Figure 5.2a). The white lines delineate regions of the scalogram that are significant against an AR(1) benchmark and encircle areas of notable power (Figure 5.2a). Despite the 41 kyr and 100 kyr periodicity not encircled in the figure, this frequency still has notable power throughout most of the record. Figure 5.2c reveals that 23 kyr is above the threshold, confirming it has significant power on the LR04 timescale.

The time series analysis (Figure 5.2) shows there is a significant precession power throughout the XRF PC1 record on the LR04 timescale. The frequency analysis output on 95% significance wavelet shows stronger precession power at 300 to 200 ka and 150 to 70 ka in the XRF PC1 record on the LR04 timescale. This is also evident when comparing XRF PC1 data with the band pass filter for precession (Figure 5.2b).

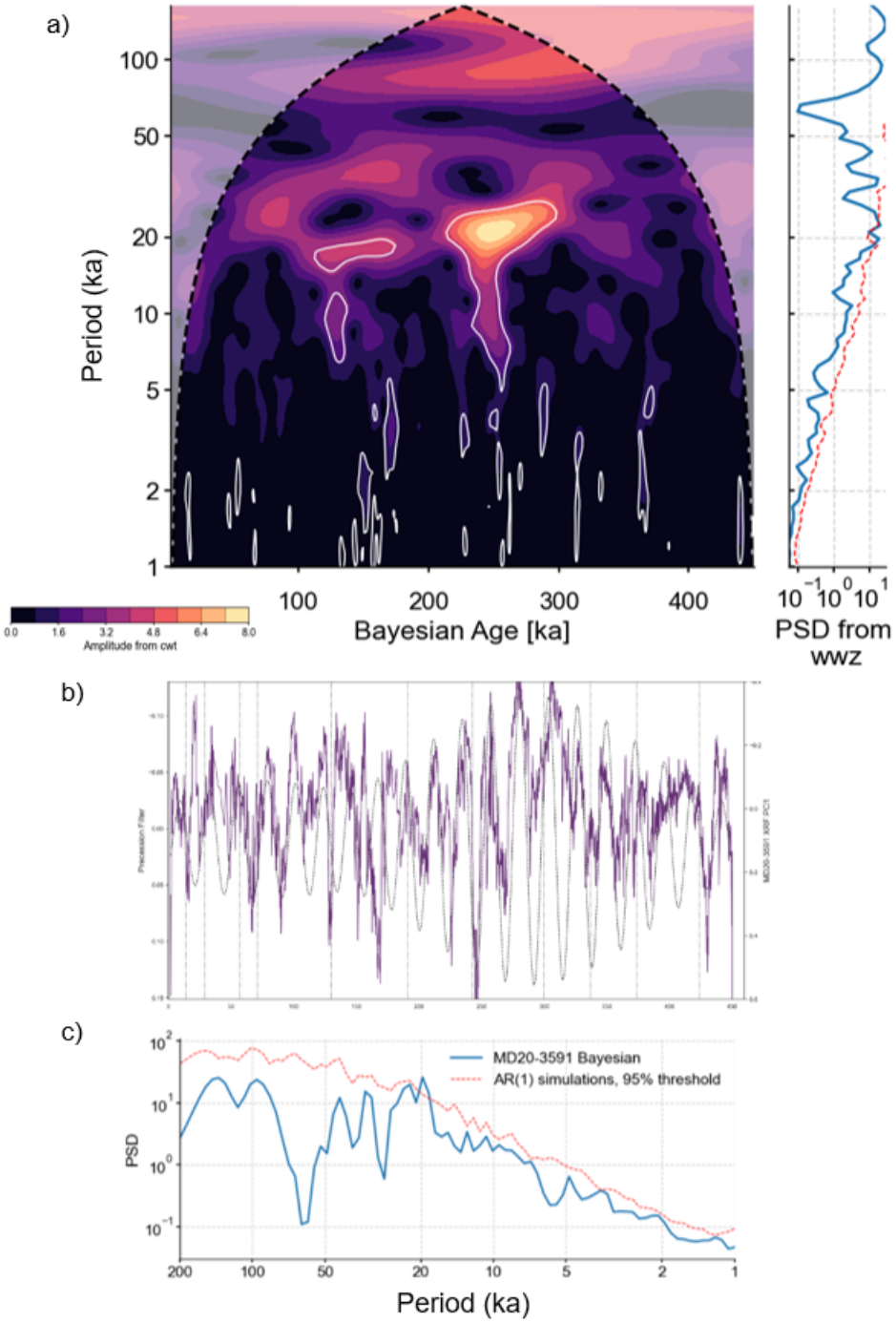

Figure 5.2: Time series analysis of XRF PC1 record on LR04 timescale (Bayesian). (a) Weighted Wavelet Z transform, lighter colours indicate stronger power, white outlines show significant results based on AR(1). (b) XRF PC1 on LR04 timescale with precession pacing (23 kyr) filtered at a bandwidth of 0.0427772 (grey dashed). (c) Time series analysis of XRF PC1 (blue) from Pyleoclim, AR(1) simulations and 95% significance threshold limit (red).

5.4.2 Hulu-Sanbao Speleothem Age Model (Speleothem Chronology)

As the LR04 timescale reveals significant 23-kyr periodicity in the frequency domain (Figure 5.2), this information is used further to tune the XRF PC1 record to the Chinese caves (Hulu and Sanbao) speleothem record which shows a high precession periodicity, paced through monsoon rainfall variability (Cheng *et al.,* 2016). The Chinese caves (Hulu and Sanbao) speleothem record (Cheng *et al.,* 2016) is absolute dated using ^{230}Th-derived chronology which spans 640 ka, so as it is radiometrically tuned with high resolution (Cheng *et al.,* 2016), it has an independently resolved age scale so is not primarily tuned to orbital parameters.

The possibility of tuning to the Chinese caves (Hulu and Sanbao) speleothem record is further supported by other records from South Africa which reveal a high precession periodicity in that frequency domain (Simon 2014; Simon *et al.,* 2015a). The Hulu and Sanbao cave records show a synchronous variability of East Asian Monsoon with North Atlantic climate variability due to the atmospheric bridge on shorter millennial timescales (Ziegler *et al.,* 2013; Simon *et al.,* 2015a). The concept of the atmospheric bridge is based on the knowledge that Southern Africa bridges climates of the low-latitude tropical regime that is primarily under the influence of the ITCZ and CAB, and the high southern latitudes that are influenced by the northern extensions of the SHW, determining climates of southern South Africa (Tyson and Preston-Whyte, 2000; Chase and Meadows, 2007). This teleconnection is due to the bipolar seesaw which is linked to the strength of the AMOC and its effect on heat distribution between hemispheres through ITCZ migration causing regional rainfall (Broecker, 1998; Ziegler *et al.,* 2013).

Additionally, evaluating this millennial scale variability in Southeast Africa is not possible on the LR04 timescale due to the lower resolution of LR04, compared to the Chinese caves (Hulu and Sanbao) speleothem record. Therefore, a different age model approach is presented, based on the tuning of XRF PC1 to Chinese caves (Hulu and Sanbao) speleothem record (Cheng *et al.,* 2016) (Figure 5.3). The Speleothem Chronology applies 34 tie points to Chinese caves (Hulu and Sanbao) speleothem record (Table 2.5). During the LMSA interval, eight additional tuning points were added to the four tie points in the LR04 age model (Figure 5.3). The speleothem chronology used the absolute radiocarbon dates for the first 50 ka and was based on wiggle matching beyond the radiocarbon limit. Transferring the $\delta^{18}O_{benthic}$ record on the Speleothem chronology still shows a high level of synchroneity between LR04 and the MD20-3591 $\delta^{18}O_{benthic}$ record despite the different tuning approach (Figure 2.12a). There are some discrepancies in timing ($\sim$ 60 ka) where the difference between LR04 age model and the speleothem age model is larger, though both age models do agree quite well with the Chinese caves (Figure 5.3). However, using the speleothem chronology results in a robust and more improved age

model for marine sediment core MD20-3591 as validated by the good agreement with the chronology derived from LR04. In addition, the linearly resolved age model, based on tuning to the Chinese caves (Hulu and Sanbao) speleothem record is within the Bayesian Speleothem chronology credibility threshold which signifies the linear age model can be used as well as the Bayesian Speleothem chronology (Figure 5.4).

5.4.2.1 Time Series Analysis of Speleothem Chronology

The Speleothem chronology displays significant 23 kyr periodicity above the AR(1) threshold (Figure 5.5b) and is particularly pronounced between 50-150 ka and 200-300 ka. The break down in the 23 kyr periodicity in the XRF PC1 record of MD20-3591 at 50 ka is likely due to the use of radiocarbon dates only being used for the age model in this interval. However, a breakdown in the precession signal in regional South African climates has been documented at 70 ka (Chase *et al.,* 2021), with records which were previously out of phase (e.g. leaf waxes from core site RC09-166 in the Gulf of Aden (Tierney *et al.,* 2017) and the Tswaing Crater (Figure 5.1) (Partridge *et al.,* 1997)), exhibiting a strong positive correlation at 70 ka. This suggests the rainfall variability in South Africa adopts a signal in-phase with a high latitude forcing which has been found to continue until the onset of the Holocene, when high latitude ice sheets retreated and direct local insolation forcing once again became the driver of South African rainfall variability (Chase *et al.,* 2021). The impact of high latitude forcing on the South African climate records (e.g. Ziegler *et al.,* 2013; Simon *et al.,* 2015a) is observed mainly in millennial-scale wet phases caused by abrupt climate oscillations in the northern high latitudes whereas low-latitude summer insolation changes paced by orbital precession explain the long-term climate variability. The breakdown in 23 kyr periodicity is important when considering the assumptions made in tuning to the Speleothem record. One such assumption is that XRF PC1 is synchronous and well represented by the Chinese caves (Hulu and Sanbao) speleothem record. This is evident when observing the LR04 timescale comparison to the Chinese caves (Hulu and Sanbao) speleothem record (Figure 5.3). A second assumption which is important to account for is the monocausal linear assumption of a given terrestrial response to Northern Hemisphere climate dynamics which does not apply for the whole record as precession appears to break down after 50 ka, therefore, the speleothem chronology is only used for the LMSA interval.

This chapter focuses on the LMSA because archaeological evidence suggests that this time interval is among the most important periods within which cognitive development occurred among Anatomically Modern Humans (AMHs), reflected in pulsed events of innovation displayed by the use colour, ornamentation of shell beads and development of stone tools (Henshilwood *et al.,* 2002; Henshilwood *et al.,* 2004; Henshilwood *et al.,* 2011; Henshilwood, 2012; Tylén *et al.,* 2020). This present study focuses on the higher resolution variability during this interval and uses additional proxies other than XRF to understand

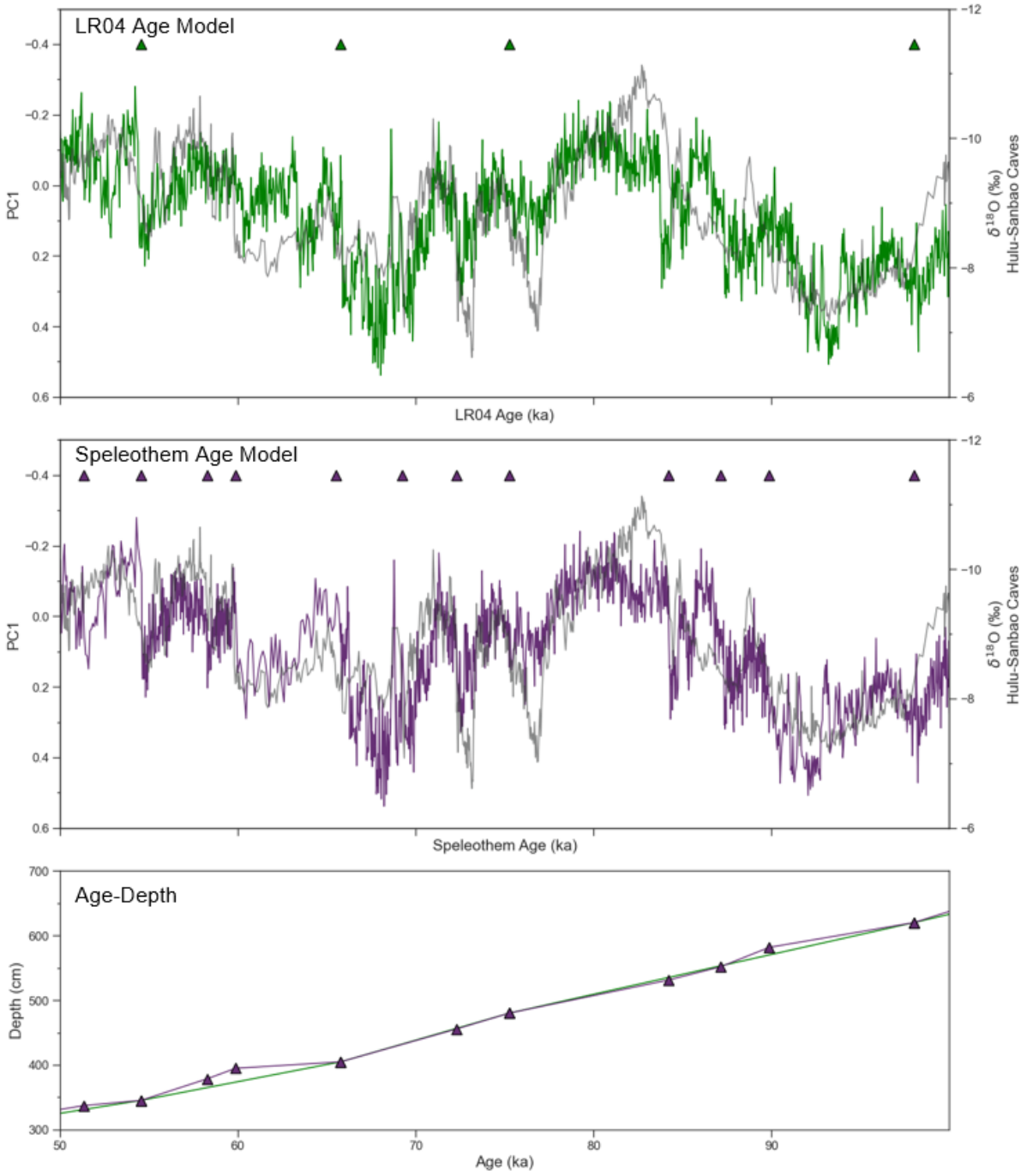

Figure 5.3: Comparison of XRF PC1 on both age model chronologies. a) LR04 Age Model, b) Speleothem Age Model, c) Age-Depth plot of LR04 Age Model (green) and Speleothem Age Model (purple).

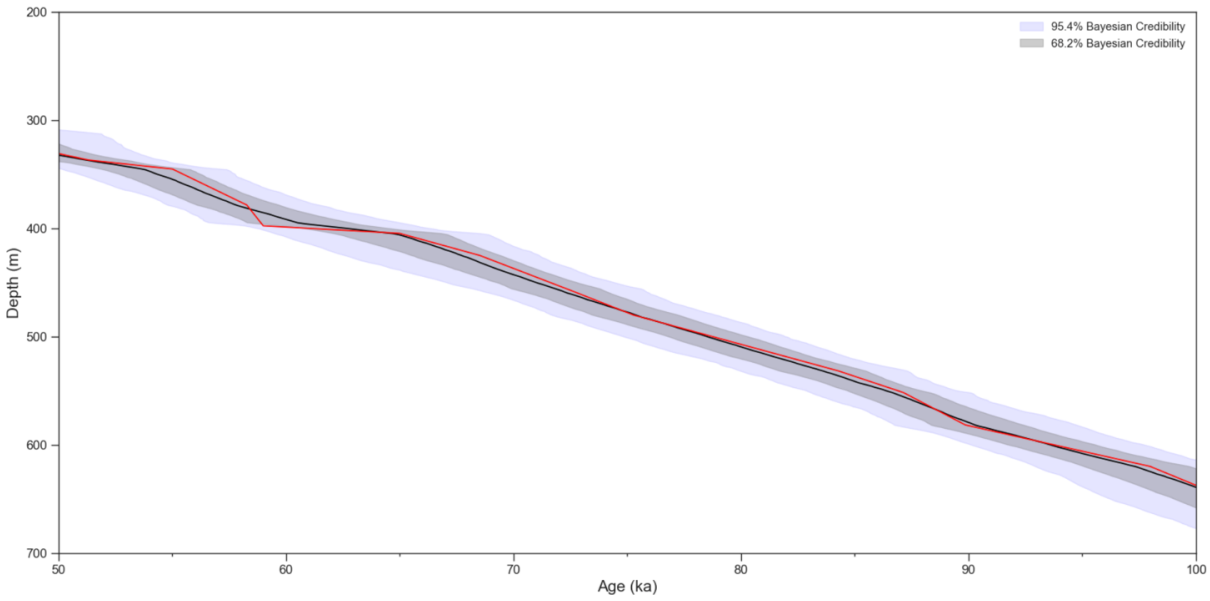

Figure 5.4: Bayesian Speleothem Chronology Age-Depth (black line) for 100 to 0 ka interval with Bayesian uncertainty thresholds (95.4% light grey; 68.2% dark grey shading). Red line is the Hulu-Speleothem age model based linear interpolation which is within the Bayesian uncertainty windows.

the sediment provenance signal to reconstruct the climate changes during LMSA. This provenance reconstruction helps contextualise the environment for early humans as it has been widely speculated that this cultural development was facilitated by specific environmental and climatic conditions in the region, particularly at the dynamic land-ocean interface (Cawthra *et al.,* 2014; Sealy *et al.,* 2016). Recently, several important datasets from a variety of marine and terrestrial sites from South Africa, combined with climate models have advanced our understanding of the climate dynamics at play between late MIS 5 and early MIS 3 (Chase *et al.,* 2021; Göktürk *et al.,* 2023b; Göktürk *et al.,* 2023a). Why these technological and cultural innovations evolved is not yet fully understood, therefore, investigating the role that regional climate potentially played is one step forward. Here, the first marine sediment provenance record from offshore South Africa spanning the full LMSA interval is presented at high resolution.

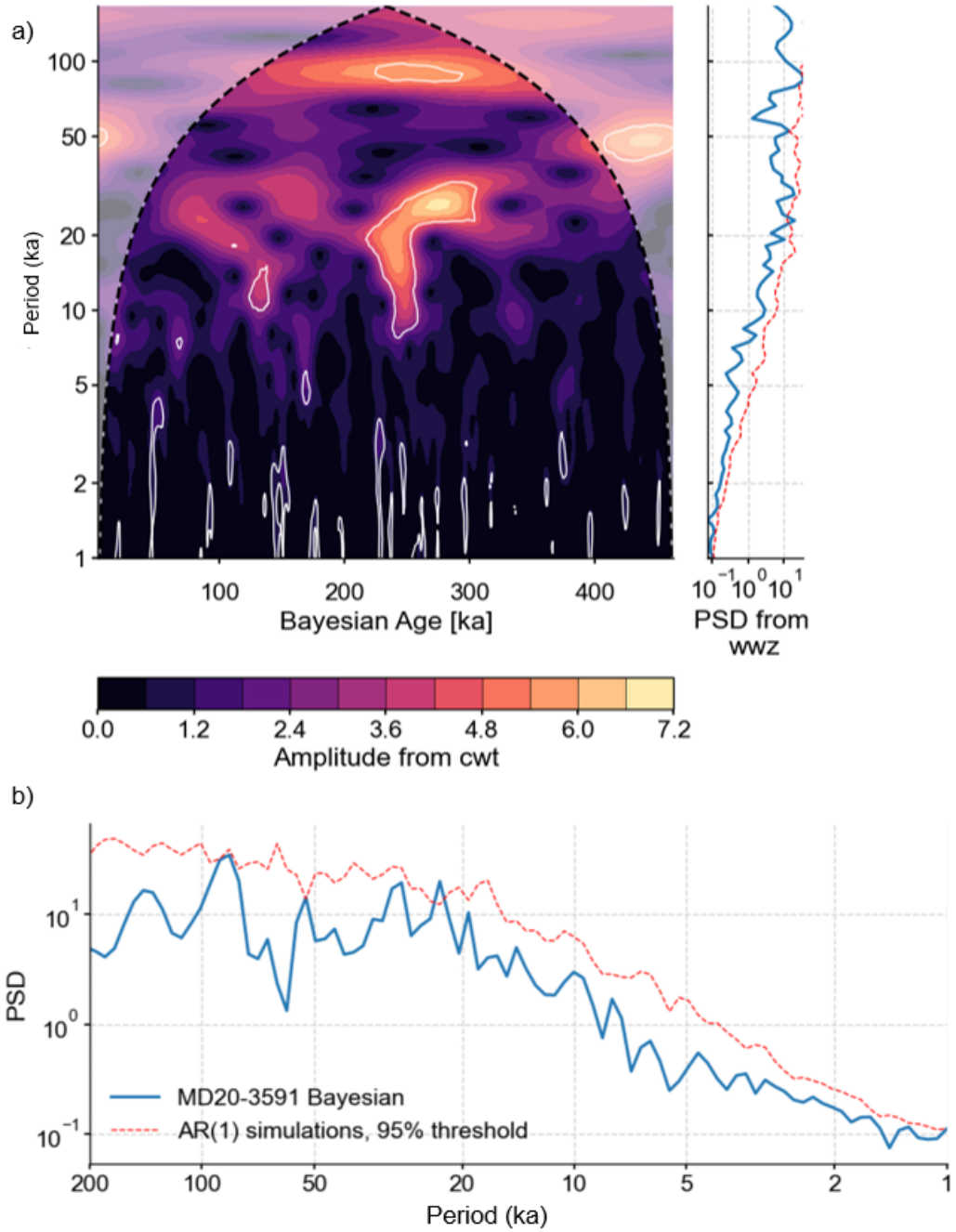

Figure 5.5: Time series analysis of XRF PC1 record on Speleothem chronology. (a) Weighted Wavelet Z transform, lighter colours indicate stronger power, white outlines show significant results based on AR(1). (b) Time series analysis of XRF PC1 (blue) from Pyleoclim, AR(1) simulations and 95% significance threshold limit (red).

5.4.3 X-Ray Fluorescence Scanning and Principal Component Analysis

5.4.3.1 XRF Scanning Results of MD20-3591

Elements derived from the continental crust, i.e. terrigenous phases such as Fe, Ti, K, Si, vary inversely with Ca content (Figure 2.8). Over the depth scale, from 0 to 3400 cm, Ca and K trend towards higher values. For the first 1000 cm, it seems Si, K, Ca, Ti and Fe all trend towards higher values (Figure 2.8). From 1700 cm, there is a similar trend

in Si, K, Ti and Fe to the bottom of the core. The greatest variability is seen in the Ti record, Ti varies by a factor of 7 through the core. The covariance of the terrestrially derived elements and anticorrelation of calcium carbonate suggest the main control on the chemical composition of the sediment from site MD20-3591 is the input of terrigenous material. It is also possible to see these downcore XRF trends using the calibrated XRF on age (Figure 5.7).

Based on the XRF calibrations (Figure 5.6), most elements have high quality R^2 coefficients greater than 0.75 and intercepts at or near zero within the bootstrapped uncertainty envelope, which shows how effectively the calibration yielded individual element concentrations (Figure 5.6). Only potassium has a lower R^2 coefficient, which reveals the relationship with the XRF-derived concentration is weaker.

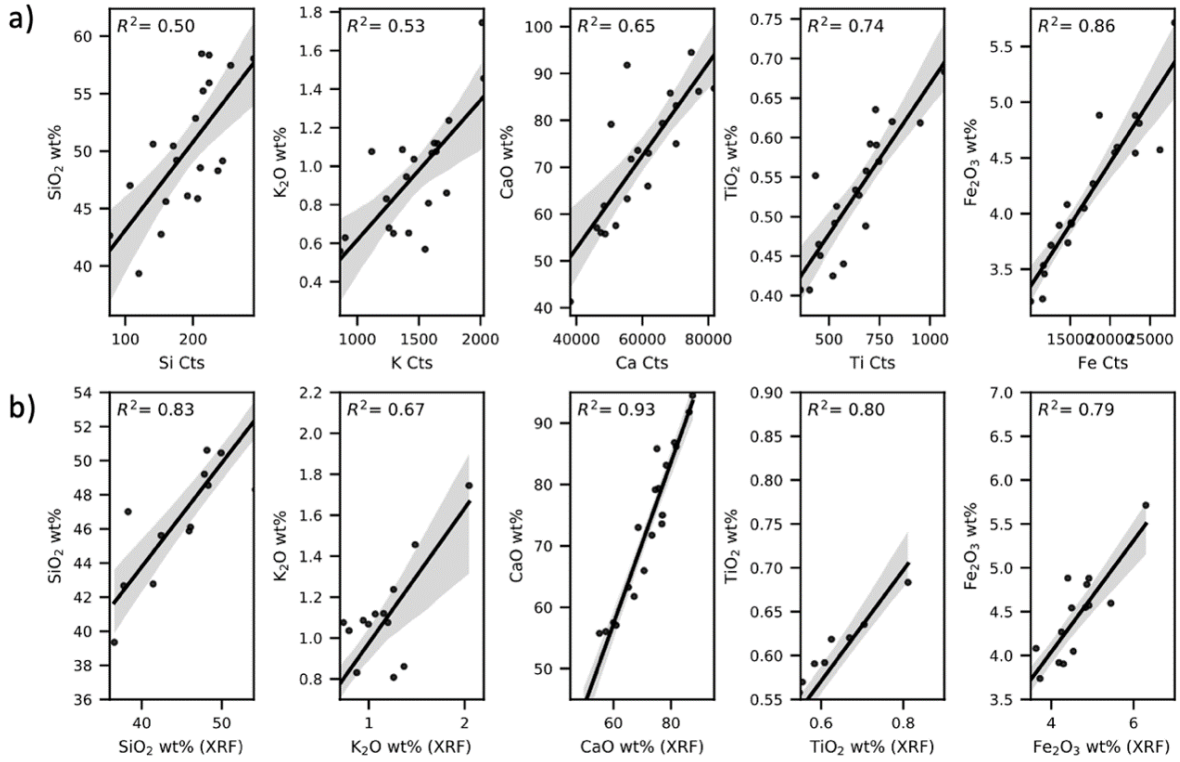

Figure 5.6: Comparison of XRF data to calibration samples using individual element concentrations. Shaded intervals = 95% confidence interval regression model computed by bootstrapping the data 1000 times. (a) Before calibration; (b) After calibration. Generated using the Python package Seaborn's regplot function.

5.4.3.2 Principal Component Analysis

The PCA results (Figure 5.8) show that the sediment elemental composition is controlled by different factors. PC1 is by far the most important component explaining 67% of the total data variance. XRF PC1 differentiates between the terrestrial siliciclastic fraction (i.e. highest positive loadings in Fe, Ti, and K) and biogenic carbonate (i.e. high negative loadings in Ca and Sr) (Figure 5.8a, b and c). XRF PC1 scores display downcore variations

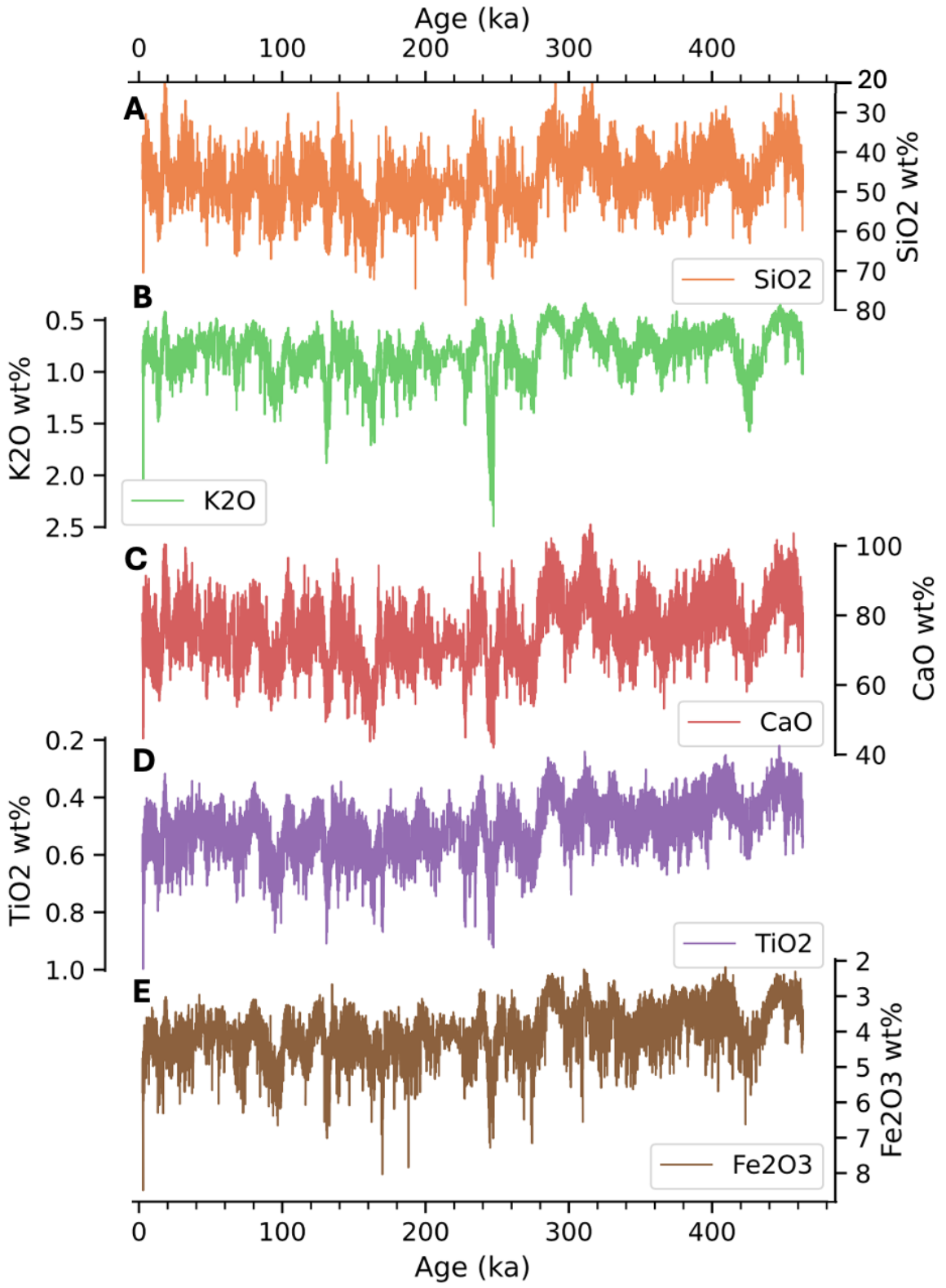

Figure 5.7: Downcore calibrated XRF scanning results as concentrations on Speleothem chronology.

which represent the supply of terrigenous sediment delivery into the marine realm, as Al, Fe, K, Ti, Rb and Si represent detrital material primarily transported by fluvial processes

into the sea (Govin *et al.,* 2014), whereas Ca and Sr are carbonate-associated elements, typically related to biological processes in the marine realm (Croudace *et al.,* 2019).

The XRF PC1 record from MD20-3591 can be used to reconstruct the hydroclimate conditions of South Africa; the variations in the terrestrial vs marine element concentrations can be used as a proxy for terrestrial input of sediments, as the variability in XRF PC1 is indicative of humid or dry conditions in the river catchments, much like the ln(Fe/K) ratios from other marine sediment cores in the region (CD154-17-17K, CD154-10-06P) (Ziegler *et al.,* 2013; Simon *et al.,* 2015a) (Figure 5.9). High temperatures and precipitation drive the weathering of bedrock in subtropical regions, which would influence the quantity of terrigenous material transported to the marine core site via riverine transport. The terrigenous material (especially Fe rich soils) is transferred to the marine environment, driven by intense weathering, whereas potassium in marine sediment is associated with lower chemical weathering and more physical weathering, driving illite or potassium feldspar production (Zabel *et al.,* 2001). The ln(Fe/K) proxy is therefore an appropriate tool for reconstructing African climate zones as it indicates the presence of more humid conditions within a river catchment (Mulitza *et al.,* 2008; Govin *et al.,* 2012). Much like the ln(Fe/K) proxy, XRF PC1 also gives a qualitative estimate of terrigenous material supplied to the ocean, as higher XRF PC1 scores indicates more terrigenous elements, like Fe and Ti. The lower XRF PC1 scores suggest more marine carbonate production based on higher loadings in Ca and Sr and therefore less humid conditions prevailed within river catchments as the Fe and K loadings are lower. As the PC1 record explains 67% of the data variance for the XRF data from MD20-3591, it is statistically robust and can be used in the same way as the reflectance data or XRF scanning elemental ratios for comparisons with other records (Ziegler *et al.,* 2013; Simon *et al.,* 2015a) (Figure 5.9). During periods of high MD20-3591 XRF PC1 scores, such as $\sim$ 70 ka (Figure 5.9) suggesting more terrigenous sediment supply, the XRF ln(Fe/K) records from MD20-3591 (Figure 5.9b), CD154-10-06P (Figure 5.8c) and CD154-17-17K (Figure 5.9d) also reveal more Fe, inferred from a higher ln(Fe/K) ratio.

The XRF PC1 record on the LR04 time scale shows remarkable similarities with the Chinese caves (Hulu and Sanbao) speleothem record as a time series (Figure 5.3a), however the scatter is substantial and the Pearson correlation is weak $R^2 = 0.01$ (Figure 5.10a). The XRF PC1 on Speleothem chronology is strongly correlated to the Chinese caves (Hulu and Sanbao) speleothem record (Figure 5.10b). In order to inspect the correlations between XRF PC1 and Chinese caves (Hulu and Sanbao) speleothem record, both age models and the Chinese caves were resampled to a common time step and aligned on age in order to inspect the correlations in Figure 5.10.

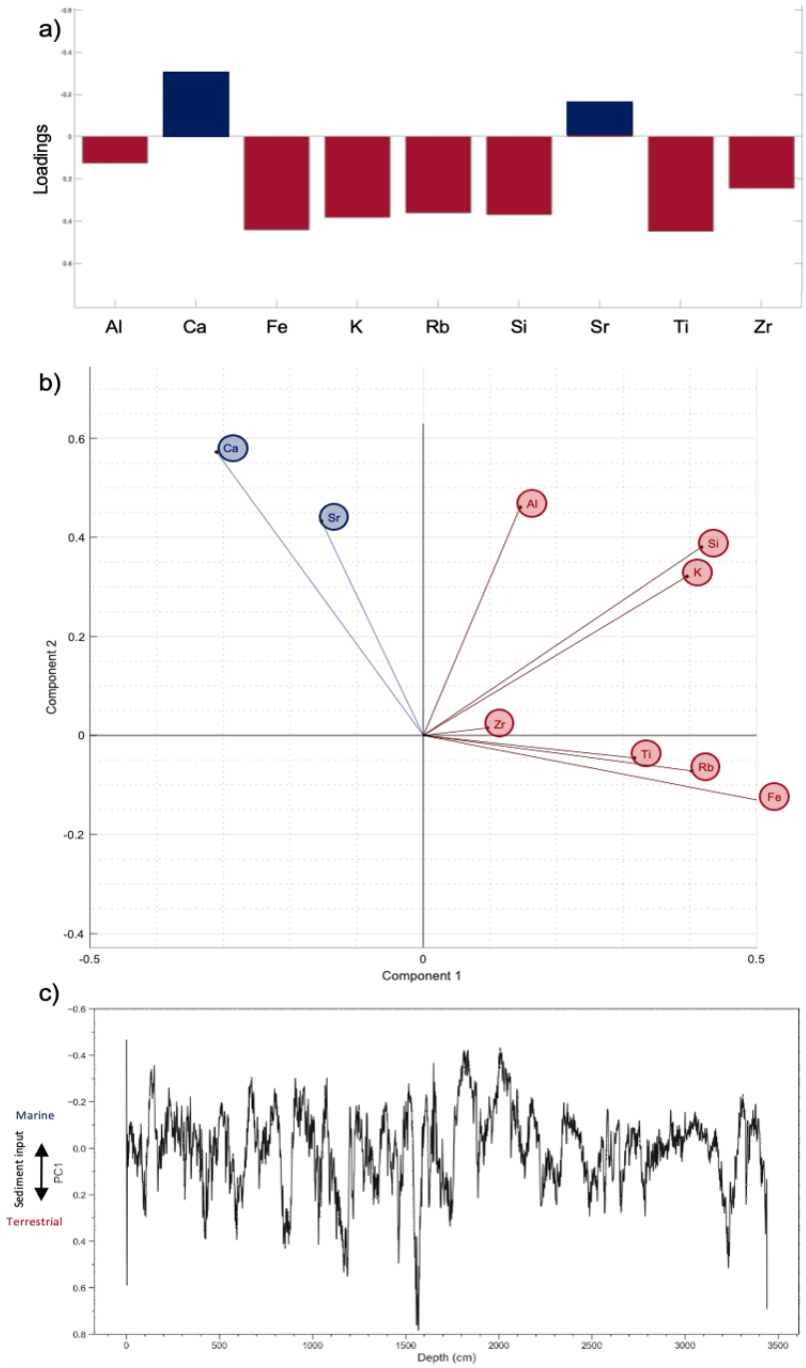

Figure 5.8: Principal Component Analysis results. (a) Relative loadings of Principal Component (PC) 1, negative loadings in blue, positive loadings in red. (b) Biplot results of PCA, elements with positive loadings are terrigenous (red), negatively loaded elements (blue) are of biogenic source. (c) Downcore variability of XRF PC1 on depth.

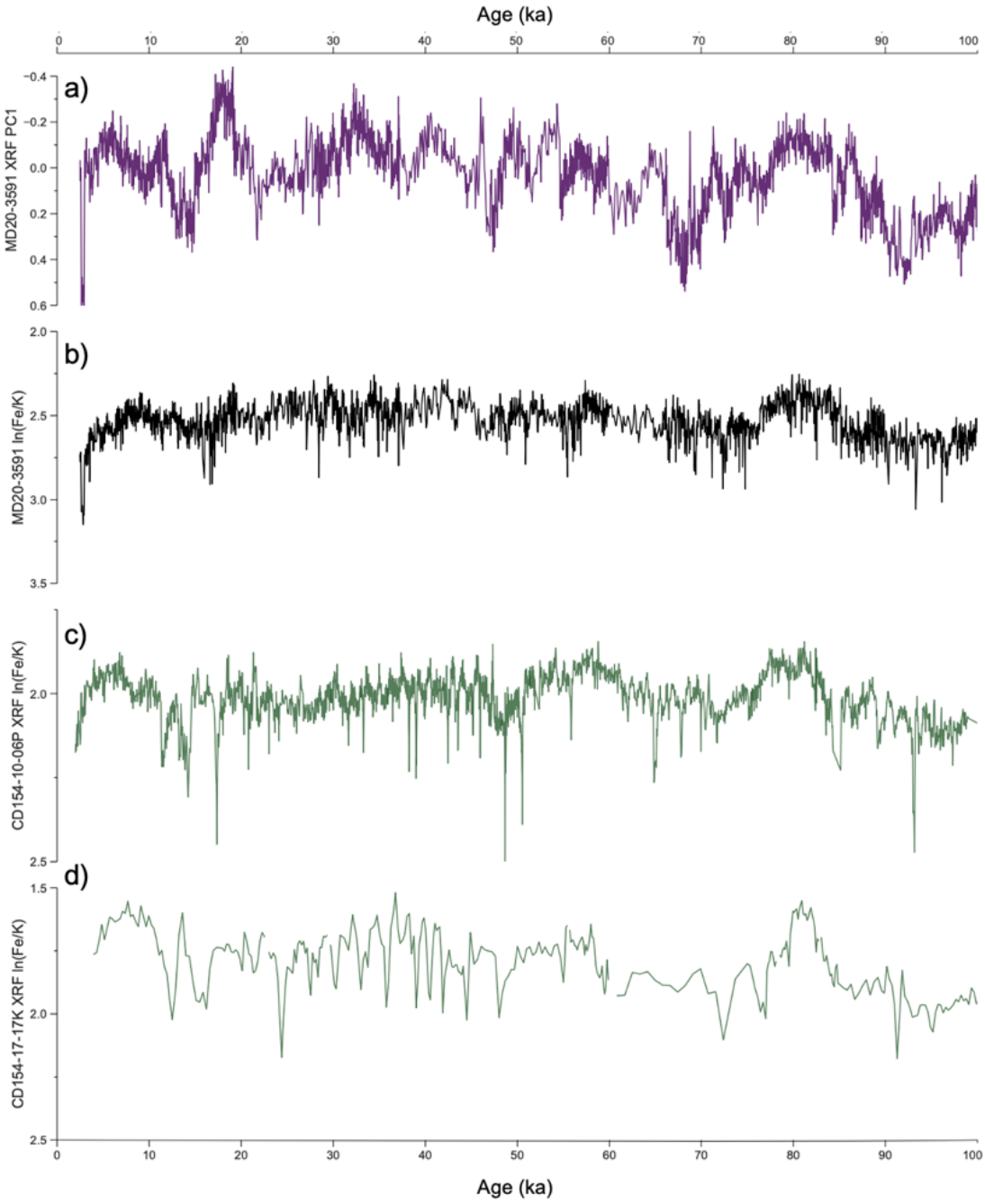

Figure 5.9: Downcore comparison of (a) MD20-3591 XRF PC1 with (b) MD20-3591 ln(Fe/K) ratios, (c) CD154-10-06P ln(Fe/K) ratios, (d) CD154-17-17K ln(Fe/K) ratios. MD20-3591 records presented on Speleothem Chronology.

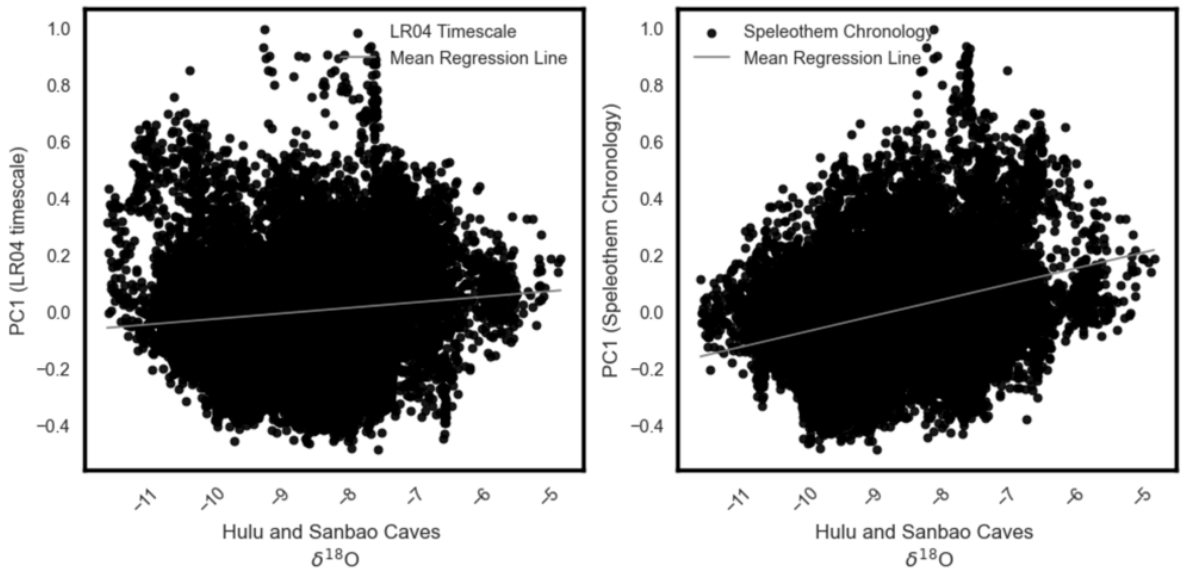

Figure 5.10: Comparison of XRF PC1 a) LR04 timescale, b) Speleothem chronology and Hulu-Sanbao δ^{18}O caves using Pearson's correlation. For LR04 timescale $r^2 = 0.01$, for Speleothem chronology $r^2 = 0.39$.

5.4.4 Sea Level Control on Grain Size at Site MD20-3591

The main sources and transport mechanisms which could affect the variation in temporal grain size variability at site MD20-3591 are changes in river sediment supply, dust input and/or changes in sea level (Weldeab *et al.,* 2013). To assess the main sediment input of marine sediment core MD20-3591, the grain size was measured. The mean grain size record of the terrigenous fraction is shown in Figure 5.11a. Mean grain size varies between 9 and 56 µm, which falls into the range of what is considered to be river and dust sized (<20 µm) particles (Maher *et al.,* 2010; Meyer *et al.,* 2011). The grain size distributions of the two endmembers are shown in Figure 5.11b. All endmembers have a clearly defined dominant mode, endmember 1 (EM1) has a model grain size of 76 µm and endmember 2 (EM2) of 24 µm. Pronounced changes in EM1 are most evident at 550 to 500 cm core depth with an abrupt increase in grain size at 550 cm core depth (Figure 5.11a). Comparing the trends and magnitude of changes in the endmembers with those of the mean grain size, it is evident that for the entire core depth, changes primarily occurred due to changes in EM1. Figure 5.11c shows the coefficients of determination (R^2), plotted against grain size for models with 2 to 10 endmembers. The mean coefficient of determination of grain size classes increases when the number of endmembers increases (Figure 5.11c). The two endmember solution ($R^2 = 0.985$) (Figure 5.11c) shows a reasonable R^2 values for the size ranges, whereas the three endmember model increases R^2 by 0.04. These goodness-of-fit statistics demonstrate that the two-endmember model provides the best compromise between the number of endmembers and R^2. The endmember modelling of grain size distribution reveals glacial-interglacial variability, indicating relatively coarse-

grained deposition during glacial stages (MIS 2, 4) and relatively fine-grained deposition during interglacial stages (MIS 1, 3, 5) at site MD20-3591 (Figure 5.12). During MIS 4, falling sea level exposed the large area of land adjacent to the present coastline, PAP (Cawthra *et al.,* 2020b)). This exposed land mass has been mapped recently, revealing that the coastal rivers incised the PAP, extending further south across the plain (Figure 1.1) (Cawthra *et al.,* 2020a; Dupont *et al.,* 2021).

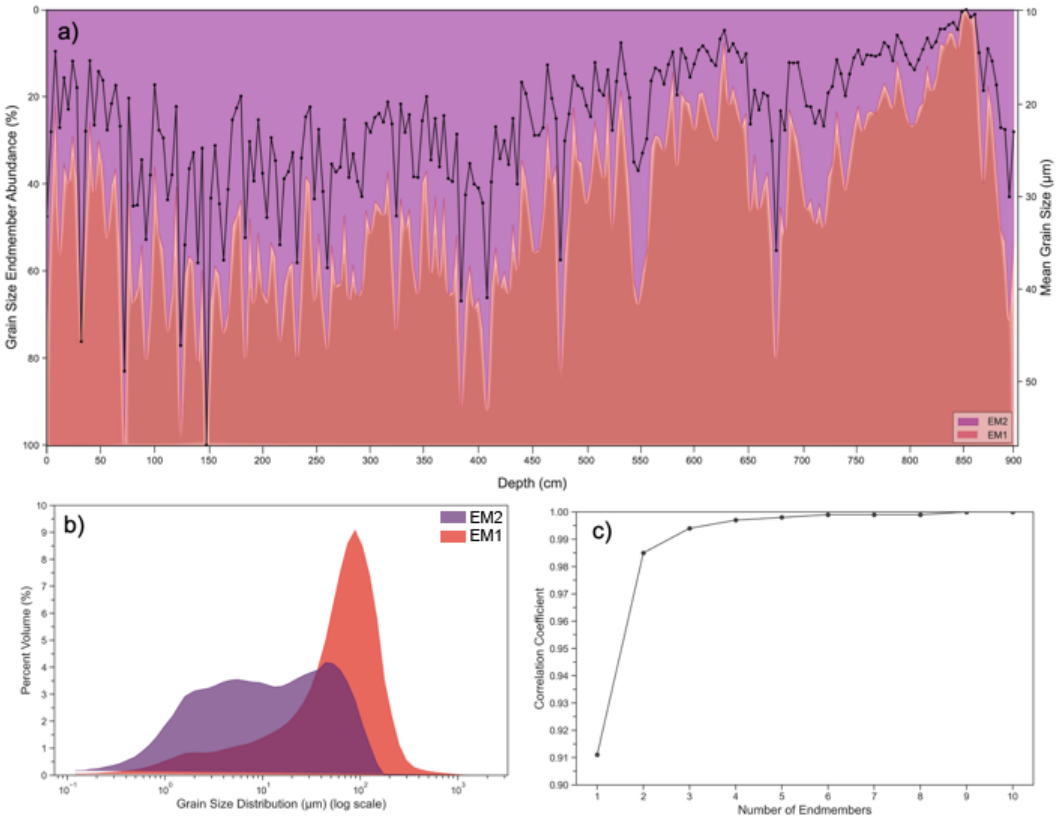

Figure 5.11: Grain size distribution for site MD20-3591 sediments (a) Endmember abundances (EM1; dark grey, EM2; light grey) compared to mean grain size (µm) (b) Percent volume of EM1 (red) and EM2 (purple), (c) coefficients of determination of number of endmembers from Endmember Mixing Model.

In order to compare the correlation between sea level (Grant *et al.,* 2014) and the MD20-3591 grain size record, the age models of both sediment cores were aligned. This was carried out firstly by downsampling using the sea level $\delta^{18}O_{planktic}$ record using 'Acycle' package within MATLAB 2022b (Li *et al.,* 2019), to the same number of data points as the $\delta^{18}O_{planktic}$ record of MD20-3591. Once the two records had the same sample rate (2.03 ka), the age models were aligned. This means the $\delta^{18}O_{planktic}$ sea level record was transferred onto the MD20-3591 $\delta^{18}O_{planktic}$ based on the Speleothem chronology. The results indicate that phases of lower sea level records correlate with a coarser grain size ($R^2 = 0.31$) (Figure 5.13).

This suggests that MIS 4 glacial low stand conditions offshore South Africa favour more

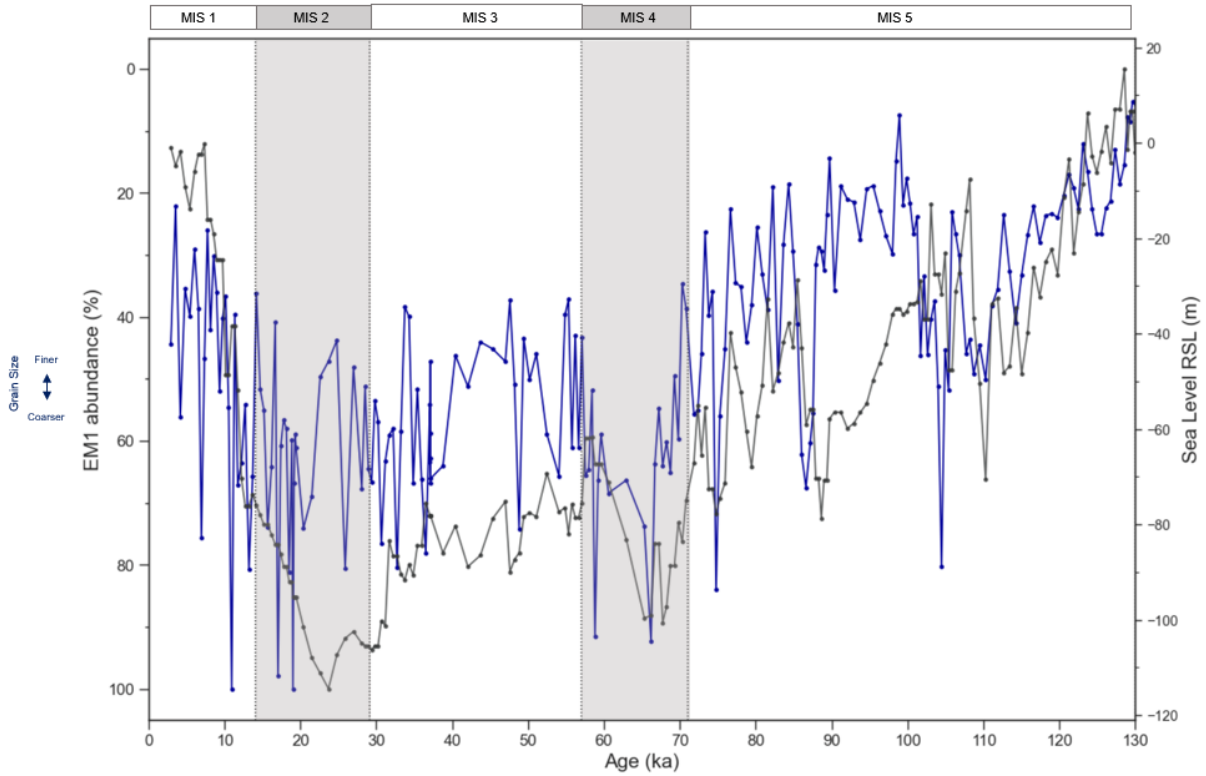

Figure 5.12: Comparison of core site MD20-3591 grain size EM1 (%) (blue) and downsampled sea level from Grant *et al.* (2014) (grey). MD20-3591 is presented on the Speleothem Chronology.

riverine input, inferred by the increased transport of coarser sediments. This might be due to a more proximal supply of river sediment to core site MD20-3591 during sea level low stands (Cawthra *et al.,* 2020a; Dupont *et al.,* 2021). Dust input is another potential contributor to the core site, however numerous studies reveal the input of dust to this region is minimal during glacial and interglacial periods (Dupont *et al.,* 2021; Chase, pers. comms). The region receives approximately 1g/m^2 per year of aeolian dust (Maher *et al.,* 2010). For the Last Glacial Maximum (LGM), one such sedimentary record from ODP site 1090 (42° 54.5' S, 8° 54.0' E) (Martínez-Garcia *et al.,* 2009) appears to indicate up to 7 times higher dust flux at the LGM compared with the present day. This is in contrast to a much larger increase (30 times) recorded by the ice cores of the Antarctic Plateau (Maher *et al.,* 2010) showing that the amount of glacial dust likely deposited at core sites south of Africa such as site MD20-3591 is much less than at sites from the Southern Ocean (Maher *et al.,* 2010).

5.4.5 Sediment Provenance (Radiogenic Isotopes) in Site MD20-3591

The $^{87}Sr/^{86}Sr$ isotope ratios increase from an unradiogenic value of 0.746 ($\pm$0.00001) at $\sim$ 89ka in MIS 5 towards MIS 4, at $\sim$ 70 ka, the highest $^{87}Sr/^{86}Sr$ value is recorded (0.758

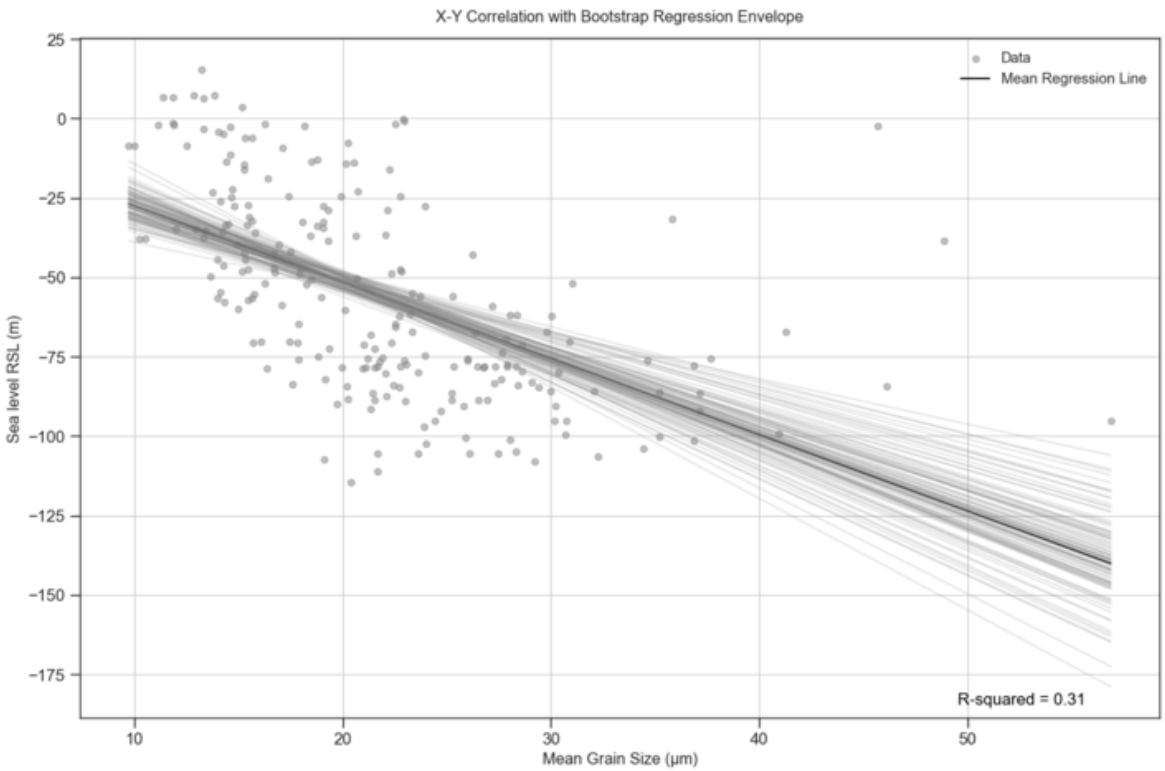

Figure 5.13: Regression plot of sea level from Grant *et al.* (2014) and mean grain size (µm) with 1000 Monte Carlo bootstrap simulations, grey shading represents the 95% certainty threshold.

±0.00001). There is a trend towards lower $^{87}Sr/^{86}Sr$ values in MIS 4, and a decrease of 0.008 from 70 to 55 ka (Figure 5.14b). Notable millennial-scale Sr fluctuations during MIS 5 and MIS 4 are also recorded with amplitudes of $\sim$ 0.005. The most prominent increase in the εNd signal occurs from 75 to 65 ka, where εNd values range from -13.765 to -11.671 (±0.161), an increase by 2.094 ε units (Figure 5.14b).

5.4.5.1 Disentangling the εNd and $^{87}Sr/^{86}Sr$ variability

As discussed in previous chapters, the grain size fraction selected is very important concerning $^{87}Sr/^{86}Sr$ ratios. To ensure no potential bias to the $^{87}Sr/^{86}Sr$ isotopes, the radiogenic isotopes were analysed on the <2 µm fraction. This is to ensure the $^{87}Sr/^{86}Sr$ ratios reflect a provenance signal and not a grain size signal. Clay minerals in the <2 µm fraction of deep-sea sediments are useful indicators of marine sedimentary processes, particularly those involving the transport of land-derived solids to and within the oceans (Griffin *et al.,* 1968). Transport mechanisms often contribute to a specific grain size, therefore isolating one size fraction and comparing all measurements on this same size fraction ensures the geochemical imprint is reflecting key environmental processes such as provenance. During chemical weathering, Sr is easily removed, leaving Rb behind, which increases the Rb/Sr ratio and the $^{87}Sr/^{86}Sr$ ratio in highly weathered rock (Blum,*et al.,* 1994; Blum and Erel, 1997; Jung *et al.,* 2004). In contrast, the rare earth elements are immobile during

weathering, so the εNd record reflects the sediment source (Chapter 3). This chemical difference in behaviour of Sr and Nd has been shown to represent periods of enhanced precipitation (i.e. chemical weathering). In this chapter, a lower $^{87}Sr/^{86}Sr$ isotope ratio in site MD20-3591 indicates more chemical weathering from South African sources (more rainfall) based on radiogenic isotopes endmember values calculated in Chapter 3. The lower $^{87}Sr/^{86}Sr$ values observed in site MD20-3591 fall within the Sr data range from the South African river sediments (Chapter 3). Whereas, the higher $^{87}Sr/^{86}Sr$ ratios are inferred to be a mixture of Limpopo and Zambezi river sources. Therefore, $^{87}Sr/^{86}Sr$ isotope variability can be interpreted to document the regional evaporation-precipitation balance also demonstrated by Jung *et al.* (2004) and Meyer *et al.* (2011). Therefore, a downcore record of $^{87}Sr/^{86}Sr$ isotopes and εNd variability allows the detection of regional climate (inferred through chemical weathering) and sediment source variability (from εNd) during different time intervals.

In this chapter, the radiogenic isotope records present different patterns (Figure 5.14b). Previous studies have documented the use of both εNd and $^{87}Sr/^{86}Sr$ isotopes as provenance indicators (e.g. Jung *et al.,* 2004; Meyer *et al.,* 2011; Noble *et al.,* 2012), however due the potential biases outlined in Chapter 3 which can affect $^{87}Sr/^{86}Sr$ isotopes, the records of radiogenic isotopes sometimes need disentangling. The MD20-3591 εNd record reflects long term changes in river discharge provenance, as a result of a combination of the local insolation and latitudinal ITCZ shifts, however, the $^{87}Sr/^{86}Sr$ signal shows shorter variability, likely reflecting more abrupt changes in the hydroclimate variability. As the $^{87}Sr/^{86}Sr$ isotopes were measured on the same grain size fraction (<2 µm), the grain size effect is considered negligible (Meyer *et al.,* 2011). This implies the <2 µm fraction is reflecting the source area variability and thus recording a provenance signal faithfully supported by other studies (Bayon *et al.,* 2015; van der Lubbe *et al.,* 2016; Beny *et al.,* 2020; Simon *et al.,* 2020a). The $^{87}Sr/^{86}Sr$ signal can operate at short timescales which is likely because of chemical weathering (Jung *et al.,* 2004). This means that chemical weathering, induced by higher precipitation in the catchment source region (on millennial-scale (see section 5.4.6.2)), is driving the $^{87}Sr/^{86}Sr$ signal from MD20-3591. The εNd provenance signals are reacting on a slower scale (insolation driven) which means the sediment does not fractionate during weathering regimes, and so εNd signals are ideal provenance tracers (Goldstein *et al.,* 1984; Blum and Erel, 2003; Fagel *et al.,* 2004; Fagel, 2007; Meyer *et al.,* 2011; Garzanti *et al.,* 2014; van der Lubbe *et al.,* 2014; Hahn *et al.,* 2016; van der Lubbe *et al.,* 2016; Hahn *et al.,* 2018).

Previous work has highlighted the possibility of picking up terrestrial signals through radiogenic isotopes systems in marine sediment cores located offshore of river catchments. For example, the radiogenic isotope composition of sediment core TPC290 (55.55°S, 45.02°E) during both the Holocene and the LGM suggests that Patagonia is the dominant

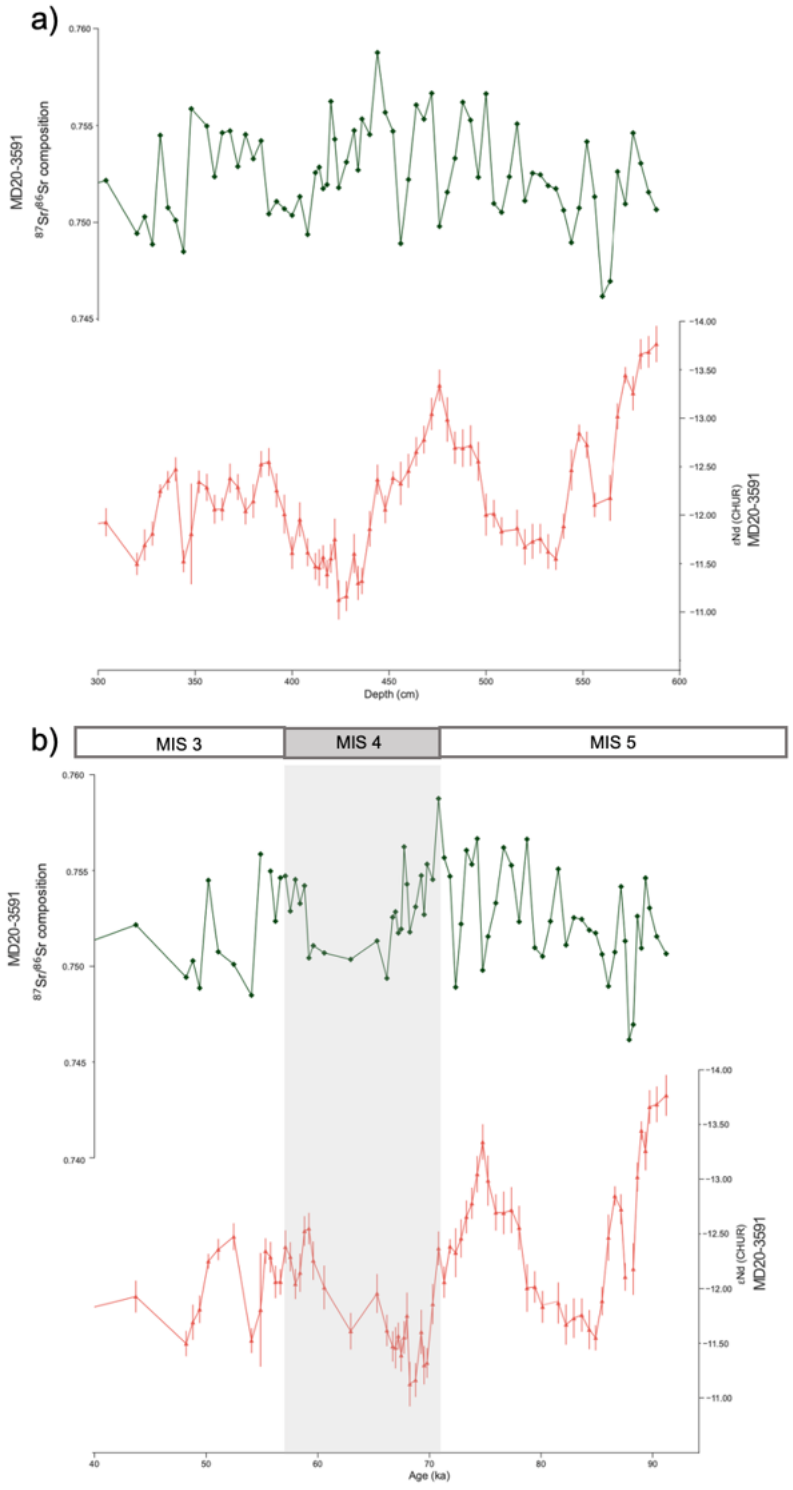

Figure 5.14: Down core radiogenic isotope reconstructions from core site MD20-3591 for a) the depth range of 300 to 588 cm, b) age range of 90 to 40 ka. The $^{87}Sr/^{86}Sr$ isotope composition (green) and εNd (red). Both isotope systems were measured on the lithogenic clay fraction (<2 µm) of sediment. Age record is presented on Speleothem chronology.

source of sediment in the northern Scotia Sea (Diekmann *et al.,* 2000; Walter *et al.,* 2000; Noble *et al.,* 2012). Closer to the study region of South Africa and marine sediment core site MD20-3591, van der Lubbe *et al.* (2016) find an increase in distinctly unradiogenic εNd Zambezi suspension load with precession maxima during the last glacial, suggesting monsoon precipitation is forced and enhanced during periods of increased Southern Hemisphere insolation and high latitude Northern Hemisphere climate variability (van der Lubbe *et al.* 2016). Earlier work tracing the $^{87}Sr/^{86}Sr$ ratios of numerous cores offshore South Africa reveals changes in Agulhas Current strength between the Holocene and LGM (Franzese *et al.,* 2006). The study finds a lower $^{87}Sr/^{86}Sr$ ratios in the LGM in the Agulhas Passage, which was interpreted to imply a reduced input of older rock sources (Agulhas sourced), suggesting a weaker Agulhas Current during the LGM (Franzese *et al.,* 2009). Local South African river sediment is less radiogenic (lower $^{87}Sr/^{86}Sr$ ratios and higher εNd), because the coastal rivers drain geologically younger rock types compared to further North, i.e. the Limpopo and Zambezi rivers (Chapter 3). The South African river catchments supplying sediments to marine core site MD20-3591 are located in-land and extend towards the coast. These local South African rivers supply a total of $\sim 10\text{x}10^6 m^3$ of terrigenous sediment flux to the Southwest Indian Ocean annually (Flemming, 1981; Rooseboom *et al.,* 1992). The Limpopo river located in Mozambique has a larger river catchment area (408,000 km^2) associated with sediment input with a signature of older, more radiogenic higher $^{87}Sr/^{86}Sr$ ratios, (lower εNd) (see Chapter 3). The provenance of marine sediment deposited at site MD20-3591 is likely a mixture of local South African sourced material and offshore Limpopo river material (Figure 5.15). This is because most sediment sits on the new linear mixing line between these two data clusters (Figure 5.15; yellow and green represent two radiogenically distinct source areas from South African rivers and the grey cross represents an offshore Limpopo endmember (calculated using the algorithm discussed in Chapter 3)). Despite this linear mixing approach, during any given interval it is unlikely that site MD20-3591 is only picking up a source from a single river, as mixing does occur between sources. There is more variability on the εNd axis between MIS 5 and MIS 4 compared to the $^{87}Sr/^{86}Sr$ axis. Sediment from MIS 5 (purple triangles; Figure 5.15) sits lower (on the εNd axis) than the MIS 4 sediments which sit above (on the εNd axis) and on the implied mixing line between the South African rivers and Limpopo river, (with some outliers below the line) indicating a more local South African input during MIS 4 and/or weaker transport from an upstream source such as the Limpopo river. This suggests there was a change in sediment provenance during MIS 4, from MIS 5 likely associated with a change in on-land hydrology influenced by global climate in MIS 4.

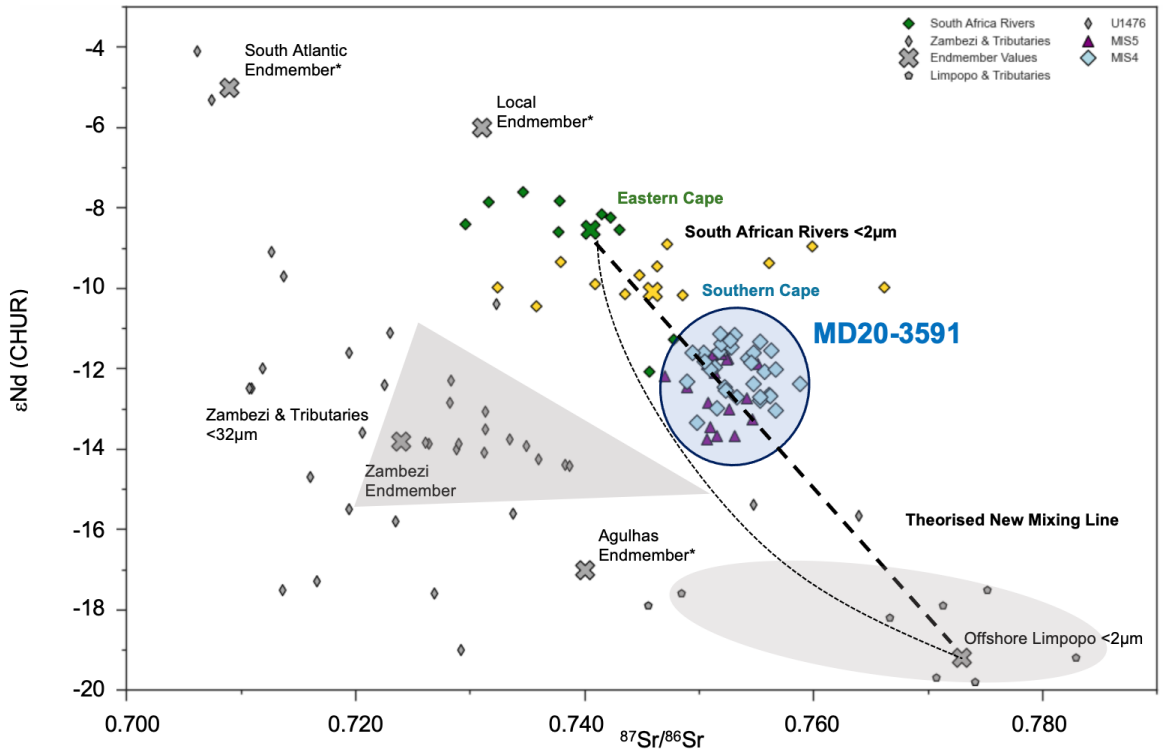

Figure 5.15: Sr-Nd ratios mixing plot based on linear regression between South African river sediments (Chapter 3) and sediment sources offshore of the Limpopo. All published data in grey, these are offshore Limpopo (Simon *et al.,* 2020a), Zambezi and Tributaries (Garzanti *et al.,* 2014), U1476 (van der Lubbe, pers comms). Endmembers with asterisks, from Franzese *et al.* (2006). Limpopo, Zambezi, eastern Cape and southern Cape endmembers generated in Chapters 3 and 4.

5.4.6 South Africa Hydroclimate Patterns at Different Timescales

As mentioned above, the radiogenic isotope records from MD20-3591 provide a reconstruction of provenance changes (εNd) and chemical weathering ($^{87}Sr/^{86}Sr$ ratios) in sediment at this location. In combination with other proxies linked with sediment geochemistry and changes in sediment input, an opportunity arises to investigate the link between hydroclimate changes, orbital precession dominance, and remote signals from the Southern Hemisphere.

5.4.6.1 Long Term Climate Variability

In MIS 5, at maximum 30°S summer insolation ($\sim$ 93 ka MIS 5b-5c), XRF PC1 signals are higher in terrestrial elements (Figure 5.16b), mirrored in a marked increase in ln(Fe/K) ratios at sites CD154-10-06P and CD154-17-17K (Figure 5.16d, e) respectively. XRF PC1 values decrease towards more biogenic sediment input at 30°S summer insolation minima ($\sim$ 82 ka MIS 5a), much like ln(Fe/K) ratios seen in CD154-10-06P and CD154-17-17K. Previous records suggest less terrestrial input from South Africa to the marine realm during Southern Hemisphere summer insolation minima as a result of migrations of the

ITCZ and associated rain-belts (Ziegler *et al.,* 2013; Simon *et al.,* 2015a). The strong similarities between these discussed core sites and site MD20-3591 suggests that sediment supplied to site MD20-3591 (from the southern Cape) during MIS 5 is driven by the same mechanism, i.e. 30°S summer insolation changes.

The MD20-3951 εNd record also follows the 30°S summer insolation during MIS 5 and into MIS 4 (Figure 5.16c). High εNd values exist during low 30°S summer insolation, and low εNd values during high 30°S summer insolation and increasing εNd values into MIS 4, from 75 ka to 65 ka respectively. The shift in the εNd signal suggests that sediment supplied to site MD20-3591 during MIS 5 high 30°S summer insolation intervals reflect the provenance from the Limpopo source whereas during low 30°S summer insolation local South African sources dominate. The εNd record is inferred as showing changes in the river catchments over longer insolation modulated timescales. This means over orbital time scales, rainfall and discharge changes in the Limpopo catchment result from a combination of local insolation and latitudinal ITCZ shifts documented in the MD20-3591 εNd record.

At the beginning of MIS 4, with increasing 30°S summer insolation, there is a transition towards higher εNd record which suggests the enhanced supply of radiogenic εNd sediments supplied from the local rivers. In southeastern Africa, similar precession paced climate patterns (Partridge *et al.,* 1997) have been explained by the African tropical rain belt being drawn southwards as it tracks maximum summer insolation (Partridge *et al.,* 1997) or the rain belt being displaced southwards in response to cooler conditions in the Northern Hemisphere (Schefuß *et al.,* 2011). The rain-belt location varies depending on the position of the ITCZ, when the rain-belt is more southerly, we see a dominance in Limpopo provenance. This is supported by other studies such as the XRF ln(Fe/Ca) record from site MD96-2048 which shows that high insolation caused more Limpopo discharge (Caley *et al.,* 2018). Studies from offshore the Zambezi region find the Zambezi suspension load follows precession forced monsoon precipitation, during low Northern Hemisphere climate variability and increased Southern Hemisphere insolation (van der Lubbe *et al.,* 2016). Dupont *et al.* (2021) find that during Southern Hemisphere summer insolation maxima, the insolation gradient is reduced causing the westerlies to shift southward and summer rainfall to increase, but rainfall in the winter zone to decrease. Conversely during Southern Hemisphere summer insolation minima, when the latitudinal gradient is stronger, this induces stronger westerlies which results in more precipitation in the winter rainfall zone, and less in the year-round rainfall zone (Dupont *et al.,* 2021). These findings are in broad agreement with our work, which is that minima 30°S summer insolation ($\sim$ 82 ka) induces more locally sourced rainfall, whereas during 30°S summer insolation maxima ($\sim$ 72 ka), there is a stronger Limpopo dominance. This means that the Limpopo catchment is experiencing wetter conditions from the southward shifting

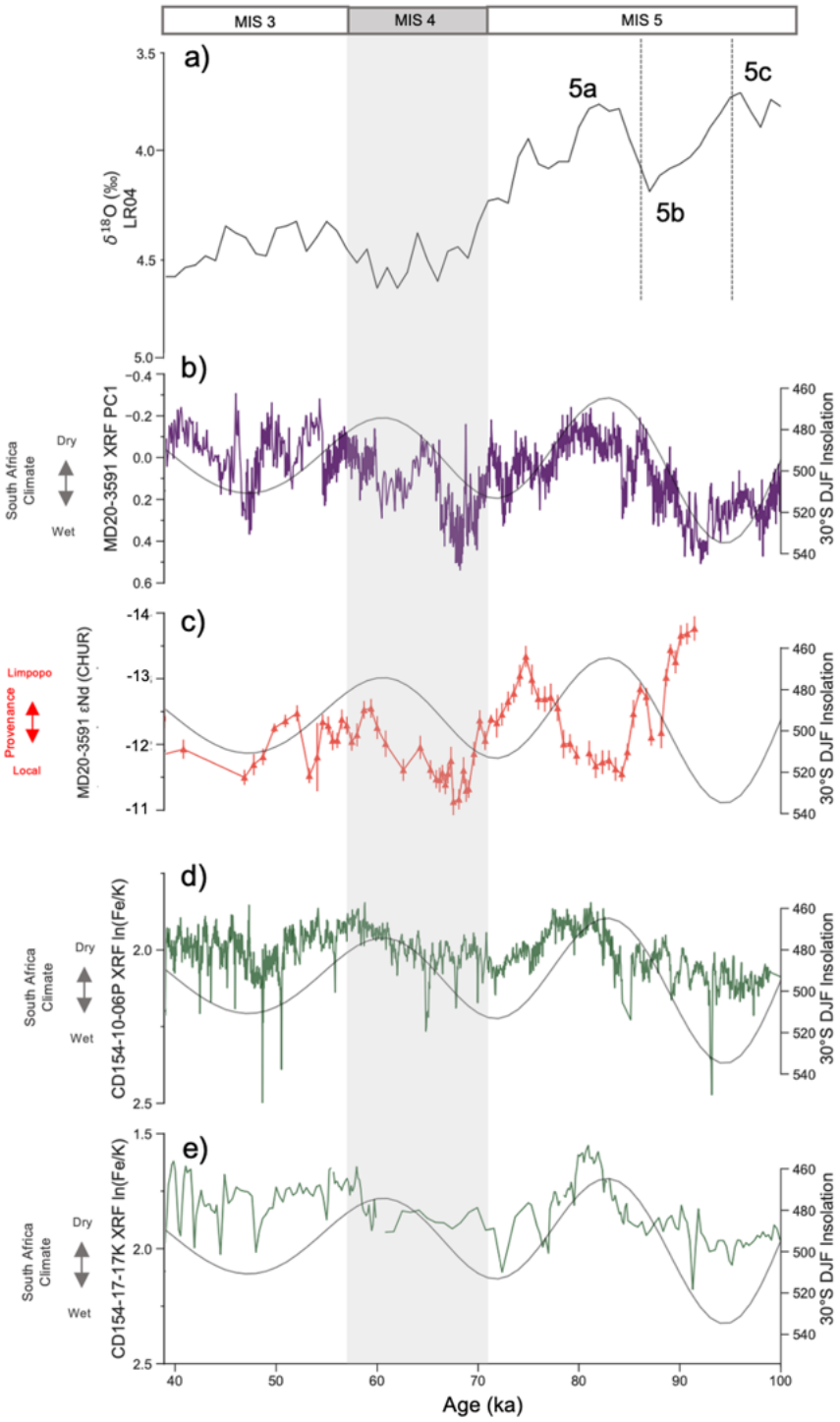

Figure 5.16: Comparison of 30°S summer (DJF) insolation (grey) and (a) LR04 (Lisiecki and Raymo, 2005), (b) MD20-3591 XRF PC1 (purple), (c) MD20-3591 εNd (red), (d) XRF scanning ln(Fe/K) (CD154-10-06P) (Simon *et al.,* 2015a) (green), (e) XRF scanning ln(Fe/K) (CD154-17-17K) (Ziegler *et al.,* 2013). MD20-3591 data are presented on the Speleothem Age Model.

rain-belts. Records from Wonderkrater located in land from the Limpopo river reveal that at $\sim$ 70 ka, wetter conditions are experienced, this is in line with the MD20-3591 εNd record (Puech *et al.,* 2017).

5.4.6.1.1 MIS 4 in South Africa

Wetter conditions prevailed in the South African river catchments during MIS 4. This is based primarily on higher εNd values in site MD20-3591 (Figure 5.16) which suggests a more local South African source. New evidence based on high resolution climate modelling in the Southern Cape and biomarker proxy (leaf wax) records from Blombos Cave support the finding of wetter river catchments in South Africa during MIS 4 (Figure 5.17) (Göktürk *et al.,* 2023a). Results from Götkürk *et al.* (2023b) indicate that during sea level low stands in MIS 4, the hydroclimate of the South African coastline was significantly more arid and continental whereas the interior of South Africa experienced more humid conditions (Figure 5.17). This is due to competing mechanisms which include the shifting coastline and the PAP exposure which have a strong influence on the coastal zones versus orbital precession forcing dominating the South African inland climate signals (Göktürk *et al.,* 2023a).

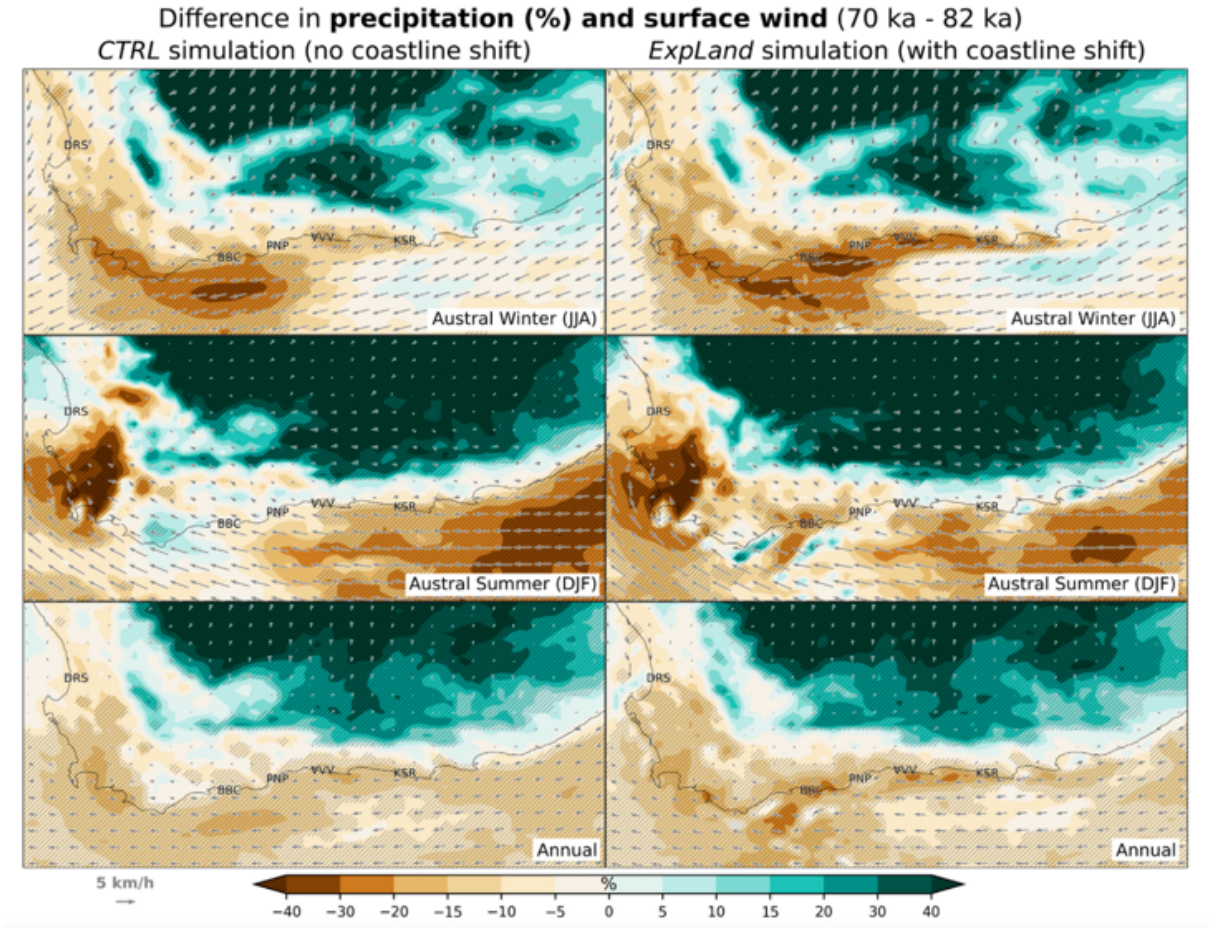

Figure 5.17: Climate modelling results from Götkürk *et al.* (2023b) showing a mean precipitation change (%) (over 30 years) and surface winds (shown by arrows) from 82 to 70 ka for the southern Cape region. The simulated output from the control is shown in the left panel and the climate effects from the exposed land is shown in the right panel. Statistically significant differences in temperature (t-test, 95% confidence level) are hatched. Present coastline is plotted. Figure taken from Götkürk *et al.* (2023b).

These modelling results suggest the possible influence of sea level on sediment supply to the Agulhas Passage region and especially to core site MD20-3591. In addition to a more local MD20-3591 εNd signal suggesting wetter conditions in South African river catchments and constant or less Limpopo river supply, the MIS 4 glacial is also associated with an increase in coarse sediment (EM1) at marine sediment core site MD20-3591 (Figure 5.12). This shift in both radiogenic isotopes, grain size and XRF PC1 records from site MD20-3591 towards more local sediment signals during MIS 4 corresponds with a suite of evidence describing a lower sea level caused by increased Northern Hemisphere ice volume during MIS 4 (Compton, 2011; Copeland *et al.,* 2016; Cawthra *et al.,* 2020b). Varying sea levels during MIS 4 affects the course of South African rivers along the exposed PAP (Cawthra *et al.,* 2020b). The presence of the PAP influences the distance between marine sediment core site MD20-3591 and the palaeoshoreline (Figure 5.18). These distances (km) were estimated using the QGIS measure line between the mouth

of the Gourritz river which was mapped in Cawthra *et al.* (2019) and site MD20-3591 (Figure 5.18). The Gourritz river was selected because it has a large runoff (488 x 10^6 m^3/year (Maitre *et al.,* 2009)) and its river mouth is 250 km located closest to site MD20-3591 during present day conditions. The distance between the Gourritz river mouth and site MD20-3591 was linearly scaled based on the distance (km) at a given sea level (m) and transferred to age (Figure 5.19). This shows that during sea level low stands (such as MIS 4), the Gourritz river (and palaeoshoreline) was 100 km closer to site MD20-3591 and coarser sediment was deposited in core site MD20-3591 based on grain size EM1 (Figure 5.19).

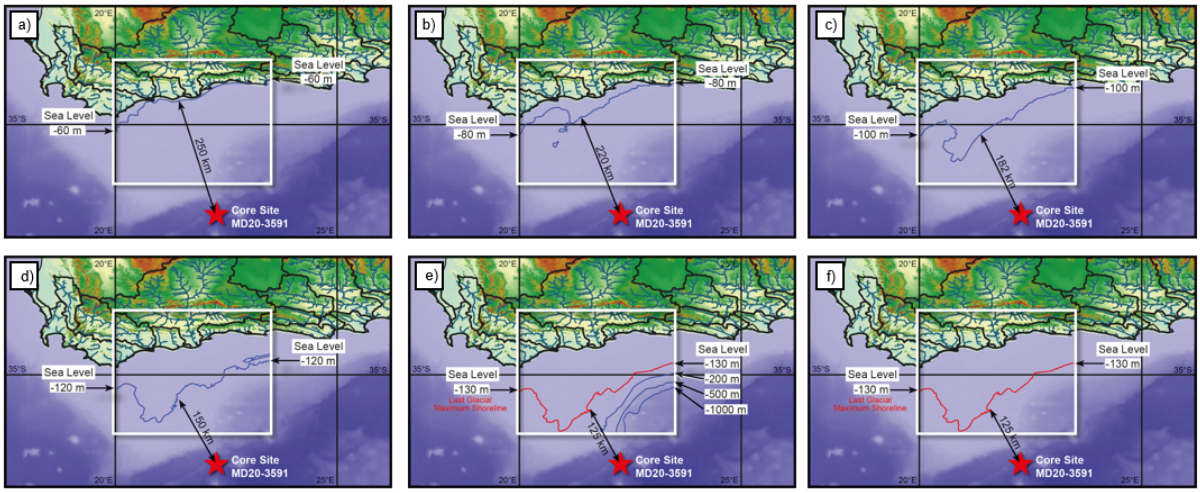

Figure 5.18: Sea level low stand Palaeo-Agulhas Plain exposure simulation at varying sea level regression. Palaeoshoreline generated by overlaying shoreline from Cawthra *et al.* (2019). Each panel presents the shoreline simulated at a palaeo sea level (a) -60m, (b) -80m, (c) -100m, (d) -120m, (e) -130m (LGM shoreline, -200m, -500m, -1000m, (f) -130m (LGM shoreline). The arrow represents distance the Gourritz river mouth (largest catchment in southern Cape) to core site MD20-3591. The distance was calculated on QGIS using the measure line (km).

Advancing on the understanding that the shoreline was closer to site MD20-3591 during MIS 4 sea level low stands, it is possible to assess the coupling between sea level and grain size at site MD20-3591. A sliding window is a technique employed to analyse a sequence of data points by moving a fixed-size window over the data, often with an overlapping mechanism. The sliding-window size is the number of data points the analysis iterates through (in this case the number of data points corresponds to either 30 kyr or 45 kyr). Sea level and grain size records are shown along with a sliding window correlation coefficient between the two records (Figure 5.19). The sliding window correlations reveal intervals of pronounced coupling (strong positive correlation) where lower sea level accompanies coarser sediment input and vice versa during decoupling (Figure 5.19). It is important to note that the timing of these intervals is somewhat sensitive to the sliding-window size used for the sliding correlation.

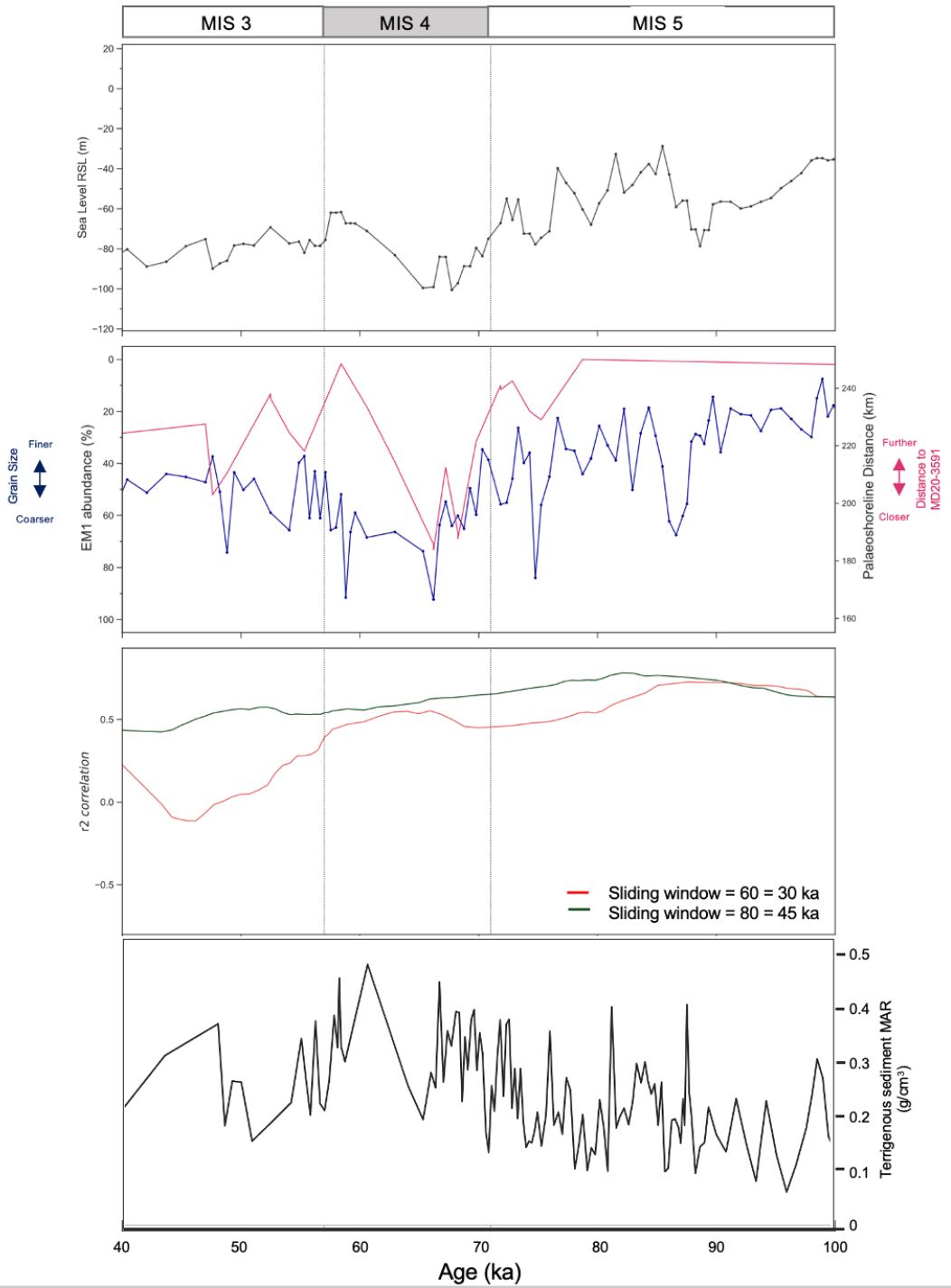

Figure 5.19: Coupling of sea level (Grant *et al.*, 2014) and grain size EM1 (%). The top two panels show the downsampled sea level curve (grey) and EM1 (%) (blue). The modelled palaeoshoreline distance between the Gourritz river mouth and site MD20-3591 is indicated by the pink line. The bottom panel shows the sliding window cross-correlation (r^2) for sea level vs EM1 (red = 30 ka; green = 45 ka) based on sliding window length. Mass Accumulation Rate (MAR) of the terrigenous fraction of sediment (black).

The sea level impact mostly dominates the grain size record, based on sliding window results. Especially, during the LMSA, there is a strong positive correlation between grain size and sea level (Figure 5.19). This is because the coastline regressed substantially

from 82 to 70 ka due to a ∼ 40 m decrease in global sea level (Grant *et al.,* 2014). During this time, lower sea level is accompanying a coarser grain size signal (Figure 5.19). Further to this, lead-lag analysis was performed for the time interval of 82-70 ka to determine whether sea level is leading or lagging the grain size signal in MD20-3591. When sea level was lowest at ∼ 68 ka (Grant *et al.,* 2014), it had a positive correlation with grain size (Figure 5.19) and a leading relationship, based on the phase shifts (Figure 5.20). At ∼ 68 ka the shoreline was ∼ 187 km from MD20-3591 (Figure 5.18), it is therefore likely that the sea level shifts and the distance between the palaeoshoreline and site MD20-3591 are modulating sediment transport to the core site which is observed in the grain size signal during this interval. Finally, the palaeoshoreline reconstruction (Figure 5.18) reveals during lower sea levels, the palaeoshoreline was closer to site MD20-3591, with coarser (based on grain size) more local sediment (based on εNd) during MIS 4 and an increased mass accumulation rate (MAR) of terrigenous sediment (Figure 5.19). The MAR is additional evidence showing the effect of palaeoshoreline distance on river sediment input recorded in MD20-3591 and how during sea level low stands, more terrigenous sediment is recorded in the marine core site.

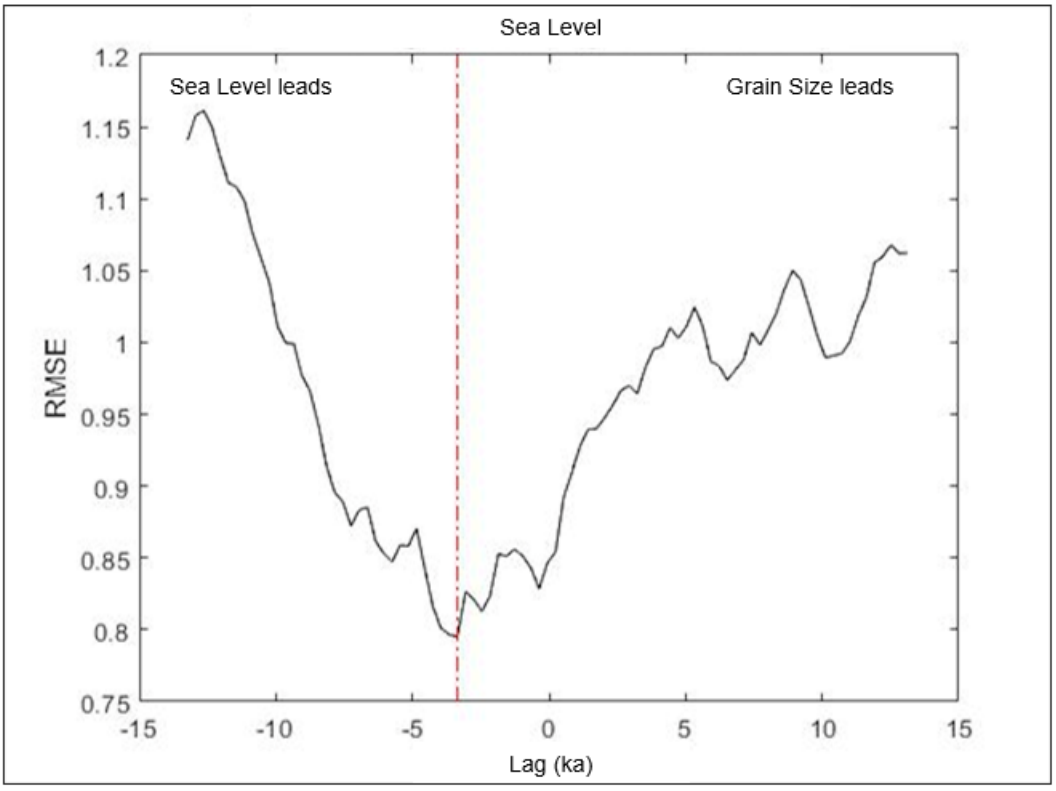

Figure 5.20: Lead lag correlation (root mean square) between sea level from Grant *et al.* (2014) and grain size EM1 performed on Acycle (Li *et al.,* 2019), a negative lag corresponds to sea level leading over EM1 for 82-70 ka.

During MIS 4, additional evidence based on higher XRF PC1 and sediment source contribution modelling suggests more terrestrial sourced sediment in MD20-3591 (Figure 5.16b).

Sediment source contribution modelling reveals more locally sourced sediment from South Africa at 70 ka and during MIS 4 (Figure 5.21). This indicates that the climate in the river catchments of South Africa was more humid. The modelling results from Goktürk *et al.* (2023) during their study period of 82 to 70 ka find there is a shift to more humid conditions in the interior of South Africa, largely driven by orbital forcing. The $^{87}Sr/^{86}Sr$ and εNd records from site MD20-3591 during MIS 4 supports the climate modelling results (Göktürk *et al.,* 2023a). The εNd record reflects provenance with more local signals during MIS 4 whereas lower $^{87}Sr/^{86}Sr$ ratios indicate higher weathering regimes in South Africa (based on Chapter 3 river catchment $^{87}Sr/^{86}Sr$ ratios) which suggests more rainfall during this time interval (Figure 5.22(f)). The lower $^{87}Sr/^{86}Sr$ values observed in site MD20-3591 fall within the Sr data range from the South African river sediments (Chapter 3). This humidity pattern is further explored using chemical weathering indices (Figure 5.22). Based on two samples with ages $\sim$ 88 ka and $\sim$ 78 ka, the chemical weathering results follow the same pattern as the $^{87}Sr/^{86}Sr$ record (i.e. more chemical weathering with a lower $^{87}Sr/^{86}Sr$ ratio).

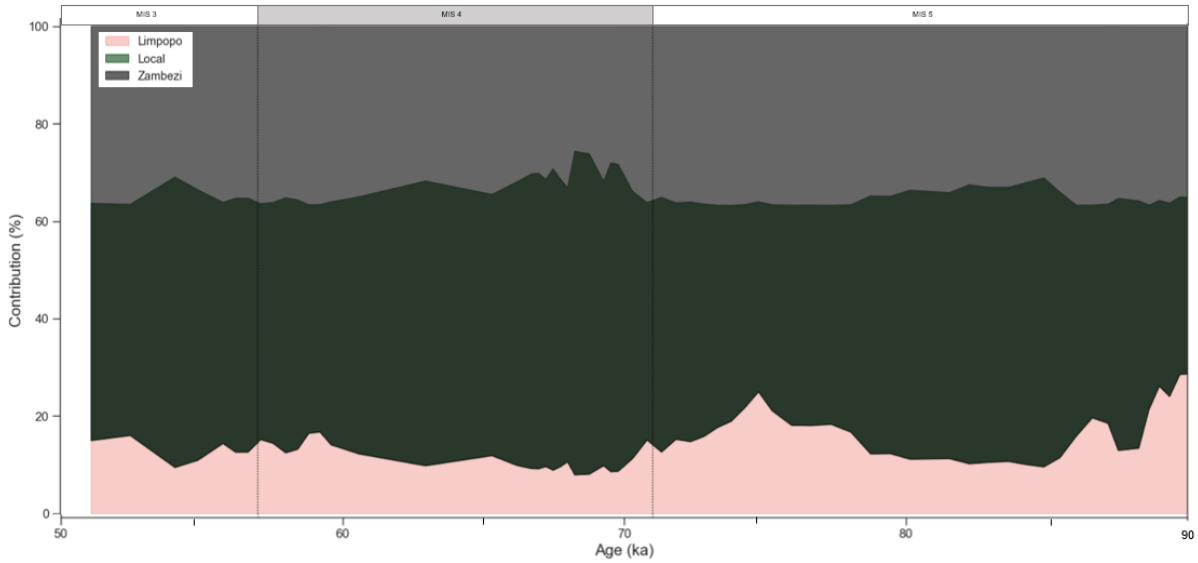

Figure 5.21: Sediment source apportionment for key sediment sources (pink: Limpopo, green: Local, grey: Zambezi for 90-53 ka. Mixing model generated using endmember values computed in Chapter 3 inputted based on the Bayesian mixing model EMMTE.

Increased humidity during MIS 4 in South Africa coincides with a suite of evidence from multiple proxies and locations in South Africa which show wetter conditions prevailed, these include terrestrial archives from the southwestern Cape (Stuut *et al.,* 2002; Chase and Meadows, 2007). These records show sand dune development with increasing atmospheric circulation intensity. Speleothem records from Crevice Cave show increased winter rainfall during MIS 4 interpreted as a change of rainfall seasonality (Figure 5.22) (Bar-Matthews *et al.,* 2010). Several studies from South Africa additionally show that the $\delta^{18}O$ speleothem record represents South African seasonality (Braun *et al.,* 2019;

Maccali *et al.,* 2023). During MIS 4, increasingly dominant winter rainfall is observed in other records from South Africa such as; the phytolith assemblages from Varsche Rivier, Southwest Africa (Mackay *et al.,* 2022) which indicates an increasingly dominant winter rainfall regime across the MIS 5/4 transition. At Oyster Bay, near Klasies River (another key Middle Stone Age archaeological site (Figure 5.1)), pollen spores indicate substantial increases in grass-type pollen (Carrion *et al.,* 2000) indicating in the first case more rainfall/ more regular rainfall, and secondly, a cooler growing season and/or increased winter rainfall in the year round zone.

At the beginning of MIS 4 ($\sim$ 72 ka), the ITCZ is more southerly (Nicholson and Flohn, 1981; Johnson *et al.,* 2002; Chiang *et al.,* 2003; Schefuß *et al.,* 2011; Hahn *et al.,* 2017) in response to high (low) summer insolation in the Southern (Northern) Hemisphere and a warmer (colder) Southern (Northern) Hemisphere, allowing rainbelts to shift further south and reach further inland along the southeast coast (Johnson *et al.,* 2002; Schefuß *et al.,* 2011; Ziegler *et al.,* 2013; Simon *et al.,* 2015a) (Figure 5.23). During MIS 4, from 72 ka to 58 ka, the SHW are believed to shift northward (van Zinderen Bakker, 1967; van Zinderen Bakker, 1976; Cockcroft *et al.,* 1987; Shi *et al.,* 2000; Stuut, 2004; Chase and Meadows, 2007; Anderson and Burckle, 2009; Sigman *et al.,* 2010; Neumann and Scott, 2018), in response to increased Antarctic sea ice (Anderson and Burckle, 2009; Sigman *et al.,* 2010; Hahn *et al.,* 2020; Miller *et al.,* 2020; Starr, *et al.,* 2021). In such a scenario, temperate systems related to the westerly wind belt bring moisture to South Africa, shifting high pressure cells further inland of South Africa and resulting in more humid conditions (Figure 5.23). The STF and associated winter storm tracks likely modulate winter rainfall in South Africa, with a more northward shift associated with increased precipitation through low pressure cells (Figure 5.23) (Hahn *et al.,* 2020). This is communicated through temperate-tropical troughs (TTTs). An increased development of TTTs causes an increased temperature gradient between the pole and equator, leading to increased oceanic and atmospheric circulation intensity (Little *et al.,* 1997) and an increase in moisture transport from low to high latitudes (Vimeux *et al.,* 1999; Sachs *et al.,* 2001). This mechanism may have operated in isolation, or as part of a more dynamical system, where frontal systems were brought into more direct association with tropical lows – favoured by increased Southern Hemisphere summer insolation to form TTTs (Carr *et al.,* 2023), driving enhanced winter rainfall over southern Africa.

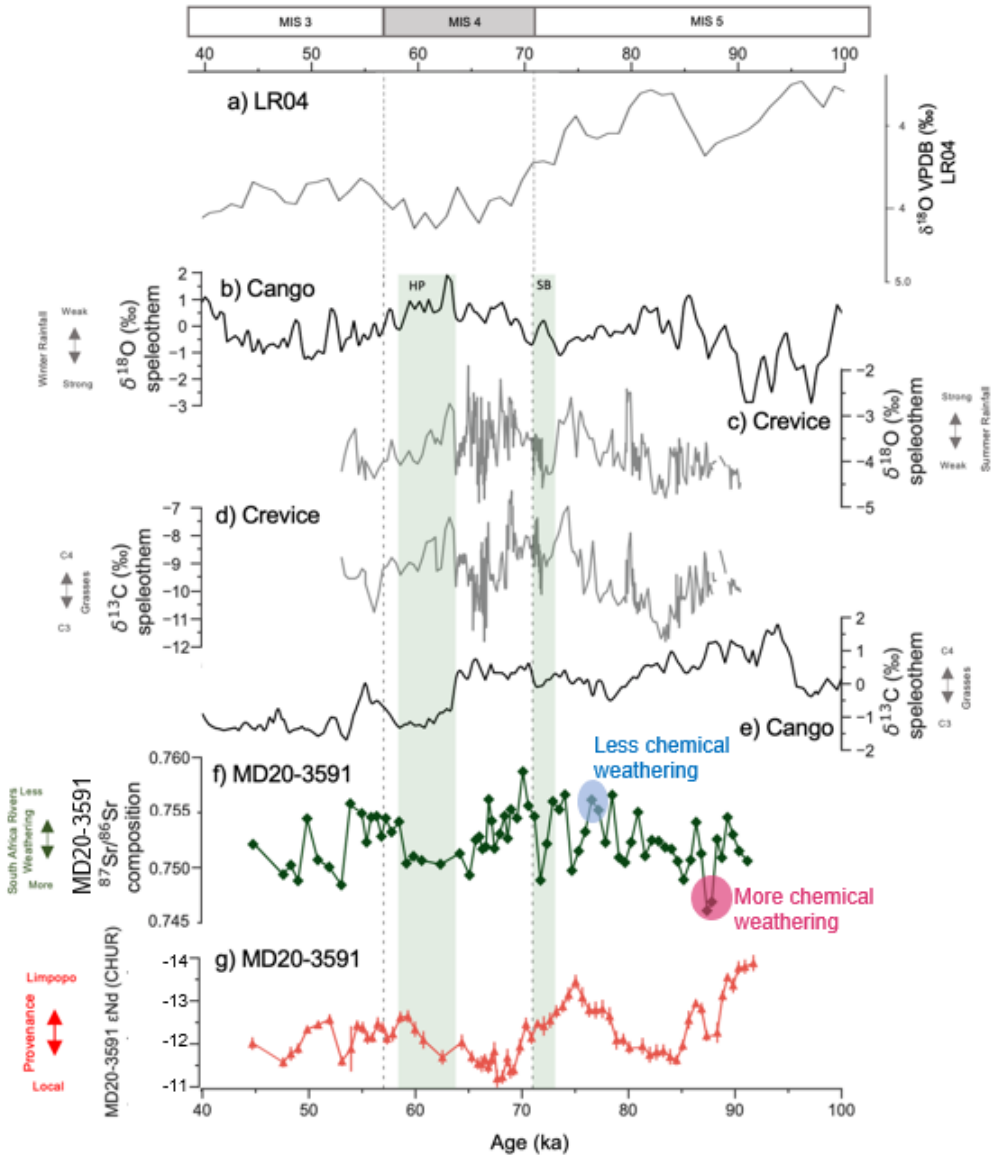

Figure 5.22: Climate Variability during the LMSA, (a) LR04; Liseicki and Raymo, (2005), (b) Cango Cave δ^{18}O speleothem record (Chase *et al.,* 2021), (c) Crevice Cave δ^{18}O speleothem record (Bar-Matthews *et al.,* 2010), (d) Crevice Cave δ^{13}C speleothem record, (e) Cango Cave δ^{13}C speleothem record, (f) MD20-3591 ^{87}Sr/^{86}Sr isotope composition (green), the chemical weathering indices are depicted as circles on the associated sample age range, (pink = more chemical weathering, blue = less chemical weathering), (g) MD20-3591 εNd record (red). MD20-3591 records presented on the Speleothem Chronology. SB = Still Bay and HP = Howiesons Poort industries indicated by vertical green bars.

Mechanisms for this increase in winter rainfall during MIS 4 are all related to shifts in the SHW (van Zinderen Bakker 1967; van Zinderen Bakker, 1976; Cockcroft *et al.,* 1987; Shi *et al.,* 2000; Stuut, 2004; Chase and Meadows, 2007; Anderson and Burckle 2009; Sigman *et al.,* 2010; Neumann and Scott, 2018), forced by a northward Antarctic sea ice edge. These shifts are documented in the following records during MIS 4; the STF record (ALF); (Peeters *et al.,* 2004)), the EDML sea salt Na flux (Fischer *et al.,* 2007) and the Southeast Atlantic wind strength composite (Chase *et al.,* 2021) (Figure 5.24). The

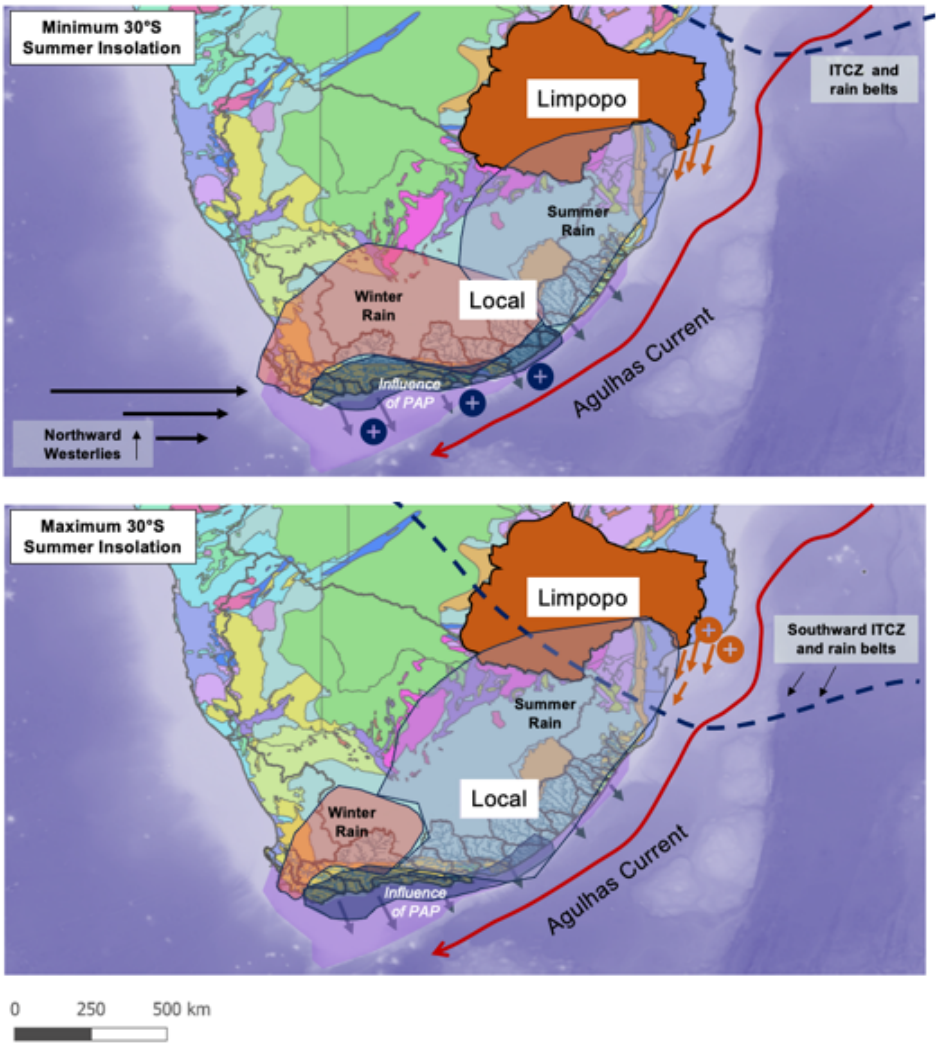

Figure 5.23: Conceptual Model of precipitation shifts during minimum 30°S summer insolation (e.g. ∼ 82 ka) (top) and maximum 30°S summer insolation (e.g. ∼ 72 ka) (bottom). Coastal zone influenced by PAP for both climate conditions. During 30°S summer insolation minima, more winter rain (orange) influenced by low pressure systems related to the northward shift of Southern Hemisphere Westerlies coincident with more local sediment input (blue crosses). During 30°S summer insolation maxima, summer rainfall expanded, influenced by southward shifting ITCZ and more Limpopo sediment supply (orange crosses). MD20-3591 core site indicated by red star and Agulhas Current trajectory by red arrow. Conditions during MIS 4 change from maximum 30°S summer insolation at the beginning (∼ 72 ka) towards minimum 30°S summer insolation for the remaining glacial period.

variability of the regional circulation system is best presented in the ALF record from Peeters *et al.* (2004), which covers the LMSA period. Over several glacial-interglacial cycles, shifts in the subtropical front are simultaneous with ALF abundances; reductions in ALF coincide with northward shifts in the STF. Between 85 to 65 ka, there is an evident shift in the mean position of the STF, from southerly in late MIS 5 to a more northerly location in MIS 4 inferred from this ALF record. It is considered likely that cooler

SSTs along the coast influenced the moisture balance and local advection, subsequently altering the structure of the region's circulation systems and increasing the strength of the westerly storm tracks (Reason *et al.,* 2002). This may have resulted in more frequent rain associated with temperate systems in southern Africa. A close correlation between the position of the STF and changes in humidity inferred from MD96-2094 (Stuut *et al.,* 2002), and a decline in ALF abundance from 80 to 74 ka may well be influenced by the STF migration. The EDML sea salt Na flux from Fischer *et al.* (2007) is a good representation of the Antarctic Sea ice edge, with enhanced ssNa flux from 85 to 65 ka (Figure 5.24). The Southeast Atlantic wind strength composite (Chase *et al.,* 2021) reveals enhanced Southeast Atlantic winds, coinciding with the STF migrating northward. This composite is calculated in Chase *et al.* (2021) using existing data (Little *et al.,* 1997; Stuut *et al.,* 2002; Farmer *et al.,* 2005; Pichevin *et al.,* 2005). These aforementioned climate proxy records all present indications of northward frontal systems during MIS 4 (van Zinderen Bakker, 1967; van Zinderen Bakker, 1976; Cockcroft *et al.,* 1987; Shi *et al.,* 2000; Stuut, 2004; Chase and Meadows, 2007; Anderson and Burckle, 2009; Sigman *et al.,* 2010; Neumann and Scott, 2018) (Figure 5.24) and support the notion that the SHW are an additional winter rainfall source, possibly in combination with the more southerly ITCZ (Nicholson and Flohn, 1981; Johnson *et al.,* 2002; Chiang *et al.,* 2003; Schefuß *et al.,* 2011; Hahn *et al.,* 2017) at the beginning of MIS 4 during maximum 30°S summer insolation.

The consistent pattern of more local South African river input (inferred from $^{87}Sr/^{86}Sr$ ratios (more chemical weathering), εNd provenance and sediment source contribution mixing (Figure 5.21)) coinciding with more winter rainfall dominance in the year-round zone during MIS 4 (Carrion *et al.,* 2000; Shi *et al.,* 2000; Stuut *et al.,* 2002; Chase and Meadows, 2007; Mackay *et al.,* 2022) would have provided ideal conditions for more weathering within river catchments of the sourced sediment and enhanced fluvial discharge from the local South African rivers. This is further supported by increased supply of terrigenous material (XRF PC1; Figure 5.19), coarser sediment input likely sourced from nearby South African rivers between the Limpopo river and rivers included in Chapter 3 during lower sea levels in MIS 4 (Figure 5.24). This means during the LMSA South Africa experienced more humid conditions, how this links to our ancestor's cultural evolution during this interval is explored below.

5.4.6.2 Millennial-Scale Variability

Transitions from cold stadial conditions to warm interstadial conditions are short-term and extremely rapid, and another factor to account for is the age control and sampling resolution of our record. The temporal resolution of the MD20-3591 $^{87}Sr/^{86}Sr$ isotope record has an average time step of 1.14 kyr in MIS 3 and 0.58 kyr in MIS 4 and 5. Therefore millennial scale variability is not accounted for in MIS 3 as the age model is not

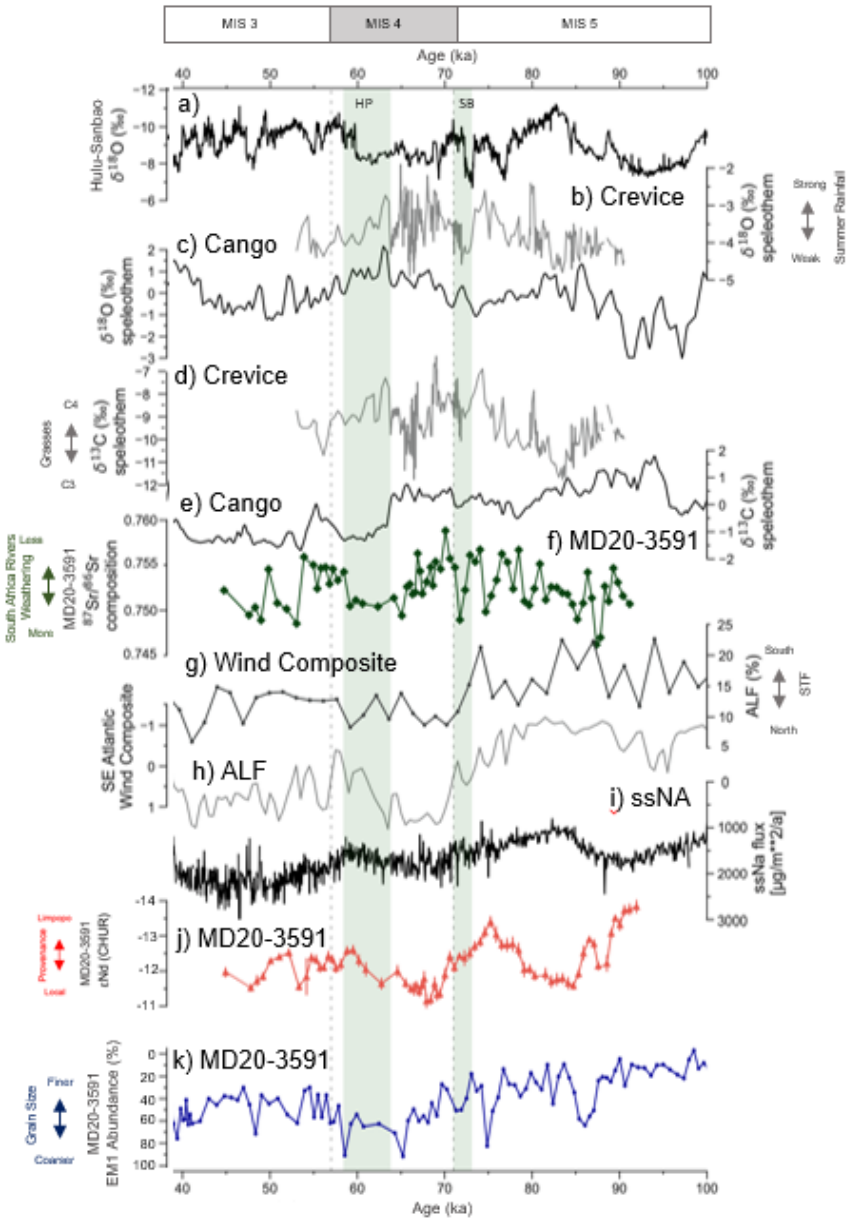

Figure 5.24: Climate variability during LMSA. Proxies showing mechanisms for humid conditions during MIS 4 (a) Hulu-Sanbao speleothem δ^{18}O, (b)Crevice Cave δ^{18}O speleothem record (Bar-Matthews *et al.,* 2010), (c) Cango Cave δ^{18}O speleothem record (Chase *et al.,* 2021), (d) Crevice Cave δ^{13}C speleothem record, (e) Cango Cave δ^{13}C speleothem record, (f) MD20-3591 ^{87}Sr/^{86}Sr isotope composition (green), (g) Agulhas Leakage Fauna record which shoes similarities to Subtropical Front (STF) migrations, (h) Southeast Atlantic wind strength composite record from Chase *et al.* (2021) and ref therein, (i) sea salt sodium flux (Fischer *et al.,* 2007), (j) MD20-3591 εNd (red), (k) MD20-3591 EM1 Abundance (%) (blue). All MD20-3591 records are presented on the Speleothem chronology.

capable of capturing this short-term variability. Spectral analysis reveals strong 1.4 kyr power cycles in the ^{87}Sr/^{86}Sr isotope record during MIS 5 and 4, above AR(1), and 1.26 kyr cycles is on the 95% certainty threshold, revealing significant shorter term variability in the ^{87}Sr/^{86}Sr isotope record (Figure 5.25).

On shorter timescales, Heinrich Stadials (HS), reflected in the ice rafted debris record in the North Atlantic Ocean (McManus *et al.,* 1999) are coupled with weak East Asian Monsoon conditions during the last glacial period (Cheng *et al.,* 2009; Barker *et al.,* 2011). This signal is propagated to the tropical latitudes via rearrangements of atmospheric circulation (Cheng *et al.,* 2009) and fluctuating heat budgets of the western Indian Ocean in conjunction with variable ocean-atmosphere heat and moisture (Zonneveld, 1997; Dupont *et al.,* 2011). Meridional shifts in the ITCZ are often proposed to explain the tight link between the African monsoon and northern high latitude climate change. Southward latitudinal migrations of the position of the ITCZ in response to Northern Hemisphere cooling forced either by large ice sheets (during glacials) (Braconnot *et al.,* 2007), or during AMOC slowdowns (such as HS) (Broecker, 1998; Ziegler *et al.,* 2013; Bohm *et al.,* 2015), are believed to result in an opposing rainfall pattern in both hemispheres. Finally, the association of humid phases over South Africa, with a northward shifting westerly wind belt and/or a southward shifting ITCZ, driven by abrupt cold events in the Northern Hemisphere likely leads to more chemical weathering in the South African river catchments sourcing sediment to MD20-3591.

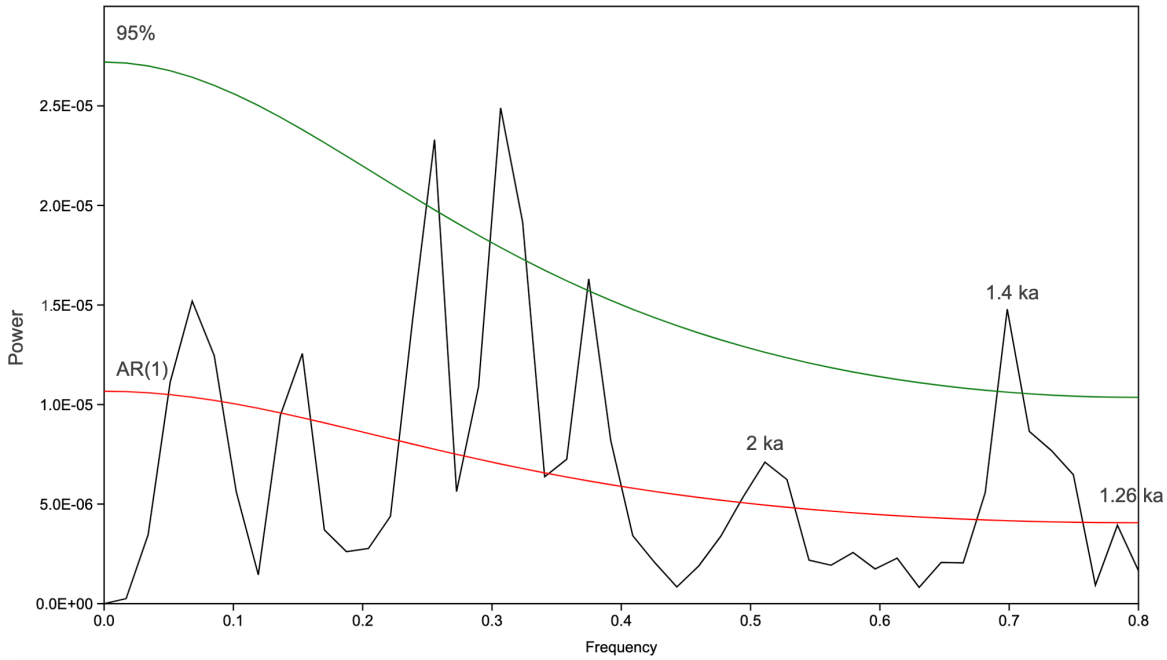

Figure 5.25: Spectral Frequencies from the $^{87}Sr/^{86}Sr$ record during MIS 5 and MIS 4. Key short-term frequencies indicated. AR(1) (green line) and 95% confidence (red).

The cold events preceding D-O events 19 and 20 in MIS 5 (at $\sim$ 72 ka and $\sim$ 77 ka respectively) are associated with wet conditions in South Africa, likely propagated by arrangements in atmospheric circulation dynamics (Schefuß *et al.,* 2011). During MIS 4, one Heinrich Stadial (HS 6) and three D-O events occurred, these were D-O 18, 17 and 16 (Figure 5.26). It is particularly evident that during the cold Northern Hemisphere intervals, the MD20-3591 XRF PC1 record increased, revealing more terrestrial sediment supply to site MD20-3591 and more humid conditions in South Africa coincided with weaker East Asian Monsoon (Figure 5.26). Additionally, the $^{87}Sr/^{86}Sr$ record shows a remarkable similarity to the structure of the millennial-scale events such as during MIS 5 and MIS 4 – D-O events 16 to 20 (Figure 5.26) that also fit dynamically with the interhemispheric signal propagation in that they indicate wet-dry successions between the records. This variation in the $^{87}Sr/^{86}Sr$ isotope variation is probably caused by changes in chemical weathering (Jung *et al.,* 2004). During colder North Atlantic cold events (Figure 5.26, grey vertical bars), lower $^{87}Sr/^{86}Sr$ signals are recorded, representing wetter conditions over South Africa and more chemical weathering, coincident with a drier East Asian summer monsoon. The timing of the wet phases in this study at 77 ka, 73 ka, 65ka, 63-58 ka, and 56 ka correspond roughly to the HS, HS6 $\sim$ 60 ka (Rasmussen *et al.,* 2014) and HS5a (56 ka, (Chapman and Shackleton, 1999) (Figure 5.26).

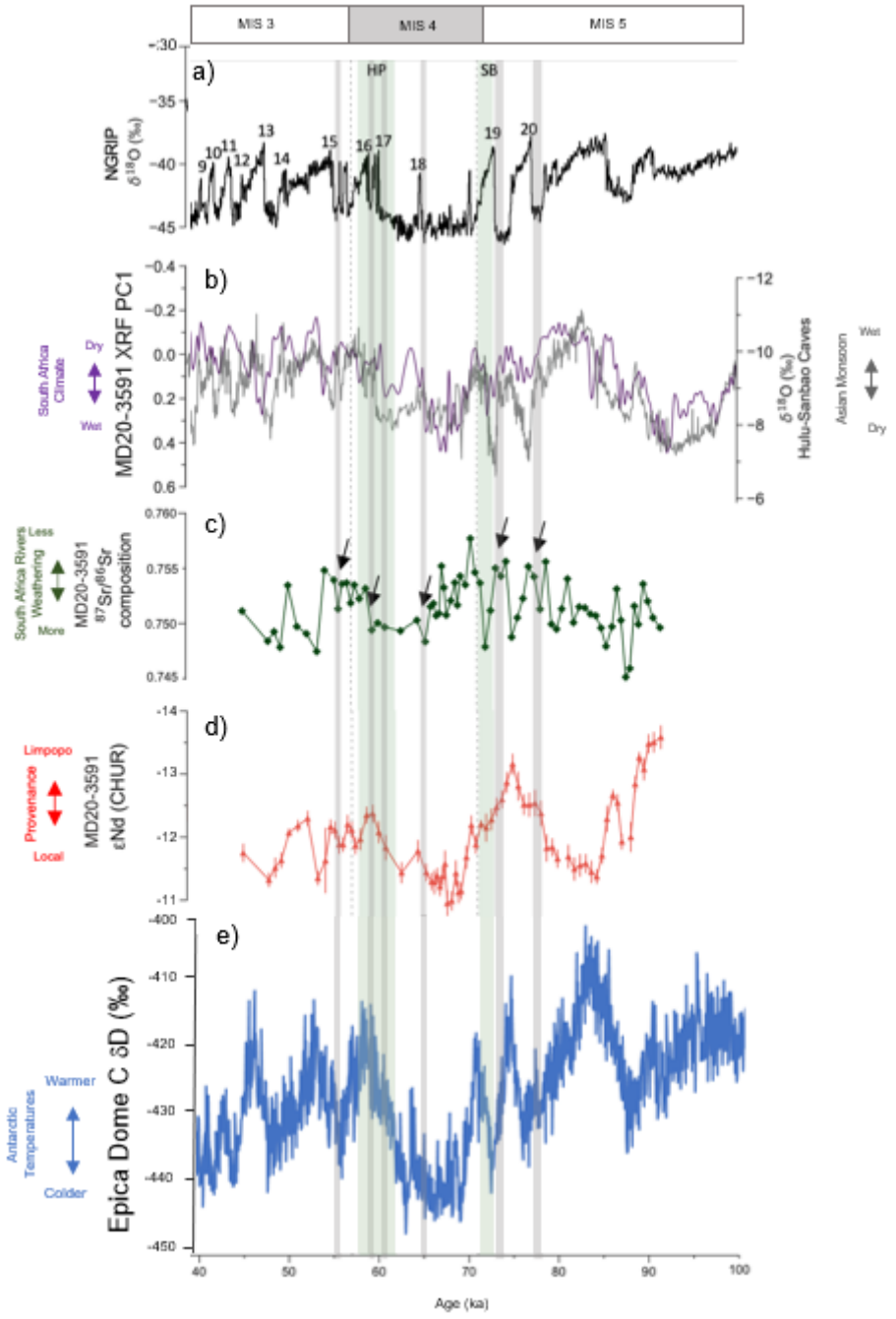

Figure 5.26: Millennial Scale Variability during the LMSA period, (a) NGRIP record, (b) PC1 (purple) compared to Hulu Sanbao cave speleothem record (Cheng *et al.,* 2016), (c) $^{87}Sr/^{86}Sr$ record from MD20-3591 (green), (d) εNd (MD20-3591) (red). (e) Epica Dome C (EDC) δD record from Jouzel *et al.* (2007). All MD20-3591 records are presented on the Speleothem chronology. Grey vertical bars represent cold events during LMSA period and numbers indicate D-O events (warmer intervals).

These wet phases in eastern Africa have been previously associated with Heinrich events (Dupont *et al.,* 2011; Schefuß *et al.,* 2011; Caley *et al.,* 2018). Previous studies have found evidence of a large scale atmospheric teleconnection linking Northern Hemisphere cold events and precipitation changes in South African climate (Ziegler *et al.,* 2013; Simon

et al., 2015a) (Figure 5.26). More humid conditions in southernmost East Africa, resulting from higher precipitation intensity, systematically corresponds to Northern Hemisphere cold intervals and periods of weak East Asian Monsoon. Modelling studies confirm that remote atmospheric forcing during Northern Hemisphere cold events is a key driver of hydrological variability in South Africa, resulting in wetter conditions during these events (Carto *et al.,* 2009; Thomas *et al.,* 2009; Lewis *et al.,* 2010). Increased rainfall over Southeast Africa coincided with a mean south-eastward shift in the positions of the South Indian and South Atlantic Ocean anticyclones. However, drier conditions occurred in Lake Malawi (Johnson *et al.,* 2002) and Lake Tanganyika (Tierney *et al.,* 2008) which are associated with Northern Hemisphere cold events and reflect a southward shift of the ITCZ (Nicholson and Flohn, 1981; Johnson *et al.,* 2002; Chiang *et al.,* 2003; Schefuß *et al.,* 2011; Hahn *et al.,* 2017), during these periods. This linkage between the different hemispheres is suggested to occur due to a weakened meridional overturning circulation in the Atlantic Ocean which leads to a bipolar seesaw warming response in the equatorial South Atlantic Ocean (Broecker, 1998), and consequently a reduction in West African summer monsoonal winds and rainfall over West Africa (Weldeab *et al.,* 2007). Parts of sub-Saharan Africa faced severe dry conditions during North Atlantic cold events (Stager *et al.,* 2011), whereas South Africa experienced more humid conditions. However, there are some records from South Africa which do not show humid conditions during Heinrich stadials, (e.g. Chevalier and Chase, 2015) and has led to the understanding that while the southerly displacement of the ITCZ is consistent with some of the available data (Schefuß *et al.,* 2011; Ziegler *et al.,* 2013; Simon *et al.,* 2015a), the impact is not uniform over the entire region and highlights the spatial complexity of changes in regional hydrology over South Africa.

Finally, in the Southern Hemisphere, Antarctic ice core records display similar variability to Northern Hemisphere HS, though to a less extent (EPICA, 2006). The millennial-scale $^{87}Sr/^{86}Sr$ isotope fluctuations coincide with the timing of Southern Hemisphere warming events recorded in Antarctic Isotope Maxima (AIM) (Figure 5.26), with lower $^{87}Sr/^{86}Sr$ ratios with warmer Antarctic temperatures. This coincidence has been noticed in records from offshore South Africa, the Antarctic ice core record is closely mimicked by SST reconstructions from sediment cores surrounding the southern tip of the African continent, both in the Indian (e.g. Simon *et al.,* 2013) and the Atlantic sector (e.g. Dyez *et al.,* 2014; Peeters *et al.,* 2004). The SST record from the Agulhas Current (Simon *et al.,* 2013) displays clear millennial-scale variability with abrupt increases up to 2°C and ALF abundance increases by $\sim$ 15%, which align with Northern Hemisphere cold events and the Antarctic temperature record (δD) (Simon *et al.,* 2013). Notably, the Northern Hemisphere stadial cooling that precedes D-O event 19 (Figure 5.26) (Dansgaard *et al.,* 1993), is a key example of more warm, saline conditions on millennial timescales, which coincides with lower $^{87}Sr/^{86}Sr$ ratios. This suggests the additional potential influence of Agulhas

Current temperatures on regional hydrology of South Africa with the $^{87}Sr/^{86}Sr$ record reflecting more precipitation (i.e. more chemical weathering) which has been previously documented (Reason and Mulenga, 1999; Tierney *et al.,* 2008; Stager *et al.,* 2011).

5.4.7 The Early Human Link

During the SB industry, previously reported marine proxy records suggest more humid conditions (Ziegler *et al.,* 2013; Simon *et al.,* 2015a). The MD20-3591 $^{87}Sr/^{86}Sr$ ratios and εNd record show more local South African river input during the SB industry which can be inferred as wetter conditions on-land inducing more chemical weathering. The speleothem records from Crevice Cave suggest a trend towards more dominant C3 grasses and winter rainfall conditions (Bar-Matthews *et al.,* 2010) (Figure 5.24). Cango Cave records approximate this pattern, with stronger (weaker) winter (summer) rainfall and more dominant C3 grasses during most of SB, with a trend towards stronger (weaker) winter (summer) rainfall at the end of the SB industry (Chase *et al.,* 2021) (Figure 5.24). Likewise HP is mostly characterised by stronger winter rainfall conditions (Bar-Matthews *et al.,* 2010) and marine core site CD154-17-17K suggests particularly humid conditions throughout HP (Ziegler *et al.,* 2013). At the start of HP, summer rainfall prevails (Bar-Matthews *et al.,* 2010; Chase *et al.,* 2021), but the seasonality changes to more winter rainfall conditions (Bar-Matthews *et al.,* 2010). This seasonality change is observed in the MD20-3591 $^{87}Sr/^{86}Sr$ and εNd records (Figure 5.22), at the end of HP there is a change in sediment source reflected in the εNd and less chemical weathering from South Africa supported by the $^{87}Sr/^{86}Sr$ ratios. The overall trend of more humid conditions during HP and SB is supported in the MD20-3591 records which show coarser grain size implying more river input from South Africa (Figure 5.24), a more local South African source contribution (Figure 5.21) and more terrestrial sediment supply (Figure 5.16).

While it is beyond the scope of the present work to make causal links between climate and early human behaviour, the results here do provide some links between sea level change, local climate and archaeological record, especially during MIS 4. During interglacial conditions (i.e. MIS 5 at $\sim$ 95 ka), when the coastline was close to Blombos Cave site, AMHs had easy access to the sea and were able to feed on abundant shellfish and other resources (Marean, 2010). The increased food security suggests that AMHs were able to settle for longer in an area (Whallon, 2006).

Alternatively, during lower sea levels and coastline retreat (i.e. MIS 4 at $\sim$ 70 ka), the exposed landmass of the PAP increased the opportunity for human migration patterns (Compton, 2011). During these times, our ancestors would have adjusted their mobility routes which meant more frequent encounters with neighbouring groups potentially gave rise to extended network structures (Mcbrearty and Brooks, 2000). These increased interactions may have enhanced knowledge exchange between AMH groups (Grove, 2016). The fluctuating coastline has been argued to be the main driver for changes in the use and

settlement at Blombos Cave by AMHs. Interestingly, the HP and SB techno-complexes overlap with the most significant sea level lowering and therefore coastline retreat (Haaland *et al.,* 2020). During these SB and HP complexes AMHs were visiting Blombos Cave for shorter time periods (Haaland *et al.,* 2020).

Based on the new radiogenic isotope and grain size proxy patterns, more humid conditions prevailed during HP and SB industries, consistent with previous work (Bar-Matthews *et al.,* 2010; Ziegler *et al.,* 2013). These periods of higher precipitation suggest the rivers would have been higher, increasing the freshwater reserve for AMHs and causing the soils on the PAP to become more fertile. This would have provided a richer ecosystem and an ideal habitat for herd animals which would have grazed on the soils and grasslands (Marean, 2014; Copeland *et al.,* 2016; Cowling *et al.,* 2019; Hodgkins *et al.,* 2020). The emergence of large mammal ecosystems required more sophisticated toolkits and hunting techniques by AMHs (Marean, 2015; Copeland *et al.,* 2016; Haaland *et al.,* 2020). This is documented in the archaeological record such as the use of silcrete as raw material for tool making, particularly bifacial points in the later SB layers (Henshilwood *et al.,* 2001; Reynard and Henshilwood, 2017).

5.5 Concluding Remarks

The radiogenic isotope ($^{87}Sr/^{86}Sr$ ratios and εNd) provenance, grain size and XRF PC1 records from marine sediment core MD20-3591 provide insights on the sediment source changes during the LMSA interval. The εNd record shows no sign of fractionation, which corroborates with other studies indicating εNd is not affected by chemical weathering and can be used to reconstruct sediment sources (Goldstein *et al.,* 1984; Blum and Erel 2003; Fagel *et al.,* 2004; Fagel, 2007; Meyer *et al.,* 2011; Garzanti *et al.,* 2014; van der Lubbe *et al.,* 2014; Hahn *et al.,* 2016; van der Lubbe *et al.,* 2016; Hahn *et al.,* 2018), however regional chemical weathering records can be obtained from the $^{87}Sr/^{86}Sr$ ratios which is induced by precipitation variability. Weathering is shown to act on short timescales (Jung *et al.,* 2004). Abrupt climate oscillations in the northern high latitudes are the main driver for the observed shorter millennial-scale wet phases, inferred from the $^{87}Sr/^{86}Sr$ isotope ratios which show changes in the South African hydroclimate conditions (i.e. more precipitation). During cold events in the Northern Hemisphere, Antarctic ice core records reveal warmer temperatures, and the $^{87}Sr/^{86}Sr$ ratios record more weathering from the South African continent, inferring wetter conditions. Whilst on longer time scales, the εNd record is reflecting changes in river discharge transported southwards in the Agulhas Current, as a result of a combination of local insolation and latitudinal ITCZ shifts.

A change in rainfall seasonality is observed on insolation timescales. During 30°S summer insolation maxima, there is a stronger Limpopo dominance, based on sediment source contribution mixing and the MD20-3591 εNd record. This means that the Limpopo

catchment is experiencing wetter conditions from the southward shifting rain-belts in response to maximum 30°S summer insolation. The sediment from the Limpopo river is transported in the Agulhas Current downstream to site MD20-3591.

At minima 30°S summer insolation ($\sim$ 82 ka), more locally sourced rainfall from South Africa is observed. However, during MIS 4, the effect of lower sea levels due to enhanced Northern Hemisphere global ice volume plays a role in affecting the South African climate. A change in sediment source is observed during the MIS 5/4 transition, identified as a local South African source, indicative of more humid conditions inland of the coastal region over the river catchments of South Africa. This is likely driven by a northward shift in the westerlies modulated by the increased Antarctic sea ice extent. The consistent pattern of more local South African sediment input at marine sediment core site MD20-3591 during MIS 4 is based on coarser sediment input from rivers due to a reduced distance from the palaeoshoreline to site MD20-3591, more terrestrial XRF sediment supply, and a local South African sediment source contribution. These MD20-3591 records coincide with palaeoclimate proxy records which show more winter rainfall dominance in the year-round zone, which are all related to SHW. These are; the Antarctic sea ice edge, the westerly wind belt and the STF. The STF record (Peeters *et al.,* 2004), the EDML ssNa flux (Fischer *et al.,* 2007) and the Southeast Atlantic wind strength composite (Chase *et al.,* 2021), which imply that the northward displacement of the westerly storm track during MIS 4 may have been influential in establishing sustained sediment input to MD20-3591 through altering South African rainfall zones. This Southern Hemisphere mechanism likely operated in tandem with a more dynamical system linked to migrations of the ITCZ and associated rain-belts, along with the formation of TTTs, would have been favoured by increased precession (Hahn *et al.,* 2020; Miller *et al.,* 2020).

Chapter 6 | Synthesis and Future Perspectives

Autumn leaves don't fall, they fly. They take their time and wander on this their only chance to soar. Reflecting sunlight, they swirled and sailed and fluttered on the wind drafts - Delia Owens - Where the Crawdads Sing

And somehow I did feel like yesterday was ours, but it's gone, yesterday was ours, all along, and they were singing - Another Friday Night - Ben Howard

6.1 Summary of Chapters

6.1.1 Chapter 3

Radiogenic isotopes strontium ($^{87}Sr/^{86}Sr$) and neodymium (εNd), clay minerals and lithogenic grain size measured in river channels from drainage basins between Durban and Cape Town in South Africa were analysed to investigate the origin and associated weathering regimes of sediments supplied to and ultimately deposited in the Southwest Indian Ocean and the Agulhas Current region. Sediment provenances were identified through unmixing of bedrock geology radiogenic isotope signatures to define two distinct radiogenic isotope endmembers that characterise the regional river systems. Rivers of the eastern Cape drain soils weathered of the Karoo Supergroup and Drakensberg basalts ($^{87}Sr/^{86}Sr$ of 0.740 ($\pm$0.00001) and εNd of –8.526 ($\pm$0.200)), whereas rivers of the southern Cape drain the Cape Supergroup province with more radiogenic $^{87}Sr/^{86}Sr$ ratios of 0.745 ($\pm$0.00001) and unradiogenic εNd values of –10.091 ($\pm$0.200). A grain size effect on Sr isotope compositions has been previously reported, whereby the $^{87}Sr/^{86}Sr$ values increase with decreasing grain size. This bias was minimised by analysing the same operationally defined grain size fraction (<2 µm) as well as the fine silt (2-32 µm) which are usually targeted in palaeoclimate studies. The variability in the $^{87}Sr/^{86}Sr$ values is due to the degree of chemical weathering, identified by clay mineral abundances, a simple linear mixing model and QGIS mapping of soils. This study reveals two new radiogenic isotope endmember values for the clay size fraction (<2 µm), which can be used for palaeoclimate studies as a provenance indicator when reconstructing offshore sediment input and transport changes offshore of South Africa. The study shows that the <2 µm fraction is weathered from the source rock but can reflect the source rock radiogenic isotope signature. The <2 µm fraction has a higher potential of long-distance transport so can be used as a provenance tracer for reconstructions related to climate variability, as implemented in subsequent chapters.

6.1.2 Chapter 4

In this study $^{87}Sr/^{86}Sr$ and εNd radiogenic isotope systems are used, along with clay mineralogy and lithogenic grain size data. These are measured in modern and Last Glacial Maximum (LGM) dated time-slices in marine sediment cores recovered from offshore of the Southeast African coastline.

The new data presented here shows a systematic change in the sediment signature across all three size fractions between the modern and LGM with a similar magnitude of change to that reported by Franzese *et al.* (2006). Sediment contribution mixing suggests that during glacial times, sediment deposition at the CD154 marine sediment core sites is most likely dominated by sediment material originating in the Zambezi river mixed with a sup-

ply of local South African river material. Hydrological records and modelling results from sites within, offshore or located close to the Zambezi catchment reveal more precipitation during the LGM (Schefuß *et al.*, 2011; Chevalier *et al.*, 2017), whereas the Limpopo is inferred to be more arid during the LGM (Finch and Hill, 2008; Baker *et al.*, 2017; Miller *et al.*, 2019) suggesting less Limpopo sediment input. There is also a deep-water signal in the 10-63 µm radiogenic isotopes, with values corresponding to a South Atlantic signal (e.g. Franzese *et al.*, 2006). This is supported by the $\delta^{13}C$ values from benthic foraminifera which reveal a water mass change during the LGM, towards a more south component water mass and higher flow speeds inferred from the sortable silt mean flow speed proxy in this study. A stronger contribution of sediment from distant Antarctic via the South Atlantic Ocean to South Africa, has been shown during glacial periods, transported by an increase in the strength of the Antarctic Circumpolar Current (ACC) supported by other studies (Franzese *et al.*, 2006; Hemming *et al.*, 2009; Noble *et al.*, 2012; Starr *et al.*, 2021).

This study has also successfully isolated three size fractions, the <2 µm, 2-10 µm and 10-63 µm using a simple and accurate method (see Chapter 2). This standardised method (section 2.3.2) using a centrifuge is straightforward to follow and time and cost effective. Minimal material is needed (1-2 g of dry <63 µm sediment), which means no bulk sediment is wasted and the procedure takes less than hour, allowing high sample throughput. Importantly, the grain size separation confirms comparisons between radiogenic isotopes must be performed on a single isolated grain size fraction. The <2 µm fraction is suggested for all future radiogenic isotopes studies as results show from Chapter 4 show that the <63 µm fraction encompasses bottom flowspeeds (i.e. 10-63 µm; McCave and Hall, 2006), hence mixing the provenance signal. Therefore isolating the clay fraction reduces the influence of hydrodynamic sorting and sediment transport processes, as well as reducing the bias on the provenance signal. As such, following this new protocol will greatly improve the capability of comparing radiogenic isotope datasets.

6.1.3 Chapter 5

Utilising the results and knowledge gained from Chapter 3 and 4, the South African hydroclimate variability recorded in sediment core MD20-3591 is further explored using multiproxy records. Grain size data from MD20-3591 shows a strong sea level control linked to the intermittently exposed Palaeo Agulhas Plain (PAP) during glacial low stands such as Marine Isotope Stage (MIS) 4 which was incised with deep river valleys. The radiogenic isotopes and XRF records from marine sediment core MD20-3591 provide insights on the sediment supply and source changes during the time interval of 100–50 ka, termed the Late Middle Stone Age (LMSA). The $^{87}Sr/^{86}Sr$ record shows changes in the South African hydroclimate conditions (i.e. more precipitation) whilst the εNd record is reflective of long term changes in river discharge, as a result of a combination of the

local insolation and latitudinal Intertropical Convergence Zone (ITCZ) shifts. A change in rainfall seasonality is observed from maximum 30°S summer insolation to 30°S summer insolation minima on precessional timescales. At 30°S summer insolation maxima, there is a stronger Limpopo dominance, based on sediment source contribution mixing and the MD20-3591 εNd record. This means that the Limpopo catchment is experiencing wetter conditions from the southward shifting rain-belts at maxima 30°S summer insolation and this sediment is transported downstream in the Agulhas Current to site MD20-3591. Other studies show precession driven humidity during maxima Southern Hemisphere summer insolation (e.g. Schefuß *et al.,* 2011; van der Lubbe *et al.,* 2014; Simon *et al.,* 2015a; Caley *et al.,* 2018). At minima 30°S summer insolation ($\sim$ 82 ka), more locally sourced sediment from South Africa is supplied to site MD20-3591 caused by enhanced on-land precipitation. This is likely driven by a northward shift in the Southern Hemisphere Westerlies (SHW) modulated by the increased Antarctic sea ice extent. These MD20-3591 records coincide with palaeoclimate proxy records which show more winter rainfall dominance in the year-round zone, which are all related to SHW. It is likely that the SHW likely operated in tandem with a more dynamical system linked to migrations of the ITCZ and associated rain-belts, along with the formation of temperate-tropical troughs (TTTs), would have been favoured by increased precession (Hahn *et al.,* 2020; Miller *et al.,* 2020) linking high latitude and low latitude forcings.

On shorter timescales, abrupt climate oscillations in the northern high latitudes are the main driver for the observed millennial-scale wet phases, inferred from $^{87}Sr/^{86}Sr$ isotope ratios. During these D-O events in the Northern Hemisphere, Antarctic ice core records reveal warmer temperatures, and the $^{87}Sr/^{86}Sr$ ratios record more weathering from the South African continent, inferring wetter conditions. These records of hydrological changes in the southern Cape region of South Africa shown in this study reveals a striking correspondence between the archaeological record of South Africa and the timing of abrupt Northern Hemisphere climate change (Ziegler *et al.*, 2013).

6.2 Wider Perspective

Blombos Cave has been subject to a considerable number of Anatomically Modern Human (AMH) groups and these inhabitants who lived there were creative and engaged in activities such as symbolically mediated behaviours during the LMSA. AMH who frequented the cave site at $\sim$ 95 ka displayed less complex cultural expression, however during Still Bay (72-71 ka) (SB) and Howiesons Poort (64–59 ka) (HP) complexes, there was a boost in cultural expression displayed in the artifacts at Blombos Cave. This reveals how AMH culturally evolved during this interval. During the LMSA, it is suggested that the duration of stay at Blombos Cave was determined by the food availability (Haaland *et al.*, 2020). There is evidence during the first occupation stages around 95 ka, that AMH frequented the cave for longer periods because of security in food availability and freshwater resource

(Haaland *et al.*, 2020).

During interglacial conditions (i.e. MIS 5 at $\sim$ 95 ka), AMH had easy access to the coastline increasing their ability to feed on abundant shellfish and other resources (Marean, 2010) because the coastline was close to Blombos Cave site. The increased food security suggests that AMHs were able to settle for longer in an area (Whallon, 2006). Glacial variations in sea level and associated land extent controlled the climate of coastal southern Africa at $\sim$ 70 ka. As the coastline moves away and the PAP is exposed, the modelled climate changed considerably (Gotkurk *et al.*, 2023a). Notably, diurnal and inter-seasonal temperature ranges changed by up to $\pm$6°C at Blombos Cave. Additionally, the coastline shift likely caused local modifications in near-surface atmospheric circulation, reducing the modelled amount of precipitation within the region by 40% (Gotkurk *et al.*, 2023b). This suggests the coastal zone was more arid during times of glacial sea level low stands (Gotkurk *et al.*, 2023b).

In addition during lower sea levels and coastline retreat (i.e. MIS 4 at $\sim$ 70 ka), the exposed landmass of the PAP increased the opportunity for human migration patterns (Compton, 2011). During both HP and SB complexes sea level was lower which means access to the coast and sea was reduced, as such AMHs were visiting Blombos Cave for shorter time periods (Haaland *et al.*, 2020). Our ancestors would have adjusted their mobility routes which meant more frequent encounters with neighbouring groups potentially gave rise to extended network structures (Mcbrearty and Brooks, 2000). These increased interactions may have enhanced knowledge exchange between AMH groups (Grove, 2015). Evidence that AMHs developed the first symbolic art, like engraved pieces of red ochre and ostrich eggshell containers, artifacts such as pierced shells, likely used for necklaces, and relatively complex stone and bone tools have also been dated within this time frame at Blombos Cave (Henshilwood *et al.*, 2002; Jacobs *et al.*, 2008). More humid conditions in Southeast Africa all fell within periods of the archaeological evidence (Ziegler *et al.*, 2013). These humid intervals are reported to be linked with Northern Hemisphere D-O variability (Ziegler *et al.*, 2013; Simon *et al.*, 2015a), supported by the Sr isotopes in this study. As the river courses changed and flowed over the PAP (Cawthra *et al.*, 2020), this increased the freshwater reserve which would have changed the soil fertility and inducing vegetation growth. This landscape provided an ideal habitat for bigger ungulates and herbivores which means it is likely our ancestors had to change their hunting techniques to provide meals for AMHs.

6.3 Future Work

6.3.1 River Sediments

Despite the general understanding that a higher $^{87}Sr/^{86}Sr$ ratio indicates more chemical weathering (Dasch, 1969; Åberg *et al.*, 1989; Blum *et al.*, 1993; Derry and France-Lanord,

1996; Blum and Erel, 1997, 2003; Capo *et al.*, 1998; Jung *et al.*, 2004), bulk geochemistry such as major and trace element analysis would help identify the Chemical Index of Alteration (CIA) and Weathering Indices Processes (WIP) which could be used to interpret which South African river sediments are most weathered and chemically altered. Stronger weathering is indicated by higher CIA, widely interpreted as a measure of the extent of conversion of feldspars to clays such as kaolinite, and by lower WIP, appropriate for heterogeneous sources including metamorphic rocks (Garzanti *et al.*, 2013). To investigate the effect of chemical weathering, the use of ratios such as K/Al or Al/Na, and secondly pairing these ratios with radiogenic isotopes would help identify volcaniclastic sediment and mafic sources (Garzanti *et al.*, 2013; Dinis *et al.*, 2020). Traditionally, K/Al ratios from bulk sediment have been used as a proxy for chemical weathering intensity although other studies have found log(Al/Na) to be a weathering proxy (Lipp *et al.*, 2020), because strong chemical weathering leaches water-mobile elements, such as Na and K, relative to immobile elements such as Al (Thiry, 2000). As kaolinite is a product of intense chemical weathering, associated river sediments have lower K/Al ratios, while illite and chlorite, which result from physical erosion in dry conditions, have higher K/Al ratios (Carter *et al.*, 2020), this work would complement the radiogenic isotopes and clay mineralogy study in Chapter 3. These analyses were planned but due to a lab closure were not possible within the study time frame.

6.3.2 More Sediment Collection

Collecting more samples from different rivers in South Africa such as the Tugela river further north of Durban and the Orange river to fill in the gaps shown in Figure 3.1. Measuring corresponding sediment samples from Garzanti *et al.* (2013) and Hahn *et al.* (2017, 2018) on the <2 µm fraction would elucidate any Sr size fraction offsets (shown in Chapter 3) and compile a database for radiogenic isotopes on the same size fraction from South African sediments. This would lead to more comparable radiogenic isotope datasets with consistent size fraction separation. To affirm conclusions drawn from Chapter 4, more provenance radiogenic isotope data is needed from the South Atlantic, as to date, no such records exist on the <2 µm. This means all radiogenic isotope data compared to the South Atlantic is likely affected by the grain size fractionation of Sr as published work from this region (e.g. Rutberg *et al.*, 2005; Franzese *et al.*, 2006) is measured on a coarser fraction. It is of equal importance to further understand potential transport pathways to site MD20-3591 from upstream sources like the Limpopo and Zambezi rivers. As such, more samples from these rivers need to be analysed on the <2 µm fraction for data compilation. This was planned but due to a lab closure was not possible. In addition, the effect of marine barite needs to be considered on the marine sediment $^{87}Sr/^{86}Sr$ isotope reconstructions, as this has been found in studies (Jewell *et al.*, 2021). Tests using the DTPA wash on sediments were planned but were not possible with lab closures.

6.3.3 Archaeological Evidence

At present, no radiogenic isotopes work has been achieved on the PAP therefore I propose two ideas to increase our understanding of palaeoenvironmental changes during the LMSA: 1) Sediment sampling from different regions of the PAP in order to carry out a full provenance study of the plain. Radiogenic isotopes and clay mineralogy analyses of sediments from the PAP would help quantify the source region of sediment deposited on the PAP. It would be useful to obtain sediment cores from as close to shore as possible, to determine whether the modern signals are similar to the river sediments of South Africa (Chapter 3) and extend studies back in time to compare the sediment source and input during glacial periods such as the LGM or MIS 4, when sea level was significantly lower than present and the PAP was exposed and quantify whether the geology of the PAP can directly influence the εNd signal recorded in marine sediment core site MD20-3591.

2) Radiogenic isotope reconstructions from macro-mammal remains or shellfish from Blombos Cave and other archaeological MSA sites in South Africa such as Bundu Farm Northern Cape (29°S 22°E), Wonderwerk Cave (27°S, 24°E) and Equus Cave (26°S, 25°E). This would offer another approach to address key questions regarding palaeoenvironmental changes during the MSA between coastal sites and more inland regions and provide understanding of the social network of AMH. Generating strontium isotope reconstructions from artifacts from other archaeological sites using ostrich egg shells would augment understand concerning the recent proposal that AMH occupying sites in central vs coastal South Africa experienced different palaeoclimate regimes (Wilkins *et al.*, 2021; Mackay *et al.*, 2022; Carr *et al.*, 2023; Gotkurk *et al.*, 2023).

Bibliography

Åberg, Jacks and Joseph Hamilton. (1989). Weathering rates and 87Sr/86Sr ratios: An isotopic approach. Journal of Hydrology 109(1–2), pp. 65–78. doi: 10.1016/0022-1694(89)90007-3.

Adams, Faure and Network. (1997). Review and Atlas of Palaeovegetation: Preliminary Land Ecosystem Maps of the World Since the Last Glacial Maximum. Quaternary Environments Network. Available at: https://books.google.co.uk/books?id=yWXnwQEACAAJ.

Adhémar (1842). Révolutions de la mer. Carilian-Goeury et V. Dalmont. Available at: https://books.google.co.uk/books?id=zvpZAAAAYAAJ.

Adkins. (2013). The role of deep ocean circulation in setting glacial climates. Paleoceanography 28(3), pp. 539–561. Available at: https://doi.org/10.1002/palo.20046.

Agassiz, Bettannier and Nicolet. (1840). Études sur les glaciers Aux frais de l'auteur ; Available at: https://www.biodiversitylibrary.org/bibliography/151173.

Ahn and Brook. (2008). Atmospheric CO2 and climate on millennial time scales during the last glacial period. Science (New York, N.Y.) 322(5898), pp. 83–85. doi: 10.1126/science.1160832.

Alley, Marotzke, Nordhaus, Overpeck, Peteet, Pielke, Pierrehumbert, Rhines, Stocker, Talley, and Wallace. (2003). Abrupt Climate Change. Review 299, pp. 59–72. doi: 10.1007/978-3-319-90975-2_4.

Anderson and Burckle. (2009). Rise in Atmospheric CO 2. Science 323(March), pp. 1443–1448.

Andersson, Johansson and Kumpulainen. (2003). Sm–Nd isotope evidence for the provenance of the Skoorsteenberg Formation, Karoo Supergroup, South Africa. Journal of African Earth Sciences 36(3), pp. 173–183. Available at: https://www.sciencedirect.com/science/article/pii/S0899536203000253.

Arhan, Mercier and Park. (2003). On the deep water circulation of the eastern South Atlantic Ocean. Deep-Sea Research Part I: Oceanographic Research Papers 50(7), pp. 889–916. doi: 10.1016/S0967-0637(03)00072-4.

Attal and Lavé. (2006). Changes of bedload characteristics along the Marsyandi River (central Nepal): Implications for understanding hillslope sediment supply, sediment load evolution along fluvial networks, and denudation in active orogenic belts. In: Willett, S. D., Hovius, N., Tectonics, Climate, and Landscape Evolution. Geological Society of

America, p. 0. doi: 10.1130/2006.2398(09).

Avanzinelli, Boari, Conticelli, Francalanci, Guarnieri, Perini, Petrone, Tommasini, Ulivi. (2005). High precision Sr, Nd, and Pb isotopic analyses using the new generation Thermal Ionisation Mass Spectrometer ThermoFinnigan Triton-Ti®. Periodico di Mineralogia 74(3), pp. 147–166.

Babin, Franzese, Hemming, Hall, LeVay, Barker, Tejeda, & Simon. (2020). Data report: X-ray fluorescence core scanning of IODP Site U1474 sediments, Natal Valley, Southwest Indian Ocean, Expedition 361. IODP Proceedings, 361(June), 1–9. https://doi.org/10.14379/iodp.proc.

Baker, Pedentchouk, Routh and Roychoudhury. (2017). Climatic variability in Mfabeni peatlands (South Africa) since the late Pleistocene. Quaternary Science Reviews 160, pp. 57–66. Available at: http://dx.doi.org/10.1016/j.quascirev.2017.02.009.

Balaram and Subramanyam. (2022). Sample preparation for geochemical analysis: Strategies and significance. Advances in Sample Preparation 1, p. 100010. Available at: https://www.sciencedirect.com/science/article/pii/S2772582022000079.

Balaram. (2021). Current and emerging analytical techniques for geochemical and geochronological studies. Geological Journal 56(5), pp. 2300–2359.

Banner. (2004). Radiogenic isotopes: systematics and applications to earth surface processes and chemical stratigraphy. Earth-Science Reviews 65(3), pp. 141–194. Available at: https://www.sciencedirect.com/science/article/pii/S0012825203000862.

Bar-Matthews, Marean, Jacobs, Karkanas, Fisher, Herries, Brown, Williams, Bernatchez, Ayalon, & Nilssen. (2010). A high resolution and continuous isotopic speleothem record of paleoclimate and paleoenvironment from 90 to 53 ka from Pinnacle Point on the south coast of South Africa. Quaternary Science Reviews, 29(17–18), 2131–2145. https://doi.org/10.1016/j.quascirev.2010.05.009

Bard and Rickaby. (2009). Migration of the subtropical front as a modulator of glacial climate. Nature 460(7253), pp. 380–383. Available at: http://dx.doi.org/10.1038/nature08189.

Barker and Gasse. (2003). New evidence for a reduced water balance in East Africa during the Last Glacial Maximum: Implication for model-data comparison. Quaternary Science Reviews 22(8–9), pp. 823–837. doi: 10.1016/S0277-3791(03)00010-6.

Barker, Knorr, Edwards, Parrenin, Putnam, Skinner, Wolff, & Ziegler. (2011). 800,000 Years of abrupt climate variability. Science, 334(6054), 347–351. https://doi.org/10.1126/science.1203580

Barker, Diz, Vautravers, Pike, Knorr, Hall and Broecker. (2009). Interhemispheric Atlantic seesaw response during the last deglaciation. Nature 457(7233), pp. 1097–1102. doi: 10.1038/nature07770.

Basile, Grousset, Revel, Petit, Biscaye and Barkov. (1997). Patagonian origin of glacial dust deposited in East Antarctica (Vostok and Dome C) during glacial stages 2, 4 and 6. Earth and Planetary Science Letters 146(3), pp. 573–589.

Bayon, Burton, Soulet, Vigier, Dennielou, Etoubleau, Ponzevera, German, & Nesbitt. (2009). Hf and Nd isotopes in marine sediments: Constraints on global silicate weathering. Earth and Planetary Science Letters, 277(3–4), 318–326.
https://doi.org/10.1016/j.epsl.2008.10.028

Bayon, Toucanne, Skonieczny, André, Bermell, Cheron, Dennielou, Etoubleau, Freslon, Gauchery, Germain, Jorry, Ménot, Monin, Ponzevera, Rouget, Tachikawa, & Barrat. (2015). Rare earth elements and neodymium isotopes in world river sediments revisited. Geochimica et Cosmochimica Acta, 170, 17–38.
https://doi.org/10.1016/j.gca.2015.08.001

Bayon, Douglas, Denton, Monin and De Deckker. 2020. Preferential Riverine Export of Fine Volcanogenic Particles to the Southeast Australian Margin. Frontiers in Marine Science 7(February). doi: 10.3389/fmars.2020.00089.

Bayon, Freslon, Germain, Bindeman, Trinquier and Barrat. (2021). A global survey of radiogenic strontium isotopes in river sediments. Chemical Geology 559, p. 119958. Available at: https://doi.org/10.1016/j.chemgeo.2020.119958.

Bayon, German, Boella, Milton, Taylor and Nesbitt. (2002). An improved method for extracting marine sediment fractions and its application to Sr and Nd isotopic analysis. Chemical Geology 187(3–4), pp. 179–199. doi: 10.1016/S0009-2541(01)00416-8.

Bé and Duplessy. (1976). Subtropical Convergence Fluctuations and Quaternary Climates in the Middle Latitudes of the Indian Ocean. Science 194(4263), pp. 419–422. Available at: https://doi.org/10.1126/science.194.4263.419.

Beal and Bryden. (1997). Observations of an Agulhas undercurrent. Deep-Sea Research Part I: Oceanographic Research Papers 44(9–10), pp. 1715–1724. doi: 10.1016/S0967-0637(97)00033-2.

Beal and Bryden. (1999). The velocity and vorticity structure of the Agulhas Current at 32°S. Journal of Geophysical Research: Oceans 104(C3), pp. 5151–5176. doi: 10.1029/1998jc900056.

Beal, De Ruijter, Biastoch, Zahn, Cronin, Hermes, Lutjeharms, Quartly, Tozuka, Baker-Yeboah, Bornman, Cipollini, Dijkstra, Hall, Park, Peeters, Penven, Ridderinkhof, & Zinke. (2011). On the role of the Agulhas system in ocean circulation and climate. Nature, 472(7344), 429–436. https://doi.org/10.1038/nature09983

Beal, Chereskin, Lenn and Elipot. (2006). The sources and mixing characteristics of the Agulhas Current. Journal of Physical Oceanography 36(11), pp. 2060–2074. Avail-

able at: https://typeset.io/papers/the-sources-and-mixing-characteristics-of-the-agulhas-3j8ak9rlwp [Accessed: 19 January 2023].

Behar, D. M., Villems, R., Soodyall, H., Blue-Smith, J., Pereira, L., Metspalu, E., Scozzari, R. et al. (2008). The dawn of human matrilineal diversity. American Journal of Human Genetics, 82, 1130-1140. http://dx.doi.org/10.1016/j.ajhg.2008.04.002

Bemis, Spero, Lea and Bijma. (2000). Temperature influence on the carbon isotopic composition of Globigerina bulloides and Orbulina universa (planktonic foraminifera). Marine Micropaleontology 38(3–4), pp. 213–228. doi: 10.1016/S0377-8398(00)00006-2.

Bender. (1971). Variations in the 13C/12C ratios of plants in relation to the pathway of photosynthetic carbon dioxide fixation. Phytochemistry 10(6), pp. 1239–1244. doi: 10.1016/S0031-9422(00)84324-1.

Beny, Bout-Roumazeilles, Davies, Waelbroeck, Bory, Tribovillard, Delattre, & Abraham. (2020). Radiogenic isotopic and clay mineralogical signatures of terrigenous particles as water-mass tracers: New insights into South Atlantic deep circulation during the last termination. Quaternary Science Reviews, 228.
https://doi.org/10.1016/j.quascirev.2019.106089

Bereiter, Lüthi, Siegrist, Schüpbach, Stocker and Fischer. (2012). Mode change of millennial CO2 variability during the last glacial cycle associated with a bipolar marine carbon seesaw. Proceedings of the National Academy of Sciences 109(25), pp. 9755–9760. Available at: https://doi.org/10.1073/pnas.1204069109.

Berger and Loutre. (1991). Insolation values for the climate of the last 10 million years. Quaternary Science Reviews 10(4), pp. 297–317. doi: 10.1016/0277-3791(91)90033-Q.

Berger. (1984). Milankovitch and climate: understanding the response to astronomical forcing. Springer Science & Business Media.

Biastoch, Beal, Lutjeharms and Casal. (2009). Variability and coherence of the agulhas undercurrent in a high-resolution ocean general circulation model. Journal of Physical Oceanography 39(10), pp. 2417–2435. doi: 10.1175/2009JPO4184.1.

Biastoch, Böning and Lutjeharms. (2008a). Agulhas leakage dynamics affects decadal variability in Atlantic overturning circulation. Nature 456(7221), pp. 489–492. doi: 10.1038/nature07426.

Biastoch, Lutjeharms, Böning and Scheinert. (2008b). Mesoscale perturbations control inter-ocean exchange south of Africa. Geophysical Research Letters 35(20). doi: 10.1029/2008GL035132.

Bickert and Mackensen. (2003). Last Glacial to Holocene Changes in South Atlantic Deep Water Circulation. The South Atlantic in the Late Quaternary, pp. 671–693. doi: 10.1007/978-3-642-18917-3_29.

Bickert and Wefer. (1996). Late Quaternary Deep Water Circulation in the South Atlantic: Reconstruction from Carbonate Dissolution and Benthic Stable Isotopes BT - The South Atlantic: Present and Past Circulation. In: Wefer, G., Berger, W. H., Siedler, G., and Webb, D. J. eds. Berlin, Heidelberg: Springer Berlin Heidelberg, pp. 599–620. Available at: https://doi.org/10.1007/978-3-642-80353-6_30.

Bickert. (2009). Carbonate Compensation Depth BT - Encyclopedia of Paleoclimatology and Ancient Environments. In: Gornitz, V. ed. Dordrecht: Springer Netherlands, pp. 136–138. Available at: https://doi.org/10.1007/978-1-4020-4411-3_33.

Birkett, Hill, Zuma and Everson. (2016). Bringing Rain to the Land: Rainfall Simulation as a Participatory Teaching Aid to Understanding Erosion. Journal of Environmental Protection 07(10), pp. 1305–1316. doi: 10.4236/jep.2016.710114.

Biscaye and Dasch. (1971). The rubidium, strontium, strontium-isotope system in deep-sea sediments: Argentine Basin. Journal of Geophysical Research 76(21), pp. 5087–5096. doi: 10.1029/jc076i021p05087.

Biscaye, Grousset, Revel, Van Der Gaast, Zielinski, Vaars and Kukla. (1997). Asian provenance of glacial dust (stage 2) in the Greenland Ice Sheet Project 2 Ice Core, Summit, Greenland. Journal of Geophysical Research: Oceans 102(C12), pp. 26765–26781. doi: 10.1029/97JC01249.

Biscaye. (1965). Mineralogy and Sedimentation of Recent Deep-Sea Clay in the Atlantic Ocean and Adjacent Seas and Oceans. Geological Society of America Bulletin 76(July), pp. 803–832.

Blanchet, Osborne, Tjallingii, Ehrmann, Friedrich, Timmermann, Brückmann, & Frank. (2021). Drivers of river reactivation in North Africa during the last glacial cycle. Nature Geoscience, 14(2), 97–103. https://doi.org/10.1038/s41561-020-00671-3

Blaser, Lippold, Gutjahr, Frank, Link and Frank. (2016). Extracting foraminiferal seawater Nd isotope signatures from bulk deep sea sediment by chemical leaching. Chemical Geology 439, pp. 189–204. Available at: http://dx.doi.org/10.1016/j.chemgeo.2016.06.024.

Blum and Erel. (1997). Rb-Sr isotope systematics of a granitic soil chronosequence: The importance of biotite weathering. Geochimica et Cosmochimica Acta 61(15), pp. 3193–3204. doi: 10.1016/S0016-7037(97)00148-8.

Blum and Erel. (2003). Radiogenic Isotopes in Weathering and Hydrology. Treatise on Geochemistry 5–9, pp. 365–392. doi: 10.1016/B0-08-043751-6/05082-9.

Blum, Erel and Brown. (1993). 87Sr/86Sr ratios of sierra nevada stream waters: Implications for relative mineral weathering rates. Geochimica et Cosmochimica Acta 57(21–22), pp. 5019–5025. doi: 10.1016/S0016-7037(05)80014-6.

Blum, Erel and Brown. (1994). Mineral Weathering Rates. Geochimica et Cosmochimica

Acta 58, pp. 5019–5025.

Blunier and Brook. (2001). Timing of Millennial-Scale Climate Change in Antarctica and Greenland During the Last Glacial Period. 291(January), pp. 109–112.

Boelhouwers and Meiklejohn. (2002). Quaternary periglacial and glacial geomorphology of southern Africa: Review and synthesis. South African Journal of Science 98(1–2), pp. 47–55.

Boelhouwers. (1999). Relict periglacial slope deposits in the Hex River Mountains, South Africa: Observations and palaeoenvironmental implications. Geomorphology 30(3), pp. 245–258. doi: 10.1016/S0169-555X(99)00033-1.

Bohm, Lippold, Gutjahr, Frank, Blaser, Antz, Fohlmeister, Frank, Andersen, & Deininger. (2015). Strong and deep Atlantic meridional overturning circulation during the last glacial cycle. Nature, 517(7532), 73–76. https://doi.org/10.1038/NATURE14059

Bond and Lotti. (1995). Iceberg discharges into the North Atlantic on millennial time scales during the last glaciation. Science 267(5200), pp. 1005–1010. doi: 10.1126/science.267.5200.1005.

Bond, Heinrich, Broecker, Labeyrie, McManus, Andrews, Huon, Jantschik, Clasen, Simet, Tedesco, Klas, Bonani, & Ivy. (1992). Evidence for massive discharges of icebergs into the North Atlantic ocean during the last glacial period. Nature, 360(6401), 245–249. https://doi.org/10.1038/360245a0

Bond, Showers, Cheseby, Lotti, Almasi, deMenocal, Priore, Cullen, Hajdas, & Bonani. (1997). A Pervasive Millennial-Scale Cycle in North Atlantic Holocene and Glacial Climates. Science, 278(5341), 1257–1266. https://doi.org/10.1126/science.278.5341.1257

Bond, Showers, Elliot, Evans, Lotti, Hajdas, Bonani, & Johnson. (1999). The North Atlantic's 1–2 kyr climate rhythm: Relation to Heinrich events, Dansgaard/Oeschger cycles and the Little Ice Age. In Geophys. Monogr. Ser.,in Mechanisms of Global Climate Change at Millennial Time Scales, vol. 112, edited by P. U. Clark, R. S. Webb, and L. D. Keigwin, p.

Bond, Broecker, Johnsen, McManus, Labeyrie, Jouzel and Bonani. (1993). Correlations between climate records from North Atlantic sediments and Greenland ice. Nature 365(6442), pp. 143–147. Available at: https://doi.org/10.1038/365143a0.

Bond, Midgley and Woodward. (2003). What controls South African vegetation — climate or fire? South African Journal of Botany 69(1), pp. 79–91. Available at: https://www.sciencedirect.com/science/article/pii/S0254629915303628.

Botha, Scott, Vogel and Von Brunn. (1992). Palaeosols and palaeoenvironments during the late Pleistocene hypothermal in northern Natal. South African Journal of Science 88(9–10), pp. 508 – 512.

Boyle. (1988). Cadmium: Chemical Tracer of Deepwater Paleoceanography. Paleoceanography 3(4), pp. 471–489.

Braconnot, Otto-Bliesner, Harrison, Joussaume, Peterchmitt, Abe-Ouchi, Crucifix, Driesschaert, Fichefet, Hewitt, Kageyama, Kitoh, Loutre, Marti, Merkel, Ramstein, Valdes, Weber, Yu, & Zhao. (2007). Results of PMIP2 coupled simulations of the Mid-Holocene and Last Glacial Maximum – Part 2: feedbacks with emphasis on the location of the ITCZ and mid- and high latitudes heat budget. Climate of the Past, 3(2), 279–296. https://doi.org/10.5194/cp-3-279-2007

Brandon and Fisher eds. Tectonics, Climate, and Landscape Evolution. Geological Society of America, p. 0. Available at:
https://doi.org/10.1130/2006.2398(09).

Braun, Bar-Matthews, Matthews, Ayalon, Cowling, Karkanas, Fisher, Dyez, Zilberman, & Marean. (2019). Late Pleistocene records of speleothem stable isotopic compositions from Pinnacle Point on the South African south coast. Quaternary Research (United States), 91(1), 265–288. https://doi.org/10.1017/qua.2018.61

Brink. (1987). The Archaeozoology of Florisbad, Orange Free State. National Museum. Available at: https://books.google.co.uk/books?id=YlN3QgAACAAJ.

Broecker and Denton. (1990). The role of ocean-atmosphere reorganizations in glacial cycles. Quaternary Science Reviews 9(4), pp. 305–341. doi: 10.1016/0277-3791(90)90026-7.

Broecker and van Donk. (1970). Insolation changes, ice volumes, and the O18 record in deep-sea cores. Reviews of Geophysics 8(1), pp. 169 – 198.

Broecker and van Donk. (1970). Insolation changes, ice volumes, and the O18 record in deep-sea cores. Reviews of Geophysics 8(1), pp. 169 – 198.

Broecker. (1998). Paleocean circulation during the last deglaciation: a bipolar seesaw? Paleoceanographyraphy 13(2), pp. 119–21.

Brook, Cowart, Brandt and Scott. (1997). Quaternary climatic change in southern and eastern Africa during the last 300 ka: The evidence from caves in Somalia and the Transvaal region of South Africa. Zeitschrift fur Geomorphologie, Supplementband 108, pp. 15 – 48.

Brooks, Yellen, Potts, Behrensmeyer, Deino, Leslie, Ambrose, Ferguson, D'Errico, Zipkin, Whittaker, Post, Veatch, Foecke, & Clark. (2018). Long-distance stone transport and pigment use in the earliest Middle Stone Age. Science, 360(6384), 90–94. https://doi.org/10.1126/science.aao2646

Bryden and Beal. (2001). Role of the Agulhas Current in Indian Ocean circulation and associated heat and freshwater fluxes. Deep Sea Research Part I Oceanographic Research

Papers 48(8), pp. 1821–1845.

Bryden, Beal and Duncan. (2005). Structure and Transport of the Agulhas Current and Its Temporal Variability. Journal of Oceanography 61, pp. 479–492. doi: 10.1055/s-0038-1624983.

Bryden, Beal and Duncan. (2005). Structure and Transport of the Agulhas Current and Its Temporal Variability. Journal of Oceanography 61, pp. 479–492. doi: 10.1055/s-0038-1624983.

Buller and Mcmanus. (1972). Modes of turbidite deposition deduced from grain-size analyses. Geological Magazine 109(6), pp. 491–500. Available at: http://10.0.3.249/s0016756800042771.

Butzer, Stuckenrath, Bruzewicz and Helgren. (1978). Late Cenozoic paleoclimates of the Gaap Escarpment, Kalahari margin, South Africa. Quaternary Research 10(3), pp. 310–339. Available at: https://www.sciencedirect.com/science/article/pii/003358947890025X.

Caley, Kim, Malaizé, Giraudeau, Laepple, Caillon, Charlier, Rebaubier, Rossignol, Castañeda, Schouten, & Sinninghe Damsté. (2011). High-latitude obliquity as a dominant forcing in the Agulhas current system. Climate of the Past, 7(4), 1285–1296. https://doi.org/10.5194/cp-7-1285-2011

Caley, Peeters, Biastoch, Rossignol, Van Sebille, Durgadoo, Malaizé, Giraudeau, Arthur, & Zahn. (2014). Quantitative estimate of the paleo-Agulhas leakage. Geophys. Res. Lett., October 2012, 1–8. https://doi.org/10.1002/2014GL059278.Received

Caley, Extier, Collins, Schefuß, Dupont, Malaizé, Rossignol, Souron, McClymont, Jimenez-Espejo, García-Comas, Eynaud, Martinez, Roche, Jorry, Charlier, Wary, Gourves, Billy, & Giraudeau. (2018). A two-million-year-long hydroclimatic context for hominin evolution in southeastern Africa. Nature, 560(7716), 76–79. https://doi.org/10.1038/s41586-018-0309-6

Caley, Giraudeau, Malaizé, Rossignol and Pierre. (2012). Agulhas leakage as a key process in the modes of Quaternary climate changes. Proceedings of the National Academy of Sciences of the United States of America 109(18), pp. 6835–6839. doi: 10.1073/pnas.1115545109.

Camberlin, Janicot and Poccard. (2001). Seasonality and Atmospheric Dynamics of the Teleconnection between African Rainfall and Tropical Sea Surface Temperature: Atlantic vs ENSO. International Journal of Climatology 21, pp. 973–1005. doi: 10.1002/2016JD025277.

Cao, He, Shi, An, Wang, Liu, Zhao, Zhou, Chen, & He. (2023). EMMTE: An Excel VBA tool for source apportionment of nitrate based on the stable isotope mixing model. Science of the Total Environment, 868(January), 161728. https://doi.org/10.1016/j.scitotenv.2023.161728

Capo, Stewart and Chadwick. (1998). Strontium isotopes as tracers of ecosystem pro-

cesses: Theory and methods. Geoderma 82(1–3), pp. 197–225. doi: 10.1016/S0016-7061(97)00102-X.

Carr, Bateman, Roberts, Murray-Wallace, Jacobs and Holmes. (2010). The last interglacial sea-level high stand on the southern Cape coastline of South Africa. Quaternary Research 73(2), pp. 351–363. Available at: http://dx.doi.org/10.1016/j.yqres.2009.08.006.

Carr, Chase, Birkinshaw, Holmes, Rabumbulu and Stewart. (2023). Paleolakes and socioecological implications of last glacial "greening" of the South African interior. Proceedings of the National Academy of Sciences 120(21), p. e2221082120. Available at: https://www.pnas.org/doi/abs/10.1073/pnas.2221082120

Carrion, Brink, Scott and Binneman. (2000). Palynology and palaeo- environment of Pleistocene hyaena coprolites from an open-air site at Oyster Bay, Eastern Cape coast, South Africa. South African Journal of Science 96, pp. 449–453.

Carter, Griffith, Clift, Scher and Dellapenna. 2020. Clay-fraction strontium and neodymium isotopes in the Indus Fan: implications for sediment transport and provenance. Geological Magazine, pp. 1–16. doi: 10.1017/s0016756820000394.

Carto, Weaver, Hetherington, Lam and Wiebe. (2009). Out of Africa and into an ice age: on the role of global climate change in the late Pleistocene migration of early modern humans out of Africa. Journal of Human Evolution 56(2), pp. 139–151. Available at: https://www.sciencedirect.com/science/article/pii/S0047248408001863.

Cartwright and Parkington. (1997). The Wood Charcoal Assemblages from Elands Bay Cave, Southwestern Cape: Principles, Procedures and Preliminary Interpretation. The South African Archaeological Bulletin 52(165), pp. 59–72. Available at: http://www.jstor.org/stable/3888977.

Cásal, Beal, Lumpkin and Johns. (2009). Structure and downstream evolution of the Agulhas Current system during a quasi-synoptic survey in February-March 2003. Journal of Geophysical Research: Oceans 114(3), pp. 1–16. doi: 10.1029/2008JC004954.

Castañeda, Caley, Dupont, Kim, Malaizé and Schouten. (2016). Middle to Late Pleistocene vegetation and climate change in subtropical southern East Africa. Earth and Planetary Science Letters 450, pp. 306–316. Available at: http://dx.doi.org/10.1016/j.epsl.2016.06.049.

Castañeda, Werne and Johnson. (2007). Wet and arid phases in the southeat African tropics since the Last Glacial Maximum. Geology 35(9), pp. 823–826. doi: 10.1130/G23916A.1.

Catuneanu, Wopfner, Eriksson, Cairncross, Rubidge, Smith and Hancox. (2005). The Karoo basins of south-central Africa. Journal of African Earth Sciences 43(1–3), pp. 211–253. doi: 10.1016/j.jafrearsci.2005.07.007.

Cawthra, Anderson, De Vynck, Jacobs, Jerardino, Kyriacou and Marean. (2020a). Migration of Pleistocene shorelines across the Palaeo-Agulhas Plain: Evidence from dated sub-bottom profiles and archaeological shellfish assemblages. Quaternary Science Reviews 235(xxxx), p. 106107. Available at: https://doi.org/10.1016/j.quascirev.2019.106107.

Cawthra, Bateman, Carr, Compton and Holmes. (2014). Understanding late quaternary change at the land-ocean interface: A synthesis of the evolution of the Wilderness coastline, South Africa. Quaternary Science Reviews 99, pp. 210–223. Available at: http://dx.doi.org/10.1016/j.quascirev.2014.06.029.

Cawthra, Cowling, Andò and Marean. (2020b). Geological and soil maps of the Palaeo-Agulhas Plain for the Last Glacial Maximum. Quaternary Science Reviews 235(xxxx), p. 105858. doi: 10.1016/j.quascirev.2019.07.040.

Cawthra, Frenzel, Hahn, Compton, Gander and Zabel. (2019). Seismic stratigraphy of the inner to mid Agulhas bank, South Africa. Quaternary Science Reviews (October), p. 105979. Available at: https://doi.org/10.1016/j.quascirev.2019.105979.

Chamley (1989). Clay Minerals. Clay Sedimentology, pp. 3–20. Available at: https://link.springer.com/ter/10.1007/978-3-642-85916-8-1 [Accessed: 4 January 2023].

Chapman and Shackleton. (1999). Global ice-volume fluctuations, North Atlantic ice-rafting events, and deep-ocean circulation changes between 130 and 70 ka. Geology 27(9), pp. 795–798. doi: 10.1130/0091-7613(1999)027<0795:GIVFNA>2.3.CO;2.

Chappell. (1973). Astronomical theory of climatic change: Status and problem. Quaternary Research 3(2), pp. 221–236. Available at: https://www.sciencedirect.com/science/article/pii/0033589473900422.

Charles, Lynch-Stieglitz, Ninnemann and Fairbanks. (1996). Climate connections between the hemisphere revealed by deep sea sediment core/ice core correlations. Earth and Planetary Science Letters 142(1–2), pp. 19–27. doi: 10.1016/0012-821x(96)00083-0.

Charlier, Ginibre, Morgan, Nowell, Pearson, Davidson and Ottley. (2006). Methods for the microsampling and high-precision analysis of strontium and rubidium isotopes at single crystal scale for petrological and geochronological applications. Chemical Geology 232(3–4), pp. 114–133. doi: 10.1016/j.chemgeo.2006.02.015.

Chase and Meadows. (2007). Late Quaternary dynamics of southern Africa's winter rainfall zone. Earth-Science Reviews 84(3–4), pp. 103–138.
doi: 10.1016/j.earscirev.2007.06.002.

Chase, Niedermeyer, Boom, Carr, Chevalier, He, Meadows, Ogle, & Reimer. (2019). Orbital controls on Namib Desert hydroclimate over the past 50,000 years. Geology, 47(9), 867–871. https://doi.org/10.1130/G46334.1

Chase, Boom, Carr, Chevalier, Quick, Verboom and Reimer. (2019). Extreme hydrocli-

mate response gradients within the western Cape Floristic region of South Africa since the Last Glacial Maximum. Quaternary Science Reviews 219, pp. 297–307. Available at: https://doi.org/10.1016/j.quascirev.2019.07.006.

Chase, Boom, Carr, Meadows and Reimer. (2013). Holocene climate change in southernmost South Africa: Rock hyrax middens record shifts in the southern westerlies. Quaternary Science Reviews 82, pp. 199–205. Available at: http://dx.doi.org/10.1016/j.quascirev.2013.10.018.

Chase, Carr, Boom, Tyrrell and Reimer. (2023). Linking upwelling intensity and orbital-scale climate variability in South Africa's winter rainfall zone: Insights from a 70,000-year hyrax midden record. Quaternary Science Advances 12(August). doi: 10.1016/j.qsa.2023.100110.

Chase, Harris, deWit, Kramers, Doel and Stankiewicz. (2021). South African speleothems reveal influence of high and lowlatitude forcing over the past 113.5 k.y. Geology 49(11), pp. 1353–1357. doi: 10.1130/G49323.1.

Chase, Lim, Chevalier, Boom, Carr, Meadows and Reimer. (2015). Influence of tropical easterlies in southern Africa's winter rainfall zone during the Holocene. Quaternary Science Reviews 107, pp. 138–148. doi: 10.1016/j.quascirev.2014.10.011.

Chase, Meadows, Scott, Thomas, Marais, Sealy and Reimer. (2009). A record of rapid Holocene climate change preserved in hyrax middens from southwestern Africa. Geology 37(8), pp. 703–706. doi: 10.1130/G30053A.1.

Chase, Quick, Meadows, Scott, Thomas and Reimer. (2011). Late glacial interhemispheric climate dynamics revealed in South African hyrax middens. Geology 39(1), pp. 19 – 22. Available at: https://www.scopus.com/inward/record.uri?eid=2-s2.0-78751545890&doi=10.1130

Chase and Quick. (2018). Influence of Agulhas forcing of Holocene climate change in South Africa's southern Cape. Quaternary Research (United States) 90(2), pp. 303–309. doi: 10.1017/qua.2018.57

Chase. (2010). South African palaeoenvironments during marine oxygen isotope stage 4: a context for the Howiesons Poort and Still Bay industries. Journal of Archaeological Science 37(6), pp. 1359–1366. doi: 10.1016/j.jas.2009.12.040.

Chase. (2021). Orbital forcing in southern Africa: Towards a conceptual model for predicting deep time environmental change from an incomplete proxy record. Quaternary Science Reviews 265, p. 107050. Available at: https://doi.org/10.1016/j.quascirev.2021.107050.

Chavaillaz, Codron and Kageyama. (2013). Southern westerlies in LGM and future (RCP4.5) climates. Climate of the Past 9(2), pp. 517–524. Available at: https://cp.copernicus.org/articles/9/517/2013/.

Chen, Kissel, Govin, Liu and Xie. (2016). Correction of interstitial water changes

in calibration methods applied to XRF core-scanning major elements in long sediment cores: Case study from the South China Sea. Geochemistry Geophysics Geosystems, pp. 1925–1934. doi: 10.1002/2016GC006320.Received.

Cheng, Edwards, Broecker, Denton, Kong, Wang, Zhang, & Wang. (2009). Ice age terminations. Science, 326(5950), 248–252. https://doi.org/10.1126/science.1177840

Cheng, Edwards, Sinha, Spötl, Yi, Chen, Kelly, Kathayat, Wang, Li, Kong, Wang, Ning, & Zhang. (2016). The Asian monsoon over the past 640,000 years and ice age terminations. Nature, 534(7609), 640–646. https://doi.org/10.1038/nature18591

Chevalier and Chase. (2015). Southeast African records reveal a coherent shift from high- to low-latitude forcing mechanisms along the east African margin across last glacial-interglacial transition. Quaternary Science Reviews 125, pp. 117–130.

Chevalier and Chase. (2015). Southeast African records reveal a coherent shift from high- to low-latitude forcing mechanisms along the east African margin across last glacial-interglacial transition. Quaternary Science Reviews 125, pp. 117–130. Available at: http://dx.doi.org/10.1016/j.quascirev.2015.07.009.

Chevalier, Brewer and Chase. (2017). Qualitative assessment of PMIP3 rainfall simulations across the eastern African monsoon domains during the mid-Holocene and the Last Glacial Maximum. Quaternary Science Reviews 156, pp. 107–120. doi: 10.1016/j.quascirev.2016.11.028.

Chiang, Biasutti and Battisti. (2003). Sensitivity of the Atlantic Intertropical Convergence Zone to Last Glacial Maximum boundary conditions. Paleoceanography 18(4), pp. 1–18. doi: 10.1029/2003PA000916.

Civel-Mazens, Crosta, Cortese, Michel, Mazaud, Ther, Ikehara, & Itaki. (2021). Impact of the Agulhas Return Current on the oceanography of the Kerguelen Plateau region, Southern Ocean, over the last 40 kyrs. Quaternary Science Reviews, 251, 106711. https://doi.org/10.1016/j.quascirev.2020.106711

Clark, Dyke, Shakun, Carlson, Clark, Wohlfarth, Mitrovica, Hostetler, & McCabe. (2009). The Last Glacial Maximum. Science, 325(5941), 710–714.
https://doi.org/10.1126/science.1172873

Clark, Pisias, Stocker and Weaver. (2002). The role of the thermohaline circulation in abrupt climate change. Nature 415(6874), pp. 863–869. Available at: https://doi.org/10.1038/415863a.

Clement, Cane and Seager. (2001). An orbitally tropical source for abrupt climate change. Journal of Climate 14(11), pp. 2369–2375. doi: 10.1175/1520-0442(2001)014<2369:AODTSF>2.0.CO;2

Clift, Il Lee, Hildebrand, Shimizu, Layne, Blusztajn, Blum, Garzanti, & Ali Khan. (2002). Nd and Pb isotope variability in the Indus River System: implications for sediment provenance and crustal heterogeneity in the Western Himalaya. Earth and Planetary Science

Letters, 200, 91–106. www.elsevier.com/locate/epsl

Cockcroft, Wilkinson and Tyson. (1987). The application of a present-day climatic mode to the Late Quaternary in southern Africa. Climatic Change 10, pp. 161–181.

Collins, Schefuß, Govin, Mulitza and Tiedemann. (2014). Insolation and glacial-interglacial control on southwestern African hydroclimate over the past 140000 years. Earth and Planetary Science Letters 398, pp. 1–10. Available at: http://dx.doi.org/10.1016/j.epsl.2014.04.034.

Compton and Maake. (2007). Source of the suspended load of the upper Orange River, South Africa. South African Journal of Geology 110(2–3), pp. 339–348. doi: 10.2113/gssajg.110.2-3.339.

Compton and Wiltshire. (2009). Terrigenous sediment export from the western margin of South Africa on glacial to interglacial cycles. Marine Geology 266(1–4), pp. 212–222. doi: 10.1016/j.margeo.2009.08.013.

Compton, Herbert and Schneider. (2009). Organic-rich mud on the western margin of southern Africa: Nutrient source to the Southern Ocean? Global Biogeochemical Cycles 23(4), pp. 1–12. doi: 10.1029/2008GB003427.

Compton. (2011). Pleistocene sea-level fluctuations and human evolution on the southern coastal plain of South Africa. Quaternary Science Reviews 30(5–6), pp. 506–527. Available at: http://dx.doi.org/10.1016/j.quascirev.2010.12.012.

Compton. (2016). Did we speciate on the Southern Coastal Plain of South Africa? Quaternary International 404(2016), pp. 204–205. Available at: http://dx.doi.org/10.1016/j.quaint.2015.08.190.

Cooke and Rohling. (1999). Stable isotopes in foraminiferal carbonate. Southampton Oceanography Centre, pp. 1–40.

Copeland, Cawthra, Fisher, Lee-Thorp, Cowling, le Roux, Hodgkins, & Marean. (2016). Strontium isotope investigation of ungulate movement patterns on the Pleistocene Paleo-Agulhas Plain of the Greater Cape Floristic Region, South Africa. Quaternary Science Reviews, 141, 65–84. https://doi.org/10.1016/j.quascirev.2016.04.002

Corliss, McCorkle and Higdon. (2002). A time series study of the carbon isotopic composition of deep-sea benthic foraminifera. Paleoceanography 17(3), pp. 8-1-8–27. doi: 10.1029/2001pa000664.

Cortese and Abelmann. (2002). Radiolarian-based paleotemperatures during the last 160 kyr at ODP Site 1089 (Southern Ocean, Atlantic Sector). Palaeogeography, Palaeoclimatology, Palaeoecology 182(3), pp. 259–286. Available at: https://www.sciencedirect.com/science/article/pii/S0031018201004990.

Cortijo, Labeyrie, Vidal, Vautravers, Chapman, Duplessy, Elliot, Arnold, Turon, & Auf-

fret. (1997). Changes in sea surface hydrology associated with Heinrich event 4 in the North Atlantic Ocean between 40 and 60 N. Earth and Planetary Science Letters, 146(1–2), 29–45.

Costa, Russell, Konecky and Lamb. (2014). Isotopic reconstruction of the African Humid Period and Congo Air Boundary migration at Lake Tana, Ethiopia. Quaternary Science Reviews 83, pp. 58–67. Available at: http://dx.doi.org/10.1016/j.quascirev.2013.10.031.

Cowling, Cartwright, Parkington and Allsopp. (1999). Fossil wood charcoal assemblages from Elands Bay Cave, South Africa: Implications for Late Quaternary vegetation and climates in the winter-rainfall fynbos biome. Journal of Biogeography 26(2), pp. 367–378. doi: 10.1046/j.1365-2699.1999.00275.x.

Cowling, Potts, Franklin, Midgley, Engelbrecht and Marean. (2019). Describing a drowned Pleistocene ecosystem: Last Glacial Maximum vegetation reconstruction of the Palaeo-Agulhas Plain. Quaternary Science Reviews 235(xxxx), p. 105866. Available at: https://doi.org/10.1016/j.quascirev.2019.105866.

Crétat, Pohl, Dieppois, Berthou and Pergaud. (2019). The Angola Low: relationship with southern African rainfall and ENSO. Climate Dynamics 52(3), pp. 1783–1803. Available at: https://doi.org/10.1007/s00382-018-4222-3.

Crétat, Richard, Pohl, Rouault, Reason and Fauchereau. (2012). Recurrent daily rainfall patterns over South Africa and associated dynamics during the core of the austral summer. International Journal of Climatology 32(2), pp. 261–273. Available at: https://doi.org/10.1002/joc.2266.

Cronin, Tozuka, Biastoch, Durgadoo and Beal. (2013). Prevalence of strong bottom currents in the greater Agulhas system. Geophysical Research Letters 40(9), pp. 1772–1776. Available at: http://10.0.3.234/grl.50400.

Croudace, Löwemark, Tjallingii and Zolitschka. (2019). Current perspectives on the capabilities of high resolution XRF core scanners. Quaternary International 514(March), pp. 5–15. Available at: https://doi.org/10.1016/j.quaint.2019.04.002.

Curry and Oppo. (2005). Glacial water mass geometry and the distribution of 13C of ΣCO2 in the western Atlantic Ocean. Paleoceanography 20(1), pp. 1–12. doi: 10.1029/2004PA001021.

Curry et al. (1988). CHANGES IN THE DISTRIBUTION OF 513C OF DEEP WATER ZCO2 BETWEEN THE LAST GLACIATION AND THE HOLOCENE To cite this version : HAL Id : hal-03550978.

Cutler, Edwards, Taylor, Cheng, Adkins, Gallup, Cutler, Burr, & Bloom. (2003). Rapid sea-level fall and deep-ocean temperature change since the last interglacial period. Earth and Planetary Science Letters, 206(3), 253–271.

https://doi.org/https://doi.org/10.1016/S0012-821X(02)01107-X

d'Errico and Henshilwood. (2007). Additional evidence for bone technology in the southern African Middle Stone Age. Journal of Human Evolution 52(2), pp. 142–163.

Daniau, Loutre, Swingedouw, Laepple, Bassinot, Malaizé, Kageyama, Charlier, & Carfantan. (2023). Precession and obliquity forcing of the South African monsoon revealed by sub-tropical fires. Quaternary Science Reviews, 310.
https://doi.org/10.1016/j.quascirev.2023.108128

Daniau, Goñi, Martinez, Urrego, Bout-Roumazeilles, Desprat and Marlon. (2013). Orbital-scale climate forcing of grassland burning in southern Africa. Proceedings of the National Academy of Sciences of the United States of America 110(13), pp. 5069–5073. doi: 10.1073/pnas.1214292110.

Dansgaard, Johnsen, Clausen, Dahl-Jensen, Gundestrup, Hammer, Hvidberg, Steffensen, Sveinbjörnsdottir, Jouzel, & Bond. (1993). Evidence for general instability of past climate from a 250-kyr ice-core record. Nature, 364(6434), 218–220. https://doi.org/10.1038/364218a0

Dansgaard, Johnsen, Clausen, Dahl-Jensen, Gundestrup, Hammer and Oeschger. (1984). North Atlantic Climatic Oscillations Revealed by Deep Greenland Ice Cores. In: Climate Processes and Climate Sensitivity. Geophysical Monograph Series. pp. 288–298. Available at: https://doi.org/10.1029/GM029p0288.

Dasch. (1969). Strontium isotopes in weathering profiles, deep-sea sediments, and sedimentary rocks. 33, pp. 1521–1552.

De Boer, Graham, Thomas and Kohfeld. (2013). The control of the Southern Hemisphere Westerlies on the position of the subtropical front. Journal of Geophysical Research: Oceans 118(10), pp. 5669–5675. doi: 10.1002/jgrc.20407.

De Ruijter, Biastoch, Drijfhout, Lutjeharms, Matano, R. P., Pichevin, van Leeuwen and Weijer (1999), Indian-Atlantic interocean exchange: Dynamics, estimation and impact, J. Geophys. Res., 104(C9), 20885–20910, doi:10.1029/1998JC900099.

De Ruijter, Ridderinkhof and Schouten. (2005). Variability of the southwest Indian Ocean. Philosophical Transactions of the Royal Society A: Mathematical, Physical and Engineering Sciences 363(1826), pp. 63–76. doi: 10.1098/rsta.2004.1478.

De Ruijter, Ridderinkhof, Lutjeharms, Schouten and Veth. (2002). Observations of the flow in the Mozambique Channel. Geophysical Research Letters 29(10), pp. 140-1-140–3. doi: 10.1029/2001gl013714.

Deacon and Lancaster. (1988). Late Quaternary palaeoenvironments of southern Africa. Clarendon Press, Oxford, p. 225.

Delmonte, Andersson, Hansson, Schöberg, Petit, Basile-Doelsch and Maggi. (2008). Aeolian dust in East Antarctica (EPICA-Dome C and Vostok): Provenance during glacial ages

over the last 800 kyr. Geophysical Research Letters 35(7), pp. 2–7. doi: 10.1029/2008GL033382.

Denton and Hughes. (1983). Milankovitch theory of ice ages: Hypothesis of ice-sheet linkage between regional insolation and global climate. Quaternary Research 20(2), pp. 125–144. Available at: https://www.sciencedirect.com/science/article/pii/003358948390073X.

Depaolo and Wasserburg. (1976). Nd Isotopic Variations and Petrogenetic Models. Geophysical Research Letters 3(5), pp. 3–6.

Depaolo. (1988). Neodymium Isotope Geochemistry. Berlin: Spring-Verlag.

Derry and France-Lanord. (1996). EPSL Neogene Himalayan weathering history and river 87Sr/ 86Sr: impact on the marine Sr record Pli SOOl2-82lX(96>00091-X. Earth and Planetary Science Letters 142, pp. 59–74.

Dickin. (1995). Radiogenic Isotope Geochemistry. Cambridge: Cambridge University Press (CUP).

Diekmann, Kuhn, Mackensen, Petschick, Fütterer, Gersonde, Rühlemann, & Niebler. (1996). Clay mineral fluctuations in Late Quaternary sediments of the Southeastern South Atlantic: implications for past changes of deep water advection. In The South Atlantic: Present and Past Circulation. Springer-Verlag, Berlin, (pp. 621–644).

Diekmann, Kuhn, Mackensen, Petschick, Fütterer, Gersonde, Rühlemann, & Niebler. (1999). Kaolinite and Chlorite as Tracers of Modern and Late Quaternary Deep Water Circulation in the South Atlantic and the Adjoining Southern Ocean.

Diekmann, Kuhn, Rachold, Abelmann, Brathauer, Fütterer, Gersonde, & Grobe. (2000). Terrigenous sediment supply in the Scotia Sea (Southern Ocean): response to Late Quaternary ice dynamics in Patagonia and on the Antarctic Peninsula. Palaeogeography, Palaeoclimatology, Palaeoecology, 162(3), 357–387.
https://doi.org/https://doi.org/10.1016/S0031-0182(00)00138-3

Diekmann, Fütterer, Grobe, Hillenbrand, Kuhn, Michels, Petschick, & Pirrung. (2003). Terrigenous Sediment Supply in the Polar to Temperate South Atlantic: Land-Ocean Links of Environmental Changes during the Late Quaternary. The South Atlantic in the Late Quaternary, 375–399. https://doi.org/10.1007/978-3-642-18917-318

Diekmann, Hofmann, Henrich, Fütterer, Röhl and Wei. (2008). Detrital sediment supply in the southern Okinawa Trough and its relation to sea-level and Kuroshio dynamics during the late Quaternary. Marine Geology 255(1–2), pp. 83–95. doi: 10.1016/j.margeo.2008.08.001.

Diekmann. (2007). Sedimentary patterns in the late Quaternary Southern Ocean. Deep Sea Research Part II: Topical Studies in Oceanography 54(21), pp. 2350–2366. Available at: https://www.sciencedirect.com/science/article/pii/S0967064507001762.

DiNezio, Tierney, Otto-Bliesner, Timmermann, Bhattacharya, Rosenbloom and Brady.

(2018). Glacial changes in tropical climate amplified by the Indian Ocean. Science Advances 4(12). Available at: https://www.science.org/doi/10.1126/sciadv.aat9658 [Accessed: 1 December 2022].

Dingle and Rogers. (1972). Pleistocene Palaeogeography of the Agulhas Bank. Transactions of the Royal Society of South Africa 40(3), pp. 155–165. Available at: https://doi.org/10.1080/0035

Dinis, Garzanti, Hahn, Vermeesch and Cabral-Pinto. (2020). Weathering indices as climate proxies. A step forward based on Congo and SW African river muds. Earth-Science Reviews 201(November 2019), p. 103039. Available at: https://doi.org/10.1016/j.earscirev.2019.103039.

Diz, Hall, Zahn and Molyneux. (2007). Paleoceanography of the southern Agulhas Plateau during the last 150 ka: Inferences from benthic foraminiferal assemblages and multispecies epifaunal carbon isotopes. Paleoceanography 22(4), pp. 1–16. doi: 10.1029/2007PA001511.

Dunlea, Murray, Tada, Alvarez-Zarikian, Anderson, Gilli, Giosan, Gorgas, Hennekam, Irino, Murayama, Peterson, Reichart, Seki, Zheng, & Ziegler. (2020). Intercomparison of XRF Core Scanning Results From Seven Labs and Approaches to Practical Calibration. Geochemistry, Geophysics, Geosystems, 21(9). https://doi.org/10.1029/2020GC009248

Dunning, Black and Allan. 2016. The onset and cessation of seasonal rainfall over Africa. Journal of Geophysical Research: Atmospheres 121(19), pp. 11,405-411,424. Available at: https://doi.org/10.1002/2016JD025428.

Dunning, Black and Allan. (2018). Later Wet Seasons with More Intense Rainfall over Africa under Future Climate Change. Journal of Climate 31(23), pp. 9719–9738. Available at: https://journals.ametsoc.org/view/journals/clim/31/23/jcli-d-18-0102.1.xml.

Duplessy, Shackleton, Fairbanks, Labeyrie, Oppo and Kallel. (1988). Deepwater source variations during the last climatic cycle and their impact on the global deepwater circulation. Paleoceanography 3(3), pp. 343–360. Available at: https://doi.org/10.1029/PA003i003p00343.

Duplessy, Shackleton, Matthews, Prell, Ruddiman, Caralp and Hendy. (1984). 13C Record of benthic foraminifera in the last interglacial ocean: Implications for the carbon cycle and the global deep water circulation. Quaternary Research 21(2), pp. 225–243. doi: 10.1016/0033-5894(84)90099-1.

Dupont, Caley, Kim, Castañeda, Malaizé and Giraudeau. (2011). Glacial-interglacial vegetation dynamics in South Eastern Africa coupled to sea surface temperature variations in the Western Indian Ocean. Climate of the Past 7(4), pp. 1209–1224. doi: 10.5194/cp-7-1209-2011.

Dupont, Caley, Kim, Castañeda, Malaizé and Giraudeau. (2011). Glacial-interglacial

vegetation dynamics in South Eastern Africa coupled to sea surface temperature variations in the Western Indian Ocean. Climate of the Past 7(4), pp. 1209–1224. doi: 10.5194/cp-7-1209-2011.

Dupont, Zhao, Charles, Faith and Braun. (2021). Continuous vegetation record of the Greater Cape Floristic Region (South Africa) covering the past 300 thousand years (IODP U1479). (July), pp. 1–32.

Dusseldorp, Lombard and Wurz. (2013). Pleistocene Homo and the updated Stone Age sequence of South Africa. South African Journal of Science 109(5/6), p. 7. Available at: https://sajs.co.za/article/view/3889.

Eglington and Armstrong. (2004). The Kaapvaal Craton and adjacent orogens, southern Africa: a geochronological database and overview of the geological development of the craton. South African Journal of Geology 107(1–2), pp. 13–32. Available at: https://doi.org/10.2113/107.1-2.13. Emiliani. (1955). Pleistocene Temperatures. Journal of Geology.

Engelbrecht, Marean, Cowling, Engelbrecht, Nkoana, O'Neal, Fisher, Shook, Franklin, Neumann, Scott, Thatcher, McGregor, Van der Merwe, Dedekind, Difford, (2019). Downscaling Last Glacial Maximum climate over southern Africa. Quaternary Science Reviews 226, p. 105879. Available at: https://doi.org/10.1016/j.quascirev.2019.105879.

Engelbrecht, Landman, Engelbrecht and Malherbe. (2015). A synoptic decomposition of rainfall over the Cape south coast of South Africa. Climate Dynamics 44(9), pp. 2589–2607. Available at: https://doi.org/10.1007/s00382-014-2230-5.

Engelbrecht, McGregor and Engelbrecht. (2009). Dynamics of the Conformal-Cubic Atmospheric Model projected climate-change signal over southern Africa. International Journal of Climatology 29(7), pp. 1013–1033. Available at: https://rmets.onlinelibrary.wiley.com/doi/abs/10.1002/joc.1742.

EPICA Members, (2004). Eight glacial cycles from an Antarctic ice core. Nature 429(6992), pp. 623–628. Available at: https://doi.org/10.1038/nature02599.

EPICA Members, (2006). Stable oxygen isotopes of ice core EDML.

Esper, Versteegh, Zonneveld and Willems. (2004). A palynological reconstruction of the Agulhas Retroflection (South Atlantic Ocean) during the Late Quaternary. Global and Planetary Change 41(1), pp. 31–62. doi: 10.1016/j.gloplacha.2003.10.002.

Fagel, Hillaire-Marcel, Humblet, Brasseur, Weis and Stevenson. (2004). Nd and Pb isotope signatures of the clay-size fraction of Labrador Sea sediments during the Holocene: Implications for the inception of the modern deep circulation pattern. Paleoceanography 19(3). doi: 10.1029/2003PA000993.

Fagel. (2007). Proxies in late cenozoic paleoceanography. Developments in Marine Geol-

ogy 1(07), pp. 139–184. doi: 10.1016/S1572-5480(07)01009-3.

Faith, Chase and Avery. (2019). Late Quaternary micromammals and the precipitation history of the southern Cape, South Africa. Quaternary Research (United States) 91(2), pp. 729–750. doi: 10.1017/qua.2018.105.

FAO and ISRIC. (2009). JRC (2009) Harmonized world soil database (version 1.1). FAO, Rome, Italy and IIASA, Laxenburg, Austria [www document]. URL http://www. fao. org/nr/land/soils/harmonized-world-soildatabase/en.

Farmer, deMenocal and Marchitto. (2005). Holocene and deglacial ocean temperature variability in the Benguela upwelling region: Implications for low-latitude atmospheric circulation. Paleoceanography 20(2). Available at:
https://doi.org/10.1029/2004PA001049.

Feng, Zhu, Zhen and Hu. (2009). Grain size effect on Sr and Nd isotopic compositions in eolian dust: Implications for tracing dust provenance and Nd model age. Geochemical Journal 43(2), pp. 123–131. doi: 10.2343/geochemj.1.0007.

Feron, de Ruijter and Oskam. (1992). Ring shedding in the Agulhas current system. Journal of Geophysical Research: Oceans 97(C6), pp. 9467–9477. doi: 10.1029/92JC00736.

Ferrari, Jansen, Adkins, Burke, Stewart and Thompson. (2014). Antarctic sea ice control on ocean circulation in present and glacial climates. Proceedings of the National Academy of Sciences of the United States of America 111(24), pp. 8753–8758. doi: 10.1073/pnas.1323922111.

Ffield, Toole and Wilson. (1997). Seasonal Circulation in the South Indian Ocean. Geophysical Research Letters 24(22), pp. 2773–2776.

Finch and Hill. (2008). A late Quaternary pollen sequence from Mfabeni Peatland, South Africa: Reconstructing forest history in Maputaland. Quaternary Research 70(3), pp. 442–450.

Fischer, Fundel,Ruth,Twarloh, Wegner, Udisti, Becagli, Castellano, Morganti, Severi, Wolff, Littot, Röthlisberger, Mulvaney, Hutterli, Kaufmann,Federer, Lambert, Bigler, Hansson, Jonsell, de Angelis, Boutron, Siggaard-Andersen, Steffensen, Barbante, Gaspari, Gabrielli, Wagenbach, (2007). Reconstruction of millennial changes in dust emission, transport and regional sea ice coverage using the deep EPICA ice cores from the Atlantic and Indian Ocean sector of Antarctica. Earth and Planetary Science Letters 260(1–2), pp. 340–354. doi: 10.1016/j.epsl.2007.06.014.

Fisher, Cawthra, Esteban, Jerardino, Neumann, Oertle, Pargeter, Saktura, Szabó, Winkler, & Zohar. (2020). Coastal occupation and foraging during the last glacial maximum and early Holocene at Waterfall Bluff, eastern Pondoland, South Africa. Quaternary Research (United States), 97, 1–41. https://doi.org/10.1017/qua.2020.26

Fisher, Bar-Matthews, Jerardino and Marean. (2010). Middle and Late Pleistocene paleoscape modeling along the southern coast of South Africa. Quaternary Science Reviews 29(11–12), pp. 1382–1398. Available at: http://dx.doi.org/10.1016/j.quascirev.2010.01.015.

Flemming. (1980). Sand transport and bedform patterns on the continental shelf between Durban and Port Elizabeth (southeast African continental margin). Sedimentary Geology 26(1–3), pp. 179–205. doi: 10.1016/0037-0738(80)90011-1.

Flemming. (1981). Factors controlling shelf sediment dispersal along the southeast african continental margin. (42), pp. 259–277.

Flores, Gersonde and Sierro. (1999). Pleistocene fluctuations in the Agulhas Current Retroflection based on the calcareous plankton record. Marine Micropaleontology 37(1), pp. 1–22. doi: 10.1016/S0377-8398(99)00012-2.

Font, Nowell, Graham Pearson, Ottley and Willis. (2007). Sr isotope analysis of bird feathers by TIMS: a tool to trace bird migration paths and breeding sites. Journal of Analytical Atomic Spectrometry 22(5), pp. 513–522. Available at: http://dx.doi.org/10.1039/B616328A.

Foster and Carmack. (1976). Frontal zone mixing and Antarctic Bottom water formation in the southern Weddell Sea. Deep Sea Research and Oceanographic Abstracts 23(4), pp. 301–317. Available at: https://www.sciencedirect.com/science/article/pii/001174717690872X.

Foster. (1996). Wavelets for period analysis of unevenly sampled time series. 112, pp. 1709–1729. doi: 10.1086/118137.

Franzese, Hemming and Goldstein. (2009). Use of strontium isotopes in detrital sediments to constrain the glacial position of the Agulhas Retroflection. 24(February), pp. 1–12. doi: 10.1029/2008PA001706.

Franzese, Hemming, Goldstein and Anderson. (2006). Reduced Agulhas Leakage during the Last Glacial Maximum inferred from an integrated provenance and flux study. Earth and Planetary Science Letters 250(1–2), pp. 72–88.
doi: 10.1016/j.epsl.2006.07.002.

Frenken, Faurès and Division. (1997). Irrigation Potential in Africa: A Basin Approach. Food and Agriculture Organization of the United Nations. Available at: https://books.google.co.uk/boo

Funnell and Riedel. (1971). The Micropalaeontology of Oceans: Proceedings of the Symposium Held in Cambridge from 10 to 17 September 1967 Under the Title 'Micropalaeontology of Marine Bottom Sediments'. Cambridge University Press.

Gamo and Obata. (2010). Preliminary cruise report KH-09-5 on RV Hakuho Maru. 3, p. 12.

Ganasri and Ramesh. 2016. Assessment of soil erosion by RUSLE model using remote sensing and GIS - A case study of Nethravathi Basin. Geoscience Frontiers 7(6), pp.

953–961. Available at: http://dx.doi.org/10.1016/j.gsf.2015.10.007.

Ganopolski and Rahmstorf. (2001). Rapid changes of glacial climate simulated in a coupled climate model. Nature 409(6817), pp. 153–158. doi: 10.1038/35051500.

Garcin, Vincens, Williamson, Guiot and Buchet. (2006). Wet phases in tropical southern Africa during the last glacial period. Geophysical Research Letters 33(7), pp. 1–4. doi: 10.1029/2005GL025531.

Garçon, Chauvel, France-Lanord, Limonta and Garzanti. (2013). Which minerals control the Nd-Hf-Sr-Pb isotopic compositions of river sediments? Chemical Geology 364, pp. 42–55. Available at: http://dx.doi.org/10.1016/j.chemgeo.2013.11.018.

Garzanti, Andò and Vezzoli. (2009). Grain-size dependence of sediment composition and environmental bias in provenance studies. Earth and Planetary Science Letters 277(3–4), pp. 422–432. Available at: http://dx.doi.org/10.1016/j.epsl.2008.11.007.

Garzanti, Padoan, Peruta, Setti and Villa. (2013). Weathering geochemistry and Sr-Nd fi ngerprints of equatorial upper Nile and Congo muds. 14(2), pp. 292–316. doi: 10.1002/ggge.20060.

Garzanti, Padoan, Setti, López-Galindo and Villa. (2014). Provenance versus weathering control on the composition of tropical river mud (southern Africa). Chemical Geology 366, pp. 61–74. Available at: http://dx.doi.org/10.1016/j.chemgeo.2013.12.016.

Gasse, Chalié, Vincens, Williams and Williamson. (2008). Climatic patterns in equatorial and southern Africa from 30,000 to 10,000 years ago reconstructed from terrestrial and near-shore proxy data. Quaternary Science Reviews 27(25–26), pp. 2316–2340. doi: 10.1016/j.quascirev.2008.08.027.

Gebbie. (2014). How much did Glacial North Atlantic Water shoal? Paleoceanography 29(3), pp. 190–209. doi: 10.1002/2013PA002557.

Gee and Bauder. (1986). Particle-size Analysis. Methods of Soil Analysis, Part 1: Physical and Mineralogical Methods, pp. 383–411. Available at: https://onlinelibrary.wiley.com/doi/full/10.2136/sssabookser5.1.2ed.c15 [Accessed: 3 March 2023].

Goddard and Graham. (1999). Importance of the Indian Ocean for simulating rainfall anomalies over eastern and southern Africa. Journal of Geophysical Research 104(16), pp. 19099–19116. doi: 10.1007/0-387-25098-0_13.

Göktürk, Sobolowski, Simon, Zhang and Jansen. (2023a). Sensitivity of coastal southern African climate to changes in coastline position and associated land extent over the last glacial. Quaternary Science Reviews 300. doi: 10.1016/j.quascirev.2022.107893.

Göktürk, Simon, Sobolowski, Zhang, Van Der Bilt, Mørkved, D'Andrea, van Niekerk, Henshilwood, Armitage, Jansen, (2023b). Behaviourally modern humans in coastal southern Africa experienced an increasingly continental climate during the transition from

Marine Isotope Stage 5 to 4. Frontiers in Earth Science 11(July), pp. 1–20. doi: 10.3389/feart.2023.1198068.

Goldstein and Hemming. (2003). Long-lived Isotopic Tracers in Oceanography, Paleoceanography, and Ice-sheet Dynamics. Treatise on Geochemistry: Second Edition 8, pp. 453–483. doi: 10.1016/B978-0-08-095975-7.00617-3.

Goldstein and Jacobsen. (1987). The Nd and Sr isotopic systematics of river-water dissolved material: Implications for the sources of Nd and Sr in seawater. Chemical Geology: Isotope Geoscience Section 66(3–4), pp. 245–272. doi: 10.1016/0168-9622(87)90045-5.

Goldstein and Jacobsen. (1988). Nd and Sr isotopic systematics of river water suspended material: implications for crustal evolution. Earth and Planetary Science Letters Elsevier Science Publishers B.V 87, pp. 249–265.

Goldstein, Nions, Hamilton, O'Nions and Hamilton. (1984). A Sm-Nd isotopic study of atmospheric dusts and particulates from major river systems. Earth and Planetary Science Letters 70(2), pp. 221–236. doi: 10.1016/0012-821X(84)90007-4.

González-Dávila, Santana-Casiano, Fine, Happell, Delille and Speich. (2011). Carbonate system in the water masses of the Southeast Atlantic sector of the Southern Ocean during February and March 2008. Biogeosciences 8(5), pp. 1401–1413. doi: 10.5194/bg-8-1401-2011.

Goodlad. (1986). Tectonic and sedimentary history of the mid- Natal valley (S.W. Indian Ocean). Bulletin - Joint Geological Survey/University of Cape Town, Marine Geoscience Unit 15.

Gordon, Lutjeharms and Gründlingh. (1987). Stratification and circulation at the Agulhas Retroflection. Deep Sea Research Part A, Oceanographic Research Papers 34(4), pp. 565–599. doi: 10.1016/0198-0149(87)90006-9.

Gordon. (1985). Indian-Atlantic Transfer of Thermocine Water. 227(4690).

Govin, Holzwarth, Heslop, Ford Keeling, Zabel, Mulitza, Collins, & Chiessi. (2012). Distribution of major elements in Atlantic surface sediments (36°N-49°S): Imprint of terrigenous input and continental weathering. Geochemistry, Geophysics, Geosystems, 13(1), 1–23. https://doi.org/10.1029/2011GC003785

Govin, Chiessi, Zabel, Sawakuchi, Heslop, Hörner, Zhang, & Mulitza. (2014). Terrigenous input off northern South America driven by changes in Amazonian climate and the North Brazil Current retroflection during the last 250 ka. Climate of the Past, 10(2), 843–862. https://doi.org/10.5194/cp-10-843-2014

Graham and De Boer. (2013). The dynamical subtropical front. Journal of Geophysical Research: Oceans 118(10), pp. 5676–5685. doi: 10.1002/jgrc.20408.

Granet, Chabaux, Stille, Dosseto, France-Lanord and Blaes. (2010). U-series disequilib-

ria in suspended river sediments and implication for sediment transfer time in alluvial plains: The case of the Himalayan rivers. Geochimica et Cosmochimica Acta 74(10), pp. 2851–2865. Available at: http://dx.doi.org/10.1016/j.gca.2010.02.016.

Grant, Rohling, Bronk Ramsey, Cheng, Edwards, Florindo, Heslop, Marra, Roberts, Tamisiea, & Williams. (2014). Sea-level variability over five glacial cycles. Nature Communications, 5. https://doi.org/10.1038/ncomms6076

Green. (2009). Sediment dynamics on the narrow, canyon-incised and current-swept shelf of the northern KwaZulu-Natal continental shelf, South Africa. Geo-Marine Letters 29(4), pp. 201–219. doi: 10.1007/s00367-009-0135-9.

Griffin, Windom and Goldberg. (1968). The distribution of clay minerals in the World Ocean. Deep-Sea Research and Oceanographic Abstracts 15(4), pp. 433–459. doi: 10.1016/0011-7471(68)90051-X.

Grousset and Biscaye. (2005). Tracing dust sources and transport patterns using Sr, Nd and Pb isotopes. Chemical Geology 222(3–4), pp. 149–167. doi: 10.1016/j.chemgeo.2005.05.006.

Grousset, Biscaye, Revel, Petit, Pye, Joussaume and Jouzel. (1992). Antarctic (Dome C) ice-core dust at 18 k.y. B.P.: Isotopic constraints on origins. Earth and Planetary Science Letters 111(1), pp. 175–182. doi: 10.1016/0012-821X(92)90177-W.

Grousset, Biscaye, Zindler, Prospero and Chester. (1988). Neodymium isotopes as tracers in marine sediments and aerosols: North Atlantic. Earth and Planetary Science Letters 87(4), pp. 367–378. doi: 10.1016/0012-821X(88)90001-5.

Grousset, Parra, Bory, Martinez, Bertrand, Shimmield and Ellam. (1998). Saharan wind regimes traced by the Sr-Nd isotopic composition of subtropical Atlantic sediments: Last Glacial Maximum vs today. Quaternary Science Reviews 17(4–5), pp. 395–409. doi: 10.1016/S0277-3791(97)00048-6.

Grousset, Rognon, Coudé-Gaussen and Pédemay. (1992). Origins of peri-Saharan dust deposits traced by their Nd and Sr isotopic composition. Palaeogeography, Palaeoclimatology, Palaeoecology 93(3–4), pp. 203–212.
doi: 10.1016/0031-0182(92)90097-O.

Grove. (2015). Palaeoclimates, plasticity, and the early dispersal of Homo sapiens. Quaternary International 369. doi: 10.1016/j.quaint.2014.08.019.

Gründlingh. (1983). On the Course of the Agulhas Current. South African Geographical Journal 65(1), pp. 49–57. Available at:
https://doi.org/10.1080/03736245.1983.10559671.

Gutjahr, Frank, Stirling, Klemm, van de Flierdt and Halliday. (2007). Reliable extraction of a deepwater trace metal isotope signal from Fe-Mn oxyhydroxide coatings of marine sed-

iments. Chemical Geology 242(3–4), pp. 351–370. doi: 10.1016/j.chemgeo.2007.03.021.

Haaland, Miller, Unhammer, Reynard, Van Niekerk, Ligouis, Mentzer, & Henshilwood. (2020). Geoarchaeological investigation of occupation deposits in Blombos Cave in South Africa indicate changes in site use and settlement dynamics in the southern Cape during MIS 5b-4. Quaternary Research (United States), 100, 170–223. https://doi.org/10.1017/qua.2020.75

Hahn, Compton, Meyer-Jacob, Kirsten, Lucasssen, Pérez Mayo, Schefuß, & Zabel. (2016). Holocene paleo-climatic record from the South African Namaqualand mudbelt: A source to sink approach. Quaternary International, 404, 121–135. https://doi.org/10.1016/j.quaint.2015.10.017

Hahn, Schefuß, Andò, Cawthra, Frenzel, Kugel, Meschner, Mollenhauer, & Zabel. (2017). Southern Hemisphere anticyclonic circulation drives oceanic and climatic conditions in late Holocene southernmost Africa. Climate of the Past, 13(6), 649–665. https://doi.org/10.5194/cp-13-649-2017

Hahn, Miller, Andó, Bouimetarhan, Cawthra, Garzanti, Green, Radeff, Schefuß, & Zabel. (2018). The Provenance of Terrigenous Components in Marine Sediments Along the East Coast of Southern Africa. Geochemistry, Geophysics, Geosystems, 19(7), 1946–1962. https://doi.org/10.1029/2017GC007228

Hahn, Groenveld, Miller and Zabel. (2020). Glacial to interglacial climate variability in the southeastern African subtropics (25- 20°S). Climate of the Past Discussions 53(9), pp. 1689–1699. doi: 10.1017/CBO9781107415324.004.

Hall, Hemming and LeVay. (2016). International ocean discovery program expedition 361 preliminary report: South African climates (Agulhas LGM density profile). Integrated Ocean Drilling Program: Preliminary Reports (361), pp. 1–46. doi: 10.14379/iodp.pr.361.2016.

Hargrove, Hanson, Martin, Blenkinsop, Bowring, Walker and Munyanyiwa. (2003). Tectonic evolution of the Zambezi orogenic belt: geochronological, structural, and petrological constraints from northern Zimbabwe. Precambrian Research 123(2), pp. 159–186. Available at: https://www.sciencedirect.com/science/article/pii/S0301926803000664.

Harris, Millman, van der Walt, Gommers, Virtanen, Cournapeau, Wieser, Taylor, Berg, Smith, Kern, Picus, Hoyer, van Kerkwijk, Brett, Haldane, del Río, Wiebe, Peterson, Gérard-Marchant, Sheppard, Reddy, Weckesser, Abbasi, Gohlke, & Oliphant. (2020). Array programming with NumPy. Nature, 585(7825), 357–362. https://doi.org/10.1038/s41586-020-2649-2

Harris, Compton and Bevington. (1999). Oxygen and hydrogen isotope composition of kaolinite deposits, Cape Peninsula, South Africa: Low-temperature, meteoric origin. Economic Geology 94(8), pp. 1353–1366. doi: 10.2113/gsecongeo.94.8.1353.

Harvey, Hales, Hobley, Liu and Fan. (2022). Measuring the grain-size distributions of mass movement deposits. Earth Surface Processes and Landforms 47(6), pp. 1599–1614. doi: 10.1002/esp.5337.

Hathaway. (1955). Procedure for Clay Mineral Analyses. Clay Minerals Bulletin 3, pp. 8–13.

Haughton, Todd and Morton. (1991). Sedimentary provenance studies. Geological Society Special Publication 57(57), pp. 1–11. doi: 10.1144/GSL.SP.1991.057.01.01.

Hays, Imbrie and Shackleton. (1976). Variations in the Earth ' s Orbit : Pacemaker of the Ice Ages. Science 194(4270), pp. 1121–1132.

He, Garzanti, Dinis, Yang and Wang. (2020). Provenance versus weathering control on sediment composition in tropical monsoonal climate (South China) - 1. Geochemistry and clay mineralogy. Chemical Geology 558(September), p. 119860. Available at: https://doi.org/10.1016/j.chemgeo.2020.119860.

Heaton, Köhler, Butzin, Bard, Reimer, Austin, Bronk Ramsey, Grootes, Hughen, Kromer, Reimer, Adkins, Burke, Cook, Olsen, & Skinner. (2020). Marine20—The Marine Radiocarbon Age Calibration Curve (0–55,000 cal BP). Radiocarbon, 62(4), 779–820. https://doi.org/DOI: 10.1017/RDC.2020.68

Heaton, Talma and Vogel. (1986). Dissolved gas paleotemperatures and 18O variations derived from groundwater near Uitenhage, South Africa. Quaternary Research 25(1), pp. 79–88. Available at: https://www.sciencedirect.com/science/article/pii/0033589486900451.

Heinrich. (1988). Origin and Consequences of Cyclic Ice Rafting in the Northeast Atlantic Ocean During the Past 130,000 Years. Quarternary Research 29(2), pp. 142–152.

Hemming, Van De Flierdt, Goldstein, Franzese, Roy, Gastineau and Landrot. (2007). Strontium isotope tracing of terrigenous sediment dispersal in the Antarctic circumpolar current: Implications for constraining frontal positions. Geochemistry, Geophysics, Geosystems 8(6). doi: 10.1029/2006GC001441.

Henshilwood and Dubreuil. (2011). The Still Bay and Howiesons Poort, 77-59 ka: Symbolic material culture and the evolution of the mind during the African Middle Stone Age. Current Anthropology 52(3), pp. 361–400. doi: 10.1086/660022.

Henshilwood and Marean. (2003). Comment on "The Origin of Modern Human Behavior." Current Anthropology 44(5), pp. 627–651.

Henshilwood and Sealy. (1997). Bone Artefacts from the Middle Stone Age at Blombos Cave, Southern Cape, South Africa. Current Anthropology 38(5), pp. 890–895. Available at: https://doi.org/10.1086/204678.

Henshilwood, Sealy, Yates, Cruz-Uribe, Goldberg, Grine, Klein, Poggenpoel, Van Niekerk, & Watts. (2001). Blombos Cave, southern Cape, South Africa: Preliminary report on the

1992-1999 excavations of the middle stone age levels. Journal of Archaeological Science, 28(4), 421–448. https://doi.org/10.1006/jasc.2000.0638

Henshilwood, D'Errico, Yates, Jacobs, Tribolo, Duller, Mercier, Sealy, Valladas, Watts, & Wintle. (2002). Emergence of modern human behavior: Middle stone age engravings from South Africa. Science, 295(5558), 1278–1280.
https://doi.org/10.1126/science.1067575

Henshilwood, & Dubreuil. (2011). The Still Bay and Howiesons Poort, 77-59 ka: Symbolic material culture and the evolution of the mind during the African Middle Stone Age. Current Anthropology, 52(3), 361–400. https://doi.org/10.1086/660022

Henshilwood, d'Errico and Watts. (2009). Engraved ochres from the Middle Stone Age levels at Blombos Cave, South Africa. Journal of Human Evolution 57(1), pp. 27–47. Available at: http://dx.doi.org/10.1016/j.jhevol.2009.01.005.

Henshilwood, d'Errico, Vanhaeren, van Niekerk and Jacobs. (2004). Middle Stone Age Shell Beads from South Africa. Science 304(5669), p. 404. Available at: https://doi.org/10.1126/science.1095905.

Henshilwood. (2012). Late Pleistocene Techno-traditions in Southern Africa: A Review of the Still Bay and Howiesons Poort, c. 75-59 ka. Journal of World Prehistory 25(3–4), pp. 205–237. doi: 10.1007/s10963-012-9060-3.

Herbert. (2009). Holocene sediment dynamics on the western margin of South Africa. Thesis.

Hines, Bolge, Goldstein, Charles, Hall and Hemming. (2021). Little Change in Ice Age Water Mass Structure From Cape Basin Benthic Neodymium and Carbon Isotopes. Paleoceanography and Paleoclimatology 36(11), pp. 1–18. doi: 10.1029/2021PA004281.

Hjulström. (1955). Transportation of Detritus by Moving Water1. Trask, P. D. ed. Recent Marine Sediments 4, p. 0. Available at: https://doi.org/10.2110/pec.55.04.0005.

Hodell, Venz, Charles and Ninnemann. (2003). Pleistocene vertical carbon isotope and carbonate gradients in the South Atlantic sector of the Southern Ocean. Geochemistry, Geophysics, Geosystems 4(1), pp. 1–19. doi: 10.1029/2002GC000367.

Hodgkins, Marean, Venter, Richardson, Roberts, Zech, Difford, Copeland, Orr, Keller, Fahey, & Lee-Thorp. (2020). An isotopic test of the seasonal migration hypothesis for large grazing ungulates inhabiting the Palaeo-Agulhas Plain. Quaternary Science Reviews, 235, 106221. https://doi.org/10.1016/j.quascirev.2020.106221

Hoffman and Todd. (2000). A National Review of Land Degradation in South Africa: The influence of Biophysical and Socio-economic Factors. Journal of Southern African Studies 26(4), pp. 743–758. doi: 10.1080/713683611.

Holmgren, Lee-Thorp, Cooper, Lundblad, Partridge, Scott, Sithaldeen, Talma, & Tyson.

(2003). Persistent millennial-scale climatic variability over the past 25,000 years in Southern Africa. Quaternary Science Reviews, 22(21–22), 2311–2326. https://doi.org/10.1016/S0277-3791(03)00204-X

Holmgren, Karlén and Shaw. (1995). Paleoclimatic Significance of the Stable Isotopic Composition and Petrology of a Late Pleistocene Stalagmite from Botswana. Quaternary Research 43(3), pp. 320–328. Available at: https://www.sciencedirect.com/science/article/pii/S0033589485710381.

Holton. (1973). An introduction to dynamic meteorology. American Journal of Physics 41(5), pp. 752–754. Holz, Stuut and Henrich. (2004). Terrigenous sedimentation processes along the continental margin off NW Africa: Implications from grain-size analysis of seabed sediments. Sedimentology 51(5), pp. 1145–1154. doi: 10.1111/j.1365-3091.2004.00665.x.

Howe, Piotrowski, Noble, Mulitza, Chiessi and Bayon. (2016). North Atlantic Deep Water Production during the Last Glacial Maximum. Nature Communications 7(1), p. 11765. Available at: https://doi.org/10.1038/ncomms11765. https://www.R-project.org/

Hu, Li, Li, Bi, Zhao and Bu. (2012). Provenance and climate change inferred from Sr-Nd-Pb isotopes of late Quaternary sediments in the Huanghe (Yellow River) Delta, China. Quaternary Research (United States) 78(3), pp. 561–571. Available at: http://dx.doi.org/10.1016/j.yqre

Hu, Noble, Piotrowski, McCave, Bostock and Neil. (2016). Neodymium isotopic evidence for linked changes in Southeast Atlantic and Southwest Pacific circulation over the last 200 kyr. Earth and Planetary Science Letters 455(October), pp. 106–114. doi: 10.1016/j.epsl.2016.09.027.

Huffman, G.J., E.F., Stocker, Bolvin and Nelkin. (2019). GPM IMERG Final Precipitation L3 Half Hourly 0.1 degree x 0.1 degree V06, Greenbelt, MD, Goddard Earth Sciences Data and Information Services Center (GES DISC).

Hunt and Speakman. (2015). Portable XRF analysis of archaeological sediments and ceramics. Journal of Archaeological Science 53, pp. 626–638. Available at: http://dx.doi.org/10.1016/j.jas

Hutson. (1980). The Agulhas Current During the Late Pleistocene: Analysis of Modern Faunal Analogs. Science 207(4426), pp. 64–66. Available at: https://doi.org/10.1126/science.207.4426.64.

HydroSHEDS v2.0 – Refined global river network and catchment delineations from TanDEM-X elevation data. Lehner, B., Roth A., Huber M. Anand, M., Grill, G., Osterkamp, N.,Tubbesing, R., Warmedinger, L., and Thieme, M. EGU21-9277. EGU General Assembly 2021.

Imbrie, Hays, Martinson, McIntyre, Mix, Morley, Pisias, Prell, & Shackleton. (1984). The orbital theory of Pleistocene climate: support from a revised chronology of the marine

d18O record.

Imbrie, Boyle, Clemens, Duffy, Howard, Kukla, Kutzbach, Martinson, Mcintyre, Pisias, Prell, Raytoo, & Shackleton. (1992). Linear Responses to Milankovitch Forcing ulate new observational and modeling efforts , we. Paleoceanography, 7(6), 701–738. https://doi.org/10.1029/92pa

Imbrie. (1982). Astronomical theory of the Pleistocene ice ages: A brief historical review. Icarus 50(2), pp. 408–422. Available at: https://www.sciencedirect.com/science/article/pii/0019103582901324.

Jacobs and Georgi. (1977). Observations on the Southwest Indian Antarctic Ocean. Deep-Sea Research Part I 24, pp. 43–84.

Jacobs, Roberts, Galbraith, Deacon, Grün, Mackay, Mitchell, Vogelsang, & Wadley. (2008). Ages for Middle Stone Age. Science, 322(5902), 733–735. https://doi.org/10.1126/science.1162219

Jacobs, Amos and Bruchhausen. (1970). Ross sea oceanography and antarctic bottom water formation. Deep Sea Research and Oceanographic Abstracts 17(6), pp. 935–962. Available at:
https://www.sciencedirect.com/science/article/pii/001174717090046X.

Jacobs, Duller, Wintle and Henshilwood. (2006). Extending the chronology of deposits at Blombos Cave, South Africa, back to 140ka using optical dating of single and multiple grains of quartz. Journal of Human Evolution 51(3), pp. 255–273. Available at: https://www.sciencedirect.com/science/article/pii/S004724840600073X.

Jacobsen and Wasserburg. (1980). Sm-Nd isotopic systematics of chondrites and achondrites. Division of Geol. Plan. Sci., 3464(358), pp. 307–308.

Jansen, Overpeck, Briffa, Duplessy, Joos, Masson-Delmotte, Olago, Otto-Bliesner, Peltier, Rahmstorf, Ramesh, Raynaud, Rind, Solomina, Villalba, & Zhang. (2007). Paleoclimates. Global Environmental Change, 49–54. https://doi.org/10.1007/978-94-007-5784-4-45

Jelsma and Dirks. (2002). Neoarchaean tectonic evolution of the Zimbabwe Craton. Geological Society Special Publication 199, pp. 183 – 211.

Jerardino and Marean. (2010). Shellfish gathering, marine paleoecology and modern human behavior: Perspectives from cave PP13B, Pinnacle Point, South Africa. Journal of Human Evolution 59(3–4), pp. 412–424. Available at:
http://dx.doi.org/10.1016/j.jhevol.2010.07.003.

Jerardino. (2016). On the origins and significance of Pleistocene coastal resource use in southern Africa with particular reference to shellfish gathering. Journal of Anthropological Archaeology 41, pp. 213–230. Available at:
http://dx.doi.org/10.1016/j.jaa.2016.01.001.

Jewell, Drake, Crocker, Bakker, Kunkelova, Bristow, Cooper, Milton, Breeze, & Wilson. (2020a). Three North African dust source areas and their geochemical fingerprint. Earth and Planetary Science Letters, 554, 1–34.
https://doi.org/10.1016/j.epsl.2020.116645

Jewell, Cooper, Milton, James, Crocker and Wilson. (2022b). Chemical isolation and isotopic analysis of terrigenous sediments with emphasis on effective removal of contaminating marine phases including barite. Chemical Geology 589(July 2021), p. 120673. Available at: https://doi.org/10.1016/j.chemgeo.2021.120673.

Johnsen, Clausen, Dansgaard, Gundestrup, Hammer, Andersen, Andersen, Hvidberg, Dahl-Jensen, Steffensen, Shoji, Sveinbjörnsdóttir, White, Jouzel, Fisher (1997). The 18O record along the Greenland Ice Core Project deep ice core and the problem of possible Eemian climatic instability. Journal of Geophysical Research: Oceans 102(C12), pp. 26397–26410. Available at: https://doi.org/10.1029/97JC00167.

Johnsen, Dansgaard, Clausen and Langway. (1972). Oxygen Isotope Profiles through the Antarctic and Greenland Ice Sheets. Nature 235(5339), pp. 429–434. Available at: https://doi.org/10.1038/235429a0.

Johnson, Brown, McManus, Barry, Barker and Gasse. (2002). A high-resolution paleoclimate record spanning the past 25,000 years in Southern East Africa. Science 296(5565), pp. 113–132. Available at: https://www.science.org/doi/10.1126/science.1070057 [Accessed: 23 November 2022].

Jonell, Carter, Böning, Pahnke and Clift. (2017). Climatic and glacial impact on erosion patterns and sediment provenance in the Himalayan rain shadow, Zanskar River, NW India. Bulletin of the Geological Society of America 129(7–8), pp. 820–836. doi: 10.1130/B31573.1.

Jonell, Li, Blusztajn, Giosan and Clift. (2018). Signal or noise? Isolating grain size effects on Nd and Sr isotope variability in Indus delta sediment provenance. Chemical Geology 485(February), pp. 56–73. Available at: https://doi.org/10.1016/j.chemgeo.2018.03.036.

Jung, Davies, Ganssen and Kroon. (2004). Stepwise Holocene aridification in NE Africa deduced from dust-borne radiogenic isotope records. Earth and Planetary Science Letters 221(1–4), pp. 27–37. doi: 10.1016/S0012-821X(04)00095-0.

Just, Schefuß, Kuhlmann, Stuut and Pätzold. (2014). Climate induced sub-basin source-area shifts of Zambezi River sediments over the past 17 ka. Palaeogeography, Palaeoclimatology, Palaeoecology 410, pp. 190–199. Available at:
http://dx.doi.org/10.1016/j.palaeo.2014.05.045.

Kanner, Burns, Cheng and Edwards. (2012). High-Latitude Forcing of the South American Summer Monsoon During the Last Glacial. Science 335(6068), pp. 570–573. Available

at: https://doi.org/10.1126/science.1213397.

Khider, Emile-Geay, Zhu, James, Landers, Ratnakar and Gil. (2022). Pyleoclim: Paleoclimate Timeseries Analysis and Visualization With Python. Paleoceanography and Paleoclimatology 37(10). Available at: http://10.0.4.5/2022pa004509.

Kirchner and Neal. (2013). Universal fractal scaling in stream chemistry and its implications for solute transport and water quality trend detection. Proceedings of the National Academy of Sciences of the United States of America 110(30), pp. 12213–12218. doi: 10.1073/pnas.1304328110.

Klein and Cruz-Uribe. (1991). The bovids from Elandsfontein, South Africa, and their implications for the age, palaeoenvironment, and origins of the site. The African Archaeological Review 9(1), pp. 21–79. doi: 10.1007/BF01117215.

Klein. (1980). Environmental and ecological implications of large mammals from Upper Pleistocene and Holocene sites in southern Africa. South African Museum.

Klein. (1983). Palaeoenvironmental implications of Quaternary-large mammals in the FynbosBiome. South African National ScientificProgrammesReports 75.

Klein. (2009). The human career: Human biological and cultural origins. University of Chicago Press.

Knorr and Lohmann. (2003). Southern ocean origin for the resumption of Atlantic thermohaline circulation during deglaciation. Nature 424(6948), pp. 532–536. doi: 10.1038/nature01855.

Kohfeld, Graham, de Boer, Sime, Wolff, Le Quéré and Bopp. (2013). Southern Hemisphere westerly wind changes during the Last Glacial Maximum: Paleo-data synthesis. Quaternary Science Reviews 68, pp. 76–95. Available at: http://dx.doi.org/10.1016/j.quascirev.2013.01.017.

Konecky, Russell, Johnson, Brown, Berke, Werne and Huang. (2011). Atmospheric circulation patterns during late Pleistocene climate changes at Lake Malawi, Africa. Earth and Planetary Science Letters 312(3–4), pp. 318–326. Available at: http://dx.doi.org/10.1016/j.epsl.2011.10

Kreissig, Nägler, Kramers, van Reenen and Smit. (2000). An isotopic and geochemical study of the northern Kaapvaal Craton and the Southern Marginal Zone of the Limpopo Belt: are they juxtaposed terranes? Lithos 50(1–3), pp. 1–25.

Kristen, Wilkes, Vieth, Zink, Plessen, Thorpe, Partridge, & Oberhänsli. (2010). Biomarker and stable carbon isotope analyses of sedimentary organic matter from Lake Tswaing: evidence for deglacial wetness and early Holocene drought from South Africa. Journal of Paleolimnology, 44(1), 143–160. https://doi.org/10.1007/s10933-009-9393-9

Kroopnick. (1985). The distribution of 13C of ΣCO2 in the world oceans. Deep Sea Research Part A. Oceanographic Research Papers 32(1), pp. 57–84. Available at:

https://www.sciencedirect.com/science/article/pii/0198014985900172.

Kuhlbrodt, Griesel, Montoya, Levermann, Hofmann and Rahmstorf. (2007). On the driving processes of the Atlantic meridional overturning circulation. Reviews of Geophysics 45(2). Available at: https://doi.org/10.1029/2004RG000166.

Kuhn and Diekmann. (2002). Late Quaternary variability of ocean circulation in the southeastern South Atlantic inferred from the terrigenous sediment record of a drift deposit in the southern Cape Basin (ODP Site 1089). Palaeogeography, Palaeoclimatology, Palaeoecology 182(3–4), pp. 287–303. doi: 10.1016/S0031-0182(01)00500-4.

Kujau, Nürnberg, Zielhofer, Bahr and Röhl. (2010). Mississippi River discharge over the last 560,000years - Indications from X-ray fluorescence core-scanning. Palaeogeography, Palaeoclimatology, Palaeoecology 298(3–4), pp. 311–318. doi: 10.1016/j.palaeo.2010.10.005.

Kunkelova, Crocker, Jewell, Breeze, Drake, Cooper, Milton, Hennen, Shahgedanova, Petraglia, & Wilson. (2022). Dust sources in Westernmost Asia have a different geochemical fingerprint to those in the Sahara. Quaternary Science Reviews, 294, 107717. https://doi.org/10.1016/j.quascirev.2022.107717

Kutzbach, Guan, He, Cohen, Orland and Chen. (2020). African climate response to orbital and glacial forcing in 140,000-y simulation with implications for early modern human environments. Proceedings of the National Academy of Sciences 117(5), pp. 2255–2264.

Kutzbach. (1981). Monsoon Climate of the Early Holocene: Climate Experiment with the Earth's Orbital Parameters for 9000 Years Ago. Science 214, pp. 59–61.

Kwon, Lim, Seoung, Cho and Park. (2023). Comparative study of the cesium adsorption behavior of montmorillonite and illite based on their mineralogical properties and interlayer cations. Journal of Hazardous Materials Advances 10, p. 100258. Available at: https://www.sciencedirect.com/science/article/pii/S2772416623000293.

Lamont, Roberts, Barlow, Morris and van den Berg. (2010). Circulation patterns in the Delagoa Bight, Mozambique, and the influence of deep ocean eddies. African Journal of Marine Science 32(3), pp. 553–562.

Lamy, Arz, Kilian, Lange, Lembke-Jene, Wengler, Kaiser, Baeza-Urrea, Hall, Harada, & Tiedemann. (2015). Glacial reduction and millennial-scale variations in Drake Passage throughflow. Proceedings of the National Academy of Sciences of the United States of America, 112(44), 13496–13501. https://doi.org/10.1073/pnas.1509203112

Lancaster. (1979). Evidence for a widespread late Pleistocene humid period in the Kalahari. Nature 279(5709), pp. 145–146. Available at:
https://doi.org/10.1038/279145a0.

Laskar, J., Robutel, P., Joutel, F., Gastineau, M., Correia, A. C. M. and Levrard, B. (2004). A long-term numerical solution for the insolation quantities of the Earth. A

A 428(1), pp. 261–285. Available at: https://doi.org/10.1051/0004-6361:20041335.

Latimer and Filippelli. (2007). Sedimentary iron records from the Cape Basin. Deep Sea Research Part II: Topical Studies in Oceanography 54(21), pp. 2422–2431. Available at: https://www.sciencedirect.com/science/article/pii/S0967064507001804.

Latimer, Filippelli, Hendy, Gleason and Blum. (2006). Glacial-interglacial terrigenous provenance in the southeastern Atlantic Ocean: The importance of deep-water sources and surface currents. Geology 34(7), pp. 545–548. doi: 10.1130/G22252.1.

Lawver, Keller, Fisk and Strelin. (1995). Bransfield Strait, Antarctic Peninsula active extension behind a dead arc. Backarc basins: tectonics and magmatism, pp. 315–342.

Lehner, B., Grill G. (2013). Global river hydrography and network routing: baseline data and new approaches to study the world's large river systems. Hydrological Processes, 27(15): 2171–2186. https://doi.org/10.1002/hyp.9740

Le Roux. (2007). Monitoring soil erosion in South Africa at a regional scale for deposition. South African Journal of Science 103(August), pp. 329–335.

Lewis, LeGrande, Kelley and Schmidt. (2010). Water vapour source impacts on oxygen isotope variability in tropical precipitation during Heinrich events. Climate of the Past 6(3), pp. 325–343. Available at: https://cp.copernicus.org/articles/6/325/2010/.

Li, Ginoux and Ramaswamy. (2008). Distribution, transport, and deposition of mineral dust in the Southern Ocean and Antarctica: Contribution of major sources. Journal of Geophysical Research: Atmospheres 113(D10).

Li, Hinnov and Kump. (2019). Acycle: Time-series analysis software for paleoclimate research and education. Computers and Geosciences 127(September 2018), pp. 12–22. Available at: https://doi.org/10.1016/j.cageo.2019.02.011.

Li, Tu, Zhang, Cheng and Yang. (2022). Application of a back propagation neural network model based on genetic algorithm to in situ analysis of marine sediment cores by X-ray fluorescence core scanner. Applied Radiation and Isotopes 184(July 2020), p. 110191. Available at: https://doi.org/10.1016/j.apradiso.2022.110191.

Lipp, Shorttle, Syvret and Roberts. (2020). Major Element Composition of Sediments in Terms of Weathering and Provenance: Implications for Crustal Recycling. Geochemistry, Geophysics, Geosystems 21(6). doi: 10.1029/2019GC008758.

Lipp, Roberts, Whittaker, Gowing and Fernandes. (2021). Source region geochemistry from unmixing downstream sedimentary elemental compositions. Geochemistry, Geophysics, Geosystems, 22, e2021GC009838. https://doi.org/10.1029/2021GC009838

Lippold, Gutjahr, Blaser, Christner, de Carvalho Ferreira, Mulitza, Christl, Wombacher, Böhm, Antz, Cartapanis, Vogel, & Jaccard. (2016). Deep water provenance and dynamics of the (de)glacial Atlantic meridional overturning circulation. Earth and Planetary

Science Letters, 445, 68–78. https://doi.org/10.1016/j.epsl.2016.04.013

Lisiecki and Raymo. (2005). A Pliocene-Pleistocene stack of 57 globally distributed benthic 18O records. Paleoceanography 20(1), pp. 1–17. doi: 10.1029/2004PA001071.

Little, Schneider, Kroon, Price, Bickert and Wefer. (1997a). Rapid palaeoceanographic changes in the Benguela Upwelling System for the last 160,000 years as indicated by abundances of planktonic foraminifera. Palaeogeography, Palaeoclimatology, Palaeoecology 130(1), pp. 135–161. Available at: https://www.sciencedirect.com/science/article/pii/S0031018296001368.

Little, Schneider, Kroon, Price, Summerhayes and Segl. (1997b). Trade wind forcing of upwelling, seasonality, and Heinrich events as a response to sub-Milankovitch climate variability. Paleoceanography 12(4), pp. 568–576. doi: 10.1029/97PA00823.

Lougheed and Obrochta. (2019). A Rapid, Deterministic Age-Depth Modeling Routine for Geological Sequences With Inherent Depth Uncertainty. Paleoceanography and Paleoclimatology 34(1), pp. 122–133. doi: 10.1029/2018PA003457.

Loveday, Durgadoo, Reason, Biastoch and Penven. (2014). Decoupling of the Agulhas leakage from the Agulhas Current. Journal of Physical Oceanography 44(7), pp. 1776–1797. doi: 10.1175/JPO-D-13-093.1.

Lowell, Heusser, Andersen, Moreno, Hauser, Heusser, Schlüchter, Marchant, & Denton. (1995). Interhemispheric correlation of late Pleistocene glacial events. Science, 269(5230), 1541–1549.

Lutjeharms and van Ballegooyen. (1984). Topographic control in the Agulhas Current system. Deep Sea Research Part A. Oceanographic Research Papers 31(11), pp. 1321–1337.

Lutjeharms, Penven and Roy. (2003). Modelling the shear edge eddies of the southern Agulhas Current. Continental Shelf Research 23(11–13), pp. 1099–1115.

Lutjeharms. (1989). Role of mesoscale eddies turbulent flows. 7(3), pp. 207–229.

Lutjeharms. (2006). The Agulhas Current. Springer Berlin Heidelberg. Available at: https://books.google.co.uk/books?id=BRVGAAAAQBAJ.

Lutjeharms. (2007). Three decades of research on the greater Agulhas Current. Ocean Science 3(1), pp. 129–147. doi: 10.5194/os-3-129-2007.

Luttinen, Rämö and Huhma. (1998). Neodymium and strontium isotopic and trace element composition of a Mesozoic CFB suite from Dronning Maud Land, Antarctica: Implications for lithosphere and asthenosphere contributions to Karoo magmatism. Geochimica et Cosmochimica Acta 62(15), pp. 2701–2714. doi: 10.1016/S0016-7037(98)00184-7.

Lyle, Oliarez Lyle, Gorgas, Holbourn, Westerhold, Hathorne, Kimoto, & Yamamoto.

(2012). Data report: raw and normalized elemental data along the Site U1338 splice from X-ray fluorescence scanning. 320.
https://doi.org/10.2204/iodp.proc.320321.203.2012.

Maccali, Meckler, Lauritzen, Brekken, Rokkan, Fernandez, Krüger, Adigun, Affolter, & Leuenberger. (2023). Multi-proxy speleothem-based reconstruction of mid-MIS 3 climate in South Africa. Clim. Past Discuss. [Preprint, January, 1–27. https://doi.org/10.5194/cp-2023-1

Maccali, Hillaire-Marcel and Not. (2018). Radiogenic isotope (Nd, Pb, Sr) signatures of surface and sea ice-transported sediments from the Arctic Ocean under the present interglacial conditions. Polar Research 37(1). Available at:
https://doi.org/10.1080/17518369.2018.1442982.

Mackay, Armitage, Niespolo, Sharp, Stahlschmidt, Blackwood, Boyd, Chase, Lagle, Kaplan, Low, Martisius, McNeill, Moffat, O'Driscoll, Rudd, Orton, & Steele. (2022). Environmental influences on human innovation and behavioural diversity in southern Africa 92–80 thousand years ago. Nature Ecology and Evolution, 6(4), 361–369. https://doi.org/10.1038/s4155
022-01667-5

Mackensen, Rudolph and Kuhn. (2001). Stable isotope ratios, carbon content and primary production of three sediment cores from the subantarctic eastern Atlantic. Supplement to:

Maher, Prospero, Mackie, Gaiero, Hesse and Balkanski. (2010). Global connections between aeolian dust, climate and ocean biogeochemistry at the present day and at the last glacial maximum. Earth-Science Reviews 99(1–2), pp. 61–97. Available at: http://dx.doi.org/10.1016/j.earscirev.2009.12.001.

Maitre, Colvin and Maherrya. (2009). Water resources in the klein karoo: the challenge of sustainable development in a water-scarce area. South African Journal of Science 105(1–2), pp. 39–48. doi: 10.1590/s0038-23532009000100019.

Marean, Bar-Matthews, Bernatchez, Fisher, Goldberg, Herries, Jacobs, Jerardino, Karkanas, Minichillo, Nilssen, Thompson, Watts, & Williams. (2007). Early human use of marine resources and pigment in South Africa during the Middle Pleistocene. Nature, 449(7164), 905–908. https://doi.org/10.1038/nature06204

Marean. (2014) Stone Age people in a changing South African Greater Cape Floristic Region. Allsopp, N., Colville, J. F., and Verboom, G. A. eds. Fynbos: Ecology, Evolution, and Conservation of a Megadiverse Region, p. 0. Available at: https://doi.org/10.1093/acprof:oso/97801

Marean. (2010). Pinnacle Point Cave 13B (Western Cape Province, South Africa) in context: The Cape Floral kingdom, shellfish, and modern human origins. Journal of Human Evolution 59(3–4), pp. 425–443. Available at:

http://dx.doi.org/10.1016/j.jhevol.2010.07.011.

Marean. (2014). The origins and significance of coastal resource use in Africa and Western Eurasia. Journal of Human Evolution 77, pp. 17–40. Available at: https://www.sciencedirect.com/science/article/pii/S0047248414002292.

Marean. (2015). The Most Invasive Species of All. Scientific American 313(2), pp. 32–39.

Marino and Zahn. (2015). The agulhas leakage: the missing link in the interhemispheric climate seesaw? Geochemistry, Geophysics, Geosystems 8(12), pp. (2004)–2005. doi: 10.1029/2007GC001604.

Marinoni, Setti, Salvi and López-Galindo. (2008). Clay minerals in late Quaternary sediments from the south Chilean margin as indicators of provenance and palaeoclimate. Clay Minerals 43(2), pp. 235–253. doi: 10.1180/claymin.2008.043.2.07.

Martínez-Garcia, Rosell-Melé, Geibert, Gersonde, Masqué, Gaspari and Barbante. (2009). Links between iron supply, marine productivity, sea surface temperature, and CO2 over the last 1.1 Ma. Paleoceanography 24(1). Available at: https://doi.org/10.1029/2008PA001657.

Martinez-Mendez, Zahn, Hall, Peeters, Pena, Cacho and Negre. (2009). Contrasting multiproxy reconstructions of surface ocean hydrography in the Agulhas Corridor and implications for the Agulhas Leakage during the last 345,000 years. Paleoceanography 25(4), pp. 1–12. doi: 10.1029/2009PA001879.

Maslin. (1995). Changes in North Atlantic deep water formation associated with the Heinrich events. Naturwissenschaften 82(7), pp. 330–333. Available at: https://doi.org/10.1007/BF01131529.

Mason. (1995). Sea-surface temperature — South African rainfall associations, 1910–1989. International Journal of Climatology 15(2), pp. 119–135. Available at: https://onlinelibrary.wiley.com/doi/full/10.1002/joc.3370150202 [Accessed: 23 November 2022].

Masson-Delmotte, V., Kageyama, M., Braconnot, P. et al. Past and future polar amplification of climate change: climate model intercomparisons and ice-core constraints. Clim Dyn 27, 437–440 (2006). https://doi.org/10.1007/s00382-006-0149-1

Mcbrearty and Brooks. (2000). The revolution that wasn't: A new interpretation of the origin of modern human behavior. Journal of Human Evolution 39(5), pp. 453–563. doi: 10.1006/jhev.2000.0435.

McCall and Thomas. (2012). Still Bay and Howiesons Poort Foraging Strategies: Recent Research and Models of Culture Change. The African Archaeological Review 29(1), pp. 7–50. Available at: http://www.jstor.org/stable/41486787.

McCall. (2007). Behavioral ecological models of lithic technological change during the later Middle Stone Age of South Africa. Journal of Archaeological Science 34(10), pp.

1738–1751.

McCave and Hall. (2006). Size sorting in marine muds: Processes, pitfalls, and prospects for paleoflow-speed proxies. Geochemistry, Geophysics, Geosystems 7(10). doi: 10.1029/2006GC001284.

McCave, Crowhurst, Kuhn, Hillenbrand and Meredith. (2014). Minimal change in antarctic circumpolar current flow speed between the last glacial and holocene. Nature Geoscience 7(2), pp. 113–116. doi: 10.1038/ngeo2037.

McCave, Manighetti and Robinson. (1995). Parameters for palaeocurrent speed and palaeoceanography. Paleoceanography 10(3), pp. 593–610.

McCave, Thornalley and Hall. (2017). Relation of sortable silt grain-size to deep-sea current speeds: Calibration of the 'Mud Current Meter.' Deep-Sea Research Part I: Oceanographic Research Papers 127(July), pp. 1–12. Available at: http://dx.doi.org/10.1016/j.dsr.2017.07.003.

McCave. (2008). Size Sorting During Transport and Deposition of Fine Sediments: Sortable Silt and Flow Speed. pp. 121–142. doi: 10.1016/S0070-4571(08)00208-2.

Mccoy-west, Millet and Burton. (2017). The neodymium stable isotope composition of the silicate Earth and chondrites. Earth and Planetary Science Letters 480, pp. 121–132. Available at: https://doi.org/10.1016/j.epsl.2017.10.004.

McDougall, Brown and Fleagle. (2005). Stratigraphic placement and age of modern humans from Kibish, Ethiopia. Nature 433(7027), pp. 733–736. Available at: https://doi.org/10.1038/nature03258.

McLennan, McCulloch, Taylor and Maynard. (1989). Effects of sedimentary sorting on neodymium isotopes in deep-sea turbidites. Nature 337(6207), pp. 547–549. doi: 10.1038/337547a0.

McManus, Oppo and Cullen. (1999). A 0.5-Million-year record of millennial-scale climate variability in the North Atlantic. Science 283(5404), pp. 971–975. doi: 10.1126/science.283.5404.971.

Meadows and Baxter. (1999). Late Quaternary palaeoenvironments of the southwestern Cape, South Africa: A regional synthesis. Quaternary International 57–58, pp. 193–206. doi: 10.1016/S1040-6182(98)00060-3.

Mellars. (2006). Why did modern human populations disperse from Africa ca. 60,000 years ago? A new model. Proceedings of the National Academy of Sciences of the United States of America 103(25), pp. 9381–9386. doi: 10.1073/pnas.0510792103.

Meyer, Davies and Stuut. (2011). Grain size control on Sr-Nd isotope provenance studies and impact on paleoclimate reconstructions: An example from deep-sea sediments offshore NW Africa. Geochemistry, Geophysics, Geosystems 12(3), pp. 1–14. doi: 10.1029/2010GC003355.

Meyers SR (2014). Astrochron: An R Package for Astrochronology. https://cran.r-project.org/package=astrochron.

Meyers. (1996). Variation of Indonesian throughflow and the El Niño - Southern Oscillation. Journal of Geophysical Research: Oceans 101(C5), pp. 12255–12263. doi: 10.1029/95JC03729.

Milanković. (1941). Canon of Insolation and the Ice-age Problem: (Kanon Der Erdbestrahlung und Seine Anwendung Auf Das Eiszeitenproblem) Belgrade, 1941. Israel Program for Scientific Translations; [available from U.S. Department of Commerce, Clearinghouse for Federal Scientific and Technical Information, Springfield, Va.]. Available at: https://books.google.co.uk/books?id=huXvAAAAMAAJ.

Milankovitch. (1930). Mathematische klimalehre und astronomische theorie der klimaschwankungen. Handbuch der Klimatologie 1.

Miller, Finch, Hill, Peterse, Humphries, Zabel and Schefuß. (2019). Late quaternary climate variability at mfabeni peatland, eastern south africa. Climate of the Past 15(3), pp. 1153–1170. doi: 10.5194/cp-15-1153-2019.

Miller, Hahn, Liebrand, Zabel and Schefuß. (2020). Mid- and low latitude effects on eastern South African rainfall over the Holocene. Quaternary Science Reviews 229, p. 106088. Available at: https://doi.org/10.1016/j.quascirev.2019.106088.

Mills, Grab, Rea, Carr and Farrow. (2012). Shifting westerlies and precipitation patterns during the Late Pleistocene in southern Africa determined using glacier reconstruction and mass balance modelling. Quaternary Science Reviews 55, pp. 145–159. Available at: http://dx.doi.org/10.1016/j.quascirev.2012.08.012.

Minoletti, Hermoso and Gressier. (2009). Separation of sedimentary micron-sized particles for palaeoceanography and calcareous nannoplankton biogeochemistry. Nature Protocols 4(1), pp. 14–24. doi: 10.1038/nprot.2008.200.

Møller, Jensen, Kuijpers, Aagaard-Sørensen, Seidenkrantz, Prins, Endler, & Mikkelsen. (2006). Late-Holocene environment and climatic changes in Ameralik Fjord, southwest Greenland: Evidence from the sedimentary record. Holocene, 16(5), 685–695. https://doi.org/10.1191/0

Molyneux, Hall, Zahn and Diz. (2007). Deep water variability on the southern Agulhas Plateau: Interhemispheric links over the past 170 ka. Paleoceanography 22(4), pp. 1–14. doi: 10.1029/2006PA001407.

Molyneux. (2007). Surface and Deep Water Variability On The Agulhas Plateau Over The Past 170 ka. (November).

Moore, Blenkinsop and Cotterill. (2009). Southern African topography and erosion history: Plumes or plate tectonics? Terra Nova 21(4), pp. 310–315. doi: 10.1111/j.1365-3121.2009.00887.x.

Moriarty. (1977). Clay minerals in Southeast Indian Ocean sediments, transport mechanisms and depositional environments. Marine Geology 25(1), pp. 149–174. Available at: https://www.sciencedirect.com/science/article/pii/0025322777900512.

Morris. (2002). Isolation and the origin of the khoisan: Late pleistocene and early holocene human evolution at the southern end of Africa. Human Evolution 17(3), pp. 231–240. Available at: https://doi.org/10.1007/BF02436374.

Mourre, Villa and Henshilwood. (2010). Early use of pressure flaking on lithic artifacts at Blombos Cave, South Africa. Science (New York, N.Y.) 330(6004), pp. 659–662. doi: 10.1126/science.1195550.

Mukai, Hirose, Motai, Kikuchi, Tanoi, Nakanishi, Yaita, & Kogure. (2016). Cesium adsorption/desorption behavior of clay minerals considering actual contamination conditions in Fukushima. Scientific Reports, 6(1), 21543.
https://doi.org/10.1038/srep21543

Mulitza, S., Prange, M., Stuut, J.-B., Zabel, M., von Dobeneck, T., Itambi, A. C., Nizou, J., Schulz, M., and Wefer, G. (2008), Sahel megadroughts triggered by glacial slowdowns of Atlantic meridional overturning, Paleoceanography, 23, PA4206, doi:10.1029/2008PA001637.

Nash. (2017). Changes in precipitation over southern Africa during recent centuries.

Nel and Henshilwood. (2016). The Small Mammal Sequence from the c. 76 – 72 ka Still Bay Levels at Blombos Cave, South Africa – Taphonomic and Palaeoecological Implications for Human Behaviour. PLOS ONE 11(8), p. e0159817. Available at: https://doi.org/10.1371/journal.pone.0159817.

Neumann and Scott. (2018). E.M. van Zinderen Bakker (1907–2002) and the study of African Quaternary palaeoenvironments. Quaternary International 495(April), pp. 153–168. doi: 10.1016/j.quaint.2018.04.017.

Neumann, Svensen, Galerne and Planke. (2011). Multistage evolution of dolerites in the Karoo large igneous province, Central South Africa. Journal of Petrology 52(5), pp. 959–984. doi: 10.1093/petrology/egr011.

NGRIP Members, (2004). High-resolution record of Northern Hemisphere climate extending into the last interglacial period. Nature 431(7005), pp. 147–151. Available at: https://doi.org/10.1038/nature02805.

Nicholson and Entekhabi. (1987). Rainfall Variability in Equatorial and Southern Africa: Relationships with Sea Surface Temperatures along the Southwestern Coast of Africa. Journal of Climate and Applied Meteorology 25(5), pp. 561–578.

Nicholson and Flohn. (1981). African climatic changes in late Pleistocene and Holocene and the general atmospheric circulation. Sea level, ice and climatic change. Proc. Canberra symposium, December 1979 2, pp. 295–301.

Nicholson. (2000). The nature of rainfall variability over Africa on time scales of decades to millenia. Global and Planetary Change 26(1–3), pp. 137–158. doi: 10.1016/S0921-8181(00)00040-0.

Niemi, Ben-Avraham, Hartnady and Reznikov. (2000). Post-Eocene seismic stratigraphy of the deep ocean basin adjacent to the southeast African continental margin: A record of geostrophic bottom current systems. Marine Geology 162(2–4), pp. 237–258. doi: 10.1016/S0025-3227(99)00062-6.

Ninnemann and Charles. (2002). Changes in the mode of Southern Ocean circulation over the last glacial cycle revealed by foraminiferal stable isotopic variability. Earth and Planetary Science Letters 201(2), pp. 383–396. doi: 10.1016/S0012-821X(02)00708-2.

Noble, Piotrowski, Robinson, McManus, Hillenbrand and Bory. (2012). Greater supply of Patagonian-sourced detritus and transport by the ACC to the Atlantic sector of the Southern Ocean during the last glacial period. Earth and Planetary Science Letters 317–318, pp. 374–385. doi: 10.1016/j.epsl.2011.10.007.

Oppo, Gebbie, Huang, Curry, Marchitto and Pietro. (2018). Data Constraints on Glacial Atlantic Water Mass Geometry and Properties. Paleoceanography and Paleoclimatology 33(9), pp. 1013–1034. doi: 10.1029/2018PA003408.

Orsi, Whitworth and Nowlin. (1995). On the meridional extent and fronts of the Antarctic Circumpolar Current. Deep-Sea Research Part I 42(5), pp. 641–673. doi: 10.1016/0967-0637(95)00021-W.

Otto-Bliesner, Russell, Clark, Liu, Overpeck, Konecky, Demenocal, Nicholson, He, & Lu. (2014). Coherent changes of southeastern equatorial and northern African rainfall during the last deglaciation. Science, 346(6214), 1223–1227.
https://doi.org/10.1126/science.1259531

Partridge, Demenocal, Lorentz, Paiker, Vogel, Partridge, Demenocal, Lorentz, Paiker, & Vogel. (1997). Orbital forcing of climate over South Africa: A 200,000-year rainfall record from the pretoria saltpan. QSRv, 16(10), 1125–1133.
https://doi.org/10.1016/S0277-3791(97)00005-X

Partridge, Scott and Schnei. (2004). Between Agulhas and Benguela: Responses of Southern African Climates of the Late Pleistocene to current fluxes, orbital precession ans the extent of the circum-antarctic vortex. pp. 45–68.

Pearce, Schumann and Lundie. (1978). Features of the Shelf Circulation off the Natal Coast. South African Journal Of Science 74(January 1978), pp. 328–331.

Peel, Finlayson and McMahon. (2007). Updated world map of the Köppen-Geiger climate classification. Hydrology and Earth System Sciences 11(5), pp. 1633–1644. Available at: https://hess.copernicus.org/articles/11/1633/2007/.

Peeters, Acheson, Brummer, De Ruijter, Schneider, Ganssen, Ufkes, & Kroon. (2004). Vigorous exchange between the Indian and Atlantic oceans at the end of the past five glacial periods. Nature, 430(7000), 661–665. https://doi.org/10.1038/nature02785

Peltier. (2004). Global glacial isostasy and the surface of the ice-age earth: The ICE-5G (VM2) model and GRACE. Annual Review of Earth and Planetary Sciences 32, pp. 111–149.

Petit, Jouzel, Raynaud, Barkov, Barnola, Basile, Bender, Chappellaz, Davis, Delaygue, Delmotte, Kotlyakov, Legrand, Lipenkov, Lorius, PÉpin, Ritz, Saltzman, & Stievenard. (1999). Climate and atmospheric history of the past 420,000 years from the Vostok ice core, Antarctica. Nature, 399(6735), 429–436.
https://doi.org/10.1038/20859

Petschick, Kuhn and Gingele. (1996). Clay mineral distribution in surface sediments of the South Atlantic: Sources, transport, and relation to oceanography. Marine Geology 130(3–4), pp. 203–229. doi: 10.1016/0025-3227(95)00148-4.

Phoma, Vikram, Jansson, Ansorge, Cowan, Van De Peer and Makhalanyane. (2018). Agulhas Current properties shape microbial community diversity and potential functionality. Scientific Reports 8(1), pp. 1–13. doi: 10.1038/s41598-018-28939-0.

Pichevin, Cremer, Giraudeau and Bertrand. (2005). A 190 ky record of lithogenic grain-size on the Namibian slope: Forging a tight link between past wind-strength and coastal upwelling dynamics. Marine Geology 218(1), pp. 81–96. Available at: https://www.sciencedirect.com/science/article/pii/S0025322705001179.

Pickrell, Patterson, Barbieri, Berthold, Gerlach, Güldemann, Kure, Mpoloka, Nakagawa, Naumann, Lipson, Loh, Lachance, Mountain, Bustamante, Berger, Tishkoff, Henn, Stoneking, Reich, & Pakendorf. (2012). The genetic prehistory of southern Africa. Nature Communications, 3(1), 1143. https://doi.org/10.1038/ncomms2140

Potts. (1998). Environmental hypotheses of hominin evolution. American Journal of Physical Anthropology 107(SUPPL. 27), pp. 93–136. doi: 10.1002/(SICI)1096-8644(1998)107:27+<93::AJPA5>3.0.CO;2-X.

Prell, Imbrie, Martinson, Morley, Pisias, Shackleton and Streeter. (1986). Graphic Correlation of Oxygen Isotope Stratigraphy Application to the Late Quaternary. Paleoceanography 1(2), pp. 137–162.

Prins, Bouwer, Beets, Troelstra, Weltje, Kruk, Kuijpers, & Vroon. (2002). Ocean circulation and iceberg discharge in the glacial North Atlantic: Inferences from unmixing of sediment size distributions. Geology, 30(6), 555–558.
https://doi.org/10.1130/0091-7613(2002)030<0555:OCAIDI>2.0.CO;2

Prins, Postma, Cleveringa, Cramp and Kenyon. (2000). Controls on terrigenous sediment

supply to the Arabian Sea during the late quaternary: The Indus fan. Marine Geology 169(3–4), pp. 327–349. doi: 10.1016/S0025-3227(00)00086-4.

Prins, Troelstra, Kruk, van der Borg, de Jong and Weltje. (2001). The Late Quaternary Sediment Record of Reykjanes Ridge, North Atlantic. Radiocarbon 43(2), pp. 939–948.

Prospero, Ginoux, Torres, Nicholson and Gill. (2002). Environmental characterization of global sources of atmospheric soil dust identified with the nimbus 7 total ozone mapping spectrometer (toms) absorbing aerosol product. Reviews of Geophysics 40(1), pp. 2–31. Available at: https://doi.org/10.1029/2000RG000095.

Puech, Urrego, Goñi, Backwell and D'Erricoc. (2017). Vegetation and environmental changes at the Middle Stone Age site of Wonderkrater, Limpopo, South Africa. Quaternary Research (United States) 88(2), pp. 313–326. doi: 10.1017/qua.2017.42.

R Core Team (2019) R: A Language and Environment for Statistical Computing. R Foundation for Statistical Computing, Vienna, Austria.

Rahmstorf. (2002). Ocean circulation and climate during the past 120,000 years. 419(September), pp. 207–214.

Rahmstorf. (2006). Thermohaline Ocean Circulation. pp. 1–10.

Rasmussen, Bigler, Blockley, Blunier, Buchardt, Clausen, Cvijanovic, Dahl-Jensen, Johnsen, Fischer, Gkinis, Guillevic, Hoek, Lowe, Pedro, Popp, Seierstad, Steffensen, Svensson, Vallelonga, Vinther, Walker, Wheatley, & Winstrup. (2014). A stratigraphic framework for abrupt climatic changes during the Last Glacial period based on three synchronized Greenland ice-core records: Refining and extending the INTIMATE event stratigraphy. Quaternary Science Reviews, 106, 14–28. https://doi.org/10.1016/j.quascirev.2014.09.007

Ravelo and Hillaire-Marcel. (2007). Chapter Eighteen The Use of Oxygen and Carbon Isotopes of Foraminifera in Paleoceanography. Developments in Marine Geology 1(07), pp. 735–764. doi: 10.1016/S1572-5480(07)01023-8.

Reason and Mulenga. (1999). Relationships between South African rainfall and SST anomalies in the southwest Indian Ocean. International Journal of Climatology 19(15), pp. 1651–1673. doi: 10.1002/(SICI)1097-0088(199912)19:15<1651::AID-JOC439>3.0.CO;2-U.

Reason and Rouault. (2002). ENSO-like decadal variability and South African rainfall. Geophysical Research Letters 29(13), pp. 16-1-16–4. doi: 10.1029/2002GL014663.

Reason, Allan, Lindesay and Ansell. (2000). Enso and climatic signals across the Indian Ocean basin in the global context: Part I, Interannual composite patterns. International Journal of Climatology 20(11), pp. 1285–1327. doi: 10.1002/1097-0088(200009)20:11<1285::AID-JOC536>3.0.CO;2-R.

Reason, Rouault, Melice and Jagadheesha. (2002). Interannual winter rainfall variability

in SW South Africa and large scale ocean–atmosphere interactions. Meteorology and Atmospheric Physics 80(1), pp. 19–29. Available at:
https://doi.org/10.1007/s007030200011.

Reason. (2001). Subtropical Indian Ocean SST dipole events and southern African rainfall. 28(11), pp. 2225–2227.

Reid. (1989). On the total geostrophic circulation of the South Atlantic Ocean: Flow patterns, tracers, and transports. Progress in Oceanography 23(3), pp. 149–244. doi: 10.1016/0079-6611(89)90001-3.

Reid. (2005). On the world-wide circulation of the deep water from the North Atlantic Ocean. Journal of Marine Research 63(1), pp. 187–201.

Reynard and Henshilwood. (2017). Subsistence strategies during the Late Pleistocene in the southern Cape of South Africa: Comparing the Still Bay of Blombos Cave with the Howiesons Poort of Klipdrift Shelter. Journal of Human Evolution 108, pp. 110–130. Available at: http://dx.doi.org/10.1016/j.jhevol.2017.04.003.

Reznikov, Ben-Avraham, Hartnady and Niemi. (2005). Structure of the Transkei Basin and Natal Valley, Southwest Indian Ocean, from seismic reflection and potential field data. Tectonophysics 397(1-2 SPEC. ISS.), pp. 127–141.
doi: 10.1016/j.tecto.2004.11.002.

Riley, Curtis, Leat, Watkeys, Duncan, Millar and Owens. (2005). Overlap of Karoo and Ferrar magma types in KwaZulu-Natal, South Africa. Journal of Petrology 47(3), pp. 541–566. doi: 10.1093/petrology/egi085.

Ritz, Stocker, Grimalt, Menviel and Timmermann. (2013). Estimated strength of the Atlantic overturning circulation during the last deglaciation. Nature geoscience 6(3), pp. 208–212.

Roddaz, Nauton-Fourteu, Santos, Dantas and Calves. (2020). Controls on the provenance of late Eocene to Quaternary Mozambique Channel shales (DSDP 25 Site 242). Marine Geology 421(December 2019), p. 106090. Available at:
https://doi.org/10.1016/j.margeo.2019.106090.

Rogers. (1987). Seismic, bathymetric and photographic evidence of widespread erosion and a manganese-nodule pavement along the continental rise of the Southeast Cape Basin. Marine Geology 78(1–2), pp. 57–76. doi: 10.1016/0025-3227(87)90068-5.

Rohling. (2007). Progress in paleosalinity: Overview and presentation of a new approach. Paleoceanography 22(3), pp. 1–9. doi: 10.1029/2007PA001437.

Rojas. (2013). Sensitivity of Southern Hemisphere circulation to LGM and 4 × CO2 climates. Geophysical Research Letters 40(5), pp. 965–970. doi: 10.1002/grl.50195.

Rooseboom and Annandale. (1981). Techniques applied in determining sediment loads

in South African rivers. Erosion and sediment transport measurement. Proc. Florence symposium, June 1981, (International Association of Hydrological Sciences, IAHS-AISH Publication 133) (133), pp. 219–224.

Rooseboom, Verster, Zietsman and Lotriet. (1992). the Development of the New Sediment Yield Map of Southern Africa. (297).

Rosenthal, Boyle and Labeyrie. (1997). Last Glacial Maximum paleochemistry and deep-water circulation in the Southern Ocean: Evidence from foraminiferal cadmium. Paleoceanography, 12(6), 787-796, https://doi.org/10.1029/97PA02508. Available at: https://doi.org/10.1594 GAEA.868710.

Rosenthal, Boyle and Slowey. (1997). Temperature control on the incorporation of magnesium, strontium, fluorine, and cadmium into benthic foraminiferal shells from Little Bahama Bank: Prospects for thermocline paleoceanography. Geochimica et Cosmochimica Acta 61(17), pp. 3633–3643. doi: 10.1016/S0016-7037(97)00181-6.

Rossignol-Strick. (1983). African monsoons, an immediate climate response to orbital insolation. Nature 304(5921), pp. 46–49. Available at: https://doi.org/10.1038/304046a0.

Rouault, Florenchie, Fauchereau and Reason. (2003). South East tropical Atlantic warm events and southern African rainfall. Geophysical Research Letters 30(5).

Rouault, White, Reason, Lutjeharms and Jobard. (2002). Ocean–atmosphere interaction in the Agulhas Current region and a South African extreme weather event. Weather and Forecasting 17(4), pp. 655–669.

Ruddiman. (2006). Orbital changes and climate. Quaternary Science Reviews 25(23–24), pp. 3092–3112. doi: 10.1016/j.quascirev.2006.09.001.

Ruddiman. (2007). Earth's Climate- Past and Future.

Russell, Dixon, Gnanadesikan, Stouffer and Toggweiler. (2006). The Southern Hemisphere Westerlies in a Warming World: Propping Open the Door to the Deep Ocean. Journal of Climate 19(24), pp. 6382–6390. Available at: https://journals.ametsoc.org/view/journals/clim/19/24/jcli3984.1.xml.

Rutberg, Goldstein, Hemming and Anderson. (2005). Sr isotope evidence for sources of terrigenous sediment in the southeast Atlantic Ocean: Is there increased available Fe for enhanced glacial productivity? Paleoceanography 20(1), pp. 1–10. doi: 10.1029/2003PA000999.

Sachs, Anderson and Lehman. (2001). Glacial surface temperatures of the southeast Atlantic Ocean. Science 293(5537), pp. 2077–2079. doi: 10.1126/science.1063584.

SADC (2010) Pietersen, Kellgren, Roos and De Vries - Explanatory Brochure for the South African Development Community (SADC) Hydrogeological Map & Atlas. pp. 1–51. Available at: http://www.orangesenqurak.org/UserFiles/File/SADC/SADC - Explana-

tory Brochure for the South African Development Community (SADC) Hydrogeological Map & Atlas (2010).pdf.

Saini, Mukherjee, Rathi and Khanna. (2000). Evaluation of energy-dispersive x-ray fluorescence spectrometry in the rapid analysis of silicate rocks using pressed powder pellets. X-Ray Spectrometry: An International Journal 29(2), pp. 166–172.

Sánchez-Goñi. (2007). 13. Introduction to climate and vegetation in Europe during MIS5. In: Sirocko, F., Claussen, M., Sánchez Goñi, M. F., and Litt, T. B. T.-D. in Q. S. eds. The Climate of Past Interglacials. Elsevier, pp. 197–205. Available at: https://www.sciencedirect.com/science/article/pii/S1571086607800388.

Scerri. (2017). The North African Middle Stone Age and its place in recent human evolution. Evolutionary Anthropology 26(3), pp. 119–135. doi: 10.1002/evan.21527.

Scheffler, Hoernes and Schwark. (2004). Reconstruction of sedimentary environment and climate conditions by multi-geochemical investigations of Late Palaeozoic glacial to post-glacial sedimentary sequences from SW-Gondwana. Mathematisch-Naturwissenschaftlichen Fakultät Erlangung, p. 213. Available at: http://hss.ulb.uni-bonn.de/2004/0399/0399.htm.

Schefuß, Kuhlmann, Mollenhauer, Prange and Pätzold. (2011). Forcing of wet phases in southeast Africa over the past 17,000 years. Nature 480(7378), pp. 509–512. doi: 10.1038/nature10685.

Schefuß, Schouten and Schneider. (2005). Climatic controls on central African hydrology during the past 20,000 years. Nature 437(7061), pp. 1003–1006. doi: 10.1038/nature03945.

Schneider, Bischoff and Haug. (2014). Migrations and dynamics of the intertropical convergence zone. Nature 513(7516), pp. 45–53. doi: 10.1038/nature13636.

Scholz, Johnson, Cohen, King, Peck, Overpeck, Talbot, Brown, Kalindekafe, Amoako, Lyons, Shanahan, Castañeda, Heil, Forman, McHargue, Beuning, Gomez, & Pierson. (2007). East African megadroughts between 135 and 75 thousand years ago and bearing on early-modern human origins. Proceedings of the National Academy of Sciences of the United States of America, 104(42), 16416–16421.
https://doi.org/10.1073/pnas.0703874104

Schouten, de Ruijter and van Leeuwen. (2002a). Upstream control of Agulhas Ring shedding. Journal of Geophysical Research C: Oceans 107(8), pp. 23–1. doi: 10.1029/2001jc000804.

Schouten, de Ruijter, van Leeuwen and Dijkstra. (2002b). An oceanic teleconnection between the equatorial and southern Indian Ocean. Geophysical Research Letters 29(16), pp. 59-1-59–4. doi: 10.1029/2001gl014542.

Schwager. (1886). Fossile Foraminiferen von Kar Nikobar Reise der Österreichischen Fregatte Novara um die Erde in den Jahren 1857, 1858, 1859 unter den Befehlen des

Commodore B. von Wüllerstorf-Urbair. Geologischer Theil 2(2), pp. 187–268.

Scorrer, Faillace, Hildred, Nederbragt, Andersen, Millet, Lamb, & Madgwick. (2021). Diversity aboard a Tudor warship: Investigating the origins of the Mary Rose crew using multi-isotope analysis. Royal Society Open Science, 8(5).
https://doi.org/10.1098/rsos.202106

Scott and Woodborne. (2007). Pollen analysis and dating of Late Quaternary faecal deposits (hyraceum) in the Cederberg, Western Cape, South Africa. Review of Palaeobotany and Palynology 144(3–4), pp. 123–134.
doi: 10.1016/j.revpalbo.2006.07.004.

Scott and Woodborne. (2007b). Vegetation history inferred from pollen in Late Quaternary faecal deposits (hyraceum) in the Cape winter-rain region and its bearing on past climates in South Africa. Quaternary Science Reviews 26(7–8), pp. 941–953. doi: 10.1016/j.quascirev.2006.12.012.

Scott, Marais and Brook. (2004). Fossil hyrax dung and evidence of Late Pleistocene and Holocene vegetation types in the Namib Desert. Journal of Quaternary Science 19(8), pp. 829–832. Available at: https://doi.org/10.1002/jqs.870.

Scott. (1982). A late quaternary pollen record from the Transvaal bushveld, South Africa. Quaternary Research 17(3), pp. 339–370. Available at: https://www.sciencedirect.com/science/article/pii/003358948290028X.

Sealy, Lee-Thorp, Loftus, Faith and Marean. (2016). Late Quaternary environmental change in the Southern Cape, South Africa, from stable carbon and oxygen isotopes in faunal tooth enamel from Boomplaas Cave. Journal of Quaternary Science 31(8), pp. 919–927. doi: 10.1002/jqs.2916.

Seutloali, Beckedahl, Dube and Sibanda. (2016). An assessment of gully erosion along major armoured roads in south-eastern region of South Africa: a remote sensing and GIS approach. Geocarto International 31(2), pp. 225–239. Available at: http://dx.doi.org/10.1080/10106049.2

Shackleton & Opdyke. (1973). Oxygen Pacific Isotope and Palaeomagnetic Stratigraphy of Equatorial Core V28-238: Oxygen Isotope Temperatures and Ice Volumes on a 10" Year and 10" Year Scale*. 55, pp. 39–55.

Shackleton and Hall. (1997). THE LATE MIOCENE STABLE ISOTOPE RECORD, SITE 926. Proceedings of the Ocean Drilling Program, Scientific Results 154(1), pp. 367–373. doi: 10.1029/97PA02995.

Shackleton. (1967). Oxygen isotope analyses and pleistocene temperatures re-assessed. Nature 215(5096), pp. 15–17. doi: 10.1038/215015a0.

Shackleton. (1969). The last interglacial in the marine and terrestrial records. Proceedings of the Royal Society of London. Series B. Biological Sciences 174(1034), pp.

135–154.

Shackleton. (1977). Stable carbon and oxygen isotope ratios of benthic and planktic foraminifera from the Atlantic Ocean. Supplement to: Shackleton, NJ (1977): Carbon-13 in Uvigerina: Tropical rain forest history and the equatorial Pacific carbonate dissolution cycle. In: Andersen, N R & Malahoff, A (eds.), The Fate of Fossil Fuel in the Oceans. New York (Plenum), 401-427. Available at:
https://doi.org/10.1594/PANGAEA.692091.

Shi, Dupont, Beug and Schneider. (2000). Correlation between Vegetation in Southwestern Africa and Oceanic Upwelling in the Past 21,000 Years. Quaternary Research 54(1), pp. 72–80. Available at: https://www.sciencedirect.com/science/article/pii/S0033589400921458.

Siegenthaler and Sarmiento. (1973). Atmospheric carbon dioxide and the ocean. Nature 365, pp. 119–125. doi: 10.1016/0013-9327(71)90019-X.

Sigman, Hain and Haug. (2010). The polar ocean and glacial cycles in atmospheric CO2 concentration. Nature 466(7302), pp. 47–55. doi: 10.1038/nature09149.

Sikes, Allen and Lund. (2017). Enhanced 13C and 18O Differences Between the South Atlantic and South Pacific During the Last Glaciation: The Deep Gateway Hypothesis. Paleoceanography 32(10), pp. 1000–1017. Available at: https://onlinelibrary.wiley.com/doi/full/10.1002/2017PA003118 [Accessed: 26 January 2023].

Simon, Arthur, Hall, Peeters, Loveday, Barker, Ziegler, & Zahn. (2013). Millennial-scale Agulhas Current variability and its implications for salt-leakage through the Indian – Atlantic Ocean Gateway. Earth and Planetary Science Letters, 383, 101–112. https://doi.org/10.1016/j.epsl.2013.09.035

Simon, Ziegler, Bosmans, Barker, Reason and Hall. (2015a). Eastern South African hydroclimate over the past 270,000 years. Scientific Reports 5, pp. 1–10. Available at: http://dx.doi.org/10.1038/srep18153.

Simon, Gong, Hall, Ziegler, Barker, Knorr, Van Der Meer, Kasper, & Schouten. (2015b). Salt exchange in the Indian-Atlantic Ocean Gateway since the Last Glacial Maximum: A compensating effect between Agulhas Current changes and salinity variations? Paleoceanography, 30(10), 1318–1327.
https://doi.org/10.1002/2015PA002842

Simon, Babin, Goldstein, Cai, Liu, Han, Haws, Johns, Lear, & Hemming. (2020a). Development of a protocol to obtain the composition of terrigenous detritus in marine sediments -a pilot study from International Ocean Discovery Program Expedition 361. Chemical Geology, 535(April 2019), 119449. https://doi.org/10.1016/j.chemgeo.2019.119449

Simon, Babin, Goldstein, Cai, Liu, Han, Haws, Johns, Lear, & Hemming. (2020b). Sequential extraction procedure to obtain the composition of terrigenous detritus in marine

sediments. MethodsX, 7, 100888. https://doi.org/10.1016/j.mex.2020.100888

Simon, Ziegler, Barker, van der Meer, Schouten and Hall. (2020c). A late Pleistocene dataset of Agulhas Current variability. Scientific Data 7(1), pp. 1–12. Available at: http://dx.doi.org/10.1038/s41597-020-00689-7.

Simon. (2014). Ocean and land climate dynamics off southeast Africa during the late Pleistocene : A multi-proxy approach. Thesis (May).

Singarayer and Burrough. (2015). Interhemispheric dynamics of the African rainbelt during the late Quaternary. Quaternary Science Reviews 124, pp. 48–67. Available at: http://dx.doi.org/10.1016/j.quascirev.2015.06.021.

Singer. (1984). The paleoclimatic interpretation of clay minerals in sediments - a review. Earth Science Reviews 21(4), pp. 251–293. doi: 10.1016/0012-8252(84)90055-2.

Speich, Lutjeharms, Penven and Blanke. (2006). Role of bathymetry in Agulhas Current configuration and behaviour. Geophysical Research Letters 33(23), pp. 2–6. doi: 10.1029/2006GL027157.

Spero, Bijma, Lea and Bemis. (1997). Effect of seawater carbonate concentration on foraminiferal carbon and oxygen isotopes. Nature 390(6659), pp. 497–500. Available at: http://10.0.4.14/37333.

Spero, Lerche and Williams. (1991). Opening the carbon isotope “vital effect” black box, 2, quantitative model for interpreting foraminiferal carbon isotope data. Paleoceanography 6(6), pp. 639–655.

Stager, Ryves, Chase and Pausata. (2011). Catastrophic drought in the Afro-Asian monsoon region during Heinrich event 1. Science 331(6022), pp. 1299–1302. doi: 10.1126/science.1198322.

Starr, Hall, Barker, Rackow, Zhang, Hemming, van der Lubbe, Knorr, Berke, Bigg, Cartagena, Jiménez-Espejo, Gong, Gruetzner, Lathika, LeVay, Robinson, & Ziegler. (2021). Antarctic icebergs reorganise ocean circulation during pleistocene glacials. Nature, 589(January). https://doi.org/10.1038/s41586-020-03094-7

Stewart, Zhao, Mitchell, Dewar, Gleason and Blum. (2020). Ostrich eggshell bead strontium isotopes reveal persistent macroscale social networking across late Quaternary southern Africa. Proceedings of the National Academy of Sciences of the United States of America 117(12), pp. 6453–6462. doi: 10.1073/pnas.1921037117.

Stramma and Peterson. (1989). The South Atlantic Current. Journal of Physical Oceanography 20, pp. 846–859.

Stringer. (2016). The origin and evolution of Homo sapiens. Philosophical Transactions of the Royal Society B: Biological Sciences 371(1698), p. 20150237. Available at: https://doi.org/10.1098/rstb.2015.0237.

Strobel, Kasper, Frenzel, Schittek, Quick, Meadows, Mäusbacher, & Haberzettl. (2019). Late Quaternary palaeoenvironmental change in the year-round rainfall zone of South Africa derived from peat sediments from Vankervelsvlei. Quaternary Science Reviews, 218, 200–214. https://doi.org/10.1016/j.quascirev.2019.06.014

Stuiver and Braziunas. (1993a). Modeling atmospheric to 10,000.

Stuiver and Braziunas. (1993b). Sun, ocean, climate and atmospheric 14CO2 : an evaluation of causal and spectral relationships. The Holocene 3(4), pp. 289–305. Available at: https://doi.org/10.1177/095968369300300401.

Stumpt. (2011). Radiogenic Isotopes Studies.

Stuut, Prins, Schneider, Weltje, Fred Jansen and Postma. (2002). A 300-kyr record of aridity and wind strength in southwestern Africa: Inferences from grain-size distributions of sediments on Walvis Ridge, SE Atlantic. Marine Geology 180(1–4), pp. 221–233. doi: 10.1016/S0025-3227(01)00215-8.

Stuut. (2004). Climate variability at the southern boundaries of the Namib (southwestern Africa) and Atacama (northern Chile) coastal deserts during the last 120,000 yr. Quaternary research 62(3), pp. 301–309. doi: 10.1016/j.yqres.2004.08.001.

Sugden, McCulloch, Bory and Hein. (2009). Influence of Patagonian glaciers on Antarctic dust deposition during the last glacial period. Nature Geoscience 2(4), pp. 281–285. doi: 10.1038/ngeo474.

Taljaard. (1996). Atmospheric circulation systems, synoptic climatology and weather phenomena of South Africa. Part 6, Rainfall in South Africa. Department of Environmental Affairs and Tourism.

Taljaard. (2003). Department of water affairs and forestry breede river basin study intermediate determination of resource directed measures.

Talley. (2013). Closure of the global overturning circulation through the Indian, Pacific, and southern oceans. Oceanography 26(1), pp. 80–97.
doi: 10.5670/oceanog.2013.07.

Talma and Vogel. (1992). Late Quaternary paleotemperatures derived from a speleothem from Cango Caves, Cape Province, South Africa. Quaternary Research 37(2), pp. 203–213.

Tangunan, Berke, Cartagena-Sierra, Flores, Gruetzner, Jiménez-Espejo, LeVay, Baumann, Romero, Saavedra-Pellitero, Coenen, Starr, Hemming, Hall, Barker, Brentegani, Caley, Charles, Crespin, Franzese, Han, Hines, Jimenez Espejo, Just, Koutsodendris, Kubota, Lathika, Norris, dos Santos, Robinson, Rolison, Simon, Tangunan, van der Lubbe, Yamane, & Zhang. (2021). Strong glacial-interglacial variability in upper ocean hydrodynamics, biogeochemistry, and productivity in the southern Indian Ocean. Communications Earth and Environment, 2(1).

https://doi.org/10.1038/s43247-021-00148-0

Taylor. (1980). Refractory and moderately volatile element abundances in the earth, moon and meteorites. Lunar and Planetary Science Conference Proceedings 1, pp. 333–348.

Texier, Porraz, Parkington, Rigaud, Poggenpoel, Miller, Tribolo, Cartwright, Coudenneau, Klein, Steele, & Verna. (2010). A Howiesons Poort tradition of engraving ostrich eggshell containers dated to 60,000 years ago at Diepkloof Rock Shelter, South Africa. Proceedings of the National Academy of Sciences of the United States of America, 107(14), 6180–6185. https://doi.org/10.1073/pnas.0913047107

Thackeray. (1987). Late Quaternary environmental changes inferred from small mammalian fauna, southern Africa. Climatic Change 10(3), pp. 285 – 305.

Thackeray. (1990). Temperature Indices from Late Quaternary Sequences in South Africa. South African Geographical Journal 72(2), pp. 47–49. Available at: https://doi.org/10.1080/03736245.1990.10586374.

Thieblemont. (2017). An updated geological map of Africa at 1 / 10 000 000 scale. pp. 1–2.

Thiry. (2000). Palaeoclimatic interpretation of clay minerals in marine deposits: an outlook from the continental origin. Earth-Science Reviews 49(1), pp. 201–221. Available at: https://www.sciencedirect.com/science/article/pii/S0012825299000549.

Thomas, Bailey, Shaw, Durcan and Singarayer. (2009). Late Quaternary highstands at Lake Chilwa, Malawi: Frequency, timing and possible forcing mechanisms in the last 44ka. Quaternary Science Reviews 28(5), pp. 526–539. Available at: https://www.sciencedirect.com/science/article/pii/S0277379108002953.

Thornalley, Barker, Broecker, Elderfield and McCave. (2011). The deglacial evolution of North Atlantic deep convection. Science (New York, N.Y.) 331(6014), pp. 202–205. doi: 10.1126/science.1196812.

Thornalley, Elderfield and McCave. (2010). Intermediate and deep water paleoceanography of the northern North Atlantic over the past 21,000 years. Paleoceanography 25(1). Available at: https://doi.org/10.1029/2009PA001833.

Tierney, Lewis, Cook, LeGrande and Schmidt. (2011). Model, proxy and isotopic perspectives on the East African Humid Period. Earth and Planetary Science Letters 307(1–2), pp. 103–112. Available at: http://dx.doi.org/10.1016/j.epsl.2011.04.038.

Tierney, Russell, Huang, Sinninghe Damsté, Hopmans and Cohen. (2008). Northern hemisphere controls on tropical southeast African climate during the past 60,000 years. Science 322(5899), pp. 252–255. doi: 10.1126/science.1160485.

Tierney, Smerdon, Anchukaitis and Seager. (2013). Multidecadal variability in East African hydroclimate controlled by the Indian Ocean. Nature 493(7432), pp. 389–392.

Available at: http://dx.doi.org/10.1038/nature11785.

Tillinger and Gordon. (2009). Fifty years of the Indonesian throughflow. Journal of Climate 22(23), pp. 6342–6355. doi: 10.1175/2009JCLI2981.1.

Tjallingii, Röhl, Kölling and Bickert. (2007). Influence of the water content on X-ray fluorescence corescanning measurements in soft marine sediments. Geochemistry, Geophysics, Geosystems 8(2), pp. 1–12. doi: 10.1029/2006GC001393.

Toggweiler, Russell and Carson. (2006). Midlatitude westerlies, atmospheric CO2, and climate change during the ice ages. Paleoceanography 21(2), pp. 1–15. doi: 10.1029/2005PA001154.

Truc, Chevalier, Favier, Cheddadi, Meadows, Scott, Carr, Smith, & Chase. (2013). Quantification of climate change for the last 20,000years from Wonderkrater, South Africa: Implications for the long-term dynamics of the Intertropical Convergence Zone. Palaeogeography, Palaeoclimatology, Palaeoecology, 386, 575–587. https://doi.org/https://doi.org/10.1016/j.palaeo.2013.06.024

Tylén, Fusaroli, Rojo, Heimann, Fay, Johannsen, Riede, & Lombard. (2020). The evolution of early symbolic behavior in Homo sapiens. Proceedings of the National Academy of Sciences of the United States of America, 117(9), 4578–4584. https://doi.org/10.1073/pnas.1910880117

Tyson and Preston-Whyte. (2000). The Weather and Climate of Southern Africa.

Tyson. (1986). Climatic Change and Variability in Southern Africa.

Urrego, Sánchez Goñi, Daniau, Lechevrel and Hanquiez. (2015). Increased aridity in southwestern Africa during the warmest periods of the last interglacial. Climate of the Past 11(10), pp. 1417–1431. doi: 10.5194/cp-11-1417-2015.

USGS. (2007). Global Ecosystems.

van Andel. (1989). Late Pleistocene Sea Levels and the Human Exploitation of the Shore and Shelf of Southern South Africa. Journal of Field Archaeology 16(2), pp. 133–155. Available at: https://doi.org/10.1179/jfa.1989.16.2.133.

van Breemen and Buurman. (2002). Soil Formation. Soil Formation (May). doi: 10.1007/978-0-585-31788-5.

van der Does, Wengler, Lamy, Martínez-García, Jaccard, Kuhn, Lanny, Stuut, & Winckler. (2021). Opposite dust grain-size patterns in the Pacific and Atlantic sectors of the Southern Ocean during the last 260,000 years. Quaternary Science Reviews, 263. https://doi.org/10.1016/j.quascirev.2021.106978

van der Lubbe, H.J.L., Hall, I.R., Barker, S., Hemming, S.R., Baar, T.F., Starr, A., Just, J., & Joordens, J.C.A. (2021). Indo-Pacific Walker circulation drove Pleistocene African aridification. Nature

van der Lubbe, Frank, Tjallingji and Ralph. (2016). Neodymium isotope constraints

on provenance, dispersal, and climate-driven supply of Zambezi sediments along the Mozambique Margin during the past 45,000 years. Geochemistry Geophysics Geosystems 18(1–2), pp. 1–10.

Van der Lubbe, Tjallingii, Prins, Brummer, Jung, Kroon and Schneider. (2014). Sedimentation patterns off the Zambezi River over the last 20,000 years. Marine Geology 355, pp. 189–201. Available at: http://dx.doi.org/10.1016/j.margeo.2014.05.012.

van der Merwe and Weber. (1963). Clay Minerals of South African Soils. South African Journal of Agricultureal Science 6, pp. 411–454.

Van Kreveld, Sarnthein, Erlenkeuser, Grootes, Jung, Nadeau, Pflaumann, & Voelker. (2000). Potential links between surging ice sheets, circulation changes, and the Dansgaard-Oeschger cycles in the Irminger Sea, 60–18 kyr. Paleoceanography, 15(4), 425–442.

van Leeuwen, de Ruijter and Lutjeharms. (2000). Natal pulses and the formation of Agulhas rings Very High Resolution. Journal of Geophysical Research 105(1999), pp. 6425–6436.

Van Rooy. (1972). Climate of South Africa: District rainfall for South Africa and the annual march of rainfall over southern Africa, part 10. South African Weather Bureau Tech. Note WB 35.

Van Sebille, Biastoch, Van Leeuwen and De Ruijter. (2009). A weaker Agulhas current leads to more Agulhas leakage. Geophysical Research Letters 36(3), pp. 10–13. doi: 10.1029/2008GL036614.

van Zinderen Bakker. (1967). Upper Pleistocene and Holocene stratigraphy and ecology on the basis of vegetation changes in sub-Saharan Africa. Background to evolution in Africa 125, p. 147.

Van Zinderen Bakker. (1976). Evolution of Late Quaternary palaeoclimates of southern Africa. Palaeoecology of Africa & of the surrounding islands & Antarctica.

Vazquez Riveiros and Waelbroeck. (2016). Cruise report ACCLIMATE MD203.

Vazquez Riveiros and Waelbroeck. (2020). Cruise Report ACCLIMATE-2.

Vigaud, Richard, Rouault and Fauchereau. (2009). Moisture transport between the South Atlantic Ocean and southern Africa: relationships with summer rainfall and associated dynamics. Climate Dynamics 32(1), pp. 113–123. Available at: https://doi.org/10.1007/s00382-008-0377-7.

Villa, Soressi, Henshilwood and Mourre. (2009). The Still Bay points of Blombos Cave (South Africa). Journal of Archaeological Science 36(2), pp. 441–460. Available at: https://www.sciencedirect.com/science/article/pii/S0305440308002318.

Villa, Soriano, Teyssandier and Wurz. (2010). The Howiesons Poort and MSA III at

Klasies River main site, Cave 1A. Journal of Archaeological Science 37(3), pp. 630–655. Available at:
https://www.sciencedirect.com/science/article/pii/S0305440309003951.

Vimeux, Masson, Jouzel, Stievenard and Petit. (1999). Glacial-interglacial changes in ocean surface conditions in the Southern Hemisphere. Nature 398(6726), pp. 410–413. doi: 10.1038/18860.

Wadley, Hodgskiss and Grant. (2009). Implications for complex cognition from the hafting of tools with compound adhesives in the Middle Stone Age, South Africa. Proceedings of the National Academy of Sciences 106(24), pp. 9590–9594.

Wadley. (2015). Those marvellous millennia: the Middle Stone Age of Southern Africa. Azania: Archaeological Research in Africa 50, pp. 155–226. Available at: https://api.semanticscholar.org/CorpusID:162432908.

Waelbroeck, Labeyrie, Michel, Duplessy, McManus, Lambeck, Balbon, & Labracherie. (2002). Sea-level and deep water temperature changes derived from benthic foraminifera isotopic records. Quaternary Science Reviews, 21(1–3), 295–305.
https://doi.org/10.1016/S0277-3791(01)00101-9

Walker. (1990). Links Between South African Summer Rainfall and Temperature Variability of the Agulhas and Benguela Current System. 95, pp. 3297–3319.

Walling. (1984). The sediment yields of African rivers. in: Challenges in African Hydrology & Water Resources, Proc. Harare Symp., (Harare, Zimbabwe: Jul. 1984), D.E. Walling; S.S.D (144) (ISBN 0-947571-05–1)).

Walter, Hegner, Diekmann, Kuhn and Rutgers Van Der Loeff. (2000). Provenance and transport of terrigenous sediment in the South Atlantic Ocean and their relations to glacial and interglacial cycles: Nd and Sr isotopic evidence. Geochimica et Cosmochimica Acta 64(22), pp. 3813–3827. doi: 10.1016/S0016-7037(00)00476-2.

Wang, Sarnthein, Erlenkeuser, Grimalt, Grootes, Heilig, Ivanova, Kienast, Pelejero, & Pflaumann. (1999). East Asian monsoon climate during the Late Pleistocene: high-resolution sediment records from the South China Sea. Marine Geology, 156(1), 245–284.
https://doi.org/https://doi.org/10.1016/S0025-3227(98)00182-0

Wang, Auler, Edwards, Cheng, Cristalli, Smart, Richards, & Shen. (2004). Wet periods in northeastern Brazil over the past 210 kyr linked to distant climate anomalies. Nature, 432(7018), 740–743. https://doi.org/10.1038/nature03067

Wang, Cheng, Edwards, Kong, Shao, Chen, Wu, Jiang, Wang, & An. (2008). Millennial- and orbital-scale changes in the East Asian monsoon over the past 224,000 years. Nature, 451(7182), 1090–1093. https://doi.org/10.1038/nature06692

Wang, Larsen, Leduc, Andersen, Blanz and Schneider. (2013a). What does leaf wax D

from a mixed C3/C4 vegetation region tell us? Geochimica et Cosmochimica Acta 111, pp. 128–139. Available at: http://dx.doi.org/10.1016/j.gca.2012.10.016.

Wang, Liu and Huang. (2013b). Last Glacial Maximum Sea Surface Temperatures: A Model-Data Comparison. Atmospheric and Oceanic Science Letters 6(5), pp. 233–239. doi: 10.3878/j.issn.1674-2834.13.0019.

Wang. (2019). Three-ocean interactions and climate variability: a review and perspective. Climate Dynamics 53(7–8), pp. 5119–5136. Available at: https://doi.org/10.1007/s00382-019-04930-x.

Weldeab, Lea, Schneider and Andersen. (2007). 155,000 Years of West African Monsoon and Ocean Thermal Evolution. Science 316(5829), pp. 1303–1307. Available at: https://doi.org/10.1126/science.1140461.

Weldeab, Stuut, Schneider and Siebel. (2013). Holocene climate variability in the winter rainfall zone of South Africa. Climate of the Past 9(5), pp. 2347–2364. doi: 10.5194/cp-9-2347-2013.

Weltje and Prins. (2003). Muddled or mixed? Inferring palaeoclimate from size distributions of deep-sea clastics. Sedimentary Geology 162(1–2), pp. 39–62. doi: 10.1016/S0037-0738(03)00235-5.

Weltje. (1997). End-member modeling of compositional data: Numerical-statistical algorithms for solving the explicit mixing problem. Mathematical Geology 29(4), pp. 503–549. doi: 10.1007/bf02775085.

Whallon. (2006). Social networks and information: Non-“utilitarian” mobility among hunter-gatherers. Journal of Anthropological Archaeology 25(2), pp. 259–270. Available at: https://www.sciencedirect.com/science/article/pii/S027841650500067X.

White, Asfaw, DeGusta, Gilbert, Richards, Suwa and Clark Howell. (2003). Pleistocene Homo sapiens from Middle Awash, Ethiopia. Nature 423(6941), pp. 742–747. Available at: https://doi.org/10.1038/nature01669.

Wilkins, Schoville, Pickering, Gliganic, Collins, Brown, von der Meden, Khumalo, Meyer, Maape, Blackwood, & Hatton. (2021). Innovative Homo sapiens behaviours 105,000 years ago in a wetter Kalahari. Nature, 592(7853), 248–252. https://doi.org/10.1038/s41586-021-03419-0

Wilkins. (2020). Learner-driven innovation in the stone tool technology of early Homo sapiens. Evolutionary Human Sciences 2, pp. 1–15. doi: 10.1017/ehs.2020.40.

Wirth, Gilli, Niemann, Dahl, Ravasi, Sax, Hamann, Peduzzi, Peduzzi, Tonolla, Lehmann, & Anselmetti. (2013). Combining sedimentological, trace metal (Mn, Mo) and molecular evidence for reconstructing past water-column redox conditions: The example of meromictic Lake Cadagno (Swiss Alps). , 120, 220–238. https://doi.org/10.1016/j.gca.2013.06.017

Worden and Morad. (2000). Clay minerals in sandstones: controls on formation, distribution and evolution. Available at: https://medium.com/@arifwicaksanaa/pengertian-use-case-a7e576e1b6bf.

Wu, Kuhn, Diekmann, Lembke-Jene, Tiedemann, Zheng, Ehrhardt, Arz, & Lamy. (2019). Surface sediment characteristics related to provenance and ocean circulation in the Drake Passage sector of the Southern Ocean. Deep Sea Research Part I: Oceanographic Research Papers, 154, 103135.
https://doi.org/https://doi.org/10.1016/j.dsr.2019.103135

Wündsch, Haberzettl, Kirsten, Kasper, Zabel, Dietze, Baade, Daut, Meschner, Meadows, & Mäusbacher. (2016). Sea level and climate change at the southern Cape coast, South Africa, during the past 4.2 kyr. Palaeogeography, Palaeoclimatology, Palaeoecology, 446, 295–307. https://doi.org/10.1016/j.palaeo.2016.01.027

Wyrtki. (1971). Oceanographic Atlas of the International Indian Ocean Expedition. National Science Foundation, Washington DC.

Yang, Zhang, Yi, Zhong, Lu, Wan, Du, & Xiang. (2023). A contracting Intertropical Convergence Zone during the Early Heinrich Stadial 1. Nature Communications, 14(1), 4695. https://doi.org/10.1038/s41467-023-40377-9

Yu and Elderfield. (2007). Benthic foraminiferal B/Ca ratios reflect deep water carbonate saturation state. Earth and Planetary Science Letters 258(1–2), pp. 73–86. doi: 10.1016/j.epsl.2007.03.025.

Zabel, Bickert, Dittert and Haese. (1999). Significance of the sedimentary AI:Ti ratio as an indicator for variations in the circulation patterns of the equatorial North Atlantic. Paleoceanography 14(6), pp. 789–799.

Zabel, Schneider, Wagner, Adegbie, de Vries and Kolonic. (2001). Geochemistry of sediment cores GeoB4901-3 and GeoB4901-8 from the southern flank of the Niger Fan. Supplement to: Zabel, M et al. (2001). Late Quaternary Climate Changes in Central Africa as Inferred from Terrigenous Input to the Niger Fan. Quaternary Research, 56(2), 207-217, https://doi.org/10.1006/qres.2001.2261.

Zachos, Pagani, Sloan, Thomas and Billups. (2001). Trends, rhythms, and aberrations in global climate 65 Ma to present. Science 292(5517), pp. 686–693. doi: 10.1126/science.1059412.

Zeeden, Meyers, Lourens and Hilgen. (2015). Testing astronomically tuned age models. Paleoceanography 30(4), pp. 369–383. doi: 10.1002/2014PA002762.

Ziegler, Simon, Hall, Barker, Stringer, Zahn, Simon, Barker, & Zahn. (2013). Development of Middle Stone Age innovation linked to rapid climate change. Nature Communications, 4(May). https://doi.org/10.1038/ncomms2897

Zonneveld. (1997). New species of organic walled dinoflagellate cysts from modern sediments of the Arabian Sea (Indian Ocean). Review of Palaeobotany and Palynology 97(3–4), pp. 319–337. doi: 10.1016/S0034-6667(97)00002-X.

Appendix

Table A1: List of references for $^{87}Sr/^{86}Sr$ isotope in the South African region used in Figure 4.2

Reference	Sample	Latitude	Longitude	$^{87}Sr/^{86}Sr$	Grain Size
Franzese et al. (2006)	Orange River Mud	-28.62	16.46	0.7157	<63 μm
Franzese et al. (2006)	RC11-106	-54.22	-34.33	0.70841	<63 μm
Franzese et al. (2006)	RC11-64	-48.23	-46.83	0.70835	<63 μm
Franzese et al. (2006)	RC11-83	-41.07	9.72	0.72259	<63 μm
Franzese et al. (2006)	RC11-84	-39.27	12.58	0.71511	<63 μm
Franzese et al. (2006)	RC11-86	-35.78	18.45	0.73237	<63 μm
Franzese et al. (2006)	RC11-87	-38.95	19.15	0.71541	<63 μm
Franzese et al. (2006)	RC11-98	-47.65	61.48	0.71051	<63 μm
Franzese et al. (2006)	RC12-261	-42	-38.13	0.70968	<63 μm
Franzese et al. (2006)	RC12-267	-38.68	-25.78	0.71106	<63 μm
Franzese et al. (2006)	RC12-291	-42.58	-17.8	0.70997	<63 μm
Franzese et al. (2006)	RC12-304	-33.22	29.18	0.71918	<63 μm
Franzese et al. (2006)	RC13-227	-21.88	8.87	0.72642	<63 μm
Franzese et al. (2006)	RC13-229	-25.5	11.3	0.72581	<63 μm
Franzese et al. (2006)	RC13-236	-29.63	1.62	0.71416	<63 μm
Franzese et al. (2006)	RC13-243	-36.9	0.33	0.71277	<63 μm
Franzese et al. (2006)	RC13-253	-46.6	7.63	0.71058	<63 μm
Franzese et al. (2006)	RC13-271	-51.98	4.52	0.71198	<63 μm
Franzese et al. (2006)	RC13-276	-47.7	14.7	0.71183	<63 μm
Franzese et al. (2006)	RC14-11	-38	51.18	0.7146	<63 μm
Franzese et al. (2006)	RC14-3	-35.48	28.95	0.71668	<63 μm
Franzese et al. (2006)	RC14-4	-32.62	31.13	0.72165	<63 μm
Franzese et al. (2006)	RC14-9	-39.02	47.88	0.71017	<63 μm
Franzese et al. (2006)	RC15-100	-42.97	-33.85	0.71106	<63 μm
Franzese et al. (2006)	RC15-112	-40.08	-49.17	0.70897	<63 μm
Franzese et al. (2006)	RC16-119	-27.7	-46.52	0.71493	<63 μm
Franzese et al. (2006)	RC17-38	-26.17	13.62	0.72506	<63 μm
Franzese et al. (2006)	RC17-44	-29.8	15.03	0.71164	<63 μm
Franzese et al. (2006)	RC17-49	-32.92	14.93	0.7202	<63 μm
Franzese et al. (2006)	RC17-59	-49.5	37	0.70751	<63 μm
Franzese et al. (2006)	RC17-62	-47.6	56.87	0.70487	<63 μm
Franzese et al. (2006)	RC17-63	-45.65	48.28	0.70421	<63 μm
Franzese et al. (2006)	RC17-66	-42.4	42.53	0.71243	<63 μm
Franzese et al. (2006)	RC17-69	-31.5	32.6	0.72739	<63 μm
Franzese et al. (2006)	RC17-75	-30.47	40.37	0.72899	<63 μm
Franzese et al. (2006)	RC18-1	-52.45	-44.9	0.70779	<63 μm
Franzese et al. (2006)	RC8-19	-24.3	-14.7	0.7125	<63 μm
Franzese et al. (2006)	RC8-42	-45.68	54.9	0.70469	<63 μm
Franzese et al. (2006)	RC8-43	-48.68	57.37	0.70691	<63 μm
Franzese et al. (2006)	TNO57-23	-41.14	13.55	0.7161	<63 μm
Franzese et al. (2006)	TNO57-6	-42.92	8.88	0.71237	<63 μm

Franzese et al. (2006)	VM12-18	-28.7	-34.5	0.71094	<63 µm
Franzese et al. (2006)	VM14-17	-23.68	-42.5	0.72139	<63 µm
Franzese et al. (2006)	VM14-65	-41.07	7.78	0.72177	<63 µm
Franzese et al. (2006)	VM14-72	-34.15	18.08	0.715	<63 µm
Franzese et al. (2006)	VM14-77	-29.63	32.87	0.72496	<63 µm
Franzese et al. (2006)	VM15-156	-34.25	-51.55	0.71088	<63 µm
Franzese et al. (2006)	VM16-192	-26.42	-44.22	0.71681	<63 µm
Franzese et al. (2006)	VM16-50	-33.35	16.43	0.71511	<63 µm
Franzese et al. (2006)	VM16-52	-35.62	19.8	0.74074	<63 µm
Franzese et al. (2006)	VM16-53	-36.83	21.3	0.71853	<63 µm
Franzese et al. (2006)	VM16-69	-37.58	56.73	0.70614	<63 µm
Franzese et al. (2006)	VM17-147	-33.15	-49.87	0.70854	<63 µm
Franzese et al. (2006)	VM18-183	-33.23	15.98	0.71532	<63 µm
Franzese et al. (2006)	VM18-188	-37.63	37.87	0.71897	<63 µm
Franzese et al. (2006)	VM18-196	-21.43	51.62	0.70574	<63 µm
Franzese et al. (2006)	VM18-35	-36.4	-41.12	0.71057	<63 µm
Franzese et al. (2006)	VM18-48	-36.85	-54.17	0.70609	<63 µm
Franzese et al. (2006)	VM19-214	-23.37	38.85	0.73555	<63 µm
Franzese et al. (2006)	VM19-224	-35.5	29.95	0.71373	<63 µm
Franzese et al. (2006)	VM19-240	-30.58	13.28	0.73061	<63 µm
Franzese et al. (2006)	VM19-257	-20.98	12.37	0.71811	<63 µm
Franzese et al. (2006)	VM19-258	-20.4	11.62	0.71991	<63 µm
Franzese et al. (2006)	VM20-190	-25.12	40.9	0.72243	<63 µm
Franzese et al. (2006)	VM20-194	-22.68	41.37	0.72743	<63 µm
Franzese et al. (2006)	VM20-196	-25.18	41.62	0.72581	<63 µm
Franzese et al. (2006)	VM20-201	-36.32	25.28	0.72292	<63 µm
Franzese et al. (2006)	VM22-108	-43.18	-3.25	0.71032	<63 µm
Franzese et al. (2006)	VM22-161	-27.43	1.47	0.7141	<63 µm
Franzese et al. (2006)	VM22-166	-20.63	-1.95	0.7272	<63 µm
Franzese et al. (2006)	VM24-203	-36.98	59.98	0.7059	<63 µm
Franzese et al. (2006)	VM24-204	-37	60	0.70703	<63 µm
Franzese et al. (2006)	VM24-216	-37.32	21.57	0.71903	<63 µm
Franzese et al. (2006)	VM24-231	-33.95	-13.83	0.7088	<63 µm
Franzese et al. (2006)	VM27-201	-34.77	-3.42	0.70734	<63 µm
Franzese et al. (2006)	VM29-105	-48.08	17.68	0.71259	<63 µm
Franzese et al. (2006)	VM29-79	-32.78	40.22	0.72653	<63 µm
Franzese et al. (2006)	VM29-89	-45.73	25.65	0.71199	<63 µm
Franzese et al. (2006)	VM29-90	-43.7	25.73	0.71508	<63 µm
Franzese et al. (2006)	VM29-97	-38.27	17.37	0.71624	<63 µm
Franzese et al. (2006)	VM34-148	-25.68	38.15	0.72761	<63 µm
Franzese et al. (2006)	VM34-153	-39.37	24.5	0.7183	<63 µm
Hahn et al. (2017)	Olifants River	-31.802222	18.4991667	0.727	<120 µm

Hahn et al. (2017)	Orange River	-28.824167	16.5797222	0.73658	<120 µm
Hahn et al. (2017)	Molopo River Mouth	-28.703611	20.4547222	0.76774	<120 µm
Hahn et al. (2017)	Vaal River	-29.113056	23.8577778	0.72371	<120 µm
Hahn et al. (2017)	Orangje River	-29.335833	23.9102778	0.7169	<120 µm
Hahn et al. (2017)	Orangje River	-29.348889	23.8661111	0.71712	<120 µm
Hahn et al. (2017)	Vaal - Orange Confluence	-29.143611	23.6919444	0.71348	<120 µm
Hahn et al. (2017)	Molopo River Catchment	-28.65	28.65	0.73005	<120 µm
Hahn et al. (2017)	Drakensberge	-28.75	21.2	0.71707	<120 µm
Garzanti et al. (2014)	3931	-17.4083333	14.2166667	0.7495	Bulk
Garzanti et al. (2014)	4299	-18.1138888	21.5888889	0.7318	<32µm
Garzanti et al. (2014)	4300	-18.7638888	22.1916667	0.7244	<32µm
Garzanti et al. (2014)	3939	-19.2638888	13.8888889	0.7297	Bulk
Garzanti et al. (2014)	4301	-19.3638888	22.2416667	0.7196	<32µm
Garzanti et al. (2014)	4305	-19.8625	23.3291667	0.7225	<32µm
Garzanti et al. (2014)	4303	-20.1833333	22.4694444	0.7283	<32µm
Garzanti et al. (2014)	4307	-20.2625	23.8555556	0.7245	<32µm
Garzanti et al. (2014)	4278	-20.3972222	28.9916667	0.7258	Bulk
Garzanti et al. (2014)	4276	-20.9472222	28.9944444	0.73	<32µm
Garzanti et al. (2014)	4272	-22.1361111	29.9305556	0.7279	<32µm
Garzanti et al. (2014)	4268	-23.6847222	29.6	0.7364	<32µm
Garzanti et al. (2014)	4266	-24.2611111	29.8055556	0.7299	<32µm
Garzanti et al. (2014)	4267	-24.2666666	29.6222222	0.795	<32µm
Garzanti et al. (2014)	4264	-25.2222222	28.3027778	0.7442	<32µm
Garzanti et al. (2014)	4296	-17.4555555	25.0055556	0.7288	<32µm
Garzanti et al. (2014)	4297	-17.4861111	24.3166667	0.7194	<32µm
Garzanti et al. (2014)	4295	-17.5361111	25.1847222	0.7337	<32µm
Garzanti et al. (2014)	4298	-17.7916666	23.3444444	0.7166	<32µm
Garzanti et al. (2014)	4293	-17.8241666	25.7411111	0.7074	<32µm
Garzanti et al. (2014)	4289	-17.9208333	25.8472222	0.7109	<32µm
Garzanti et al. (2014)	4286	-18.0763888	26.6763889	0.7107	<32µm
Garzanti et al. (2014)	4286	-18.0763888	26.6763889	0.7119	<32µm
Garzanti et al. (2014)	4287	-18.0791666	26.5791667	0.7062	<32µm
Garzanti et al. (2014)	4283	-18.1555555	27.0222222	0.7383	<32µm
Garzanti et al. (2014)	4282	-18.6138888	27.1861111	0.7194	<32µm
Garzanti et al. (2014)	3938	-18.7333333	12.9444444	0.7292	Bulk
Garzanti et al. (2014)	4279	-19.7055555	28.4041667	0.716	<32µm
Garzanti et al. (2014)	4355	-20.1888888	13.2	0.7137	<32µm
Garzanti et al. (2014)	4362	-20.2361111	14.0416667	0.7126	<32µm
Garzanti et al. (2014)	4352	-20.4722222	13.3222222	0.7206	<32µm
Garzanti et al. (2014)	4350	-20.9055555	13.4611111	0.7269	<32µm
Garzanti et al. (2014)	4363	-21.1166666	16.8333333	0.7312	<32µm

Garzanti et al. (2014)	4348	-21.1638888	13.6666667	0.723	<32µm
Garzanti et al. (2014)	4309	-22.0055555	21.5416667	0.7235	<32µm
Garzanti et al. (2014)	4344	-22.0861111	14.2666667	0.7225	<32µm
Garzanti et al. (2014)	4271	-22.2277777	29.9916667	0.7136	<32µm
Garzanti et al. (2014)	4313	-22.3527777	18.2333333	0.7323	<32µm
Garzanti et al. (2014)	4312	-22.4291666	18.95	0.7313	<32µm
Garzanti et al. (2014)	4341	-22.6888888	14.5305556	0.7283	<32µm
Hahn et al. (2015)	GeoB8331-4_4.5cm	-29.08	16.42	0.72219	<32µm
Hahn et al. (2015)	GeoB8323-2_3cm	-32.02	18.22	0.719375	<32µm
Hahn et al. (2017)	ORF10	-31.8022222	18.4991667	0.727	<120 µm
Hahn et al. (2017)	ORF24	-28.8241666	16.5797222	0.73658	<120 µm
Hahn et al. (2017)	ORF30	-28.7036111	20.4547222	0.76774	<120 µm
Hahn et al. (2017)	ORF34	-29.1130555	23.8577778	0.72371	<120 µm
Hahn et al. (2017)	ORF36	-29.3358333	23.9102778	0.7169	<120 µm
Hahn et al. (2017)	ORF38	-29.3488888	23.8661111	0.71712	<120 µm
Hahn et al. (2017)	ORF39	-29.1436111	23.6919444	0.71348	<120 µm
Hahn et al. (2017)	GTC-24	-28.65	28.65	0.73005	<120 µm
Hahn et al. (2017)	GTC-9	-28.75	21.2	0.71707	<120 µm